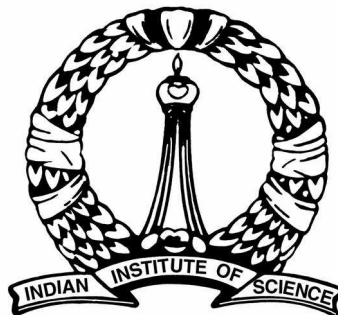


Spiral-wave Dynamics in Ionically Realistic Mathematical Models for Human Ventricular Tissue

A thesis submitted for the degree of
Doctor of Philosophy
in the Faculty of Science

Alok Ranjan Nayak



Department of Physics
Indian Institute of Science
Bangalore - 560012
India

April 2013

Declaration

The work reported in this thesis is original and was carried out by me during my tenure as a PhD student at the Department of Physics, Indian Institute of Science, Bangalore. This thesis has not formed the basis for the award of any degree, diploma, associateship, membership or similar title of any university or institution.

(Alok Ranjan Nayak)

April, 2013

Department of Physics,
Indian Institute of Science,
Bangalore - 560012,
India

Acknowledgement

First of all, I would like to express my deep and sincere gratitude to my advisor, Professor Rahul Pandit, for his excellent guidance in both academic and non-academic matters. Frankly speaking, he is also one of the mentors in my life from whom I learnt many things.

I would like to thank Prof. A.V. Panfilov, Gent University, Belgium, and Dr. T.K Shajahan, McGill University, Canada, for joint work; some part of my research work, presented in this thesis, has been done in collaborative work with them (see Chapters 2, 3, and 5). I would also like to thank Rupamanjari Majumder for other joint projects, which I have not covered in this thesis.

I feel privileged to be associated with our excellent condensed-matter theory group. I feel fortunate to have attended courses taught by Prof. Rahul Pandit, Prof. Sriram Ramaswamy, Prof. Prabal K. Maiti, and Prof. Govindan Rangarajan.

I thank all our staff members, especially, Mr. Srinivas, Ms. Meena, Ms. Shantakumari, and Mr. Prabhakar for their help.

I would like to give my sincere thanks to a couple of my friends, Tapan Ch. Adhyapak and Anupam Gupta, who helped me a lot in many ways. I would also like to thank Harsh Soni who helped me a lot. My sincere thanks to Pranab Jyoti Bhuyan, Tapan Mishra, and Bijoy Mallick for their help in similar way.

I would also like to thank all the members of our group: Anupam, Jamshid, Rupamanjari, Debarghya, Vishwanath, Rajany, Akshay, Sabya, Nairita, and Soling. I am thankful to all my seniors and juniors in the condensed-matter physics theory group (Chirag, Prasad, Ganpati, Samridhi, Nandan, Biswaroop, Smarajit, Vijay Narayan, Viajy Kumar, Sumilan, Shradha, Shajahan, Debarshini, Subhro, Pranab, Ganguly, Tapan Adhyapak, Santosh, Harsh, Saroj, Ananyo, Kingshuk, Hemant, Yogeshwar, Suropriya, Jayantha, Ranjan, Debabrata, Tarak, Himanshu, Pramod, Raghav, Aabhaas, and Manjari) for their useful guidance and help.

Some friends and seniors to whom I would like to acknowledge for their help in different ways during my stay at IISc: Alok Singh, Geetanjali, Ketan, Vikram, Pradeep, Pushpander, Rahman, Nitin Kumar, Apurba, Durgesh, Manohar, Rupak, Dipankar, Sakshath, Chanchal, Sayak, Sayantan, Vineeth, Shivaraj, Sivasunder, Vaibhav, Bidya, Amit Roy, Amit Majhi, Arvind, Anbu, Akshaya Shiva, Manisha, Gaurav, Rahul, Nirmalendu, Nitin Chandra, Sandeep, Gauhar, Abhiram, Debakanta, Tapan Mishra, Souren, Hembram, Sanjit, Bhupal, Jayakrishna, Ramakanta, Sudhansu, Sabya, Pratap, Chakrapani, Sankarsan, Benudhar, Anirudha, Shiva, Tapan Hota, Durga, Lalit, Ashutosh, Anil, Anupam, Umasankar, Saurav,

Narendra, Tusar, Ashish, Sudarsan, Amal, Pranjal, Bishwajit, Bhaskar, Padma, Gitish, Gunin, Bhabatosh, Diganta, Debajyoti, Tridev, Dipak, Mohan, Arkajyoti, Debayan, Harikrishna, Gaurav, Shailendra, Nirupam, and Neelesh. I am lucky to have had batchmates like Tapan Adhyapak, Sunil, Biswanath, and Ritupan, who made my stay at IISc enjoyable.

I like to thank the Super Computer Education and Research Center (SERC) for their computing facilities, and the Department of Physics for the same.

Finally, I am grateful to all the agencies who have supported me in all these years: Council for Scientific and Industrial Research (CSIR), India, Microsoft Research, India, and the Robert Bosch Centre for Cyber Physical Systems (IISc) for fellowships during various parts of my PhD; the Asian Technology Information Program (ATIP), for inviting and supporting me to attend a ‘ATIP’s First Workshop on High-Performance Computing in India: Research Challenges on Computing in India’, Supercomputing 2009 (SC09), in Portland, Oregon.

At the end, I would like to express my love, thanks, and gratitude to my family, Bou, Bapa, Badabapa, Nanaa, Mily Dei, Deepak, Badal, Jhua, Bhauja, Ashutosh, and Ayush, for their constant support throughout my life and during my PhD. I would also like to express my happiness to have my *fiancée* Mamata by my side.

Preface

There is a growing consensus that life-threatening cardiac arrhythmias like ventricular tachycardia (VT) or ventricular fibrillation (VF) arise because of the formation of spiral waves of electrical activation in cardiac tissue; unbroken spiral waves are associated with VT and broken ones with VF. Several experimental studies have shown that inhomogeneities in cardiac tissue can have dramatic effects on such spiral waves.

In this thesis we focus on spiral-wave dynamics in mathematical models of human ventricular tissue which contain (a) conduction inhomogeneities, (b) ionic inhomogeneities, (c) fibroblasts, (d) Purkinje fibers. We also study the effect of a periodic deformation of the simulation domain on spiral wave-dynamics. Chapter 2 contains our study of “Spiral-Wave Dynamics and Its Control in the Presence of Inhomogeneities in Two Mathematical Models for Human Cardiac Tissue”; this Chapter follows closely parts of a paper we have published [1]. Chapter 3 contains our study of “Spiral-wave dynamics in a Mathematical Model of Human Ventricular Tissue with Myocytes and Fibroblasts”; this chapter follows closely a paper that we have submitted for publication. Chapter 4 contains our study of “Spiral-wave Dynamics in Ionically Realistic Mathematical Models for Human Ventricular Tissue: The Effects of Periodic Deformation”; this chapter follows closely a paper that we have submitted for publication. Chapter 5 contains our study of “Spiral-wave dynamics in a Mathematical Model of Human Ventricular Tissue with Myocytes and Purkinje fibers”; this chapter follows closely a paper that we will submit for publication soon.

In Chapter 2, we study systematically the AP morphology for the TNNP04 model of cardiac tissue; we also look at the contribution of individual ionic currents to the AP by partially or completely blocking ion channels associated with the ionic currents. We then carry out systematic studies of plane-wave and circular-wave dynamics in the TNNP04 model for cardiac tissue model. We present a detailed and systematic study of spiral-wave turbulence and spatiotemporal chaos in two mathematical models for human cardiac tissue, namely, the TNNP04 model and the TP06 model. In particular, we use extensive numerical simulations to elucidate the interaction of spiral waves in these models with conduction and ionic inhomogeneities. Our central qualitative result is that, in all these models, the dynamics of such spiral waves depends very sensitively on such inhomogeneities. A major goal here is to develop low-amplitude defibrillation schemes for the elimination of

VT and VF, especially in the presence of inhomogeneities that occur commonly in cardiac tissue. Therefore, we study a control scheme that has been suggested for the control of spiral turbulence, via low-amplitude current pulses, in such mathematical models for cardiac tissue; our investigations here are designed to examine the efficacy of such control scheme in the presence of inhomogeneities in biophysical realistic models. We find that a scheme that uses control pulses on a spatially extended mesh is more successful in the elimination of spiral turbulence than other control schemes. We discuss the theoretical and experimental implications of our study that have a direct bearing on defibrillation, the control of life-threatening cardiac arrhythmias such as ventricular fibrillation.

In Chapter 3, we study the role of cardiac fibroblasts in ventricular tissue; we use the TNNP04 model for the myocyte cell, and the fibroblasts are modelled as passive cells. Cardiac fibroblasts, when coupled functionally with myocytes, can modulate their electrophysiological properties at both cellular and tissue levels. Therefore, it is important to study the effects of such fibroblasts when they are coupled with myocytes. Chapter 3 contains our detailed and systematic study of spiral-wave dynamics in the presence of fibroblasts in both homogeneous and inhomogeneous domains of a state-of-the-art mathematical model for human ventricular tissue due to ten-Tusscher, Noble, Noble, and Panfilov (the TNNP04 model). We carry out extensive numerical studies of such modulation of electrophysiological properties in mathematical models for (a) single myocyte-fibroblast (MF) units and (b) two-dimensional (2D) arrays of such units; our models build on earlier ones and allow for zero-, one-, and two-sided MF couplings. Our studies of MF units elucidate the dependence of the action-potential (AP) morphology on parameters such as E_f , the fibroblast resting-membrane potential, the fibroblast conductance G_f , and the MF gap-junctional coupling G_{gap} . Furthermore, we find that our MF composite can show autorhythmic and oscillatory behaviors in addition to an excitable response. Our 2D studies use (a) both homogeneous and inhomogeneous distributions of fibroblasts, (b) various ranges for parameters such as G_{gap} , G_f , and E_f , and (c) intercellular couplings that can be zero-sided, one-sided, and two-sided connections of fibroblasts with myocytes. We show, in particular, that the plane-wave conduction velocity CV decreases as a function of G_{gap} , for zero-sided and one-sided couplings; however, for two-sided coupling, CV decreases initially and then increases as a function of G_{gap} , and, eventually, we observe that conduction failure occurs for low values of G_{gap} . In our homogeneous studies, we find that the rotation speed and stability of a spiral wave can be controlled either by controlling G_{gap} or E_f . Our studies with fibroblast inhomogeneities show that a spiral wave

can get anchored to a local fibroblast inhomogeneity. We also study the efficacy of a low-amplitude control scheme, which has been suggested for the control of spiral-wave turbulence in mathematical models for cardiac tissue, in our MF model both with and without heterogeneities.

In Chapter 4, we carry out a detailed, systematic study of spiral-wave dynamics in the presence of periodic deformation (PD) in two state-of-the-art mathematical models of human ventricular tissue due to (a) ten-Tusscher and Panfilov (the TP06 model) and (b) ten-Tusscher, Noble, Noble, and Panfilov (the TNNP04 model). To the best of our knowledge, our work is the first, systematic study of the dynamics of spiral waves of electrical activation and their transitions, in the presence of PD, in such biophysically realistic mathematical models of cardiac tissue. In our studies, we use three types of initial conditions whose time evolutions lead to the following states in the absence of PD: (a) a single rotating spiral (RS), (b) a spiral-turbulence (ST) state, with a single meandering spiral, and (c) an ST state with multiple broken spirals for both these models. We then show that the imposition of PD in these three cases leads to a rich variety of spatiotemporal patterns in the transmembrane potential including states with (a) an RS state with n -cycle temporal evolution (here n is a positive integer), (b) rotating-spiral states with quasiperiodic (QP) temporal evolution, (c) a state with a single meandering spiral MS, which displays spatiotemporal chaos, (d) an ST state, with multiple broken spirals, and (e) a quiescent state SA in which all spirals are absorbed. For all three initial conditions, precisely which one of the states is obtained depends on the amplitudes and the frequencies of the PD in the x and y directions. We also suggest specific experiments that can test the results of our simulations. We also study, in the presence of PD, the efficacy of a low-amplitude control scheme that has been suggested, hitherto only without PD, for the control of spiral-wave turbulence, via low-amplitude current pulses applied on a square mesh, in mathematical models for cardiac tissue. We also develop line-mesh and rectangular-mesh variants of this control scheme. We find that square- and line-mesh-based, low-amplitude control schemes suppress spiral-wave turbulence in both the TP06 and TNNP04 models in the absence of PD; however, we show that the line-based scheme works with PD only if the PD is applied along one spatial direction. We then demonstrate that a minor modification of our line-based control scheme can suppress spiral-wave turbulence: in particular, we introduce a rectangular-mesh-based control scheme, in which we add a few control lines perpendicular to the parallel lines of the line-based control scheme; this rectangular-mesh scheme is a significant improvement

over the square-mesh scheme because it uses fewer control lines than the one based on a square mesh.

In Chapter 5, we have carried out detailed numerical studies of (a) a single unit of an endocardial cell and Purkinje cell (EP) composite and (b) a two-dimensional bilayer, which contains such EP composites at each site. We have considered biophysically realistic ionic models for human endocardial cells (Ecells) and Purkinje cells (Pcells) to model EP composites. Our study has been designed to elucidate the sensitive dependence, on parameters and initial conditions, of (a) the dynamics of EP composites and (b) the spatiotemporal evolution of spiral waves of electrical activation in EP-bilayer domains. We examine this dependence on myocyte parameters by using the three different parameter sets $\mathcal{P}1$, $\mathcal{P}2$, and $\mathcal{P}3$; to elucidate the initial-condition dependence we vary the time at which we apply the S2 pulse in our S1-S2 protocol; we also investigate the dependence of the spatiotemporal dynamics of our system on the EP coupling D_{gap} , and on the number of Purkinje-ventricular junctions (PVJs), which are measured here by the ratio \mathcal{R} , the ratio of the total number of sites to the number of PVJs in our simulation domain.

Our studies on EP composites show that the frequency of autorhythmic activity of a P cell depends on the diffusive gap-junctional conductance D_{gap} . We perform a set of simulations to understand the source-sink relation between the E and P cells in an EP composite; such a source-sink relation is an important determinant of wave dynamics at the tissue level. Furthermore, we have studied the restitution properties of an isolated E cell and a composite EP unit to uncover this effect on wave dynamics in 2D, bilayers of EP composites.

Autorhythmicity is an important property of Purkinje cell; it helps to carry electrical signals rapidly from *bundle of His* to the endocardium. Our investigation of an EP composite shows that the cycle length (CL) of autorhythmic activity decreases, compared to that of an uncoupled Purkinje cell. Furthermore, we find that the APD increases for an EP composite, compared to that of an uncoupled P cell. In our second set of simulations for an EP-composite unit, we have obtained the AP behaviors and the amount of flux that flows from the E to the P cell during the course of the AP. The direction of flow of this flux is an important quantity that identifies which one of these cells act as a source or a sink in this EP composite. We have found that the P cell in an EP composite acts as a stimulation-current source for the E cell in the depolarization phase of the AP, when the stimulus is applied to both cells or to the P cell only. However, the P cell behaves both as a source and a sink when the stimulus is applied to the E cell only. In our third set of simulations for an EP composite unit, we have calculated the restitution of

the APD; this plays an important role in deciding the stability of spiral waves in mathematical models for cardiac tissue. Our simulation shows that, for the EP composite with high coupling ($D_{gap} = D_{mm}/10$), the APDR slope decreases, relative to its value for an isolated E cell, for parameter sets $\mathcal{P}1$ and $\mathcal{P}2$, and first increases (for $50 \leq DI \leq 100$ ms) and then decreases for the parameter set $\mathcal{P}3$; however, for low coupling ($D_{gap} = D_{mm}/100$), the variation of the APD as function of DI , for an EP composite, shows biphasic behavior for all these three parameter sets. We found that the above dynamics in EP cable type domains, with EP composites, depends sensitively on \mathcal{R} .

We hope our *in silico* studies of spiral-wave dynamics in a variety of state-of-the-art ionic models for ventricular tissue will stimulate more experimental studies that examine such dynamics.

List of Publications

[1] Shajahan TK, **Nayak AR**, Pandit R (2009) Spiral-Wave Turbulence and Its Control in the Presence of Inhomogeneities in Four Mathematical Models of Cardiac Tissue. PLoS ONE 4(3): e4738. doi:10.1371/journal.pone.0004738.

[2] Majumder R, **Nayak AR**, Pandit R (2011) An Overview of Spiral- and Scroll-Wave Dynamics In Mathematical Models for Cardiac Tissue - invited book chapter, in O.N. Tripathi, U. Ravens, and M.C. Sanguinetti (eds.), Heart Rate and Rhythm, DOI 10.1007/978-3-642-17575-6_14, (Springer-Verlag, Berlin, Heidelberg 2011) Chapter 14, pp 269-282.

[3] Majumder R, **Nayak AR**, Pandit R (2011) Scroll-Wave Dynamics in Human Cardiac Tissue: Lessons from a Mathematical Model with Inhomogeneities and Fiber Architecture. PLoS ONE 6(4): e18052. doi:10.1371/journal.pone.0018052.

[4] Majumder R, **Nayak AR**, Pandit R (2012) Nonequilibrium Arrhythmic States and Transitions in a Mathematical Model for Diffuse Fibrosis in Human Cardiac Tissue. PLoS ONE 7(10): e45040. doi:10.1371/journal.pone.0045040.

Submitted for Publication:

[1] **Nayak AR** and Pandit R (2013) Spiral-wave Dynamics in Ionically Realistic Mathematical Models for Human Ventricular Tissue: The Effects of Periodic Deformation, submitted for publication to PLoS ONE journal (under review).

[2] **Nayak AR**, Shajahan TK, Panfilov AV, and Pandit R (2013) Spiral-wave dynamics in a Mathematical Model of Human Ventricular Tissue with Myocytes and Fibroblasts, submitted for publication to PLoS ONE journal (under review) .

Manuscripts in Preparation:

[1] **Nayak AR**, Panfilov AV, and Pandit R (2013) Spiral-wave dynamics in a Mathematical Model of Human Ventricular Tissue with Myocytes and Purkinje fibers, to be submitted shortly.

Contents

1	An Overview of Mathematical Models of Cardiac Tissue and Mechanisms of Ventricular Fibrillation	1
1.1	Introduction	1
1.2	Anatomy, mechanical function, and conduction systems of mammalian hearts	2
1.2.1	Anatomy of the heart	2
1.2.2	Heart conduction system	3
1.2.3	Mechanical function of the heart	4
1.3	Modelling Cardiac Tissue	5
1.4	Mathematical Models of Cardiac Cells	9
1.5	Mathematical Models of Ventricular Cell	10
1.6	Experimental Overview:	15
1.7	Mechanisms of Ventricular Fibrillation	18
1.7.1	Critical mass hypothesis	18
1.7.2	Multiple wavelet hypothesis	18
1.7.3	Focal source hypothesis	19
1.7.4	Restitution hypothesis	20
1.8	A summary of the problems studied in this Thesis	20
2	Spiral-Wave Dynamics and Its Control in the Presence of Inhomogeneities in Two Mathematical Models for Human Cardiac Tissue	34
2.1	Introduction	34
2.2	Model and Methods	38
2.2.1	Model	38
2.2.2	Methods	39
2.2.3	Computational Benchmark	40
2.3	Results	41

2.3.1	Single-cell studies	41
2.3.2	Plane-wave propagation	48
2.3.3	Circular-wave propagation	51
2.3.4	Spiral-wave dynamics	54
2.3.5	Elimination of spiral turbulence	69
2.4	Discussion and Conclusion	74
1	Supporting Information	79
3	Spiral-wave dynamics in a Mathematical Model of Human Ventricular Tissue with Myocytes and Fibroblasts	87
3.1	Introduction	87
3.2	Model and Methods	93
3.3	Results	96
3.3.1	A Myocyte-Fibroblast (MF) Composite	97
3.3.2	Wave dynamics in a 2D simulation domain with MF composites	110
3.3.3	Control of spiral-wave turbulence in the presence of MF-composite inhomogeneities	130
3.4	Discussion and Conclusion	134
1	Supporting Information	139
4	Spiral-wave Dynamics in Ionically Realistic Mathematical Models for Human Ventricular Tissue: The Effects of Periodic Deformation	150
4.1	Introduction	150
4.2	Methods	154
4.3	Results	156
4.3.1	Plane-wave Dynamics in a Cable	157
4.3.2	Spiral-wave Dynamics in a Homogeneous Domain	161
4.3.3	Spiral Waves with PD	166
4.3.4	Control of Spiral waves	178
4.4	Discussion and Conclusion	183
1	Supporting Information	188
1	Supplementary Material S1	199
5	Spiral-wave dynamics in a Mathematical Model of Human Ventricular Tissue with Myocytes and Purkinje fibres	236

5.1	Introduction	236
5.2	Methods	241
5.3	Results	243
5.3.1	An EP composite	244
5.3.2	Wave dynamics in a 2D simulation domain	248
5.3.3	Controlling Spiral Waves in the EP-bilayer Domain	266
5.4	Discussion and Conclusion	269
1	Supporting Information	274
1	Supplementary Material S1	284
A		309
Appendix A		309
A.1	The TNNP04 Model	309
A.2	The TP06 Model	318
A.3	The Purkinje Model	327

Chapter 1

An Overview of Mathematical Models of Cardiac Tissue and Mechanisms of Ventricular Fibrillation

1.1 Introduction

Cardiac arrhythmias, like ventricular tachycardia (VT) and ventricular fibrillation (VF) [1, 2], are a leading cause of sudden cardiac death in industrialized countries. Estimates indicate that (a) more than one million people die per year because of such arrhythmias and (b) VF is the main reason for death in 30% of the cases in which heart failure occurs [3, 4]. Despite decades of research, the underlying mechanisms of cardiac arrhythmias, such as VT and VF, are still not clearly understood. However, the general consensus is that the abnormal propagation of a wave of electrical activation across the ventricles might be the principal reason for such arrhythmias. Both experimental [5–8] and computational [8, 9] studies have suggested spiral or scroll waves of electrical activation in cardiac tissue or mathematical models thereof are associated with VT, whereas, when these waves break to yield spiral- or scroll-wave turbulence, VT develops into life-threatening VF. In the absence of medical intervention, VF makes the heart incapable of pumping blood, so a patient dies roughly two-and-a-half minutes after the initiation of VF. Thus, studies of spiral- and scroll-wave dynamics in cardiac tissue pose important challenges for *in vivo* and *in vitro* experimental studies and for *in silico*, numerical studies of mathematical models for cardiac tissue. This thesis is devoted to several such *in silico* studies. Before we give a summary of the numerical studies we carry out of spiral-wave dynamics in a variety of state-of-the-art mathematical models for cardiac tissue, we provide an overview of waves of excitation in cardiac tissue and mathematical models for such tissue.

The properties of mammalian hearts and cardiac tissue, such as shape, size, physiology, and coupling between cells, vary from species to species; there is some

variation even within a particular species. These variations leads to challenges for experimental studies that try to elucidate the mechanisms behind cardiac arrhythmias. Thus, computational studies of mathematical models for cardiac tissue play an important, complementary role in investigations of the dynamics of spiral and scroll waves, which are the mathematical analogues of arrhythmias. Computational studies are well-suited for detailed investigations of the effects of heterogeneities and special conduction systems, such as Purkinje fibers, on spiral-wave dynamics; heterogeneities can arise in cardiac tissue because of scar tissues, blood vessels, connective tissue, or nonmyocyte cells (e.g., fibroblasts). In subsequent Chapters, we study various mathematical models that allow for such heterogeneities and Purkinje fibers.

The remaining part of this Chapter is organized as follows: In Sec. 1.2, we give a short overview of the anatomy of a human heart, its electrical conduction system, and its mechanical function. In Sec. 4.2, we illustrate how to develop mathematical model for cardiac tissue. In Sec. 1.4, we present a summary of models for various types of cardiac cells. In Sec. 1.5, we list a number of ventricular models that have been developed so far; and we discuss the most commonly used ones. In Sec. 1.6, we present the experimental background that is required for our studies of wave dynamics in cardiac tissue. In Sec. 1.7, we give an overview of the hypotheses for the underlying causes for VF to motivate investigations of wave dynamics in experimental and computational studies. Section 1.8 contains a synopsis of the studies we carry out in subsequent Chapters.

1.2 Anatomy, mechanical function, and conduction systems of mammalian hearts

1.2.1 Anatomy of the heart

A human heart is a muscular organ, whose weight is between 200 to 425 grams [10–12], and it varies with the age and sex of a person. The size of a human heart is roughly the size of a clenched fist [12]; the hearts of smaller (larger) mammals, e.g., rabbits (elephants) are considerable smaller (larger) [13]. The heart is located in between the lungs and is enclosed by a double-layered membrane called the pericardium [12]. The heart has four chambers: the upper two are atria and lower two are the ventricles; the important parts of a human heart are shown by a schematic diagram in Fig. 1.1(a). The left and right atria, and the left and right ventricles, are separated by a wall of muscle called the septum. Each chamber of

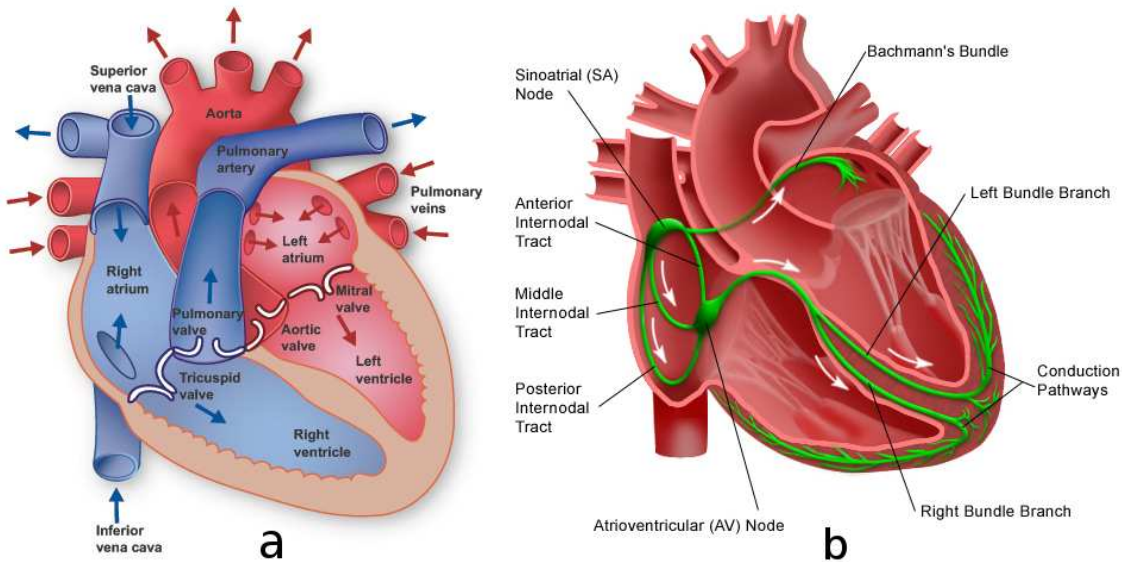


Figure 1.1: Schematic diagrams showing (a) the heart anatomy and (b) its conduction systems. Images taken from: <http://www.texasheartinstitute.org/HIC/Anatomy/anatomy2.cfm>, <http://mdmedicine.wordpress.com/2011/04/24/heart-conduction-system/>.

the heart is composed mainly of a special muscle called the myocardium; the inner, middle, and outer layers are called the endocardium, the mid-myocardium, and the epicardium, respectively. The left atrium, right atrium, left ventricle, and right ventricle wall thicknesses are typically, 3, 2, 8 – 15, and 3 – 5 mm [14, 15]; the left-ventricle wall is thicker than those of the other chambers of the heart and, because of that, it can generate sufficient mechanical force to pump the blood into various parts of the body. A healthy human heart in normal physiological conditions, beats periodically, on an average, 72 times per minute. This generates the necessary mechanical force to pump blood out of the heart. Each heart beat is generated by a wave of electrical stimulation, which spreads across the heart.

1.2.2 Heart conduction system

The electrical excitation waves, which arise from single-cell action potentials (APs), originate from the natural pacemaker of the heart, namely, the sino-atrial node (SAN), which lies at the top of the right atrium. The SAN has capable to fire trains of APs automatically, between 72 to 100 times per minute [16], at regular intervals, in a normal, healthy, human heart. There are other types of cardiac cells, which have potential to fire APs rhythmically. In particular, the atrio-ventricular node (AVN) and Purkinje fibers are well known for their autorhythmic activities; the AVN can fire 40 – 60 pulses per minute and Purkinje fibers 10 – 20 pulses per

minute [16,17]. However, in a healthy, working heart, they normally do not exhibit their autorhythmic activities, because of the higher firing rate of the SAN dominates the autorhythmic activities of both the SAN and Purkinje fibers. The excitations generated at the SAN travels to Brachman's Bundle (Fig. 1.1b) and the internodal tracts, which are, roughly speaking, the electrical conducting wires of the right and left atria, respectively. The excitation reaches at the AVN with a delay time 0.2 s via the the three internodal tracts (Fig. 1.1(b)); then the waves travel to the lower part of the heart conduction system, namely, the Purkinje fibers through the Bundle branch. Such Purkinje fibers form a network-type structure, which spreads over the interior of the ventricular heart walls and helps to excite the entire left and right ventricular muscles . The time required to activate the whole network of the heart-conduction system is roughly 0.8 s.

1.2.3 Mechanical function of the heart

The electrical activities of the heart are coupled with its mechanical activities [18], i.e., the electrical excitations generate the mechanical force that is required to pump blood from the left ventricle to the whole body. Heart tissue has muscle fibers, whose orientation leads to anisotropy in the tissue; this anisotropy helps to generate the force required to push blood from the heart to the organs of the body. The mechanical activities of the heart start from the two upper chambers, atria, followed by the two lower chambers, ventricles. Note that the contraction and expansion phases occur in a coherent way in the upper chambers followed by those in the lower chambers; the loss of such coherent process leads to dysfunction of the heart.

The contraction of the right atrium helps to push blood to the right ventricle through the tricuspid valve; the opening of the mitral valve allows the flow of blood from the left atrium to the left ventricle. De-oxygenated blood comes from various parts of the body; it is received by the right atrium via the superior and inferior vena cavae (see Fig 1.1(a)); it flows into the right ventricle, because of the contraction of the right atrium. When the right ventricle contracts, the pulmonary valve opens and allows the de-oxygenated blood to flow from the right ventricle to the lungs via the pulmonary artery; the de-oxygenated blood is mixed with oxygen and returns to the left atrium; when the right atrium contracts, the blood enters to the left ventricle; this whole process, called a cardiac cycle, takes approximately 0.8 sec.

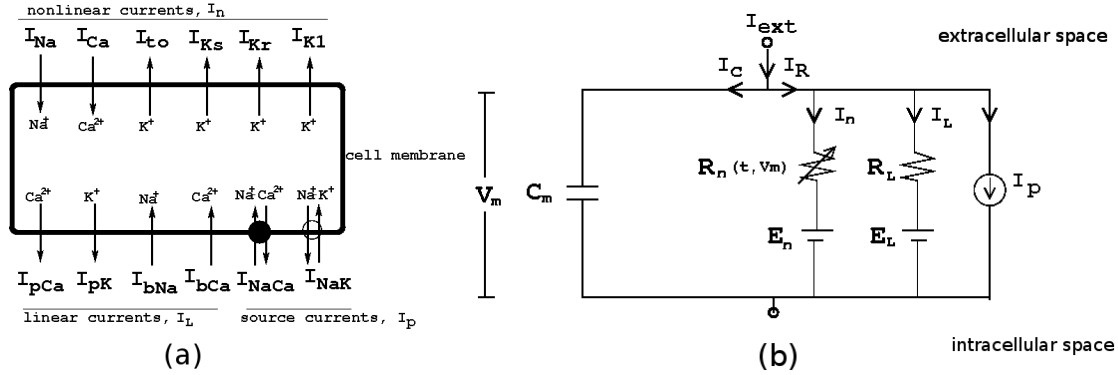


Figure 1.2: (a) A schematic diagram describing the ion movement through voltage-gated ion channels; it has 6 components of nonlinear current, 4 components of linear current and 2 source currents [41], (b) an equivalent electrical circuit.

1.3 Modelling Cardiac Tissue

The membrane of a cardiac cell can be thought of in terms of an equivalent electrical circuit [19–21] in which the cell membrane behaves like a capacitor because of the charge accumulation across it. The potential across the membrane, because of the gradient of an ionic concentration, is called the Nernst potential for that ionic species. These Nernst potentials are represented by batteries; and the ion-selective channels by resistors, which are connected in parallel with the capacitor. Figure. 1.2 shows schematic diagrams of a cardiac cell and its RC-circuit analog. If we inject an external current I_{ext} into the extra-cellular space of the cell, then *Kirchhoff's current law* yields

$$I_{ext} = I_C + I_R, \quad (1.1)$$

where I_C and I_R are, respectively, the currents shown in Fig. 1.2(b). Equation (1.1) can be rewritten as

$$C_m \frac{dV_m}{dt} = - \sum_k I_k + I_{ext}, \quad (1.2)$$

where C_m is the cell capacitance per unit surface area, the transmembrane potential V_m is the voltage difference between intra- and extra-cellular space, and $\sum_k I_k$ is the sum of all ionic currents that cross the cell membrane. Thus, a single cardiac cell with realistic physiological variables can be modelled by using the following set of equations [22]:

$$C_m \frac{\partial V_m}{\partial t} = - \sum_k I_k; \quad (1.3)$$

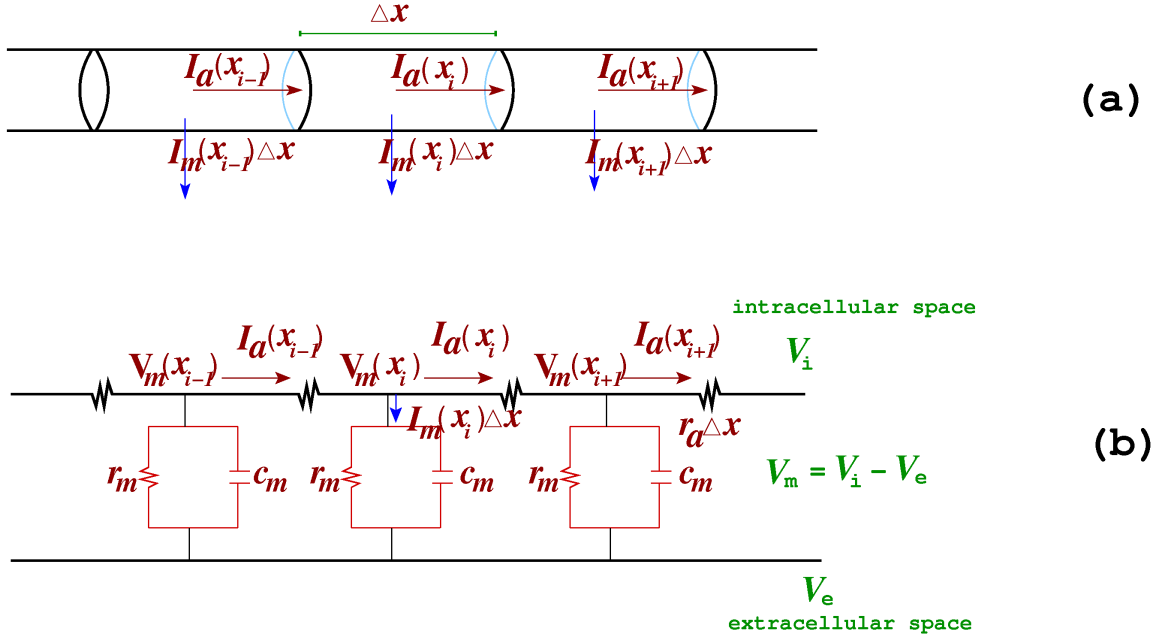


Figure 1.3: (a) A schematic diagram shows the flow of axial and transmembrane currents in a cable; the cable is discretized to small pieces with length Δx . (b) The equivalent electrical circuit of the cable; the transmembrane of each piece of cable is represented by an RC circuit and they are connected to each other parallelly by axial resistance $r_a\Delta x$. Here I_a is the axial current, I_m is the membrane current per unit length, r_a is the axial resistance per unit length, r_m is the membrane resistance per unit length, and c_m is the membrane capacitance per unit length.

The current density I_k depends on V_m in a complicated manner; this can be represented by following equation:

$$I_k = G_k x_s^1 x_s^2 \dots x_s^n (V_m - V_k); \quad (1.4)$$

here, x_k^i , for $1 \leq i \leq n$, is the gating variable of a particular ion channel of species k ; such variables control the ionic dynamics across the cell membrane. G_k is the conductance associated with a particular ion channel, for the k^{th} ion species, V_k is the equilibrium potential of the ion species k . The gating variables evolve according to the following ordinary differential equations

$$\frac{dx_k}{dt} = \frac{x_{k\infty}(V_m) - x_k}{\tau_k(V_m)} \quad (1.5)$$

where $x_{k\infty}$ is the steady-state value of a single gating variable x_k (i.e. its value for $dx/dt = 0$), and τ_k is a time constant describing the return of x to its steady-state value x_∞ following a voltage perturbation. The voltage dependence of both x_∞ and

τ_x can be determined from experimental data.

$$\frac{d[k]}{dt} = \sum_i I_k^i(V_m, k) \quad (1.6)$$

here $[k]$ represents the concentration of ion species k .

The set of equations in 1.3, 1.4, 1.5, and 1.3 can explain the electrophysiological properties, at the cellular level, such as cardiac AP, AP morphology, and action potential restitution.

Cardiac cells are coupled via *gap junctions* [20, 21, 23], which are networks of protein channels that allows the passage of ions, hormones, and neurotransmitters, from cell to cell. The propagation of biological signals, such as, electrical excitation, from cell to cell can be modelled by a continuum model that is called the *cable equation*, derived by Lord Kelvin in 1855 in the context of the flow of electricity in a leaky cable [24]. Cardiac cells are roughly cylindrical, with length $\simeq 100 \mu\text{m}$ and radius $\simeq 10 - 30 \mu\text{m}$ [20, 21], so a strand of such cells can be approximated as a cylindrical cable (Fig. 1.3(a)); here, the membrane of a subcylindrical part of a cable, with length Δx , corresponds to a parallel RC circuit (see Eq. 1.2). The total current through this membrane patch of each piece of cable is $I_m(x_i)\Delta x$, where $I_m(x_i)$ is the membrane current per unit length. Note that the membrane current varies with distance x down the cylinder, therefore, if we multiply $I_m(x_i)$ by Δx we obtain the total current that passes across the membrane. Similarly, by multiplying Δx with the membrane capacitance per unit length, c_m , and the axial resistance per unit length, r_a , we get the total capacitance and the axial resistance of the subcylindrical part of the cable. If we now assume ohmic resistance, the axial current $I_a(x_i)$ is

$$V_m(x_i) - V_m(x_{i+1}) = I_a(x_i)r_a\Delta x. \quad (1.7)$$

Current conservation law now yields

$$I_a(x_i) - I_a(x_{i-1}) = -I_m(x_i)\Delta x. \quad (1.8)$$

If we take the limit, $\Delta x \rightarrow 0$, Eqs. 1.7 and 1.8 become

$$\lim_{\Delta x \rightarrow 0} \frac{V_m(x_{i+1}) - V_m(x_i)}{\Delta x} = -I_a(x_i)r_a, \quad (1.9)$$

or

$$\frac{\partial V_m}{\partial x} = -I_a r_a, \quad (1.10)$$

and

$$\lim_{\Delta x \rightarrow 0} \frac{I_a(x_i) - I_a(x_{i-1})}{\Delta x} = -I_m(x_i), \quad (1.11)$$

or

$$\frac{\partial I_a}{\partial x} = -I_m. \quad (1.12)$$

By combining Eqs. 1.10 and 1.12 we get

$$\frac{1}{r_a} \frac{\partial^2 V_m}{\partial^2 x} = I_m. \quad (1.13)$$

According to Eq. 1.2, the total transmembrane current is the sum of the capacitive and resistive currents, i.e.,

$$I_m = c_m \frac{\partial V_m}{\partial t} + i_{ion} \quad (1.14)$$

If we combine Eqs. 1.13 and 1.14,

$$\frac{1}{r_a} \frac{\partial^2 V_m}{\partial^2 x} = c_m \frac{dV_m}{dt} + i_{ion}, \quad (1.15)$$

where r_a , i_{ion} , and c_m are the axial resistance, membrane ionic current, and the capacitance per unit length of the fiber. Experiments yield R_a , I_{ion} , and C_m , which are the specific axial resistance ($k\Omega - cm$), the membrane current density ($\mu A/cm^2$), and the capacitance density ($\mu F/cm^2$). The relation between the normalized and the measured variables are given below:

$$\begin{aligned} r_a &= \frac{R_a}{\pi a^2}, \\ c_m &= 2\pi a C_m, \\ i_{ion} &= 2\pi a I_{ion}, \end{aligned} \quad (1.16)$$

where a is the fiber radius.

From Eqs. 1.15 and 1.16, we obtain the following cable equation

$$\frac{1}{R_a(2\pi a/\pi a^2)C_m} \frac{\partial^2 V_m}{\partial^2 x} = \frac{\partial V_m}{\partial t} + I_{ion} \quad (1.17)$$

or

$$\frac{\partial V_m}{\partial t} = D \frac{\partial^2 V_m}{\partial^2 x} - \frac{I_{ion}}{C_m} \quad (1.18)$$

where, D is a diffusion coefficient in the above equation that is of the Reaction-Diffusion type. In principle, D should be a tensor rather than a scalar, so

$$\frac{dV}{dt} = \nabla \cdot D \nabla V - \frac{I_{ion}}{C_m}. \quad (1.19)$$

Equation 1.19 is derived by assuming that the extracellular space is more conducting than the intra cellular space, therefore, the contribution of the extracellular potential (V_e) to the transmembrane potential ($V_m = V_i - V_e$) is effectively zero. The model described above is based on a single domain, in which we neglect the contribution of the extra-cellular space; thus, Eq. 1.19 is called a *monodomain* model.

In fact, the cardiac cell is not a single domain. When we take into account the contribution of the extra-cellular space (i.e., V_e is no more negligible), we have to use a *bidomain model*; which was first proposed by Schimtt, *et al.* [25] and the mathematical formulation for this model was developed by several groups [26–28]. More discussions about this model can be found in Ref. [29]. The model is based on the following set of two partial-differential-equations:

$$\begin{aligned} \frac{\partial V_m}{\partial t} &= -\frac{I_{ion}}{C_m} + \frac{1}{A_m C_m} [\nabla \cdot (\sigma_i \nabla V_m) + \nabla \cdot (\sigma_e \nabla V_e)], \\ \nabla \cdot [(\sigma_i + \sigma_e) \nabla V_e] &= -\nabla \cdot (\sigma_i \nabla V_m), \end{aligned} \quad (1.20)$$

where V_m is the transmembrane potential, V_e is the extracellular potential, A_m is the surface to volume ratio, C_m is the membrane capacitance per unit area, σ_i is the intracellular conductivity tensor, and σ_e is the extracellular conductivity tensor. We will not use bidomain models in this thesis; a recent study in Ref. [30] have shown that there are no significant qualitative differences between bidomain and monodomain models.

1.4 Mathematical Models of Cardiac Cells

A cardiac cell, called a myocyte, is excitable [20,21] in the sense that sub-threshold perturbations decay, whereas, super-threshold ones lead to an action potential (AP). Once excited, the medium cannot be reexcited for a certain period of time known as the *refractory period* [20,21]. A typical AP, generated from a mathematical model of a myocyte cell is shown in Fig. 5.2. The specific model that we have used here is the TNNP04 and the TP06 models that is derived completely in the next Section and the Appendix. Similar models have been developed for Purkinje, atria, sino-atrial node (SAN), and atrio-ventricular node cells [35]; among these cells, the SAN, the AVN, and the Purkinje cells are autorhythmic, whereas, the atrial and ventricular cells are excitable. Apart from these cells, there are other type of non-myocyte cells that can be found in mammalian hearts. Fibroblasts are among such cells; these cells play an important role in cardiac remodelling after

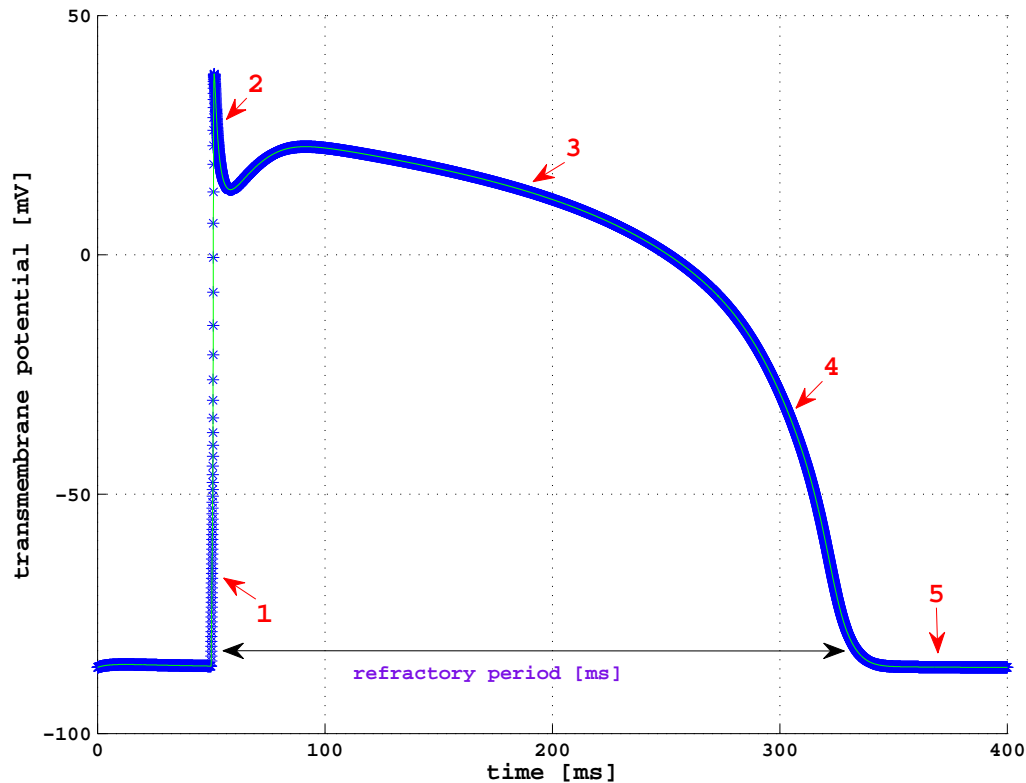


Figure 1.4: An example of a cardiac action potential generated by using the TNNP04 model (see Appendix) for a human ventricular cell: (1) The action potential upstroke or rapid depolarization, (2) rapid repolarization, (3) the plateau stage, (4) the final stage of repolarization, and (5) the resting state.

injuries or a myocardial infarction [31, 32]; they also contribute to generating mechanical force in heart. Such nonexcitable cells can be modelled by passive RC circuits [33, 34]. A list of models for various parts of the heart conduction system can be found in Ref. [35].

1.5 Mathematical Models of Ventricular Cell

In Sec. 4.2 we have derived a set of mathematical equations that can be used to develop mathematical models for cardiac cells; these set of Eqs. 1.3, 1.4, 1.5, and 1.3 describe the dynamics of electrophysiological properties at cellular and tissue levels. A large number of ventricular-cell models have been developed to study the dynamics at cellular, tissue, and organ levels. There are also many complex ventricular models with details of ion-channel kinematics and ionic-concentration dynamics; these have been developed for both human and other mammalian species

to understand the role of ion-channel-blocking drugs on electrophysiological properties, and thereby, their effects on fibrillation, whose mathematical analogs are spiral and scroll waves in mathematical models. We give a brief overview of such ionic models, starting from simple, two-variable models to complex physiologically realistic ionic models for ventricular cells.

The first attempt was made, about three-and-half decades ago, by Beeler and Reuter [36] (the BR model). They constructed an ionic model for a ventricular cell by fitting the ionic-current data, available at that time from voltage-clamp measurements; their ionic-current formulation for the model was based on Hodgkin-Huxley-type equations. The model consists of 4 ionic currents, namely, the inward sodium current, I_{Na} , the slow, inward current, I_s , carried by calcium ions, the time-independent, outward current due to potassium, I_{K1} , and voltage- and time-dependent currents due to potassium, I_{X1} . It uses 8 variables: (a) 1 for the transmembrane potential V_m , (b) 6 for the ion-channel gates, namely, m , h , j , d , f , and x_1 , and (c) 1 for Ca^{2+} ion concentration dynamics. The BR model is the first ionic model, which was used to reproduce an action potential (AP), computationally, for a ventricular cell.

A realistic ionic model for a ventricular cell has been developed by Luo and Rudy [37] (the LR-I model) in 1991 for a guinea pig. This model is an improvement over the BR model because it includes more ionic currents and uses intracellular calcium dynamics. The model includes 6 components of ionic current: (a) the fast sodium current I_{Na} , (b) the slow inward current I_{si} , (c) the time-dependent potassium current I_K , (d) the time-independent potassium current I_{K1} , (e) the plateau-potassium current I_{pK} , and (f) the background current I_b ; it uses 8 variables: (a) one for V_m , (b) 6 for ion-channel gates, namely, m , h , j , d , f , and x_1 , and (c) one for intracellular calcium dynamics.

An improved version of the LR-I model was developed by Luo and Rudy in their second phase calculation in 1994 [38]; this model includes an ion exchanger, an ion pump, and detailed dynamics of intracellular calcium ions; it is generally referred to as the Luo-Rudy phase 2 model (the LR-II model). This model consists of 13 components of ionic current: (a) the fast sodium current I_{Na} , (b) the three components of current through L-type Ca^{2+} channel, namely, I_{Ca} due to Ca^{2+} , I_{CaK} due to K^+ , and I_{CaNa} due to Na^+ , (c) the time-dependent K^+ current I_K , (d) the time-independent K^+ current I_{K1} , (e) the $Na^+ - Ca^{2+}$ exchanger current I_{NaCa} , (f) the $Na^+ - K^+$ pump current I_{NaK} , (g) the plateau K^+ current I_{pK} , (h) the sarcolemmal Ca^{2+} pump current I_{pCa} , (i) the nonspecific Ca^{2+} -activated current I_{nsCa} which has two components, namely, I_{nsK} and I_{nsNa} , (j) the Na^+ background current I_{bNa} ,

(k) the Ca^{2+} background current I_{bCa} . In the LRI model there are 3 components of currents, which are purely voltage dependent and time independent, I_{K1} , I_{pK} , and I_b ; but, in the LRII model, there are 6 components of purely voltage-dependent and time-independent currents, I_{K1} , I_{pK} , I_{bNa} , I_{bCa} , I_{NaK} , and I_{pCa} . It uses 11 variables: (a) 1 for V_m , (b) 6 for ion-channel gates, namely, m , h , j , d , f , and x_1 , and (c) 3 for Ca^{2+} ion concentration dynamics, namely, Ca_i , Ca_{JSR} , and Ca_{NSR} . The model includes various compartments, which can regulate the intracellular Ca^{2+} dynamics; these are the sarcoplasmic reticulum (SR), which is further divided into two sub-compartments, namely, the network SR (NSR) and the junctional SR (JSR), and the myoplasm compartment.

The first mathematical model for a human ventricular cell was published in 2002 by Priebe and Beuckelmann (the PB model) [39]. The PB model is a second-generation model, like the LRII model, which contains five major ionic currents based on human-myocyte experimental data; and the remaining currents are adopted from LR-II model by scaling such a way to fit human cell data. The model consists of 10 components of ionic current (a) the fast sodium current I_{Na} , (b) the L-type Ca^{2+} current channel I_{Ca} , (c) the transient outward K^+ current I_{to} , (d) the delayed rectifier K^+ current, I_K , which has two components, namely, the fast delayed rectifier I_{Kr} and the slow delayed rectifier I_{Ks} , (e) the inward rectifier K^+ current I_{K1} , (f) the $Na^+ - Ca^{2+}$ exchanger current I_{NaCa} , (g) the $Na^+ - K^+$ pump current I_{NaK} , (h) the background current which has two components, namely, the Na^+ background current I_{bNa} and the Ca^{2+} background current I_{bCa} ; the model does not have plateau currents. It uses 13 variables: (a) 1 for V_m , (b) 9 for ion-channel gates, namely, m , h , j , d , f , r , t , X_s and X_r , and (c) 3 for Ca^{2+} ion-concentration dynamics, namely, Ca_i , Ca_{JSR} , and Ca_{NSR} .

The reduced version of the original PB model, developed by Bernus-Wilders-Zemlin-Verschelde-Panfilov in 2002 [40] (the redPB), achieved computational efficiency without losing any basic properties (e.g., the AP morphology, the restitution of APD, and the conduction velocity CV). The reformulated PB model reduced 16 variables of the PB model to 6 variables: (a) 1 for V_m and (b) 5 for ion-channel gates, namely, m , v , f , t , and X ; it excluded the dynamics of intracellular concentrations by approximating the variables by suitable constants. The redPB model consists of 9 components of ionic current: (a) the fast sodium current I_{Na} , (b) the L-type Ca^{2+} current channel I_{Ca} , (c) the transient outward K^+ current I_{to} , (d) the delayed rectifier K^+ current I_K , (e) the inward rectifier K^+ current I_{K1} , (f) the $Na^+ - Ca^{2+}$ exchanger current I_{NaCa} , (g) the $Na^+ - K^+$ pump current I_{NaK} , (h) the background current, which has two components, namely, the Na^+ background current I_{bNa} and

the Ca^{2+} background current I_{bCa} . For more details, we refer the reader to Bernus, *et al* [40].

The realistic models we study are the ones introduced recently by ten Tusscher, Noble, Noble, and Panfilov [41] (the TNNP04 model) and the one due to ten Tusscher and Panfilov [42] (the TP06 model). These are based on experimental data obtained from human-ventricular cells. The TNNP04 model allows for variations of intracellular ion concentration, as in other second-generation models, contains 12 ionic currents, 12 gating variables, one ion pump, and an ion exchanger. All major ionic currents are included in the TNNP model, e.g., the fast inward sodium current I_{Na} , the L-type calcium current I_{CaL} , the transient outward potassium current I_{to} , the slow, potassium, delayed, rectifier current I_{Ks} , the rapid, potassium, delayed, rectifier current I_{Kr} , and the inward, rectifier potassium current I_{K1} . These and other currents and the details of the dynamics of calcium ions are given in Section (A.1) of the Appendix A. The TP06 model [42] is an improvement over the TNNP04 model; in particular, it includes more calcium dynamics to make it more realistic than the TNNP04 model. The TP06 model uses 12 ionic currents and 20 variables: The ionic currents I_{Na} , I_{to} , I_{Kr} , I_{K1} , I_{NaCa} , I_{NaK} , I_{pCa} , I_{pK} , I_{bNa} , and I_{bCa} remain the same as they are in the TNNP04 model; only I_{CaL} and I_{Ks} are changed. The TP06 model includes 3 compartments, namely, the cytoplasm (CY), the sarcoplasmic reticulum (SR), and the diadic subspace (SS), to explain the dynamics of the intracellular Ca^{2+} ion concentration; in contrast, the TNNP04 model does not have the SS compartment.

In Table 1.1 we list a number of mathematical models that have been developed for a variety of mammalian ventricular myocytes [36–56] to study the AP morphological behavior for a myocyte and fibrillation in ventricular tissue. The models given in the table can be classified into the following four categories: (a) generic models, (b) first-generation models, (c) second-generation models, and (d) reduced models.

Generic models contain at least two variables, namely, slow and fast variables; the fast variable explains the activation process, whereas, slow variable explains the recovery process for the excitable media including cardiac tissue. There are models that have three variables; these can be included in the category of generic models. The model developed by FitzHugh and Nagumo, *et al.* [44] (FHN model), Panfilov, *et al.* [43] (Panfilov model) are familiar examples of the generic-model class. Example of three-variable models include those of Fenton, *et al.* [45] (FK model). Such generic models are useful for exploring generic features of spiral-wave dynamics in cardiac tissue models.

Model	Year	total ionic currents	total variables	ion dynamics	species	model type
BR	1977	4	8	absent	–	general
LRI	1991	6	9	absent	pig	first generation
Panfilov	1993	–	3	absent	–	general
LRII	1994	–	–	present	pig	second generation
FK	1998	–	3	absent	–	general
PB	1998	10	16	present	human	second generation
PCGD	2001	–	–	–	rat	–
redPB	2002	9	6	absent	human	reduced
MSKON	2003	–	–	–	pig	–
BSBKR	2004	–	–	present	mouse	–
HR	2004	29	–	present	canine	second generation
SWPWB	2004	–	–	–	rabbit	–
IMW	2004	–	–	present	human	second generation
TNNP	2004	12	17	present	human	second generation
redTNNP	2006	12	9	absent	human	reduced
TP06	2006	12	19	present	human	second generation
OCF	2008	–	3	absent	human	3 variable
MS	2008	–	–	–	rabbit	–
GPB	2010	–	–	absent	human	3 variable
HVVR	2011	–	–	present	human	second generation

Table 1.1: List of mathematical models for ventricular myocytes. BR: Beeler-Reuter [36]; LRI: Luo-Rudy phase 1 [37]; LRII: Luo-Rudy phase 2 [38]; FK: Fenton-Karma [45]; PB: Priebe-Beuckelmann [39]; PCGD: Pandit-Clark-Giles-Demir [46]; redPB: Bernus-Wilders-Zemlin-Verschelde-Panfilov [40]; MSKON: Matsuoka-Sarai-Kuratomi-Ono-Noma [47]; BSBKR: Bondarenko-Szigeti-Bett-Kim-Rasmusson [48]; HR: Hund-Rudy [49]; SWPWB: Shannon-Wang-Puglisi-Weber-Bers [50]; IMW: Iyer-Mazhari-Winslow [51]; TNNP: ten Tusscher-Noble-Noble-Panfilov [41]; redTNNP: ten Tusscher-Panfilov [52]; TP06: ten Tusscher-Panfilov [42]; MS: Mahajan-Shiferaw-Sato *et al.* [54]; OCF: Orovio-Cherry-Fenton [53]; GPB: Grandi-Pasqualini-Bers [55]; and HVVR: Hara-Virag-Varro-Rudy [56];

The first-generation of ventricular models [36, 37] were developed to study the AP morphology, such as, the maximum rate of depolarization, the repolarization, the APD, the resting membrane potential, etc, based on animal cardiac tissue experiments. Ion pumps, exchangers, and intracellular ion dynamics were not included in first-generation models, but there were then considered in the second-generation of the ventricular-cell models [38–41, 51] to make them more realistic.

The second-generation models account for detailed intracellular sodium, calcium, and potassium ion concentrations dynamics, with more calcium subspace, ion pumps, ion exchangers, and more state variables for ionic currents than first-

generation models. Therefore, the models that belong to this second category are *biophysically more realistic* than first-generation model. The aim of developing such complex models is to study the restitution properties and electrical, and calcium-ion alterations, and their roles in spiral break up. The LRII [38], PB [39], IMW [51], TNNP [41], and TP06 [42] are familiar examples of second-generation model. These models are computationally expensive, especially, if we want to study the details of the spiral- and scroll-wave dynamics. As we will show in subsequent Chapters, we must work with high-performance computing clusters and use parallel programming to study such models numerically.

Reduced models are the reduced versions of second-generation models; these are obtained by normalizing intracellular ion concentrations to constant values and eliminating those variables which do not have significant effects on the action potential (AP) and its morphology. These reduced models aim at improving computational efficiency without losing any basic tissue properties such as the AP, AP morphology, the restitution of action potential duration, and the restitution of conduction velocity. However, the models of this class can not be used for the investigation of calcium-related dynamics. The models developed by Bernus *et al.* [40] (the redPB model), ten Tusscher *et al.* [52] (the redTNNP model), Orovio *et al.* [53] (the OCF model), and Grandi *et al.* [55] (the GPB model) are examples of reduced models.

Mathematical details of several such models will be given in subsequent Chapters. Analogous models have been developed for cardiac fibroblasts and Purkinje-fiber cells, as we will discuss in Chapters 3 and 5, respectively.

1.6 Experimental Overview:

A mammalian heart pumps blood because of rhythmical contraction of the atria and ventricles, which is maintained by the regular electrical activity generated by the SAN. The atria are electrically insulated from the ventricles except, in a region known as atrioventricular node (AVN), a specialized conduction path between the atria and ventricles. The electrical activation generated by the SAN spreads to the atria and then into the ventricles through the bundle of His and Purkinje fibers. Any irregularities of this synchronized process affect the pumping action of the heart and, in extreme cases it ceases to pump blood. This may occur due to a conduction block between the atria and ventricles, irregular activities in the atria (atrial fibrillation AF), irregular activities in ventricles (ventricular tachycardia (VT) and ventricular fibrillation VF), or some other reason. Despite decades

of research, the underlying mechanism of cardiac arrhythmias, such as VF, is still remains unclear. Ventricular fibrillation (VF), the incoherent activities of ventricular fibers, is the most dangerous among all types of arrhythmias, is believed to be associated with multiple wandering waves of electrical activation. However, the recent application of nonlinear dynamics and high-resolution optical mapping techniques [57] have revealed that VF is a self organized phenomena triggered by the reentrant activities of cardiac excitation. Depending on the nature of reentry, it can be of two types; (1) anatomical reentry, if there is a relationship of the reentry pathway to the underlying tissue structure, and (2) functional reentry, with reentrant circuits at random locations and no clearly defined anatomical circuit. Anatomical reentry was studied by G. Mines in 1913 by generating a reentrant excitation in a ring of cardiac muscle obtained from a dog heart [58, 59]; this showed that a stimulation at one point on the ring led to the development of a stable circulating wave in the ring, if the period of excitation wave exceeded the refractory period. Hence the excitation wavelength (λ), which is roughly the product of the *refractory period* (t) and the *conduction velocity* (v), must be shorter than the entire length (l) of the anatomically defined reentrant path for a complete rotation. The reexcitation can be ensured only when there exists a zone called, the excitable gap, which separates the head of the wave from its own tail. In the presence of an excitable gap, a stable circulation wave can be seen for more than one hour in the ring. When λ is longer than l , the wave front collides with its own refractory tail or attempt to move to the region that has not yet recovered; this produces a conduction block. At intermediate values (i.e., $\lambda \sim l$) waves with unstable rotation periods and with complex dynamics can be seen. It has been observed that the change of the propagation velocity (v), within the reentrant circuit, gives a complex relation between the rotation period and the excitable gap. The presence and extent of the excitable gap is important in the termination of the reentrant activity in the circuit. When a local stimulus is applied at the correct position and time, it can capture the tail and head of the reentrant wave and thus terminate the rotating wave in the circuit. This idea of terminating, by local pacing, is a great achievement if the arrhythmias is associated with one-dimensional reentry.

In 1924, a description of reentry phenomena without an anatomical obstacle was given by Garrey [20, 60]. The first direct experiment on such functional reentry was carried out by Allesie in 1973. He used an isolated, left-atrial tissue of a rabbit [61]. In his experiment, the transmembrane-potential recordings showed that the cells at the center of the core were not excited. A possible explanation of this observation was that the depolarization front, which continuously rotate

around the area, makes it refractory to some extent and leaves the area functionally inexcitable.

Excitability is an important property of cardiac tissue; this allows it to support various spiral waves. It can support a single spiral, whose core emits electrical activation or multiple spirals that may annihilate or regenerate by random collision with each other. It has been shown experimentally, a self-sustained single spiral whose core is stationary leads to monomorphic VT, whereas a drifting spiral is the cause of polymorphic tachycardia [6]. Experiments on slices of dog and sheep ventricular epicardial muscle revealed that a drifting spiral occasionally attached to small local inhomogeneity in its path in which the electrocardiographic (ECG) pattern changes from polymorphic to monomorphic by rotating the spiral around the inhomogeneity [5, 6]. Furthermore, it was also observed the drifting spiral core drifted towards border of tissue and self-terminated. It is still unclear whether a single drifting spiral or multiple spirals are responsible for fibrillation. Experimental studies on a rabbit heart, using a high-resolution electronic cameras and voltage-sensitive dyes have shown that a single, rapidly moving three-dimensional spiral (i.e., scroll wave), whose tip trajectory wanders in the medium can produce complex patterns in the ECG; these patterns are indistinguishable from those accompany fibrillation [62]. Similar behaviors have been observed in a sheep heart [63] during ventricular fibrillation. Multiple spirals have been detected at the time of fibrillation in experiments on dog, rabbit, and sheep hearts [7, 64, 65]. These experiments have shown that frequent wave-front collision and wave breaks are dominant features during the early phase of fibrillation; and there is also a high degree of temporal and spatial organization of spiral activations. Recent experiments on human heart which have used a data-mapping technique for the ventricular epicardium have revealed that both the periodic and multiple sources exist in the fibrillation phase [66, 67].

Despite decades of research on VF, the precise mechanisms of fibrillation are not completely clear. The main reason is that the currently available data recording techniques can either record the electrical activation from the surface of the body or the epicardial surface. Therefore, it is not possible to characterize and distinguish clearly the spatiotemporal pattern of cardiac activities during the onset of arrhythmias. These may arise from an abnormal, localized focus or a reentry pathway or a combination of both.

1.7 Mechanisms of Ventricular Fibrillation

As we have mentioned above the mechanisms of VF is still unclear; so it is not possible to develop a concrete theory [68, 69] that can explain the mechanisms of VF. It is for this reason that computational studies of mathematical models for cardiac tissue, of the type that we carry out in the subsequent Chapters of this thesis, play an important in developing and understanding of cardiac arrhythmias. Such *in silico* computational studies complement *in vitro* and *in vivo* studies of cardiac arrhythmias. Before we give an overview of our computational studies, we sketch the four leading hypotheses for mechanisms behind VF. These are the (a) critical-mass, (b) multiple-wavelet, (c) focal-source, and (d) restitution hypotheses.

1.7.1 Critical mass hypothesis

The critical-mass hypothesis was first proposed by Garrey in 1914 [70, 71] and then investigated by various groups [72–74]. According to this hypothesis a critical mass of cardiac tissue is required to sustain fibrillation; this critical mass depends on the *refractory period* of spiral waves in cardiac tissue. Spiral-wave activation is terminated if the size of the tissue is less than the critical size. Recent studies [75, 76] have reevaluated the role of tissue size in fibrillation and, thereby, the critical-mass hypothesis. For example, studies in Qu, *et al.* [75] have evaluated the importance of this hypothesis in fibrillation by focusing on the transient time, the size, and the shape of tissue. And Byrd, *et al.* [76] have investigated the relationship between tissue geometry and atrial fibrillation (AF) for a canine heart.

1.7.2 Multiple wavelet hypothesis

The multiple-wavelet hypothesis was suggested by Moe, almost five decades ago [77, 78]. According this hypothesis, multiple spirals are responsible for fibrillation, which is maintained by the spontaneous creation and annihilation of spiral waves. A direct test of this hypothesis was performed by Allesie *et al.* [79], by recording ECG from fibrillating canine atria simultaneously; the activation pattern from their studies was compatible with the multiple-wavelet hypothesis.

Recent experimental and computational studies [67, 80, 81] have investigated the role of multiple waves in fibrillation. For example, Wu, *et al.* [80] have found the existence of multiple waves on the epicardial surface of a rabbit heart; Nash *et al.* [67] have found the existence of multiple waves during VF on the epicardial surface of a human heart. Among computational studies, Wu, *et al.* [80] have

studied the maintenance of fibrillation because of multiple waves in their three-dimensional (3D) tissue-slab simulation; Keldermann, *et al.* [81] have studied the role of multiple waves in ventricular fibrillation in an anatomically realistic geometry for human ventricles, with an ionic model developed by ten Tusscher *et al.* [41] (the TNNP04 model). For an overview of such computational studies see Ref. [22].

1.7.3 Focal source hypothesis

The focal-source hypothesis suggests that a single, rapidly firing focal source is responsible for the maintenance of VF in cardiac tissue. This focal source appears normally in two ways: (a) because of a group of abnormal cells, which are capable to firing action potentials periodically, or (b) because of a single rotating spiral, known as the mother rotor which has a core that emits electrical waves in the form of spiral arms. Source (a) is widely used in studies of AF [82–85] to understand the mechanisms of AF and, therefore, to control AF by suppressing the focal sites by ablation procedures [86–89]. For example, recent studies by Haïssaguerre, *et al.* [86], have shown that pulmonary veins are an important source of ectopic beats; and these foci are responsible in triggering and maintaining AF; these authors have shown that AF can be removed from the atria by suppressing these foci by using radio-frequency ablation. For other similar studies see Refs. [87, 88]. Experiments on ventricular tissue [80, 90, 91] have also suggested that a rapidly firing focal source from abnormal sites, has the capability to maintain VF.

Fibrillation maintained by a mother rotor, known as the motor-rotor hypothesis [67, 69, 92–94], was first proposed by Lewis [95], and later by Gurvich [96]. The importance of such a rotor in VF is described systematically in the review article by Jalife *et al.* [71]. According this hypothesis single rotating spiral- or scroll-waves of electrical activation are responsible for maintaining fibrillation. Such rotors can be (a) anchored to an anatomic heterogeneity, or (b) can exist without a heterogeneity. Both types of rotors emit electrical wave fronts that spread across the myocardium; these wave fronts may break up, to generate temporally unstable rotors, called daughter rotors, which exist for short durations and do not have any regular, repeating activation sequences, like the mother rotor. A mother rotor attached to an anatomical heterogeneity has been investigated in both experimental [5–8, 97] and computational studies [8, 9, 97]. For example, Davidenko *et al.* [5], have studied spiral waves in thin slices of dog and sheep ventricular epicardial muscle and found the anchoring of a spiral wave around the small arteries or bands of connective tissue; similar studies by Pertsov *et al.* [6], have found that a rotor attached to a small arteries or other heterogeneities; Wu *et al.* [80] have found the existence of a

mother rotor anchored to the papillary muscle of the left ventricle of a rabbit heart; Lim *et al.* [98] have studied the electrical activation of spiral waves in *in culture* monolayer of neonatal rat cardiomyocytes and they have found that a spiral wave can be attached to an anatomical heterogeneity, such as an obstacle. A mother rotor without an anatomic heterogeneity has also been investigated in experiments. For example, Gray, *et al.* [62] have shown the existence of a rapidly moving rotor on the surface of the isolated rabbit heart during VF; Samie, *et al.* [97] have studied Langendorff-perfused guinea-pig hearts and showed that the existence of mother rotor located on the anterior left ventricular wall; Nash *et al.* [67] have found the existence of mother rotor during VF on the epicardial surface of a human heart. Computational studies have also shown that spiral waves can be attached to heterogeneities in mathematical models of cardiac tissue; e.g., Shajahan *et al.* [99], have investigated the spiral-wave dynamics in cardiac-tissue model. For other illustrative computational studies we refer the readers to Refs. [6, 62, 80, 81, 97]. Such experimental and computational studies have suggested that the existence of mother rotors in cardiac tissue and elucidated their important role in fibrillation.

1.7.4 Restitution hypothesis

Recently developed advanced techniques can easily carry out *in cell-culture* experiments in pure homogeneous systems, which do not have any pre-existing disorders. And now computer simulation is a powerful tool for performing numerical experiments on mathematical models for cardiac tissue with realistic models several biophysical details. Such studies reveal that VF is possible in a completely homogeneous systems. Whether VF occurs in such systems can be determined by studying (a) the restitution of the action potential duration (APDR) and (b) the restitution of the conduction velocity (CVR) as explained in Refs. [42, 100–105]. We will use this in Chapter 5.

1.8 A summary of the problems studied in this Thesis

In this thesis we focus on spiral-wave dynamics in mathematical models of human ventricular tissue which contain (a) conduction inhomogeneities, (b) ionic inhomogeneities, (c) fibroblasts, (d) Purkinje fibers. We also study the effect of a periodic deformation of the simulation domain on spiral wave-dynamics. Chapter 2 contains our study of “Spiral-Wave Dynamics and Its Control in the Presence of Inhomogeneities in Two Mathematical Models for Human Cardiac Tissue”; this Chapter follows closely parts of a paper we have published [99]. Chapter 3 contains our

study of “Spiral-wave dynamics in a Mathematical Model of Human Ventricular Tissue with Myocytes and Fibroblasts ”; this chapter follows closely a paper that we have submitted for publication. Chapter 4 contains our study of “Spiral-wave Dynamics in Ionically Realistic Mathematical Models for Human Ventricular Tissue: The Effects of Periodic Deformation”; this chapter follows closely a paper that we have submitted for publication. Chapter 5 contains our study of “Spiral-wave dynamics in a Mathematical Model of Human Ventricular Tissue with Myocytes and Purkinje fibers”; this chapter follows closely a paper that we will submit for publication soon.

In Chapter 2, we study systematically the AP morphology for the TNNP04 model of cardiac tissue; we also look at the contribution of individual ionic currents to the AP by partially or completely blocking ion channels associated with the ionic currents. We then carry out systematic studies of plane-wave and circular-wave dynamics in the TNNP04 model for cardiac tissue model. We present a detailed and systematic study of spiral-wave turbulence and spatiotemporal chaos in two mathematical models for human cardiac tissue, namely, the TNNP04 model and the TP06 model. In particular, we use extensive numerical simulations to elucidate the interaction of spiral waves in these models with conduction and ionic inhomogeneities. Our central qualitative result is that, in all these models, the dynamics of such spiral waves depends very sensitively on such inhomogeneities. A major goal here is to develop low-amplitude defibrillation schemes for the elimination of VT and VF, especially in the presence of inhomogeneities that occur commonly in cardiac tissue. Therefore, we study a control scheme [106, 107] that has been suggested for the control of spiral turbulence, via low-amplitude current pulses, in such mathematical models for cardiac tissue; our investigations here are designed to examine the efficacy of such control scheme in the presence of inhomogeneities in biophysical realistic models. We find that a scheme that uses control pulses on a spatially extended mesh is more successful in the elimination of spiral turbulence than other control schemes. We discuss the theoretical and experimental implications of our study that have a direct bearing on defibrillation, the control of life-threatening cardiac arrhythmias such as ventricular fibrillation.

In Chapter 3, we study the role of cardiac fibroblasts in ventricular tissue; we use the TNNP04 model for the myocyte cell, and the fibroblasts are modelled as passive cells. Cardiac fibroblasts, when coupled functionally with myocytes, can modulate their electrophysiological properties at both cellular and tissue levels. Therefore, it is important to study the effects of such fibroblasts when they are coupled with myocytes. Chapter 3 contains our detailed and systematic study of

spiral-wave dynamics in the presence of fibroblasts in both homogeneous and inhomogeneous domains of a state-of-the-art mathematical model for human ventricular tissue due to ten-Tusscher, Noble, Noble, and Panfilov (the TNNP04 model). We carry out extensive numerical studies of such modulation of electrophysiological properties in mathematical models for (a) single myocyte-fibroblast (MF) units and (b) two-dimensional (2D) arrays of such units; our models build on earlier ones and allow for zero-, one-, and two-sided MF couplings. Our studies of MF units elucidate the dependence of the action-potential (AP) morphology on parameters such as E_f , the fibroblast resting-membrane potential, the fibroblast conductance G_f , and the MF gap-junctional coupling G_{gap} . Furthermore, we find that our MF composite can show autorhythmic and oscillatory behaviors in addition to an excitable response. Our 2D studies use (a) both homogeneous and inhomogeneous distributions of fibroblasts, (b) various ranges for parameters such as G_{gap} , G_f , and E_f , and (c) intercellular couplings that can be zero-sided, one-sided, and two-sided connections of fibroblasts with myocytes. We show, in particular, that the plane-wave conduction velocity CV decreases as a function of G_{gap} , for zero-sided and one-sided couplings; however, for two-sided coupling, CV decreases initially and then increases as a function of G_{gap} , and, eventually, we observe that conduction failure occurs for low values of G_{gap} . In our homogeneous studies, we find that the rotation speed and stability of a spiral wave can be controlled either by controlling G_{gap} or E_f . Our studies with fibroblast inhomogeneities show that a spiral wave can get anchored to a local fibroblast inhomogeneity. We also study the efficacy of a low-amplitude control scheme, which has been suggested for the control of spiral-wave turbulence in mathematical models for cardiac tissue, in our MF model both with and without heterogeneities.

In Chapter 4, we carry out a detailed, systematic study of spiral-wave dynamics in the presence of periodic deformation (PD) in two state-of-the-art mathematical models of human ventricular tissue due to (a) ten-Tusscher and Panfilov (the TP06 model) and (b) ten-Tusscher, Noble, Noble, and Panfilov (the TNNP04 model). To the best of our knowledge, our work is the first, systematic study of the dynamics of spiral waves of electrical activation and their transitions, in the presence of PD, in such biophysically realistic mathematical models of cardiac tissue. In our studies, we use three types of initial conditions whose time evolutions lead to the following states in the absence of PD: (a) a single rotating spiral (RS), (b) a spiral-turbulence (ST) state, with a single meandering spiral, and (c) an ST state with multiple broken spirals for both these models. We then show that the imposition of PD in these three cases leads to a rich variety of spatiotemporal patterns in

the transmembrane potential including states with (a) an RS state with n -cycle temporal evolution (here n is a positive integer), (b) rotating-spiral states with quasiperiodic (QP) temporal evolution, (c) a state with a single meandering spiral MS, which displays spatiotemporal chaos, (d) an ST state, with multiple broken spirals, and (e) a quiescent state SA in which all spirals are absorbed. For all three initial conditions, precisely which one of the states is obtained depends on the amplitudes and the frequencies of the PD in the x and y directions. We also suggest specific experiments that can test the results of our simulations. We also study, in the presence of PD, the efficacy of a low-amplitude control scheme that has been suggested, hitherto only without PD, for the control of spiral-wave turbulence, via low-amplitude current pulses applied on a square mesh, in mathematical models for cardiac tissue. We also develop line-mesh and rectangular-mesh variants of this control scheme. We find that square- and line-mesh-based, low-amplitude control schemes suppress spiral-wave turbulence in both the TP06 and TNNP04 models in the absence of PD; however, we show that the line-based scheme works with PD only if the PD is applied along one spatial direction. We then demonstrate that a minor modification of our line-based control scheme can suppress spiral-wave turbulence: in particular, we introduce a rectangular-mesh-based control scheme, in which we add a few control lines perpendicular to the parallel lines of the line-based control scheme; this rectangular-mesh scheme is a significant improvement over the square-mesh scheme because it uses fewer control lines than the one based on a square mesh.

In Chapter 5, we have carried out detailed numerical studies of (a) a single unit of an endocardial cell and Purkinje cell (EP) composite and (b) a two-dimensional bilayer, which contains such EP composites at each site. We have considered biophysically realistic ionic models for human endocardial cells (Ecells) [42] and Purkinje cells (Pcells) [108] to model EP composites. Our study has been designed to elucidate the sensitive dependence, on parameters and initial conditions, of (a) the dynamics of EP composites and (b) the spatiotemporal evolution of spiral waves of electrical activation in EP-bilayer domains. We examine this dependence on myocyte parameters by using the three different parameter sets $\mathcal{P}1$, $\mathcal{P}2$, and $\mathcal{P}3$; to elucidate the initial-condition dependence we vary the time at which we apply the S2 pulse in our S1-S2 protocol; we also investigate the dependence of the spatiotemporal dynamics of our system on the EP coupling D_{gap} , and on the number of Purkinje-ventricular junctions (PVJs), which are measured here by the ratio \mathcal{R} , the ratio of the total number of sites to the number of PVJs in our simulation domain.

Our studies on EP composites show that the frequency of autorhythmic activity of a P cell depends on the diffusive gap-junctional conductance D_{gap} . We perform a set of simulations to understand the source-sink relation between the E and P cells in an EP composite; such a source-sink relation is an important determinant of wave dynamics at the tissue level. Furthermore, we have studied the restitution properties of an isolated E cell and a composite EP unit to uncover this effect on wave dynamics in 2D, bilayers of EP composites.

Autorhythmicity is an important property of Purkinje cell; it helps to carry electrical signals rapidly from *bundle of His* to the endocardium. Our investigation of an EP composite shows that the cycle length (CL) of autorhythmic activity decreases, compared to that of an uncoupled Purkinje cell. Furthermore, we find that the APD increases for an EP composite, compared to that of an uncoupled P cell. In our second set of simulations for an EP-composite unit, we have obtained the AP behaviors and the amount of flux that flows from the E to the P cell during the course of the AP. The direction of flow of this flux is an important quantity that identifies which one of these cells act as a source or a sink in this EP composite. We have found that the P cell in an EP composite acts as a stimulation-current source for the E cell in the depolarization phase of the AP, when the stimulus is applied to both cells or to the P cell only. However, the P cell behaves both as a source and a sink when the stimulus is applied to the E cell only. In our third set of simulations for an EP composite unit, we have calculated the restitution of the APD; this plays an important role in deciding the stability of spiral waves in mathematical models for cardiac tissue. Our simulation shows that, for the EP composite with high coupling ($D_{gap} = D_{mm}/10$), the APDR slope decreases, relative to its value for an isolated E cell, for parameter sets $\mathcal{P}1$ and $\mathcal{P}2$, and first increases (for $50 \leq DI \leq 100$ ms) and then decreases for the parameter set $\mathcal{P}3$; however, for low coupling ($D_{gap} = D_{mm}/100$), the variation of the APD as function of DI , for an EP composite, shows biphasic behavior for all these three parameter sets. We found that the above dynamics in EP cable type domains, with EP composites, depends sensitively on \mathcal{R} .

We hope our *in silico* studies of spiral-wave dynamics in a variety of state-of-the-art ionic models for ventricular tissue will stimulate more experimental studies that examine such dynamics.

Bibliography

- [1] American Heart Association (2001) *Heart and Stroke*, Statistical update. (AHA, Dallas, 2001).
- [2] Roger VL, Go AS, Lloyd-Jones DM, *et al.* (2011) Heart disease and stroke statistics-2011 update: a report from the American Heart Association. *Circulation* 123(4): e18.
- [3] Zipes DP, Wellens HJ (1998) Sudden cardiac death. *Circulation* 98: 2334.
- [4] Fogoros RN (2011) Ventricular Fibrillation. *Heart disease, Heart health center.*
- [5] Davidenko JM, Pertsov AV, Salomonsz R, *et al.* (1992) Stationary and drifting spiral waves of excitation in isolated cardiac muscle. *Nature* 355: 349.
- [6] Pertsov AM, Davidenko JM, Salomonsz R, *et al.* (1993) Spiral waves of excitation underlie reentrant activity in isolated cardiac muscle. *Circ Res* 72: 631.
- [7] Gray RA, Pertsov AM, Jalife J (1998) Spatial and temporal organization during cardiac fibrillation. *Nature* 392: 75.
- [8] Jalife J, Gray RA, Morley GE, *et al.* (1998) Self organization and the dynamical nature of ventricular fibrillation. *Chaos* 8: 5764.
- [9] Fenton FH, Cherry EM, Hastings HM, *et al.* (2002) Multiple mechanisms of spiral wave breakup in a model of cardiac electrical activity. *Chaos* 12(3): 852.
- [10] Latimer HB (1953) The weight and thickness of the ventricular walls in the human heart. *Anat Rec.* 117(4): 713.
- [11] <http://hypertextbook.com/facts/2006/StephanieGambino.shtml>
- [12] <http://www.texasheartinstitute.org/HIC/Anatomy/anatomy2.cfm>
- [13] Knut Schmidt-Nielsen (1997) *Animal Physiology: Adaptation and environment.* 5th Ed., Cambridge University Press.

- [14] Human anatomy, Human body, Angiology, The Heart. <http://www.theodora.com/anatomy/the-heart.html>
- [15] Anatomy of the Heart. <http://www.rjmatthewsmd.com/Definitions/anatomy-ofthe-heart.htm>
- [16] New Human Physiology. <http://www.zuniv.net/physiology/book/chapter11.html>
- [17] Human Physiology, Wikibook. <http://en.wikibooks.org/wiki/Human-Physiology/The-cardiovascular-system>
- [18] Mittal RK, Rochester DF, and McCallum RW (1988) Electrical and mechanical activity in the human lower esophageal sphincter during diaphragmatic contraction. *J Clin Invest* 81: 1182.
- [19] Hodgkin AL, Huxley AF (1952) A quantitative description of membrane current and its application to conduction and excitation in nerve. *J Physiol* 117: 500.
- [20] Jalife J, Delmar M, Davidenko J, Anumonwo J, Kalifa J (2009) Basic Cardiac Electrophysiology for the Clinician. 2nd Edition, Wiley-Blackwell.
- [21] Zaza A, Rosen M (2000) An Introduction to Cardiac Electrophysiology. Harwood Academic Publishers.
- [22] Clayton R, Panfilov A (2008) A guide to modelling cardiac electrical activity in anatomically detailed ventricles. *Progress in Biophysics and Molecular Biology* 96:19.
- [23] Cardiac muscle, New World Encyclopedia. <http://www.newworldencyclopedia.org/entry/cardiac-muscle>
- [24] Kenner J, Sneyd J (1998) Mathematical Physiology. Springer, New York.
- [25] Schmitt OH (1969) Biological information processing using the concept of interpenetrating domains. In Leibovic KN (ed): "Information Processing in the Nervous System". Springer Verlag, New York.
- [26] Tung L (1978) A Bidomain model for describing Ischemic myocardial D-C potential. PhD thesis, MIT, MA.
- [27] Plonsey R, Barr RC (1984) Current flow patterns in two-dimensional anisotropic bisyncytia with normal and extreme conductivities. *Biophys J* 45: 557.
- [28] Miller WT, Geselowitz DB (1978) Simulation studies of the electrocardiogram I. The normal heart. *Circ Res* 43: 301.

- [29] Henriquez CS (1993) Simulating the electrical behavior of cardiac tissue using the bidomain model. *Crit Rev Biomed Eng* 21: 1.
- [30] Potse M, Dube B, Richer J, Vinet A, Gulrajani RM (2006) A comparison of monodomain and bidomain reaction-diffusion models for action potential propagation in the human heart. *IEEE Trans Biomed Eng* 53: 2425.
- [31] Kohl P, Kamkin AG, Kiseleva IS, Noble D (1994) Mechanosensitive fibroblasts in the sino-atrial node region of rat heart: interaction with cardiomyocytes and possible role. *Exp Physiol* 79: 943.
- [32] Camelliti P, Green CR, LeGrice I, Kohl P (2004) Fibroblast network in rabbit sinoatrial node: structural and functional identification of homogeneous and heterogeneous cell coupling. *Circ Res* 94(6): 828.
- [33] Xie Y, Garfinkel A, Weiss JN, Qu Z (2009) Cardiac alternans induced by fibroblast-myocyte coupling: mechanistic insights from computational models. *Am J Physiol Heart Circ Physiol* 297: H775.
- [34] MacCannell KA, Bazzazi H, Chilton L, et al. (2007) A mathematical model of electrotonic interactions between ventricular myocytes and fibroblasts. *Biophys J* 92: 4121.
- [35] Fenton FH and Cherry EM (2008) Models of cardiac cell. *Scholarpedia* 3(8): 1868.
- [36] Beeler GW and Reuter H (1977) Reconstruction of the action potential of ventricular myocardial fibers. *J Physiol* 268: 177.
- [37] Luo C, Rudy Y (1991) A model of the ventricular cardiac action potential. *Circ Res* 68: 1501.
- [38] Luo C, Rudy Y (1994) A dynamic model of the cardiac ventricular action potential. 1. simulations of ionic currents and concentration changes. *Circ Res* 74: 1071.
- [39] Priebe L and Beuckelmann J (1998) Simulation study of cellular electric properties in heart failure. *Circ Res* 82: 1206.
- [40] Bernus O, Wilders R, Zemlin CW, Versschelde H, Panfilov AV (2002) A computationally efficient electrophysiological model of human ventricular cells. *Am J Physiol Heart Circ Physiol* 282: H2296.
- [41] ten Tusscher KHWJ, Noble D, Noble PJ, and Panfilov AV (2004) A model for human ventricular tissue. *Am J Physiol Heart Circ Physiol* 286: H1573.

- [42] ten Tusscher KHWJ, Panfilov AV (2006) Alternans and spiral breakup in a human ventricular tissue model. *Am J Physiol Heart Circ Physiol* 291: H1088.
- [43] Panfilov AV (1998) Spiral breakup as a model of VF. *Chaos* 8: 57.
- [44] FitzHugh R (1961) Impulses and physiological states in theoretical models of nerve membrane. *Biophys J* 1: 444.
- [45] Fenton F and Karma A (1998) Vortex dynamics in three-dimensional continuous myocardium with fiber rotation: Filament instability and fibrillation. *Chaos* 8: 20.
- [46] Pandit SV, Clark RB, Giles WR, and Demir SS (2001) A mathematical model of action potential heterogeneity in adult rat left ventricular myocytes. *Biophys J* 81: 3029.
- [47] Matsuoka S, Sarai N, and Kuratomi S, *et al.* (2003) Role of individual ionic current systems in ventricular cells hypothesized by a model study. *Jpn J Physiol* 53: 105.
- [48] Bondarenko VE, Szigetzi GP, and Bett GC, *et al.* (2004) Computer model of action potential of mouse ventricular myocytes. *Am J Physiol Heart Circ Physiol* 287: H1378.
- [49] Hund TJ and Rudy Y (2004) Rate dependence and regulation of action potential and calcium transient in a canine cardiac ventricular cell model. *Circulation* 110: 3168.
- [50] Shannon TR, Wang F, and Puglisi J, *et al.* (2004) A mathematical treatment of integrated calcium dynamics within the ventricular myocytes. *Biophys J* 87: 3351.
- [51] Iyer V, Mazhari R, and Winslow RL (2004) A computational model of the human left-ventricular epicardial myocyte. *Biophys J* 87: 1507.
- [52] ten Tusscher KHWJ and Panfilov AV (2006) Cell model for efficient simulation of wave propagation in human ventricular tissue under normal and pathological conditions. *Phys Med Biol* 51: 6141.
- [53] Bueno-Orovio A, Cherry EM, and Fenton FH (2008) Minimal model for human ventricular action potentials in tissue. *J Theor Biol* 253: 544.
- [54] Mahajan A, Shiferaw Y, and Sato D, *et al.* (2008) A rabbit ventricular action potential model replicating cardiac dynamics at rapid heart rates. *Biophys J* 94: 392.

- [55] Grandi E, Pasqualini FS, and Bers DM (2010) A novel computational model of the human ventricular action potential and Ca transient. *J Mol Cell Cardiol* 48: 112.
- [56] O'Hara T, Virag L, Varro A, Rudy Y (2011) Simulation of the undiseased human cardiac ventricular action potential: model formulation and experimental validation. *PLoS Comput Biol* 7(5): e1002061.
- [57] Efimov IR, Nikolski VP, and Salama G (2004) Optical Imaging of the Heart. *Circ Res* 95: 21.
- [58] Mines GR (1913) On dynamic equilibrium in the heart. *J Physiol* 46: 349.
- [59] Mines GR (1914) On circulating excitations in heart muscles and their possible relation to tachycardia and fibrillation. *Trans R Soc Can* IV: 43.
- [60] Garrey WE (1924) Auricular fibrillation. *Physiol Rev* 4: 215.
- [61] Allesie MA, Bonke FIM, and Schopman FJC (1973) Circus movement in rabbit atrial muscle as a mechanism of tachycardia. *Circ Res* 33: 54.
- [62] Gray RA, Jalife J, Panfilov AV, Baxter WT, Cabo C, Davidenko JM, and Pertsov AM (1995) Mechanisms of cardiac fibrillation. *Science* 270: 1222.
- [63] Gray RA and Jalife J (1996) Self-organized drifting spiral waves as a mechanism for ventricular fibrillation. *Circulation* 94: 48.
- [64] Damle RS, Kanaan NM, Robinson NS, Ge YZ, Goldberger JJ, and AH Kadish (1992) Spatial and temporal linking of epicardial activation directions during ventricular fibrillation in dogs. Evidence for underlying organization *Circulation* 86: 1547.
- [65] Witkowski FX, Leon LJ, Penkoske PA, Giles WR, Spano ML, Ditto WL, and Winfree AT (1998) Spatiotemporal evolution of ventricular fibrillation. *Nature* 392: 78.
- [66] Massé S, Downar E, Chauhan V, Sevaptisidis E, and Nanthakumar K (2007) Ventricular fibrillation in myopathic human hearts: mechanistic insights from in vivo global endocardial and epicardial mapping. *Heart Circ Physiol* 292: H2589.
- [67] Nash MP, Mourad A, Clayton RH, Sutton PM, Bradley CP, Hayward M, Paterson DJ, and Taggart P (2006) Evidence for multiple mechanisms in human ventricular fibrillation. *Circulation* 114: 536.

- [68] Janse MJ (2007) Focus, reentry, or “focal” reentry? *Am J Physiol Heart Circ Physiol* 292: H2561.
- [69] Ideker RE and Rogers JM (2006) Human ventricular fibrillation: wandering wavelets, mother rotors, or both ? *Circulation* 114: 530.
- [70] Garrey WE (1914) The nature of fibrillatory contraction of the heart: its relation to tissue mass and form. *Am J Physiol* 33: 397.
- [71] Jalife J (2000) Ventricular fibrillation: mechanisms of initiation and maintenance. *Annu Rev Physiol* 62: 25.
- [72] Zipes DP, Fischer J, King RM, *et al.* (1975) Termination of ventricular fibrillation in dogs by depolarizing a critical amount of myocardium. *Am J Cardiol* 36: 37.
- [73] Kochiadakis GE, Igoumenidis NE, Parthenakis FI, *et al.* (1999) Amiodarone versus propafenone for conversion of chronic atrial fibrillation: results of a randomized, controlled study. *J Am Coll Cardiol* 33: 966.
- [74] Chen MC, Chang JP, Guo GB, Chang HW (2001) Atrial size reduction as a predictor of the success of radiofrequency maze procedure for chronic atrial fibrillation in patients undergoing concomitant valvular surgery. *J Cardiovasc Electrophysiol* 12: 867.
- [75] Qu Z (2006) Critical mass hypothesis revisited: role of dynamical wave stability in spontaneous termination of cardiac fibrillation. *Am J Physiol Heart Circ Physiol* 290: H255.
- [76] Byrd GD, Prasad SM, Ripplinger CM, *et al.* (2005) Importance of geometry and refractory period in sustaining atrial fibrillation: testing the critical mass hypothesis. *Circulation* 112: I-7.
- [77] Moe GK (1962) On the multiple wavelet hypothesis of AF. *Arch Int Pharmacodyn Ther* 140: 183.
- [78] Moe GK, Rheinboldt WC, Abildskov JA (1964) A computer model for atrial fibrillation. *Am Heart J* 67: 200.
- [79] Allesie MA, Lammers WJEP, Bonke FJM, Hollen J (1985) Experimental evaluation of Moe’s multiple wavelet hypothesis of atrial fibrillation. In: *Cardiac Electrophysiology and Arrhythmias*, edited by Zipes DP and Jalife J. Orlando: Grune and Stratton, p. 265-275.

- [80] Wu TJ, Lin SF, Baher A, Qu Z, Garfinkel A, Weiss JN, Ting CT, and Chen PS (2004) Mother Rotors and the Mechanisms of D600-Induced Type 2 Ventricular Fibrillation. *Circulation* 110: 2110.
- [81] Keldermann RH, ten Tusscher KH, Nash MP, *et al.* (2008) A computational study of mother rotor VF in the human ventricles. *Am J Physiol Heart Circ Physiol* 296: H370.
- [82] Scherf D, Morgenbesser L, Nightingale E, Schaeffler K (1950) Further studies on the mechanisms of auricular fibrillation. *Proc Soc Exp Biol Med* 73: 650.
- [83] Scherf D (1974) Studies on auricular tachycardia caused by aconitine administration *Proc Soc Exp Biol Med* 64: 233.
- [84] Jalife J, Berenfeld O, Mansour M (2002) Mother rotors and fibrillatory conduction: a mechanism of atrial fibrillation. *Cardiovasc Res* 54: 204.
- [85] Kapa S, Asirvatham SJ (2009) Atrial fibrillation: focal or reentrant or both?: a new autonomic lens to examine an old riddle. *Circ Arrhythm Electrophysiol* 2: 345.
- [86] Haissaguerre M, Jais P, Shah DC, *et al.* (1998) Spontaneous initiation of atrial fibrillation by ectopic beats originating in the pulmonary veins. *New Engl J Med* 339: 659.
- [87] Jais P, Haissaguerre M, Shah DC, *et al.* (1997) A focal source of atrial fibrillation treated by discrete radiofrequency ablation. *Circulation* 95: 572.
- [88] Niu G, Scherlag B, Lu Z, *et al.* (2009) An acute experimental model demonstrating two different forms of sustained atrial tachyarrhythmias. *Circ Arrhythmia Electrophysiol* 2: 384.
- [89] Narayan SM, Krummen DE, Shivkumar K, *et al.* (2012) Treatment of atrial fibrillation by the ablation of localized sources: CONFIRM (Conventional Ablation for Atrial Fibrillation With or Without Focal Impulse and Rotor Modulation) trial. *J Am Coll Cardiol* 60(7): 628.
- [90] Chen PS, Wu TJ, Ting CT, Karagueuzian HS, Garfinkel A, Lin SF, and Weiss JN (2003) A Tale of Two Fibrillations. *Circulation* 108: 2298.
- [91] Swissa M, Qu Z, Ohara T, *et al.* (2002) Action potential duration restitution and ventricular fibrillation due to rapid focal excitation. *Am J Physiol Heart Circ Physiol* 282: H1915.

- [92] Zaitsev AV, Berenfeld O, Mironov SF, *et al.* (2000) Distribution of excitation frequencies on the epicardial and endocardial surfaces of fibrillating ventricular wall of the sheep heart. *Circ Res* 86: 408.
- [93] Samie FH and Jalife J (2001) Mechanisms underlying ventricular tachycardia and its transition to ventricular fibrillation in the structurally normal heart. *Cardiovascular Research* 50: 242.
- [94] Tabereaux PB, Dossdall DJ, Ideker RE (2009) Mechanisms of VF maintenance: wandering wavelets, mother rotors, or foci. *Heart Rhythm* 6(3): 405.
- [95] Lewis T, *The Mechanism and Graphic Registration of the Heart Beat*. Vol. 3rd ed.. London: Shaw and Sons, Ltd., 1925.
- [96] Gurvich NL, *The Main Principles of Cardiac Defibrillation*. Moscow, Russia: Medicine, 1975.
- [97] Samie FH, Berenfeld O, Anumonwo J, *et al.* (2001) Rectification of the background potassium current: a determinant of rotor dynamics in ventricular fibrillation. *Circ Res* 89: 1216.
- [98] Lim ZY, Maskara B, Aguel F, *et al.* (2006) Spiral wave attachment to millimeter-sized obstacles. *Circulation* 114: 2113.
- [99] Shajahan TK, Nayak AR, Pandit R (2009) Spiral-wave turbulence and its control in the presence of inhomogeneities in four mathematical models of cardiac tissue. *PLoS One* 4(3): e4738.
- [100] Karma A (1994) Electrical alternans and spiral wave breakup in cardiac tissue. *Chaos* 4: 461.
- [101] Koller ML, Riccio MR, and Gilmour RF Jr (1998) Dynamic restitution of action potential duration during electrical alterans and ventricular fibrillation. *Am J Physiol Heart Circ Physiol* 275: H1635.
- [102] Riccio ML, Koller ML, and Gilmour RF Jr (1999) Electrical restitution and spatiotemporal organization during ventricular fibrillation. *Circ Res* 84: 955.
- [103] Banville I and Gray RA (2002) Effect of action potential duration and conduction velocity restitution and their spatial dispersion on alternans and the stability of arrhythmias. *J Cardiovasc Electrophysiol* 13: 1141.
- [104] Wu T, Lin S, Weiss JN, *et al.* (2002) Two types of ventricular fibrillation in isolated rabbit hearts. *Circulation* 106: 1859.

-
- [105] Garfinkel A, Kim YH, Voroshilovsky O, *et al.* (2000) Preventing ventricular fibrillation by flattening cardiac restitution. *PNAS* 97(11): 6061.
- [106] Sinha S, Pande A, Pandit R (2001) Defibrillation via the elimination of spiral turbulence in model for ventricular fibrillation. *Phys Rev Lett* 86: 3678.
- [107] Pandit R, Pande A, Sinha S, Sen A (2002) Spiral turbulence and spatiotemporal chaos: Characterization and control in two excitable media. *Physica A* 306: 211.
- [108] Stewart P, Aslanidi OV, Noble D, *et al.* (2009) Mathematical models of the electrical action potential of Purkinje fibre cells. *Philos Transact A Math Phys Eng Sci* 367: 2225.

Chapter 2

Spiral-Wave Dynamics and Its Control in the Presence of Inhomogeneities in Two Mathematical Models for Human Cardiac Tissue

*This Chapter is based to a large extent on the following paper: Shajahan TK, Nayak AR, Pandit R (2009) Spiral-wave turbulence and its control in the presence of inhomogeneities in four mathematical models of cardiac tissue. PLoS One 4(3): e4738. This paper reports our work on Spiral-wave turbulence and its control in the presence of inhomogeneities in four different models of cardiac tissue, namely, Panfilov [1], Luo-Rudy Phase I (LRI) [2], reduced Priebe-Beuckelmann (rPB) [4], and the TNNP04 [3] models. The calculation on the TNNP04-model part of this paper were carried out by **me** and they are discussed in this Chapter. In addition, I have carried out similar calculations with the TP06 model [5] for human ventricular tissue; this is even more sophisticated than the TNNP04 model. These results for the TP06 model are reported in this thesis for the first time.*

2.1 Introduction

Regular electrical activation waves in cardiac tissue lead to the rhythmic contraction and expansion of the heart, which that ensures blood supply to the whole body. Irregularities in the propagation of these activation waves can result in cardiac arrhythmias, like ventricular tachycardia (VT) and ventricular fibrillation (VF) [6, 7], which are major causes of death in the industrialised world. Despite decades of research, the underlying mechanism of cardiac arrhythmias, such as VT and VF, is still not clearly understood. Experimental studies over the past decade or so have suggested that VT is associated with an unbroken spiral wave of electrical activation on cardiac tissue but VF with broken spiral waves [8–10]. There is growing

consensus [11, 12] that the analogs of VT and VF in mathematical models for cardiac tissue are, respectively, (a) a single rotating spiral wave in two dimensions (2D) or a scroll wave in three dimensions (3D) and (b) spiral-wave or scroll-wave turbulence [13–15]. It is imperative, therefore, to study spiral- and scroll-wave turbulence systematically in such mathematical models.

There are several mathematical models for ventricular tissue have been developed, so far, for both non-human and human species [2, 3, 5, 16–18] (see, Table 1.1 in Chapter 1). However, to the best of our knowledge, none of the studies had investigated systematically spiral wave-dynamics in (a) a homogeneous domain, and (b) a domain with heterogeneities, especially, conduction and ionic-type inhomogeneities in ionically realistic models for cardiac tissue until our study in Ref. [31] on which we base this Chapter.

We study two biophysically realistic mathematical models of human ventricular tissue, namely, the models due to (a) ten-Tusscher, Noble, Noble, and Panfilov (the TNNP04 model) [3] and (b) ten-Tusscher and Panfilov (the TP06 model) [5]; in particular, we look at the interaction of spiral waves with conduction and ionic inhomogeneities. Such heterogeneities arise in cardiac tissue in the form of (1) epicardial coronary arteries, (2) papillary muscles, (3) transmural sites with abrupt fiber-orientation changes, (4) increased fibrosis from cardiomyopathy, (5) a myocardial infarction that leads to ischemia, the subsequent damage or death of the affected cardiac cells, and, in the latter case, the formation of scar tissue that is nonconducting, (7) chronic heart failure, (8) genetic disorders, (9) the presence of major blood vessels, (10) intercalated disc, and (11) non-myocyte cells. Before we present the central results of our numerical calculation, we give a brief overview of some of the important studies that are related to various types of heterogeneities in cardiac tissue; and we discuss their role in VT and VF.

Conduction inhomogeneities in cardiac tissue can affect spiral waves in several ways. Experimental studies [19–21] have found that such inhomogeneities can anchor a spiral wave or, in some cases, can even eliminate it completely [9]. Studies of the dependence of such anchoring on the size of the obstacle [19–21] reveal that the larger the obstacle the more likely is the anchoring; however, even if the obstacle is large, the wave might not attach to it; furthermore, small obstacles can anchor spiral waves, albeit infrequently [21]. Such behaviors have also been seen in numerical simulations of spiral-wave turbulence in models for cardiac tissue: In particular, Xie, *et al.* [22], have studied the dynamics of spiral waves in the LRI model in a two-dimensional (2D) circular domain with a circular hole in the middle: The parameters and initial condition are so chosen that, without the hole,

spiral waves break up in the simulation domain. By shrinking the radius of the hole, the system is changed continuously from a 1D ring to 2D tissue with an obstacle, and, finally, to homogeneous 2D tissue [the hole radius is changed from that of the simulation domain (≈ 9.2 cm) to zero]. When the radius of the hole is very large, the system is effectively a 1D ring; the wave just goes around this ring. As the radius of the hole is decreased, the wave appears as a spiral anchored on the hole but rotating around it periodically, if the hole is large. As the hole radius is decreased, a transition occurs first to a quasiperiodically rotating spiral wave and, eventually, to spiral-wave break up and spatiotemporal chaos [22], with the spirals not attached to the hole.

ten Tusscher *et al.* [23] have studied the Panfilov model with nonexcitable cells distributed randomly in it. In particular, they investigate spiral-wave dynamics as a function of the percentage of the simulation domain covered by such nonexcitable cells and find that, when this percentage is high, spiral-wave break up can be suppressed.

A detailed numerical and analytical study of the interaction of excitation waves with a piecewise linear obstacle has been carried out in Ref. [24]. This study finds that, if the excitability of the medium is high, the wave moves around the obstacle boundary, rejoins itself, and then proceeds as if it had not encountered any obstacles in its path. However, if the excitability is low, the two ends of this wavefront are unable to join, so two free ends survive, curl up, and then develop into two spiral waves, which can in turn break up again. In addition, apart from the excitability of the medium and the local curvature of the wave front, the shape of the obstacle also affects the attachment of spiral waves to it. Shajahan *et al.* [25] have carried out a detailed numerical study of spiral-wave dynamics in the presence of conduction inhomogeneities in the Panfilov and LRI models; they have shown that the dynamics of spiral waves depends very sensitively on the position of a conduction inhomogeneity.

Ionic inhomogeneities, formed say by local modifications of the maximal conductance of calcium ion channels, affect the action potential of a cardiac cell; in particular, the action potential duration (APD) and other time scales, such as the extent of the plateau region and the refractory period [26] are modified by these inhomogeneities and affect spiral-wave dynamics in turn. For example, the stability of a spiral wave, in homogeneous, two-dimensional cardiac tissue depends on the maximal amplitude of the slow inward calcium current (governed by the conductance G_{si}) as illustrated by the numerical study of Qu *et al.* [27] for the LRI model: As they increased G_{si} , they first observed a rigidly rotating spiral wave, then one

in which the spiral tip meandered quasiperiodically, and eventually chaotically; finally they obtained spiral turbulence with broken spiral waves. Furthermore, the numerical studies of Refs. [25,28] have found that ionic heterogeneities can play an important role in the initiation and break up of spiral waves; and Ref. [25] has presented preliminary studies of the Panfilov-model analog of ionic inhomogeneities.

We present a detailed and systematic study of spiral-wave turbulence and spatiotemporal chaos in two mathematical models for human cardiac tissue, namely, the TNNP04 model and the TP06 model. In particular, we use extensive numerical simulations to elucidate the interaction of spiral waves in these models with conduction and ionic inhomogeneities. Our central qualitative result is that, in all these models, the dynamics of such spiral waves depends very sensitively on such inhomogeneities. A major goal here is to develop low-amplitude defibrillation schemes for the elimination of VT and VF, especially in the presence of inhomogeneities that occur commonly in cardiac tissue. Therefore, we study a control scheme [29, 30] that has been suggested for the control of spiral turbulence, via low-amplitude current pulses, in such mathematical models for cardiac tissue; our investigations here are designed to examine the efficacy of such control scheme in the presence of inhomogeneities in biophysical realistic models. We find that a scheme that uses control pulses on a spatially extended mesh is more successful in the elimination of spiral turbulence. We discuss the theoretical and experimental implications of our study that have a direct bearing on defibrillation, the control of life-threatening cardiac arrhythmias such as ventricular fibrillation.

This Chapter is organized as follows: In Sec. 5.2 we present the models and numerical methods that we use in our study. In Sec. 5.3 we present our results on studies of wave dynamics, especially, in the presence of conduction and ionic inhomogeneities; we also give a brief overview of various control schemes that have been proposed to control cardiac chaos in the mathematical models of cardiac tissue; we then describe the low-amplitude control scheme, which we have developed earlier [29, 30], for the elimination of spiral-wave turbulence in models for cardiac tissue and examine its efficacy in our 2D tissue of biophysical realistic models in (a) homogeneous domain and (b) a domain with conduction and ionic inhomogeneities. Section 5.4 contains a discussion of our results and the limitations of our study. The Supporting Information contains a list of animations of our numerical simulations of the TNNP04 and the TP06 models. Analogous studies for the Reduced Priebe Beuckelmann model [4], carried out by T.K. Shajahan, are contained in my joint paper with him and Rahul Pandit in the Supplementary Material S1 of Ref. [31].

2.2 Model and Methods

2.2.1 Model

The cell membrane of a cardiac myocyte is modelled by the following ordinary differential equation (ODE) [32, 33]:

$$C_m \frac{\partial V_m}{\partial t} = -I_{ion} + I_{ext}, \quad (2.1)$$

where C_m is the membrane capacitance density, V_m is the transmembrane potential, i.e., the voltage difference between intra- and extra-cellular spaces, I_{ion} is the sum of all the ionic currents that cross the cell membrane, and I_{ext} is the externally applied current. We use two biophysically realistic ionic models for human cardiac myocytes: (a) the ten Tusscher, Noble, Noble, and Panfilov model (the TNNP04 model) [3], and (b) the ten Tusscher and Panfilov model (the TP06 model) [5]; these have been developed recently. In these models the total ionic current

$$\begin{aligned} I_{ion} = & I_{Na} + I_{CaL} + I_{to} + I_{Ks} + I_{Kr} + I_{K1} \\ & + I_{NaCa} + I_{NaK} + I_{pCa} + I_{pK} + I_{bNa} + I_{bCa}, \end{aligned} \quad (2.2)$$

where I_{Na} is the fast, inward Na^+ current, I_{CaL} the L-type, slow, inward Ca^{2+} current, I_{to} the transient, outward current, I_{Ks} the slow, delayed, rectifier current, I_{Kr} the rapid, delayed, rectifier current, I_{K1} the inward, rectifier K^+ current, I_{NaCa} the Na^+/Ca^{2+} exchanger current, I_{NaK} the Na^+/K^+ pump current, I_{pCa} and I_{pK} the plateau Ca^{2+} and K^+ currents, and I_{bNa} and I_{bCa} the background Na^+ and Ca^{2+} currents, respectively.

Physical units used in the model are as follows: time (t) is in milliseconds, the voltage (V_m) in millivolts, the current densities (I_x) in picoamperes per picofarad, the conductances (G_x) in nanosiemens per picofarad, and the intracellular and extracellular ionic concentrations (X_i , X_o) in millimoles per liter. Area and capacitance are related since the specific capacitance of cardiac tissue is of the order of $1 \mu A/cm^2$. The full sets of equations for these models, including the ordinary differential equations for the ion-channel gating variables and the ion dynamics, are given in the Appendix.

The transmembrane potential V_m of a two-dimensional (2D) sheet of cardiac tissue can be modelled by using the *reaction-diffusion-type* partial-differential equation (PDEs):

$$\frac{\partial V_m}{\partial t} + \frac{I_{ion}}{C_m} = D \nabla^2 V_m; \quad (2.3)$$

here D is the *diffusion coefficient*, which is related to conductivity [3] and responsible for the coupling between different cardiac cells; for an anisotropic medium the diffusion term along x and y directions are different, i.e., $D_x \neq D_y$.

We introduce conduction inhomogeneities, which we also refer to as obstacles, in the simulation domains of the models described above by making the conductivity constant $D = 0$ in the region of the obstacle; in most of our studies we use a square shape obstacle. When we set $D = 0$ we decouple the cells inside the obstacle from those outside it. Furthermore, we use Neumann (i.e., no-flux) boundary conditions on the boundaries of the obstacle; we have checked in representative cases that, even if we do not impose Neumann boundary conditions on the obstacle boundaries, our results are not changed qualitatively.

We insert ionic inhomogeneities into our simulation domains by changing the values of the maximal conductances of Na^+ and Ca^{2+} channels, in the region of the inhomogeneity. In most of our studies we use square, ionic inhomogeneities in two dimensions.

2.2.2 Methods

To integrate the partial-differential-equation (PDE), we use the forward-Euler method in time t , with a time step $\delta t = 0.02$ ms, and a finite-difference method in space, with step size $\delta x = 0.225$ mm for the TNNP04 model and 0.25 mm for the TP06 model, and five-point stencils for the Laplacian.

For these two models that we study, we use Neumann (no-flux) boundary conditions. The parameter sets we use for the model studies are given in the Appendix. For numerical efficiency, these simulations have been carried out on parallel computers with MPI codes that we have developed for all these models.

We use a thin, cable-type simulation domain, with 16×4096 grid points (gpts) to study plane-wave propagation, i.e., a cable of size $L_x = 4$ mm and $L_y = 1024$ mm. We use square simulation domains consisting of $N = 600$ gpts and $N = 1024$ gpts, respectively, for the TNNP04 and TP06 models (i.e., with side $L = 135$ mm and $L = 256$ mm), to study spiral-wave dynamics.

As suggested in Ref. [34], it is useful to test the accuracy of the numerical scheme used by varying both the time and space steps of integration. We illustrate this for the TNNP04 model by measuring the conduction velocity (CV) of a plane wave, which is injected into the medium by stimulating the left boundary of our simulation domain. We find that, with $\delta x = 0.0225$ cm CV, increases by 1.3% as we decrease δt from 0.02 to 0.01 ms; if we use $\delta t = 0.02$ ms and decrease δx from 0.0225 to 0.015 cm,

then CV increases by 3.3%; such changes are comparable to those found in earlier studies [3, 34].

To examine the spatiotemporal evolution of the transmembrane potentials for a homogeneous domain, we obtain the local time series of $V_m(x, y, t)$, from the representative point ($x = 90$ mm, $y = 90$ mm) for the TNNP04 model and ($x = 125$ mm, $y = 125$ mm) for the TP06 model that is shown by an asterisk in all pseudocolor plots of V_m . To obtain the plots of the inter-beat interval ibi , we use this local time series with 2×10^5 data points after removing the initial 0.488×10^5 data points; for the power spectra $E(\omega)$, we use the local time series of V_m with 2×10^5 data points, after the initial 0.488×10^5 data points have been removed to eliminate transients. Furthermore, we show animations of pseudocolor plots of transmembrane potentials as videos, which have 10 frames per second and in which each pseudocolor plot is separated from its predecessor by 8 ms.

2.2.3 Computational Benchmark

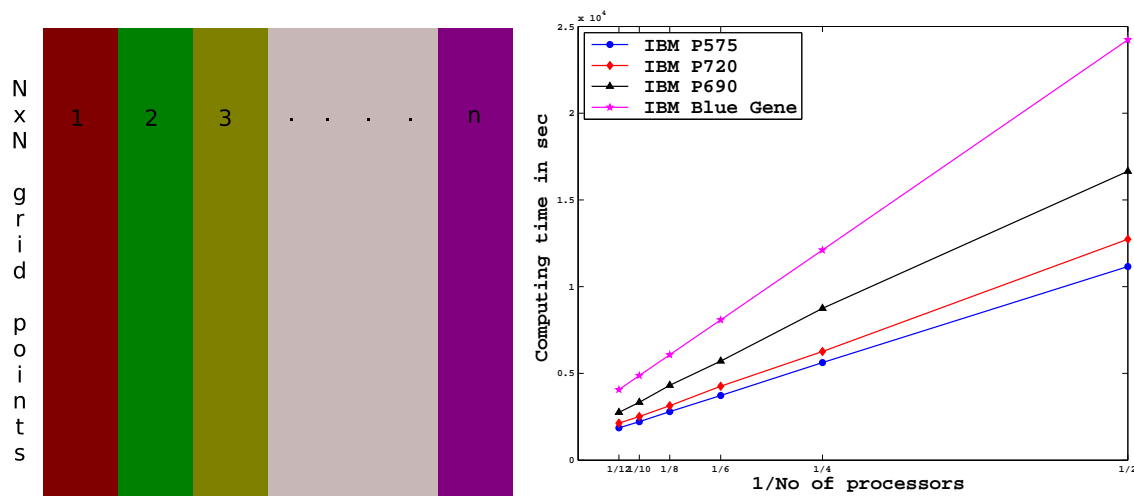


Figure 2.1: (a) Schematic diagram of our MPI simulation, here n represents to the number of processor; (b) A plot of computing time versus the inverse of the number of processors for our MPI code for the TNNP04 model (600×600 domain).

For numerical efficiency, the simulations have been carried out on parallel computers with an MPI code that we have developed for both the TNNP04 and the TP06 models. The MPI code divides the whole simulation domain n columns, i.e., each processor carries out the computations for $N \times (N/n)$ grid points (see Fig. 2.1(a)). To compute the Laplacian at the interface of processor boundaries we use two extra temporal grid lines which can send and receive the data from left

and right neighbour processor. The Neumann boundary condition is taken care of by adding an extra layer of grid points on the boundaries of the simulation domain of each processor.

We have tested our MPI code on various high-performance computing (HPC) platforms. These are (a) the SGI Altix 350 with Intel Itanium processors operating at 1.5 GHz, (b) the IBM Regatta P690 with IBM POWER-4 processors operating at 1.3 GHz, (c) the IBM Cluster P720 with IBM Power-5 processors operating at 1.65 GHz, (d) the IBM P575 with IBM Power-5 processors operating at 1.9 GHz, and (e) the IBM Blue Gene/L with IBM PowerPC processors operating at 700 MHz [35]. To check the performances of various HPC cluster, we use 4,000 iteration steps with 600×600 grid points in our simulation domain and 8 processors. Our computational results show that the times taken by each processor of the P690, P720, P575 clusters are 3369.71, 3183.16 and 2805.50 seconds, respectively. We have also studied the performances of the clusters in the following three ways: (1) by changing the number of processors and keeping all other simulation parameters fixed; (2) by changing the system size and keeping all other simulation parameters fixed; (3) by changing the number of iteration steps and keeping all other simulation parameters fixed. In the first case, we have used a 600×600 simulation domain, 4,000 iteration steps and used 4, 6, 8, and 10 processors for P575 and P720 clusters. The time required for the processors to finish the jobs are 4892.47, 3613.95, 2805.50, 2235.31 seconds, respectively, for the P575 processor and 6313.06, 4277.31, 3183.16, 2531.92 seconds, respectively for the P720 processor. Hence the computation time decreases roughly linearly as we increase the number of processors. The other two cases also show a similar linear dependence of computing time on the parameter that is being varied (see Fig. 2.1(b)). In all these cases we noticed that processors of the P565 cluster take less time for the computation than the P720 and P690 clusters. The studies reported here were carried out several years ago. [Our more recent studies, which are reported in subsequent Chapters, have been carried out on cluster computers with more advanced processors.]

2.3 Results

2.3.1 Single-cell studies

Cardiac tissue is excitable in the sense that sub-threshold perturbations decay, whereas super-threshold ones lead to an action potential AP. Therefore, to get an AP, the membrane potential V_m of a cardiac cell must be above its threshold po-

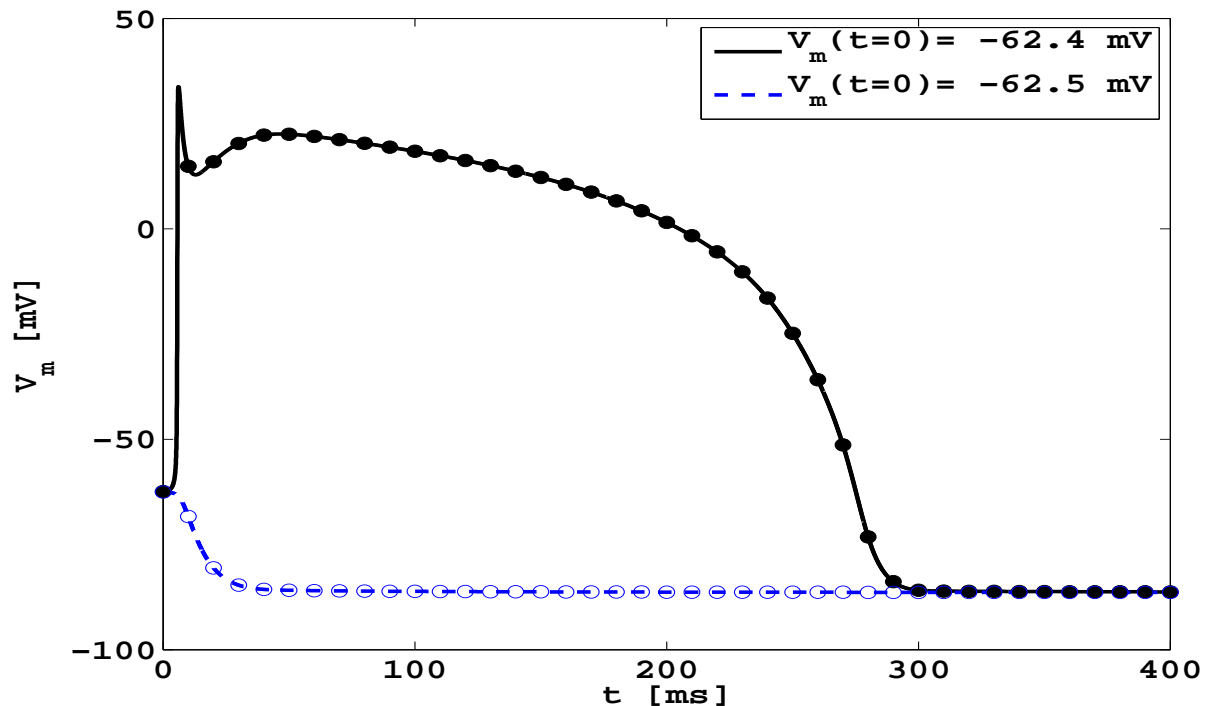


Figure 2.2: The threshold of a cardiac cell can be measured by elevating the resting membrane potential; we find $V_{threshold}$ for the TNNP04 model is -62.4 mV.

tential $V_{threshold}$. We measure $V_{threshold}$ by elevating V_m slowly so that the cell can generate an AP automatically. Our numerical results show that $V_{threshold}$ for the TNNP04 model is $\simeq -62.4$ mV as shown in Fig. 2.2. Note that, here, $V_m \leq -52.4$ mV leads to an unsuccessful attempt to generate an AP.

An injection of external current (see Eq. 2.1 on Sec. 5.1) can produce an AP. To generate an AP we apply a current stimulus of density $I_{stim} = 52$ pA/pF for the time 1 ms as shown in Fig. 5.2. In Figs. 2.4(a), (b), (c), (d), (e), and (f) we show, respectively, major ionic currents, namely, the fast-inward sodium current I_{Na} , the L-type calcium current I_{CaL} , the transient outward current I_{to} , the slow delayed rectifier current I_{Ks} , the rapid delayed rectifier current I_{Kr} , and the inward rectifier current I_{K1} that associated to the AP in Fig. 5.2; similarly, in Figs. 2.4(g), (h), (i), (j), (k), and (l), we show the minor currents, namely, I_{NaCa} the Na^+/Ca^{2+} exchanger current, I_{NaK} the Na^+/K^+ pump current, I_{pCa} and I_{pK} the plateau Ca^{2+} and K^+ currents, and I_{bNa} and I_{bCa} the background Na^+ and Ca^{2+} currents, respectively. Comparing the scales of these ionic-current plots, we conclude that the sodium current I_{Na} is the dominant one in the early phase of the AP (Fig. 5.2(a)), i.e., AP depolarization phase, that is responsible for the AP upstroke. By contrast, the calcium current I_{CaL} is significant in the plateau regime of the AP (Fig. 5.2(b)). In

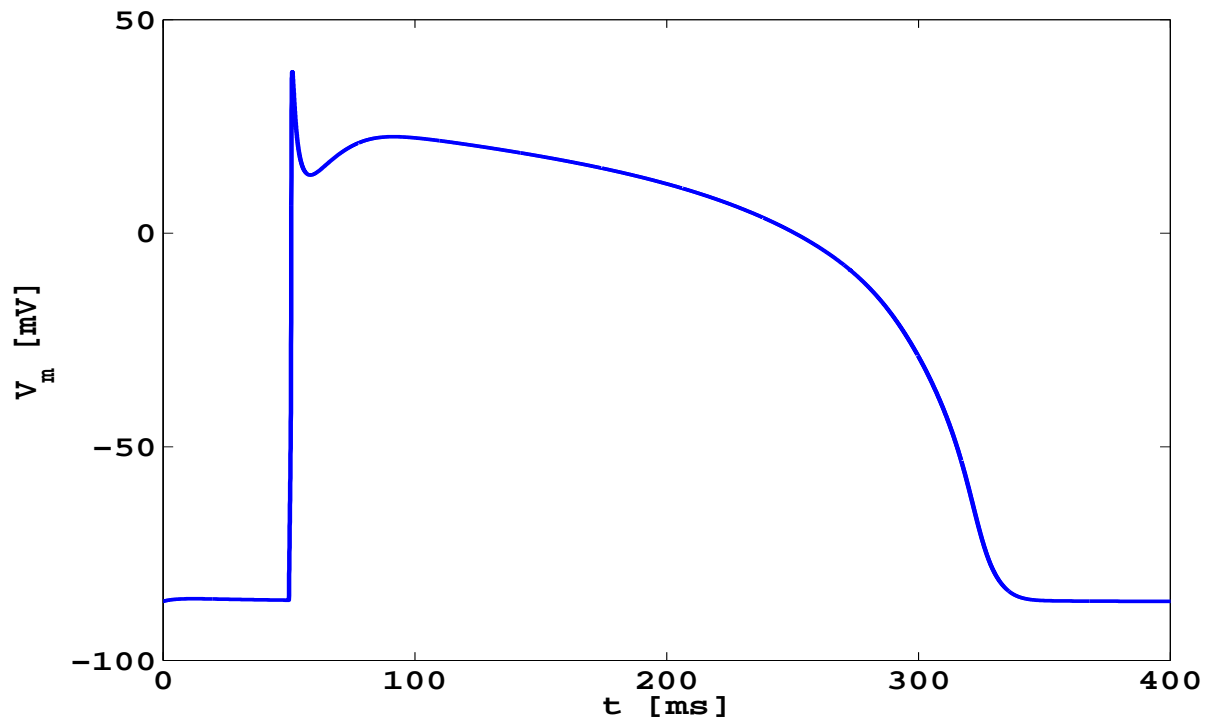


Figure 2.3: An AP generated by stimulating a cell of the TNNP04 model by a current density stimulus of strength 52 pA/pF for 1 ms.

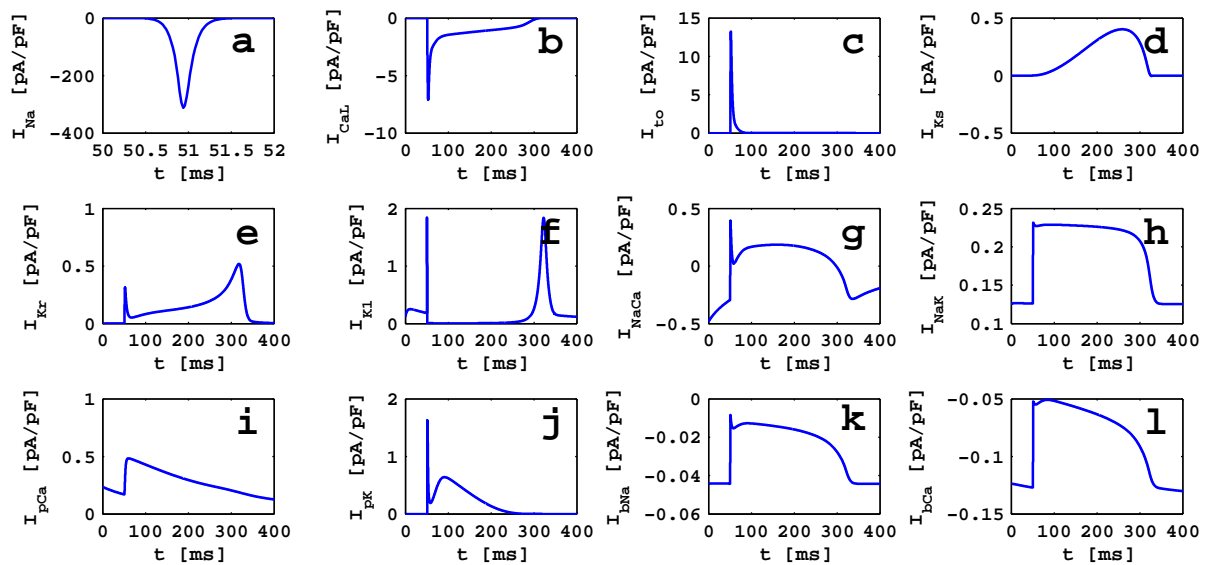


Figure 2.4: Major and minor currents associated with the AP during the course of the action potential (Fig. 5.2) for the TNNP04 model. Negative currents move into the cell and positive currents move out of the cell.

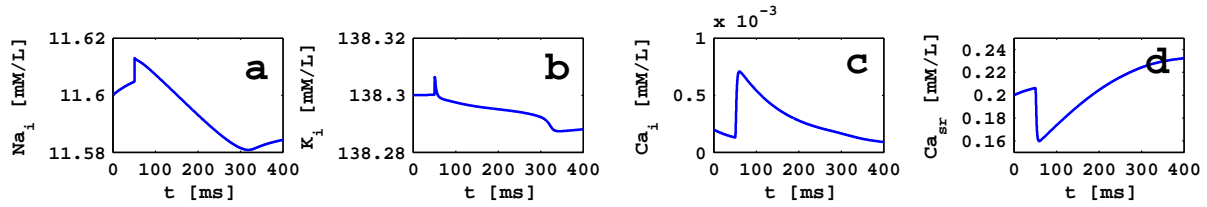


Figure 2.5: Initial ionic concentrations associated with AP during the course of the action potential (Fig. 5.2) for the TNNP04 model.

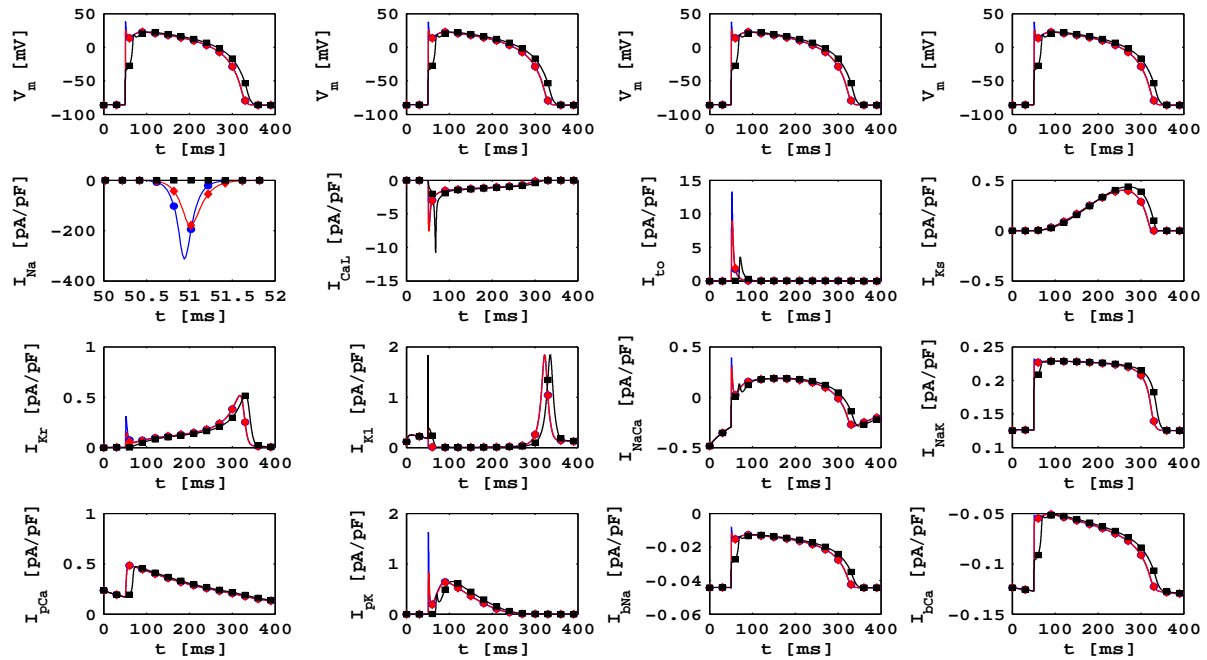


Figure 2.6: Action potential (top panel) and ionic currents associated to it when the I_{Na} ionic conductance G_{Na} is changed. The symbols that are used in these plots are as follows: (a) the blue, filled circles represent the channel conductance without blocking, (b) the red, filled diamonds represent the channel conductance at half the maximal conductance, and (c) the channel conductance blocked completely is represented by black, filled squares.

Fig. 2.5 we show the ionic concentrations associated with AP during the course of the action potential.

As suggested in Refs. [36–39], the contribution of individual ionic currents to the AP properties, such as, the maximum AP amplitude, V_{max} , the AP notch, V_{notch} , the maximum of the plateau potential, $V_{plateau}$, the AP duration, APD , and the resting membrane potential, V_{rest} , can be examined by a partial or complete blocking of the corresponding ion channel. Therefore, we examine, for an isolated myocyte, how the AP changes as we modify the major ionic currents, namely, the fast-inward sodium current I_{Na} , the L-type calcium current I_{CaL} , the transient outward current I_{to} , the slow delayed rectifier current I_{Ks} , the rapid delayed rectifier current I_{Kr} , and the inward rectifier current I_{K1} ; we carry out these studies by changing the associated channel conductance. We also give a set of plots to examine the time-dependence of the ionic currents I_{Na} , I_{CaL} , I_{to} , I_{Ks} , I_{Kr} , I_{K1} , I_{NaCa} , I_{NaK} , I_{pCa} , I_{pK} , I_{bNa} , and I_{bCa} , when we block either partially or completely of a major ionic current conductance.

In Fig. 2.6, we show plots of the AP, major ionic currents (I_{Na} , I_{CaL} , I_{to} , I_{Ks} , I_{Kr} , and I_{K1}), and minor ionic currents (I_{NaCa} , I_{NaK} , I_{pCa} , I_{pK} , I_{bNa} , and I_{bCa}), when we vary the maximal conductance G_{Na} associated with the I_{Na} ionic current. We apply a stimulus of current density 52 pA/pF for $t = 1$ ms to achieve such an AP and ionic currents associated with it. The symbols that are used in these plots are as follows: (a) the blue, filled circles represent the channel conductance without blocking, (b) the red, filled diamonds represent the channel conductance at half of the maximal conductance, and (c) the channel conductance blocked completely is represented by black, filled squares. The Figs. 2.7, 2.8, 2.9 2.10, and 2.11 are the analogs of Fig. 2.6 for the channel conductances G_{CaL} , G_{to} , G_{Ks} , G_{Kr} , and G_{K1} , respectively. We do not give all the details of this study because it is akin to those presented in Refs. [36–39]; a short summary follows: We find that (a) V_{max} depends principally on I_{Na} , (b) V_{notch} depends mainly on I_{to} , (c) the maximum of the plateau region $V_{plateau}$ is maintained by a balance between I_{CaL} and I_{Ks} , (d) the final phase of repolarization, which determines the APD, depends primarily on I_{Kr} and I_{Ks} , (e) the diastolic or resting phase, which decides the value of V_{rest} , is maintained predominantly by I_{K1} , and (f) all gating variables, which determine the opening and closing of ion channels, depend on V_m and, therefore, the contribution of the ionic currents to the morphology of the AP is modified as V_m changes.

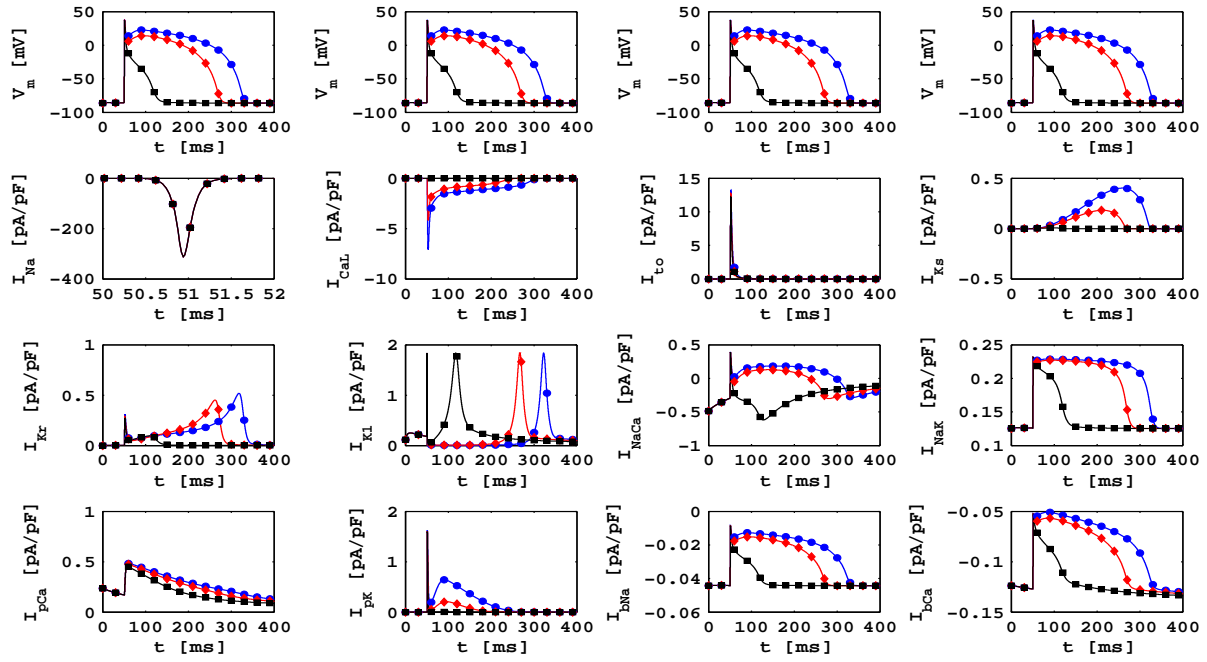


Figure 2.7: The analogs of the plots of Fig 2.6 when G_{CaL} , that is associated with the I_{CaL} ionic current, is not block (blue, filled circles), partially block (red, filled diamonds), and completely block (black, filled squares).

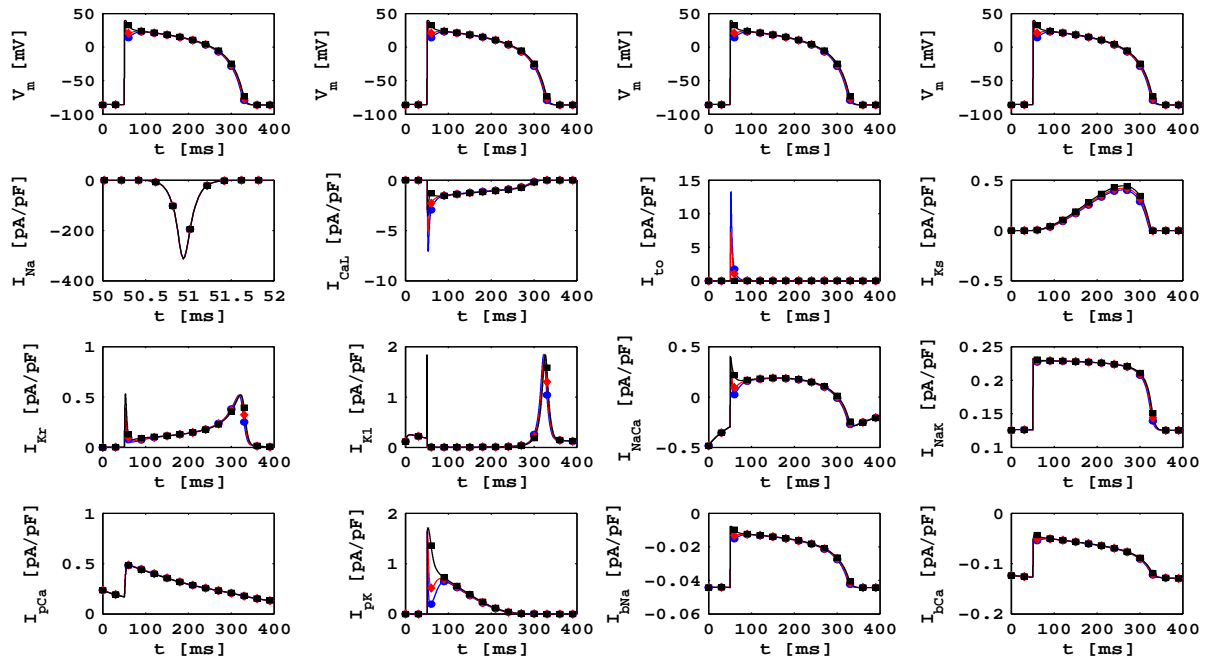


Figure 2.8: The analogs of the plots of Fig 2.7 when G_{to} , that is associated with the I_{to} ionic current, is varied.

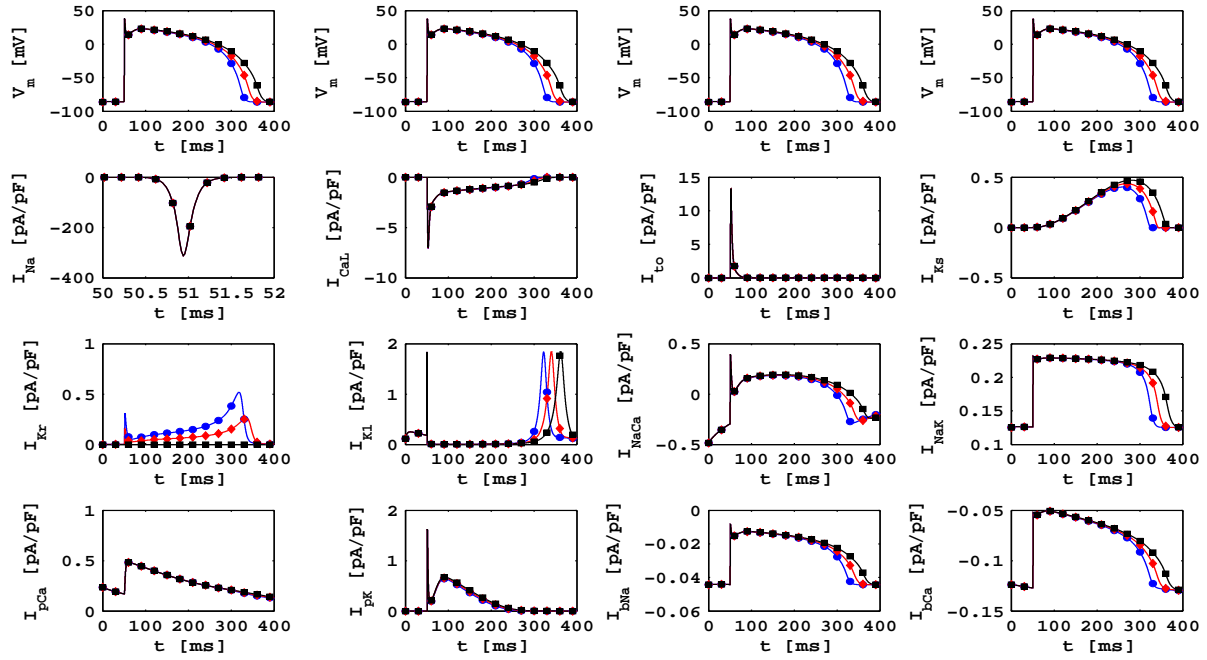


Figure 2.9: The analogs of the plots of Fig 2.7 when G_{Kr} , that is associated with the I_{Kr} ionic current, is varied.

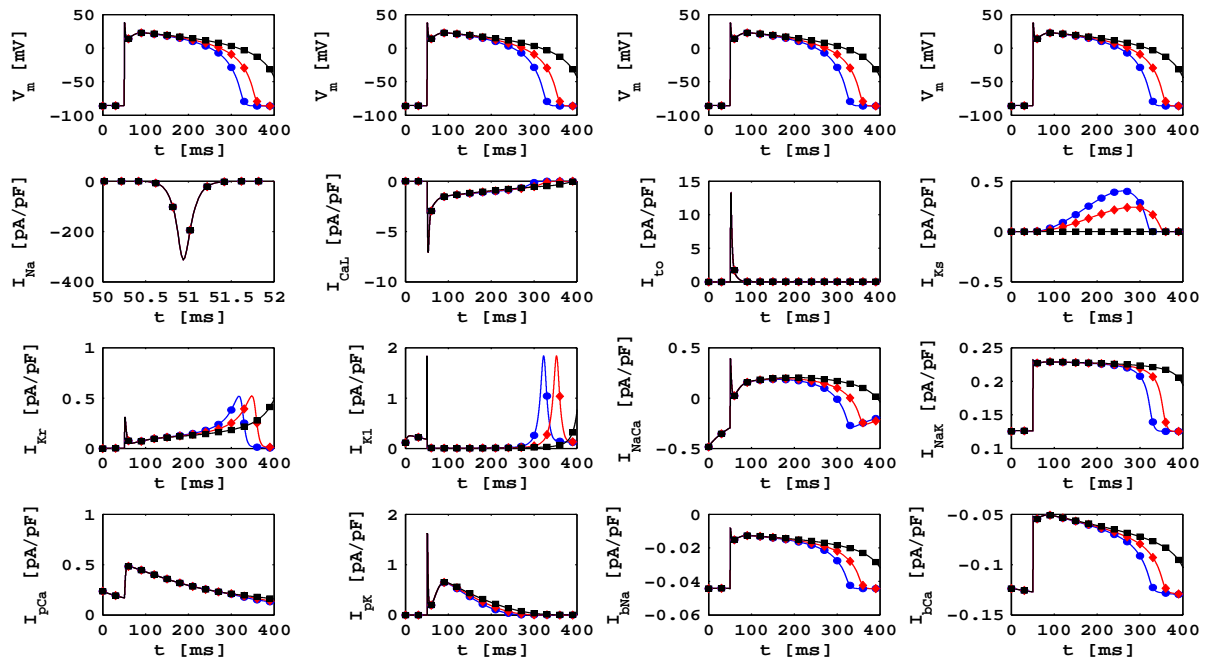


Figure 2.10: The analogs of the plots of Fig 2.7 when G_{Ks} , that is associated with the I_{Ks} ionic current, is varied.

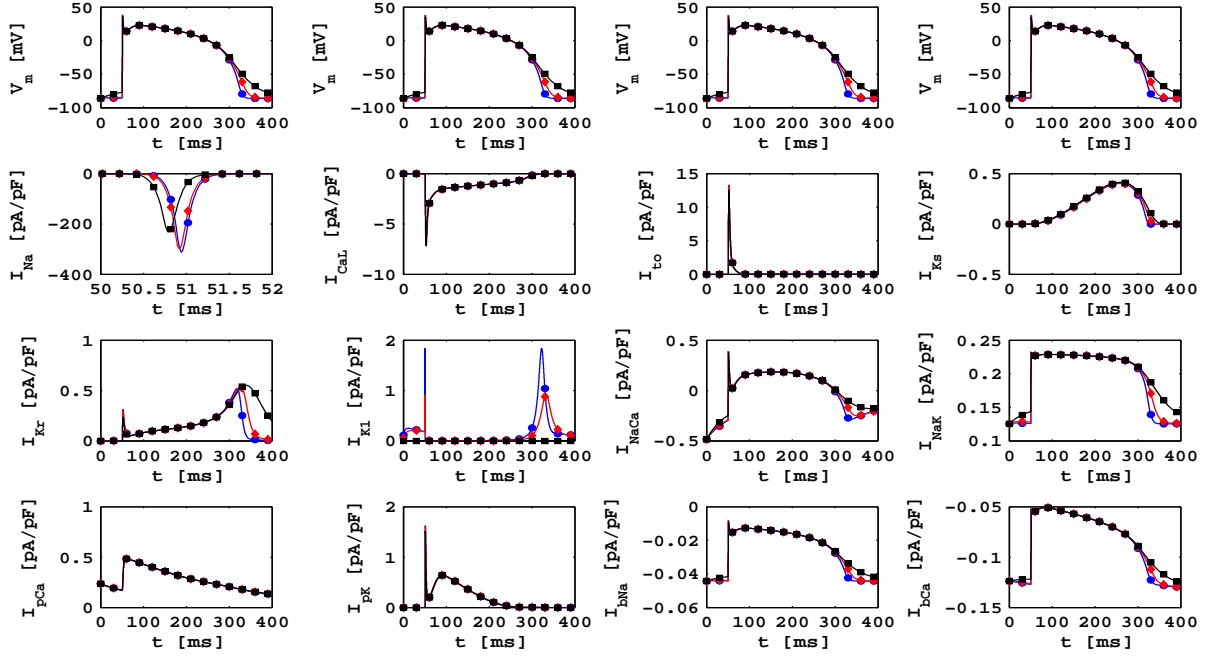


Figure 2.11: The analogs of the plots of Fig 2.7 when G_{K1} , that is associated with the I_{K1} ionic current, is varied.

2.3.2 Plane-wave propagation

We study plane-wave propagation in a thin, cable-type simulation domain, consisting of 2000×20 grid points, with spacing $\Delta x = 0.225$ mm, i.e., edge lengths $L_x = 450$ mm and $L_y = 4.5$ mm (see Sec. 5.2). A plane wave is injected in this cable type domain by stimulating the left boundary with a current pulse of amplitude 150 pA/pF for 3 ms. This leads to the formation of a plane wave that then propagates through the conduction domain as shown in Fig. 2.12. The animations in Video S01 show the spatiotemporal evolution of V_m ; the top and bottom panels show 2D and 3D views of V_m , respectively. We then measure the conduction velocity CV and the wave length λ , in this cable-type domain, by recording the positions of the wave front at times t and $t + \delta t$ and by using $CV = \delta x / \delta t$, where δx is the distance traveled by the wave front in the time interval δt . We locate the position of the wave front by finding the value of x at which $V_m \simeq 0$ mV; we define the position of the wave back as the point, behind the wave front, at which a secondary action potential can just be initiated by an additional stimulus (this turns out to occur at a value of $V_m \simeq 75\%$ of the repolarization phase of the AP). We obtain λ by measuring the distance between the wave front and the wave back at time t . We find that, with the diffusion coefficient $D = 0.00154$ cm²/ms, $CV \simeq 67.8$ cm/s and

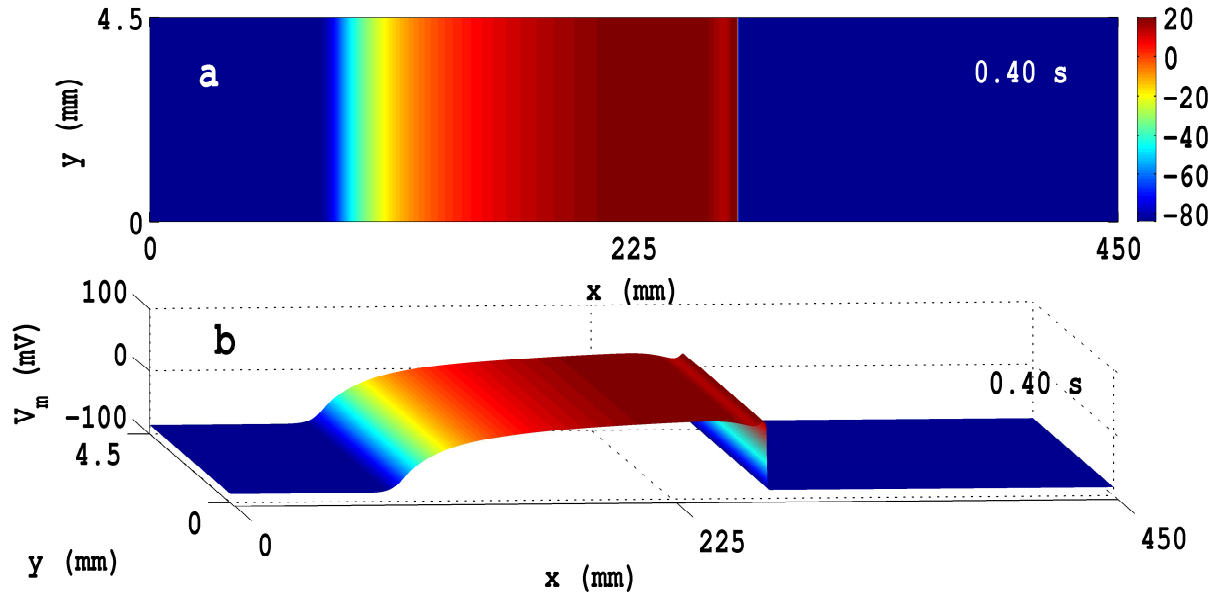


Figure 2.12: Illustrative plots of V_m at time $t = 400$ ms in a thin strip of cardiac tissue with dimension, $L_x = 45$ cm and $L_y = 0.45$ cm, which is basically, a one dimensional cable: (a) pseudo color plots of V_m in 2D; (b) V_m plots in 3D; the animations in Video S01 show the spatiotemporal evolution of V_m for this case. The wave length, λ , is the distance between wave front (AP upstroke) and wave back (AP repolarization) of the propagating wave.

$\lambda \simeq 18.9$ cm for the TNNP04 model, and $CV \simeq 70.6$ cm/s and $\lambda \simeq 21.6$ cm for the TP06 model.

In Figs. 2.13(a)-(f), we show pseudocolor plots of the transmembrane potential V_m at time $t = 300$ ms in our cable-type domain with diffusion coefficients (a) $D = 0.125 \times D_{model}$, (b) $D = 0.5 \times D_{model}$, (c) $D = D_{model}$, (d) $D = 2 \times D_{model}$, (e) $D = 3 \times D_{model}$, and (f) $D = 4 \times D_{model}$. It is known that the propagation velocity of reaction-diffusion-type equation is directly proportional to the square root of the diffusion coefficient (D) [32]. To confirm this relation in the TNNP04 model, we measure CV by using different values of D and by injecting a plane wave into the cable-type domain. In Fig 2.13(g) we show the plot of CV versus the normalized diffusion coefficient $D_{normalized}$, i.e., the ratio of D and its maximal value $D_{max} = 0.00154$ cm^2/ms . The data, shown by black, filled circles in Fig. 2.13(g), are fitted using nonlinear curve fitting technique with a power-law function of the form $CV = AD^\alpha$; the curve is shown by a blue, solid line. We find that, $A \simeq 67.65$ and $\alpha \simeq 0.55$; this is consistent with $CV \propto \sqrt{D}$. For a plane wave in a medium, CV and λ are related by, $\lambda = APD \times CV$ [40], where APD is the action potential duration, which is roughly related to its single-cell value. To verify such a relation, we calculate λ by using the same

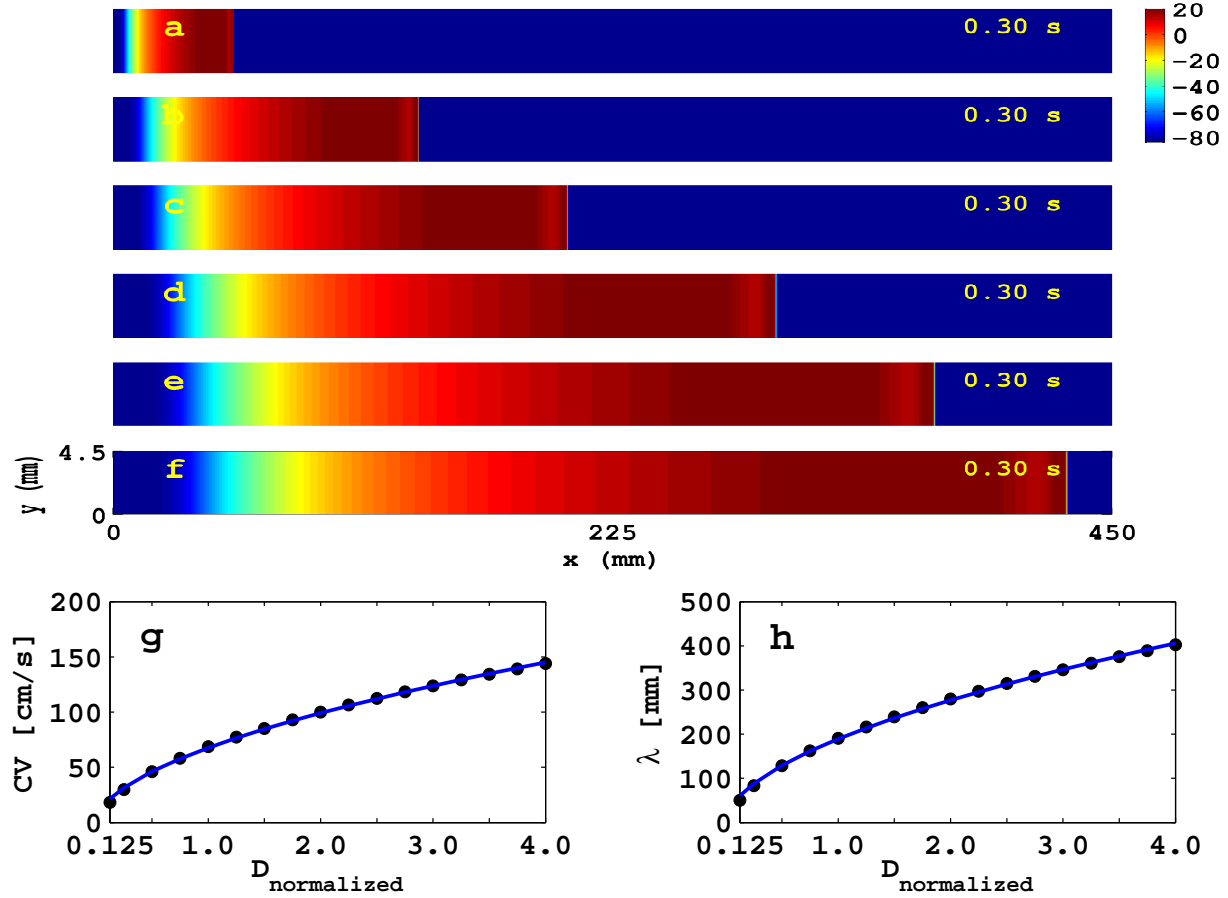


Figure 2.13: Pseudocolor plots of V_m at time $t = 300$ ms in the cable with diffusion coefficients (a) $D = 0.125 \times D_{max}$, (b) $D = 0.5 \times D_{max}$, (c) $D = D_{max}$, (d) $D = 2 \times D_{max}$, (e) $D = 3 \times D_{max}$, (f) $D = 4 \times D_{max}$. (g) A plot of the normalized diffusion coefficient $D_{normalized}$ versus the conduction velocity CV ; here, we obtain $D_{normalized}$ by taking ratio of D for the simulation and its maximal or normal value of $D_{normal} = 0.00154$ cm²/ms. The curve (shown by a solid line) is fitted using a power function, i.e., $Y = AX^\alpha$, where $A \approx 67.65$ and $\alpha \approx 0.55$; it is consistent with $CV \propto \sqrt{D}$; (h) plot of wave length λ versus the normalized diffusion coefficient $D_{normalized}$, i.e., the ratio of D and its maximal value $D_{max} = 0.00154$ cm²/ms; the solid line indicates a fit of the form $CV = AD^\alpha$; we find $A \approx 189.15$ and $\alpha \approx 0.5$, which is consistent with $CV \propto \sqrt{D}$. Furthermore, the estimated value of APD from the relation, $\lambda = APD \times CV$, is 279.6 ms.

technique that we have used for CV . In Fig. 2.13(h), we show a plot for λ similar to Fig. 2.13(g); we find that $A \approx 189.15$ and $\alpha \approx 0.5$ for λ ; this is also consistent with $\lambda \propto \sqrt{D}$. We estimate the value of APD, from the relation, $\lambda = APD \times CV$, and find $APD \approx 279.6$ ms; this is consistent with the APD of a single cell [3].

2.3.3 Circular-wave propagation

An application of a point stimulus leads to an outward expanding wave with a circular wave front for a 2D, homogeneous simulation domain. The wave front can deviate substantially from a circular wave as a consequence of numerical artifacts [34], and this leads to unphysical wave dynamics.

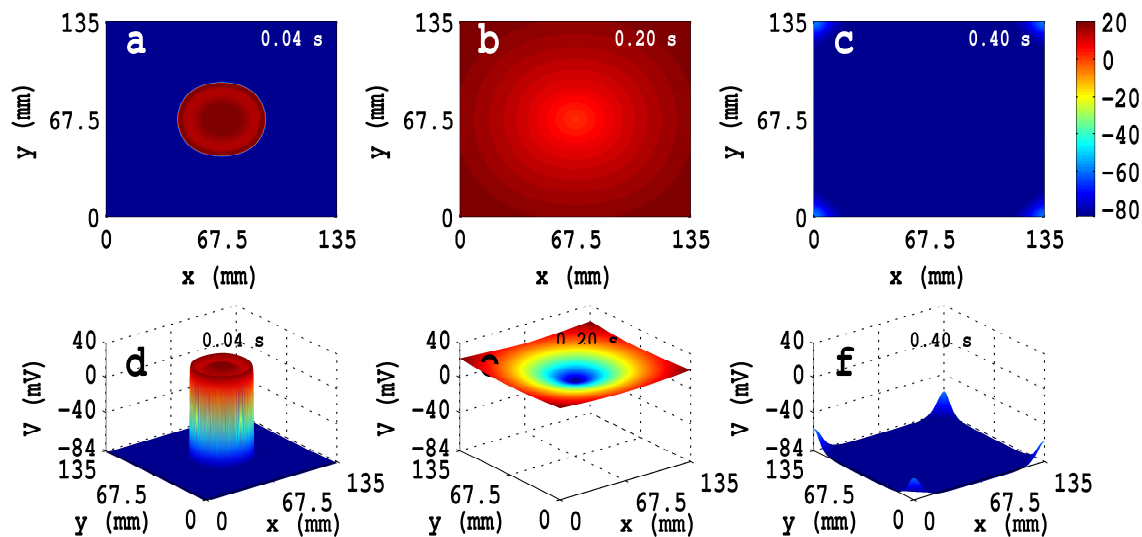


Figure 2.14: Pseudocolor plots of the transmembrane potential V_m in a square simulation domain of side $L = 135$ mm for the TNNP04 model; here, a point stimulus of strength 450 pA/pF is applied for 3 ms at the center of the simulation domain ($x = 67.5$ mm, $y = 67.5$ mm). The time evolutions of V_m are shown via 2D plots in (a), (b), and (c) at time, t , 0.04 ms, 0.2 s, and 0.4 s, respectively; there corresponding 3D plots are shown in (d), (e), and (f). The animations in Video S02 show the spatiotemporal evolution of V_m for this case.

Reference [34] suggests that we must have $D\delta t/(\delta x^2) < 1/2d$ for numerical stability, where d is the dimension of the simulation domain. For the TNNP04 model, with diffusion coefficients $D = 0.00154$ cm²/ms [3], time step $\delta t = 0.02$ ms, and space step $\delta x = 0.225$ mm (see Sec. 5.2), the value of $D\delta t/(\delta x)^2$ is $\simeq 0.06$; and for the TP06 model, with diffusion coefficients $D = 0.00154$ cm²/ms [5], time step $\delta t = 0.02$ ms, and space step $\delta x = 0.25$ mm (see Sec. 5.2), the value of $D\delta t/(\delta x)^2$ is $\simeq 0.05$; for the 2D domain for both the models, the quantity $1/2d = 0.25$, i.e., we have numerical stability because $D\delta t/(\delta x)^2 < 1/2d$. As we discussed above, our results can be shown to be free from numerical artifacts by checking the spatiotemporal evolution of an expanding wave front that emerges from a point stimulus. Therefore, we carry out a simulation for a 2D square domain of side $L = 135$ mm, with TNNP04 model, to verify numerical stability. A point stimulus of strength 450 pA/pF for 3 ms is

applied at the center of the domain. In Figs. 2.14(a)-(c), we show the time evolution of pseudocolor plots of V_m in 2D for the TNNP04 model at times $t = 0.04$ ms, $t = 0.2$ s, and $t = 0.4$ s, respectively; the corresponding 3D plots are shown in (d), (e), and (f). The animations in Video S02 show the spatiotemporal evolution of V_m (pseudocolor plots in 2D (left panel), contour plots (middle panel), and pseudocolor plots in 3D (right panel)). The Fig. 2.14 and Video S02 we show that fronts of the expanding wave do not deviate substantially from circles. We have also obtained similar results for the TP06 model.

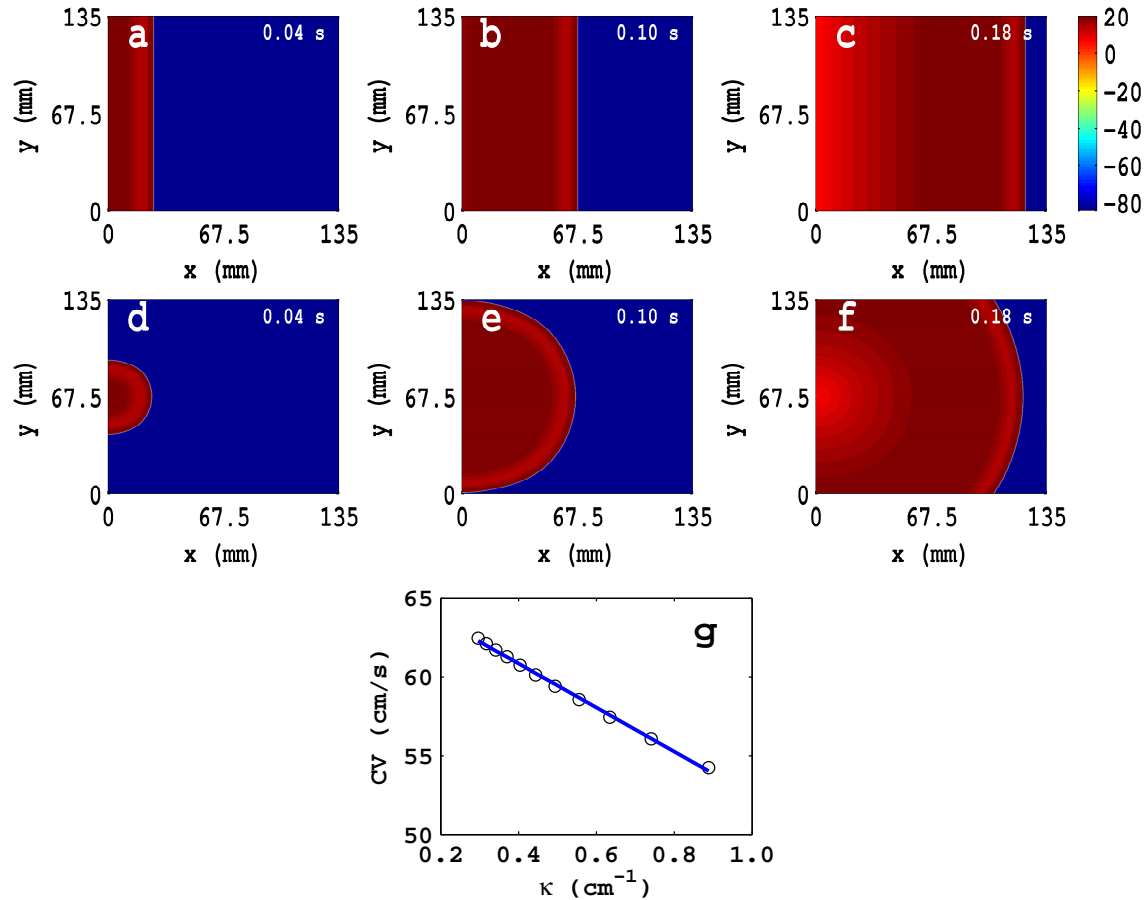


Figure 2.15: Pseudocolor plots of V_m illustrating that a plane wave (a)-(c) propagates faster than a convex wave (d)-(f). Thus, curvature plays an important role in wave propagation. The eikonal relation for a highly dispersive media is $CV = CV_0 - h\kappa D$, here, CV , CV_0 , κ , and D , are the conduction velocity of circular wave, plane wave, curvature, and diffusivity, respectively. In (g) we show this relation between CV and κ , when a stimulus of strength 450 pA/pF is applied at center of the simulation domain for 3 ms. The factor, $h \simeq 1$, for the Zykov limit [47] and $h > 1$ for the dispersive situation; we have obtained $h \simeq 9$ because of high dispersion and high curvature in our study.

It is well known that the curvature at a wave front plays an important role in the propagation of waves in excitable media. In particular, as suggested in Refs. [41, 42], the curvature plays an important role with $CV = CV_0 - \kappa D$, where, CV , CV_0 , κ , and D , are the CV at the front of any type of wave, CV at the front of a plane wave, curvature of the wave front, and diffusion coefficient, respectively. For a concave wave κ is negative and convex wave κ is positive, therefore, $CV > CV_0$ for a concave wave and $CV < CV_0$ for a convex wave, because, for concave wave the flux carried by a wave front converges, so fast conduction occurs, where as for a convex wave the flux carried by wave front diverges, therefore, slow conduction occurs. We study propagating plane and circular waves, which have zero and negative curvatures, in our 2D square domain of side $L = 135$ mm for the TNNP04 model to study the effects of curvature on the propagation speed. We apply a line stimulus of strength 450 pA/pF for 3 ms along the entire left boundary of the domain to inject a plane wave; and we apply a point stimulus of the same strength and duration at the middle of the left boundary to inject the circular wave. In Figs. 2.15(a)-(c), we show pseudocolor plots of V_m at times $t = 0.04$ ms, $t = 0.1$ s, and $t = 0.18$ s, respectively; plots, similar to Figs. 2.15(a)-(c), are shown in Figs. 2.15(d)-(f) for a circular wave. By comparing the wave fronts from these plots in Figs. 2.15(a)-(f), we conclude that the convex wave, which has negative curvature, propagates slowly compared to the plane wave.

The relation between CV and κ , called the eikonal equation, has been studied well in various excitable media [43–46]. It shows that $CV = CV_0 - \kappa D$, and is valid for small curvatures. However, for highly dispersive media this relation is not valid [44, 47, 48], and the corrected relation is $CV = CV_0 - h\kappa D$. Here the factor, $h \simeq 1$ for the Zykov limit and $h > 1$ for the dispersive situation. The deviation of eikonal relation from the Zykov limit has been seen in both two-variable and ionic models for cardiac tissue. For example, Pertsov *et al.* [47] have shown that the correction factor can be $h \simeq 2.1$ for a two-variable model; Qu *et al.* [44] have found $h \simeq 0.9$ for the LR-I ionic model for cardiac tissue.

To estimate the correction factor h for the TNNP04 model we apply a point stimulus of a strength 450 pA/pF at the center ($x = 67.5$ mm, $y = 67.5$ mm) of a square domain of side $L = 135$ mm for 3 ms. An expanding circular wave front travels away from this point source as shown via contour plots in Video S02; this allows allows us to locate the wave-front position at a given time and thus to measure CV and κ . We considered the propagation across an annulus of inner radius $r_i = 78.75$ mm and outer radius $r_o = 123.75$ mm, which is wide enough to obtain the wave speed as a linear function of κ , which is obtained by $\kappa = 1/r$, where r is the radius of the

expanding circular wave front at a given time t ; and $CV = r/t$. In Fig. 2.15(g) we show plots of CV versus κ ; from this plot we find $h \simeq 9$ for the TNNP04 model.

2.3.4 Spiral-wave dynamics

Spiral waves in homogeneous domains

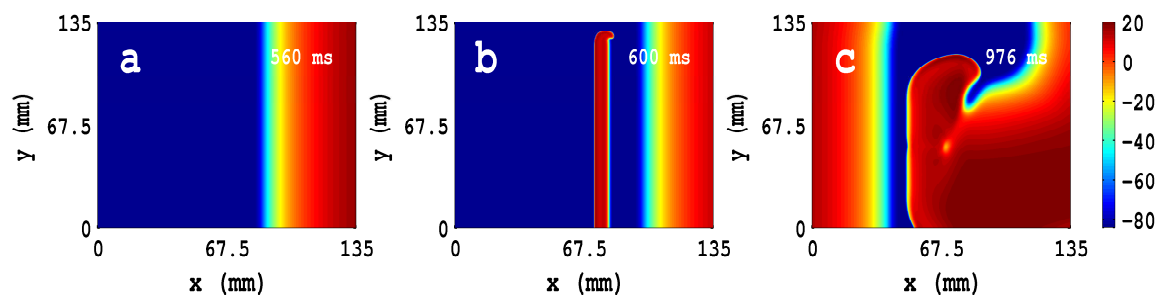


Figure 2.16: Initiation of spiral waves in the TNNP model by S1-S2 parallel protocol (see text) illustrated via pseudocolor plots of the transmembrane potential V_m . We use the configuration shown in (c) as our initial condition to study spiral-waves dynamics in this model.

Generally, two methods are used to initiate spiral waves in simulations [3, 4, 31, 49] and experiments [9, 49], namely, (1) the S1-S2 cross-field protocol and (2) the S1-S2 parallel-field protocol. In the cross-field method, a super-threshold stimulus S2 is applied at the boundary that is perpendicular to the S1 stimulus, whereas, in the parallel-field method, S2 is applied parallel to the refractory tail of the S1 stimulus, but not over the entire length of the domain.

We use an S1-S2 parallel-field protocol to initiate a spiral wave in a 2D square domain of side $L = 135$ cm for the TNNP04 model. We inject a plane wave into the domain via an S1 stimulus of strength 150 pA/pF for 3 ms at the left boundary. We choose D to be 0.000385 cm²/ms (approximately 1/4th of its original value, 0.00154 cm²/ms) in the beginning of our simulation to initiate a spiral wave. We then apply an S2 stimulus of strength 450 pA/pF for 3 ms, after 560 ms, and just behind the refractory tail of S1 ($x = 360$, $1 \leq y \leq 550$). As the first wave moves further towards the right (Fig. 2.16(a)), the free end of the new stimulus is able to move into the area behind the first wave; a hook-like proto spiral appears at this free end (Fig. 2.16(b)). We then reset the conductivity to its original value after 880 ms. This procedure yields the fully developed spiral wave shown in Fig. 2.16(c) at $t = 976$ ms; and this state is used as the initial condition for our subsequent studies.

We now study the properties of the AP and its morphology for an isolated myocyte cell as we vary the maximal conductances, G_{CaL} , G_{to} , G_{Ks} , G_{Kr} , and G_{K1} ,

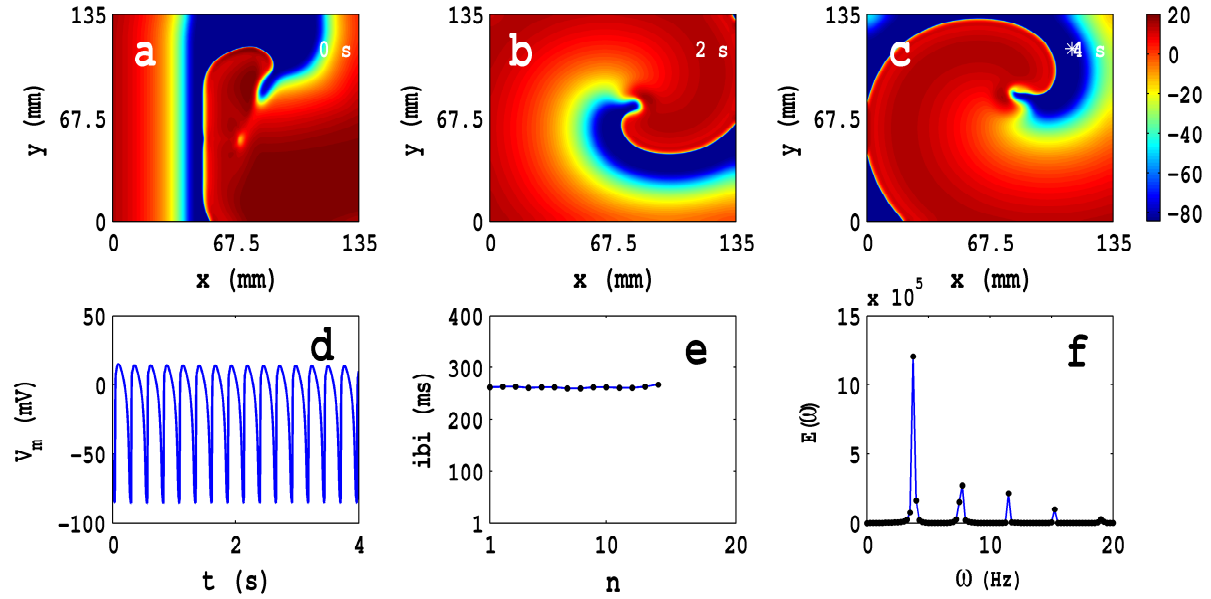


Figure 2.17: The rotating spiral (RS) state in the TNNP model with the parameter set P0 (see Table 2.1). We start with the initial condition of Fig. 2.16(c); pseudocolor plots of V_m are shown in (a), (b), and (c); the animation (a) in Video S03 shows the spatiotemporal evolution of V_m for this case. These pseudocolor plots and the animation show the existence of a single rotating spiral in the domain. (d) The local time series for V_m from a sample of 2×10^5 iterations taken from the representative point (90 mm, 90 mm) marked by an asterisk in (c) (see Methods Section); and plots of (e) the inter-beat interval (ibi) versus the beat number n from a sample time series of 2×10^5 iterations, and (f) the power spectrum of V_m obtained from a time series of length 2×10^5 iterations, which shows discrete peaks at the fundamental frequency $\omega_f = 3.75$ Hz and its harmonics. The periodic behavior of the ibi and discrete peaks in the power spectrum are characteristic of the RS state.

which are associated with the major ionic currents I_{Na} , I_{CaL} , I_{to} , I_{Ks} , I_{Kr} , and I_{K1} , respectively. We then carry out systematic studies of spiral-wave dynamics, as we tune the maximal conductances of major ionic currents. The parameter sets, given in Table 2.1, are chosen by modifying one of the major ionic conductance; and these parameter sets are used to study spiral-wave dynamics in the TNNP04 2D model. We present below our detailed results for two representative cases.

In Figs. 2.17(a)-(c), we show pseudocolor plots of V_m at times $t = 0$ s, $t = 2$ s, and $t = 4$ s, respectively, for the parameter set P0 (see Table 2.1) in the TNNP04 model; this initial configuration evolves to a state with a rotating spiral (RS) in the medium; the animation (a) in Video S03 shows the spatiotemporal evolution of V_m for this case. The local time series of $V_m(x, y, t)$, from the representative point ($x = 90$ mm, $y = 90$ mm) (the asterisk in Fig. 2.17(c)), is shown in Fig. 2.17(d) for $0 \leq t \leq 4$ s; a plot of the inter beat interval (ibi) is given in Fig. 2.17(e), which

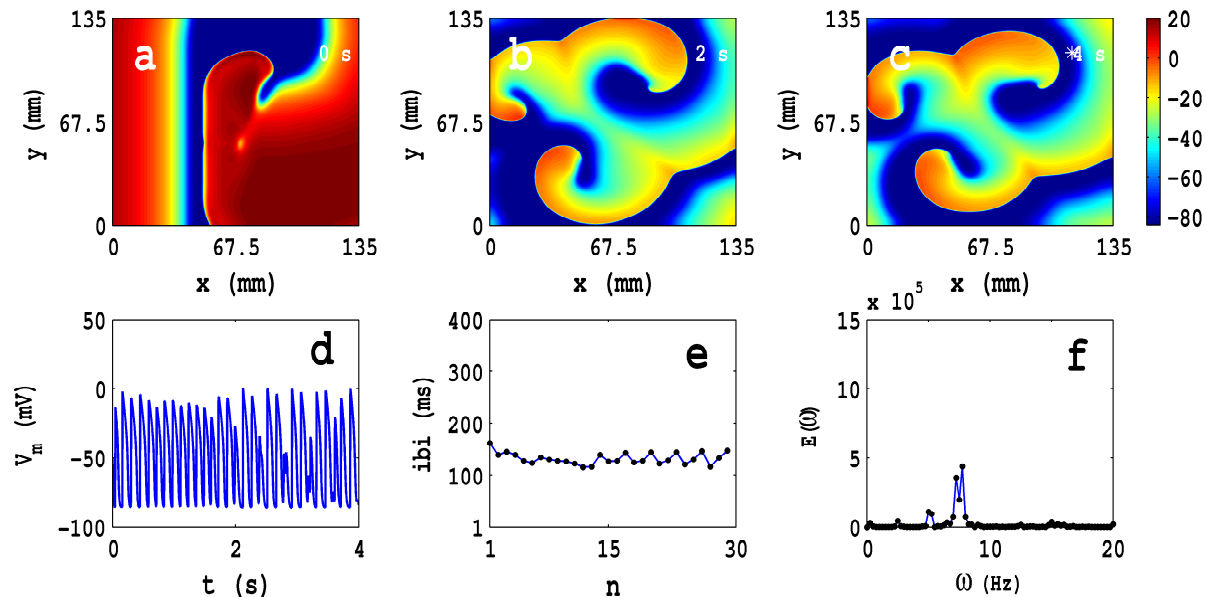


Figure 2.18: The state with three rotating spirals in the TNNP model with parameter set P7 (see Table 2.1). We start with the initial condition of Fig. 2.16(c); pseudocolor plots of V_m are shown in (a), (b), and (c); the animation (c) in Video S04 shows the spatiotemporal evolution of V_m for this case. These pseudocolor plots and the animation show the existence of three rotating spirals (two clockwise and one anti clockwise) in the domain. (d) The local time series for V_m , from a sample of 2×10^5 iterations taken from the representative point (90 mm, 90 mm) marked by an asterisk in (c) (see Methods Section); and plots of (e) the inter-beat interval (ibi) versus the beat number n from a sample time series of 2×10^5 iterations, which shows the average rotation period of spirals $\tau_{rot} \simeq 135$ ms; and (f) the power spectrum of V_m obtained from a time series of length 2×10^5 iterations, which shows a first dominant peak at the frequency $\omega_f \simeq 7.75$ Hz; this is consistent with the average rotation period measured via the ibi ($\omega_f = 1/\tau_{rot}$).

shows that the spiral wave rotates periodically with an average rotation period $T \simeq 262$ ms. In Fig. 2.17(f), we plot the power spectrum $E(\omega)$, which we have obtained from the local time series of V_m mentioned above; discrete peaks in $E(\omega)$ appear at the fundamental frequency $\omega_f \simeq 3.75$ Hz and its harmonics. The periodic nature of the local time series of V_m , the flattening of the ibi, and the discrete peaks in $E(\omega)$ show that the temporal evolution of the spiral wave is periodic.

In Figs. 2.18(a)-(g) we show, for the parameter set P7 (see Table 2.1) in the TNNP04 model, the exact analogs of Figs. 2.17(a)-(g); and the animation (c) in Video S04 shows the spatiotemporal evolution of V_m for this case. This animation, the pseudocolor plots of V_m show two clockwise and one anti clockwise rotating spirals in the domain. The local time series of $V_m(x, y, t)$, from the representative point ($x = 90$ mm, $y = 90$ mm) (the asterisk in Fig. 2.18(c)), is shown in Fig. 2.18(d) for $0 \text{ s} \leq t \leq 4 \text{ s}$; a plot of the inter beat interval (ibi) is given in Fig. 2.18(e), which shows

that the spirals in the medium rotate nearly periodically with an average rotation period $\tau_{rot} \simeq 135$ ms. In Fig. 2.18(f), we plot the power spectrum $E(\omega)$, which we have obtained from the local time series of V_m mentioned above; which shows first dominant peaks at the frequency $\omega_f \simeq 7.75$ Hz; this is consistent with the average measured ibi ($\omega = 1/\tau_{rot}$).

The complete spatiotemporal behavior of our system is summarized for different parameter sets in Table 2.1. And we present the spatiotemporal evolution of V_m by a series of Videos (S03-S08) of its pseudocolor plots; all these videos use 10 frames per second and each frame is separated from the succeeding frame by 8 ms.

To initiate a spiral wave in square homogeneous domain of size, $L = 256$ mm, for the TP06 model, we use a slightly modified version of the S1-S2 cross-field protocol. We inject a plane wave into the domain via an S1 stimulus of strength 150 pA/pF for 3 ms at the left boundary. Then, we apply an S2 stimulus of the same strength and duration from the bottom boundary the middle of the medium ($0 \text{ mm} < L_y \leq 125 \text{ mm}$). This procedure yields a fully developed spiral wave.

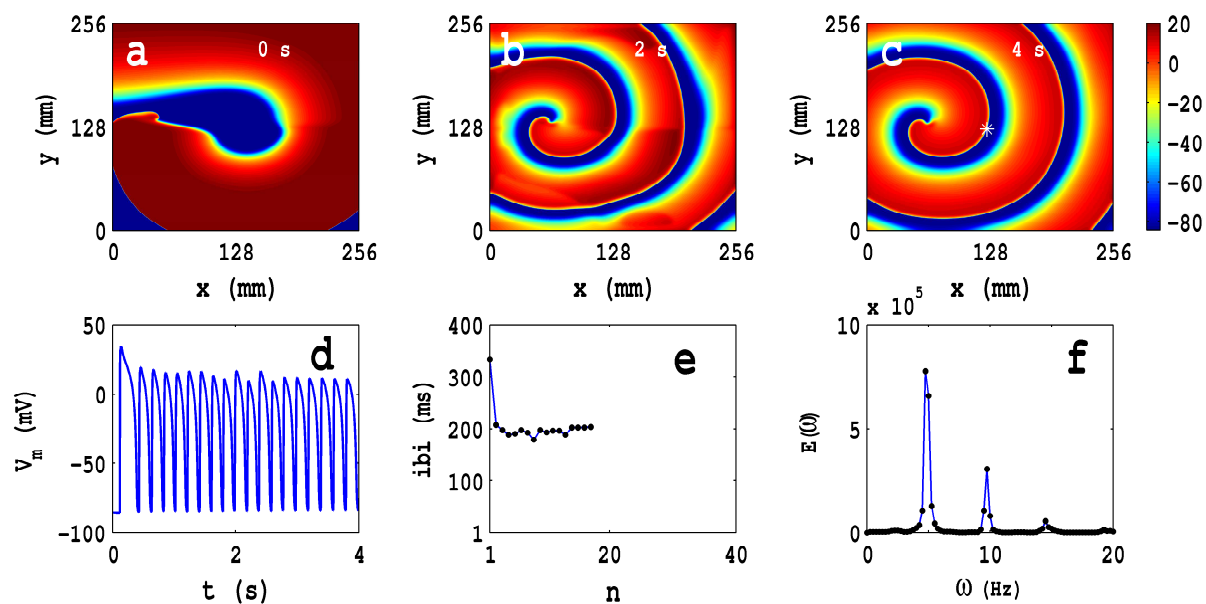


Figure 2.19: Spatiotemporal evolution of V_m for the parameter set P1 for the TP06 model: (a)-(c) Pseudocolor plots of V_m at times $t = 0$ s, $t = 2$ s, and $t = 4$ s, respectively, showing the evolution towards a state with a rotating spiral (RS); the animation (a) in Video S09 shows the spatiotemporal evolution of V_m for this case. (d) The local time series of $V_m(x, y, t)$, from the representative point ($x = 125$ mm, $y = 125$ mm) (the asterisk in (c)) for $0 \text{ s} \leq t \leq 4 \text{ s}$; (e) a plot of the inter beat interval (ibi), which we obtain from this time series, of length 2×10^5 iterations; (f) the power spectrum $E(\omega)$, obtained from the local time series of (d), with discrete peaks at the fundamental frequency $\omega_f \simeq 4.75$ Hz and its harmonics.

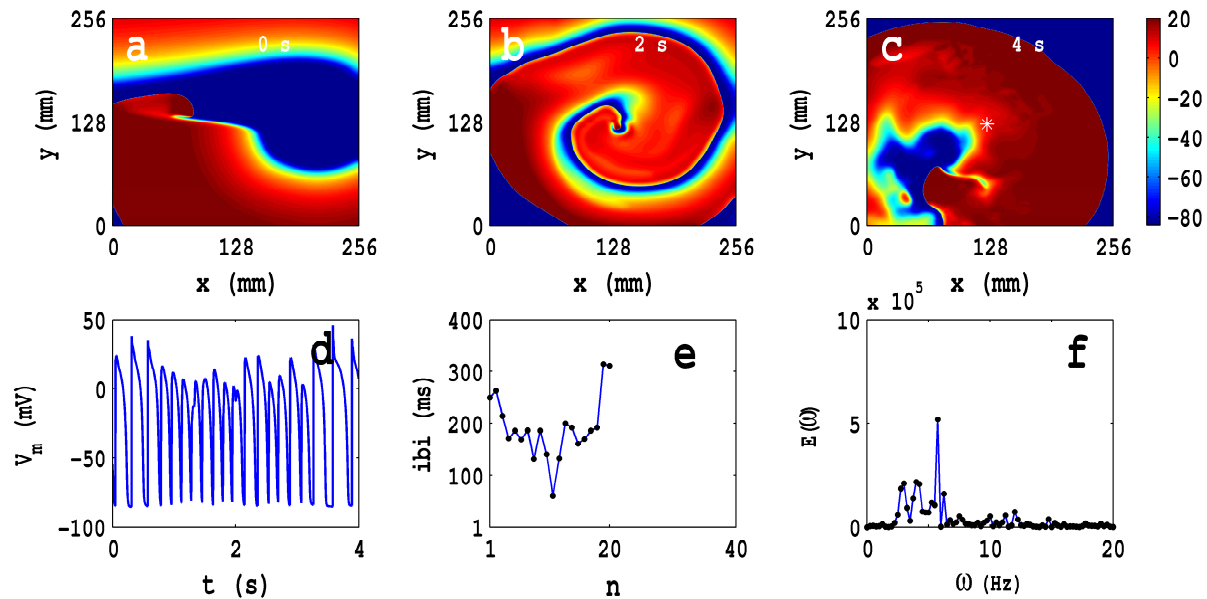


Figure 2.20: Spatiotemporal evolution of V_m for the parameter set P2 for the TP06 model: (a)-(f) show, for the parameter set P2, the exact analogs of Figs. 4.4; and the animation (b) in Video S09 shows the spatiotemporal evolution of V_m for this case. This animation, the pseudocolor plots of V_m ((a)-(c)), the representative local time series of V_m (d), the plot of the ibi (e), and the power spectrum $E(\omega)$ (f) show that the parameter P1 leads to spatiotemporal chaos and spiral turbulence (ST) with a single spiral meandering chaotically in the simulation domain (SMST).

We also explore the spatiotemporal behavior of V_m by modifying the maximal conductances of major ionic current of the TP06 model. However, for a particular combination of one or more ionic conductances, with a time constant associated with the I_{CaL} ionic current, leads to three major types of spiral-wave states, namely, (a) RS, (b) SMST, and (c) MST states. We list these variables in Table 2.2. We present below detailed results for the parameter sets P1, P2, and P3, for the TP06 model.

In Figs. 4.4(a)-(c), we show pseudocolor plots of V_m at times $t = 0$ s, $t = 2$ s, and $t = 4$ s, respectively, for the parameter set P1 in the TP06 model; this initial configuration evolves to a state with a rotating spiral (RS) in the medium; the animation (a) in Video S09 shows the spatiotemporal evolution of V_m for this case. The local time series of $V_m(x, y, t)$, from the representative point ($x = 125$ mm, $y = 125$ mm) (the asterisk in Fig. 4.4(c)), is shown in Fig. 4.4(d) for $0 \text{ s} \leq t \leq 4 \text{ s}$; a plot of the inter beat interval (ibi) is given in Fig. 4.4(e), which shows that, after initial transients (roughly the first 10 beats), the spiral wave rotates periodically with an average rotation period $T \simeq 210$ ms. In Fig. 4.4(f), we plot the power spectrum $E(\omega)$, which we have obtained from the local time series of V_m mentioned above;

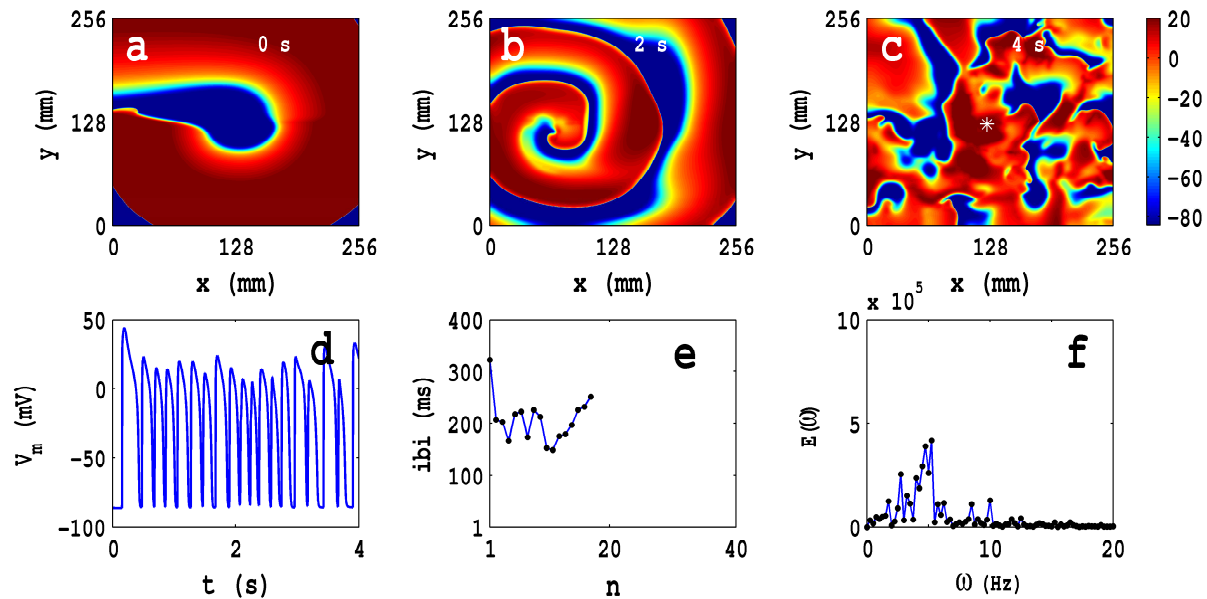


Figure 2.21: Spatiotemporal evolution of V_m for the parameter set P3 for the TP06 model: (a)-(f) show, for the parameter set P3, the exact analogs of Figs. 4.4(a)-(f); and the animation (c) in Video S09 shows the spatiotemporal evolution of V_m for this case. This animation, the pseudocolor plots of V_m ((a)-(c)), the representative local time series of V_m (d), the plot of the ibi (e), and the power spectrum $E(\omega)$ (f) show that the parameter set P3 leads to spatiotemporal chaos and spiral turbulence (ST) with multiple broken spirals in the simulation domain (MST).

discrete peaks in $E(\omega)$ appear at the fundamental frequency $\omega_f \simeq 4.75$ Hz and its harmonics. The periodic nature of the local time series of V_m , the flattening of the ibi, and the discrete peaks in $E(\omega)$ show that the temporal evolution of the spiral wave is periodic.

In Figs. 4.5(a)-(g) we show, for the parameter set P2, the exact analogs of Figs. 4.4(a)-(g); and the animation (b) in Video S09 shows the spatiotemporal evolution of V_m for this case. This animation, the pseudocolor plots of V_m (Figs. 4.5(a)-(c)), the representative local time series of V_m (Fig. 4.5(d)), the plot of the ibi (Fig. 4.5(e)), the power spectrum $E(\omega)$ (Fig. 4.5(f)), and the spiral-tip trajectory (the white curve in Fig. 4.5(c) and the blue one in Fig. 4.5(g)) show that the parameter set P2 leads to spatiotemporal chaos and spiral turbulence (ST), with a single spiral meandering chaotically in the simulation domain (SMST).

In Figs. 4.6(a)-(f) we show, for the parameter set P3, the exact analogs of Figs. 4.4(a)-(f); and the animation (c) in Video S09 shows the spatiotemporal evolution of V_m for this case. This animation, the pseudocolor plots of V_m (Figs. 4.6(a)-(c)), the representative local time series of V_m (Fig. 4.6(d)), the plot of the ibi (Fig. 4.6(e)), and the power spectrum $E(\omega)$ (Fig. 4.6(f)) show that the parameter set P3 leads to spa-

tiotemporal chaos and spiral turbulence (ST) with multiple broken spirals in the simulation domain (MST).

Spiral wave with conduction inhomogeneity

Conduction inhomogeneities (also referred as obstacles) in cardiac tissue can affect spiral wave dynamics in several ways. Experimental studies show that a drifting spiral can attach to an obstacle in its path and continue anchored around it [9, 19–21, 49] for an indefinite period of time. Therefore, an obstacle can cause the transition from an irregular activity (drifting spiral) to regular activity (anchored spiral). It is also observed that, in some cases, the obstacle can eliminate the spiral wave completely. Studies of the dependence of such anchoring on the size of the obstacle [19,21] reveal that the larger the obstacle, the more likely is the anchoring; however, even if the obstacle is large, the wave might not attach to it. An obstacle can also convert multiple spirals to an anchored spiral [20].

We introduce an obstacle in the simulation domains of both the TNNP04 and TP06 models described above by making the conductivity constant $D = 0$ in the region of the obstacle. We use square obstacles in most of our 2D studies. When we set $D = 0$, we decouple the cells inside the obstacle from those outside it. Furthermore, we use Neumann (i.e., no-flux) boundary conditions on the boundaries of the obstacle; we have checked in representative cases that, even if we do not impose Neumann boundary conditions on the obstacle boundaries, our results are not changed qualitatively.

We first examine the dependence of spiral-wave dynamics on the size of an obstacle by fixing its position and changing its size (cf., Ikeda *et al.* [19] for similar experiments).

In Figs. 2.22, we show the pseudocolour plots of V_m at time, $t = 0.4$ s, for the TNNP04 model with the P1 parameter set, with a square conduction inhomogeneity whose top-left corner is fixed at $(x = 67.5$ mm, $y = 90$ mm). The square obstacle has a side of length $\ell = 0$, i.e., a homogeneous domain (Fig. 2.22(a)), $\ell = 22.5$ mm (Fig. 2.22(b)), $\ell = 27$ mm (Fig. 2.22(c)), $\ell = 31.5$ mm (Fig. 2.22(d)), $\ell = 36$ mm (Fig. 2.22(e)), $\ell = 40.5$ mm (Fig. 2.22(f)), $\ell = 45$ mm (Fig. 2.22(g)), and $\ell = 49.5$ mm (Fig. 2.22(h)). The Video S10 has four panels that show the spatiotemporal evolution of pseudocolor plots of V_m for 2 s $\leq t \leq 3$ s for a homogeneous domain with no inhomogeneities (top left panel) and the simulation domains for Figs. 2.22 (c), (e), and (g) (top right, bottom left, and bottom right panels, respectively). These pseudocolor plots and animations show that the smallest obstacle that can anchor

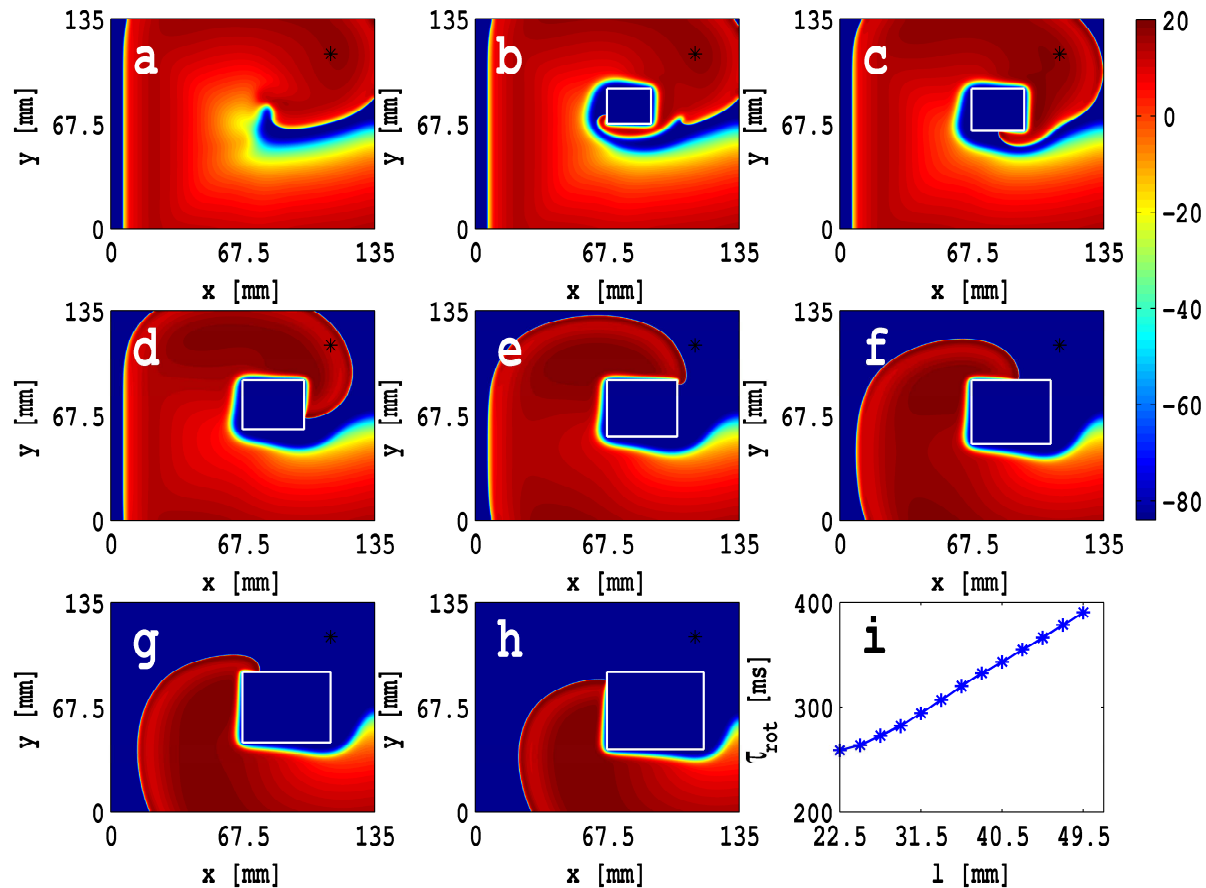


Figure 2.22: Pseudocolour plots of V_m at time, $t = 400$ ms, for the parameter set P1 in the TNNP04 model, with a square shape conduction inhomogeneity whose top-left corner is fixed at (67.5 mm, 90 mm): (a) $\ell = 0$, i.e., myocytes absence of inhomogeneity; (b) $\ell = 22.5$ mm; (c) $\ell = 27$ mm; (d) $\ell = 31.5$ mm; (e) $\ell = 36$ mm; (f) $\ell = 40.5$ mm; (g) $\ell = 45$ mm; and (h) $\ell = 49.5$ mm. The animations (a), (b), (c), and (d) show the spatiotemporal evolution of V_m for the cases of plots (a), (c), (e), and (g), respectively. The local data recorded from a representative point ($x = 112.5$ mm, $y = 112.5$ mm), shown by asterisks. Here, $\ell = 27$ mm is the smallest size of inhomogeneity that require to anchor a spiral around it. Figure (i) shows the rotation period of a stable spiral that attached to inhomogeneity.

a spiral wave has $\ell = 27$ mm. Figure 2.22(i), a plot of the rotation period τ_{rot} , of such an anchored spiral wave, versus ℓ , shows how τ_{rot} increases with ℓ .

The analogs of Figs. 2.22(a)-(i) and Video S10 are shown in Figs. 2.23(a)-(i) and Video S11, respectively, for the P7 parameter set for the TNNP04 model; here we fix the top-right corner of the obstacle at ($x = 90$ mm, $y = 90$ mm) rather than top-left corner as in Fig. 2.22; and we observe that the smallest inhomogeneity which is required to anchor a spiral around it, has $\ell = 22.5$ mm.

In Fig. 2.24, we show our results for the TP06 model with P1 parameter set (these are the exact analogs of our TNNP04 model results (Fig.2.23)) for a domain

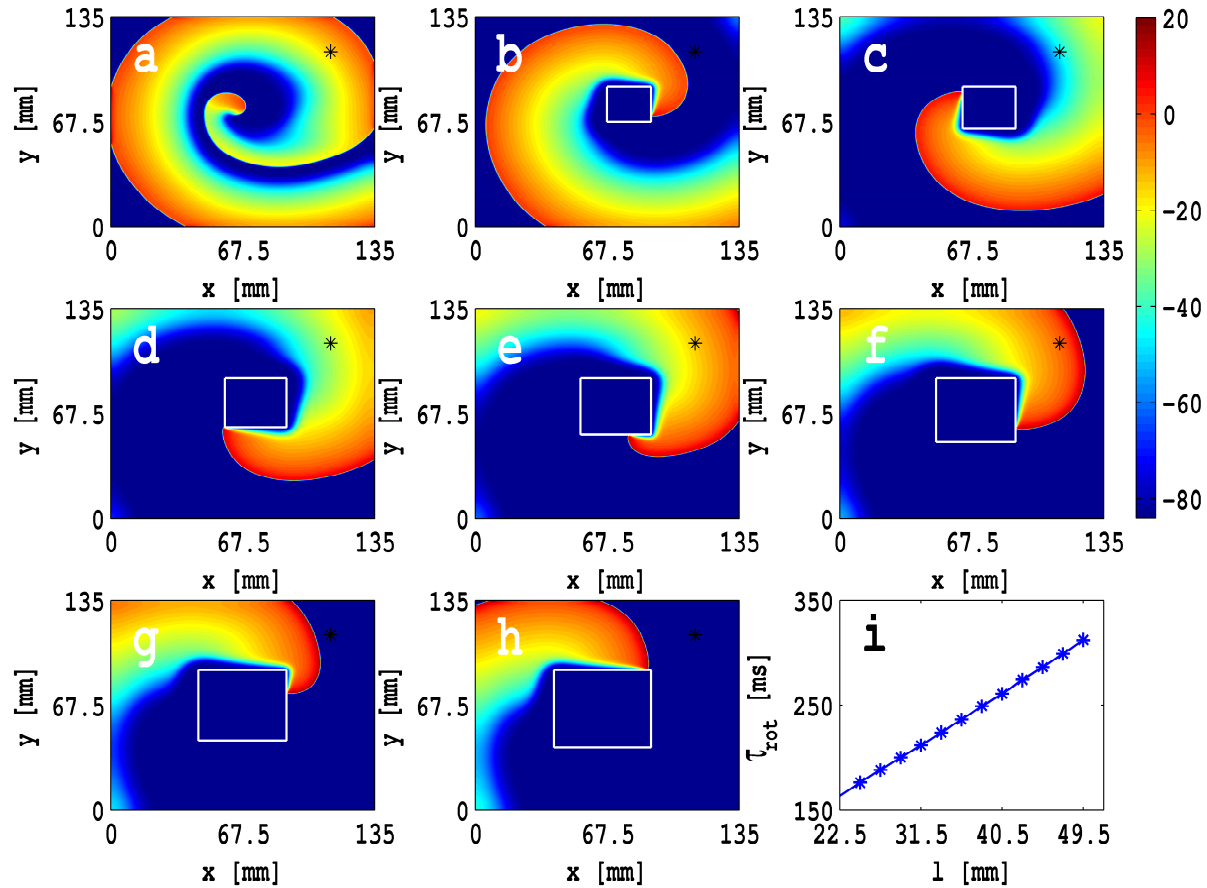


Figure 2.23: Pseudocolour plots of V_m at time, $t = 400$ ms, for the parameter set P7 in the TNNP04 model, with a square shape conduction inhomogeneity whose top-right corner is fixed at (90 mm, 90 mm): (a) $\ell = 0$, i.e., myocytes absence of inhomogeneity; (b) $\ell = 22.5$ mm; (c) $\ell = 27$ mm; (d) $\ell = 31.5$ mm; (e) $\ell = 36$ mm; (f) $\ell = 40.5$ mm; (g) $\ell = 45$ mm; and (h) $\ell = 49.5$ mm. The local data recorded from a representative point ($x = 112.5$ mm, $y = 112.5$ mm), shown by asterisks. Here, $\ell = 22.5$ mm is the smallest size of inhomogeneity that require to anchor a spiral around it. Figure (i) shows the rotation period of a stable spiral that attached to inhomogeneity.

with side $L = 512$ mm with a square obstacle whose top-left corner is fixed at ($x = 50$ mm, $y = 125$ mm); here, we observe that the smallest inhomogeneity which is required to anchor a spiral around it, has $\ell = 25$ mm.

We now check the dependence of spiral-wave dynamics on the position of the obstacle for a fixed size. Shajahan, *et al.* [25] have studied the dependence of an MST state on the positions of obstacles for the Panfilov and LRI models. In our previous studies [31], we have carried out systematic studies of such dependence for (a) an RS state and (b) an MST state, for the RPB and TNNP04 models. These studies have found that, for the parameter set for which the system evolves to an MST in the absence of an obstacle, we can obtain one of the following cases:

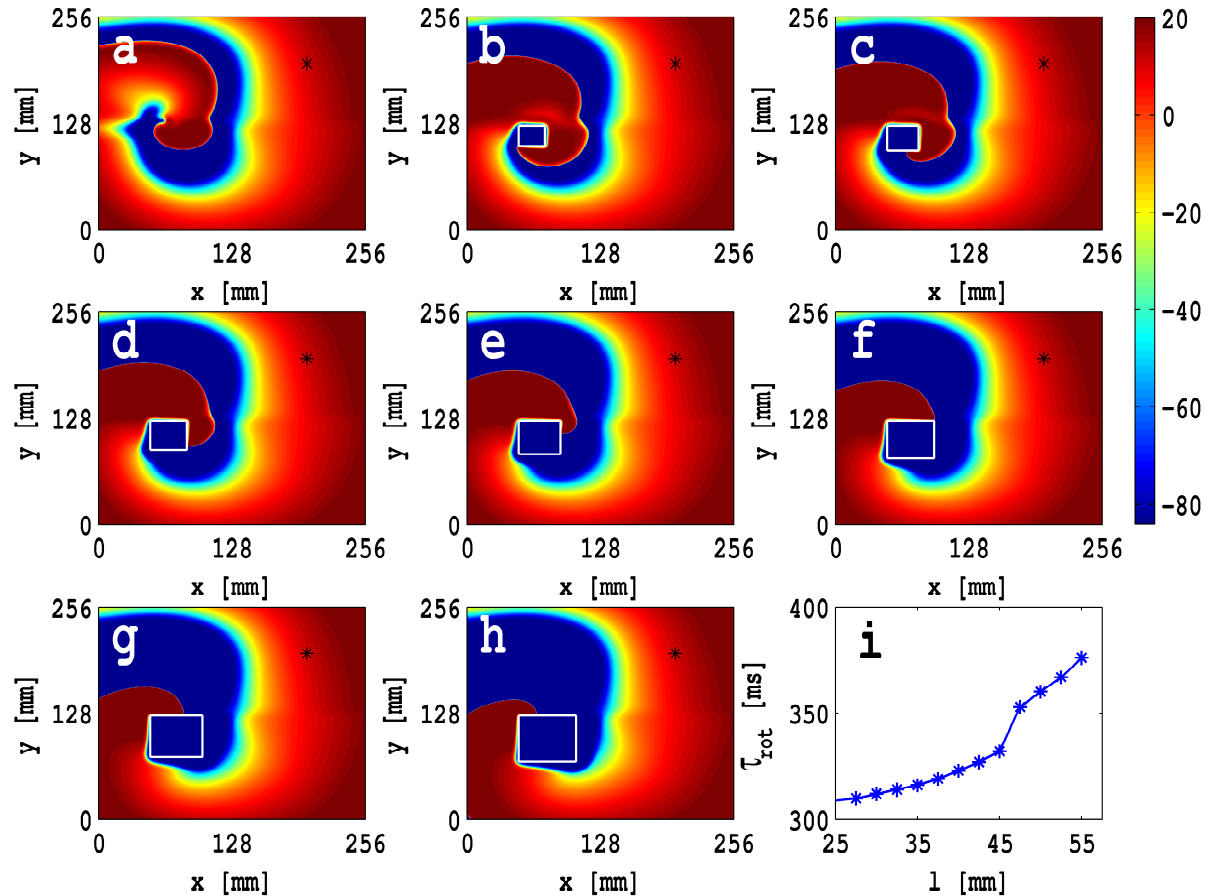


Figure 2.24: Pseudocolour plots of V_m at time, $t = 400$ ms, for the parameter set P1 in the TP06 model, with a square shape conduction inhomogeneity whose top-left corner is fixed at $(50 \text{ mm}, 125 \text{ mm})$: (a) $\ell = 0$, i.e., myocytes absence of inhomogeneity; (b) $\ell = 25$ mm; (c) $\ell = 30$ mm; (d) $\ell = 35$ mm; (e) $\ell = 40$ mm; (f) $\ell = 45$ mm; (g) $\ell = 50$ mm; and (h) $\ell = 55$ mm. The local data recorded from a representative point $(x = 200 \text{ mm}, y = 200 \text{ mm})$, shown by asterisks. Here, $\ell = 25$ mm is the smallest size of inhomogeneity that require to anchor a spiral around it. Figure (i) shows the rotation period of a stable spiral that attached to inhomogeneity.

(a) an MST state can persist; (b) the MST state can be replaced by an RS state anchored to the obstacle; (c) the MST can be replaced by a state SA where spirals are absorbed by the boundaries. We have also obtained these three types of states in the presence of an obstacle, if the parameter set evolves to an RS state rather than an MST in the absence of an obstacle as presented in our previous joint work in Ref. [31].

We turn now to check such obstacle-position dependence of spiral-wave dynamics for the TP06 model. We have found that, the parameter set P3, for which the system evolves to an MST in the absence of an obstacle, we can obtain one of the

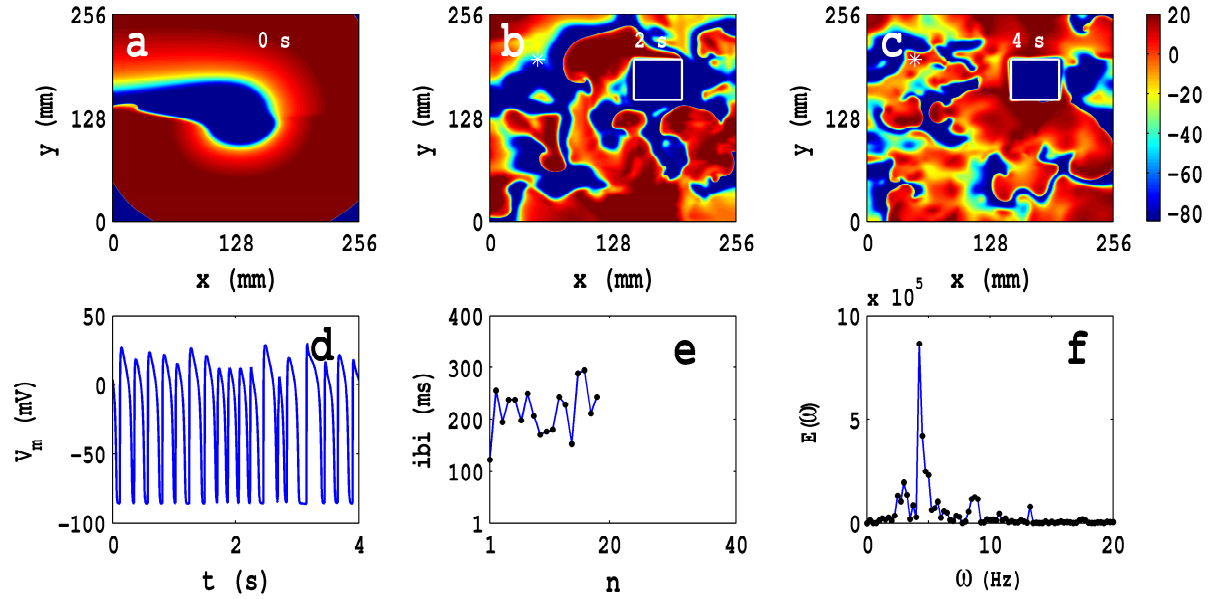


Figure 2.25: The spiral-turbulence (ST) state in the TP06 model with a square obstacle of side $\ell = 50$ mm at $(150$ mm, 150 mm) in a square simulation domain with $L = 256$ mm. We use the parameter set P3 with initial configuration (a); pseudocolor plots of V_m are shown in (a), (b), and (c) at 0, 2, and 4 s, respectively. (d) The local time series for V_m from a sample of 2×10^5 iterations taken from the representative point $(50$ mm, 200 mm), shown by an asterisk in (b) and (c); and plots of (e) the inter-beat interval (ibi) versus the beat number n from a sample time series of 2×10^5 iterations, and (f) the power spectrum of V_m obtained from a time series of length 2×10^5 iterations; the non-periodic behavior of the ibi and the broad-band nature of the power spectrum are characteristic of the spiral-turbulence state.

following states in the presence of an obstacle: (a) an MST state; (b) an RS state anchored to obstacle; (c) an SA state. We obtain similar results if we use the P1 parameter set, for which the system evolves to an RS state in the absence of an obstacle. We present below our results for the P3 parameter set in the presence of square obstacle.

In Figs. 2.25(a)-(c), we show pseudocolor plots of V_m at times $t = 0$ s, $t = 2$ s, and $t = 4$ s, respectively, for the parameter set P3 in the TP06 model with a square obstacle of side $\ell = 50$ mm and bottom left corner is fixed at $(150$ mm, 150 mm); this initial spiral configuration, with P3 parameter set, evolves to an MST state in the absence of an obstacle as shown in Fig. 4.6. The local time series of $V_m(x, y, t)$, from the representative point $(x = 50$ mm, $y = 200$ mm) (the asterisk in Figs. 2.25(b) and (c)), is shown in Fig. 2.25(d) for $0 \leq t \leq 4$ s. A plot of the inter-beat interval (ibi) and power spectrum $E(\omega)$ of a sample of 2×10^5 data points are shown in Figs. 2.25(e)

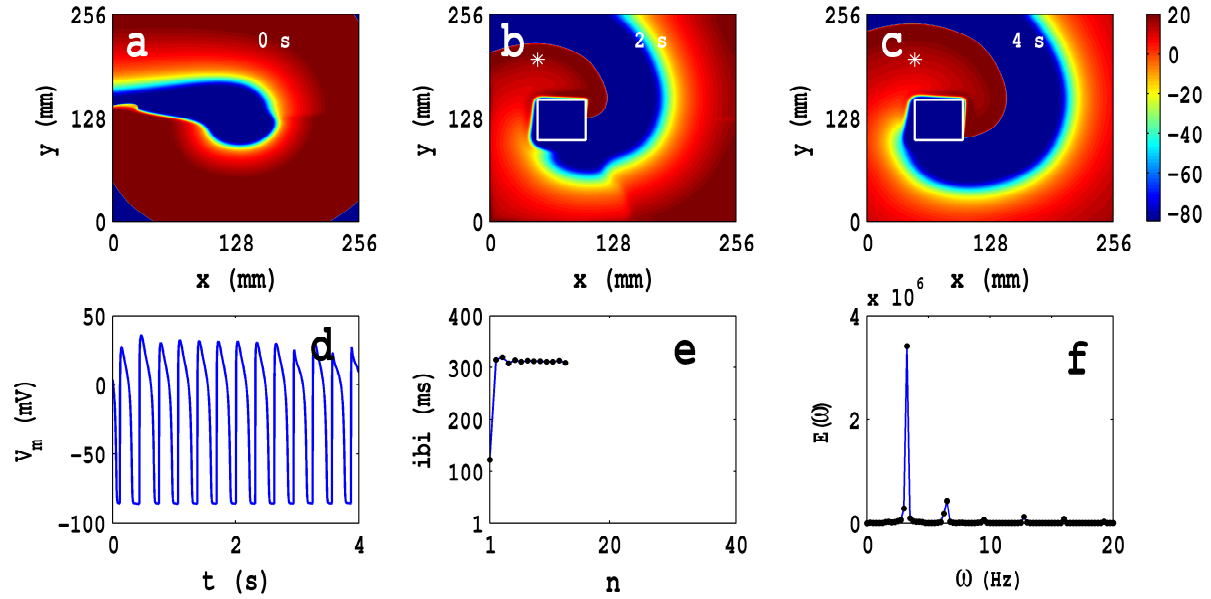


Figure 2.26: Pseudocolor plots of V_m for the TP06 model showing a spiral wave attached to a square obstacle of side 50 mm placed at (50 mm, 100 mm) and (a) $t = 0$ s, (b) $t = 2$ s, and (c) $t = 4$ s. This wave leads to periodic temporal evolution as can be seen from plots of (d) the time series of V_m from a sample of 2×10^5 iterations taken from the representative point (50 mm, 200 mm), shown by an asterisk, in the square simulation domain of side $L = 256$ mm, (e) the ibi versus the beat number n (a sample of 2×10^5) that settles, eventually, to a constant value of ≈ 309 ms, and (f) the power spectrum of V_m (from a time series of 2×10^5 iterations) that has discrete peaks at the fundamental frequency $\omega_f \approx 3.25$ Hz and its harmonics.

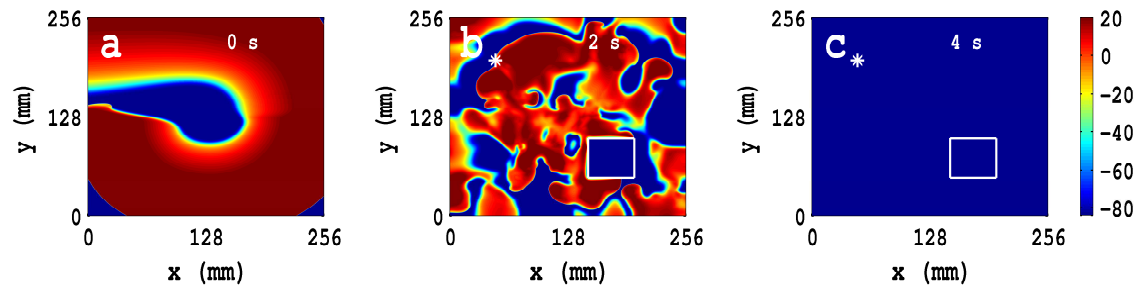


Figure 2.27: The spiral wave moves away from the square simulation domain of side $L = 256$ mm for the TP06 model with the P3 parameter set if a square obstacle of side $\ell = 50$ mm is placed at (150 mm, 50 mm) as illustrated in (a), (b), and (c) via pseudocolor plots of V_m at $t = 0$ s, $t = 2$ s, and $t = 4$ s, respectively.

and (f), respectively. The oscillating time series, non periodic ibi, and broad-band nature of power spectrum are characteristic of the state with MST.

In Figs. 2.26(a)-(g) we show, for the parameter set P3 and with a square obstacle of side $\ell = 50$ mm with its bottom-left corner fixed at (50 mm, 100 mm), the exact analogs of Figs. 2.25(a)-(g). The periodic nature of the local time series of V_m (Fig. 2.26(d)), the flattening of the ibi (Fig. 2.26(e)), and the discrete peaks in $E(\omega)$ with fundamental frequency at $\omega_f \simeq 3.25$ Hz (Fig. 2.26(a)), show that the temporal evolution of the spiral wave is periodic. And the pseudocolor plots of V_m in Figs. 2.26(b) and (c) give evidence of an RS state in which the spiral is anchored to the obstacle.

In Figs. 2.27(a)-(c) we show, for the parameter set P3 and with a square obstacle of side $\ell = 50$ mm and bottom left corner is fixed at (150 mm, 50 mm), the exact analogs of Figs. 2.25(a)-(c). The pseudocolor plot of Fig. 2.27(c) shows that the final state is an SA state.

To check the sensitive dependence of spiral-wave dynamics on the position of an obstacle, we change the position of the obstacle, whose size is fixed. Our results show that a small change of the position of the obstacle can change the final state of the system from spiral-turbulence (ST) to a rotating-spiral (RS) or spiral absorption (SA), which reflects an underlying fractal-type basin boundary between the domains of attraction of ST, RS, and SA states. We also observe similar sensitive dependence of spiral-wave dynamics on the position of an obstacle, if we use an obstacle that does not have a square shape (e.g., for a circle) [31]. For more details we refer the reader to our previous work [31].

Spiral wave with ionic inhomogeneity

Apart from obstacles, cardiac tissue also have other types of inhomogeneities that originate from the changes of physiological properties at the single-cell level; e.g., changes in the chemical environment or metabolic modifications [50] can modify the ionic current of a cell. We refer to a collection of such cells as an ionic inhomogeneity. Studies on such inhomogeneities in cardiac tissue show that they can affect the dynamics of spiral waves [28,31,44]. For example, the stability of a spiral wave in a homogeneous, 2D cardiac tissue depends on the maximal amplitude of the slow inward calcium current (governed by the conductance G_{si}) as illustrated by the numerical studies of Refs. [28,31,44] for the LRI model. In these studies, as the authors increased G_{si} , they first observed a rigidly rotating spiral wave, then one in which the spiral tip meandered quasiperiodically, and finally they obtained spiral turbulence with broken spiral waves.

Studies of ionic inhomogeneities show that they can have dramatic effects on spiral wave dynamics. Like a conduction inhomogeneity, they can eliminate spiral

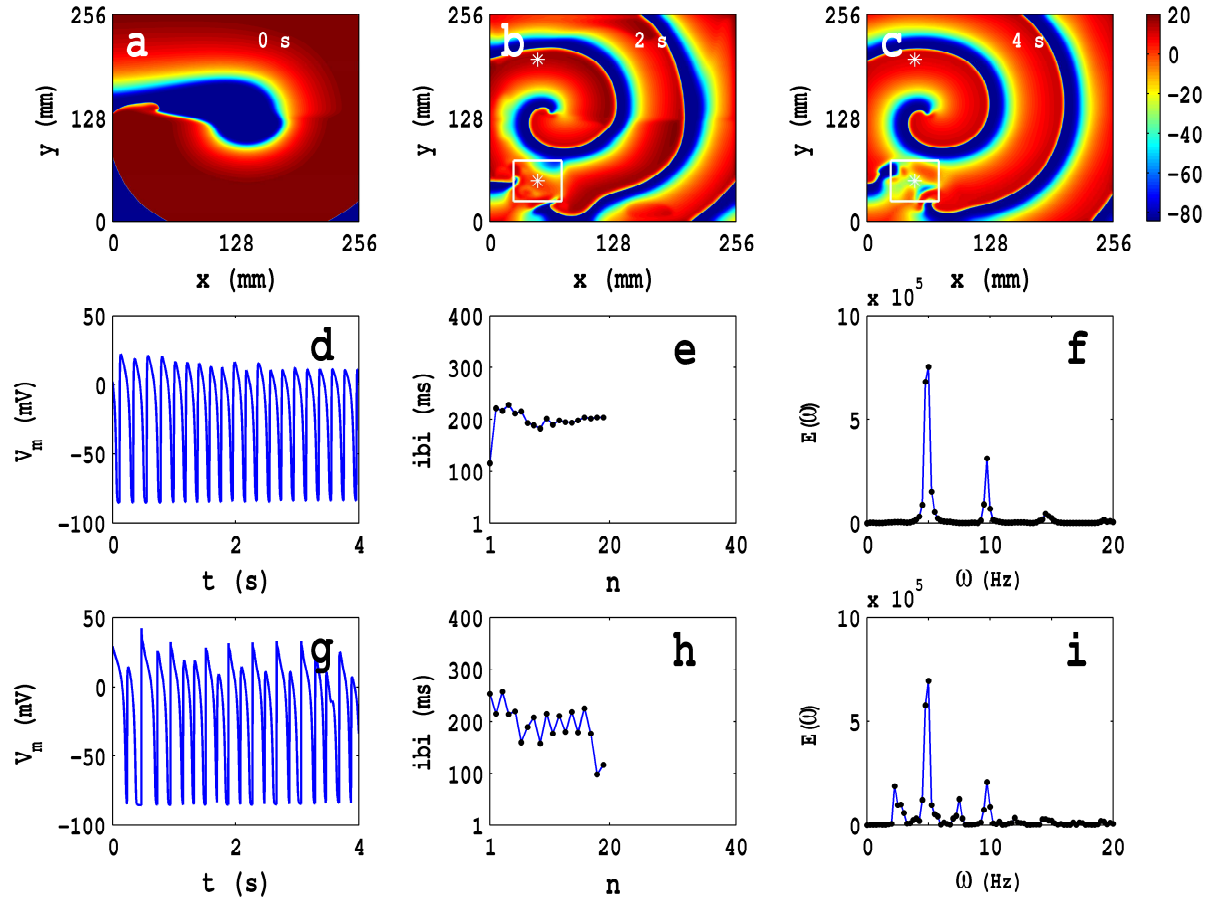


Figure 2.28: The effect of a square G_{Na} inhomogeneity, of side 50 mm in a square simulation domain of side 256 mm, with $G_{Na}^{out} = 14.838$ (maximal value) and $G_{Na}^{in} = 5 \times 14.838$, and placed at $(x = 25 \text{ mm}, y = 25 \text{ mm})$, on spiral-wave dynamics in the TP06 model: Pseudocolor plots of V_m at (a) 0 s, (b) 2 s, and (c) 4 s; (d) the time series of V_m , from a sample of the initial 2×10^5 iterations, taken from the point (50 mm, 200 mm) that lies outside the inhomogeneity. Associated plots of (e) the ibi versus the beat number n and (f) the power spectrum $E(\omega)$ of V_m indicating periodic temporal evolution with a fundamental frequency $\omega_f = 5 \text{ Hz}$ (see text); this is consistent with the average rotation period, $\tau_{rot} \simeq 202 \text{ s}$, of a spiral wave, as obtained from our ibi plot. Figures (g), (h), and (i) are the analogs of (d), (e), and (f), respectively, when data for V_m are recorded from the point (50 mm, 50 mm) that lies inside the inhomogeneity; here we have roughly quasiperiodic behavior, with a dominant peak at $\omega_1 \simeq 5 \text{ Hz}$ and a secondary peak at $\omega_2 \simeq 2.25 \text{ Hz}$.

waves, or lead to an anchored spiral, with richer dynamics than for a conduction inhomogeneity. For example, ionic inhomogeneity studies in the Panfilov model in Refs. [25, 31] show that such an inhomogeneity can lead to the coexistence of the following states in the same system: (a) spatiotemporal chaos outside the inhomogeneity and quasiperiodic behavior inside it (ST-QP); (b) an unbroken rotating spiral outside the inhomogeneity and broken spiral waves inside it (RS-ST); (c) a

spiral anchored to the inhomogeneity, with different quasiperiodic behaviour outside and inside it (QP-QP). Such complex behaviours have also been observed in numerical studies in some ionic model of cardiac tissue, like the LRI, RPB and TNNP models [31]. Here we restrict ourselves to discuss only the part of results for the TP06 model and similar results have been discussed explicitly for the Panfilov, LRI, RPB, and TNNP04 models in our previous studies [31].

We introduce a square ionic inhomogeneity of side $\ell = 50$ mm in a domain of side $L = 512$ mm, for the TP06 model, by decreasing the value of G_{Na} above its maximal value in the region of the inhomogeneity. We present below some of our representative results for the TP06 model with ionic inhomogeneities.

We use the initial spiral configuration, shown in Fig. 4.4(a), with the P1 parameter set, which evolves to a stable rotating spiral (Fig. 4.4(c)) in the absence of an ionic inhomogeneity. In Figs. 2.28 (a), (b), and (c) we show the pseudocolor plots of V_m at times $t = 0$ s, 2 s, and 4 s, respectively, for a representative, square, ionic inhomogeneity, with side $\ell = 50$ mm and the lower-left-hand corner of this square fixed at $(x = 25$ mm, $y = 25$ mm). We obtain time series for V_m from a point outside the inhomogeneity (50 mm, 200 mm) and a point inside it (50 mm, 50 mm); these points are indicated, respectively, by asterisks in Figs. 2.28 (b) and (c). In Fig. 2.28(d) we give the time series of V_m , with 2×10^5 data points, recorded from outside of inhomogeneity; Fig. 2.28 (e) shows plot of the inter-beat interval (ibi) versus the beat number n for the time series of V_m mentioned above, which shows that, after initial transients (roughly the first 10 beats), the spiral wave rotates periodically with an average rotation period $\tau_{rot} \simeq 202$ ms. The power spectrum $E(\omega)$, which follow from this time series, is given in Fig. 2.28 (f); this shows discrete peaks in $E(\omega)$ at the fundamental $\omega_f \simeq 5$ Hz and its harmonics. The periodic nature of the local time series of V_m , the flattening of the ibi, and the discrete peaks in $E(\omega)$ show that the temporal evolution of the spiral wave is periodic. The analogs of Figs. 2.28(d), (e), and (f), for the data recorded inside inhomogeneity, are shown in Figs. 2.28(g), (h), and (i), respectively. The time series, oscillating ibi, and the peaks in $E(\omega)$ show spiral-wave activation, inside the inhomogeneity, is roughly quasiperiodic behavior, with a dominant peak at $\omega_1 \simeq 5$ Hz and a secondary peak at $\omega_2 \simeq 2.25$ Hz. We also observe following dynamics, inside and outside inhomogeneities, depending on the position of the inhomogeneity: (a) quasiperiodic behaviors both outside and inside, (b) same periodic behavior outside and inside, i.e., the inhomogeneity does not have a significant qualitative effect on the dynamics of spiral waves, but the position of the spiral tip may shift to another position in the simulation domain. The spatiotemporal evolution of V_m , for an ionic inhomogeneity of side $\ell = 50$ mm

and various positions is presented in Video S12; these animations use $G_{Na}^{out} = 14.838$ (maximal value) and $G_{Na}^{in} = 5 \times 14.838$; the animations (b), (c), (d), (e), and (f) in this Video show the inhomogeneity with its left-bottom corner at $(x = 25 \text{ mm}, y = 25 \text{ mm})$, $(x = 75 \text{ mm}, y = 75 \text{ mm})$, $(x = 100 \text{ mm}, y = 100 \text{ mm})$, $(x = 125 \text{ mm}, y = 125 \text{ mm})$, and $(x = 175 \text{ mm}, y = 175 \text{ mm})$, respectively; the animation (a) shows the domain without an inhomogeneity. We also obtain similar results, if the initial configuration is a broken spiral-wave state rather than a rotating state. The coexistence of such complex periodic oscillations in an excitable medium has been reported in experiments [51]; however, the oscillations observed in these experiments are believed to be caused by the interplay of conduction inhomogeneities and partial conduction block.

2.3.5 Elimination of spiral turbulence

As we have mentioned in Sec. 5.1, there is growing consensus that the break up of spiral waves of electrical activation in ventricular tissue leads to ventricular fibrillation (VF). In the usual clinical treatment of VF electrical stimuli are applied to the affected heart. This is believed to reset all irregular waves in the ventricular tissue leaving it ready to receive the regular sinus rhythm [52]; thus, if the electrical stimulus is strong enough, it can arrest VF and restore the sinus rhythm. Initially 60 Hz AC was used clinically to defibrillate transthoracically [53] but this was later discontinued because of several reasons including the high energy requirement, the possible induction of atrial fibrillation, the prolonged muscle contraction, the risk of an electrical shock to the operator, and the size of the device [52]. Clinically available defibrillation techniques still apply massive electrical shocks to the heart; this can damage the heart muscle. The success rate of such techniques is not quite satisfactory [54]. Furthermore, scar tissues can be created during the process of such defibrillation; these can make the patient vulnerable to further arrhythmias and also act as conduction inhomogeneities that we have investigated via numerical simulations in Section 5.3. Hence, there is a great need for developing low-amplitude defibrillation schemes; this must be based on an understanding of the spatiotemporal behavior of activation waves during VF. We begin with a brief overview of some techniques that have been proposed for the elimination of spiral-wave turbulence in models for cardiac tissue.

Biktashev and Holden [55] have proposed a method for controlling spiral-wave turbulence by producing a directed movement of a rigidly rotating spiral wave away from the medium by using resonant stimulation. They find that small-amplitude, spatially uniform, repeated stimuli can be used to produce a directed movement

of the spiral wave, if the period of stimulation is equal to the period of its rotation. This directed movement eventually pushes this wave out of the simulation domain [55]. However, this method can only be used before the onset of spiral-wave turbulence.

Osipov and Collins [56] have suggested another scheme that is based on the observation that the dynamics of excitable media can be modelled by fast and slow variables, e.g, V and g in the Panfilov model. They control the slow variable by applying a weak impulse on the whole medium. This eventually changes the velocities of the front and back of the wave. The propagation of the wave front and wave back with different velocities leads to a shrinkage or expansion of the pulse width. If the amplitude and duration of the impulse are sufficiently large, then the propagating pulse collapses and disappears. Unfortunately such control of the slow variable over the whole medium can be achieved only by pharmaceutical means and not by the application of electrical pulses.

Rappel, Fenton, and Karma [57] have proposed another method based on the application of a small control current at a finite number of equally spaced “controlled cells” in a tissue, by using a coarse lattice of electrodes with a lattice spacing of about 1 cm. This method has been demonstrated to prevent one spiral from breaking up. Unfortunately this method fails in the fully developed spiral-wave turbulence state with broken spirals [29].

To suppress a spatiotemporally chaotic state with broken spiral waves, Sinha, Pande, and Pandit [29] have proposed a scheme based on the observation that spiral turbulence does not persist in the hearts of small mammals, if it can at all be initiated [58]. We will use this scheme below, so we describe it in some detail. They have shown that spiral-wave turbulence is a long-lived transient [29, 30] whose lifetime τ_L increases rapidly with the linear size L of the simulation domain, e.g., from $\simeq 850$ ms for $L = 100$ mm to $\simeq 3200$ ms for $L = 128$ mm in the two-dimensional Panfilov model; for large systems (e.g., $L > 128$ mm in the Panfilov case), τ_L is sufficiently long so that we obtain a nonequilibrium statistical steady state with spatiotemporal chaos [30]. This might suggest that a global control scheme, such as that of Osipov and Collins [56], is essential. It turns out, however, that a judicious choice of control points on a mesh leads to an efficient scheme for the control of spiral-wave turbulence in such models [29]. We first illustrate the principle of this method for a two-dimensional square domain with side L : This is divided into K^2 smaller blocks by a mesh of line electrodes, and the mesh size is chosen to be small enough that spirals cannot persist for long inside the block of side $\ell = L/K$. A voltage or current pulse is applied at all points along

the mesh boundaries for a time τ_c . This makes the mesh region refractory and so effectively simulates Neumann boundary conditions for any block bounded by the mesh. Thus spiral waves formed inside the block are absorbed at the mesh bounding the block. For example, in the Panfilov model in dimension $d = 2$, $L = 128$, and $K = 2$, a time $\tau_c = 41.2$ ms suffices to suppress spiral turbulence; when $L = 512$, and $K = 8$, a time $\tau_c = 704$ ms is required; electrical pulses of amplitude $\simeq 60 \mu\text{A}/\text{cm}^2$ are used on the control mesh; this is much less than in conventional electrical defibrillation which uses pulses of amplitude $1 \text{ A}/\text{cm}^2$. This control algorithm has been extended to suppress spiral turbulence in the two-dimensional Beeler-Reuter and LRI models [30].

Recently Zhang, *et al.* [59], have proposed another attractive scheme for the control of spiral turbulence in excitable media. In their method spiral waves are driven away by periodic forcing of V at a small number of $n \times n$ points in the center of the simulation domain. This generates target waves that eventually drive out the spiral waves if the amplitude Γ and the frequency ω_f of the forcing are chosen carefully: For example, for the Panfilov model with $d = 2$ it is shown in Ref. [59] that spiral turbulence in a square 500×500 simulation domain can be suppressed within 410,000 iterations when one chooses $n = 6$, $\omega_f = 0.82$, and $\Gamma = 6$. This control scheme is attractive because it employs *local* forcing, compared to the control scheme of Ref. [29] that uses a *spatially extended* control mesh. However, the local control scheme of Ref. [59] inadvertently generates spiral-wave break up if there are obstacles in the medium.

In the paragraph above we have given a short overview of some control schemes that have been used to suppress spiral-wave break up in two-dimensional simulation in some mathematical models for cardiac tissue. Cardiac tissue can have inhomogeneities, such as scar tissue. It is important, therefore, to study whether these control schemes are effective in controlling spiral-wave turbulence in the presence of such inhomogeneities. To the best of our knowledge this has not been investigated systematically so far. We present such an investigation here (for simplicity we restrict ourselves to conduction inhomogeneities). In particular, it is important to ensure that a control scheme does not lead inadvertently to spiral break up in the presence of inhomogeneities.

We begin by studying the control scheme of Zhang *et al.* [59] that we have outlined above. This scheme drives away broken spiral waves from the simulation domain by using the target waves that are created by the local periodic forcing. What happens to such target waves when they encounter an obstacle? It turns out that these target waves break up as they collide with the obstacle and thus contribute

to spiral turbulence in the medium [60]. Had there been no obstacle, this control scheme would have driven away all the broken spiral waves from the domain. However, this does not happen in the presence of an obstacle; hence this control scheme is unsuitable for controlling spiral-wave turbulence if inhomogeneities are present.

By contrast, the control scheme proposed in Ref. [29] works even in the presence of an inhomogeneity. Here we show how the control scheme of Ref. [29] is also successful in eliminating spiral turbulence in the complex model even in the presence of conduction inhomogeneities. We describe below the detail technique of this low-amplitude control scheme.

In this mesh-based control scheme, we apply a current pulse of amplitude 75 pA/pF for 0.2 s over a mesh that divides our square simulation domain with $L = 256$ mm into 64 square cells of side $l = 32$ mm each; this pulse makes the links of the mesh refractory and, thereby, effectively imposes Neumann boundary conditions for any block inside the mesh; therefore, spiral waves inside a block are absorbed on the links of the mesh that bound the block.

In Fig. 4.14 we illustrate spiral-wave control, via low-amplitude control pulses, in the TP06 model, in the , by presenting pseudocolor plots of V_m . The spiral state, at time $t = 0$ ms (Fig. 4.14(a) with the P1 parameter set), evolves to an RS state (Fig. 4.14(b)) at time $t = 0.2$ s; this state is suppressed, by our square-mesh control methods, as shown in Fig. 4.14(c) and , at $t = 0.2$ ms. Similar plots for the P2 and P3 parameter sets are given in Figs. 4.14(d)-(f) and Figs. 4.14(g)-(h), respectively; these illustrate square-mesh control of states with spiral turbulence. The Video S13, which comprises six animations of pseudocolor plots of V_m , shows the spatiotemporal evolution of these spiral waves, with and without control pulses, for the time interval $0 \text{ s} \leq t \leq 1 \text{ s}$.

We now study spiral-wave control in a 2D simulation domain with a square conduction inhomogeneity with side $\ell = 50$ mm. Again, we apply a control pulse of amplitude 75 pA/pF for $t = 0.2$ s over a square mesh with cells whose sides are of length $L/K = 32$ mm, i.e., the simulation domain is divided into $8^2 = 64$ square blocks. We present results for two representative cases with the P3 parameter set. Figures 3.25 (a), (b), and (c) show pseudocolor plots of V_m at times $t = 0$ s, 0.2 s, and 0.2, respectively, when the bottom left corner of the obstacle is fixed at $(x = 50 \text{ mm}, y = 75 \text{ mm})$; the animation at the left-panel of Video S14 shows the spatiotemporal evolution of V_m in the absence and presence of the control pulse. The pseudocolor plots and animations show that the single spiral that is attached to the obstacle, in the absence of the control pulse, can be removed by our low-amplitude, mesh-based, control scheme. Pseudocolor plots and animations, similar

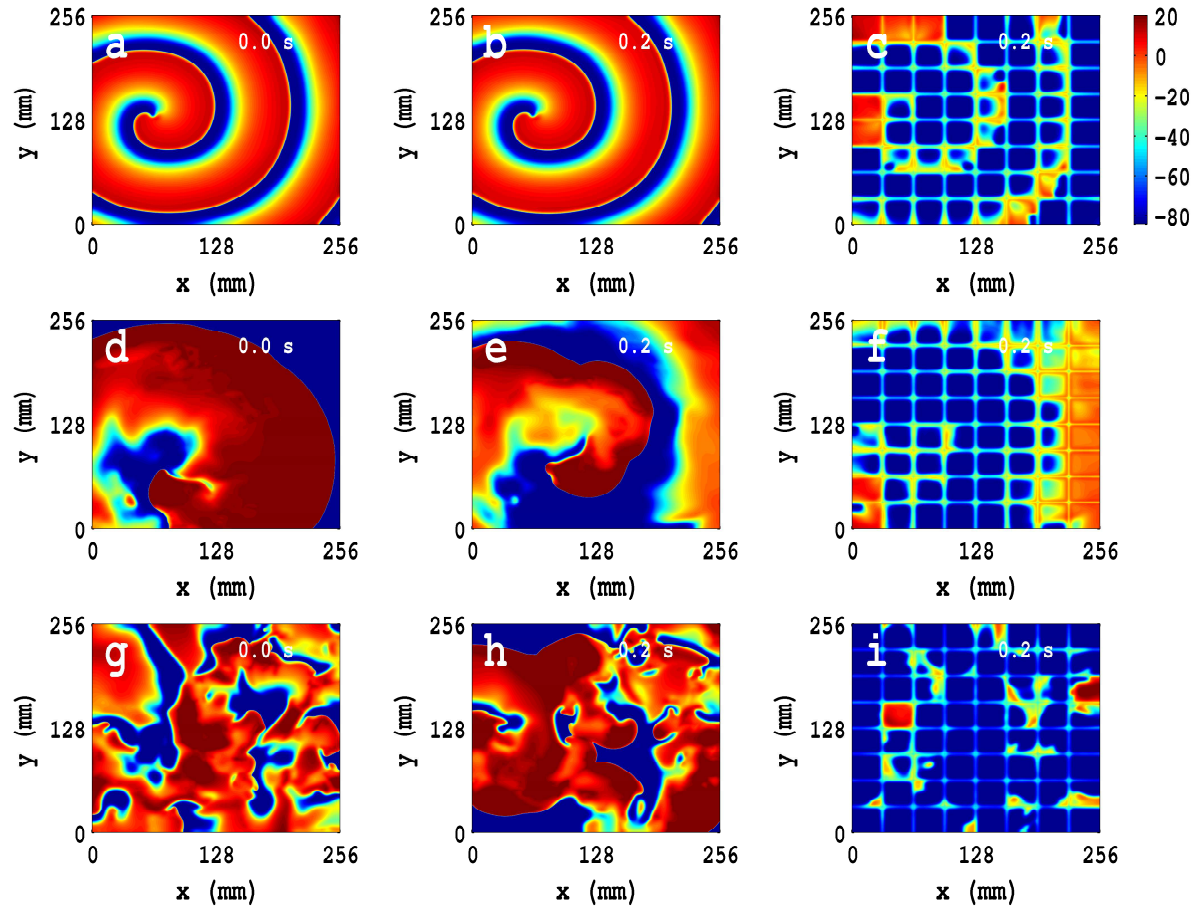


Figure 2.29: Spiral-wave control in the TP06 model for the homogeneous domain by low-amplitude control pulses (see text). The spiral state, at time $t = 0$ s (a), with the parameter set P1, evolves, in the absence of the control, to an RS state (b), at time $t = 0.2$ s; this state is suppressed by the square-mesh control method as shown in (c), at $t = 0.2$ s. Similar plots for the sets P2 and P3 parameter sets are given, respectively, in (d)-(f) and (g)-(h). The Video S18, which comprises six animations of pseudocolor plots of V_m , shows the spatiotemporal evolution of these spiral waves, with and without control pulses, for the time interval $0 \leq t \leq 1$ s. In all these cases, we apply a control pulse of amplitude 75 pA/pF for $t = 0.2$ ms.

to those in Figs. 3.25(a)-(c) and Video S14 (a) and (c), are shown in Figs. 3.25(d)-(e) and animations (c) and (d), respectively, for an MST state with the bottom-left corner of the obstacle fixed at $(x = 125 \text{ mm}, y = 125 \text{ mm})$. The plots in Figs. 3.25 and animations in Video S14 show that the states RS and MST, with an obstacle, can be controlled successfully by our mesh-bashed, low-amplitude, control scheme. Thus, we conclude that the low-amplitude mesh-based control scheme is an effective control method for the suppression of various types of spiral-wave states in the absence and the presence of inhomogeneities.

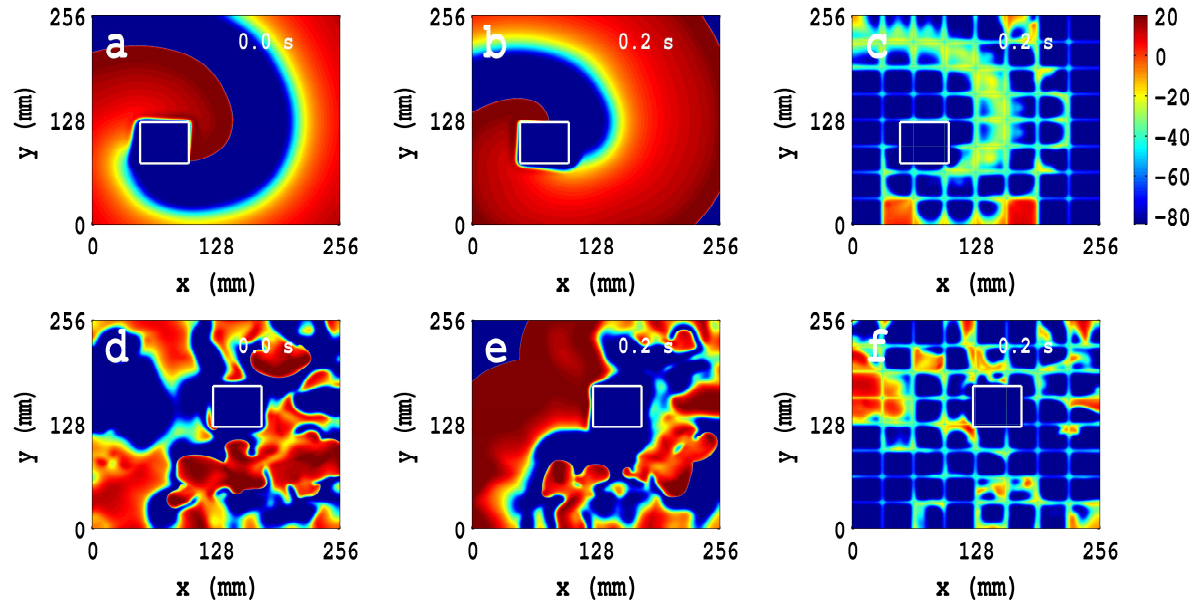


Figure 2.30: Spiral-wave control in the TP06 model in the presence of a square shape conduction inhomogeneity of size $\ell = 50$ mm by low-amplitude control pulses (see text). The spiral state, at time $t = 0$ s (a), with the parameter set P3 and an obstacle whose bottom-left corner is fixed at $(x = 50 \text{ mm}, y = 75 \text{ mm})$, evolves, in the absence of control, to an RS state (b) that is anchored to the obstacle, at time $t = 0.2$ s; this state is suppressed by the square-mesh control method as shown in (c), at $t = 0.2$ s. Similar plots for the P3 parameter set and an obstacle whose bottom-left corner is fixed at $(x = 125 \text{ mm}, y = 125 \text{ mm})$ are given, respectively, in (d)-(f) for the ST state. The Video S14, which comprises four animations of pseudocolor plots of V_m , shows the spatiotemporal evolution of these spiral waves, with and without control pulses, for the time interval $0 \leq t \leq 1$ s. In all these cases we apply a control pulse of amplitude 75 pA/pF for $t = 0.2$ ms. These plots and animations show that the states RS and MST, with an obstacle, can be controlled successfully by our mesh-bashed, low-amplitude, control scheme.

2.4 Discussion and Conclusion

We have presented the most extensive numerical study carried out so far of the effects of inhomogeneities on spiral-wave dynamics in mathematical models for cardiac tissue. In particular, we have investigated such dynamics in the TNNP04 and TP06 models for homogeneous simulation domains and also in the presence of conduction and ionic inhomogeneities. Furthermore, we have considered a low-amplitude control scheme in detail; this has been designed to eliminate spiral-wave turbulence in these models but has not been tested systematically in the presence of inhomogeneities; we carry out such tests here.

One of the principal results of our studies is the confirmation that spiral-wave dynamics in mathematical models of cardiac tissue depends very sensitively on the positions of conduction or ionic inhomogeneities in the simulation domain. Our results here extend significantly those presented in Ref. [25] for the Panfilov and LRI models. In particular, we have shown that this sensitive dependence on inhomogeneities also holds in realistic ionic models, which account for ion pumps and ion exchangers and also the details of the dynamics of calcium ions; and the nature of the inhomogeneity also affects the spatiotemporal dynamics of spiral waves as can be seen by comparing our simulations of conduction inhomogeneities with those for ionic inhomogeneities. As we have seen, in the latter case the transmembrane potential V_m displays rich and different temporal behaviors inside and outside the ionic inhomogeneity. We believe this sensitive dependence of spiral waves on inhomogeneities in the medium is a reflection of a fractal basin boundary between the domains of attraction of spiral-turbulence (ST), rotating-spiral (RS), and quiescent (Q) states. In a low-dimensional dynamical system it is possible to obtain such a basin boundary by changing initial conditions; in a high-dimensional dynamical system (the partial-differential-equation models for cardiac tissue are infinite dimensional) it is not practical to find such a boundary numerically. We have shown instead, that, by changing parameters in these cardiac-tissue models, such as the positions or natures of inhomogeneities, we can affect the spatiotemporal evolution of spiral waves drastically.

Our studies have practical implications for experimental investigations of spiral-wave dynamics in cardiac tissue. In particular, the studies of Refs. [19–21, 51] have provided a rich variety of results including complicated temporal patterns in inter-beat intervals [51] for V_m and the partial or complete elimination of spiral-wave turbulence by conduction inhomogeneities [9]. We have described these briefly in the introduction. Here we would like to note that our *in silico* simulations of spiral-wave dynamics in the TNNP04 and TP06 models have allowed us to carry out a much more systematic study of inhomogeneities in these models than is possible *in vitro* and *in vivo*. We hope our work will stimulate experiments in this field. It is worth noting that our study yields all the types of rich spatiotemporal behaviors (e.g., for V_m) that have been observed in a variety of experiments on spiral-wave dynamics in cardiac tissue or cell cultures, if we keep in mind that the states ST, RS, and Q in our simulations are the analogs of VF, VT, and quiescence in such experiments.

Our results, especially those on the elimination of spiral-wave turbulence in the presence of inhomogeneities, should also have important implications for the

development of low-amplitude electrical defibrillation schemes, which is a major challenge that lies at the interfaces between nonlinear science, biophysics, and biomedical engineering. One of the lessons of our numerical studies, namely, the sensitive dependence of spiral-wave dynamics on inhomogeneities, implies that low-amplitude defibrillation schemes might well have to be tuned suitably to account for inhomogeneities in cardiac tissue. Furthermore, it would be very interesting to develop the mesh-based control scheme that we have described in the previous section and to see how it might be realised experimentally.

As we have emphasized throughout this paper, one of the principal goals of our study is a qualitative one, namely, the elucidation of the sensitive dependence of spiral-wave dynamics on inhomogeneities in mathematical models of cardiac tissue. We have, therefore, carried out extensive simulations of such dynamics in the TNNP04 and TP06 models; but we have not, so far, extended our study to bidomain models [61] and models in which mechanics [62] is also included. We expect our principal qualitative results about inhomogeneities will go through even when such models are considered; this will have to be checked explicitly by subsequent studies.

Parameter sets	G_{Na} (nS/pF)	G_{CaL} (nS/pF)	G_{to} (nS/pF)	G_{Ks} (nS/pF)	G_{Kr} (nS/pF)	G_{K1} (nS/pF)	Video	Final state
P0	14.838	0.000175	0.294	0.245	0.096	5.405	S03(a)	SRS with fundamental peak $\omega_f \approx 3.75$ Hz
P1	1.85475	0.000175	0.294	0.245	0.096	5.405	S03(b)	DRS with fundamental peak $\omega_f \approx 2.75$ Hz
P2	7.419	0.000175	0.294	0.245	0.096	5.405	S03(c)	SRS with fundamental peak $\omega_f \approx 3.5$ Hz
P3	29.676	0.000175	0.294	0.245	0.096	5.405	S03(d)	SMST with first dominant peak $\omega_f \approx 3.75$ Hz
P4	59.352	0.000175	0.294	0.245	0.096	5.405	S03(e)	SMQP with fundamental peaks $\omega_1 \approx 4$ Hz and $\omega_2 \approx 8.25$ Hz
P5	118.704	0.000175	0.294	0.245	0.096	5.405	S03(f)	SA
P6	14.838	0	0.294	0.245	0.096	5.405	S04(b)	DRS with first dominant peak $\omega_f \approx 8$ Hz
P7	14.838	0.00001	0.294	0.245	0.096	5.405	S04(c)	Three RS with first dominant peak $\omega_f \approx 7.75$ Hz
P8	14.838	0.00002	0.294	0.245	0.096	5.405	S04(d)	SRS with first dominant peak $\omega_f \approx 6.25$ Hz
P9	14.838	0.00004	0.294	0.245	0.096	5.405	S04(e)	SA
P10	14.838	0.00035	0.294	0.245	0.096	5.405	S04(e)	SSQP with fundamental peaks $\omega_1 \approx 3.25$ Hz and $\omega_2 \approx 6.75$ Hz
P11	14.838	0.000175	0.588	0.245	0.096	5.405	S05(b)	SSQP with fundamental peaks $\omega_1 \approx 3.75$ Hz and $\omega_2 \approx 7.75$ Hz
P12	14.838	0.000175	1.176	0.245	0.096	5.405	S05(c)	SSQP with fundamental peaks $\omega_1 \approx 3.75$ Hz and $\omega_2 \approx 7.75$ Hz
P13	14.838	0.000175	2.352	0.245	0.096	5.405	S05(d)	SSQP with fundamental peaks $\omega_1 \approx 3.75$ Hz and $\omega_2 \approx 7.5$ Hz
P14	14.838	0.000175	0.294	0.98	0.096	5.405	S06(b)	SRS with fundamental peak $\omega_f \approx 4.75$ Hz
P15	14.838	0.000175	0.294	3.92	0.096	5.405	S06(c)	SRS with fundamental peak $\omega_f \approx 6$ Hz
P16	14.838	0.000175	0.294	15.68	0.096	5.405	S06(d)	SRS with fundamental peak $\omega_f \approx 7.75$ Hz

Parameter sets	G_{Na} (nS/pF)	G_{CaL} (nS/pF)	G_{to} (nS/pF)	G_{Ks} (nS/pF)	G_{Kr} (nS/pF)	G_{K1} (nS/pF)	Video	Final state
P17	14.838	0.000175	0.294	0.245	0.192	5.405	S07(b)	SRS with fundamental peak $\omega_f \simeq 4.25$ Hz
P18	14.838	0.000175	0.294	0.245	0.384	5.405	S07(c)	SMST
P19	14.838	0.000175	0.294	0.245	0.768	5.405	S07(d)	SMST
P20	14.838	0.000175	0.294	0.245	0.096	10.81	S08(b)	SMQP with fundamental peaks $\omega_1 \simeq 4.25$ Hz and $\omega_2 \simeq 8.75$ Hz
P21	14.838	0.000175	0.294	0.245	0.096	21.62	S08(c)	SMST
P22	14.838	0.000175	0.294	0.245	0.096	43.24	S08(d)	SMST

Table 2.1: Parameter sets used for our studies of the TNNP04, 2D, homogeneous model; we change channel conductances, associated with *major* ionic currents. The abbreviations are as follows: (a) SRS, single rotating spiral; (b) DRS, double rotating spiral; (c) SSQP: single spiral quasi periodic; (d) SMQP, single meandering quasiperiodic; (e) SMST, single meandering spiral turbulence; (f) MST, multiple spiral turbulence; and (g) SA, spiral absorption.

Parameter sets	G_{Na} nS/pF	G_{kr} nS/pF	G_{ks} nS/pF	G_{pCa} nS/pF	G_{pK} nS/pF	σ_f	Video	Final state
P1	14.838	0.153	0.392	0.1238	0.0146	1	S09(a)	RS with fundamental peak $\omega_1 \simeq 4.75$ Hz
P2	5×14.838	0.153	0.392	0.1238	0.0146	1	S09(b)	SMST
P3	14.838	0.172	0.441	0.8666	0.00219	2	S09(c)	MST

Table 2.2: Parameter sets used for our study of the TP06, 2D, homogeneous model; we change the channel conductances, associated with the ionic, currents and time constants to obtain three major spiral states, namely, single rotating spiral (SRS), single meandering spiral turbulence (SMST), and multiple spiral turbulence (MST), for the parameter sets P1, P2, and P3, respectively. Here, σ_f is the scale factor of the time constant τ_f (see Appendix).

1 Supporting Information

Video S01: Spatiotemporal evolution of a plane wave in a cable-type domain, for the TNNP04 model, shown via 2D pseudocolor plots (top panel) and 3D pseudocolor plots (bottom panel) of the transmembrane potential V_m ; the time evolution is shown for $0 \text{ s} \leq t \leq 0.8 \text{ s}$; we use 10 frames per second (fps); in real time each frame is separated from the succeeding frame by 2 ms.

Video S02: Spatiotemporal evolution of circular waves for, the TNNP04 model, produced by an application of a point stimulus at the middle of the our square simulation domain; the time evolution of 2D pseudocolor plots (left panel), contour plots (middle panel), and 3D pseudocolor plots (right panel) of the transmembrane potential V_m are shown for $0 \text{ s} \leq t \leq 0.4 \text{ s}$; we use 10 frames per second (fps); in real time each frame is separated from the succeeding frame by 2 ms.

Video S03: Spiral-wave dynamics for the TNNP04 model with the parameter sets (a) P0, (b) P1, (c) P2, (d) P3, (e) P4, and (f) P5 (Table 2.1), which are obtained by modifying the maximal G_{Na} conductance associated with the I_{Na} ionic current. The pseudocolor plots of the transmembrane potential V_m are shown for $0 \text{ s} \leq t \leq 4 \text{ s}$; we use 10 frames per second (fps); in real time each frame is separated from the succeeding frame by 8 ms.

Video S04: Spiral-wave dynamics for the TNNP04 model with the parameter sets (a) P0, (b) P6, (c) P7, (d) P8, (e) P9, and (f) P10 (Table 2.1), which are obtained by modifying the maximal G_{Ca} conductance associated with the I_{CaL} ionic current. The pseudocolor plots of the transmembrane potential V_m are shown for $0 \text{ s} \leq t \leq 4 \text{ s}$; we use 10 frames per second (fps); in real time each frame is separated from the succeeding frame by 8 ms.

Video S05: Spiral-wave dynamics for the TNNP04 model with the parameter sets (a) P0, (b) P11, (c) P12, and (d) P13 (Table 2.1), which are obtained by modifying the maximal G_{to} conductance associated with the I_{to} ionic current. The pseudocolor plots of the transmembrane potential V_m are shown for $0 \text{ s} \leq t \leq 4 \text{ s}$; we use 10 frames per second (fps); in real time each frame is separated from the succeeding frame by 8 ms.

Video S06: Spiral-wave dynamics for the TNNP04 model with the parameter sets (a) P0, (b) P14, (c) P15, and (d) P16 (Table 2.1), which are obtained by modifying the maximal G_{Ks} conductance associated with the I_{Ks} ionic current. The pseudocolor plots of the transmembrane potential V_m are shown for $0 \text{ s} \leq t \leq 4 \text{ s}$; we use 10 frames per second (fps); in real time each frame is separated from the succeeding frame by 8 ms.

Video S07: Spiral-wave dynamics for the TNNP04 model with the parameter sets (a) P0, (b) P17, (c) P18, and (d) P19 (Table 2.1), which are obtained by modifying the maximal G_{Kr} conductance associated with the I_{Kr} ionic current. The pseudocolor plots of the transmembrane potential V_m are shown for $0 \text{ s} \leq t \leq 4 \text{ s}$; we use 10 frames per second (fps); in real time each frame is separated from the succeeding frame by 8 ms.

Video S08: Spiral-wave dynamics for the TNNP04 model with the parameter sets (a) P0, (b) P20, (c) P21, and (d) P22 (Table 2.1), which are obtained by modifying the maximal G_{K1} conductance associated with the I_{K1} ionic current. The pseudocolor plots of the transmembrane potential V_m are shown for $0 \text{ s} \leq t \leq 4 \text{ s}$; we use 10 frames per second (fps); in real time each frame is separated from the succeeding frame by 8 ms.

Video S09: Spiral-wave dynamics for the TP06 model with the parameter sets (a) P0, (b) P1, and (c) P3 (Table 2.2), which are obtained by modifying the maximal channel conductances, associated with the ionic currents and time constants. The pseudocolor plots of the transmembrane potential V_m are shown for $0 \text{ s} \leq t \leq 4 \text{ s}$; we use 10 frames per second (fps); in real time each frame is separated from the succeeding frame by 8 ms.

Video S10: Spiral-wave dynamics for the TNNP04 model with the P1 parameter set in the presence of a square conduction inhomogeneity whose top-left corner is fixed at $(x = 67.5 \text{ mm}, y = 90 \text{ mm})$. (a) $\ell = 0$ i.e., a homogeneous domain, (b) $\ell = 27 \text{ mm}$, (c), $\ell = 36 \text{ mm}$, and (d) $\ell = 45 \text{ mm}$. The pseudocolor plots of the transmembrane potential V_m are shown for $0 \text{ s} \leq t \leq 1 \text{ s}$; we use 10 frames per second (fps); in real time each frame is separated from the succeeding frame by 8 ms.

Video S11: Spiral-wave dynamics for the TNNP04 model with the P7 parameter set in the presence of a square conduction inhomogeneity whose top-right corner is fixed at $(x = 90 \text{ mm}, y = 90 \text{ mm})$. (a) $\ell = 0$ i.e., a homogeneous domain, (b) $\ell = 27 \text{ mm}$, (c), $\ell = 36 \text{ mm}$, and (d) $\ell = 45 \text{ mm}$. The pseudocolor plots of the transmembrane potential V_m are shown for $0 \text{ s} \leq t \leq 1 \text{ s}$; we use 10 frames per second (fps); in real time each frame is separated from the succeeding frame by 8 ms.

Video S12: Spiral-wave dynamics for the TP06 model in the presence of a square ionic inhomogeneity, of side $\ell = 50 \text{ mm}$, for the case of $G_{Na}^{out} = 14.838$ (maximal value) and $G_{Na}^{in} = 5 \times 14.838$, and the lower left-bottom corner of the inhomogeneity at different positions. (a) Homogeneous domain, (b) $(x = 25 \text{ mm}, y = 25 \text{ mm})$, (c) $(x = 75 \text{ mm}, y = 75 \text{ mm})$, (d) $(x = 100 \text{ mm}, y = 100 \text{ mm})$, (e) $(x = 125 \text{ mm}, y = 125 \text{ mm})$, and (f) $(x = 175 \text{ mm}, y = 175 \text{ mm})$. The pseudocolor plots of the transmembrane potential

V_m are shown for $0 \text{ s} \leq t \leq 4 \text{ s}$; we use 10 frames per second (fps); in real time each frame is separated from the succeeding frame by 8 ms.

Video S13: Spiral-wave dynamics for the homogeneous TP06 model without and with control pulses for the parameter sets P1 (left-panel), P2 (middle-panel), and P3 (right-panel). The pseudocolor plots of the transmembrane potential V_m are shown for $0 \text{ s} \leq t \leq 1 \text{ s}$; we use 10 frames per second (fps); in real time each frame is separated from the succeeding frame by 8 ms.

Video S14: Spiral-wave dynamics for the TP06 model without and with control pulses in the presence of a square conduction inhomogeneity of side $\ell = 50 \text{ mm}$, and bottom-left corners at $(x = 50 \text{ mm}, y = 75 \text{ mm})$ (left-panel) and $(x = 125 \text{ mm}, y = 125 \text{ mm})$ (right-panel). The pseudocolor plots of the transmembrane potential V_m are shown for $0 \text{ s} \leq t \leq 1 \text{ s}$; we use 10 frames per second (fps); in real time each frame is separated from the succeeding frame by 8 ms.

Bibliography

- [1] Panfilov AV (1998) Spiral breakup as a model of VF. *Chaos* 8:57.
- [2] Luo C, Rudy Y (1991) A model of the ventricular cardiac action potential. *Circ Res* 68:1501.
- [3] ten Tusscher KHWJ, Noble D, Noble PJ, Panfilov AV (2004) A model for human ventricular tissue. *Am J Physiol Heart Circ Physiol* 286:H 1573.
- [4] Bernus O, Wilders R, Zemlin CW, Versschelde H, Panfilov AV (2002) A computationally efficient electrophysiological model of human ventricular cells. *Am J Physiol Heart Circ Physiol* 282:H2296.
- [5] ten Tusscher KH, Panfilov AV (2006) Alternans and spiral breakup in a human ventricular tissue model. *Am J Physiol Heart Circ Physiol* 291: H1088.
- [6] American Heart Association (2001) *Heart and Stroke*, Statistical update. (AHA, Dallas, 2001).
- [7] Roger VL, Go AS, Lloyd-Jones DM, *et al.* (2011) Heart disease and stroke statistics-2011 update: a report from the American Heart Association. *Circulation* 123(4):e18-e209.
- [8] Davidenko JM, Kent PF, Chialvo DR, Michaels DC, Jalife J (1990) Sustained vortex-like waves in normal isolated ventricular muscle. *Proc Natl Acad Sci USA* 87:8785.
- [9] Davidenko JM, Perstov AM, Salomonsz R *et al.* (1992) Stationary and drifting spiral waves of excitation in isolated cardiac muscle. *Nature* 355:349.
- [10] Jalife J, Gray RA, Morley GE, Davidenko JM (1998) Self organization and the dynamical nature of ventricular fibrillation. *Chaos* 8:5764.
- [11] Winfree AT (1998) Evolving perspectives during 12 years of electrical turbulence. *Chaos* 12:1.

- [12] Christini DJ, Glass L (2002) Introduction : Mapping and control of complex cardiac arrhythmias. *Chaos* 12:732.
- [13] Gray RA, Pestov AM, Jalife J (1998) Spatial and temporal organization during cardiac fibrillation. *Nature* 392:75.
- [14] Massè S, Downar E, Chauhan V, Sevaptisidis E, Nanthakumar K (2007) Ventricular fibrillation in myopathic human hearts: mechanistic insights from in vivo global endocardial and epicardial mapping. *Am J Physiol Heart Circ Physiol* 292:H2589.
- [15] Nash MP, Mourad A, Clayton RH, Sutton PM, Bradley CP, et al. (2006) Evidence for multiple mechanisms in human ventricular fibrillation. *Circulation* 114:530.
- [16] Luo C, Rudy Y (1994) A dynamic model of the cardiac ventricular action potential. 1. simulations of ionic currents and concentration changes. *Circ Res* 74:1071.
- [17] Priebe L, Beuckelmann J (1998) Simulation study of cellular electric properties in heart failure. *Circ Res* 82:1206.
- [18] Iyer V, Mazhari R, Winslow R (2004) A computational model of the human left-ventricular epicardial myocyte. *Biophys J* 87:1507.
- [19] Ikeda T, Yashima M, Uchida T, Hough D, Fishbein MC, et al. (1997) Attachment of meandering reentrant wavefronts to anatomic obstacles in the atrium. *Circ Res* 81:753.
- [20] Valderrabano M, Kim YH, Yashima M, Wu TJ, Karagueuzian HS, et al. (2000) Obstacle-induced transition from ventricular fibrillation to tachycardia in isolated swine right ventricles. *J Am Coll Cardiol* 36:2000.
- [21] Lim ZY, Maskara B, Aguel F, Emokpae R, Tung L (2006) Spiral wave attachment to millimeter-sized obstacles. *Circulation* 114:2113.
- [22] Xie F, Qu Z, Garfinkel A (1998) Dynamics of reentry around a circular obstacle in cardiac tissue. *Phys Rev E* 58:6355.
- [23] ten Tusscher KHWJ, Panfilov A (2003) Influence of nonexcitable cells on spiral breakup in two-dimensional and three-dimensional excitable media. *Phys Rev E* 68:062902.

- [24] Starobin JM, Starmer CF (1996) Boundary-layer analysis of waves propagating in an excitable medium: Medium conditions for wave-frontobstacle separation. *Phys Rev E* 54:430.
- [25] Shajahan TK, Sinha S, Pandit R (2007) Spiral-wave dynamics depends sensitively on inhomogeneities in mathematical models of ventricular tissue. *Phys Rev E* 75:011929.
- [26] Shajahan TK, Sinha S, Pandit R (2005) Spatiotemporal chaos and spiral turbulence in models of cardiac arrhythmias. *Proceedings of Indian National Science Academy* 71 A:4757.
- [27] Qu Z, Garfinkel FXA, Weiss JN (2000) Origin of spiral wave meander and breakup in a two-dimensional cardiac tissue model. *Ann BioMed Engg* 28:755.
- [28] Xie F, Qu Z, Garfinkel A, Weiss JN (2001) Electrophysiological heterogeneity and stability of reentry in simulated cardiac tissue. *Am J Physiol Heart Circ Physiol* 280:H535.
- [29] Sinha S, Pande A, Pandit R (2001) Defibrillation via the elimination of spiral turbulence in model for ventricular fibrillation. *Phys Rev Lett* 86:3678.
- [30] Pandit R, Pande A, Sinha S, Sen A (2002) Spiral turbulence and spatiotemporal chaos: Characterization and control in two excitable media. *Physica A* 306:211.
- [31] Shajahan TK, Nayak AR, Pandit R (2009) Spiral-wave turbulence and its control in the presence of inhomogeneities in four mathematical models of cardiac tissue. *PLoS One* 4(3): e4738.
- [32] Kenner J, Sneyd J (1998) *Mathematical Physiology*. Springer-Verlag New York, Inc. New York, NY, USA.
- [33] Panfilov AV, Holden AV (1996) *Computational Biology of the Heart*. Wiley.
- [34] Clayton R, Panfilov A (2008) A guide to modelling cardiac electrical activity in anatomically detailed ventricles. *Progress in Biophysics and Molecular Biology* 96:19.
- [35] The Supercomputer Education and Research Centre, IISc, Bangalore, India. <http://www.serc.iisc.ernet.in/facilities/ComputingFacilities/systems/systems.html>
- [36] Doerr T, Denger R, Doerr A, *et al.* (1990) Ionic currents contributing to the action potential in single ventricular myocytes of the guinea pig studied with action potential clamp. *Pflugers Arch* 416:230-7.

- [37] Matsuoka S, Sarai N, Kuratomi S, *et al.* (2003) Role of individual ionic current systems in ventricular cells hypothesized by a model study. *Jpn J Physiol* 53:105-23.
- [38] Fink M, Giles WR, Noble D (2006) Contributions of inwardly rectifying K^+ currents to repolarization assessed using mathematical models of human ventricular myocytes. *Phil. Trans. R. Soc. A* 364:1207-22.
- [39] Fink M, Noble D, Virag L, *et al.* (2008) Contributions of HERG K^+ current to repolarization of the human ventricular action potential. *Prog Biophys Mol Biol* 96:357-76.
- [40] Weiss JN, Chen PS, Qu Z, *et al.* (2000) Ventricular fibrillation: how do we stop the waves from breaking? *Circ Res* 87:1103-1107.
- [41] Kléber AG, Rudy Y (2004) Basic mechanisms of cardiac impulse propagation and associated arrhythmias. *Physiol Rev* 84: 431-488..
- [42] Comtois P, Kneller J, Nattel S (2005) Of circles and spirals: bridging the gap between the leading circle and spiral wave concepts of cardiac reentry. *Europace* 7: S10-S20.
- [43] Keener JP and Tyson JJ (1986) Spiral waves in the Belousov-Zhabotinskii reaction. *Physica D* 21:307-324.
- [44] Qu Z, Xie F, Garfinkel A, Weiss JN (2000) Origins of spiral wave meander and breakup in a two-dimensional cardiac tissue model. *Ann Biomed Eng* 28:755-71.
- [45] Wellner M and Pertsov AM (1997) Generalized eikonal equation in excitable media. *Physical Review E* 55:7656-7661.
- [46] Wellner M, Jalife J, and Pertsov AM (2002) Waves in excitable media: effects of wave geometry. *International Journal of Bifurcation and Chaos* 12: 1939-1951.
- [47] Pertsov AM, Wellner M, and Jalife J (1997) Eikonal relation in highly dispersive excitable media. *Phys. Rev. Lett.* 78:2656-2659.
- [48] Dierckx H, Bernus O, Verschelde H (2011) Accurate eikonal-curvature relation for wave fronts in locally anisotropic reaction-diffusion systems. *Phys Rev Lett* 107:108101.
- [49] Pertsov AM, Davidenko JM, Salomonsz R, *et al.* (1993) Spiral waves of excitation underlie reentrant activity in isolated cardiac muscle. *Circ Res* 72:631.

- [50] Carmeliet E (1999) Cardiac ionic currents and acute ischemia: From channels to arrhythmias. *Physiol Rev* 79:917.
- [51] Hwang SM, Kim TY and Lee KJ (2005) Complex-periodic spiral waves in confluent cardiac cell cultures induced by localized inhomogeneities. *PNAS* 102:10363.
- [52] Tacker WA, Geddes LA (1968) Electrical Defibrillation. *CRC*, Boca Raton, FL.
- [53] Beck CS, Pritchard WH, Feil HS (1947) Ventricular fibrillation of long duration abolished by electric shock. *J Am Med Assoc* 135:985.
- [54] Pool R (1990) Heart like a wheel. *Science* 247:1294–1295.
- [55] Biktashev VN (1998) Reentrant waves and their elimination in a model mammalian ventricular tissue. *Chaos* 8:48.
- [56] Osipov GV, Collins JJ (1999) Using weak impulses to suppress travelling waves in excitable media. *Phys Rev E* 60:54.
- [57] Rappel WJ, Fenton F, Karma A (1999) Spatiotemporal control of wave instabilities in cardiac tissue. *Phys Rev Lett* 83:456.
- [58] Kim YH, Garfinkel A (1997) Spatiotemporal complexity of ventricular fibrillation revealed by tissue mass reduction in isolated swine right ventricle. *J Clin Invest* 100:2486.
- [59] Zhang H, Hu B, Hu G (2003) Suppression of spiral waves and spatiotemporal chaos by generating target waves in excitable media. *Phys Rev E* 68:026134.
- [60] Agladze K, Keener JP, Müller SC, Panfilov A (1994) Rotating spiral waves created by geometry. *Science* 264:1746.
- [61] Sepulveda NG, Roth BJ, J P Wikswo J (1989) Current injection into a two-dimensional anisotropic bidomain. *Biophys J* 55:987.
- [62] Panfilov AV, Keldermann RH, Nash MP (2007) Drift and breakup of spiral waves in reaction diffusion mechanics systems. *Proc Natl Acad Sci USA* 104:7922.

Chapter 3

Spiral-wave dynamics in a Mathematical Model of Human Ventricular Tissue with Myocytes and Fibroblasts

*This Chapter follows closely a paper that we have submitted for publication to PLoS ONE journal. The authors are **Alok Ranjan Nayak**, TK Shajahan, AV Panfilov, and Rahul Pandit.*

3.1 Introduction

Cardiac fibroblasts, which are connective, non-myocyte cells, play a major role in producing myocyte cells, both in the early stage of heart development and after a myocardial infarction. Experimental studies [1,2] suggest that such fibroblasts can be coupled functionally with myocytes, under both physiological and pathophysiological conditions. Fibroblasts can, therefore, modulate the electrophysiological properties of cardiac tissue. However, it is not clear yet what range of values we should use for the gap-junctional conductance G_{gap} of a fibroblast-myocyte gap junction [3–5]; in intact tissue $4 \text{ nS} \lesssim G_{gap} \lesssim 6 \text{ nS}$ [3] and, in cell-culture preparations, $0.3 \text{ nS} \lesssim G_{gap} \lesssim 8.0 \text{ nS}$ [5]. The structural organization of fibroblast cells in cardiac tissue, which consists of myocyte and non-myocyte cells (e.g., fibroblasts), is still being explored [2, 6–8] for different mammalian hearts. This lack of detailed structural and functional information makes it difficult to use experimental studies to uncover the precise role that fibroblasts play in the propagation of electrical impulses and spiral waves of electrical activation in cardiac tissue. Therefore, computational studies are beginning to play an important role in the investigation of the properties of mathematical models for cardiac tissue that include myocytes and fibroblasts and a coupling between them; some of these study a single, composite

myocyte-fibroblast cell [9–12]; others have considered electrical-wave propagation in one- and two-dimensional, mathematical models for cardiac tissue, in which the fibroblasts are modelled as passive cells [11, 13, 14]. Here we build on mathematical models that couple cardiac myocytes and fibroblasts at the single-cell level to develop a mathematical model for a two-dimensional (2D) sheet of cardiac myocytes coupled to a similar sheet of fibroblasts. Our model uses the state-of-the-art ionic model for human cardiac myocytes due to ten Tusscher, Noble, Noble, and Panfilov (TNNP) [15]; we include connections between myocytes and fibroblasts via gap junctions; and we also allow for the possibility of studying *zero-sided*, *one-sided*, and *two-sided* couplings. We carry out detailed numerical studies of the propagation of electrical impulses in our myocyte-fibroblast (MF) models; these yield a variety of interesting results that we summarize below after a brief, illustrative overview of some earlier studies that have investigated single fibroblast-myocyte-cell units to determine the effects of the extra electrical load, either because of passive or active fibroblasts, in both animal- and human-ventricular-cell models [9–12].

Xie, *et al.* [9] have used two different ionic models, namely, the Luo-Rudy Phase 1 (LRI) model [16], with modified maximal conductances, and a rabbit-ventricular-cell model [17], coupled to models of passive and active fibroblasts via a gap-junctional conductance. In their passive-fibroblast studies, they have considered the ranges $0 \text{ nS} < G_f \leq 4 \text{ nS}$ and $-80 \text{ mV} \leq E_f \leq 0 \text{ mV}$ for the membrane conductance G_f and the resting membrane potential E_f of fibroblasts; and they have used $N_f = 2$ and 3 and $G_{gap} = 8 \text{ nS}$ and 3 nS , respectively, for LRI and rabbit-ventricular models, where N_f is the number of fibroblasts per myocyte and G_{gap} the gap-junctional conductance. For low values of G_f they have found that the action-potential duration (APD) is always prolonged relative to its value APD^m for an uncoupled myocyte; however, if G_f is large, then the APD is less than APD^m , if E_f is low, but greater than APD^m , if E_f is high. They have obtained similar results in models with active fibroblasts.

Sachse, *et al.* [10] have shown that the APD is prolonged relative to APD^m in an active-fibroblast model. They have employed a rat-ventricular-cell model [18] coupled to active fibroblasts with $0.1 \text{ nS} \leq G_{gap} \leq 100 \text{ nS}$ and $0 \leq N_f \leq 10$. Their study shows that the myocyte APD, measured at 90% repolarization, increases from 38.9 ms to 61.3 ms if $N_f = 10$ and $G_{gap} = 10 \text{ nS}$; however, if $N_f = 10$ and $G_{gap} = 0.1 \text{ nS}$, this APD decreases from 39.0 ms to 37.1 ms. Their studies also show that the myocyte resting membrane potential, V_{rest} , and the maximal upstroke velocity, \dot{V}_{max} , depend on N_f and G_{gap} ; e.g., if $N_f = 10$ and $G_{gap} = 100$, then V_{rest} increases from -81.1 mV , in

the absence of fibroblasts, to -80.6 mV, whereas \dot{V}_{max} decreases from 160 mV/ms to 114 mV/ms.

Jacquemet, *et al.* [11] have studied a mouse-ventricular-cell model [19] coupled to a simple fibroblast model that includes a delayed activation of the membrane current. Their study has revealed that the myocyte APD is prolonged from 14.4 ms to 14.8 ms, its action potential amplitude (APA) reduced from 115.1 mV to 114.6 mV, and there is a slight elevation of the resting membrane potential V_{rest} from -82.3 mV to -82.0 mV, when a single fibroblast is coupled to a myocyte with $G_{gap} = 4.05$ nS. They have also studied the dependence of the APA, APD, V_{rest} , and \dot{V}_{max} on N_f and G_{gap} by measuring them at a site of a myocyte cell, located in the middle of a cable, which contains 50 myocyte cells covered by a layer of fibroblasts. They have found, e.g., that (a) the APA, APD, and V_{rest} change to 93.1 mV, 19.3 ms, and -80.5 mV, respectively, from their corresponding uncoupled values 100.8 mV, 15.7 ms, and -82.3 mV, when $N_f = 10$ and $G_{gap} = 4.05$ nS, and (b) \dot{V}_{max} changes to ≈ 68 mV/ms from its uncoupled value ≈ 92 mV/ms, when $N_f = 17$ and $G_{gap} = 4.05$ nS.

MacCannell, *et al.* [12] have considered fibroblast models, principally active but also passive, coupled to a human-ventricular-myocyte model [15]. They have presented representative results for a single MF unit for the passive case, with $N_f = 2$ and 4 and $C_{f,tot}$ (the total cellular capacitance for fibroblast), G_f and E_f 6.3 pF, 0.1 nS, and -49.6 mV, respectively, to a myocyte via a gap-junctional conductance with $G_{gap} = 3$ nS; they have found that the myocyte APD *increases* from its uncoupled value 263 ms to 273 ms or 275 ms for $N_f = 2$ and 4 , respectively. By contrast, in their active-MF model, they have found that the APD *decreases* from 263 ms to 195 ms and 155 ms, respectively, when $N_f = 2$ or 4 (with the above-mentioned parameter values); furthermore, V_{rest} is elevated from its uncoupled value -86.1 mV to -85.8 mV, if $N_f = 2$, and -85.3 mV, if $N_f = 4$; and the APD shortening can be enhanced by increasing either $C_{f,tot}$ or G_{gap} ; e.g., if $N_f = 2$ the APD decreases from 263 ms to 225 ms or 207 ms, respectively, for $G_{gap} = 1$ and 2 nS, with $C_{f,tot} = 6.3$ pF, $G_f = 0.1$ nS, and $E_f = -49.6$ mV. This study also obtains similar results when it holds all parameters at the values given above but uses $C_{f,tot} = 6$ pF or 63 pF.

Both in cell culture and in intact tissue, fibroblasts can couple functionally to adjacent myocytes via a gap junction at the single-cell level by expressing either the Cx43 or the Cx45 gap-junction protein or connexin. Miragoli, *et al.* [20] have shown the expression of connexins, between fibroblasts and, at contact sites, between fibroblasts and cardiomyocytes, by studying cocultured fibroblasts coated over rat-ventricular-myocyte strands; and Gaudesius, *et al.* [21] have reported that Cx43 and Cx45 are expressed among fibroblasts and between fibroblasts and my-

ocytes when fibroblasts are inserted in cocultures of neonatal rat-heart cells in a monolayer.

Fibroblasts can play a major role in the propagation of electrical impulses in cardiac tissue. Some *cell-culture* [13, 20–22] and *in-silico* [11, 13, 14] studies have reported the suppression of impulse propagation in cardiac tissue because of fibroblasts. For example, Miragoli, *et al.* [20] have studied electrical-impulse propagation in cultured strands of myocytes coated by fibroblasts and shown that the conduction velocity CV decreases by an amount that depends on the density of fibroblasts. The work of Gaudesius, *et al.* [21] has demonstrated that conduction delay occurs because of the insertion of fibroblasts between myocytes in cultured myocyte strands; the delay depends on the number of inserted fibroblasts; and finally conduction block occurs when the length of the inserted fibroblasts exceeds $300\ \mu\text{m}$. Zlochiver, *et al.* [13] have studied the propagation of electrical impulses in a monolayer of myocytes and fibroblasts of neonatal rats; in one set of experiments they have either increased or decreased the gap-junction coupling by over-expressing Cx43 or by using silencing RNAi; in another set of experiments they have varied the ratio of fibroblasts to myocytes. In the former case, they have observed that an increase in the gap-junctional conductance first leads to a decrease in CV and then an increase; in the second set of experiments they have found that CV decreases as the fibroblast density increases. McSpadden, *et al.* [22] have studied electrical-wave propagation in a monolayer of neonatal rat cardiac myocytes electrotonically loaded with a layer of cardiac fibroblasts; they have used an optical-mapping technique to find the dependence of such impulse propagation on the gap-junctional conductance G_{gap} ; and they have found that impulse propagation, in both the transverse and longitudinal directions, changes significantly when fibroblasts are loaded on the myocyte monolayers; e.g. , as the fibroblast coverage area increases from the 0 – 15% coverage range to the 75 – 100% coverage range, the conduction velocity CV , in loaded monolayers, decreases from $\simeq 28 \pm 5\ \text{cm/s}$ to $\simeq 21 \pm 7\ \text{cm/s}$, in the longitudinal direction, and from $13 \pm 3\ \text{cm/s}$ to $9 \pm 3\ \text{cm/s}$, in the transverse direction.

Xie, *et al.* [14] have followed Ref. [23] to model MF tissue in three different ways, namely, with (a) zero-sided, (b) single-sided, and (c) double-sided connections, by using the LRI [16] ventricular-cell model for myocytes with slight modifications of the original parameters. In their zero-sided connection model, passive fibroblasts are inserted in a 2D layer of myocytes; but they are functionally uncoupled with myocytes at their contact sites, so the fibroblasts are equivalent to conduction inhomogeneities [24–28]. In the single-sided connection model, con-

nected fibroblasts are loaded on the top of a 2D layer of myocytes; therefore, they are equivalent to an extra, local electrical load. In the double-sided-connection model, connected fibroblasts are inserted in a 2D myocardial layer, with myocytes and fibroblasts connected at contact sites; this provides an additional conduction pathway for electrical signals, so the fibroblasts are qualitatively similar to ionic inhomogeneities [24,25,29]. Their studies of fibroblasts randomly attached on the top of a 2D myocyte sheet (i.e., single-sided connections), show that, for low fibroblast membrane conductances $G_f \simeq 1$ and with the fibroblast resting-membrane potential $E_f = -20$ mV, CV initially remains almost unchanged as the fibroblast-myocyte (FM) ratio increases; but then it decreases quickly as the FM ratio approaches 3. If, however, $G_f \simeq 4$, CV increases initially and then decreases rapidly as the FM ratio approaches 1. However, in both cases, with low and high values of G_f , conduction failure occurs when CV decreases to $\simeq 0.2$ m/s from its uncoupled value 0.56 m/s. Furthermore, when $E_f = -80$ mV (i.e., close to the myocyte resting-membrane potential), CV decreases linearly from 0.56 m/s to 0.49 m/s as the FM ratio increases from 0 to 3; this trend is almost independent of the value of G_f . They have also studied the effects of the random insertion of fibroblasts in a 2D sheet of myocytes sheet; the resulting myocyte-fibroblast pairs can have zero-sided or double-sided connections. When fibroblasts are inserted in series, CV decreases almost linearly as the FM ratio increases, for zero-sided connections, and conduction failure occurs if the FM ratio is above 3. Similar results are observed with double-sided connection when fibroblasts, with $E_f = -20$ mV and a low value of G_f (1 nS) are coupled with myocytes. However, for larger values of G_f (4 nS), CV decreases much faster as the FM ratio increases, and conduction failure occurs if the FM ratio is below 1. Furthermore, if $E_f = -80$ mV, CV is only slightly different from that with uncoupled fibroblasts and almost independent of G_f . If the fibroblasts lie parallel to myocytes in a 2D sheet, they have found that, with random laterally inserted fibroblasts coupled to all neighboring cells (double-sided connection), CV changes in both longitudinal and transverse directions, but to a different extents. In the longitudinal direction, CV is similar to that in models with random fibroblast attachment; however, in the transverse direction, CV decreases much more rapidly, as in to models with random fibroblast insertions. These authors have also studied the effects of G_j on CV for randomly inserted fibroblasts (double-sided connection) in a 2D sheet of myocytes. For low G_f (0.1 nS), with an FM ratio of 1, they have found that CV decreases first and then increases as G_j increases ($G_j > 25$ nS). However, for high G_f (2 nS), CV increases to a maximum (at $G_j \simeq 5$ nS), then decreases to minimum (at $G_j \simeq 25$ nS), and eventually increases linearly as G_j increases.

Zlochiver, *et al.* [13] have studied impulse propagation, by inserting fibroblasts, in a 2D sheet of myocyte tissue in the dynamic Luo-Rudy (LRd) [30, 31] model of a mammalian ventricular cell [32]. Their studies show that CV first increases and then decreases as G_{gap} increases and then decreases as a function of fibroblast-myocyte area ratio, in agreement with their experimental observations.

Before we present the details of our work, we give a summary of our principal results: We present systematic numerical studies of single MF units and two-dimensional (2D) arrays of such units. Our studies on a single MF unit show that the action-potential (AP) morphology depends principally on E_f and the coupling G_{gap} between a myocyte-fibroblast pair. We present ionic mechanisms that are responsible for the modulation of the AP as we alter E_f or G_{gap} . Our numerical results for an MF composite show that APD alternans can arise from the modulation of the I_{Ks} and I_{Kr} potassium ionic currents. However, the current I_{K1} contributes principally to an elevation in V_{rest} in the diastolic interval; the amount of this elevation depends on the potential difference between the myocyte and fibroblast. We find that our MF composite can also show autorhythmic and oscillatory behaviors in addition to an excitable response; precisely which one of these responses is obtained depends on the values of G_{gap} and other parameters. We also carry out systematic studies of a 2D mathematical model for MF tissue with (a) both homogeneous and inhomogeneous distributions of fibroblasts, (b) various ranges for parameters such as G_{gap} , G_f , and E_f , and (c) intercellular couplings that can be zero-sided, one-sided, and two-sided connections of fibroblasts with myocytes. Our studies with homogeneous simulation domains show that CV decreases as a function of G_{gap} , for zero-sided and one-sided couplings; however, for two-sided coupling, CV decreases initially and then increases as a function of G_{gap} , and, eventually, we observe that conduction failure occurs for low values of G_{gap} . In our homogeneous studies, we find that the rotation speed and stability of a spiral wave can be controlled either by controlling G_{gap} or E_f . Our studies with fibroblast inhomogeneities show that a spiral wave can get anchored to a local fibroblast inhomogeneity, just as with conduction or ionic inhomogeneities [24, 33–35]; but the spiral-wave dynamics are completely different here than they are with conduction and ionic inhomogeneities. We also study the efficacy of a low-amplitude control scheme, which has been suggested for the control of spiral-wave turbulence in mathematical models for cardiac tissue [24, 25, 36, 37], in our MF model both with and without heterogeneities.

The remaining part of this paper is organized as follows. In Sec. 4.2, we describe the formulation of our myocyte-fibroblast model, for a single cell and for 2D tissue; we also describe the numerical schemes that we use to solve the model equations.

In Sec. 3.3, we present the results of our numerical calculations. In Sec. 3.4, we discuss the significance of our results and compare them with results from other experimental and computational studies.

3.2 Model and Methods

In this Section, we build on earlier mathematical models for (a) cardiac tissue [15] and (b) the coupling, at the level of single cells, of cardiac myocytes and cardiac fibroblasts [9–12] to develop a mathematical model for a 2D sheet of cardiac myocytes coupled to a similar sheet of fibroblasts. We use the ionic model for human cardiac myocytes [15] due to ten Tusscher, Noble, Noble, and Panfilov (TNNP); we include connections between myocytes and fibroblasts via gap junctions; and we also allow for the possibility of studying *zero-sided*, *one-sided*, and *two-sided* couplings as illustrated in the schematic diagram of Fig. 3.1.

The cell membrane of a cardiac myocyte is modelled by the following ordinary differential equation (ODE) [38, 39]:

$$C_{m,tot} \frac{\partial V_m}{\partial t} = -I_{ion,m} + I_{ext}; \quad (3.1)$$

here $C_{m,tot}$ is the total cellular capacitance, V_m is the transmembrane potential, i.e., the voltage difference between intra- and extra-cellular spaces, $I_{ion,m}$ is the sum of all ionic currents that cross the cell membrane, and I_{ext} is the externally applied current. Similarly, the membrane potential of a passive fibroblast is given by the ODE

$$C_{f,tot} \frac{\partial V_f}{\partial t} = -I_{ion,f}, \quad (3.2)$$

where $C_{f,tot}$, V_f , and $I_{ion,f}$ are, respectively, the total cellular capacitance, the transmembrane potential, and the sum of all ionic currents for the fibroblast. The passive nature of the fibroblasts allows us to write

$$I_{ion,f} = G_f(V_f - E_f); \quad (3.3)$$

here G_f and E_f are, respectively, the conductance and the resting membrane potential for the fibroblast. If a single myocyte cell is coupled with N_f fibroblasts via the gap junctional conductance G_{gap} , its transmembrane potential can be modelled by the following set of equations:

$$C_{m,tot} \frac{\partial V_m}{\partial t} = -I_{ion,m} + \sum_n^{N_f} I_{gap,n}, \quad (3.4)$$

$$C_{f,tot,n} \frac{\partial V_{f,n}}{\partial t} = -I_{ion,f,n} - I_{gap,n}, \quad (3.5)$$

where

$$I_{gap,n} = G_{gap}(V_{f,n} - V_m); \quad (3.6)$$

here n labels the fibroblasts that are connected to the myocyte via G_{gap} ; note that $1 \leq n \leq N_f$ and, for the identical fibroblasts we consider here, $C_{f,tot,n} = C_{f,tot}$, $I_{gap,n} = I_{gap}$, and $V_{f,n} = V_f$, for all n . The physical units that we use for our model are as follows: time t is in ms, the transmembrane potentials V_m and V_f are in mV, the transmembrane currents $I_{ion,m}$ and $I_{ion,f}$ are in pA, therefore, current densities for the myocyte are in pA/pF, the total cellular capacitances $C_{m,tot}$ and $C_{f,tot}$ are in pF, and the fibroblast conductance G_f and the gap-junctional conductance G_{gap} are in nS.

As suggested in Ref. [40], the dynamics of N_f identical fibroblasts coupled to a myocyte is equivalent to the dynamics of a single fibroblast coupled to a myocyte with coupling strength, $\mathcal{G}_{mf} = \mathcal{G}_{fm}/N_f$, where \mathcal{G}_{mf} is the coupling strength of a myocyte to N_f fibroblasts and $\mathcal{G}_{fm} = G_{gap}$ is the coupling strength of a fibroblast to a myocyte. Therefore, we have performed simulations by using only one fibroblast per myocyte in our 2D simulation domain. This is equivalent to a myocyte being coupled with N_f fibroblasts with coupling strength $\mathcal{G}_{mf} = \mathcal{G}_{fm}/N_f$. Furthermore, in our 2D model, the maximum number of fibroblasts $N_{f,max}$ allowed per site is roughly related with the ratio of $C_{m,tot}$ and $C_{f,tot}$ because they are related to the surface area of the cell; in experiments, N_f depends on the ratio of these surface areas and the volume fractions of myocytes and fibroblasts. These considerations are important because fibroblasts are considerably smaller than myocytes as we discuss in greater detail in Sec. 3.4.

In our 2D computational studies, we use a simulation domain in which we have one layer of fibroblasts on top of a myocyte layer as illustrated in Fig. 3.1. Such a simulation domain is motivated by the experiments of Refs. [6–8, 41]. We model this myocyte-fibroblast bilayer by using the following discrete equations [42, 43]:

$$\begin{aligned} C_{m,tot}\dot{V}_m(i, j) &= -I_{ion,m}(i, j) + G_{gap}(V_f(i, j) - V_m(i, j)) \\ &+ \sum_{\substack{I=-1;1 \\ J=-1;1}} \mathcal{G}_{mm}(V_m(i+I, j+J) - V_m(i, j)) + \mathcal{G}_{fm}(V_f(i+I, j+J) - V_m(i, j)) \end{aligned} \quad (3.7)$$

$$\begin{aligned} C_{f,tot}\dot{V}_f(i, j) &= -I_{ion,f}(i, j) + G_{gap}(V_m(i, j) - V_f(i, j)) \\ &+ \sum_{\substack{I=-1;1 \\ J=-1;1}} \mathcal{G}_{ff}(V_f(i+I, j+J) - V_f(i, j)) + \mathcal{G}_{mf}(V_m(i+I, j+J) - V_f(i, j)) \end{aligned} \quad (3.8)$$

here the dots above V_m and V_f denote time derivatives, \mathcal{G}_{mm} and \mathcal{G}_{ff} represent, respectively, intercellular couplings in the myocyte and fibroblast layers; and \mathcal{G}_{mf}

and \mathcal{G}_{fm} account for cross couplings between myocyte and fibroblast layers; if one of the cross-coupling coefficients, say \mathcal{G}_{mf} , is nonzero, then the other, \mathcal{G}_{fm} , must also be nonzero to ensure current conservation; myocyte and fibroblast composites are coupled at a given site by G_{gap} ; in addition, we allow for intercellular couplings (see Fig. (3.1)) that can be categorized naturally as follows: (A) zero-sided: $\mathcal{G}_{mm} > 0$, $\mathcal{G}_{mf} = \mathcal{G}_{fm} = \mathcal{G}_{ff} = 0$; (B) one-sided: $\mathcal{G}_{mm}, \mathcal{G}_{ff} > 0$, $\mathcal{G}_{mf} = \mathcal{G}_{fm} = 0$; and (C) two-sided: $\mathcal{G}_{mm}, \mathcal{G}_{ff} > 0$, $\mathcal{G}_{mf}, \mathcal{G}_{fm} > 0$; the index (i, j) refers to the cell associated with the node under consideration; the conductances \mathcal{G}_{mm} , \mathcal{G}_{ff} , \mathcal{G}_{mf} , \mathcal{G}_{fm} , and G_{gap} are in nS.

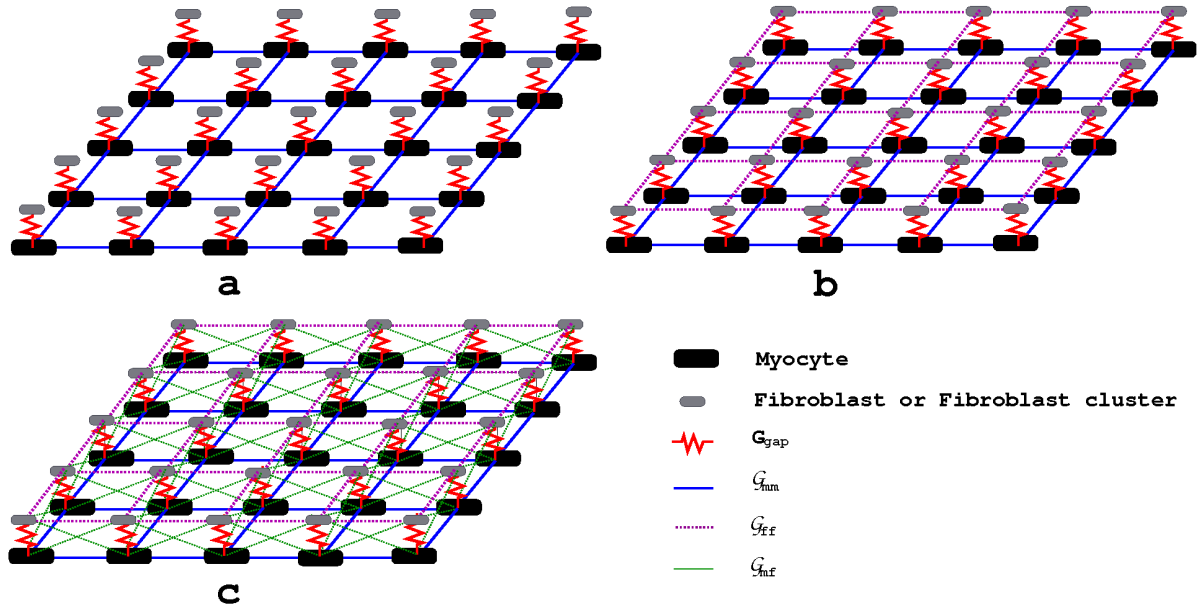


Figure 3.1: Schematic diagram: A small part of our square simulation domain with sites occupied by myocyte-fibroblast (MF) composites, connected by the gap-junctional conductance G_{gap} , with (a) zero-sided, (b) single-sided, and (c) double-sided couplings between MF composites (see text).

We use a 2D square domain consisting of 600×600 grid points and lattice spacing $\Delta x = \Delta y = 0.225$ mm, so the side of each square domain is $L = 135$ mm; one of these layers contains myocytes and the other fibroblasts as shown in Fig. 3.1. These two layers are separated by a distance $\Delta z = 0.225$ mm. We use a forward-Euler method for the time evolution of the transmembrane potentials with a time step $\Delta t = 0.02$ ms. We use *no-flux* (Neumann) boundary conditions on the edges of the simulation domain. The initial condition we use is related to the one given in Ref. [25]; we describe it in detail in subsection 4.3.2.

It is often useful to track the trajectory of the tip of a spiral wave to investigate the stability of a spiral, its transitions, and its the rate of drifting in a 2D simulation domain. The tip of such a spiral wave is normally defined as the point

where the excitation wave front and repolarization wave back meet; this point can be found as the point of intersection of an isopotential line, of constant membrane potential, $V_m = V_{iso}$ (in general $V_{iso} < 0$ mV), and the line $dV_m/dt = 0$ [15, 44, 45]. Another classical technique, which tracks the spiral-wave tip in a two-variable model, obtains this tip by finding the point where the isocontours of the two state variables intersect [45–48]; this technique can also be used in a complex mathematical model for cardiac tissue provided the model has at least one slow and one fast variable. We have developed a tip-tracking algorithm that locates the tip position, i.e., the point at which the wave-front and wave-back meet each other, by monitoring I_{Na} , the sodium current. This is the predominant current in the depolarization phase of the AP and is, therefore, responsible for depolarizing the cells that lie ahead of the wave front, in the 2D simulation domain; thus, it plays an important role in the spatiotemporal evolution of this wave front. Hence, we find the minimum strength of I_{Na} that can yield an AP; and we use this as a reference value to track the tip position. Given the sharpness of the depolarization, pseudocolor plots of I_{Na} show a fine line along a spiral-wave arm (see, e.g., Fig. 2A in Ref. [24]); this fine line stops at the spiral tip and provides, therefore, an accurate way of tracking the spatio-temporal evolution of this tip.

3.3 Results

In our previous studies [24, 25], we have investigated the interaction of a spiral-wave with conduction and ionic inhomogeneities in the TNNP model for cardiac tissue. Here we elucidate spiral-wave dynamics in the presence of fibroblasts by using the mathematical model we have developed in Sec. 4.2. In subsection 3.3.1 we present results for the morphology of the action potential (AP) in a myocyte-fibroblast (MF) composite; in particular, we examine the dependence of the AP on G_{gap} , G_f , E_f , $C_{f,tot}$, and N_f . Subsection 3.3.2 contains our results for spiral-wave dynamics in a homogeneous MF bilayer, in which MF composites are coupled; we consider zero-, one-, and two-sided couplings. In subsection 3.3.2 we explore the dynamics of spiral waves in a sheet of myocytes with an inhomogeneity that is an MF bilayer. The last subsection 4.3.4 examines the efficacy of the low-amplitude, mesh-based control scheme of Refs. [24, 36, 37] in the elimination of spiral waves in the homogeneous MF bilayer and the sheet of myocytes with an MF-bilayer inhomogeneity.

3.3.1 A Myocyte-Fibroblast (MF) Composite

Fibroblast cells act like an electrical load on myocytes. This load, which depends, principally, on the parameters G_{gap} , G_f , E_f , $C_{f,tot}$, and N_f , and alters the electrophysiological properties of a myocyte that is coupled to a fibroblast. In particular, it modifies the morphology of the action potential (AP). Earlier computational studies [9–12], which we have summarized in the Introduction (Sec. 4.1), have investigated mathematical models for a single unit of a myocyte and fibroblasts, for both animal and human ventricular cells and with passive or active fibroblasts. Most of these computational studies focus on the modification of the AP by (a) the number N_f of fibroblasts per myocyte and (b) the gap-junctional conductance G_{gap} . In the numerical studies that we present here we use a composite myocyte-fibroblast (MF) system with N_f passive fibroblasts per myocyte. We examine in detail the dependence of the AP of this composite on the parameters of the model, namely, the membrane capacitance $C_{f,tot}$, the membrane conductance G_f , the resting membrane potential E_f , and the coupling strength G_{gap} ; the trends we uncover are in qualitative agreement with various experiments [3, 5].

The ranges of parameters, which we use for our composite MF system, are consistent with those found in experimental studies and those used in earlier computational studies. For example, in a cell-culture experiment, Rook, *et al.* [5] have studied rat-heart fibroblasts and reported that the membrane resistance R_f , the fibroblast resting membrane potential E_f , and the gap-junctional conductance G_{gap} , lie, respectively, in the ranges 3 – 25 $G\Omega$, –20 to –40 mV, and 0.3 – 8.0 nS. Kohl *et al.* [3] have studied non-excitable cardiac, mechanosensitive fibroblasts from the region of the sinoatrial node in a rat heart. Their study, which uses both intact tissue and cell cultures, estimates that $R_f \simeq 1 G\Omega$, $E_f \simeq -15 \pm 10$ mV, and $G_{gap} \simeq 4 - 6$ nS for a well-coupled MF pair. In vitro studies, by Kiseleva, *et al.* [49], have examined rat mechanosensitive fibroblasts attached to the right atrium; they have found $E_f \simeq -22 \pm 1.9$ mV and $R_f \simeq 0.51 \pm 0.01 G\Omega$, for a control case, and $E_f \simeq -46.5 \pm 1.8$ mV and $R_f \simeq 3.8 \pm 0.03 G\Omega$, in the case of a large infarct caused by a myocardial infarction. In vitro studies by Kamkin, *et al.* [50] of non-excitable, mechanosensitive, cardiac fibroblasts from the atrium of a human heart have reported $E_f \simeq -15.9 \pm 2.1$ mV $R_f \simeq 4.1 \pm 0.1 G\Omega$. In vitro studies, by Kamkin *et al.* [51], of rat atrial fibroblasts attached to the sinoatrial node region yielded $E_f \simeq -22 \pm 2$ mV and $R_f \simeq 510 \pm 10 M\Omega$, for the control case, and for the case with myocardial infarction, and $E_f \simeq -41 \pm 3$ mV to $\simeq -28 \pm 3$ mV. Recent experiment, in culture, by Chilton *et al.* [52] have measured the cellular capacitance $C_{f,tot}$ of rat-ventricular fibroblasts by using a patch-clamp recording and found $C_{f,tot} \simeq 6.3 \pm 1.7$ pF; they have shown that the input resistance

of fibroblasts $R_f \simeq 10.7 \pm 2.3 G\Omega$. Their measurements have shown that E_f depends on the inwardly rectifying K^+ current (Kir) and the potassium ion concentration $[K^+]_o$; e.g, when Kir is expressed, E_f is $\simeq -65 \pm 5$ mV and $\simeq -80 \pm 1.8$ mV for $[K^+]_o = 10$ mM and 5.4 mM, respectively. However, when Kir is absent, E_f is $\simeq -34 \pm 2$ mV. Furthermore, in culture, Shibukawa, *et al.* [53] have found, in patch-clamp recordings from rat-ventricular fibroblasts (active), that $C_{f,tot} \simeq 4.5 \pm 0.4$ pF, $E_f \simeq -58 \pm 3.9$ mV, $R_f \simeq 5.5 \pm 0.6 G\Omega$.

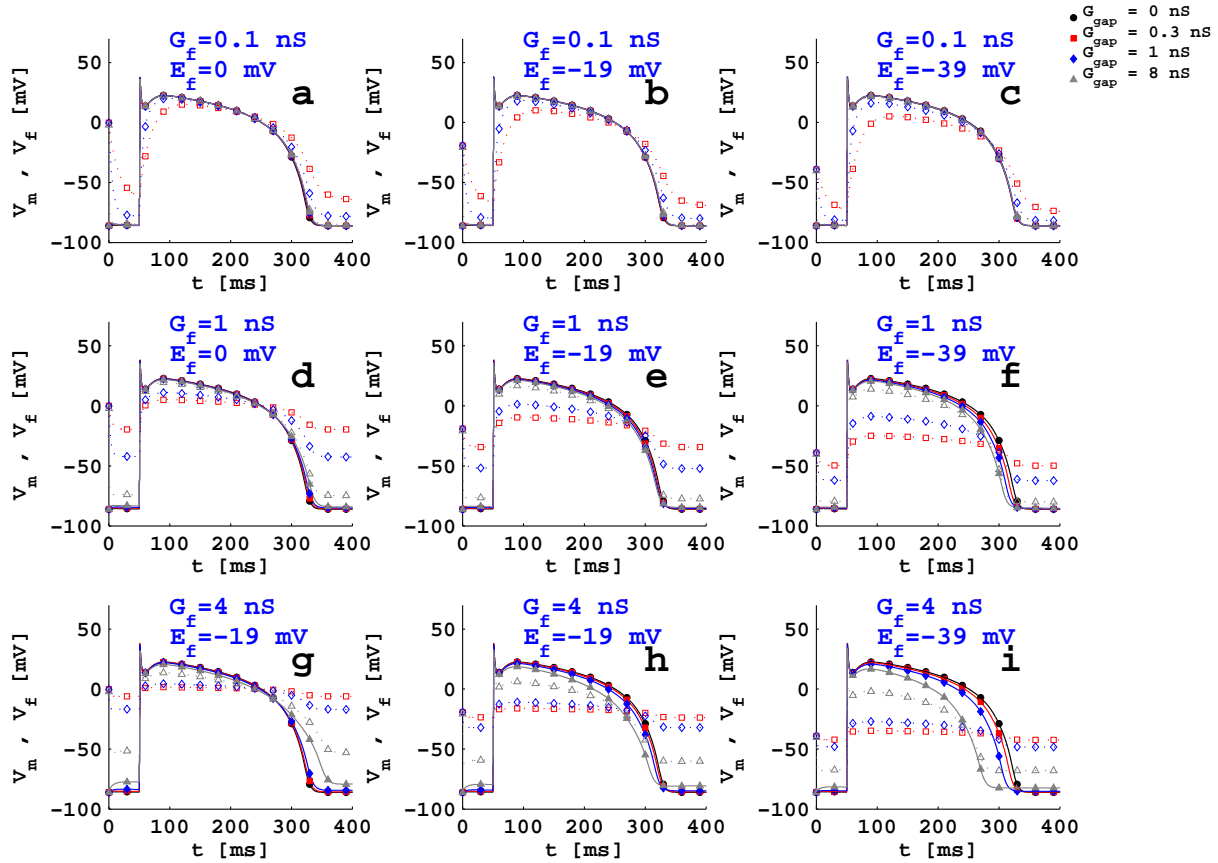


Figure 3.2: Plots of the myocyte action potential V_m (full symbols and lines) and the fibroblast action potential V_f (unshaded symbols and dashed lines), with a passive fibroblast of capacitance $C_{f,tot} = 6.3$ pF coupled with a myocyte for (a) $E_f = 0$ mV and $G_f = 0.1$ nS, (b) $E_f = -19$ mV and $G_f = 0.1$ nS, (c) $E_f = -39$ mV and $G_f = 0.1$ nS, (d) $E_f = 0$ mV and $G_f = 1$ nS, (e) $E_f = -19$ mV, and $G_f = 1$ nS, (f) $E_f = -39$ mV and $G_f = 1$ nS, (g) $E_f = 0$ mV and $G_f = 4$ nS, (h) $E_f = -19$ mV and $G_f = 4$ nS, and (i) $E_f = -39$ mV and $G_f = 4$ nS; red squares (full or unshaded) indicate $G_{gap} = 0.3$ nS; blue diamonds (full or unshaded) indicate $G_{gap} = 1$ nS; gray triangles (full or unshaded) indicate $G_{gap} = 8$ nS; black squares (full or unshaded) indicate an uncoupled myocyte.

The computational studies of mathematical models for fibroblasts, discussed in Sec. 4.1, have also used a wide range of values for parameters for the cellular

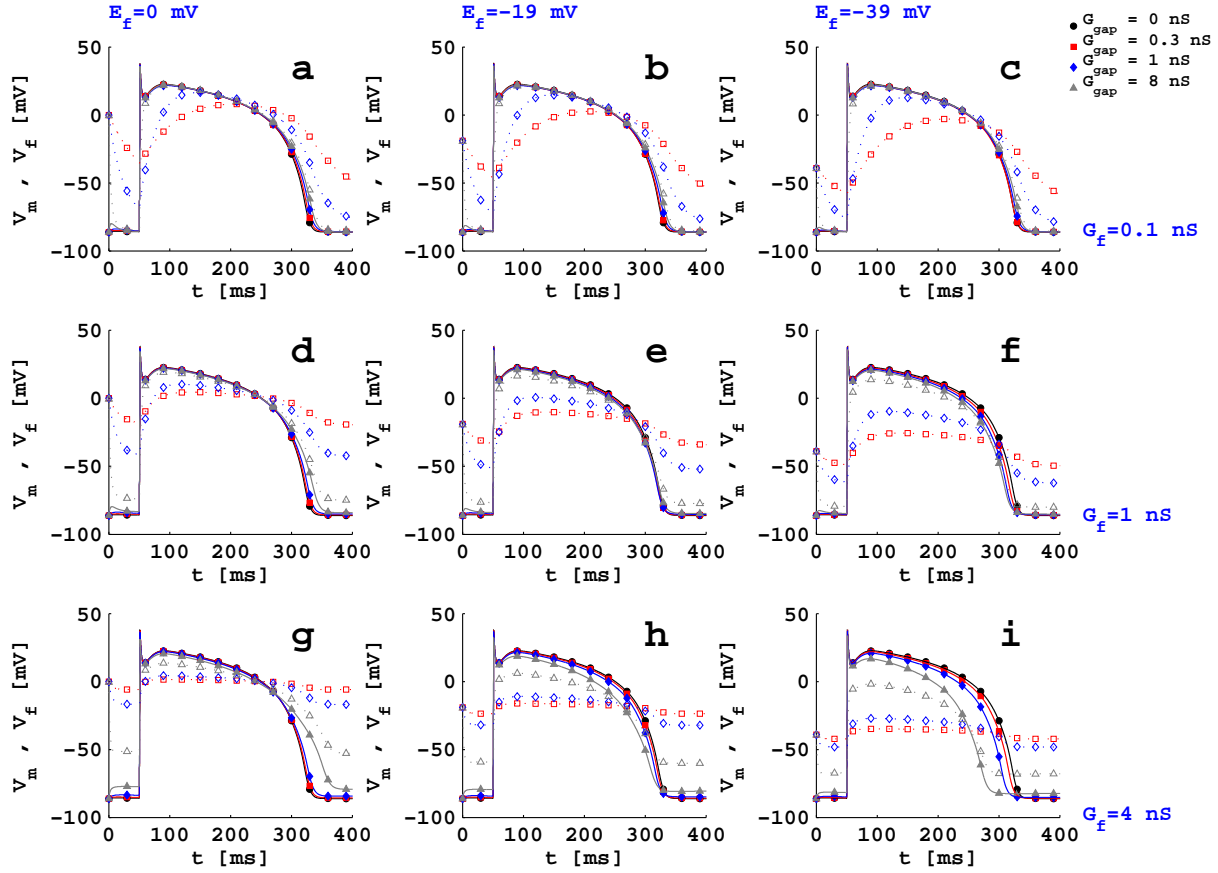


Figure 3.3: Plots of the myocyte action potential V_m (full symbols and lines) and the fibroblast action potential V_f (unshaded symbols and dashed lines), with a passive fibroblast of capacitance $C_{f,tot} = 25.2$ pF coupled with a myocyte for (a) $E_f = 0$ mV and $G_f = 0.1$ nS, (b) $E_f = -19$ mV and $G_f = 0.1$ nS, (c) $E_f = -39$ mV and $G_f = 0.1$ nS, (d) $E_f = 0$ mV and $G_f = 1$ nS, (e) $E_f = -19$ mV and $G_f = 1$ nS, (f) $E_f = -39$ mV and $G_f = 1$ nS, (g) $E_f = 0$ mV and $G_f = 4$ nS, (h) $E_f = -19$ mV and $G_f = 4$ nS, and (i) $E_f = -39$ mV and $G_f = 4$ nS; red squares (full or unshaded) indicate $G_{gap} = 0.3$ nS; blue diamonds (full or unshaded) indicate $G_{gap} = 1$ nS; gray triangles (full or unshaded) indicate $G_{gap} = 8$ nS; black squares (full or unshaded) indicate an uncoupled myocyte.

capacitance $C_{f,tot}$, the membrane conductance G_f , the fibroblast resting membrane potential E_f , and the gap-junctional coupling G_{gap} between myocyte and fibroblasts. For example, Xie, *et al.* [9] have used $C_{f,tot} = 25$ pF, $G_f = 0.1 - 4$ nS, $E_f = -50 - 0$ mV, and $G_{gap} = 0 - 20$ nS for an MF composite. The study of Sachse, *et al.* [10] has used $C_{f,tot} = 4.5$ pF, $E_f = -58$ mV, and $G_{gap} = 0.1 - 100$ nS for an MF composite with active fibroblasts. Jacquemet, *et al.* [11] have studied the MF composite with active fibroblasts by using $C_{f,tot} = 4.5$ pF, $E_f = -58$ mV, and $G_{gap} = 0.09 - 4.05$ nS. MacCannell, *et al.* [12] have used $C_{f,tot} = 6 - 60$ pF, $E_f = -49.6$ mV and $G_{gap} = 1 - 3$ nS for their studies of an active-fibroblast model. To investigate in detail the

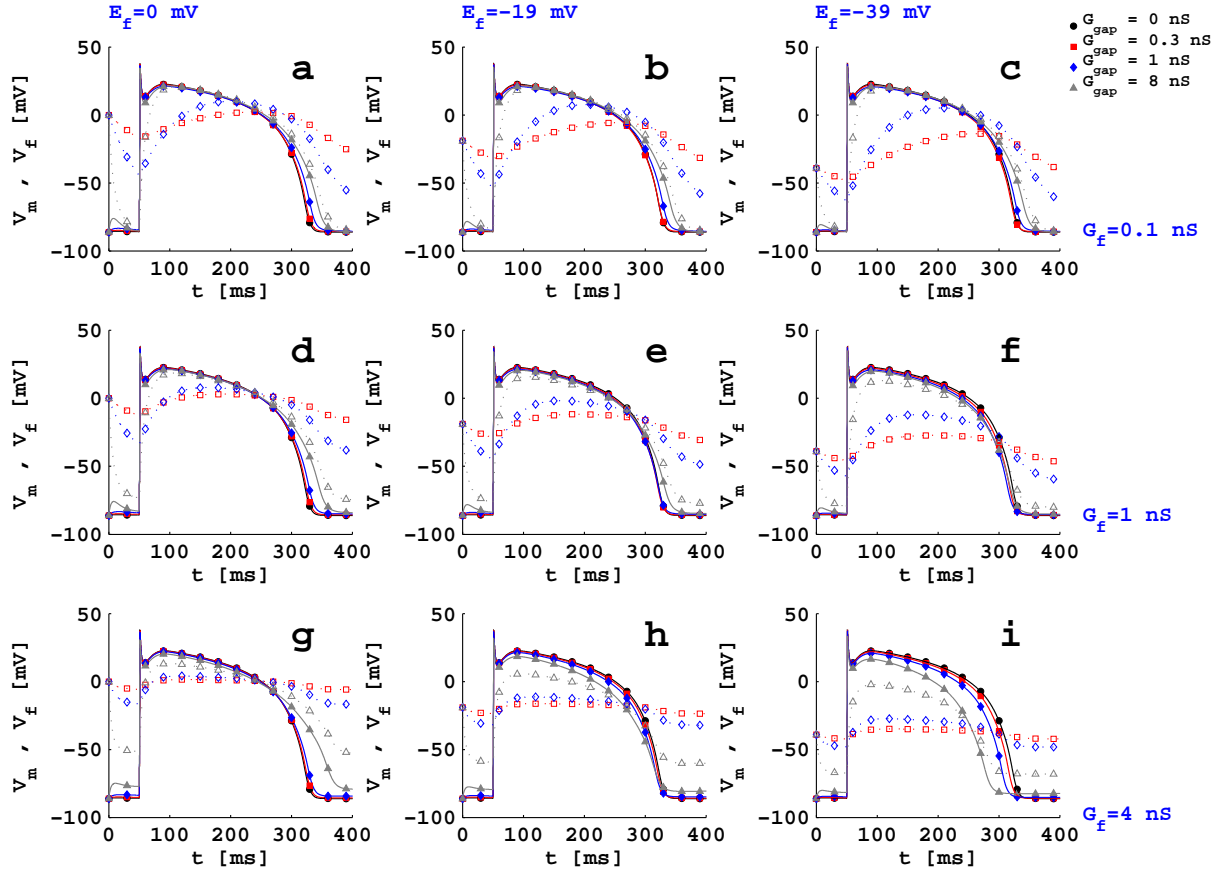


Figure 3.4: Plots of the myocyte action potential V_m (full symbols and lines) and the fibroblast action potential V_f (unshaded symbols and dashed lines), with a passive fibroblast of capacitance $C_{f,tot} = 63$ pF coupled with a myocyte for (a) $E_f = 0$ mV and $G_f = 0.1$ nS, (b) $E_f = -19$ mV and $G_f = 0.1$ nS, (c) $E_f = -39$ mV and $G_f = 0.1$ nS, (d) $E_f = 0$ mV and $G_f = 1$ nS, (e) $E_f = -19$ mV and $G_f = 1$ nS, (f) $E_f = -39$ mV and $G_f = 1$ nS, (g) $E_f = 0$ mV and $G_f = 4$ nS, (h) $E_f = -19$ mV and $G_f = 4$ nS, and (i) $E_f = -39$ mV and $G_f = 4$ nS; red squares (full or unshaded) indicate $G_{gap} = 0.3$ nS; blue diamonds (full or unshaded) indicate $G_{gap} = 1$ nS; gray triangles (full or unshaded) indicate $G_{gap} = 8$ nS; black squares (full or unshaded) indicate an uncoupled myocyte.

effect of fibroblasts on a myocyte, we use the following wide ranges of parameters (these encompass the ranges used in the experimental and computational studies mentioned above): $C_{f,tot} = 6 - 60$ pF, $G_f = 0.1 - 4$ nS, $E_f = -39$ to 0 mV, and $G_{gap} = 0.3 - 8.0$ nS for our MF composites. However, to observe some special properties, such as autorhythmicity of MF composites, we vary the fibroblast parameters and gap-junctional conductances.

Figures 3.2 (a)-(i) show plots of the myocyte transmembrane potential V_m (filled symbols with solid lines) and the fibroblast transmembrane potential V_f (unshaded symbols with dashed lines) versus time t , when we consider an MF composite in

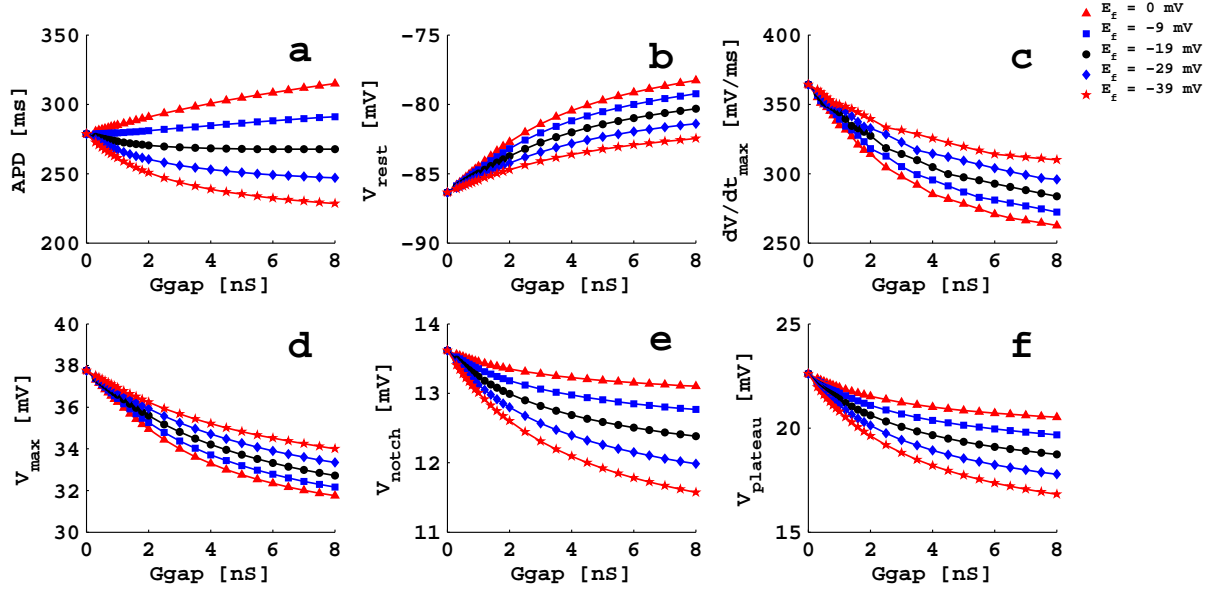


Figure 3.5: Plots of various morphological features of the myocyte action potential V_m versus the gap-junctional conductance G_{gap} ; here the myocyte is coupled with a passive fibroblast with capacitance $C_{f,tot} = 6.3$ pF and conductance $G_f = 4.0$ nS. (a) The action-potential duration APD versus G_{gap} ; (b) the resting-membrane potential V_{rest} versus G_{gap} ; (c) the maximum upstroke velocity dV/dt_{max} versus G_{gap} ; (d) the maximum value of V_m , during the action potential, V_{max} versus G_{gap} ; (e) the value of V_m at the position of the notch, i.e., V_{notch} versus G_{gap} ; (f) the maximum value of V_m , in the plateau region of the action potential, i.e., $V_{plateau}$ versus G_{gap} ; these figures show plots for the fibroblast resting membrane potential $E_f = 0$ mV (full red triangles), $E_f = -9$ mV (full blue squares), $E_f = -19$ mV (full black circles), $E_f = -29$ mV (full blue diamonds), and $E_f = -39$ mV (full red stars).

which a myocyte is coupled to a passive fibroblast, with $C_{f,tot} = 6.3$ pF. In Figs. 3.2 (a)-(i) we use squares (\blacksquare or \square) for low coupling ($G_{gap} = 0.3$ nS), diamonds (\blacklozenge or \blacklozenge) for intermediate coupling ($G_{gap} = 1.0$ nS), triangles (\blacktriangle or \triangle) for high coupling ($G_{gap} = 8.0$ nS), and filled circles (\bullet) for a myocyte that is not coupled to a fibroblast. Figures 3.2 (a), (d), (g), which are in the first column, depict V_m and V_f for low (0.1 nS), intermediate (1.0 nS), and high (4.0 nS) values of G_f when $E_f = 0.0$ mV; their analogs for $E_f = -19.0$ mV and -39.0 mV are given, respectively, in Figs. 3.2 (b), (e), (h) (second column) and Figs. 3.2 (a), (d), (g) (third column). These figures show the following: (i) the fibroblast action potential (fAP) is similar to the myocyte action potential (mAP) when the gap-junctional conductance G_{gap} is high and the fibroblast conductance G_f is low (Figs. 3.2 (a), (b), (c) in the first row); (ii) for low and intermediate values of G_{gap} and with $G_f = 0.1$ nS, the fAP plateau decreases but the APD is prolonged with respect to that of the corresponding mAP; (iii) the fAP loses its spike and notch and has a lower plateau and prolonged APD compared to the mAP when

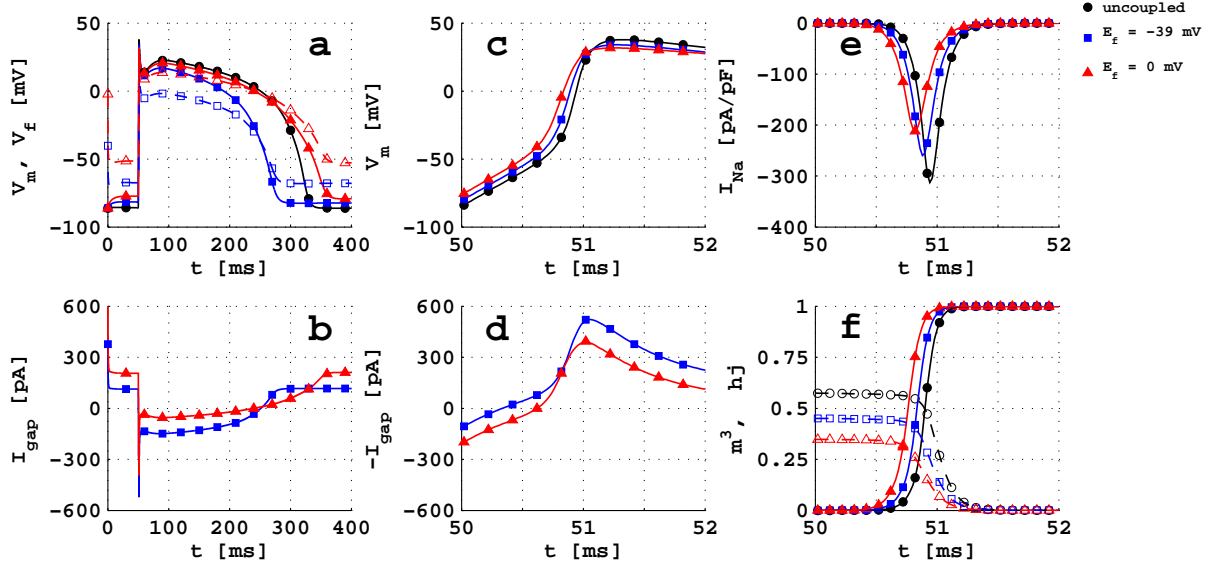


Figure 3.6: (a) Plots versus time t of the transmembrane potentials V_m (full curves with filled symbols), for a myocyte, and V_f (dashed curves with open symbols), for a passive fibroblast coupled with a myocyte cell; here $C_{f,tot} = 6.3$ pF, $G_f = 4.0$ nS, $G_{gap} = 8.0$ nS and $E_f = -39.0$ mV (blue squares) and $E_f = 0.0$ mV (red triangles); the full black curve with circles shows V_m for an uncoupled myocyte. (b) Plots versus t of the gap-junctional current I_{gap} with parameters and symbols as in (a). Plots versus t , for the first 2 ms after the application of a stimulus of -52 pA/pF, of (c) V_m , (d) I_{gap} , (e) the myocyte sodium current I_{Na} , and (f) the total activation m^3 (full lines with filled symbols) and total inactivation hj (dashed lines with open symbols) gates; the parameters and symbols here are as in (a).

$G_f = 1.0$ nS or 4.0 nS. Figures similar to Figs. 3.2 (a)-(i), but with $C_{f,tot} = 25.2$ pF and $C_{f,tot} = 63$, are given, respectively, in Figs. 3.3 (a)-(i) and Figs. 3.4 (a)-(i); these show that V_m does not depend very significantly on $C_{f,tot}$ but V_f does.

In Figs. 3.5 (a), (b), (c), (d), (e), and (f) we show, respectively, plots of the action-potential duration APD, the resting-membrane potential V_{rest} , the maximum up-stroke velocity dV/dt_{max} , the maximum value of V_m , during the action potential, namely, V_{max} , the value of V_m at the position of the notch, i.e., V_{notch} , and the maximum value of V_m , in the plateau region of the action potential, i.e., $V_{plateau}$ versus the gap-junctional conductance G_{gap} ; here the myocyte is coupled with a passive fibroblast with capacitance $C_{f,tot} = 6.3$ pF and conductance $G_f = 4.0$ nS. These figures show plots for the fibroblast resting membrane potential $E_f = 0$ mV (full red triangles), $E_f = -9$ mV (full blue squares), $E_f = -19$ mV (full black circles), $E_f = -29$ mV (full blue diamonds), and $E_f = -39$ mV (full red stars). For -39 mV $\lesssim E_f \lesssim -19$ mV, the APD decreases monotonically as G_{gap} increases, but for higher values of E_f , namely, -9 mV and 0 mV their is a monotonic increase of the

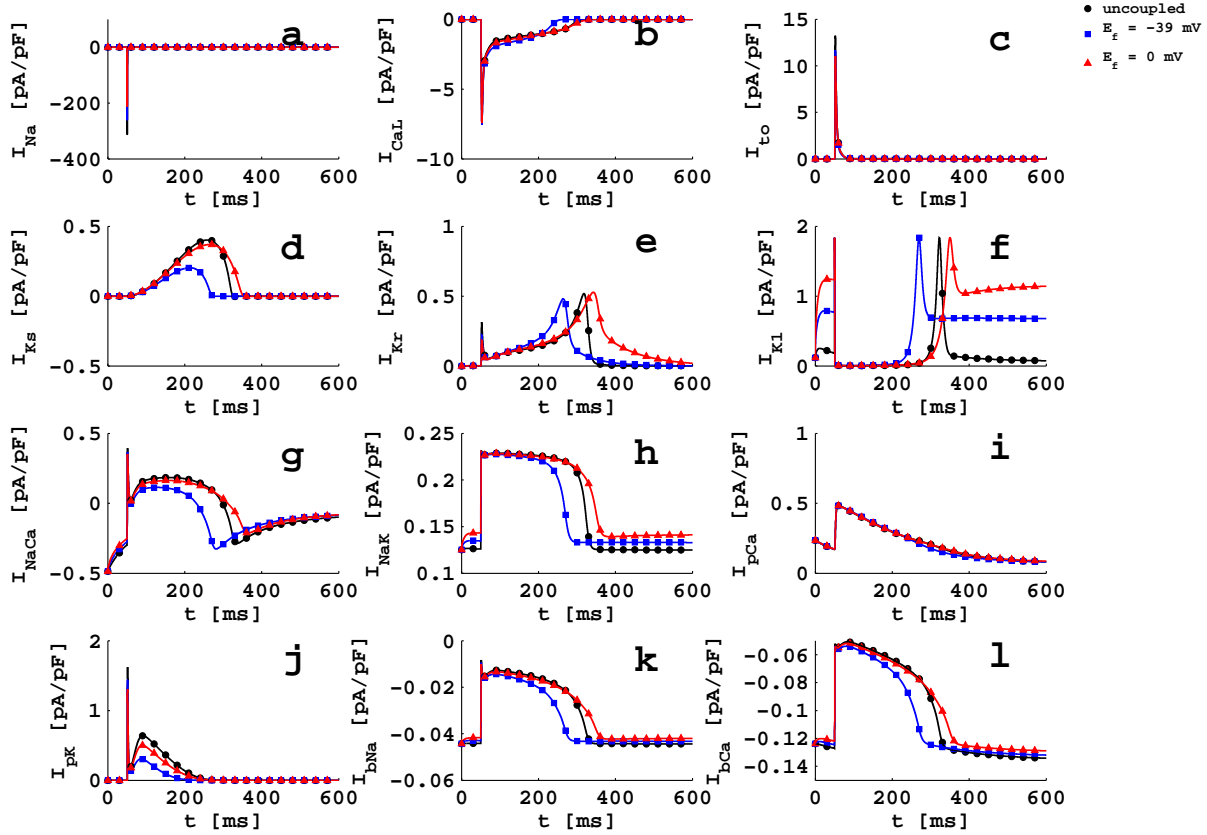


Figure 3.7: Plots of ionic current, I_m , of the myocyte versus time t of an MF composite with $N_f = 1$; the fibroblast parameters are $C_{f,tot} = 6.3$ pF and $G_f = 4.0$ nS, and it coupled with a myocyte with $G_{gap} = 8.0$ nS; the full black curve with circles shows I_m for an uncoupled myocyte; the blue filled squares and the red triangles are, respectively, for $E_f = -39.0$ mV and $E_f = 0$ mV. (a) the fast inward Na^+ current, I_{Na} ; (b) the L-type slow inward Ca^{2+} current, I_{CaL} ; (c) the transient outward current, I_{to} ; (d) the slow delayed rectifier current, I_{Ks} ; (e) the rapid delayed rectifier current, I_{Kr} ; (f) the inward rectifier K^+ current, I_{K1} ; (g) the Na^+/Ca^{2+} exchanger current, I_{NaCa} ; (h) the Na^+/K^+ pump current, I_{NaK} ; (i) the plateau Ca^{2+} current, I_{pCa} ; (j) the plateau K^+ current, I_{pK} ; (k) the background Na^+ current, I_{bNa} ; (l) the background Ca^{2+} current, I_{bCa} .

APD with G_{gap} . Both dV/dt_{max} and V_{max} decrease monotonically as G_{gap} increases; the lower the value of E_f , the slower is this decrease. Similarly, V_{notch} and $V_{plateau}$ decrease monotonically as G_{gap} increases; but the higher the value of E_f , the slower is this decrease.

In Fig. 3.6 (a) we present plots versus time t of the transmembrane potentials V_m (full curves with filled symbols), for a myocyte, and V_f (dashed curves with open symbols), for a passive fibroblast coupled with a myocyte cell; here $C_{f,tot} = 6.3$ pF, $G_f = 4.0$ nS, $G_{gap} = 8.0$ nS and $E_f = -39.0$ mV (blue squares) and $E_f = 0.0$ mV (red triangles); the full black curve with circles show, for comparison, a plot of

V_m for an uncoupled myocyte. Figure 3.6 (b) contains plots versus t of the gap-junctional current I_{gap} with parameters and symbols as in (b); and plots versus t of V_m , I_{gap} , the myocyte sodium current I_{Na} , and the total activation m^3 (full lines with filled symbols) and total inactivation h_j (dashed lines with open symbols) gates, for the first 2 ms after the application of a stimulus current $I_{ext} = -52$ pA/pF at 50 ms for 3 ms, are depicted in Figs. 3.6 (c), (d), (e), and (f), respectively, for the parameters and symbols used in Fig. 3.6 (a). These plots show that the myocyte membrane potential V_m is reduced, i.e., the cell is depolarized, when a passive fibroblast is coupled with it; the larger the value of E_f , the more is the reduction in V_m . However, V_m is elevated, compared to its value in the uncoupled-myocyte case, for both the values of E_f we study, because, when I_{ext} from $0 \leq t \leq 50$ ms, the gap-junctional current I_{gap} flows from the fibroblast to the myocyte as shown in Fig. 3.6 (b). The greater the elevation of V_m the earlier is the activation of the Na^+ fast-activation gate m , in the presence of an external applied stimulus, as can be seen by comparing Figs. 3.6 (c) and (f); this early activation shifts the minimum in I_{Na} towards the left as depicted in Fig. 3.6 (e). Note that the product h_j , the total inactivation gating variables, decreases as V_m increases (dashed lines in Fig. 3.6 (f)) in the range $50 \text{ ms} \leq t \leq 52 \text{ ms}$. Therefore, the amplitude of I_{Na} decreases with increasing E_f , as shown in Fig. 3.6 (e), and leads to a reduction in the maximum rate of AP depolarization (see the plots of dV/dt_{max} in Fig. 3.5 (c)); this shift in the minimum of I_{Na} is also associated with the leftward shift of V_m in Fig. 3.6 (c). A comparison of Figs. 3.6 (e) and (f) shows, furthermore, that, for a given value of E_f , the minimum of I_{Na} occurs at the value of t where the plots of m^3 and h_j cross.

The current $I_{gap} = G_{gap}(V_m - V_f)$ flows from the myocyte to the fibroblast or vice versa as shown in Figs. 3.6 (b) and (d). Before the application of a stimulus current ($0 \text{ ms} \leq t \leq 50 \text{ ms}$ in Fig. 3.6 (b)), $I_{gap} < 0$, i.e., it flows from the fibroblast to the myocyte; and the current-sink capability of the fibroblast increases with E_f , because (see Fig. 3.6 (a)) $(V_m - V_f)$ increases with E_f . However, when we have a current stimulus $I_{ext} > 0$, i.e., in the time interval $50 \text{ ms} < t \leq 53 \text{ ms}$, the trend noted above is reversed: the lower the value of E_f the higher is the ability of the myocyte to act as a current sink as shown in Fig. 3.6 (d).

Several studies [54–57] have shown that the contribution of individual ionic currents to the AP morphology can be examined by a partial or complete blocking of the corresponding ion channel. Therefore, we examine, for an isolated myocyte, how the AP morphology changes as we modify the major ionic currents. As in Refs. [54–57], we find that (a) V_{max} and dV/dt_{max} depend principally on I_{Na} , (b) V_{notch} depends mainly on I_{to} , (c) the maximum of the plateau region $V_{plateau}$ is maintained

by a balance between I_{CaL} and I_{Ks} , (d) the final phase of repolarization, which determines the APD, depends primarily on I_{Kr} and I_{Ks} , (e) the diastolic or resting phase, which decides the value of V_{rest} , is maintained predominantly by I_{K1} , and (f) all gating variables, which determine the opening and closing of ion channels, depend on V_m , therefore, the contribution of the ionic currents to the morphology of the AP is modified as V_m changes.

Given these results for an isolated myocyte, we can understand qualitatively the effects on the AP morphology of a myocyte when it is coupled with a fibroblast. The coupling of a fibroblast to a myocyte modifies V_m because of the electronic interaction, via G_{gap} . Therefore, the AP morphology changes as we have described above and shown in Figs. 3.5(a)-(f); to explain the results in this figure, we have to examine the behaviors of all the ionic currents when the myocyte is coupled to a fibroblast. For the ensuing discussion we consider a representative value of G_{gap} , namely, 8.0 nS, and study the variation of the ionic currents as we change E_f for an MF composite. In particular, we examine the time-dependence of the myocyte ionic currents I_{Na} , I_{CaL} , I_{to} , I_{Ks} , I_{Kr} , I_{K1} , I_{NaCa} , I_{NaK} , I_{pCa} , I_{pK} , I_{bNa} , and I_{bCa} , which are plotted in Fig. 3.7 for a fibroblast coupled with a myocyte, with $C_{f,tot} = 6.3$ pF, $G_f = 4.0$ nS, $G_{gap} = 8.0$ nS and $E_f = -39.0$ mV (blue squares) and $E_f = 0.0$ mV (red triangles); the full black curves with circles show the ionic currents for an uncoupled myocyte. We observe that, as we vary E_f , the I_{Ks} and I_{Kr} currents change substantially (see Figs. 3.7(d) and (e)). As a result, APD increases with increasing E_f , as shown in Fig. 3.5(a). Furthermore, as we increase E_f , V_{rest} increases as shown in Fig. 3.5(b); the amount of elevation of V_{rest} depends on $(V_m - E_f)$. By examining the contributions of all ionic currents (see Fig. 3.7) to their values in the resting state of the AP ($t \geq 400$ ms), we conclude that I_{K1} changes most significantly compared to other ionic currents. Therefore, we find the E_f -dependence of I_{K1} shown in Fig. 3.7(f). As we have noted above for an isolated myocyte, V_{max} and dV/dt_{max} depend principally on I_{Na} ; therefore, we examine I_{Na} to understand the variations of V_{max} and dV/dt_{max} as functions of E_f for an MF composite. We find that the magnitude of I_{Na} decreases as E_f increases (Fig. 3.7(a)), so V_{max} and dV/dt_{max} decrease as E_f increases (as shown in Figs. 3.5(c) and (d)). Similarly, we look at I_{to} to understand the dependence of V_{notch} on E_f ; and we examine I_{CaL} and I_{Ks} for the E_f -dependence of $V_{plateau}$. Figure 3.7(c) shows that I_{to} decreases when E_f increases, therefore, V_{notch} increases as a function of E_f (as shown in Fig. 3.5(e)). Figures 3.7(b) and (d) show I_{CaL} and I_{Ks} , respectively; the former decreases and the latter increases as E_f increases; however, the effect of I_{Ks} dominates that of I_{CaL} so $V_{plateau}$ increases as E_f increases as shown in Fig. 3.5(f).

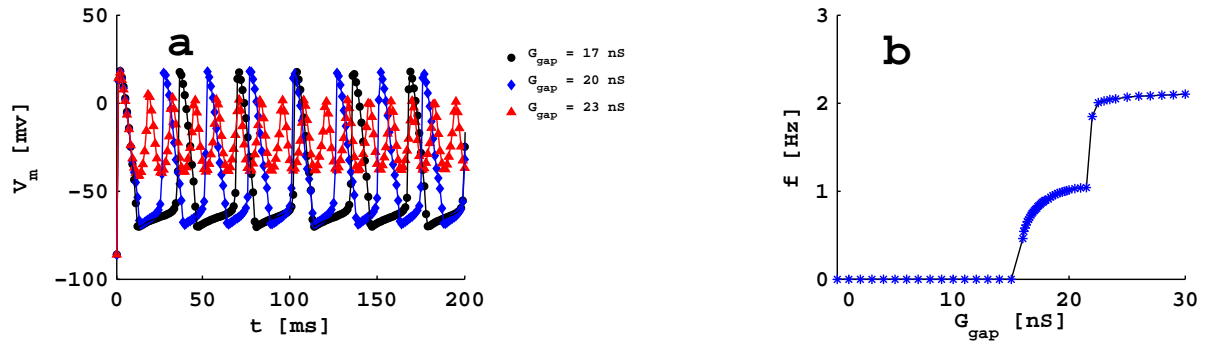


Figure 3.8: (a) Transmembrane potential of myocyte V_m in an MF composite with $C_{f,tot} = 6.3$ pF, $G_f = 8.0$ nS, and $E_f = 0$ mV for $G_{gap} = 17$ nS (full black circles), $G_{gap} = 20$ nS (full blue diamond) and $G_{gap} = 23$ nS (full red triangle). (b) Plot of frequency f versus G_{gap} . The MF composite shows excitable, autorhythmicity and oscillatory behavior in the regime $0 \leq G_{gap} < 16$ nS, $16 \leq G_{gap} < 23$ nS and $G_{gap} \geq 23$ nS, respectively.

It has been noted in Refs. [40,58,59], that a myocyte cell can display autorhythmicity when it is coupled with fibroblasts; in particular, Ref. [58] shows that the cycle length of autorhythmicity activation depends on E_f and G_{gap} . We find that G_f and $C_{f,tot}$ play a less important role than N_f , E_f , and G_{gap} in determining whether such autorhythmicity is obtained. In Fig. 3.8 we give some illustrative plots for $N_f = 1$, $E_f = 0$ mV, and $G_f = 8$ nS that yield autorhythmicity; Fig. 3.8 (a) shows a plot of V_m versus time t ; Fig. 3.8 (b) contains a plot of the frequency of autorhythmicity f versus G_{gap} for our MF composite; for more detailed studies of the dependence of such autorhythmicity on N_f and E_f we refer the reader to Ref. [60]. Figure 3.8 (b) shows that, for the range 0 nS $\lesssim G_{gap} \lesssim 16$ nS, the myocyte behaves like an excitable cell, which produces one action potential when it is stimulated electrically; in the range 16 nS $\lesssim G_{gap} \lesssim 23$ nS, the myocyte displays autorhythmicity and the cycle length λ_{cl} , the time difference between the upstrokes of two successive action potentials, decreases with increasing G_{gap} ; for $G_{gap} \gtrsim 23$ nS, the myocyte displays oscillatory behavior. Such autorhythmic and oscillatory responses of an MF composite [60] can occur at lower values of G_{gap} , e.g., $G_{gap} = 8$ nS, if we increase N_f .

The number of fibroblasts N_f that are coupled to a myocyte in our MF composite affect significantly the response of the MF composite to external electrical stimuli as has been shown in detail in Refs. [9,60]. In Fig. 3.9, we show illustrative plots versus t of V_m , V_f , and I_{gap} for our MF composite with $N_f = 0$, i.e., no fibroblasts (black circles), $N_f = 1$ (red squares), $N_f = 2$ (blue diamonds), and $N_f = 4$ (gray triangles) for the parameter values $C_{f,tot} = 6.3$ pF, $G_f = 4$ nS, $E_f = -39$ mV. For a low value of G_{gap} , namely, 0.3 nS (plots in the left column), we see that the resting potential of

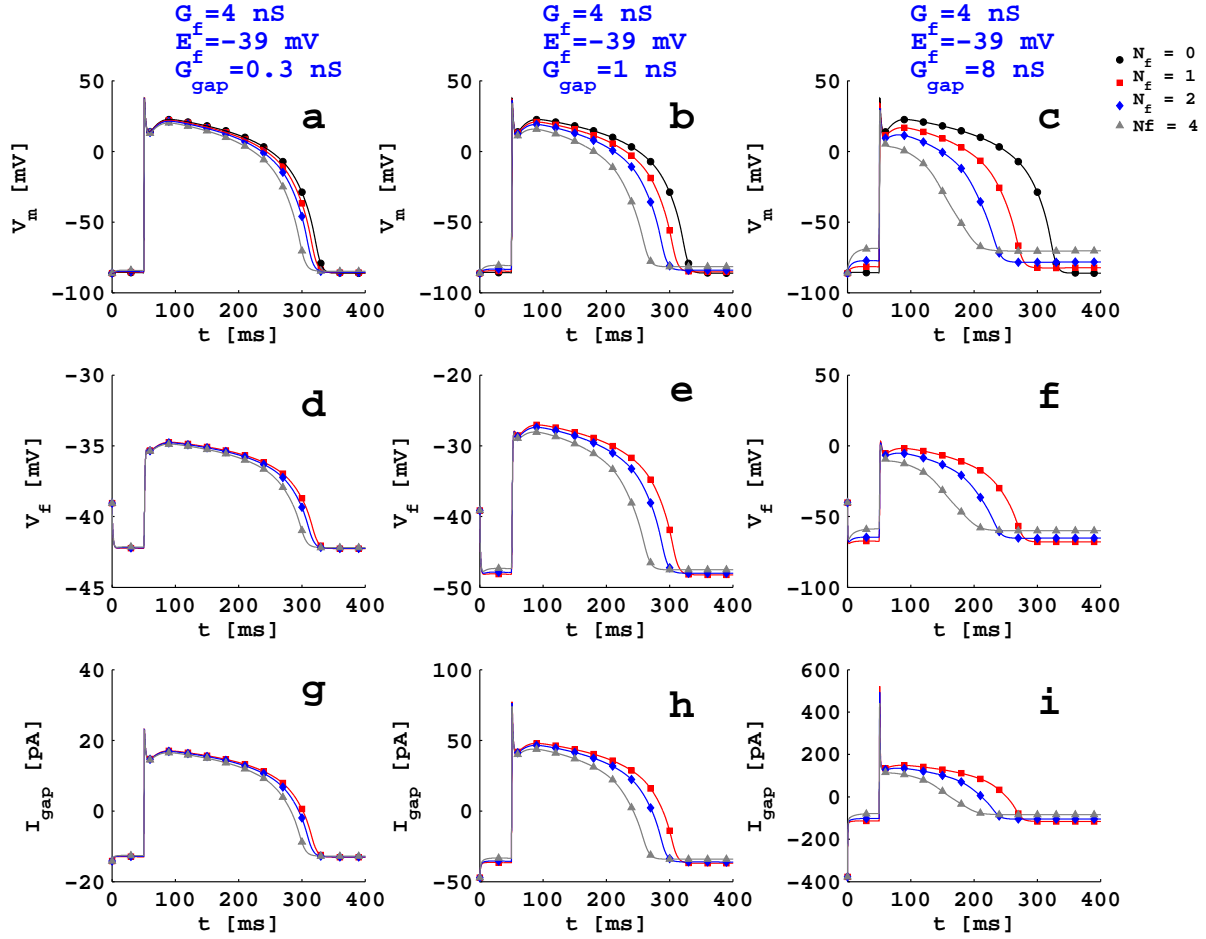


Figure 3.9: Plots versus t of V_m , V_f , and I_{gap} for $N_f = 0$, i.e., no fibroblasts (black circles), $N_f = 1$ (red squares), $N_f = 2$ (blue diamonds), and $N_f = 4$ (gray triangles) for the illustrative parameter values $C_{f,tot} = 6.3$ pF, $G_f = 4$ nS, $E_f = -39$ mV, and a low value of G_{gap} , namely, 0.3 nS (plots in the left panel (a), (d), and (g)), an intermediate value of G_{gap} , namely, 1.0 nS (plots in the middle panel (b), (e), and (h)), and a high value of G_{gap} , namely, 8.0 nS (plots in the right panel (c), (f), and (i)).

the coupled myocyte is elevated slightly relative to the case $N_f = 0$; and the APD decreases from 280 ms, for $N_f = 0$, to 260 ms when $N_f = 4$ (Fig.3.9(a)); the dependence of V_f and I_{gap} on N_f is illustrated in Figs.3.9(d) and (g). This dependence of V_m , V_f , and I_{gap} increases as we can see from the plots in the middle column, Figs.3.9(b), (e), and (h), for an intermediate value of G_{gap} , namely, 1 nS, and from the plots in the right column, Figs.3.9(c), (f), and (i), for an high value of G_{gap} , namely, 8 nS. In the former case ($G_{gap} = 1$ nS) V_{rest} rises from -84.6 mV to -83.2 mV and the APD decreases from 280 ms to 240 ms as we go from $N_f = 0$ to $N_f = 4$ (Fig.3.9(b)); in the latter case ($G_{gap} = 8$ nS) V_{rest} rises from -84.6 mV to -74.4 mV and the APD decreases from 280 ms to 150 ms as we go from $N_f = 0$ to $N_f = 4$ (Fig.3.9(c)).

$C_{f,tot}$ (pA)	G_f (nS)	G_{gap} (nS)	E_f (mV)	N_f	$\Delta APD_{70\%}$ (ms)	$\Delta APD_{80\%}$ (ms)	$\Delta APD_{90\%}$ (ms)	$\Delta \dot{V}_{max}$ (mV/ms)	ΔV_{rest} (mV)
6.3	4	8	-9	1	4.62	6.72	12.30	-91.89	7.12
6.3	4	8	-9	2	40.90	50.40	-	-151.68	14.99
6.3	4	8	-19	1	-16.80	-15.16	-11.02	-80.64	6.04
6.3	4	8	-19	2	-16.92	-11.02	-	-137.32	12.60
6.3	4	8	-29	1	-36.12	-34.84	-31.74	-68.40	4.97
6.3	4	8	-29	2	-58.00	-54.02	-	-122.88	10.33
6.3	4	8	-29	3	-64.56	-51.84	-	-270.10	15.91
6.3	4	8	-39	1	-53.62	-52.64	-50.32	-54.41	3.90
6.3	4	8	-39	2	-89.68	-86.92	-75.54	-103.87	8.21
6.3	4	8	-39	3	-112.60	-106.02	-	-135.49	12.21
6.3	4	8	-39	4	-126.26	-106.18	-	-270.10	16.35
6.3	4	8	-49	1	-69.52	-68.82	-67.10	-40.90	2.86
6.3	4	8	-49	2	-115.22	-113.30	-107.18	-82.25	6.18
6.3	4	8	-49	3	-146.06	-142.18	-	-112.77	9.10
6.3	4	8	-49	4	-173.62	-166.16	-	-134.10	11.77
6.3	4	8	-49	5	-195.72	-179.94	-	-149.25	14.30
6.3	4	8	-49	6	-205.32	-144.06	-	-162.44	16.72
6.3	4	8	-49	7	-214.12	-	-	-178.78	18.96

Table 3.1: The values of $C_{f,tot}$, G_f , G_{gap} , E_f , and N_f for a single MF composite and the changes in the AP morphology, relative to that of an uncoupled myocyte. We concentrate on the APD, \dot{V}_{max} , and V_{rest} and list the changes, indicated by Δ , in these parameters. $\Delta APD_{70\%}$, $\Delta APD_{80\%}$, and $\Delta APD_{90\%}$ denote, respectively, the changes in the APD at 70%, 80%, and 90% repolarization. Note that here we have high values (see text) for both G_f (4 nS) and G_{gap} (8 nS).

In Table 3.1, we show the change of the APD, \dot{V}_{max} , and V_{rest} for an MF composite with respect to their uncoupled values when N_f identical fibroblasts are coupled with a myocyte with high value of both G_f (4 nS) and G_{gap} (8 nS). We measure $\Delta APD_{70\%} = APD_{70\%}^c - APD_{70\%}^m$, where $APD_{70\%}^c$ and $APD_{70\%}^m$ are, respectively, APD of an MF composite and isolated myocyte at 70% repolarization. Similarly, $\Delta APD_{80\%}$ and $\Delta APD_{90\%}$ are, respectively, the change of the APD of MF composite with respect to the myocyte APD at 80% and 90% repolarization of AP. We do not present here the results of composites with N_f fibroblasts, which show AP automatically in the absence of external stimulus. The change of \dot{V}_{max} , $\Delta \dot{V}_{max}$, is measured by subtracting \dot{V}_{max}^c of an MF composite from an isolated myocyte \dot{V}_{max}^m . Similarly, the change of V_{rest} , ΔV_{rest} , is measured by subtracting V_{rest}^c of an MF composite from an isolated myocyte V_{rest}^m . The analog of Table 3.1 for low values of G_f (0.1 nS) and G_{gap} (0.3 nS), is given in Table 3.2.

$C_{f,tot}$ (pA)	G_f (nS)	G_{gap} (nS)	E_f (mV)	N_f	$\Delta APD_{70\%}$ (ms)	$\Delta APD_{80\%}$ (ms)	$\Delta APD_{90\%}$ (ms)	$\Delta \dot{V}_{max}$ (mV/ms)	ΔV_{rest} (mV)
6.3	0.1	0.3	-9	1	0.82	0.90	1.06	-2.41	0.12
6.3	0.1	0.3	-9	2	1.66	1.82	2.14	-5.49	0.25
6.3	0.1	0.3	-9	3	2.52	2.78	3.26	-9.28	0.38
6.3	0.1	0.3	-9	4	3.42	3.76	4.42	-13.83	0.52
6.3	0.1	0.3	-9	5	4.32	4.76	5.62	-19.16	0.67
6.3	0.1	0.3	-9	6	5.26	5.80	6.86	-22.21	0.82
6.3	0.1	0.3	-9	7	6.22	6.86	8.12	-25.40	0.99
6.3	0.1	0.3	-9	8	7.22	7.96	9.44	-29.41	1.16
6.3	0.1	0.3	-19	1	0.26	0.34	0.50	-2.08	0.10
6.3	0.1	0.3	-19	2	0.56	0.70	1.00	-4.64	0.21
6.3	0.1	0.3	-19	3	0.86	1.08	1.54	-7.72	0.33
6.3	0.1	0.3	-19	4	1.18	1.50	2.12	-11.34	0.45
6.3	0.1	0.3	-19	5	1.52	1.92	2.70	-15.53	0.57
6.3	0.1	0.3	-19	6	1.86	2.36	3.34	-20.29	0.70
6.3	0.1	0.3	-19	7	2.24	2.84	3.98	-22.61	0.84
6.3	0.1	0.3	-19	8	2.64	3.32	4.68	-25.34	0.98
6.3	0.1	0.3	-29	1	-0.28	-0.22	-0.08	-1.76	0.09
6.3	0.1	0.3	-29	2	-0.54	-0.40	-0.12	-3.85	0.18
6.3	0.1	0.3	-29	3	-0.80	-0.58	-0.16	-6.29	0.28
6.3	0.1	0.3	-29	4	-1.04	-0.76	-0.18	-9.10	0.37
6.3	0.1	0.3	-29	5	-1.28	-0.90	-0.18	-12.29	0.48
6.3	0.1	0.3	-29	6	-1.50	-1.04	-0.14	-15.89	0.58
6.3	0.1	0.3	-29	7	-1.70	-1.16	-0.08	-19.87	0.69
6.3	0.1	0.3	-29	8	-1.88	-1.26	0.02	-22.37	0.81
6.3	0.1	0.3	-39	1	-0.82	-0.76	-0.64	-1.45	0.07
6.3	0.1	0.3	-39	2	-1.64	-1.52	-1.26	-3.11	0.15
6.3	0.1	0.3	-39	3	-2.46	-2.26	-1.86	-4.99	0.22
6.3	0.1	0.3	-39	4	-3.26	-2.98	-2.46	-7.10	0.30
6.3	0.1	0.3	-39	5	-4.04	-3.70	-3.02	-9.45	0.39
6.3	0.1	0.3	-39	6	-4.82	-4.40	-3.58	-12.05	0.47
6.3	0.1	0.3	-39	7	-5.58	-5.08	-4.10	-14.90	0.56
6.3	0.1	0.3	-39	8	-6.32	-5.74	-4.62	-18.00	0.65

Table 3.2: The values of $C_{f,tot}$, G_f , G_{gap} , E_f , and N_f for a single MF composite and the changes in the AP morphology, relative to that of an uncoupled myocyte. We concentrate on the APD, V_{max} , and V_{rest} and list the changes, indicated by Δ , in these parameters. $\Delta APD_{70\%}$, $\Delta APD_{80\%}$, and $\Delta APD_{90\%}$ denote, respectively, the changes in the APD at 70%, 80%, and 90% repolarization. Note that here we have low values (see text) for both G_f (0.1 nS) and G_{gap} (0.3 nS).

3.3.2 Wave dynamics in a 2D simulation domain with MF composites

We move now to a systematic study of the propagation of electrical waves of activation in a 2D simulation domain with MF composites that are coupled via the types of intercellular and gap-junctional couplings described in Sec. 4.2. We begin with an examination of plane-wave propagation through such a simulation domain and study the dependence of the conduction velocity CV on the gap-junctional coupling G_{gap} for zero-, one-, and two-sided couplings. We then study spiral-wave propagation in this domain. Finally, we investigate spiral-wave propagation through an inhomogeneous, square simulation domain in which most of the domain consists of myocytes, but a small region comprises a square MF composite.

In most of our numerical simulations of 2D MF composite domains, we choose the following representative values: the total cellular capacitance $C_{f,tot} = 6.3$ pF; the fibroblast conductance $G_f = 4.0$ nS; the resting membrane potential of fibroblast $E_f = -39$ mV; and $D_{mm} = 0.00154$ cm²/ms [15], which yields, in the absence of fibroblasts, the maximum value for the plane-wave conduction velocity CV , namely, $= 68.3$ cm/s [25]; here D_{mm} is the diffusion constant of the myocyte layer, and it is given by the relation, $D_{mm} = \mathcal{G}_{mm}S_m/C_{m,tot}$, where S_m is the surface area of the myocyte. For the the gap-junctional conductance we explore values in the experimental range (see Sec. 4.1), 0.0 nS $\lesssim G_{gap} \lesssim 8.0$ nS; the remaining intercellular conductances lie in the following ranges: $0 \leq \mathcal{G}_{ff} \leq \mathcal{G}_{mm}/200$ and $0 \leq \mathcal{G}_{mf} = \mathcal{G}_{fm} \leq \mathcal{G}_{mm}/200$. In some of our studies, we vary G_f and E_f ; e.g., when we study spiral wave dynamics in the autorhythmicity regime, we use $G_f = 8.0$ nS and $E_f = 0.0$ mV.

Spiral waves in homogeneous domains

As we have noted in Sec. 4.1, both experimental and computational studies [13, 14, 22] have shown that CV behaves nonmonotonically as a function of the number of fibroblasts N_f in an MF composite. However, to the best of our knowledge, no simulation has examined in detail the dependence of CV on G_{gap} ; therefore, we examine this dependence for the zero-, single-, and double-sided couplings described in Sec. 4.2.

We measure CV for a plane wave by stimulating the left boundary of the simulation domain with a current pulse of amplitude 150 pA/pF for 3 ms. This leads to the formation of a plane wave that then propagates through the conduction domain as shown in Fig. 3.10. For such a wave we can determine CV as described, e.g., in Refs. [24, 25]. In our *in silico* experiments, we observe that CV decreases monotonically, as a function of G_{gap} , for zero- and single-sided couplings; but CV is a nonmonotonic function of G_{gap} in the case of double-sided coupling. These be-

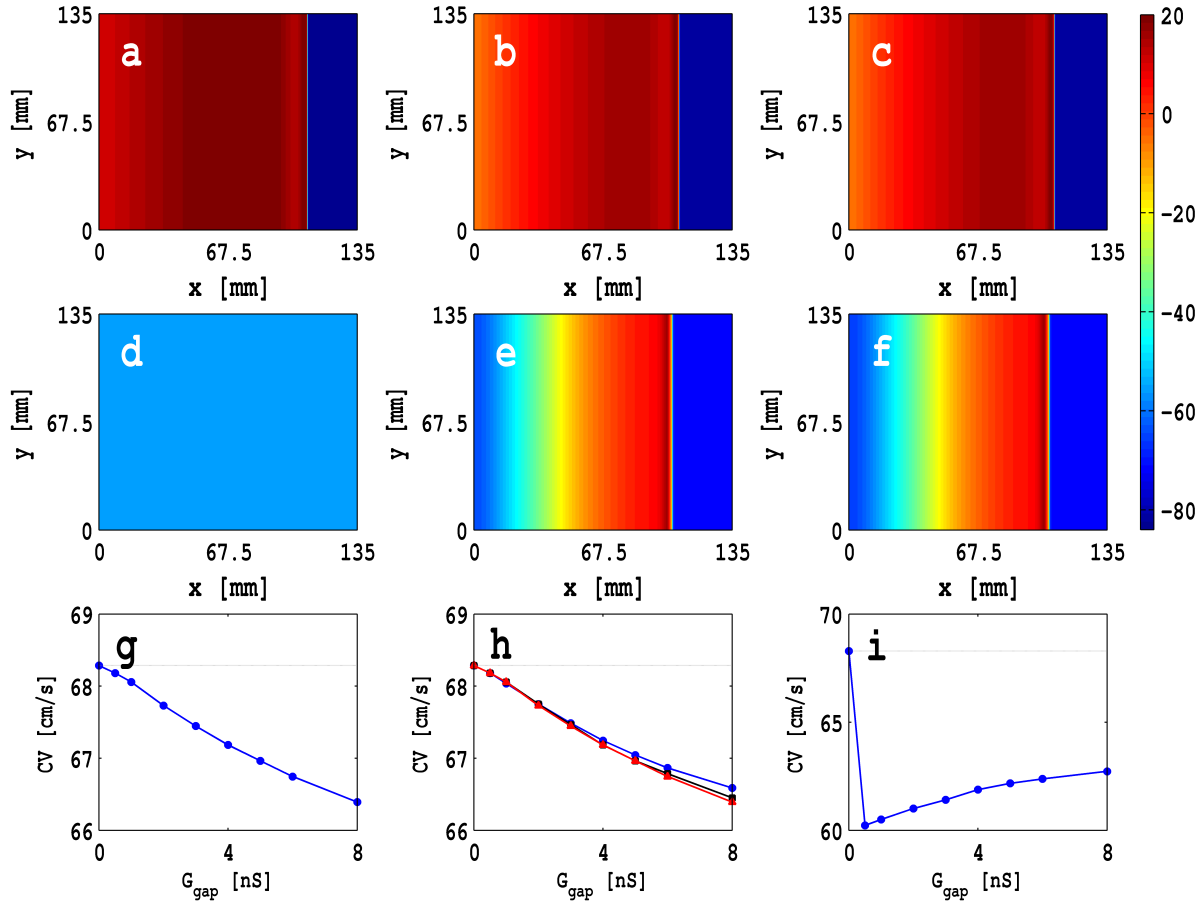


Figure 3.10: Plane waves shown via pseudocolor plots of V_m at $t = 160$ ms in a 2D square simulation domain of side $L = 135$ mm for (a) the control case with only myocytes, (b) *zero-sided coupling*, (c) *single-sided coupling* with $\mathcal{G}_{mm}/\mathcal{G}_{ff} = 1$, (d) *double-sided coupling* with $\mathcal{G}_{mm}/\mathcal{G}_{ff} = 1$, $\mathcal{G}_{mm}/\mathcal{G}_{mf} = 100$, and $G_{gap} = 0.5$ nS, (e) *double-sided coupling* with $\mathcal{G}_{mm}/\mathcal{G}_{ff} = 1$, $\mathcal{G}_{mm}/\mathcal{G}_{mf} = 100$, and $G_{gap} = 8.0$ nS, and (f) *double-sided coupling* with $\mathcal{G}_{mm}/\mathcal{G}_{ff} = 1$, $\mathcal{G}_{mm}/\mathcal{G}_{mf} = 200$, and $G_{gap} = 0.5$ nS (Video S1 illustrates the spatiotemporal evolution of these plane waves). Plots of CV versus G_{gap} for (g) zero-sided coupling, (h) single-sided coupling with $\mathcal{G}_{mm}/\mathcal{G}_{ff} = 1$ (blue circles), $\mathcal{G}_{mm}/\mathcal{G}_{ff} = 4$ (black squares), and $\mathcal{G}_{mm}/\mathcal{G}_{ff} = 100$ (red triangles), and (i) double-sided coupling with $\mathcal{G}_{mm}/\mathcal{G}_{ff} = 1$ and $\mathcal{G}_{mm}/\mathcal{G}_{mf} = 200$. For double-sided coupling, conduction failure can occur for low and intermediate values of G_{gap} , e.g., 0.5 nS and 2.0 nS, as shown in (d).

haviors of CV , as a function of G_{gap} , can be explained qualitatively by examining the dependence of the rate of depolarization dV/dt on G_{gap} for an isolated MF composite. As we increase G_{gap} , dV/dt decreases because of the additional electrical load of the fibroblast on the myocyte; the fibroblast acts as current sink and, therefore, the flux carried by the wave front decreases and CV decreases. However, for *double-sided coupling*, CV decreases initially and then increases as a function of G_{gap} because of the cross-coupling terms \mathcal{G}_{mf} and \mathcal{G}_{fm} .

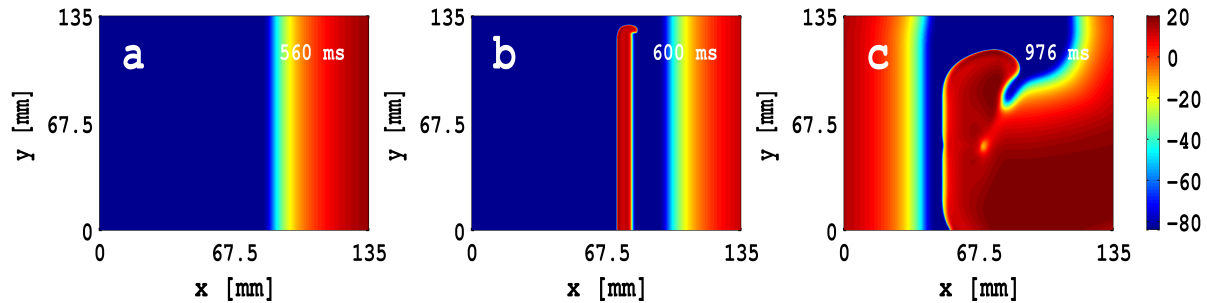


Figure 3.11: Initiation of a spiral wave by the S1-S2 parallel field protocol: To inject a spiral wave, the diffusion constant is set to $D_{mm} = 0.000385 \text{ cm}^2/\text{ms}$; this is a quarter of its original value, which is $0.00154 \text{ cm}^2/\text{ms}$; an S1 stimulus of strength 150 pA/pF is applied for 3 ms at the left boundary; after 560 ms , an S2 stimulus of strength 450 pA/pF is applied for 3 ms just behind the *refractory tail* of the plane wave initiated by the S1 stimulus; this S2 stimulus is applied over the region $x = 360$ and $1 \leq y \leq 550$. We reset D_{mm} to its original value after 880 ms ; this procedure yields a fully developed spiral wave at $t = 976 \text{ ms}$. The spiral wave configuration in (c) is used as the initial condition for our subsequent studies.

We show plane waves in Figs. 3.10 (a)-(f) via pseudocolor plots of V_m at $t = 160 \text{ ms}$ in a 2D square simulation domain of side $L = 135 \text{ mm}$ for (a) the control case with only myocytes, (b) *zero-sided coupling*, (c) *single-sided coupling* with $\mathcal{G}_{mm}/\mathcal{G}_{ff} = 1$, (d) *double-sided coupling* with $\mathcal{G}_{mm}/\mathcal{G}_{ff} = 1$, $\mathcal{G}_{mm}/\mathcal{G}_{mf} = 100$, and $G_{gap} = 0.5 \text{ nS}$, (e) *double-sided coupling* with $\mathcal{G}_{mm}/\mathcal{G}_{ff} = 1$, $\mathcal{G}_{mm}/\mathcal{G}_{mf} = 100$, and $G_{gap} = 8.0 \text{ nS}$, and (f) *double-sided coupling* with $\mathcal{G}_{mm}/\mathcal{G}_{ff} = 1$, $\mathcal{G}_{mm}/\mathcal{G}_{mf} = 200$, and $G_{gap} = 0.5 \text{ nS}$. Video S1 illustrates the spatiotemporal evolution of these plane waves. Figures 3.10 (g)-(h) show plots of CV versus G_{gap} for (g) zero-sided coupling, (h) single-sided coupling with $\mathcal{G}_{mm}/\mathcal{G}_{ff} = 1$ (blue circles), $\mathcal{G}_{mm}/\mathcal{G}_{ff} = 4$ (black squares), and $\mathcal{G}_{mm}/\mathcal{G}_{ff} = 100$ (red triangles), and (i) double-sided coupling with $\mathcal{G}_{mm}/\mathcal{G}_{ff} = 1$ and $\mathcal{G}_{mm}/\mathcal{G}_{mf} = 200$. For double-sided coupling, conduction failure can occur for low and intermediate values of G_{gap} , e.g., 0.5 nS and 2.0 nS , as shown in Fig. 3.10 (d); however, no conduction failure occurs in this range if $\mathcal{G}_{mm}/\mathcal{G}_{mf} = 200$. We do not observe any conduction failure in the cases of zero- and one-sided coupling.

Two methods are often used to initiate spiral waves in simulations [15,24,61,62] and in experiments [61,63], namely, (1) the S1-S2 cross-field protocol and (2) the S1-S2 parallel-field protocol. In the cross-field method, a super-threshold stimulus S2 is applied at the boundary that is perpendicular to the boundary along which the S1 stimulus is given; in the parallel-field method, S2 is applied parallel to the refractory tail of the S1 stimulus, but not over the entire length of the domain. We use the parallel-field protocol to initiate a spiral wave in our homogeneous, square

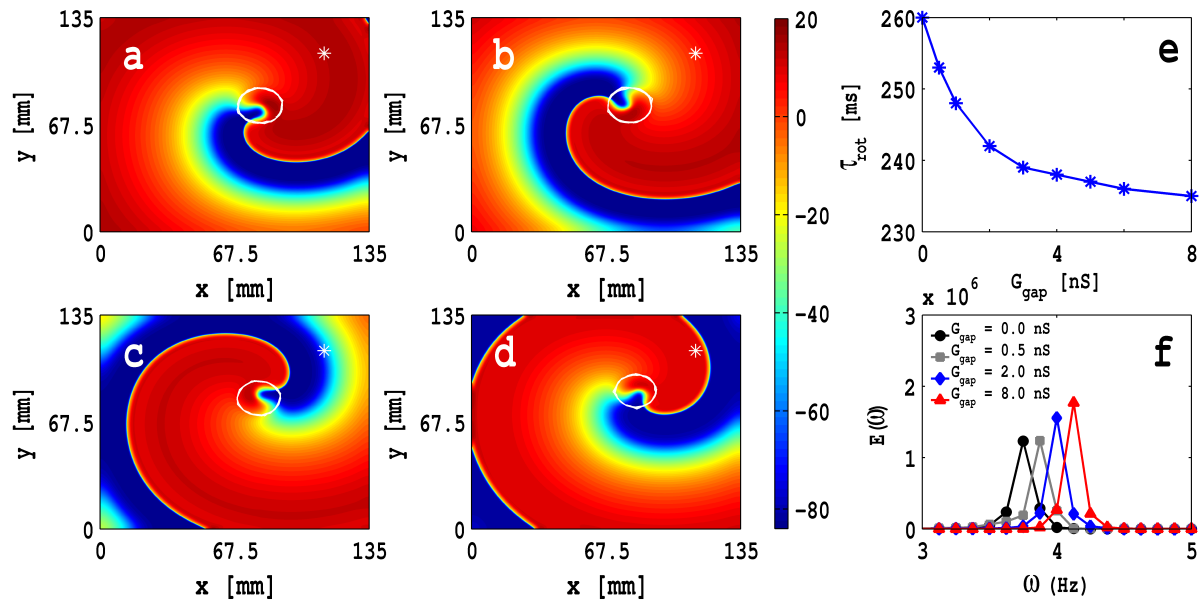


Figure 3.12: Pseudocolour plots of V_m , in a square simulation domain of side $L = 135$ mm, at time $t = 2$ s with $G_f = 4.0$ nS, $E_f = -39.0$ mV, zero-sided coupling with $D_{mm} = 0.00154$ cm²/s, and (a) $G_{gap} = 0.0$ nS (control case, i.e., only myocytes), (b) $G_{gap} = 0.5$ nS (low coupling), (c) $G_{gap} = 2.0$ nS (intermediate coupling), and (d) $G_{gap} = 8.0$ nS (high coupling); the white solid lines show the trajectory of the spiral tip for $2 \leq t \leq 3$ s. Video S2 illustrates the spatiotemporal evolution of these spiral waves. (e) Plot of the rotation period τ_{rot} of the spiral wave versus G_{gap} . (f) Plots of the power spectra $E(\omega)$ of the time series of $V_m(x, y, t)$ recorded from the representative point ($x = 112.5$ mm, $y = 112.5$ mm), which is indicated by an asterisk in (a)-(d), for $G_{gap} = 0.0$ nS (black circles), (b) $G_{gap} = 0.5$ nS (gray squares), (c) $G_{gap} = 2.0$ nS (blue diamonds), and (d) $G_{gap} = 8.0$ nS (red triangles); for these power spectra we use time series with 400000 points.

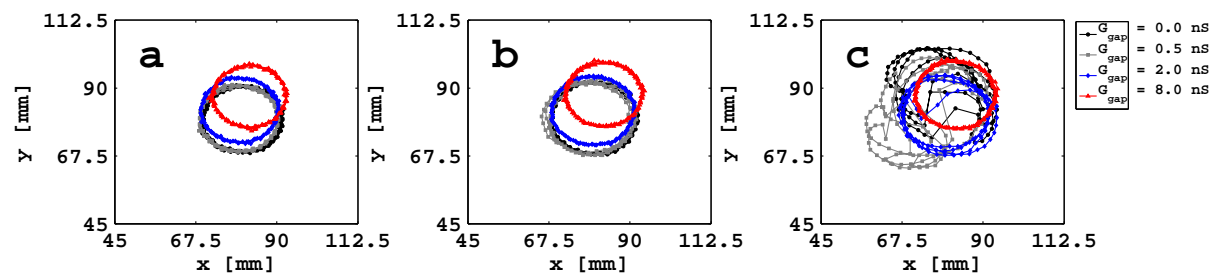


Figure 3.13: Plots of spiral-wave-tip trajectories for the time intervals (a) $2 \leq t \leq 3$ s, (b) $4 \leq t \leq 5$ s, and (c) $6 \leq t \leq 7$ s, with zero-sided coupling, and for the control case with $G_{gap} = 0.0$ nS (black circles), $G_{gap} = 0.5$ nS (gray squares), $G_{gap} = 2.0$ nS (blue diamonds), and $G_{gap} = 8.0$ nS (red triangles), and all other parameter values as in Fig. 3.12. Videos S2, S3, and S4 illustrate the spatiotemporal evolution of these spiral-tip trajectories.

simulation domain with myocytes as follows. Initially we set the diffusion constant $D_{mm} = 0.000385 \text{ cm}^2/\text{ms}$; this is a quarter of its original value, which is $0.00154 \text{ cm}^2/\text{ms}$. We then inject a plane wave into the domain via an S1 stimulus of strength 150 pA/pF for 3 ms at the left boundary. After 560 ms we apply an S2 stimulus of strength 450 pA/pF for 3 ms just behind the *refractory tail* of the plane wave initiated by the S1 stimulus; in our simulation domain the S2 stimulus is applied over the region $x = 360$ and $1 \leq y \leq 550$. We reset D to its original value after 880 ms . This procedure yields a fully developed spiral wave at $t = 976 \text{ ms}$ (see Fig. 3.11 for a pseudocolor plot of the transmembrane potential for this spiral wave); we use the values of V_m , the gating variables, the intracellular ion concentrations for this spiral wave as the initial condition for our subsequent studies. By decreasing D for this small interval of time we are able to reduce CV (because $CV \propto \sqrt{D}$) and, thereby, the wave length λ ; if we do not reduce D for this period, it is difficult to trap the hook of the proto spiral our simulation domain, whose side $L = 13.5 \text{ cm}$.

We use the fully developed spiral wave of Fig. 3.11 in (c) as an initial condition for the myocytes in our 2D simulation domain with MF composites; for the fibroblasts V_f is set equal to E_f at this initial time.

We begin by studying the dependence on G_{gap} of spiral-wave dynamics in our 2D MF-composite simulation domain with zero-sided coupling. In Fig. 3.12 we show pseudocolour plots of V_m , in a square simulation domain of side $L = 135 \text{ mm}$, at time $t = 2 \text{ s}$ with $G_f = 4.0 \text{ nS}$, $E_f = -39.0 \text{ mV}$, and (a) $G_{gap} = 0.0 \text{ nS}$ (control case, i.e., only myocytes), (b) $G_{gap} = 0.5 \text{ nS}$ (low coupling), (c) $G_{gap} = 2.0 \text{ nS}$ (intermediate coupling), and (d) $G_{gap} = 8.0 \text{ nS}$ (high coupling); the white solid lines show the trajectory of the spiral tip for $2 \text{ s} \leq t \leq 3 \text{ s}$. Video S2 illustrates the spatiotemporal evolution of these spiral waves. The plot in Fig. 3.12 (e) of the rotation period τ_{rot} of the spiral wave versus G_{gap} shows that τ_{rot} decreases as G_{gap} increases. In Fig. 3.12 (f) we show the power spectra $E(\omega)$ of the time series of $V_m(x, y, t)$ recorded from the representative point $x = 112.5 \text{ mm}, y = 112.5 \text{ mm}$, which is indicated by an asterisk in Figs. 3.12 (a)-(d), for $G_{gap} = 0.0 \text{ nS}$ (black circles), (b) $G_{gap} = 0.5 \text{ nS}$ (gray squares), (c) $G_{gap} = 2.0 \text{ nS}$ (blue diamonds), and (d) $G_{gap} = 8.0 \text{ nS}$ (red triangles); for these power spectra we use time series with 400000 points; the discrete lines in these power spectra show that, over these time scales, we have periodic temporal evolution that is a characteristic signature of a single, rotating spiral wave. The position of the fundamental peak in these power spectra moves to high frequencies as we increase G_{gap} in a manner that is consistent with the decrease of τ_{rot} in (e).

The rotation period τ_{rot} , for zero-sided coupling, decreases as G_{gap} increases. We can understand this qualitatively by looking at the APD of an MF composite and

examining the propagation properties of plane waves that we have discussed above. Recall that, as G_{gap} increases, the myocyte APD for a myocyte in an MF composite decreases for low values of E_f (e.g., $E_f = -39$ mV, as shown by red triangles in Fig. 3.5 (a)). The APD is roughly equal to the refractory time of a plane wave in a 1D or 2D domain [64], therefore, the refractory period of a plane wave in 2D decreases as G_{gap} increases; and we have checked explicitly that it decreases as G_{gap} increases by applying an additional stimulus at the wave back of the propagating plane wave. The rotation period τ_{rot} of a spiral wave is related to the refractory period of a plane wave, although the curvature plays an additional role in the spiral-wave case [65, 66]. Therefore, spiral waves rotate faster as G_{gap} is increased.

The white solid lines in Figs. 3.12 (a)-(d) show the trajectories of the spiral tips for $2 \text{ s} \leq t \leq 3 \text{ s}$. If we monitor these trajectories for longer durations of time, we obtain the tip trajectories shown in Figs. 3.13 (a), (b), and (c), respectively, for the time intervals $2 \text{ s} \leq t \leq 3 \text{ s}$, $4 \text{ s} \leq t \leq 5 \text{ s}$, and $6 \text{ s} \leq t \leq 7 \text{ s}$ for the case of zero-sided coupling, for the control case with $G_{gap} = 0.0$ ns (black circles), $G_{gap} = 0.5$ ns (gray squares), $G_{gap} = 2.0$ ns (blue diamonds), and $G_{gap} = 8.0$ ns (red triangles), and all other parameter values as in Fig. 3.12. Note that in Figs. 3.13 (a) and (b), i.e., for $t \lesssim 5$ s, these trajectories are very nearly circular for all the values of G_{gap} we consider. However, for $t > 5$ s, the tip trajectories can form Z-type curves as shown in Fig. 3.13 (c) for the control case with $G_{gap} = 0.0$ ns (black circles), $G_{gap} = 0.5$ ns (gray squares), and $G_{gap} = 2.0$ ns (blue diamonds); the trajectory for $G_{gap} = 8.0$ ns (red triangles) continues to be circular. Videos S2, S3, and S4 illustrate the spatiotemporal evolution of these spiral-tip trajectories. The stability of the spiral core increases as we increase G_{gap} because the interaction of the wave back of the preceding arm of the spiral wave and the wave front of the following arm decreases with increasing G_{gap} .

For the case of zero-sided coupling, with $E_f = 0$ mV and $G_f = 8$ nS, Figs. 3.14(a)-(c) show, respectively, pseudocolor plots of the myocyte transmembrane potential V_m , at time $t = 2$ s, for low-frequency autorhythmicity (e.g., with $G_{gap} = 17$ nS), high-frequency autorhythmicity (e.g., with $G_{gap} = 20$ nS), and when the MF composite displays (cf. Fig. 3.8) oscillatory behavior (e.g., with $G_{gap} = 23$ nS). In Fig. 3.14(d), we show the time series of $V_m(x, y, t)$, in the interval $0 \text{ s} \leq t \leq 4 \text{ s}$, obtained from three representative points, shown by asterisks in Fig. 3.14(a), namely, $(x = 22.5 \text{ mm}, y = 22.5 \text{ mm})$ (black filled circles), $(x = 67.5 \text{ mm}, y = 67.5 \text{ mm})$ (blue filled diamonds), and $(x = 112.5 \text{ mm}, y = 112.5 \text{ mm})$ (red filled triangles); Fig. 3.14(g) shows the corresponding power spectra, which we calculate from these time series, each of which has 2×10^5 data points; each one of these power spectra has discrete, sharp peaks at a funda-

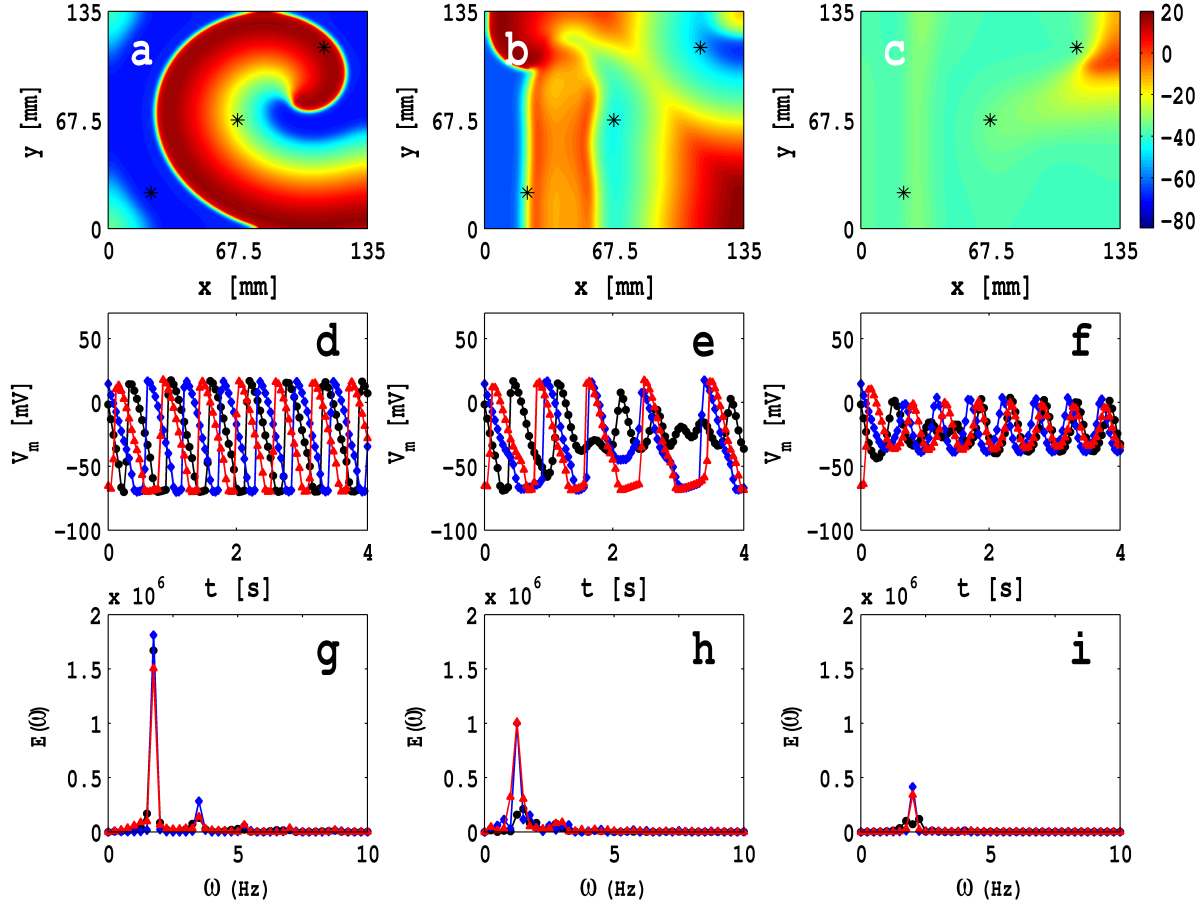


Figure 3.14: Pseudocolor plots of the myocyte transmembrane potential V_m , at time $t = 2$ s, for the case of zero-sided couplings, with $E_f = 0$ mV and $G_f = 8$ nS: (a) low-frequency autorhythmicity ($G_{gap} = 17$ nS), (b) high-frequency autorhythmicity ($G_{gap} = 20$ nS), and (c) when the MF composite displays oscillatory behavior ($G_{gap} = 23$ nS) (see, Figs. 3.8 for the boundaries of these regions). Figures (d)-(f) show, respectively, the time series of $V_m(x, y, t)$, in the time interval $0 \text{ s} \leq t \leq 4 \text{ s}$, obtained from three representative points, shown by asterisks in Fig. 3.14(a)-(c), namely, $(x = 22.5 \text{ mm}, y = 22.5 \text{ mm})$ (black filled circles), $(x = 67.5 \text{ mm}, y = 67.5 \text{ mm})$ (blue filled diamonds), and $(x = 112.5 \text{ mm}, y = 112.5 \text{ mm})$ (red filled triangles). Figures 3.14(g)-(i) show the corresponding power spectra, which we calculate from these time series, each of which has 2×10^5 data points.

mental frequency and at its harmonics; the periodic nature of the time series and these peaks in the power spectra provide evidence for the temporally periodic motion of the spiral wave in the region of low-frequency autorhythmicity. The analogs of Figs. 3.14(d) and (g) are shown in Figs. 3.14(e) and (h) for the regime of high-frequency autorhythmicity; the time series of $V_m(x, y, t)$, in the interval $0 \text{ s} \leq t \leq 4 \text{ s}$, from $(x = 22.5 \text{ mm}, y = 22.5 \text{ mm})$ (black filled circles) and $(x = 67.5 \text{ mm}, y = 67.5 \text{ mm})$ (blue filled diamonds), show irregular behaviors and the corresponding power spectra show subsidiary peaks near the main peaks; however, the time series recorded

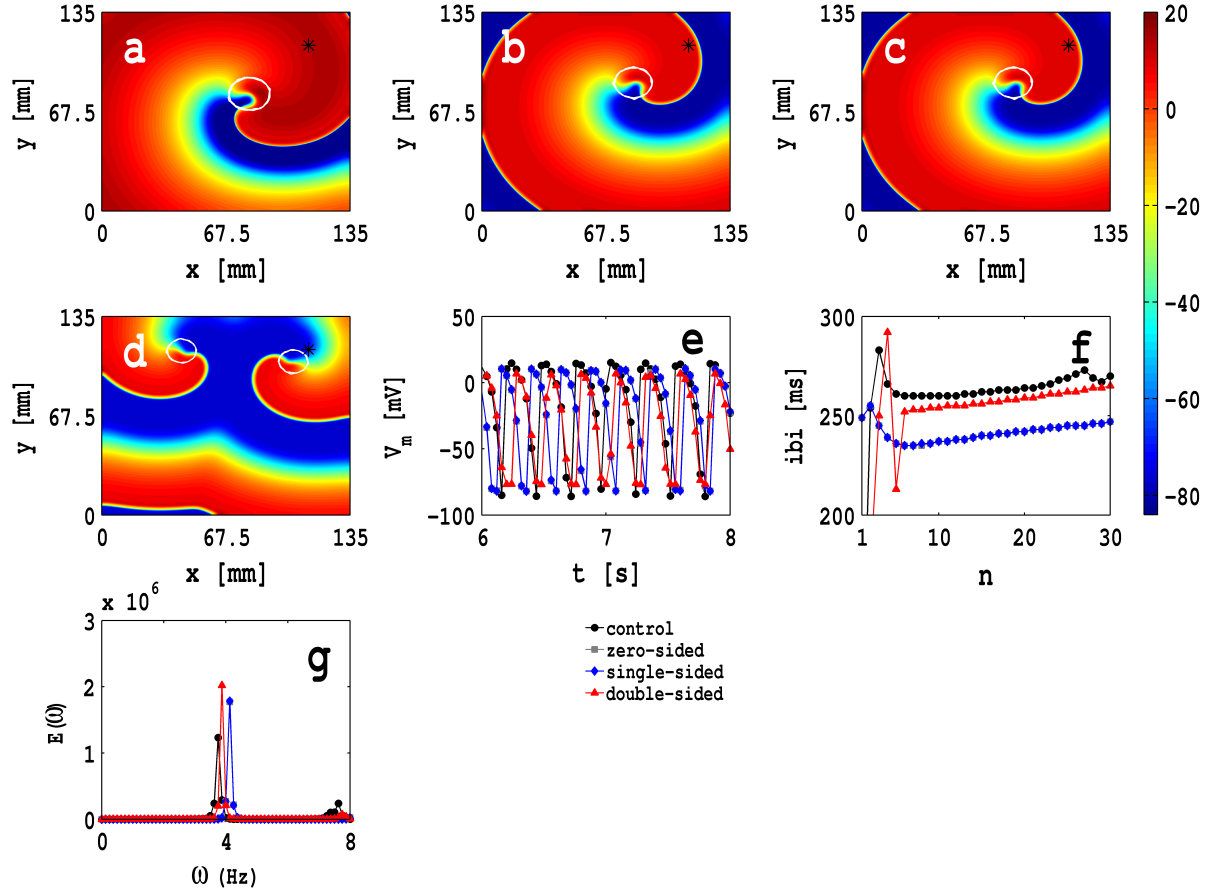


Figure 3.15: Spiral waves in pseudocolor plots of V_m at time $t = 2$ s in a simulation domain with $L = 13.5$ cm, an MF composite at every site, with a myocyte M coupled via $G_{gap} = 8$ nS with one fibroblast F ($C_{f,tot} = 6.3$ pF, $G_f = 4$ nS, and $E_f = -39$ mV) for (a) control case with only myocytes and no fibroblasts, (b) zero-sided coupling, (c) single-sided coupling with $\mathcal{G}_{mm}/\mathcal{G}_{ff} = 1$, and (d) double-sided coupling with $\mathcal{G}_{mm}/\mathcal{G}_{ff} = 1$ and $\mathcal{G}_{mm}/\mathcal{G}_{mf} = 200$; the white solid lines in plots (a), (b), (c), and (d) show the trajectories of the spiral tip for $2 \text{ s} < t < 3 \text{ s}$. Video S5 illustrates the spatiotemporal evolution of these spiral waves. (e) Time series data for $V_m(x, y, t)$ are recorded at the point ($x = 112.5$ mm, $y = 112.5$ mm), shown by an asterisk, for $6 \text{ s} < t < 8 \text{ s}$. (f) Plot of the inter-beat interval (ibi) versus the beat number n , and (g) the power spectrum $E(\omega)$ (of V_m) versus the frequency ω for the control case (black circles), zero-sided coupling (gray squares), single-sided coupling (blue diamonds), and double-sided coupling (red triangles); these plots of ibi and $E(\omega)$ are obtained from a time series of V_m , with 400000 data points separated by 0.02 ms.

from ($x = 112.5$ mm, 112.5 mm) (red filled triangles) shows periodic behavior and, consequently, the corresponding power spectrum has discrete, strong peaks. The analogs of Figs. 3.14(d) and (g), for the oscillatory regime, are shown in Figs. 3.14(f) and (i).

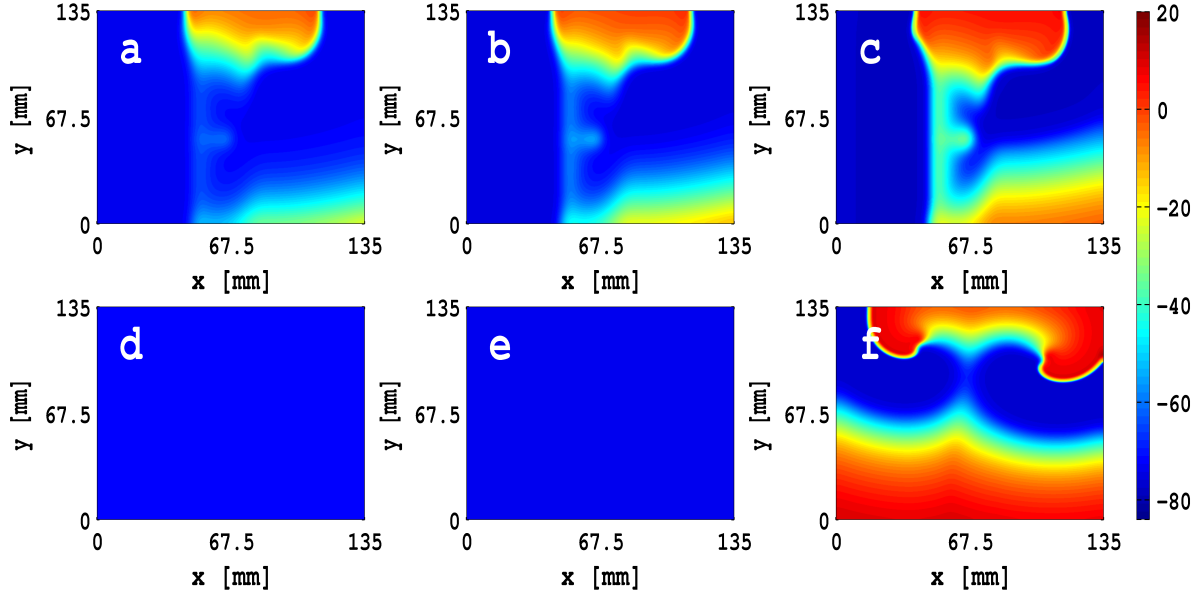


Figure 3.16: Pseudocolor plots show the time evolution of the myocyte transmembrane potential V_m for double-sided diffusive coupling with $D_{mm}/D_{ff} = 1$ and $D_{mm}/D_{mf} = 200$; the fibroblasts in these MF composites have $C_{f,tot} = 6.3$ pF, $G_f = 4.0$ nS, and $E_f = -39.0$ mV; the gap-junctional couplings G_{gap} are, (a) 0.5 nS, (b) 2 nS, and (c) 8 nS. The plots of V_m , at time $t = 80$ ms, are shown in (a), (b), and (c) for the G_{gap} 0.5 nS, 2 nS, and 8 nS, respectively; (d), (e) and (f) are the analogs of (a), (b) and (c) at time $t = 400$ ms. For low and intermediate values of G_{gap} conduction failure occurs as shown in (a),(b), (d), and (e).

In Fig. 3.15 we show spiral waves via pseudocolor plots of V_m at time $t = 2$ s; here, at each site, we have an MF composite with a myocyte M coupled with one fibroblast F for which $G_{gap} = 8$ nS, $C_{f,tot} = 6.3$ pF, $G_f = 4$ nS, and $E_f = -39$ mV. Figure 3.15(a) shows the control case in which there are only myocytes and no fibroblasts; Fig. 3.15(b) shows the spiral wave for the case of zero-sided coupling; Fig. 3.15(c) gives the spiral wave for single-sided coupling with $\mathcal{G}_{mm}/\mathcal{G}_{ff} = 1$; and Fig. 3.15(d) portrays this wave when we have double-sided coupling with $\mathcal{G}_{mm}/\mathcal{G}_{ff} = 1$ and $\mathcal{G}_{mm}/\mathcal{G}_{mf} = 200$; the white solid lines in these plots show the trajectories of the spiral tip for $2 \text{ s} < t < 3 \text{ s}$. Video S5 illustrates the spatiotemporal evolution of these spiral waves. In Fig. 3.15(d), we show the time series of $V_m(x, y, t)$, in the interval $6 \text{ s} \leq t \leq 8 \text{ s}$, obtained from a representative point, shown by asterisks in Figs. 3.15(a-d), namely, $(x = 112.5 \text{ mm}, y = 112.5 \text{ mm})$, for the control case (black circles), zero-sided coupling (gray squares), single-sided coupling (blue diamonds), and double-sided coupling (red triangles); Figs 3.15(e) and (f) contain, respectively, plots of the inter-beat interval (ibi) versus the beat number n and the power spectrum $E(\omega)$ (of V_m) versus the frequency ω for the control case (black circles), zero-sided

coupling (gray squares), single-sided coupling (blue diamonds), and double-sided coupling (red triangles); these plots of i_{bi} and $E(\omega)$ are obtained from a time series with 4×10^5 data points separated by 0.02 ms and recorded from the representative point ($x = 112.5$ mm, $y = 112.5$ mm) that is indicated by a $*$ in these pseudocolor plots. For a specific, initial spiral configuration (see Fig. 3.11), we observe that the spatiotemporal evolution of the system leads to a single rotating spiral for control, zero-sided, and single-sided couplings; however, this initial condition leads to two rotating spirals, with opposite senses of rotation, for double-sided couplings. All initial conditions do not lead to two rotating spiral waves, for the case of double-sided couplings, but some do (see Figs. 3.11 and 3.16). The spiral-wave rotation period, with double-sided couplings, is less than it is in the case with no fibroblasts (only myocytes) but greater than it is with zero- and single-sided couplings. We now investigate the dependence of the two-spiral state, with double-sided couplings, on G_{gap} with the initial spiral configuration shown in Fig. 3.11 (c). In Fig. 3.16, we show pseudocolor plots of the myocyte transmembrane potential V_m , for double-sided coupling with $\mathcal{G}_{mm}/\mathcal{G}_{ff} = 1$ and $\mathcal{G}_{mm}/\mathcal{G}_{mf} = 200$, and at different values of the time t ; the fibroblasts in these MF composites have $C_{f,tot} = 6.3$ pF, $G_f = 4.0$ nS, and $E_f = -39.0$ mV. Pseudocolor plots of V_m at $t = 80$ ms are given in Figs. 3.16 (a), (b), and (c) for $G_{gap} = 0.5$ nS, 2 nS, and 8 nS, respectively; the analogs of these plots at $t = 400$ ms are given, respectively, in Figs. 3.16 (d), (e), and (f). From these plots we conclude that, for low and intermediate values of G_{gap} , conduction failure occurs because of the absorption of spiral waves at the top boundary of the simulation domain (see Figs. 3.16(a), (b), (d), and (e)); however, for $G_{gap} = 8.0$ nS, the initial spiral configuration splits into the two stable spirals as shown in Figs. 3.16(c) and (f).

Spiral waves in inhomogeneous domains

We now examine the effects of fibroblast inhomogeneities on spiral-wave dynamics in our mathematical model; outside the region of the inhomogeneity we use the TNNP model for cardiac tissue; inside the inhomogeneity we use the 2D MF composite domain that we have used in our studies above.

We model an inhomogeneity in our 2D simulation domain by incorporating a small square patch of side ℓ ; this patch is an MF composite domain; the remaining part of the simulation domain contains only myocytes that are coupled via D_{mm} . Again, we focus on three different types of couplings in the MF-composite domain, namely, zero-, single-, and double-sided couplings between myocytes and

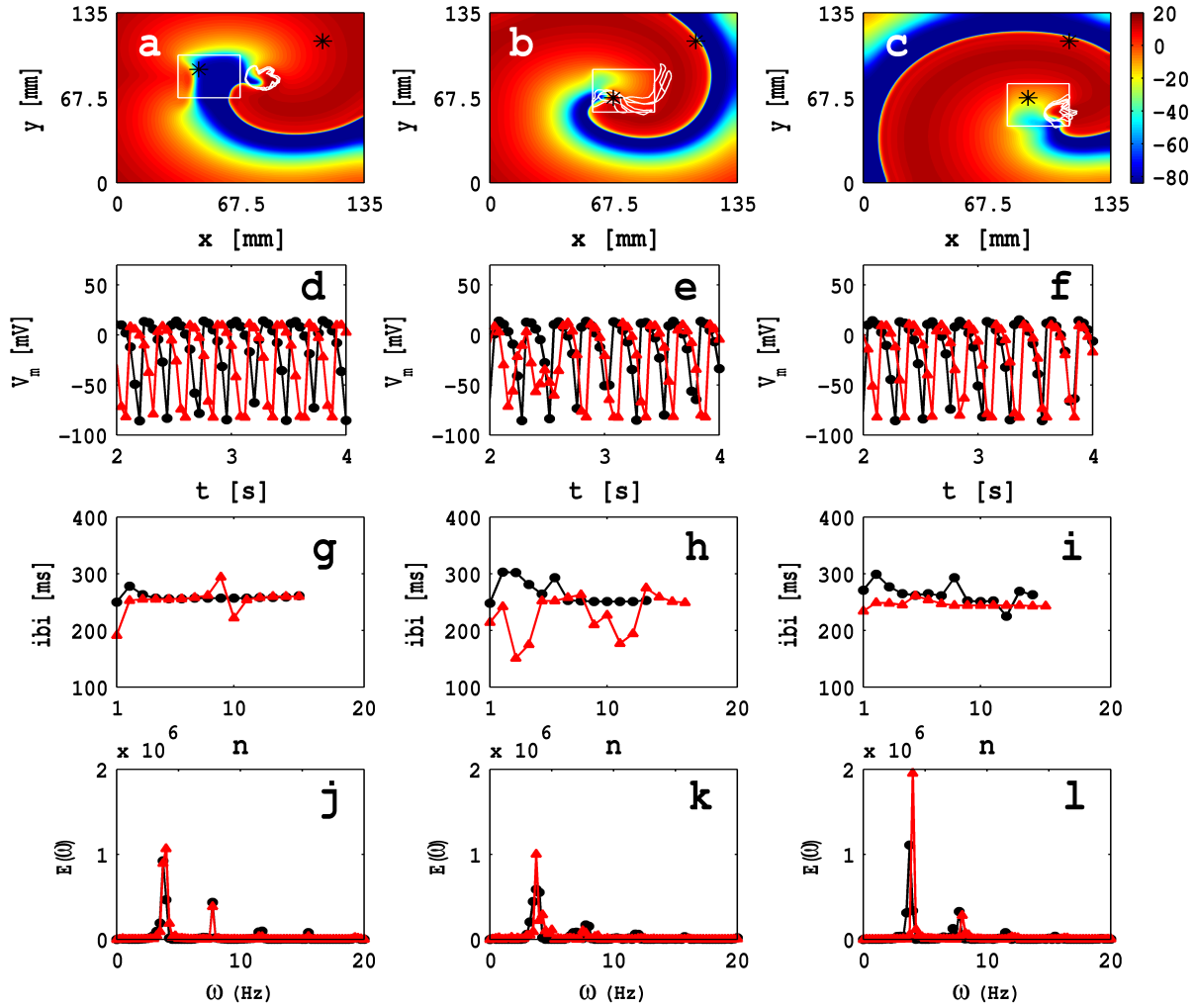


Figure 3.17: Pseudocolor plots of the transmembrane potential of the myocyte V_m at time, $t = 2$ s, in the presence of a square shape MF composite inhomogeneity, of side $\ell = 33.75$ mm, for the case of zero-sided coupling; the bottom-left corner of the inhomogeneity is fixed at (a) $(x = 33.75 \text{ mm}, y = 67.5 \text{ mm})$, (b) $(x = 56.25 \text{ mm}, y = 56.25 \text{ mm})$, and (c) $(x = 78.75 \text{ mm}, y = 45 \text{ mm})$; the white solid lines in these figures show the spiral-tip trajectories in the time interval $2 \text{ s} \leq t \leq 3 \text{ s}$ and the local time series data are recorded from points that are shown by asterisks. Video S6 illustrates the spatiotemporal evolution of these spiral waves. The plots in (d)-(f) show the time series for V_m , in the interval $0 \text{ s} \leq t \leq 4 \text{ s}$, which are obtained from a point outside ($(x = 112.5 \text{ mm}, y = 112.5 \text{ mm})$ for all cases) and inside the fibroblast inhomogeneity ($(x = 45 \text{ mm}, y = 90 \text{ mm})$, $(x = 67.5 \text{ mm}, y = 67.5 \text{ mm})$, and $(x = 90 \text{ mm}, y = 67.5 \text{ mm})$ for (a), (b), and (c), respectively), represented by black circles and red triangles, respectively; (g), (h), and (i) show plots of the inter-beat intervals (ibis) versus the beat number n for the time series of V_m mentioned above; each one of these time series contain 2×10^5 data points; the power spectra $E(\omega)$, which follow from these time series, are given in (j), (k), and (l).

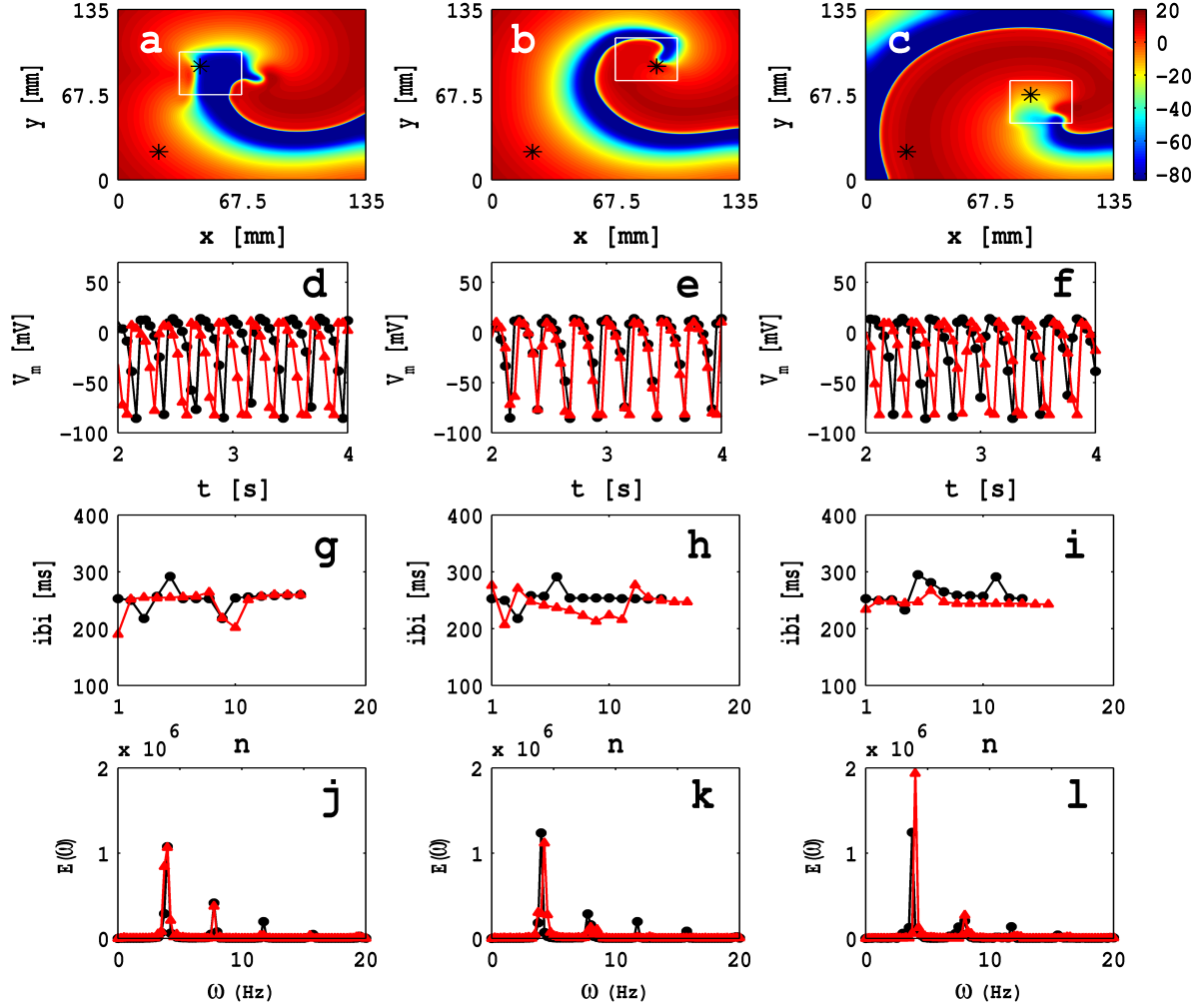


Figure 3.18: Pseudocolor plots of the transmembrane potential V_m of the myocyte at time, $t = 2$ s, in the presence of a square MF-composite inhomogeneity, of side $\ell = 33.75$ mm, for the case of single-sided coupling with $\mathcal{G}_{mm}/\mathcal{G}_{mf} = 1$; the bottom-left corner of the inhomogeneity is fixed at (a) $(x = 33.75 \text{ mm}, y = 67.5 \text{ mm})$, (b) $(x = 56.25 \text{ mm}, y = 56.25 \text{ mm})$, and (c) $(x = 78.75 \text{ mm}, y = 45 \text{ mm})$; the white solid lines in these figures show the spiral-tip trajectories in the time interval $2 \text{ s} \leq t \leq 3 \text{ s}$ and the local time series data are recorded from points that are shown by asterisks. The plots in (d)-(f) show the time series for V_m , in the interval $0 \text{ s} \leq t \leq 4 \text{ s}$, which are obtained from the points outside $((x = 112.5 \text{ mm}, y = 112.5 \text{ mm})$ for all cases) and inside the fibroblast inhomogeneity $((x = 45 \text{ mm}, y = 90 \text{ mm})$, $(x = 67.5 \text{ mm}, y = 67.5 \text{ mm})$, and $(x = 90 \text{ mm}, y = 67.5 \text{ mm})$ for (a), (b), and (c), respectively), represented by black circles and red triangles, respectively; (g), (h), and (i) show plots of the inter-beat intervals (ibis) versus the beat number n for the time series of V_m mentioned above; each one of these time series contain 2×10^5 data points; the power spectra $E(\omega)$, which follow from these time series, are given in (j), (k), and (l).

fibroblasts; and we choose to the following, representative fibroblast parameters: $C_{f,tot} = 6.3 \text{ pF}$, $G_f = 4 \text{ nS}$, and $E_f = -39 \text{ mV}$. In most of our studies, we use $G_{gap} = 8 \text{ nS}$.

In Figs. 3.17 (a), (b), and (c) we show pseudocolor plots of V_m at time, $t = 2$ s, in the presence of a square fibroblast inhomogeneity, of side 33.75 mm, for the case of zero-sided coupling, and the lower-left-hand corner of the inhomogeneity at, respectively, $(x = 33.75 \text{ mm}, y = 67.5 \text{ mm})$, $(x = 56.25 \text{ mm}, y = 56.25 \text{ mm})$ and $(x = 78.75 \text{ mm}, y = 45 \text{ mm})$, respectively; the white solid lines in these figures show the spiral-tip trajectories, for $2 \text{ s} \leq t \leq 3 \text{ s}$. We also obtain time series for V_m from a point outside the inhomogeneity ($(x = 112.5 \text{ mm}, y = 112.5 \text{ mm})$ for all cases) and a point inside it ($(x = 45 \text{ mm}, y = 90 \text{ mm})$, $(x = 67.5 \text{ mm}, y = 67.5 \text{ mm})$, and $(x = 90 \text{ mm}, y = 67.5 \text{ mm})$ for Figs. 3.17 (a), (b), and (c), respectively). Data from the points outside and inside the fibroblast inhomogeneity are represented, respectively, by black circles and red triangles in Figs. 3.17 (d), (e), and (f). Figures 3.17 (g), (h), and (i) show plots of the inter-beat intervals (ibi) versus the beat number n for the time series of V_m mentioned above; each one of these time series contain 2×10^5 data points; the power spectra $E(\omega)$, which follow from these time series, are given in Figs. 3.17 (j), (k), and (l).

The white solid lines in Figs. 3.17 (a)-(c) show the trajectories of the spiral tips for $2 \text{ s} \leq t \leq 3 \text{ s}$; note that these trajectories depend sensitively on the position of the MF composite inhomogeneity; furthermore, the dynamics of the wave, inside and outside this inhomogeneity, are different (cf., our previous studies with ionic inhomogeneities [24, 25]). Figure 3.17 (a) shows that, in the presence of an MF-composite inhomogeneity, the tip trajectory deviates from one with a circular core; the corresponding plots of the ibi and power spectra, Figs. 3.17 (g) and (j), respectively, illustrate that the temporal evolution of the spiral is periodic inside and outside of the inhomogeneous domain. However, for the inhomogeneity of Fig. 3.17 (b), we observe non-periodic and periodic temporal evolutions, respectively, inside and outside the MF inhomogeneity as can be surmised from the ibi and power-spectra plots in Figs. 3.17 (h) and (k); the tip has a Z -type trajectory, extends over a length $\simeq 34 \text{ mm}$, and it meanders both inside and outside the inhomogeneity. For the inhomogeneity of Fig. 3.17 (c), we obtain periodic and non-periodic temporal evolutions, respectively, inside and outside the MF-composite inhomogeneity (see Figs. 3.17 (i) and (l) for the ibi and power spectra); here the tip trajectory has a linear extent $\simeq 14 \text{ mm}$ and it is restricted, predominantly, inside the inhomogeneity. The Video S6 has four animations that show superimpositions of pseudocolor plots of V_m and the spiral-tip trajectories for $2 \leq t \leq 3 \text{ s}$ for a control myocyte layer with no inhomogeneities and the simulation domains for Figs. 3.17 (a)-(c). If we use one-sided coupling with $\mathcal{G}_{mm}/\mathcal{G}_{ff} = 1$, we find that our results are similar to those we have depicted in Fig. 3.17 for zero-sided coupling, as we show in Fig. 3.18. In general, the

heterogeneity of cardiac tissue causes a drift of the spiral wave towards regions in which a spiral wave has a long period of rotation [67–69]. In our studies, the period of a spiral wave decreases slightly inside the fibroblast heterogeneity; and the final position of the spiral depends on the location of the heterogeneity.

Next we investigate the dependence of spiral-wave dynamics on the size of the MF-composite inhomogeneity. Figures 3.19 (a), (b), and (c) show pseudocolor plots, at time $t = 2$ s, of V_m for three representative square inhomogeneities, with sides $\ell = 22.5$ mm, $\ell = 33.75$ mm, and $\ell = 45$ mm; the lower-left-hand corner of these squares is fixed at (56.25 mm, 56.25 mm). The white, solid lines in these figures show the spiral-tip trajectories for $2 \leq t \leq 3$ s. The spiral-tip trajectory, shown in Fig. 3.19(a), is a closed, but not circular, path that is confined inside the inhomogeneity; as the size of the inhomogeneity grows, this tip trajectory also grows in size and parts of it lie outside the inhomogeneity, as shown, e.g., in Fig. 3.19(b) and (c); in the latter two cases, the tip trajectories are not closed and their linear extent is comparable to the length of the side of the inhomogeneity. We also obtain time series for V_m from a point outside the inhomogeneity (22.5mm, 22.5mm) and a point inside it (67.5mm, 67.5mm); these points are indicated, respectively, by black and white asterisks in Figs. 3.19 (a), (b), and (c); and data from the points outside and inside the fibroblast inhomogeneity are represented, respectively, by black circles and red triangles in Figs. 3.19 (d)-(l). In Figs. 3.19 (d), (e), and (f) we give the time series of V_m ; Figs. 3.19 (g), (h), and (i) show plots of the inter-beat intervals (ibis) versus the beat number n for the time series of V_m mentioned above (these contain 2×10^5 data points); the power spectra $E(\omega)$, which follow from these time series, are given in Figs. 3.19 (j), (k), and (l). The Video S7 has four panels that show superimpositions of pseudocolor plots of V_m and the spiral-tip trajectories for $2 \leq t \leq 3$ s for a control myocyte layer with no inhomogeneities (top left panel) and the simulation domains for Figs. 3.19 (a), (b), and (c) (top right, bottom left, and bottom right panels, respectively). We observe rich varieties of spiral-wave dynamics, both inside and outside of the inhomogeneity. The precise spatiotemporal evolution of the spiral waves depends on the size of the inhomogeneity; for a careful investigation of this size dependence, we must keep one point of the inhomogeneity, say its left bottom corner, fixed, as in Figs. 3.19(a), (b), and (c), where we find that the system moves from periodic to non-periodic temporal evolution as the size of the inhomogeneity increases; this conclusion follows from the ibi plots in Figs. 3.19(g)-(i) and the power spectra in Figs. 3.19(j)-(l). Note, furthermore, that the spiral-wave rotation period τ_{rot} decreases as the size of inhomogeneity increases; this is consistent with

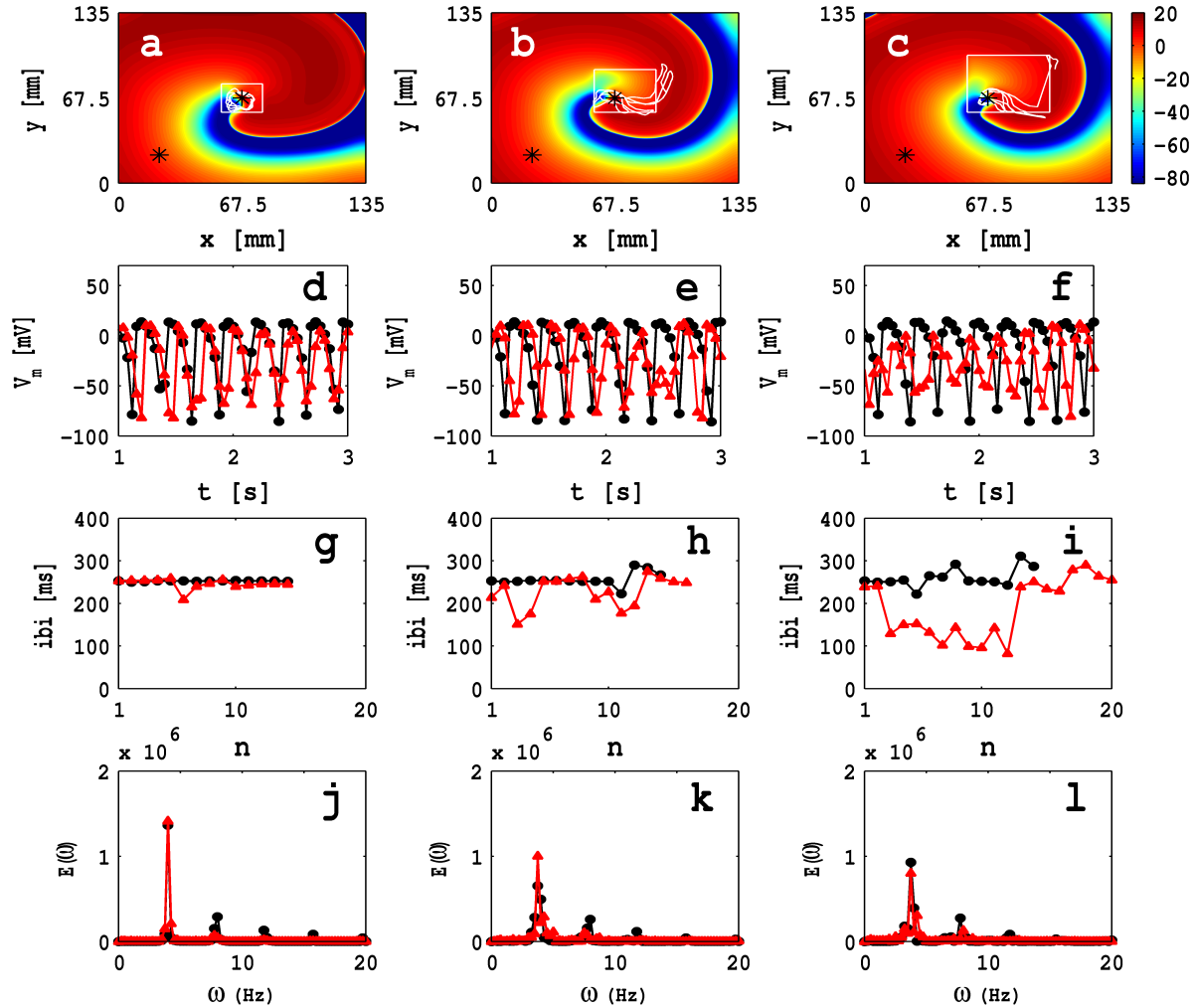


Figure 3.19: Pseudocolor plots of the transmembrane potential of the myocyte V_m at time, $t = 2$ s, in the presence of three square MF composite inhomogeneities with sides (a) $\ell = 22.5$ mm, (b) $\ell = 33.75$ mm, and (c) $\ell = 45$ mm, for the case of zero-sided coupling; the bottom-left corner of these squares is fixed at $(x = 56.25 \text{ mm}, y = 56.25 \text{ mm})$; the white solid lines in these figures show the spiral-tip trajectories in the time interval $2 \text{ s} \leq t \leq 3 \text{ s}$ and the local time series data are recorded from points that are shown by asterisks. Video S7 illustrates the spatiotemporal evolution of these spiral waves. The plots in (d)-(f) show the time series for V_m , in the interval $0 \text{ s} \leq t \leq 4 \text{ s}$, which are obtained from the point outside the inhomogeneity ($x = 22.5 \text{ mm}, y = 22.5 \text{ mm}$) and a point inside it ($x = 67.5 \text{ mm}, y = 67.5 \text{ mm}$), represented by black filled circles and red filled triangles, respectively; (g), (h), and (i) show plots of the inter-beat intervals (ibis) versus the beat number n for the time series of V_m mentioned above; each one of these time series contain 2×10^5 data points; the power spectra $E(\omega)$, which follow from these time series, are given in (j), (k), and (l).

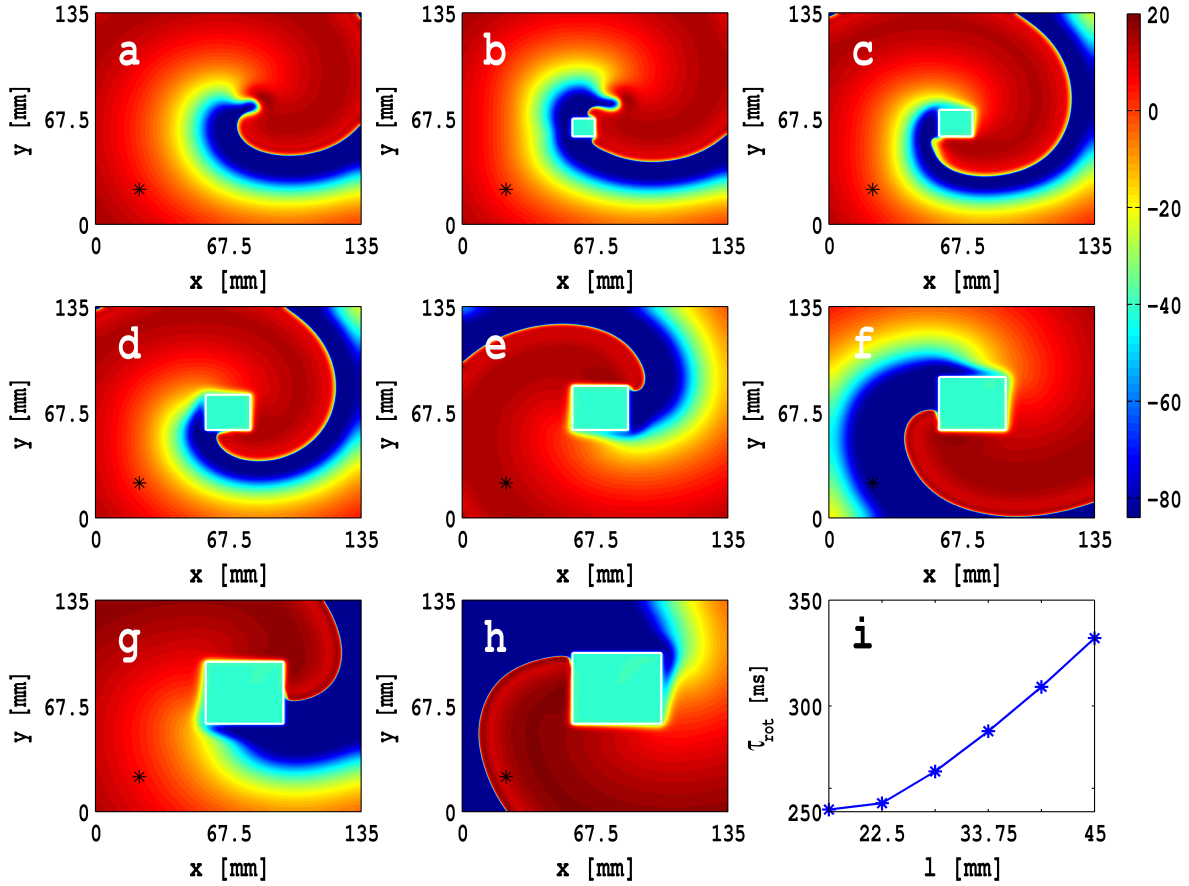


Figure 3.20: Pseudocolor plots of the transmembrane potential of the myocyte V_m at time, $t = 2$ s, when a square MF-composite inhomogeneity, with $\mathcal{G}_{mm}/\mathcal{G}_{ff} = 1$ and $\mathcal{G}_{mm}/\mathcal{G}_{mf} = 1$, is placed with its lower-left corner at $(x = 67.5\text{mm}, y = 67.5\text{mm})$; the square has a side of length (a) $\ell = 0$, i.e., no inhomogeneity, (b) $\ell = 11.25\text{mm}$, (c) $\ell = 16.875\text{mm}$, (d) $\ell = 22.5\text{mm}$, (e) $\ell = 28.125\text{mm}$, (f) $\ell = 33.75\text{mm}$, (g) $\ell = 39.375\text{mm}$, and (h) $\ell = 45\text{mm}$. Video S8 illustrates the spatiotemporal evolution of these spiral waves for (a), (d), (f) and (h). The smallest MF-composite inhomogeneity that can anchor a spiral wave has $\ell = 16.875\text{mm}$; (i) shows a plot of the rotation period τ_{rot} of such an anchored spiral wave.

Fig. 3.15 (f), which shows that the ibi for a homogenous myocyte layer is greater than the ibi of a homogeneous MF-composite layer.

We turn now to a study of an MF-composite inhomogeneity with double-sided coupling. We have shown that, in a homogeneous, 2D simulation domain with such MF composites, the occurrence of conduction block depends on the value of \mathcal{G}_{mf} ; e.g., we have observed that conduction failure occurs if $\mathcal{G}_{mm}/\mathcal{G}_{mf} \leq 4$ and $G_{gap} = 8$ nS, but it does not occur if $G_{gap} = 8$ nS and $\mathcal{G}_{mm}/\mathcal{G}_{mf} > 4$; in the latter case, CV depends on the ratio $\mathcal{G}_{mm}/\mathcal{G}_{mf}$. Therefore, we choose the following four representative values for \mathcal{G}_{mf} in our MF-composite inhomogeneity studies: $\mathcal{G}_{mm}/\mathcal{G}_{mf} = 1$, $\mathcal{G}_{mm}/\mathcal{G}_{mf} = 50$, $\mathcal{G}_{mm}/\mathcal{G}_{mf} = 100$, and $\mathcal{G}_{mm}/\mathcal{G}_{mf} = 200$. We begin with $\mathcal{G}_{mm}/\mathcal{G}_{mf} = 1$ for which conduc-

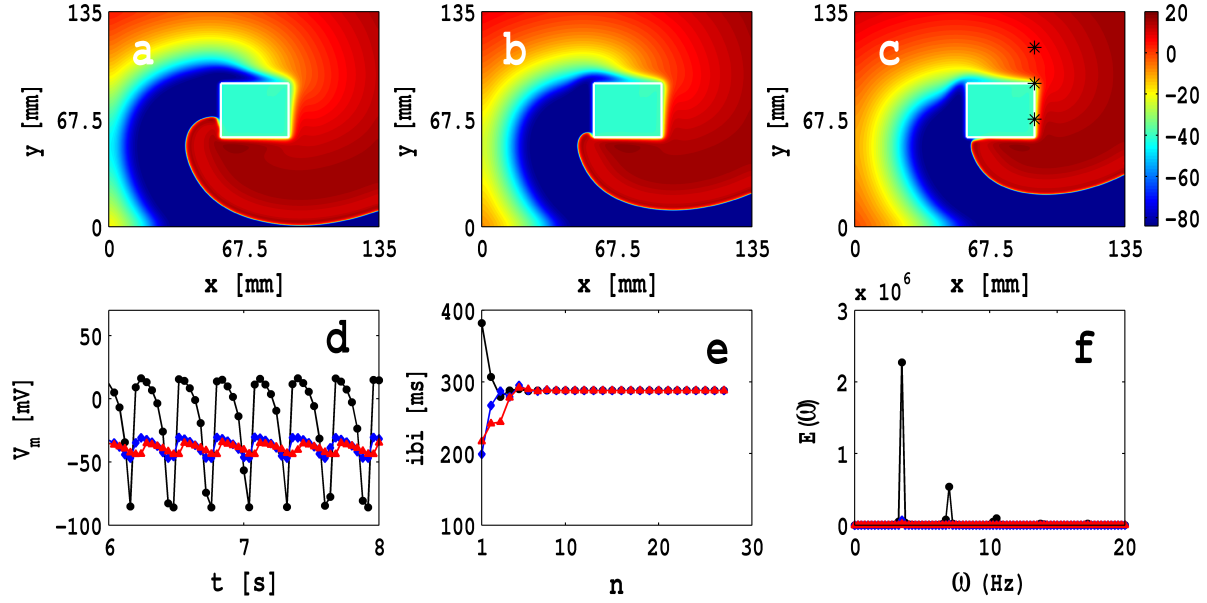


Figure 3.21: Pseudocolor plots of the transmembrane potential of the myocyte V_m at time, (a) $t = 2$ s, (b) $t = 4$ s, and (c) $t = 6$ s, when a square MF-composite inhomogeneity with, $\mathcal{G}_{mm}/\mathcal{G}_{ff} = 1$ and $\mathcal{G}_{mm}/\mathcal{G}_{mf} = 1$, and of length $\ell = 33.75$ mm, is placed with its lower-left corner at $(x = 67.5\text{mm}, y = 67.5\text{mm})$; (d) shows the time series of $V_m(x, y, t)$, in the time interval $0 \leq t \leq 4$ s, obtained from three representative points, shown by asterisks in (c), namely, $(x = 90 \text{ mm}, y = 112.5 \text{ mm})$ (black filled circles), $(x = 90 \text{ mm}, y = 90 \text{ mm})$ (blue filled diamonds), and $(x = 90 \text{ mm}, y = 67.5 \text{ mm})$ (red filled triangles); the corresponding ibi's, calculated from data sets of 4×10^5 points, are shown in (e); (f) shows the power spectrum of the above time series of V_m of length 2×10^5 data points (after removing the initial 2×10^5 iteration steps).

tion failure occurs for all physical values \mathcal{G}_{ff} and \mathcal{G}_{gap} in the homogeneous case. In Figs. 3.20 (a)-(h), we show pseudocolor plots of V_m at time $t = 2$ ms, when a square MF-composite inhomogeneity, with $\mathcal{G}_{mm}/\mathcal{G}_{ff} = 1$ and $\mathcal{G}_{mm}/\mathcal{G}_{mf} = 1$, is placed with its lower-left corner at $(x = 67.5 \text{ mm}, y = 67.5 \text{ mm})$; the square has a side of length $\ell = 0$, i.e., no inhomogeneity (Fig. 3.20(a)), $\ell = 11.25$ mm (Fig. 3.20(b)), $\ell = 16.875$ mm (Fig. 3.20(c)), $\ell = 22.5$ mm (Fig. 3.20(d)), $\ell = 28.125$ mm (Fig. 3.20(e)), $\ell = 33.75$ mm (Fig. 3.20(f)), $\ell = 39.375$ mm (Fig. 3.20(g)), and $\ell = 45$ mm (Fig. 3.20(h)). The smallest MF-composite inhomogeneity that can anchor a spiral wave has $\ell = 16.875$ mm. The Video S8 has four panels that show the spatiotemporal evolution of pseudocolor plots of V_m for $2 \text{ s} \leq t \leq 3 \text{ s}$ for a control myocyte layer with no inhomogeneities (top left panel) and the simulation domains for Figs. 3.20 (d), (f), and (h) (top right, bottom left, and bottom right panels, respectively). Figure 3.20(i), a plot of the rotation period τ_{rot} , of such an anchored spiral wave, versus ℓ , shows how τ_{rot} increases with ℓ ; such an increase has also been seen for a conduction inhomogeneity [70].

If the value of $\mathcal{G}_{mm}/\mathcal{G}_{mf}$ is such that conduction failure occurs in a homogeneous, MF-composite simulation domain, then the MF-composite inhomogeneity behaves somewhat like a conduction inhomogeneity inasmuch as the spiral wave does not enter significantly into the region of the inhomogeneity. To check how far the wave penetrates into the MF-composite inhomogeneity, we show in Figs. 3.21 (a), (b), and (c) pseudocolor plots of V_m at times $t = 2\text{s}$, $t = 6\text{s}$, and $t = 8\text{s}$, respectively, when a square MF-composite inhomogeneity of side $\ell = 33.75\text{mm}$, with $\mathcal{G}_{mm}/\mathcal{G}_{ff} = 1$ and $\mathcal{G}_{mm}/\mathcal{G}_{mf} = 1$ is placed with its bottom left corner at $(x = 56.25\text{ mm}, y = 56.25\text{ mm})$. Data for the time series of $V_m(x, y, t)$ are recorded at three points of the simulation domain, namely, $(x = 90\text{mm}, y = 112.5\text{mm})$, which lies outside the inhomogeneity, $(x = 90\text{mm}, y = 90\text{mm})$, at the top-right corner of the inhomogeneity, and $(x = 90\text{mm}, y = 67.5\text{mm})$, on the right-middle side of the inhomogeneity; these points are indicated by asterisks in Fig. 3.21 (c) and the data recorded from them are represented, respectively, by black circles, blue diamonds, and red triangles in Figs. 3.21 (d)-(f). Figure 3.21 (d) contains plots of the time series of V_m (each one of these time series contain 2×10^5 data points). Figure 3.21 (e) shows the corresponding plots of the inter-beat intervals (ibi) versus the beat number n ; and the power spectra $E(\omega)$, which follow from the time series of V_m , are given in Fig. 3.21 (f).

From the time series of V_m (Fig. 3.21 (d)), we see small-amplitude oscillations in V_m if the time series are obtained from points at the side and corner of the MF-composite inhomogeneity; however, if the point lies outside the inhomogeneity, this time series shows a periodic pattern of action potentials. These times series and the plots of the ibi (Fig. 3.21 (e)) show that the oscillations in V_m , from these three different points, are in phase; to this extent the MF-composite inhomogeneity acts like a conduction inhomogeneity [24]; however, the spiral wave does penetrate the region of the inhomogeneity marginally, so, in this sense, the MF-composite inhomogeneity acts like an ionic inhomogeneity [24].

In our plane-wave studies in 2D homogeneous simulation domains with double-sided coupling, we have noted that the propagation speed CV and the wave length λ depend \mathcal{G}_{mf} . Therefore, we now carry out a study of the interaction of spiral waves with an MF-composite inhomogeneity for different values of \mathcal{G}_{mf} . We have seen above that an MF-composite inhomogeneity behaves somewhat like a conduction inhomogeneity if $\mathcal{G}_{mm}/\mathcal{G}_{mf} = 1$. In Figs. 3.22 (a), (b), and (c) we show, for $\mathcal{G}_{mm}/\mathcal{G}_{mf} = 50, 100, \text{ and } 200$, respectively, pseudocolor plots of V_m , at time $t = 2\text{ s}$, in the presence of a square, MF-composite inhomogeneity, of side $\ell = 33.75\text{ mm}$ and with its lower-left-hand corner placed at $(x = 56.25\text{ mm}, y = 56.25\text{ mm})$ for the case of doubled-sided coupling with $\mathcal{G}_{mm}/\mathcal{G}_{ff} = 1$ and $G_{gap} = 8\text{ nS}$. We also obtain time series

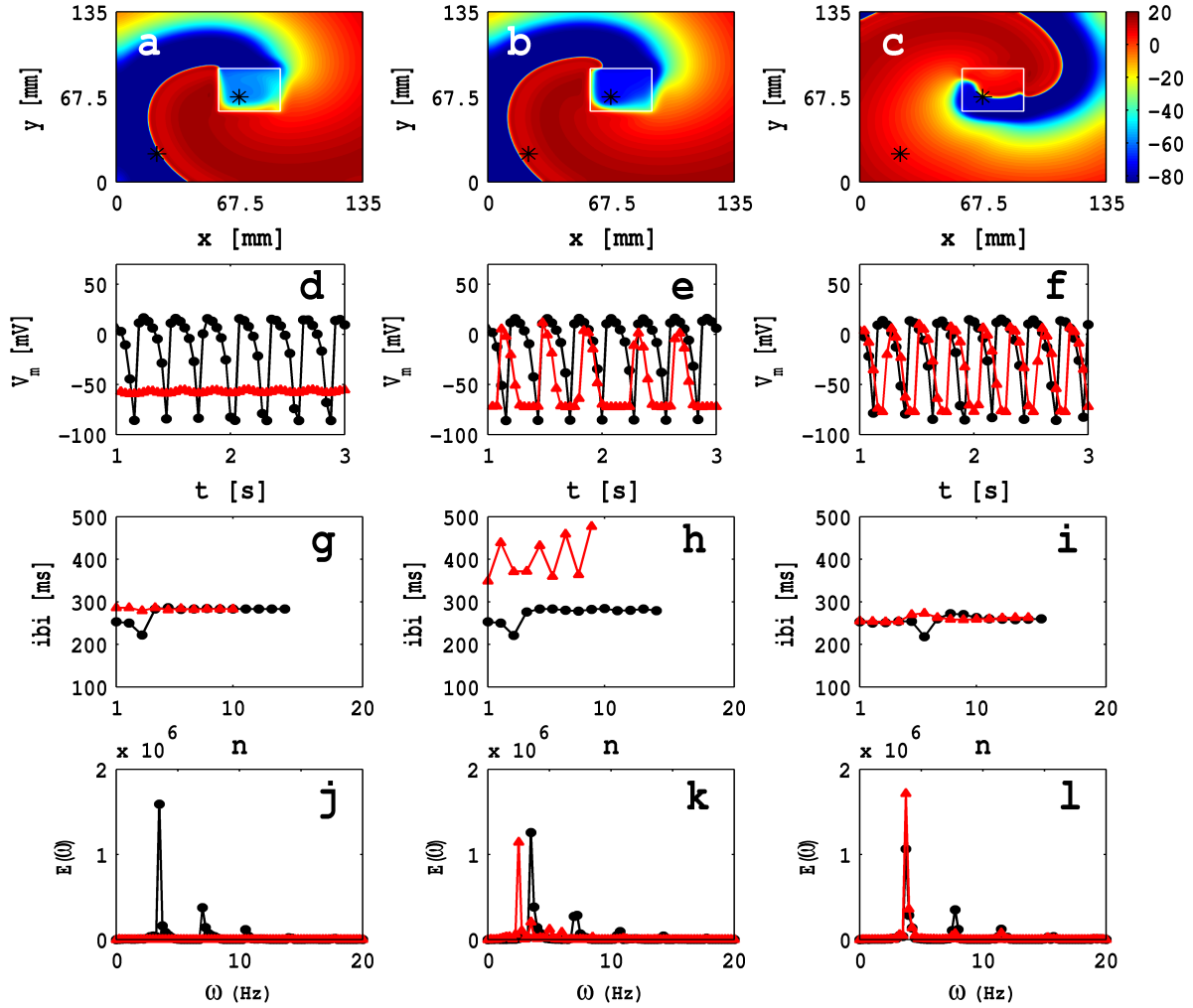


Figure 3.22: Pseudocolor plots of the transmembrane potential of the myocyte V_m , at time $t = 2$ s, in the presence of a square, MF-composite inhomogeneity, of side $\ell = 33.75$ mm and with its lower-left-hand corner placed at $(x = 56.25$ mm, $y = 56.25$ mm) for the case of doubled-sided coupling with $\mathcal{G}_{mm}/\mathcal{G}_{ff} = 1$ and $G_{gap} = 8$ nS: (a) $\mathcal{G}_{mm}/\mathcal{G}_{mf} = 50$, (b) $\mathcal{G}_{mm}/\mathcal{G}_{mf} = 100$, and (c) $\mathcal{G}_{mm}/\mathcal{G}_{mf} = 200$. Video S9 illustrates the spatiotemporal evolution of these spiral waves. The time series for $V_m(x, y, t)$, with 2×10^5 , from a point outside the inhomogeneity ($x = 22.5$ mm, $y = 22.5$ mm) and a point inside it ($x = 67.5$ mm, $x = 67.5$ mm), both of which are depicted by asterisks in (a)-(c), are plotted in (d), (e), and (f) for $\mathcal{G}_{mm}/\mathcal{G}_{mf} = 50$, 100, and 200, respectively (data from the points outside and inside the inhomogeneity are represented, respectively, by black circles and red triangles); (g), (h), and (i) show the corresponding plots of the ibi versus the beat number n ; and the associated power spectra $E(\omega)$ are depicted in (j), (k), and (l).

for $V_m(x, y, t)$ from a point outside the inhomogeneity ($x = 22.5$ mm, $y = 22.5$ mm) and a point inside it ($x = 67.5$ mm, $x = 67.5$ mm), both of which are depicted by asterisks in Figs. 3.22 (a)-(c). These time series, with 2×10^5 data points each, are plotted

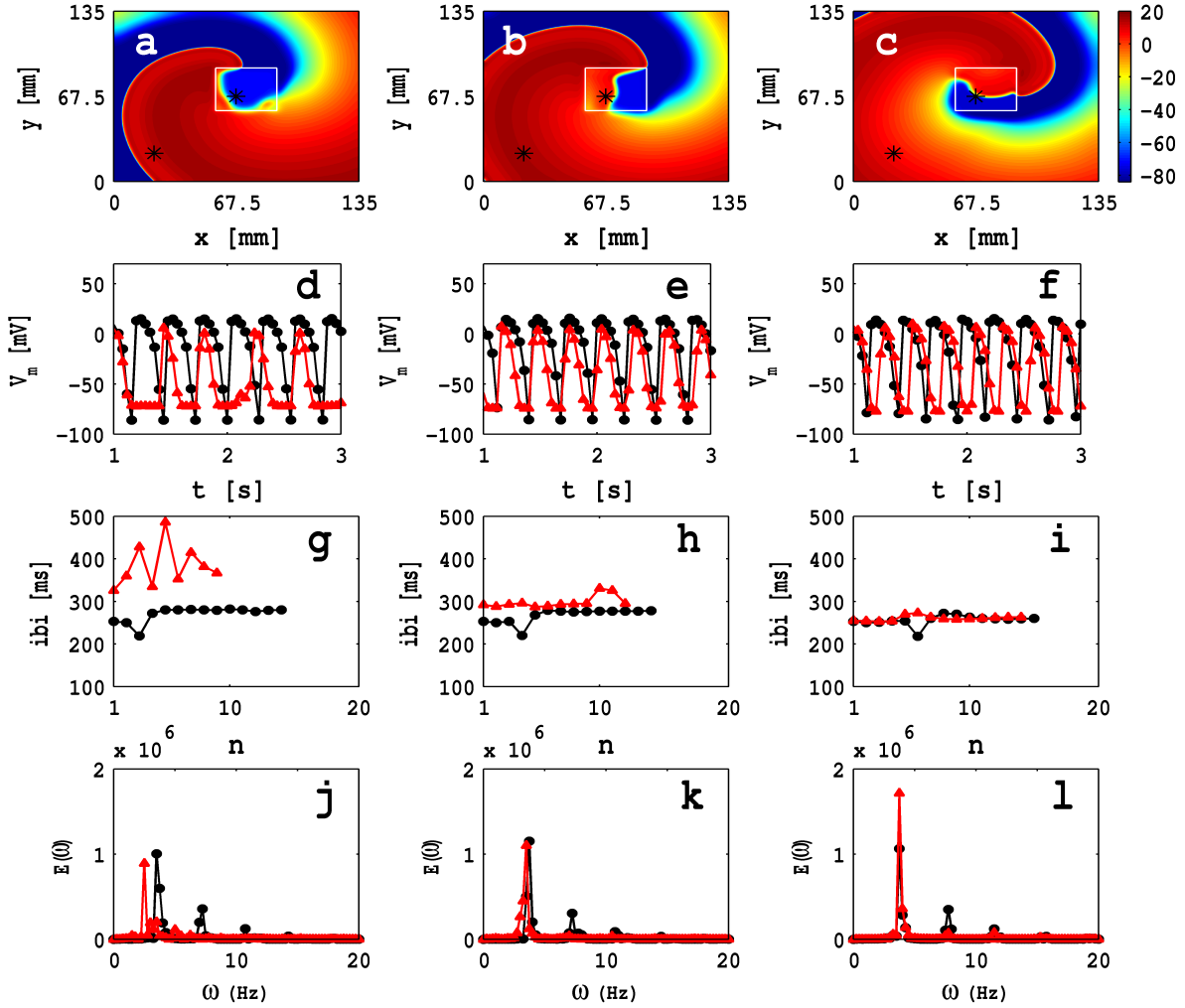


Figure 3.23: Pseudocolor plots of the transmembrane potential of the myocyte V_m , at time $t = 2$ s, in the presence of a square, MF-composite inhomogeneity, of side $\ell = 33.75$ mm and with its lower-left-hand corner placed at $(x = 56.25 \text{ mm}, y = 56.25 \text{ mm})$ for the case of doubled-sided coupling with $\mathcal{G}_{mm}/\mathcal{G}_{ff} = 1$ and $\mathcal{G}_{mm}/\mathcal{G}_{ff} = 200$: (a) $G_{gap} = 0.5$ nS, (b) $G_{gap} = 2$ nS, and (c) $G_{gap} = 8$ nS. Video S10 illustrates the spatiotemporal evolution of these spiral waves. The time series for $V_m(x, y, t)$, with 2×10^5 data points each, from a point outside the inhomogeneity ($x = 22.5 \text{ mm}, y = 22.5 \text{ mm}$) and a point inside it ($x = 67.5 \text{ mm}, y = 67.5 \text{ mm}$), both of which are depicted by asterisks in (a)-(c), are plotted in (d), (e), and (f) for $G_{gap} = 0.5$ nS, 2 nS, and 8 nS, respectively (data from the points outside and inside the inhomogeneity are represented, respectively, by black circles and red triangles); (g), (h), and (i) show the corresponding plots of the ibi versus the beat number n ; and the associated power spectra $E(\omega)$ are depicted in (j), (k), and (l).

in Figs. 3.22 (d), (e), and (f) for $\mathcal{G}_{mm}/\mathcal{G}_{mf} = 50, 100,$ and $200,$ respectively (data from the points outside and inside the inhomogeneity are represented, respectively, by black circles and red triangles); Figs. 3.22 (g), (h), and (i) show the corresponding

plots of the ibi versus the beat number n ; and the associated power spectra $E(\omega)$ are depicted in Figs. 3.22 (j), (k), and (l). The Video S9 has four panels that show the spatiotemporal evolution of pseudocolor plots of V_m and the spiral-tip trajectories for $2 \text{ s} \leq t \leq 3 \text{ s}$ for a control myocyte layer with no inhomogeneities (top left panel) and, in addition, the simulation domains of Figs. 3.22 (a)-(c) (top right, bottom left, and bottom right panels). We observe rich spiral-wave dynamics, which can be different inside and outside of the MF-composite inhomogeneity, as in the cases with zero- and single-sided couplings. The degree to which the spiral-wave penetrates inside the inhomogeneity depends on the value of \mathcal{G}_{mf} , as we can see from the time-series plots of Figs. 3.22(d)-(f).

We turn now to an examination of the interaction of spiral waves with an MF-composite inhomogeneity for different values of G_{gap} . For the same MF-composite inhomogeneity and parameters as in Fig. 3.22 (c), we show in Figs. 3.23 (a), (b), and (c) for, respectively, $G_{gap} = 0.5 \text{ nS}$ (low coupling), 2 nS (intermediate coupling), and 8 nS (high coupling), pseudocolor plots of V_m , at time $t = 2 \text{ s}$, with $\mathcal{G}_{mm}/\mathcal{G}_{mf} = 1$ and $\mathcal{G}_{mm}/\mathcal{G}_{mf} = 200$. We also obtain time series for $V_m(x, y, t)$ from a point outside the inhomogeneity ($x = 22.5\text{mm}, y = 22.5\text{mm}$) and a point inside it ($x = 67.5\text{mm}, y = 67.5\text{mm}$), both of which are depicted by asterisks in Figs. 3.23 (a)-(c). These time series, with 2×10^5 data points each, are plotted in Figs. 3.23 (d), (e), and (f) for $G_{gap} = 0.5 \text{ nS}$, 2 nS , and 8 nS , respectively (data from the points outside and inside the inhomogeneity are represented, respectively, by black circles and red triangles); Figs. 3.23 (g), (h), and (i) show the corresponding plots of the ibi versus the beat number n ; and the associated power spectra $E(\omega)$ are depicted in Figs. 3.23 (j), (k), and (l). The Video S10 has four panels that show the spatiotemporal evolution of pseudocolor plots of V_m and the spiral-tip trajectories for $2 \text{ s} \leq t \leq 3 \text{ s}$ for a control myocyte layer with no inhomogeneities (top left panel) and, in addition, the simulation domains of Figs. 3.23 (a)-(c) (top right, bottom left, and bottom right panels). Here too we obtain a rich variety of spiral-wave behaviors inside and outside of the MF-composite inhomogeneity, as in the cases with zero- and single-sided couplings.

3.3.3 Control of spiral-wave turbulence in the presence of MF-composite inhomogeneities

One of the goals of our extensive studies of various types of heterogeneities in mathematical models for cardiac tissue [24,25,33,34] has been to understand their effects on spiral-wave dynamics and thus develop effective, low-amplitude control techniques for the elimination of single, rotating spiral waves or spatiotemporally chaotic multiple spiral waves of electrical activation in mathematical models for

cardiac tissue. In these earlier studies [24, 25, 33, 34] we have considered conduction or ionic inhomogeneities; here we have extended such studies to mathematical models in which we allow for the MF-composite inhomogeneities that we have described above.

In this subsection we investigate the elimination of spiral-wave turbulence in the presence of MF-composite inhomogeneities. We use the control scheme of Sinha, *et al.*, [37]; this eliminates spiral waves by the application of a current pulse on a mesh, which we describe below. We have found in our earlier studies [24, 25, 36, 37] that such a mesh-based control scheme is effective even when the simulation domain has conduction or ionic inhomogeneities; by contrast, control schemes, which use electrical stimuli at a point [71, 72], work well in homogeneous simulation domains but do not eliminate spiral-wave turbulence in domains with inhomogeneities.

In our mesh-based control scheme in a 2D simulation domain with an MF-composite inhomogeneity, we apply a current pulse of amplitude 30 pA/pF for 20 ms over a mesh that divides our square simulation domain, of side 135 mm, into 16 square cells of side 33.75 mm each. The application of this pulse makes the region, which is covered by the mesh, refractory and, therefore, effectively imposes Neumann boundary conditions for any cell bounded by this mesh. Thus, spiral waves that lie inside the cell are absorbed at the mesh that bounds it and, eventually, spiral-wave turbulence is eliminated from the whole simulation domain.

We begin with a discussion of the control of spiral waves, in a 2D, MF-composite simulation domain, by the application of a current pulse on the square mesh described above. In Fig. 4.14 (a) we show a pseudocolor plot of V_m at time $t = 0$ ms, for the control case with $G_{gap} = 0$ nS; we give pseudocolor plots of V_m , at $t = 400$ ms, and in the absence and presence of the control pulse in Figs. 4.14 (b) and (c), respectively. Figures 4.14 (d), (e) and (f), are the analogs of Figs. 4.14 (a), (b), and (c), respectively, for zero-sided coupling with $C_{f,tot} = 6.3$ pF, $G_f = 4$ nS, $E_f = -39$ mV, and $G_{gap} = 8$ nS. Figures 4.14 (g), (h), and (i) are the analogs of Figs. 4.14 (a), (b), and (c), respectively, for two-sided coupling with $C_{f,tot} = 6.3$ pF, $G_f = 4$ nS, $E_f = -39$ mV, $G_{gap} = 8$ nS, $\mathcal{G}_{mm}/\mathcal{G}_{ff} = 1$, and $\mathcal{G}_{mm}/\mathcal{G}_{mf} = 200$. From the pseudocolor plots of V_m in Figs. 4.14 (c), (f), and (i) we see that our mesh-based, spiral-control scheme succeeds in eliminating spiral-wave turbulence in less than 400 ms in a 2D, MF-composite simulation domain with zero- and two-sided couplings; we have obtained similar results with one-sided coupling too. The Video S11, which comprises six animations of pseudocolor plots of V_m , shows the spatiotemporal evolution of the spiral waves for these cases, with and without control pulses.

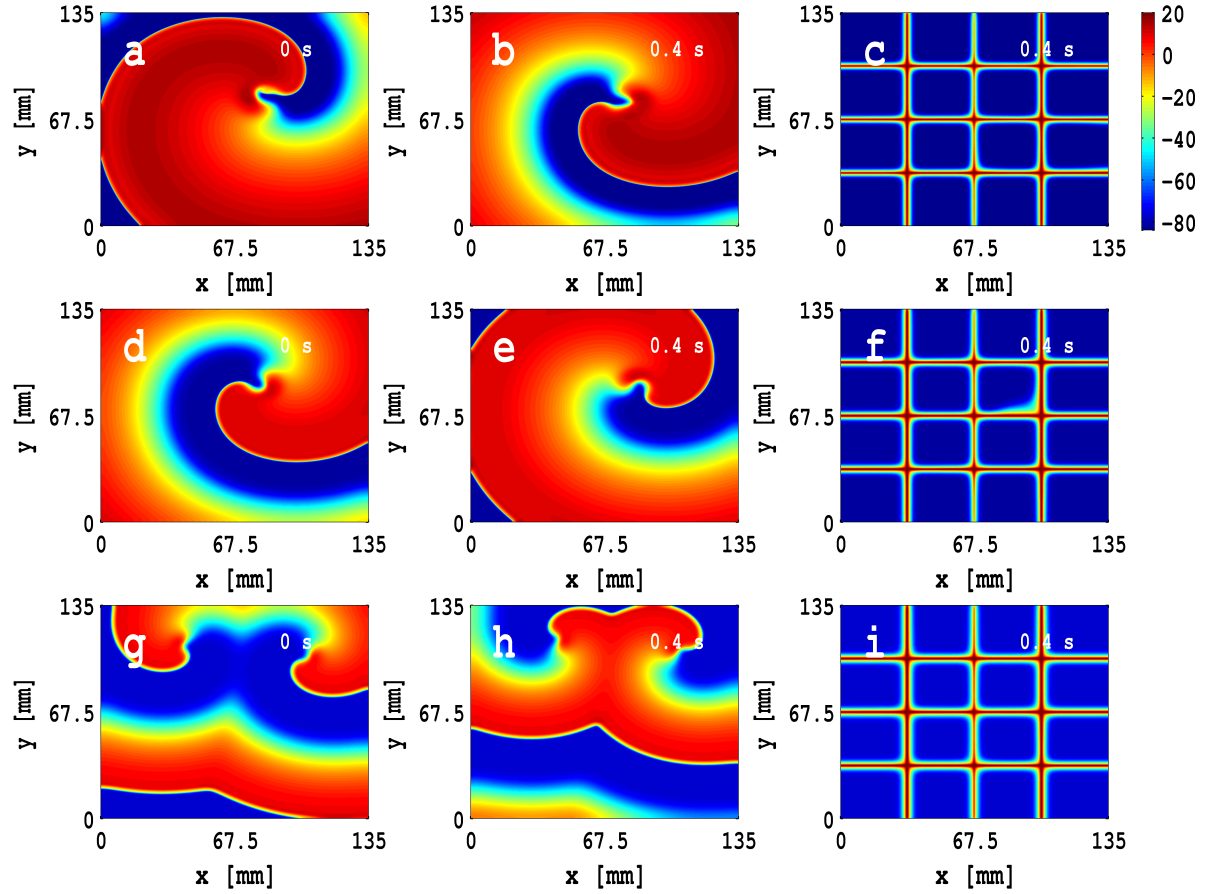


Figure 3.24: Spiral-wave control in our 2D M-F composite model, by the application of a control pulse of amplitude 30 pA/pF for $t = 400$ ms over a square mesh with each block of side $L/K = 33.75$ mm, i.e., the simulation domain is divided into 4^2 square blocks. Plots in (a), (d) and (g) are the initial conditions of V_m , i.e., $t = 0$ ms, for the control case, i.e., $G_{gap} = 0$ nS, zero sided coupling with $C_{f,tot} = 6.3$ pF, $G_f = 4$ nS, $E_f = -39$ mV and $G_{gap} = 8$ nS, and double-sided coupling with the same fibroblasts parameters as in (d) and with $G_{mm}/G_{ff} = 1$ and $G_{mm}/G_{mf} = 200$, respectively; (b), (e) and (h) show the pseudocolor plots of V_m at $t = 400$ ms in the absence of any control pulse. However, the spiral-wave is suppressed by an application of the control pulse as shown (c), (f) and (i) at time $t = 400$ ms. The Video S11, which comprises six animations of pseudocolor plots of V_m , shows the spatiotemporal evolution of these spiral waves for these cases, with and without control pulses.

We now study spiral-wave control in a 2D simulation domain with myocytes and a square MF-composite inhomogeneity with side $l = 33.75$ mm whose bottom-left corner is placed at $(x = 56.25 \text{ mm}, y = 56.25 \text{ mm})$. Again, we apply a control pulse of amplitude 30 pA/pF for $t = 20$ ms over a square mesh with cells whose sides are of length $L/K = 33.75$ mm, i.e., the simulation domain is divided into $4^2 = 16$ square blocks. We consider the following three cases: (A) zero-sided coupling with $C_{f,tot} = 6.3$ pF, $G_f = 4$ nS, $E_f = -39$ mV and $G_{gap} = 8$ nS; (B) double-sided coupling with

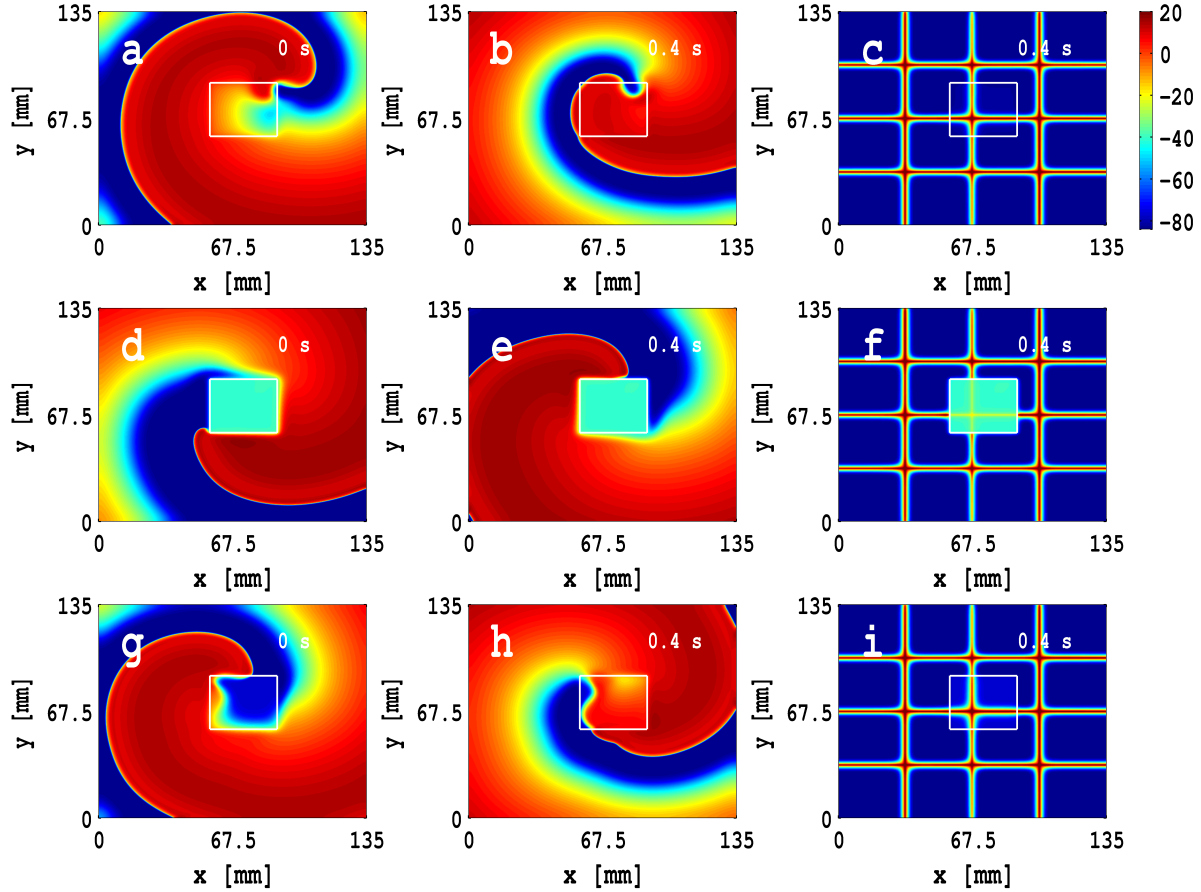


Figure 3.25: Spiral-wave control in the 2D Fibroblast model in the presence of a square shape MF composite inhomogeneity of size $l = 33.75$ mm whose bottom-left corner is placed at $(56.25$ mm, 56.25 mm). We apply a control pulse of amplitude 30 pA/pF for $t = 400$ ms over a square mesh with each block of size $L/K = 33.75$ mm, i.e., the simulation domain is divided into 4^2 square blocks. Plots in Figs. (a), (b) and (c) are the initial conditions of V_m , i.e., $t = 0$ ms, for zero sided coupling with $C_{f,tot} = 6.3$ pF, $G_f = 4$ nS, $E_f = -39$ mV and $G_{gap} = 8$ nS, double sided coupling with same fibroblasts parameters as in (a) with $\mathcal{G}_{mm}/\mathcal{G}_{ff} = 1$ and $\mathcal{G}_{mm}/\mathcal{G}_{mf} = 1$, and double sided coupling with same fibroblasts parameters as in (a) with $\mathcal{G}_{mm}/\mathcal{G}_{ff} = 1$ and $\mathcal{G}_{mm}/\mathcal{G}_{mf} = 200$, respectively. Figures (b), (e) and (h) are the time evolution of V_m corresponds to Figs. (a), (d), (g), respectively, at $t = 400$ ms in absence of any control pulse. However, the spiral-wave is suppressed an application of control pulse as shown in Figs. (c), (f) and (i) at time $t = 400$ ms. For the spatiotemporal evolution of these spiral waves see Video S12.

the same fibroblasts parameters as in case (A) and with $\mathcal{G}_{mm}/\mathcal{G}_{ff} = 1$ and $\mathcal{G}_{mm}/\mathcal{G}_{mf} = 1$; and (C) double-sided coupling with the same fibroblasts parameters as in case (A) and with $\mathcal{G}_{mm}/\mathcal{G}_{ff} = 1$ and $\mathcal{G}_{mm}/\mathcal{G}_{mf} = 200$. Figures 3.25 (a), (d), and (g) show pseudocolor plots of V_m at $t = 0$ for cases (A), (B), and (C), respectively. Figures 3.25 (b), (e), and (h) show their analogs for $t = 400$ ms when no control pulse is applied.

Figures 3.25 (c), (f), and (i), which show pseudocolor plots of V_m at $t = 0$ for cases (A), (B), and (C), respectively, at $t = 400$ ms when we apply a control pulse, illustrate how our control scheme is effective in suppressing spiral-wave turbulence in the presence of an MF-composite inhomogeneity. For the spatiotemporal evolution of these spiral waves see Video S12.

3.4 Discussion and Conclusion

We have carried out detailed numerical studies of an MF composite by modelling human ventricular myocyte cells, as in Ref. [15], and fibroblasts as passive RC circuits, as in Refs. [9, 12]. The passive nature of these fibroblasts makes them behave as inexcitable cells and, therefore, they act either as current sources or sinks, when they are coupled with myocytes. We have investigated the responses of such MF composites to external electrical stimuli by varying systematically the total cellular capacitance $C_{f,tot}$ of fibroblasts and their membrane conductance G_f , resting membrane potential E_f , gap-junctional coupling (with myocytes) G_{gap} , and the number N_f of fibroblasts coupled to a myocyte over a wide range of biophysically relevant values. The parameters $C_{f,tot}$, G_f , and E_f depend on the geometry and size of the fibroblast [49, 52, 53]. In our first set of simulations (Fig. 3.2 and Figs. 3.3 and 3.4), we have uncovered the dependence of the AP morphology on $C_{f,tot}$ by choosing three representative values of $C_{f,tot}$, namely, (a) 6.3 pF, (b) 25.2 pF, and (c) 63 pF; we have found that the value of $C_{f,tot}$ does not affect the myocyte AP morphology significantly, but it does affect the APD. In the second set of simulations (Fig. 3.2), we have set $C_{f,tot} = 6.3$ pF and examined the dependence of the AP morphology on G_f by using the three representative values (a) 0.1 nS, (b) 1 nS, and (c) 4 nS; we have found that the myocyte APD depends on G_f ; and V_{rest} is elevated substantially as G_f is increased.

In our third set of simulations, we have fixed $C_{f,tot} = 6.3$ pF and $G_f = 4$ nS to examine explicitly the dependence of the AP morphology on E_f and G_{gap} . We have focused on this dependence of the AP morphology on E_f and G_{gap} , because the values of these two parameters span a wide range in experiments [3, 5, 52, 53]. Our studies have shown that E_f alters the APD; in particular, we have found that the APD increases with G_{gap} (Fig. 3.5) if E_f is high, but it decreases, as G_{gap} increases, if E_f is low. The maximum upstroke velocity, dV/dt_{max} , and the maximum value of the myocyte transmembrane potential, V_{max} , decrease as we increase E_f (Fig. 3.5), with a fixed value of G_{gap} , whereas the notch of the AP, V_{notch} , the maximum of the plateau, $V_{plateau}$, and resting membrane potential all increase as we increase

E_f . Furthermore, we have shown that dV/dt_{max} , V_{max} , V_{notch} , and $V_{plateau}$ decrease, but V_{rest} increases, as we increase G_{gap} (Fig. 3.5), with a fixed value of E_f . We have explored the dependence of the myocyte AP morphology on different ionic currents. Moreover, we have examined carefully the gap-junctional current I_{gap} to understand when the fibroblasts in our MF composite act as current sources and when they behave as current sinks. In general, our studies have shown that if these fibroblasts act as current sources (current sinks), then the myocyte APD decreases (increases), principally via modifications of the currents I_{Ks} and I_{Kr} .

We have carried out simulations to check the dependence of the myocyte AP on the number N_f of fibroblasts coupled to a myocyte and have observed that (a) the APD and V_{rest} decrease and increase, respectively, as N_f increases and (b) this increase of V_{rest} depolarizes the membrane potential so that, eventually, V_m crosses the threshold value for the generation of an AP, and, therefore, the MF composite cell begins to show either autorhythmic or oscillatory behaviors. We have found that such behaviors occur at unphysically high values of E_f and G_{gap} , if $N_f = 1$, but in the range of experimentally observed values of E_f and G_{gap} if $N_f > 1$ [60].

Fibroblasts are found to be much smaller than myocytes in experimental studies [8, 73]; thus, in cell-culture experiments, more than one fibroblast can be deposited per myocyte in the cell culture. Furthermore, the sizes of fibroblasts can vary in such experiments; this depends on the preparation technique and circumstances; and the fibroblast size decides the maximum number of fibroblasts that can attach to a myocyte. Indeed, a wide range of values has been used for the total cellular capacitance $C_{f,tot}$ in various computer models [9, 11, 12] because these models assume that $C_{f,tot}$ is related to the size of the fibroblast. Hence, in our model studies, for a given size of fibroblast, i.e., a fixed value of $C_{f,tot}$, the complex, network-type interaction can occur via \mathcal{G}_{ff} , \mathcal{G}_{mf} , and \mathcal{G}_{fm} , depending on the number of fibroblasts N_f coupled to a myocyte in an MF composite. Therefore, we use N_f fibroblasts per a myocyte site in an MF composite to study the wave dynamics; each of these fibroblasts are coupled to a myocyte via G_{gap} . We think of this collection of N_f fibroblasts as a single cluster that interacts via \mathcal{G}_{mf} and \mathcal{G}_{fm} , with its neighboring myocytes; we assume that the number of fibroblast clusters is exactly equal to the number of myocyte cells. We assume that, at the level of a first approximation, the fibroblasts in a cluster interact with each other only to the extent that they form cluster. When the size of the fibroblast cluster is much smaller than the size of a myocyte, then the couplings \mathcal{G}_{mf} , \mathcal{G}_{fm} , and \mathcal{G}_{ff} are irrelevant and we should only use a zero-sided model.

Earlier computational studies [9–12], which we have discussed in Sec. 4.1, have not investigated the dependence of the AP morphology, as we do, on the parameters $C_{f,tot}$, G_f , E_f , G_{gap} , and N_f ; most of these earlier studies have focused on the dependence of the AP on N_f , principally, and E_f , to some extent. Our detailed studies of the dependence of the AP morphology on $C_{f,tot}$, G_f , E_f , G_{gap} , and N_f are designed to help experimentalists in the growth of different tissue layers with myocytes and fibroblasts and thus uncover the contribution of fibroblasts to the mechanisms of ventricular fibrillation. For example, in our simulation, we have found that E_f has the potential to alter the APD and, therefore, it can play a crucial role in spiral-wave dynamics.

We have performed extensive numerical simulations in two-dimensional (2D) simulation domains, both homogeneous and inhomogeneous, which contain myocytes or MF composites, with $N_f = 1$ and with zero-, one-, or two-sided couplings between myocytes and fibroblasts. We have found that, for zero- and one-sided couplings, the plane-wave conduction velocity CV decreases as G_{gap} increases, but, with two-sided couplings, CV first decreases very rapidly and then rises slowly as G_{gap} increases; furthermore, we have found that conduction failure can occur in the double-sided case if G_{mf} and G_{gap} are low (Fig. 3.10). Such behaviors have been seen in earlier numerical studies, with passive or active fibroblast in models [13,14] that are similar to, but not the same as, our mathematical model, and in cell cultures [13,20–22]. In our studies with zero-sided coupling, we have found that (a) the rotation period τ_{rot} of a spiral wave decreases as we increase G_{gap} (Fig. 3.12), which we have explained qualitatively, (b) the higher the value of G_{gap} , the more compact and closed is the trajectory of the spiral tip (this compactness prevents a single spiral from splitting into multiple spirals [74–76]), and (c) in the parameter range in which autorhythmicity occurs, the spiral wave rotates periodically, for low frequencies (Figs. 3.14).

Our studies of spiral-wave dynamics in a homogeneous simulation domain with MF composites has shown that the spiral rotates faster for single-sided coupling than for zero-sided coupling. The spiral rotation rate in the double-sided case lies between these rates for zero- and one-sided couplings. We have presented a qualitative explanation of such fast and slow rotation rates of spiral waves by analyzing the AP morphology of a single MF composite and the plane-wave CV with these three types of couplings. In general, our studies have shown that, if the fibroblasts in the MF composites act as current sources (current sinks), then the rate of rotation of the spiral wave increases (decreases).

Our studies of spiral-wave dynamics in the presence of localized, MF-composite inhomogeneities have shown that they may block spiral-wave propagation like conduction inhomogeneities [24, 26, 28, 33, 34, 77]; however, in some cases (see below) the spiral wave can enter the region with the MF-composite inhomogeneity and yield rich spiral-wave dynamics, which can be different inside and outside of the inhomogeneity, as happens, e.g., when we have ionic inhomogeneities [24, 29, 34]. We have found that zero- and single-sided couplings have the potential to behave like ionic inhomogeneities; but double-sided couplings have the potential to behave either like conduction- or ionic-type inhomogeneities (depending on the value of \mathcal{G}_{mf}).

Our model has some limitations: it does not have any mechanosensitive currents [78], either for the myocytes or the fibroblast. These types of ionic currents have been obtained in experimental studies of fibroblasts in the sino-atrial node (SAN) and atria of certain mammals [3, 49, 51, 78, 79]. These mechanosensitive currents may affect spiral-wave propagation if there is electro-mechanical feedback [80, 81]; our model excludes such electro-mechanical feedback. The purely electrical approach, which we adopt, has also been used by several other groups (see, e.g., Refs. [37, 77, 82–87]) with the understanding that the mechanical system basically follows the electrical activation at the level of a first approximation (see, e.g., Ref. [88]). Furthermore, our model is based on passive fibroblasts rather than active fibroblast; there are several reasons to use passive fibroblast rather than active ones, the main reason being that, so far, no experiments have identified the presence of ionic currents in human, ventricular fibroblasts; and the presence of active fibroblast in human, ventricular fibroblasts continues to be a matter of debate. The expression of ionic currents in fibroblasts have been observed in animal species, either in the region of the SAN or the right atrium. In spite of these limitations of our model, our work provides the most comprehensive study, attempted so far, of (a) the response of MF composites to external electrical stimulation and (b) the propagation of spiral waves in MF-composite 2D simulation domains, which are designed to model cell-culture experiments of the sort presented in Refs. [13, 22]. We do not attempt here to study diffuse fibrosis; this lies beyond the scope of this paper; it has been addressed in other simulation studies [43, 60, 89–91]. Our studies have been designed specifically to uncover the role of fibroblasts in spiral-wave dynamics in the the absence of other tissue heterogeneities; once the underlying contributions of fibroblasts to spiral-wave dynamics have been revealed, we can incorporate tissue anisotropy and diffuse fibrosis as, e.g., in Ref. [60].

One of our goals is to test our low-amplitude control scheme in our 2D MF-composite model; we have focused here on a monodomain model, because we use low-amplitude control pulses rather than high-amplitude ones; the latter may require a bidomain model. Furthermore, some studies [92] have shown that there are no significant qualitative differences between bidomain and monodomain models, so we expect that our principal qualitative result will continue to hold even when such models are considered; this will have to be checked explicitly by subsequent studies.

1 Supporting Information

Video S1 Plane-wave propagation in our 2D, homogeneous myocyte-fibroblast (MF) model for different cases. (a) the control case, i.e., with only myocytes; (b) *zero-sided coupling*; (c) *single-sided coupling* with $\mathcal{G}_{mm}/\mathcal{G}_{ff} = 1$; (d) *double-sided coupling* with $\mathcal{G}_{mm}/\mathcal{G}_{ff} = 1$, $\mathcal{G}_{mm}/\mathcal{G}_{mf} = 100$, and $G_{gap} = 0.5$ nS; (e) *double-sided coupling* with $\mathcal{G}_{mm}/\mathcal{G}_{ff} = 1$, $\mathcal{G}_{mm}/\mathcal{G}_{mf} = 100$, and $G_{gap} = 8.0$ nS; and (f) *double-sided coupling* with $\mathcal{G}_{mm}/\mathcal{G}_{ff} = 1$, $\mathcal{G}_{mm}/\mathcal{G}_{mf} = 200$, and $G_{gap} = 0.5$ nS. The time evolution of pseudo-color plots of the myocyte transmembrane potential V_m is shown for $0 \text{ s} \leq t \leq 1 \text{ s}$; we use 10 frames per second (fps); in real time each frame is separated from the succeeding frame by 8 ms.

Video S2 Spiral-wave dynamics in our 2D homogeneous myocyte-fibroblast model with zero-sided coupling. (a) $G_{gap} = 0.00$ nS (control case, i.e., with only myocytes); (b) $G_{gap} = 0.50$ nS (low coupling); (c) $G_{gap} = 2.00$ nS (intermediate coupling); (d) $G_{gap} = 8.00$ nS (high coupling). Here spiral-tip trajectories, for $2 \text{ s} \leq t \leq 3 \text{ s}$, are shown by the white lines; we use 10 frames per second (fps); in real time each frame is separated from the succeeding frame by 8 ms.

Video S3 Spiral-wave dynamics in our 2D homogeneous myocyte-fibroblast model with zero-sided coupling. (a) $G_{gap} = 0.00$ nS (control case, i.e., with only myocytes); (b) $G_{gap} = 0.50$ nS (low coupling); (c) $G_{gap} = 2.00$ nS (intermediate coupling); (d) $G_{gap} = 8.00$ nS (high coupling). Here spiral-tip trajectories, for $4 \text{ s} \leq t \leq 5 \text{ s}$, are shown by the white lines; we use 10 frames per second (fps); in real time each frame is separated from the succeeding frame by 8 ms.

Video S4 Spiral-wave dynamics in our 2D homogeneous myocyte-fibroblast model with zero-sided coupling. (a) $G_{gap} = 0.00$ nS (control case, i.e., with only myocytes); (b) $G_{gap} = 0.50$ nS (low coupling); (c) $G_{gap} = 2.00$ nS (intermediate coupling); (d) $G_{gap} = 8.00$ nS (high coupling). Here spiral-tip trajectories, for $6 \text{ s} \leq t \leq 7 \text{ s}$, are shown by the white lines; we use 10 frames per second (fps); in real time each frame is separated from the succeeding frame by 8 ms.

Video S5 Spiral-wave dynamics in our 2D homogeneous myocyte-fibroblast model with gap-junctional conductance, $G_{gap} = 8.0$ nS. (a) control case; (b) zero-sided coupling; (c) single-sided coupling; (d) double-sided coupling. Here spiral-tip trajectories, for $2 \text{ s} \leq t \leq 3 \text{ s}$, are shown by the white lines; we use 10 frames per second (fps); in real time each frame is separated from the succeeding frame by 8 ms.

Video S6 Spiral-wave dynamics in our 2D myocyte-fibroblast model in the presence of a square fibroblast inhomogeneity, of side $\ell = 33.75$ mm, for the case of zero-sided, and the lower left-hand corner of the inhomogeneity at different positions. (a) control case; (b) $(x = 33.75 \text{ mm}, y = 67.5 \text{ mm})$; (c) $(x = 56.25 \text{ mm}, y = 56.25 \text{ mm})$; (d)

($x = 78.75$ mm, $y = 45$ mm). Here spiral-tip trajectories, for $2 \text{ s} \leq t \leq 3 \text{ s}$, are shown by the white lines; we use 10 frames per second (fps); in real time each frame is separated from the succeeding frame by 8 ms.

Video S7 Spiral-wave dynamics in our 2D myocyte-fibroblast model in the presence of a square fibroblast inhomogeneity of side ℓ for the case of zero-sided with the lower-left-hand corner of the inhomogeneity fixed at ($x = 56.25$ mm, $y = 56.25$ mm). (a) control case; (b) $\ell = 22.5$ mm; (c) $\ell = 33.75$ mm; (d) $\ell = 45$ mm. Here spiral-tip trajectories, for $2 \text{ s} \leq t \leq 3 \text{ s}$, are shown by the white lines; we use 10 frames per second (fps); in real time each frame is separated from the succeeding frame by 8 ms.

Video S8 Spiral-wave dynamics in our 2D myocyte-fibroblast model with a double-sided coupling and a square fibroblast inhomogeneity with side ℓ and $\mathcal{G}_{mm}/\mathcal{G}_{ff} = 1$ and $\mathcal{G}_{mm}/\mathcal{G}_{mf} = 1$, and the lower left-hand corner of the inhomogeneity fixed at ($x = 67.5$ mm, $y = 67.5$ mm). (a) $\ell = 0$, i.e., absence of inhomogeneity; (b) $\ell = 22.5$ mm; (c) $\ell = 33.75$ mm; (d) $\ell = 45$ mm. Here the myocyte transmembrane potential time evolution is shown for $2 \text{ s} \leq t \leq 3 \text{ s}$; we use 10 frames per second (fps); in real time each frame is separated from the succeeding frame by 8 ms.

Video S9 Spiral-wave dynamics in our 2D myocyte-fibroblast model in the presence of a square, MF-composite inhomogeneity, of side $\ell = 33.75$ mm and with its lower-left-hand corner placed at ($x = 56.25$ mm, $y = 56.25$ mm) for the case of doubled-sided coupling with $\mathcal{G}_{mm}/\mathcal{G}_{ff} = 1$ and $G_{gap} = 8$ nS. (a) control case, i.e., with only myocytes; (b) $\mathcal{G}_{mm}/\mathcal{G}_{mf} = 50$; (c) $\mathcal{G}_{mm}/\mathcal{G}_{mf} = 100$; (d) $\mathcal{G}_{mm}/\mathcal{G}_{mf} = 200$. Here the myocyte transmembrane potential time evolution is shown for $2 \text{ s} \leq t \leq 3 \text{ s}$; we use 10 frames per second (fps); in real time each frame is separated from the succeeding frame by 8 ms.

Video S10 Spiral-wave dynamics in our 2D myocyte-fibroblast model in the presence of a square, MF-composite inhomogeneity, of side $\ell = 33.75$ mm and with its lower-left-hand corner placed at ($x = 56.25$ mm, $y = 56.25$ mm) for the case of doubled-sided coupling with $\mathcal{G}_{mm}/\mathcal{G}_{ff} = 1$ and $\mathcal{G}_{mm}/\mathcal{G}_{mf} = 200$. (a) control case, i.e., with only myocytes; (b) $G_{gap} = 0.5$ nS (low coupling); (c) $G_{gap} = 2.0$ nS (intermediate coupling); (d) $G_{gap} = 8.0$ nS (high coupling). Here the myocyte transmembrane potential time evolution is shown for $2 \text{ s} \leq t \leq 3 \text{ s}$; we use 10 frames per second (fps); in real time each frame is separated from the succeeding frame by 8 ms.

Video S11 Spiral-wave dynamics, without (top panel) and with (bottom panel) control pulses, in our 2D MF-composite model; we apply a control pulse of amplitude 30 pA/pF for $t = 400$ ms over a square mesh with each block of side $L/K = 33.75$ mm, i.e., the simulation domain is divided into 4^2 square blocks. (a) for the

control case, i.e., $G_{gap} = 0$ nS; (b) zero-sided couplings with $C_{f,tot} = 6.3$ pF, $G_f = 4$ nS, $E_f = -39$ mV and $G_{gap} = 8$ nS; and (c) double-sided couplings with the same fibroblasts parameters as in (b) and with $\mathcal{G}_{mm}/\mathcal{G}_{ff} = 1$ and $\mathcal{G}_{mm}/\mathcal{G}_{mf} = 200$. The animations in (d), (e), and (f) are the analogs of (a), (b), and (c), respectively, with control pulses. Here the spatiotemporal evolution of the myocyte transmembrane potential is shown for $0 \text{ s} \leq t \leq 0.8 \text{ s}$; we use 10 frames per second (fps); in real time each frame is separated from the succeeding frame by 8 ms.

Video S12 Spiral-wave dynamics, without (top panel) and with (bottom panel) control pulses, in the 2D Fibroblast model in the presence of a square MF composite inhomogeneity of side $l = 33.75$ mm whose bottom-left corner is placed at (56.25 mm, 56.25 mm); we apply a control pulse of amplitude 30 pA/pF for $t = 400$ ms over a square mesh with each block of side $L/K = 33.75$ mm, i.e., the simulation domain is divided into 4^2 square blocks. (a) zero-sided coupling with $C_{f,tot} = 6.3$ pF, $G_f = 4$ nS, $E_f = -39$ mV and $G_{gap} = 8$ nS, (b) double-sided coupling, with the same fibroblasts parameters as in (a) with $\mathcal{G}_{mm}/\mathcal{G}_{ff} = 1$ and $\mathcal{G}_{mm}/\mathcal{G}_{mf} = 1$, and (c) double-sided coupling with the same fibroblasts parameters as in (a) with $\mathcal{G}_{mm}/\mathcal{G}_{ff} = 1$ and $\mathcal{G}_{mm}/\mathcal{G}_{mf} = 200$. The animations in (d), (e), and (f) are the analogs of (a), (b), and (c), respectively, with control pulses. Here the spatiotemporal evolution of the myocyte transmembrane potential is shown for $0 \text{ s} \leq t \leq 0.8 \text{ s}$; we use 10 frames per second (fps); in real time each frame is separated from the succeeding frame by 8 ms.

Bibliography

- [1] Chilton L, Giles WR, Smith GL (2007) Evidence of intercellular coupling between co-cultured adult rabbit ventricular myocytes and myofibroblasts. *J Physiol* 583(1):225-236.
- [2] Camelliti P, Devlin GP, Matthews KG, *et al.* (2004) Spatially and temporally distinct expression of fibroblast connexins after sheep ventricular infarction. *Cardiovasc Res* 62:415-425.
- [3] Kohl P, Kamkin AG, Kiseleva IS, Noble D (1994) Mechanosensitive fibroblasts in the sino-atrial node region of rat heart: interaction with cardiomyocytes and possible role. *Exp Physiol* 79:943-956.
- [4] Jacquemet V, Henriquez CS (2008) Loading effect of fibroblast-myocyte coupling on resting potential, impulse propagation, and repolarization: insights from a microstructure model. *Am J Physiol Heart Circ Physiol* 294: H2040-H2052.
- [5] Rook MB, van Ginneken AC, de Jonge B, *et al.* (1992) Differences in gap junction channels between cardiac myocytes, fibroblasts, and heterologous pairs. *Am J Physiol* 263:C959-C977.
- [6] Camelliti P, Borg TK, Kohl P (2005) Structural and functional characterisation of cardiac fibroblasts. *Cardiovasc. Res.* 65:40-51.
- [7] Camelliti P, McCulloch AD, Kohl P (2005) Microstructured cocultures of cardiac myocytes and fibroblasts: a two-dimensional in vitro model of cardiac tissue. *Microsc. Microanal.* 11:249-259
- [8] Baudino TA, McFadden A, Fix C, *et al.* (2008) Cell patterning: interaction of cardiac myocytes and fibroblasts in three-dimensional culture. *Microsc. Microanal.* 14:117-125.

- [9] Xie Y, Garfinkel A, Weiss JN, Qu Z (2009) Cardiac alternans induced by fibroblast-myocyte coupling: mechanistic insights from computational models. *Am J Physiol Heart Circ Physiol* 297:H775-H784.
- [10] Sachse FB, Moreno AP, Abildskov JA (2008) Electrophysiological modeling of fibroblasts and their interaction with myocytes. *Ann Biomed Engg* 36(1):41-56.
- [11] Jacquemet V, Henriquez CS (2007) Modelling cardiac fibroblasts: interactions with myocytes and their impact on impulse propagation. *Europace* 9:vi29-vi37.
- [12] MacCannell KA, Bazzazi H, Chilton L, et al. (2007) A mathematical model of electrotonic interactions between ventricular myocytes and fibroblasts. *Biophys J* 92:4121-4132.
- [13] Zlochiver S, Munoz V, Vikstrom KL, et al. (2008) Electrotonic myofibroblast-to-myocyte coupling increases propensity to reentrant arrhythmias in two-dimensional cardiac monolayers. *Biophys J* 95:4469.
- [14] Xie Y, Garfinkel A, Camelliti P, et al. (2009) Effects of fibroblast-myocyte coupling on cardiac conduction and vulnerability to reentry: A computational study. *Heart Rhythm* 6(11):1641-1649.
- [15] ten Tusscher KHWJ, Noble D, Noble PJ, Panfilov AV (2004) A model for human ventricular tissue. *Am J Physiol Heart Circ Physiol* 286:H 1573.
- [16] Luo CH, Rudy Y (1991) A model of the ventricular cardiac action potential: depolarization, repolarization, and their interaction. *Circ Res* 68:1501-1526.
- [17] Mahajan A, Shiferaw Y, Sato D, et al. (2008) A rabbit ventricular action potential model replicating cardiac dynamics at rapid heart rates. *Biophys J* 94:392-410.
- [18] Pandit SV, Clark RB, Giles WR, Demir SS (2001) A mathematical model of action potential heterogeneity in adult left ventricular myocytes. *Biophys J* 81:3029-3051.
- [19] Bondarenko VE, Szigeti GP, Bett GCL, et al. (2004) Computer model of action potential of mouse ventricular myocytes. *Am J Physiol Heart Circ Physiol* 287:H1378-H1403.
- [20] Miragoli M, Gaudesius G, Rohr R (2006) Electrotonic modulation of cardiac impulse conduction by myofibroblasts. *Circ Res* 98:801.

- [21] Gaudesius G, Miragoli M, Thomas SP, Rohr S (2003) Coupling of cardiac electrical activity over extended distances by fibroblasts of cardiac origin. *Circ Res* 93:421-428.
- [22] McSpadden LC, Kirkton RD, Bursac N (2009) Electrotonic loading of anisotropic cardiac monolayers by unexcitable cells depends on connexin type and expression level. *Am J Physiol Cell Physiol* 297: C339-C351.
- [23] Kohl P, Camelliti P (2007) Cardiac myocyte-nonmyocyte electrotonic coupling: implications for ventricular arrhythmogenesis. *Heart Rhythm* 4:233-235.
- [24] Shajahan TK, Nayak AR, Pandit R (2009) Spiral-wave turbulence and its control in the presence of inhomogeneities in four mathematical models of cardiac tissue. *PLoS ONE* 4(3): e4738.
- [25] Majumder R, Nayak AR, Pandit R (2011) An overview of spiral- and scroll-wave dynamics in mathematical models for cardiac tissue. *Heart Rate and Rhythm: Molecular Basis, Pharmacological Modulation and Clinical Implications*, edited by Tripathi ON, Ravens U, Sanguinetti MC, (Springer) Chapter 14, pp 269-282.
- [26] Ikeda T, Yashima M, Uchida T, Hough D, Fishbein MC, et al. (1997) Attachment of meandering reentrant wavefronts to anatomic obstacles in the atrium. *Circ Res* 81: 753.
- [27] Valderrabano M, Kim YH, Yashima M, Wu TJ, *et al.* (2000) Obstacle-induced transition from ventricular fibrillation to tachycardia in isolated swine right ventricles. *J Am Coll Cardiol* 36: 2000.
- [28] Lim ZY, Maskara B, Aguel F, Emokpae R, Tung L (2006) Spiral wave attachment to millimeter-sized obstacles. *Circulation* 114: 2113.
- [29] Hwang SM, Kim TY, Lee KJ (2005) Complex-periodic spiral waves in confluent cardiac cell cultures induced by localized inhomogeneities. *Proc Natl Acad Sci USA* 102: 10363.
- [30] Luo CH, Rudy Y (1994) A dynamic model of the cardiac ventricular action potential. I. Simulations of ionic currents and concentration changes. *Circ Res* 74:1071-1096.
- [31] Luo CH, Rudy Y (1994) A dynamic model of the cardiac ventricular action potential. II. Afterdepolarizations, triggered activity, and potentiation. *Circ Res* 74:1097-1113.

- [32] Viswanathan PC, Shaw RM, Rudy Y (1999) Effects of I_{Kr} and I_{Ks} heterogeneity on action potential duration and its rate dependence: a simulation study. *Circulation* 99:2466-2474.
- [33] Shajahan TK, Sinha S, Pandit R (2007) Spiral-wave dynamics depends sensitively on inhomogeneities in mathematical models of ventricular tissue. *Phys Rev E* 75: 011929.
- [34] Majumder R, Nayak AR, Pandit R (2011) Scroll-wave dynamics in human cardiac tissue: lessons from a mathematical model with inhomogeneities and fiber architecture. *PLoS ONE* 6(4): e18052.
- [35] Shajahan TK, Sinha S, Pandit R (2009) The mathematical modelling of inhomogeneities in ventricular tissue *Complex Dynamics in Physiological Systems: From Heart to Brain*, edited by Dana SK, Roy PK, Kurths J, (Springer), pp 51-67.
- [36] Pandit R, Pande A, Sinha S *et al.* (2002) Spiral turbulence and spatiotemporal chaos: characterization and control in two excitable media. *Physica A* 306: 211-219.
- [37] Sinha S, Pande A, Pandit R (2001) Defibrillation via the elimination of spiral turbulence in model for ventricular fibrillation. *Phys Rev Lett* 86:3678.
- [38] Kenner J, Sneyd J (1998) *Mathematical Physiology*. Springer-Verlag New York, Inc. New York, NY, USA.
- [39] Panfilov AV, Holden AV (1996) *Computational Biology of the Heart* Wiley.
- [40] Kryukov AK, Petrov VS, Averyanova LS, *et al.* (2008) Synchronization phenomena in mixed media of passive, excitable, and oscillatory cells. *Chaos* 18:037129.
- [41] Desroches BR, Zhang P, Choi BR, *et al.* (2012) Functional scaffold-free 3-D cardiac microtissues: a novel model for the investigation of heart cells. *Am J Physiol Heart Circ Physiol* 302: H2031
- [42] Hu G, Xiao J, Chua LO, Pivka L (1998) Controlling spiral waves in a model of two-dimensional arrays of Chua's circuits. *Phys Rev Lett* 80(9): 1884.
- [43] Panfilov AV (2002) Spiral breakup in an array of coupled cells: the role of the intercellular conductance. *Phys Rev Lett* 88(11): 118101.

- [44] Fenton F, Karma A (1998) Vortex dynamics in three-dimensional continuous myocardium with fiber rotation: Filament instability and fibrillation. *Chaos* 8(1):20-47
- [45] Fenton FH, Cherry EM, Hastings HM, and Evans SJ (2002) Multiple mechanisms of spiral wave breakup in a model of cardiac electrical activity. *Chaos* 12(3):852-892.
- [46] Barkley D (1990) Spiral-wave dynamics in a simple model of excitable media: The transition from simple to compound rotation *Phys. Rev. A* 42(4):2489-2492.
- [47] Otani NF (2002) A primary mechanism for spiral wave meandering. *Chaos* 12(3):829-842.
- [48] Gray RA, Wikswo JP, and Otani NF (2009) Origin choice and petal loss in the flower garden of spiral wave tip trajectories. *Chaos* 19(3): 033118.
- [49] Kiseleva I, Kamkin A, Pylaev A, et al. (1998) Electrophysiological properties of mechanosensitive atrial fibroblasts from chronic infarcted rat heart. *J Mol Cell Cardiol* 30:1083-1093.
- [50] Kamkin A, Kiseleva I, Wagner KD, et al. (1999) Mechanically induced potentials in fibroblasts from human right atrium. *Exp Physiol* 84:347-356.
- [51] Kamkin A, Kiseleva I, Wagner KD, et al. (2002) A possible role for atrial fibroblasts in postinfarction bradycardia. *Am J Physiol Heart Circ Physiol* 282:H842-H849.
- [52] Chilton L, Ohya S, Freed D, et al. (2005) K^+ currents regulate the resting membrane potential, proliferation, and contractile responses in ventricular fibroblasts and myofibroblasts. *Am J Physiol Heart Circ Physiol* 288:H2931-H2939.
- [53] Shibukawa Y, Chilton EL, Maccannell KA, et al. (2005) K^+ currents activated by depolarization in cardiac fibroblasts. *Biophys J* 88:3924-3935.
- [54] Doerr T, Denger R, Doerr A, et al. (1990) Ionic currents contributing to the action potential in single ventricular myocytes of the guinea pig studied with action potential clamp. *Pflugers Arch* 416:230-7.
- [55] Matsuoka S, Sarai N, Kuratomi S, et al. (2003) Role of individual ionic current systems in ventricular cells hypothesized by a model study. *Jpn J Physiol* 53:105-23.

- [56] Fink M, Giles WR, Noble D (2006) Contributions of inwardly rectifying K^+ currents to repolarization assessed using mathematical models of human ventricular myocytes. *Phil. Trans. R. Soc. A* 364:1207-22.
- [57] Fink M, Noble D, Virag L, *et al.* (2008) Contributions of HERG K^+ current to repolarization of the human ventricular action potential. *Prog Biophys Mol Biol* 96:357-76.
- [58] Jacquemet V (2006) Pacemaker activity resulting from the coupling with nonexcitable cells. *Phys Rev E* 74:011908.
- [59] Miragoli M, Salvarani N, Rohr S (2007) Myofibroblasts induce ectopic activity in cardiac tissue. *Circ Res* 101:755-758.
- [60] Majumder R, Nayak AR, Pandit R (2012) Nonequilibrium Arrhythmic States and Transitions in a Mathematical Model for Diffuse Fibrosis in Human Cardiac Tissue. *PLoS ONE* 7(10): e45040.
- [61] Pertsov AM, Davidenko JM, Salomonsz R, *et al.* (1993) Spiral waves of excitation underlie reentrant activity in isolated cardiac muscle. *Circ Res* 72: 631.
- [62] Bernus O, Wilders R, Zemlin CW, *et al.* (2002) A computationally efficient electrophysiological model of human ventricular cells. *Am J Physiol Heart Circ Physiol* 282: H2296.
- [63] Davidenko JM, Pertsov AV, Salomonsz R, *et al.* (1992) Stationary and drifting spiral waves of excitation in isolated cardiac muscle. *Nature* 355: 349.
- [64] Weiss JN, Chen PS, Qu Z, *et al.* (2000) Ventricular fibrillation: how do we stop the waves from breaking? *Circ Res* 87: 1103-1107.
- [65] Kléber AG, Rudy Y (2004) Basic mechanisms of cardiac impulse propagation and associated arrhythmias. *Physiol Rev* 84: 431-488.
- [66] Comtois P, Kneller J, Nattel S (2005) Of circles and spirals: bridging the gap between the leading circle and spiral wave concepts of cardiac reentry. *Eurpace* 7: S10-S20.
- [67] Rudenko AN, Panfilov AV (1983) Drift and interaction of vortices in two-dimensional heterogeneous active medium. *Studia Biophysica* 98: 183.
- [68] Panfilov AV, Vasiev BN (1991) Vortex initiation in a heterogeneous excitable medium. *Physica D* 49: 107.

- [69] Ten Tusscher KH, Panfilov AV (2003) Reentry in heterogeneous cardiac tissue described by the Luo-Rudy ventricular action potential model. *Am J Physiol Heart Circ Physiol* 284: H542.
- [70] Shajahan TK (2008) Studies of spiral turbulence and its control in models of cardiac tissue. PhD Thesis, Indian Institute of Science, Bangalore, India.
- [71] Zhang H, Hu B, Hu G (2003) Suppression of spiral waves and spatiotemporal chaos by generating target waves in excitable media. *Phys Rev E* 68: 026134.
- [72] Zhang H, Cao Z, Wu NJ, Ying HP, Hu G (2005) Suppress Winfree turbulence by local forcing excitable systems. *Phys Rev Lett* 94: 188301.
- [73] Camelliti P, Green CR, LeGrice I, Kohl P (2004) Fibroblast network in rabbit sinoatrial node: structural and functional identification of homogeneous and heterogeneous cell coupling. *Circ Res* 94(6):828-835.
- [74] Chen PS, Wu TJ, Ting CT, *et al.*, (2003) A tale of two fibrillations. *Circulation* 108: 2298.
- [75] Ideker RE and Rogers JM (2006) Human ventricular fibrillation: wandering wavelets, mother rotors, or both ? *Circulation* 114: 530.
- [76] Janse MJ (2007) Focus, reentry, or “foca” reentry ? *Am J Physiol Heart Circ Physiol* 292: H2561.
- [77] Xie F, Qu Z, Garfinkel A (1998) Dynamics of reentry around a circular obstacle in cardiac tissue. *Phys Rev E* 58:6355.
- [78] Kohl P, Kamkin AG, Kiseleva IS, Streubel T (1992) Mechanosensitive cells in the atrium of frog heart. *Exp Physiol* 77:213.
- [79] Kamkin A, Kiseleva I, Lozinsky I, Scholz H (2005) Electrical interaction of mechanosensitive fibroblasts and myocytes in the heart. *Basic Res Cardiol* 100:337.
- [80] Panfilov AV, Keldermann RH, Nash MP (2007) Drift and breakup of spiral waves in reaction-diffusion-mechanics systems. *Proc Natl Acad Sci USA* 104: 7922.
- [81] Weise LD, Nash MP, Panfilov AV (2011) A discrete model to study reaction-diffusion-mechanics systems. *PLoS ONE* 6(7):e21934
- [82] Karma A (1993) Spiral breakup in model equations of action potential propagation in cardiac tissue. *Phys Rev Lett* 71:1103.

- [83] Panfilov AV (1998) Spiral breakup as a model of VF. *Chaos* 8:57.
- [84] Bernus O, Wilders R, Zemlin CW, Versschelde H, Panfilov AV (2002) A computationally efficient electrophysiological model of human ventricular cells. *Am J Physiol Heart Circ Physiol* 282:H2296.
- [85] Qu Z, Garfinkel FXA, Weiss JN (2000) Origin of spiral wave meander and breakup in a two-dimensional cardiac tissue model. *Ann BioMed Engg* 28:755.
- [86] Xie F, Qu Z, Garfinkel A, Weiss JN (2001) Electrophysiological heterogeneity and stability of reentry in simulated cardiac tissue. *Am J Physiol Heart Circ Physiol* 280:H535.
- [87] Zhang H, Hu B, Hu G (2003) Suppression of spiral waves and spatiotemporal chaos by generating target waves in excitable media. *Phys Rev E* 68: 026134.
- [88] Pumir A, Nikolski V, Horning M, *et al.* (2007) Wave emission from heterogeneities opens a way to controlling chaos in the heart. *Phys Rev Lett* 99:208101.
- [89] Ten Tusscher KH, Panfilov AV (2003) Influence of nonexcitable cells on spiral breakup in two-dimensional and three-dimensional excitable media. *Phys Rev E* 68: 062902.
- [90] Ten Tusscher KHWJ, and Panfilov AV (2007) Influence of diffuse fibrosis on wave propagation in human ventricular tissue. *Europace* 9: vi38.
- [91] McDowell KS, Arevalo HJ, Maleckar MM, Trayanova NA (2011) Susceptibility to arrhythmia in the infarcted heart depends on myofibroblast density. *Biophys J* 101: 1307.
- [92] Potse M, Dube B, Richer J, Vinet A, Gulrajani RM (2006) A comparison of monodomain and bidomain reaction-diffusion models for action potential propagation in the human heart. *IEEE Trans Biomed Eng* 53:2425.

Chapter 4

Spiral-wave Dynamics in Ionically Realistic Mathematical Models for Human Ventricular Tissue: The Effects of Periodic Deformation

*This Chapter follows closely a paper that we have submitted for publication to PLoS ONE journal. The authors are **Alok Ranjan Nayak** and **Rahul Pandit**.*

4.1 Introduction

Sudden cardiac arrest is caused, in many cases, by cardiac arrhythmias, such as ventricular tachycardia (VT) and ventricular fibrillation (VF) [1, 2]. Estimates suggest that VF is the main reason for death in 30% of the cases in which heart failure occurs [3, 4]. Thus, the importance of studying such arrhythmias cannot be overemphasized. Such studies must use interdisciplinary approaches because they require inputs from biology, bio-medical engineering, cardiology, on the one hand, and physics, nonlinear dynamics, and numerical methods, on the other; methods from these areas must be used to study the complicated, nonlinear, partial-differential-equation models that have been developed for cardiac tissue. Such equations can show, *inter alia*, spiral-wave turbulence and spatiotemporal chaos, which is believed to be one of the mathematical analogs of VF. The study we present here combines theoretical ideas from spatiotemporal chaos in extended dynamical systems with extensive direct numerical simulations, to elucidate the effects of periodic deformation (PD) on spiral-wave dynamics in detailed mathematical models for cardiac tissue and to investigate the elimination of such spiral waves, in the presence of PD, by the application of low-amplitude current pulses.

The mechanisms underlying VT and VF are not understood with complete certainty; however, various clinical studies [4, 5] have suggested that the abnormal

propagation of a wave of electrical activation across the ventricles might be the main reason for such arrhythmias. In particular, both experimental [6–9] and computational [9–11] studies have suggested that VT and VF are, respectively, manifestations of (a) a rotating spiral (RS) or scroll wave or (b) broken spiral or scroll waves that lead to spiral- or scroll-wave turbulence (ST). Several studies have investigated the transition from RS to ST, both in experiments on cardiac tissue and in computational studies of mathematical models for cardiac tissue; they find that this transition can occur because of (a) a steep, increasing initial segment in the restitution curve, a plot of the action potential duration (APD) versus the diastolic interval (DI) [10, 12, 13], (b) a similar steep part in an analogous plot of the conduction velocity (CV) versus the DI [10, 14], (c) alternans [11, 13, 15, 16], and (d) heterogeneities, such as, conduction and ionic inhomogeneities [17–21]. Recently, some groups [22–26] have begun to study the effects of deformation of cardiac tissue on the RS-ST transition; they have used simple, two-variable mathematical models for electrical activation in such tissue. One of the goals of our study is to investigate spiral-wave dynamics in general, and RS-ST transitions in particular, in a simple mathematical model for periodic deformation (PD) of cardiac tissue [22–24] that we couple with ionically realistic human-ventricular-tissue mathematical models, namely, (a) the TP06 model, due to ten Tusscher and Panfilov [27], or (b) the TNNP04 model, of ten Tusscher, Noble, Noble, and Panfilov [28]. In our PD model we do not include stretch-activated currents as considered in Refs. [25, 26, 29]. Therefore, our model for PD is a simplified one in which the effects of PD are accounted for by a temporal modulation of diffusion constants. However, in spite of this simplified representation of PD, our study yields important results that have been observed in two-variable models for cardiac tissue both with periodic deformation [22–24] or mechanical deformation [25, 26, 29]; the latter studies include stretch-activated currents. On the positive side, our study uses ionically realistic models that have not been employed in such PD studies so far.

Zhang, *et al.* [22] have studied the instability of a spiral wave of electrical activation by introducing, in a simple, two-variable, FitzHugh-Nagumo-type model [30] for cardiac tissue, the possibility of periodic, temporal oscillations in the diffusion constant. Their study shows that the resulting periodic deformation (PD) can lead to a transition from a stable, RS state to an ST state with multiple spirals. In another study Zhang, *et al.* [23] have shown that such an ST state can be driven into a quiescent state with no spirals, if the oscillation frequency of the PD is chosen to be close to the characteristic frequency of the spiral wave in the RS state of the system. Chen, *et al.* [24] have studied the effects of PD in the two-variable, Bär model [31]

on spiral-wave dynamics by varying the parameter ϵ , which sets the time scale of the slow variable in this model, and the amplitude A and frequency f of the periodic oscillations that lead to PD; their study shows that the RS-ST transition can be effected by changing ϵ , A , and f suitably. Panfilov, *et al.* [25] have shown that PD can either (a) induce a spiral wave to drift or (b) break up spiral waves and thus lead to complex spatiotemporal patterns in the three-variable Fenton-Karma model [32] for cardiac tissue; the model that Panfilov, *et al.* [25] use for PD is different from, and more realistic than, the one used in Refs. [22–24] in so far as it includes a *stretch-activated* current, which accounts for the mechano-electrical feedback in cardiac tissue, whose stress tensor controls PD; their study shows that rotating spirals become unstable both because of the stretch-activated current and the deformation of the tissue. In a related study, which also includes stretch-activated currents, Weise, *et al.* [26] have shown that PD can lead to pacemaker activity in a discrete version of the two-variable, Aliev-Panfilov, reaction-diffusion model [30]. Note that the studies in Refs. [22–26] have used only a particular type of spiral wave configuration in their two-variable models, with either periodic deformation or mechanical deformation.

To the best of our knowledge, there has been no study of the effects of PD on spiral-wave dynamics in an ionically realistic mathematical model for cardiac tissue. To make up for this lacuna, we carry out a systematic numerical study of spiral-wave dynamics in the recently developed TP06 and TNNP04 mathematical models for human-ventricular tissue [27, 28], in which we include PD as in Refs. [22–24]. We also investigate the efficacy of a low-amplitude control scheme, which has been successful in the suppression of spiral-wave turbulence in 2D models for cardiac tissue [18, 19, 33, 34] in the absence of PD. We give below a brief overview of our principal results.

We begin with a study of plane-wave propagation in a cable-type domain, which is well suited for the calculation of the conduction velocity CV and the wavelength λ . We find that PD leads to a periodic, spatial modulation of CV and a temporally periodic modulation of λ ; the degrees of these modulations depend on the amplitude and frequency of the PD.

We use three different parameter sets, for both TP06 and TNNP04 models, to obtain three different prototypical spiral configurations, which we use as the initial conditions $IC1$, $IC2$, and $IC3$. In the TP06 model, these initial conditions evolve, respectively, to (a) a rotating-spiral state RS, with a circular tip trajectory, (b) a state with spiral turbulence (ST), but with a single meandering spiral, and (c) an ST state that has multiple broken spirals, in the absence of PD; in the TNNP04

model they evolve, respectively, to (a) an RS state, with a circular tip trajectory, (b) a temporally quasi-periodic state QP, with a Z -type spiral-tip trajectory, and (c) an ST state, with multiple broken spirals, in the absence of PD.

For the TP06 model, with PD, we show that the initial condition $IC1$ can lead to (a) an RS state with n -cycle temporal evolution (here n is a positive integer), (b) rotating-spiral states with QP temporal evolution, (c) a state with a single meandering spiral MS, which displays spatiotemporal chaos, (d) an ST state, with multiple broken spirals, and (e) a quiescent state SA in which all spirals are absorbed. With the initial condition $IC2$, the TP06 model, with PD, can display either (a) an ST state, with multiple spirals, or (b) an SA state, with no spirals; and for $IC3$ it can be driven into (a) an ST state, with a single meandering spiral, (b) an ST state, with multiple spirals, and (c) the state SA. For all the initial conditions, precisely which one of these states is obtained depends on the amplitudes A_x and A_y and the frequencies f_x and f_y of the PD in the x and y directions.

Our studies of the TNNP04 model, with PD, show that the initial condition $IC1$ leads to one of the following states (depending on the values of A_x , A_y , f_x , and f_y): (a) an RS state, with a non-circular spiral-tip trajectory, (b) a meandering spiral MS state, with a single spiral, (c) an ST state, with multiple broken spirals, and (d) the state SA, with no spirals. The initial condition $IC2$ can yield (a) an MS state, (b) an ST state, and (c) an SA state, whereas $IC3$ can lead to an (a) ST or (b) SA state; in the last case, the spirals are first depleted by collisions among different spiral waves and then the last remaining waves are absorbed by the boundary of the simulation domain.

We also study, in the presence of PD, the efficacy of a low-amplitude control scheme [18, 34] that has been suggested, hitherto only without PD, for the control of spiral-wave turbulence, via low-amplitude current pulses applied on a square mesh, in mathematical models for cardiac tissue. Furthermore, we develop line-mesh and rectangular-mesh variants of this control scheme.

The remaining part of this paper is organized as follows. In Sec. 4.2, we present the models we study and describe the numerical methods we use. In Sec. 4.3, we present our results on spiral-wave dynamics in the TP06 and TNNP04 models in the presence of PD; we then describe the low-amplitude control scheme for the elimination of spiral-wave turbulence in models for cardiac tissue and examine its efficacy in the presence of PD. Section 4.4 contains a discussion of our results and the limitations of our study; we include here a brief overview of various stretching devices, which have been developed to control the deformation of a cell, fiber, and tissue, and we then suggest experiments that can impose a periodic deformation

on cardiac tissue or cell cultures, and thereby, verify the predictions of our *in silico* studies. The Supplementary Material S1 contains a detailed specification of the TP06 and TNNP04 models, with lists of all the variables, the equations that govern their spatiotemporal evolution, their initial values, and the additional figures that augment the results that we present in the main body of this paper.

4.2 Methods

We begin with the reaction-diffusion equation, for the transmembrane potential V_m ,

$$\frac{\partial V_m}{\partial t} + \frac{I_{ion}}{C_m} = D_x \frac{\partial^2 V_m}{\partial x^2} + D_y \frac{\partial^2 V_m}{\partial y^2}, \quad (4.1)$$

where C_m is the membrane capacitance density, I_{ion} is the sum of all the ionic currents that cross the cell membrane, and D_x and D_y are, respectively, the *diffusion coefficients* along x and y directions. We use two biophysically realistic ionic models for human cardiac myocytes: (a) the ten Tusscher and Panfilov model (the TP06 model) [27], and (b) the ten Tusscher, Noble, Noble, and Panfilov model (the TNNP04 model) [28]; these have been developed recently. In these models, the total ionic current

$$\begin{aligned} I_{ion} = & I_{Na} + I_{CaL} + I_{to} + I_{Ks} + I_{Kr} + I_{K1} \\ & + I_{NaCa} + I_{NaK} + I_{pCa} + I_{pK} + I_{bNa} + I_{bCa}, \end{aligned} \quad (4.2)$$

where I_{Na} is the fast, inward Na^+ current, I_{CaL} the L-type, slow, inward Ca^{2+} current, I_{to} the transient, outward current, I_{Ks} the slow, delayed, rectifier current, I_{Kr} the rapid, delayed, rectifier current, I_{K1} the inward, rectifier K^+ current, I_{NaCa} the Na^+/Ca^{2+} exchanger current, I_{NaK} the Na^+/K^+ pump current, I_{pCa} and I_{pK} the plateau Ca^{2+} and K^+ currents, and I_{bNa} and I_{bCa} the background Na^+ and Ca^{2+} currents, respectively. The full sets of equations for these models, including the ordinary differential equations for the ion-channel gating variables and the ion dynamics, are given in the Supplementary Material S1.

We follow the method suggested in Refs. [22–24] for the introduction of PD into a mathematical model for cardiac tissue. In particular, we note that any point $\mathbf{x} = (x, y)$ in the medium changes to $\mathbf{x}'(t) = (x'(t), y'(t))$ with

$$\begin{aligned} x'(t) &= x[1 + A_x(t)], \\ y'(t) &= y[1 + A_y(t)], \end{aligned} \quad (4.3)$$

if we impose a PD with $A_x(t) = A_x \cos(2\pi f_x t)$ and $A_y(t) = A_y \cos(2\pi f_y t)$. By substituting Eq. 4.3 into Eq. 4.1, we obtain

$$\begin{aligned} \frac{\partial V_m}{\partial t} + \frac{I_{ion}}{C_m} &= \frac{1}{[1 + A_x(t)]^2} D_x \frac{\partial^2 V_m}{\partial x^2} \\ &+ \frac{1}{[1 + A_y(t)]^2} D_y \frac{\partial^2 V_m}{\partial y^2}; \end{aligned} \quad (4.4)$$

a comparison of Eqs. 4.1 and 4.4 shows that Eq. 4.4 can be rewritten as

$$\frac{\partial V_m}{\partial t} + \frac{I_{ion}}{C_m} = D_x(t) \frac{\partial^2 V_m}{\partial x^2} + D_y(t) \frac{\partial^2 V_m}{\partial y^2}, \quad (4.5)$$

with $D_x(t) = D_x(1 + A_x(t))^{-2}$ and $D_y(t) = D_y(1 + A_y(t))^{-2}$.

In our numerical simulations, we use 2D square domains with 1024×1024 grid points and lattice spacings $\delta x = \delta y = 0.25$ mm for both TP06 and TNNP04 models, so the sides of our square simulation domains are $L = 256$ mm in the absence of PD. We use a forward-Euler method for time evolution, with a time step $\delta t = 0.02$ ms; and we employ a five-point stencil for the Laplacian. We use no-flux (Neumann) boundary conditions on the edges of our simulation domains.

We set the diffusion coefficients $D_x = D_y = D = 0.00154$ cm²/ms [27, 28] for both the TP06 and the TNNP04 models and examine the oscillation-amplitude and the frequency ranges $0 \lesssim A_x = A_y \lesssim 0.5$, and 0 Hz $\lesssim f \lesssim 7.0$ Hz, respectively; the deformation amplitudes we use are comparable to those in other computational studies [22, 23, 26]. Reference [35] suggests that we must have $D\delta t/(\delta x^2) < 1/2d$ for numerical stability, where d is the dimension of the simulation domain. For the largest amplitude we use for the PD, the minimum and maximum values of our time-dependent diffusion coefficient are, respectively, $0.00154 \times (1 + 0.5)^{-2} \simeq 0.00068$ cm²/ms and $0.00154 \times (1 - 0.5)^{-2} \simeq 0.00068$ cm²/ms between which our time-dependent diffusion coefficient oscillates. Therefore, for the time and space steps we have used in our calculations, the maximum and minimum values of $D\delta t/(\delta x)^2$ are, respectively, 0.197 and 0.022; for our 2D domain, the quantity $1/2d = 0.25$, i.e., we have numerical stability because $D\delta t/(\delta x)^2 < 1/2d$ for all values of our time-dependent diffusion coefficient. We have also checked that the changes of CV , which occur when we change either our time step or space step, are not significant so our simulation results for CV are not numerical artifacts. We can test, in one more way, that our results are free from numerical artifacts by checking the spatiotemporal evolution of an expanding wave front that emerges from a point stimulus [35]; if this wave front deviates substantially from a circular wave, then spiral-wave dynamics in the simulation may be represented inaccurately. Therefore, we have carried out a set of simulations by applying a stimulus at a point at the center of the simula-

tion domain in the presence of PD; and we have found that the resulting wave has a front that is circular, as we show in Sec. 4.3.

In Figs. S1(a)-(f) in the Supplementary Material S1, we show schematic diagrams for illustrative periodic deformations of a small part of our simulation domain, with 5×5 grid points (indicated by gpts on the axes of figures); in these diagrams, blue, open circles and blue, dashed lines show, at a particular instant of time, the deformed simulation domain superimposed on the undeformed one, which is represented by black, solid circles and black, full lines. We give representative diagrams for the case of expansion, with deformations along only x , only y , or both x and y directions, in Figs. S1(a), (b) and (c), in the Supplementary Material S1, at time $t = 20$ ms; the corresponding plots for contraction, at time $t = 180$ ms, are shown in Figs. S1(d), (e), and (f), in the Supplementary Material S1.

We often have to track the trajectory of the tip of a spiral wave in a 2D simulation domain. The tip of such a spiral wave is normally defined as the point where the excitation wave front and repolarization wave back meet; this point can be found by a variety of methods [10, 32, 36–39]. We use the tip-tracking algorithm of Ref. [39] that locates the tip position by monitoring I_{Na} , the sodium current. Pseudocolor plots of I_{Na} show a fine line along the arm of a spiral wave (Fig. 2A in Ref. [18]); this line terminates in the spiral tip and can, therefore, be used to obtain the spatiotemporal evolution of this tip.

4.3 Results

Our principal goals are (a) the examination of the effects of PD on the propagation of electrical waves of activation in mathematical models for cardiac tissue and (b) the evaluation of the efficacy, in the presence of PD, of the low-amplitude control scheme of Refs. [18, 33] for the elimination of spiral-wave turbulence in these models. We begin with (a), by exploring the effects of PD both on plane-wave propagation and on spiral-wave dynamics; here we vary the oscillation amplitude and the frequency in the ranges $0 \lesssim A_x, A_y \lesssim 0.5$, and $0 \text{ Hz} \lesssim f \lesssim 7.0 \text{ Hz}$; the deformation amplitudes we use are comparable to those in other computational [22, 23, 26] and experimental [40, 41] studies; to set the scale of frequencies, we note that the frequency of rotation of a single spiral wave is 4.75 Hz for the TP06 model and 3.75 Hz for the TNNP04 model (see Sec. 4.3.2). We then study the effects of PD on the control scheme mentioned in (b) above.

Type of domain	Dimension of domain (mm)	Parameter sets	Amplitude of PD	Frequency of PD (Hz)
Cable	$L_x = 1024, L_y = 4$	(a00)	$A_x = 0, A_y = 0$	$f_x = 0, f_y = 0$
	$L_x = 1024, L_y = 4$	(a01)	$A_x = 0.1, A_y = 0$	$f_x = 1, f_y = 0$
	$L_x = 1024, L_y = 4$	(a02)	$A_x = 0.2, A_y = 0$	$f_x = 1, f_y = 0$
	$L_x = 1024, L_y = 4$	(a03)	$A_x = 0.3, A_y = 0$	$f_x = 1, f_y = 0$
	$L_x = 1024, L_y = 4$	(a04)	$A_x = 0.4, A_y = 0$	$f_x = 1, f_y = 0$
	$L_x = 1024, L_y = 4$	(a05)	$A_x = 0.5, A_y = 0$	$f_x = 1, f_y = 0$
	$L_x = 1024, L_y = 4$	(a06)	$A_x = 0.1, A_y = 0$	$f_x = 3, f_y = 0$
	$L_x = 1024, L_y = 4$	(a07)	$A_x = 0.2, A_y = 0$	$f_x = 3, f_y = 0$
	$L_x = 1024, L_y = 4$	(a08)	$A_x = 0.3, A_y = 0$	$f_x = 3, f_y = 0$
	$L_x = 1024, L_y = 4$	(a09)	$A_x = 0.4, A_y = 0$	$f_x = 3, f_y = 0$
	$L_x = 1024, L_y = 4$	(a10)	$A_x = 0.5, A_y = 0$	$f_x = 3, f_y = 0$
	$L_x = 1024, L_y = 4$	(a11)	$A_x = 0.1, A_y = 0$	$f_x = 5, f_y = 0$
	$L_x = 1024, L_y = 4$	(a12)	$A_x = 0.2, A_y = 0$	$f_x = 5, f_y = 0$
	$L_x = 1024, L_y = 4$	(a13)	$A_x = 0.3, A_y = 0$	$f_x = 5, f_y = 0$
	$L_x = 1024, L_y = 4$	(a14)	$A_x = 0.4, A_y = 0$	$f_x = 5, f_y = 0$
	$L_x = 1024, L_y = 4$	(a15)	$A_x = 0.5, A_y = 0$	$f_x = 5, f_y = 0$
	$L_x = 1024, L_y = 4$	(a16)	$A_x = 0.1, A_y = 0$	$f_x = 7, f_y = 0$
	$L_x = 1024, L_y = 4$	(a17)	$A_x = 0.2, A_y = 0$	$f_x = 7, f_y = 0$
	$L_x = 1024, L_y = 4$	(a18)	$A_x = 0.3, A_y = 0$	$f_x = 7, f_y = 0$
	$L_x = 1024, L_y = 4$	(a19)	$A_x = 0.4, A_y = 0$	$f_x = 7, f_y = 0$
$L_x = 1024, L_y = 4$	(a20)	$A_x = 0.5, A_y = 0$	$f_x = 7, f_y = 0$	

Table 4.1: Parameters for the periodic deformation (PD) that we use to study the wave dynamics in our cable-type simulation domain in both TP06 and TNNP04 ventricular models.

4.3.1 Plane-wave Dynamics in a Cable

We study plane-wave propagation in a thin, cable-type simulation domain, with 16×4096 grid points, i.e., $L_x = 4$ mm and $L_y = 1024$ mm. We inject a stimulus of strength $I_{stimulus} = 150$ pA/pF at the left end of the cable for 3 ms and then study the effects of PD on the plane wave that propagates through this cable; in particular, we measure the conduction velocity CV and wavelength λ of the propagating wave in the cable. We find that the $CV \simeq 70.6$ cm/s and $\lambda \simeq 21.6$ cm for the TP06 model, and $CV \simeq 67.8$ cm/s and $\lambda \simeq 18.9$ cm for the TNNP04 model, in the absence of PD. As suggested in Refs. [18, 28, 35], it is useful to test the accuracy of the numerical scheme by varying both the time and space steps that we use for integration. We illustrate this for the TP06 model by measuring CV for a plane wave, which is injected into the medium by stimulating the left boundary of our simulation domain. We find that, with $\delta x = 0.025$ cm CV increases by 1.6% as we decrease δt from 0.02 to 0.01 ms;

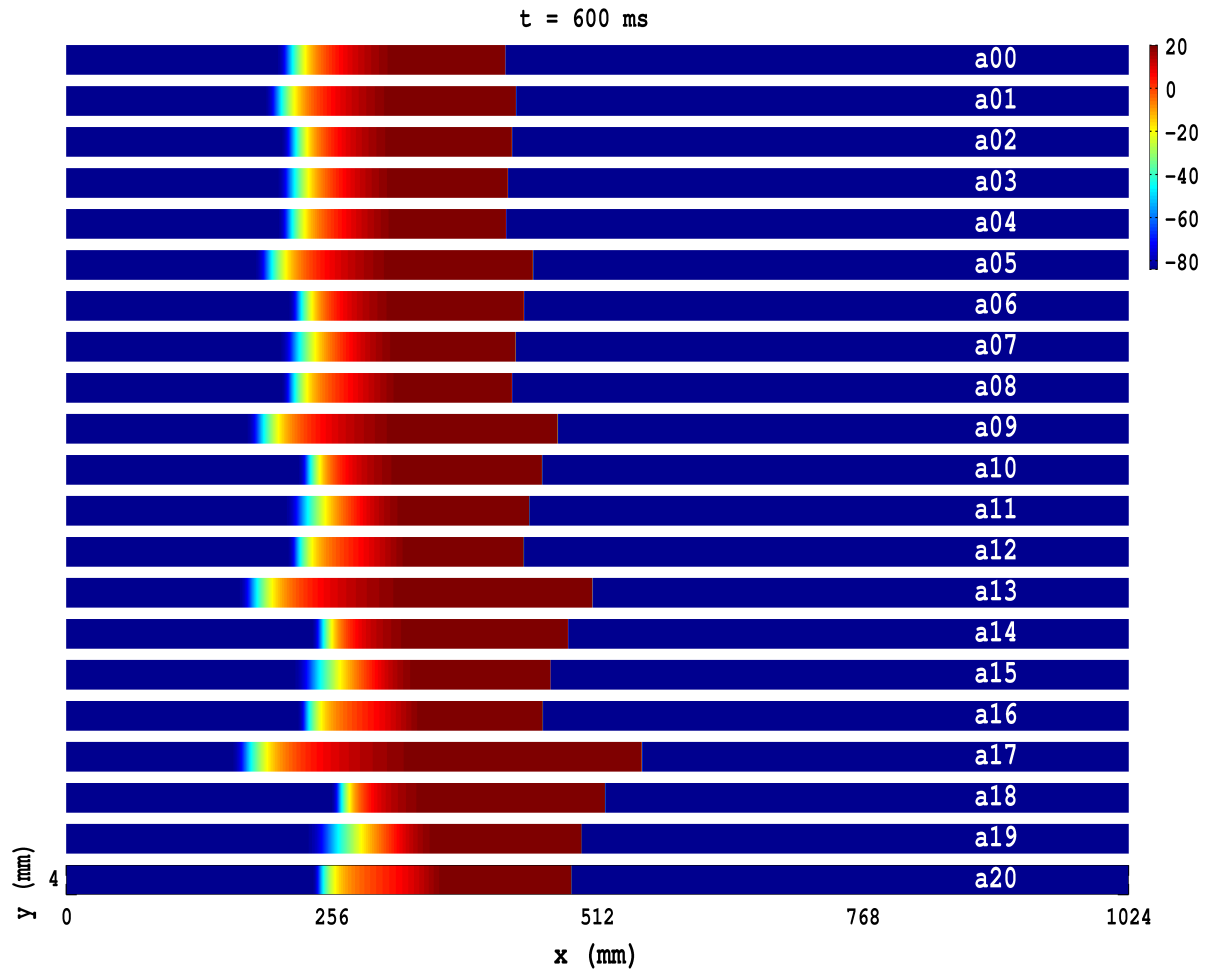


Figure 4.1: Pseudocolor plots of the transmembrane potential V_m for the TP06 model illustrating plane-wave propagation in a cable-type domain, with PD along the axial-direction of the cable, and the parameter sets given in Table 4.1. The Video S1 comprises 21 animations that show the spatiotemporal evolution of these plane waves.

if we use $\delta t = 0.02$ ms and decrease δx from 0.025 to 0.015 cm then CV increases by 4.7%; such changes are comparable to those found in earlier studies [18, 28].

In Figs. 4.1(a00)-(a20) we show, at time $t = 600$ ms, when deformation is applied along the axial direction of the cable, pseudocolor plots of the transmembrane potential V_m for the TP06 model, with PD along the axial direction of the cable, and the parameter sets given in Table 4.1. The Video S1 comprises 21 animations that show the the spatiotemporal evolution of the plane waves in Figs. 4.1(a00)-(a20); these animations and Figs. 4.1(a00)-(a20) show that the conduction velocity CV is modulated in space and the wavelength λ is modulated in time because of the PD. Figure 4.2 illustrates these modulations via plots of CV_f and CV_b versus x for the conduction velocities of the wave front (Fig. 4.2 (a)) and the wave back (Fig. 4.2

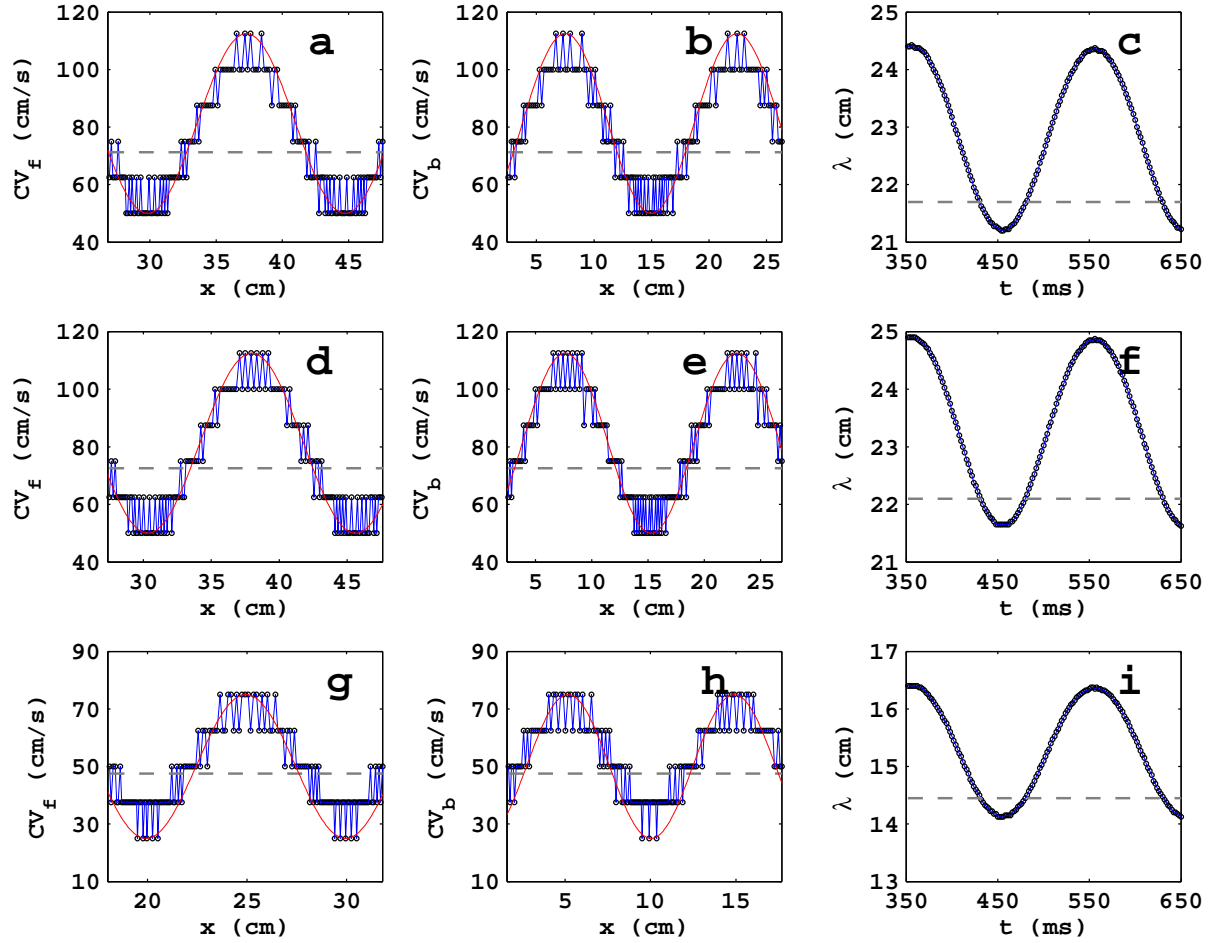


Figure 4.2: The spatial modulation of CV and the temporal modulation of λ of a plane wave propagating in a cable-type domain with PD: Plots versus distance x along the cable of the conduction velocities with $D = 0.00154 \text{ cm}^2/\text{ms}$, $\delta t = 0.02 \text{ ms}$, and $\delta x = 0.25 \text{ mm}$ (a) CV_f , of the wave front, and (b) CV_b , of the wave back; (c) plot versus time t of the wavelength λ . The exact analogs of (a), (b), and (c) are shown in (d), (e), and (f), for $D = 0.00154 \text{ cm}^2/\text{ms}$, $\delta t = 0.01 \text{ ms}$, and $\delta x = 0.25 \text{ mm}$, and in (g), (h), and (i), for $D = 0.00077 \text{ cm}^2/\text{ms}$, $\delta t = 0.02 \text{ ms}$, and $\delta x = 0.25 \text{ mm}$. We use the representative PD parameter values $A_x = 0.3$ and $f_x = 5.0 \text{ Hz}$ for the TP06 model. Open circles show the values from our calculation; the red lines show smooth sinusoidal envelopes; in the absence of PD, $CV \simeq 70.6 \text{ cm/s}$, $\simeq 71.7 \text{ cm/s}$, and $\simeq 47 \text{ cm/s}$, respectively, for above three parameter sets (gray, dashed lines in (a) and (b)); in (c) the gray, dashed line shows the value of λ that we obtain in the absence of PD.

(b)), respectively; and Fig. 4.2(c) shows the corresponding plot for λ versus time t ; in these plots we use the representative PD parameter values $A_x = 0.3$ and $f_x = 5.0 \text{ Hz}$ for the TP06 model. We calculate the conduction velocities $CV_f(x)$ and $CV_b(x)$, in the cable-type domain with PD, by recording the positions of the wave front and the wave back at times t and $t + \delta t$; the wave-front and wave-back conduction ve-

locities, at the point x at time t , are $CV_f(x) = \delta_f x / \delta t$ and $CV_b(x) = \delta_b x / \delta t$, where $\delta_f x$ and $\delta_b x$ are, respectively, the distances traveled by the wave front and wave back in the time interval δt . We locate the position of the wave front by finding the value of x at which $V_m \simeq 0$ mV; we define the position of the wave back as the point, behind the wave front, at which a secondary action potential can just be initiated by an additional stimulus (this turns out to occur at a value of V_m that is $\simeq 75\%$ of the repolarization phase of the action potential). We obtain the wavelength $\lambda(t)$ by measuring the distance between the wave front and the wave back at time t .

In Figs. 4.2 (a) and (b), the open circles show the values of $CV_f(x)$ and $CV_b(x)$, respectively, that we obtain by the method described above; the red lines show smooth sinusoidal envelopes, with amplitude $\simeq 31.2$ cm/s and spatial period $\simeq 14.5$ cm, that give the average modulations of these conduction velocities with x . Note that, in the absence of PD, $CV \simeq 70.6$ cm/s (this is shown via a gray, dashed line in Figs. 4.2 (a) and (b)); therefore, the electrical wave can travel $\simeq 70.6/f$ cm in $1/f$ s; hence, for a given PD frequency f , the spatial period of oscillation of $CV_f(x)$ and $CV_b(x)$ is $\simeq 70.6/f$ cm; the representative plots of Figs. 4.2 (a) and (b), in which $f = 5$ Hz and the period is $\simeq 70.6/5 = 14.12$ cm, are consistent with this estimate.

Figure 4.2(c) shows that λ is a periodic function of t with a period τ ; we expect that $\tau = 1/f$, where f is the PD frequency; the illustrative plot in Fig. 4.2(c), with $f = 5$ Hz, is consistent with this expectation because $\tau \simeq 202$ ms; the gray, dashed line shows the value of λ that we obtain in the absence of PD.

It is useful to study how CV and λ of a plane wave behave, in the presence of PD, when we change the values of the time step and the diffusion coefficients. We find that, in the presence of PD, CV and λ continue to oscillate, as in Figs. 4.2(d)-(i), as functions of x and t , respectively; the mean values of CV and λ , about which these oscillations occur, are close to their values without PD, which depend on the diffusion coefficients and marginally on the time step: In Figs. 4.2(d)-(e) we show, for $D = 0.00154$ cm²/ms, $\delta t = 0.01$ ms, and $\delta x = 0.25$ mm, the analogs of Figs. 4.2(a)-(c); and in Figs. 4.2(g)-(i) we give their counterparts for $D = 0.00077$ cm²/ms, $\delta t = 0.01$ ms, and $\delta x = 0.25$ mm.

The TNNP04-model analogs of the TP06-model Figs. 4.1(a00)-(a20) are given in Figs. S2(a00)-(a11) in the Supplementary Material S1; and Video S2 is the TNNP04-model counterpart of the TP06-model Video S1 (these videos cover the time interval $0 \text{ s} \leq t \leq 2 \text{ s}$ and they have 10 frames per second).

Model	Initial condition	Final state	G_{Na} (nS/pF)	G_{kr} (nS/pF)	G_{ks} (nS/pF)	G_{pCa} (nS/pF)	G_{pK} (nS/pF)	σ_f
TP06	<i>IC1</i>	RSC	14.838	0.153	0.392	0.1238	0.0146	1
TP06	<i>IC2</i>	STSS	5×14.838	0.153	0.392	0.1238	0.0146	1
TP06	<i>IC3</i>	STMS	14.838	0.172	0.441	0.8666	0.00219	2
TNNP04	<i>IC1</i>	RSC	14.838	0.096	0.245	0.825	0.0146	1
TNNP04	<i>IC2</i>	RSZ	5×14.838	0.096	0.245	0.825	0.0146	1
TNNP04	<i>IC3</i>	STMS	3×14.838	0.096	0.245	5×0.825	0.0146	2

Table 4.2: Parameters for the initial conditions *IC1*, *IC2*, and *IC3* for TP06 and TNNP04 models: The third column lists the final state of the system, namely, RSC, RSZ, STSS, and STMS that denote, respectively, a rotating-spiral state with a circular tip trajectory, a rotating-spiral state with a *Z*-type tip trajectory, a spiral-turbulence state with a single meandering spiral, and a spiral-turbulence state with multiple spirals. Here, σ_f is the scale factor of the time constant τ_f (see the Supplementary Material S1).

4.3.2 Spiral-wave Dynamics in a Homogeneous Domain

We move now to systematic studies of spiral-wave dynamics in a 2D, square simulation domain with side $L = 256$ mm, in the presence of PD, for both TP06 and TNNP04 models.

In the absence of PD, two methods are used to initiate spiral waves in simulations [7, 18, 28, 42] and experiments [6, 7], namely, (1) the S1-S2 cross-field protocol and (2) the S1-S2 parallel-field protocol. In the cross-field method, a super-threshold stimulus S2 is applied at the boundary that is perpendicular to the S1 stimulus, whereas, in the parallel-field method, S2 is applied parallel to the refractory tail of the S1 stimulus, but not over the entire length of the domain. Our simulation does not show spiral-wave formation if we use the S1-S2 cross-field protocol; this protocol leads to an initial spiral hook near the edge of the simulation domain; and this hook is absorbed by the boundary before it can develop into a spiral wave. However, the parallel-field protocol does lead to the formation of a spiral wave in the medium; in Refs. [18, 19] we have shown that the location of the center of the spiral depends sensitively on the time of initiation of the S2 stimulus and on its spatial extent. We have found that the following modification of the cross-field protocol yields spiral waves easily. In this modified protocol, the precise position and the application time of the S2 stimulus does not have to be controlled as carefully as in the parallel-field protocol; the principal requirement is that the S2 pulse must be applied before the wave back of the S1 stimulus travels across the full simulation domain. In particular, to initiate a spiral wave in our square simulation domain with sides $L_x = L_y = 256$ mm, we first apply an S1 stimulus, of

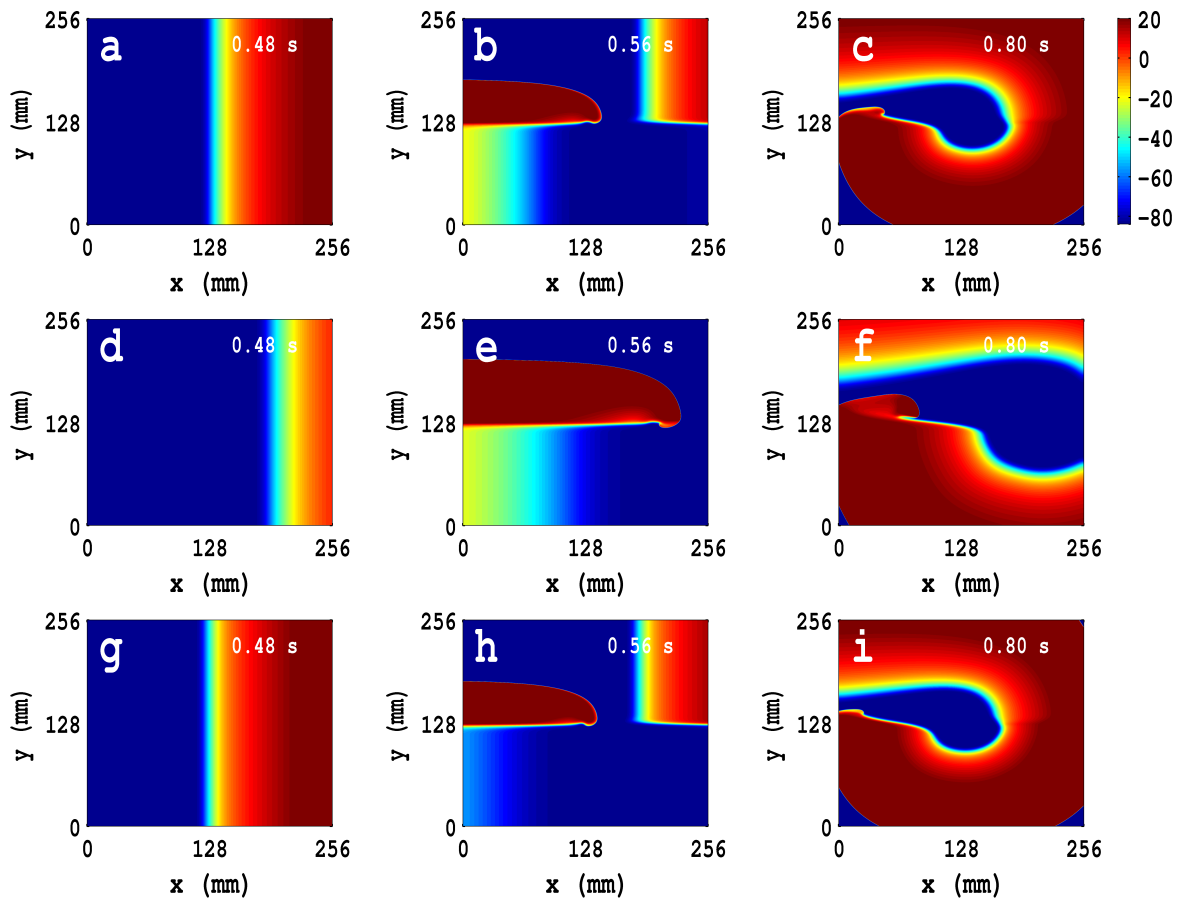


Figure 4.3: Initiation of spiral waves in the TP06 model by the S1-S2 cross field protocol (see text): Pseudocolor plots of the transmembrane potential V_m showing the time evolution of spiral waves for initial conditions (see text) $IC1$ ((a)-(c)), $IC2$ ((d)-(f)), and $IC3$ ((g)-(i)). The animations (a), (b), and (c) in the Video S3 show the spatiotemporal evolution of V_m for these cases.

strength 150 pA/pF, for 3 ms; this injects a plane wave at the left boundary of this domain; we then apply an S2 stimulus, of the same strength as the S1 stimulus and for the same duration, to the bottom half of the domain (i.e., $0 \text{ mm} \leq y \leq 125 \text{ mm}$). This procedure yields the fully developed spiral waves shown in Fig. 4.3; we use three types of spiral-wave initial configurations for our subsequent studies; we refer to these as $IC1$, $IC2$, and $IC3$ initial conditions (see Table 5.1 for parameter values). In Figs. 4.3(a)-(c), we show the time evolution of pseudocolor plots of V_m for the TP06 model with the $IC1$ initial configuration; similar plots are shown in Figs. 4.3(d)-(e) and (f)-(i), respectively, for the $IC2$ and $IC3$ initial configurations; the complete spatiotemporal evolution of V_m for these cases is given in the upper row of Video S3. The TNNP04-model analogs of Figs. 4.3(a)-(i) and the upper row of

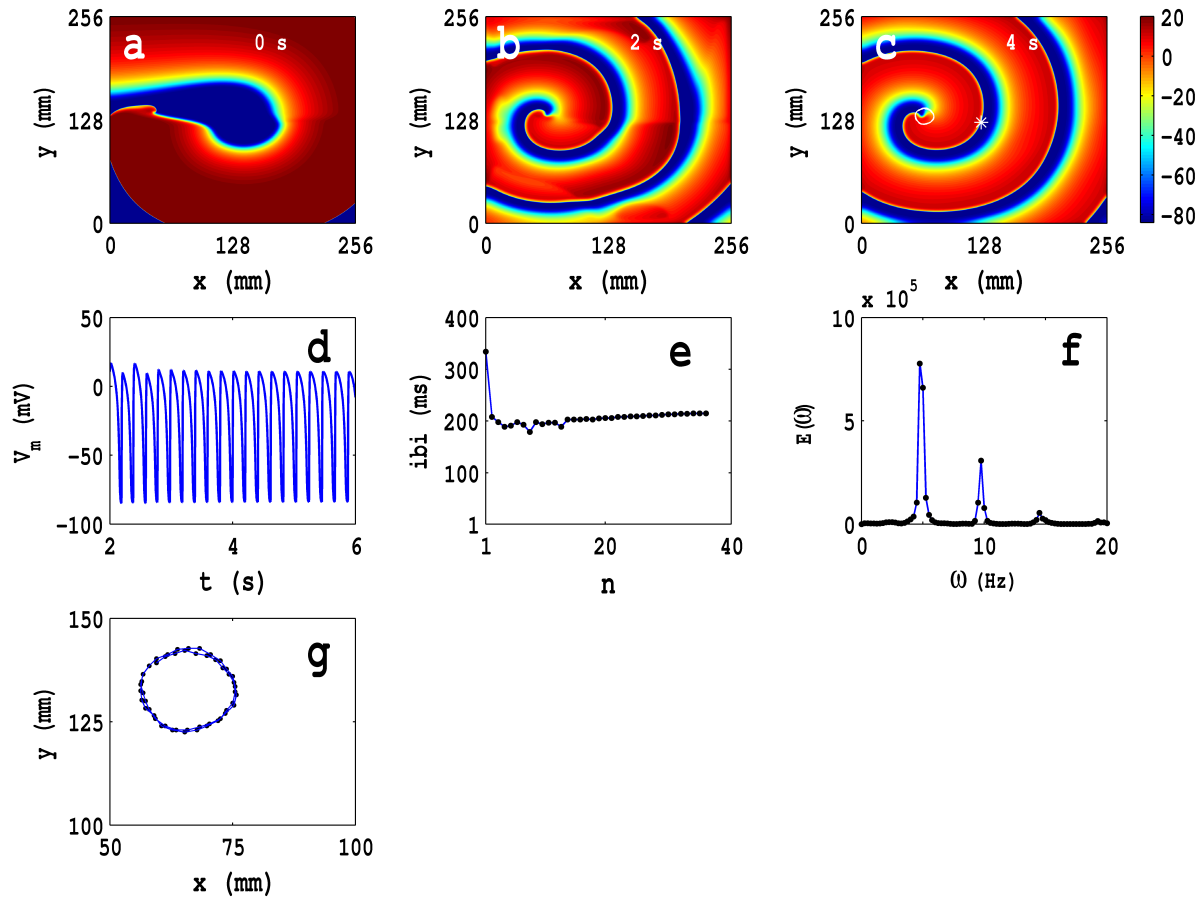


Figure 4.4: Spatiotemporal evolution of V_m for the initial condition $IC1$ for the TP06 model in the absence of PD: (a)-(c) Pseudocolor plots of V_m at times $t = 0$ s, $t = 2$ s, and $t = 4$ s, respectively, showing the evolution towards a state with a rotating spiral (RS); the animation (a) in Video S4 shows the spatiotemporal evolution of V_m for this case. (d) The local time series of $V_m(x, y, t)$, from the representative point ($x = 125$ mm, $y = 125$ mm) (the asterisk in (c)) for $2 \text{ s} \leq t \leq 6 \text{ s}$; (e) a plot of the inter beat interval (ibi), which we obtain from this time series, of length 4×10^5 iterations; (f) the power spectrum $E(\omega)$, obtained from the local time series of (d), with discrete peaks at the fundamental frequency $\omega_f \simeq 4.75$ Hz and its harmonics. The spiral-tip trajectory traces a roughly circular path, with radius $l_c \simeq 20$ mm, which is shown, for $3.6 \text{ s} \leq t \leq 4 \text{ s}$, by the white line that has been superimposed on the pseudocolor plot of V_m in (c); a magnified view of this path is shown in (g).

Video S3 are given, respectively, in Figs. S3(a)-(i), in the Supplementary Material S1, and the bottom row of Video S3.

In Figs. 4.4(a)-(c), we show pseudocolor plots of V_m at times $t = 0$ s, $t = 2$ s, and $t = 4$ s, respectively, for the initial condition $IC1$ in the TP06 model, in the absence of PD; this initial configuration evolves to a state with a rotating spiral (RS) in the medium; the animation (a) in Video S4 shows the spatiotemporal evolution of

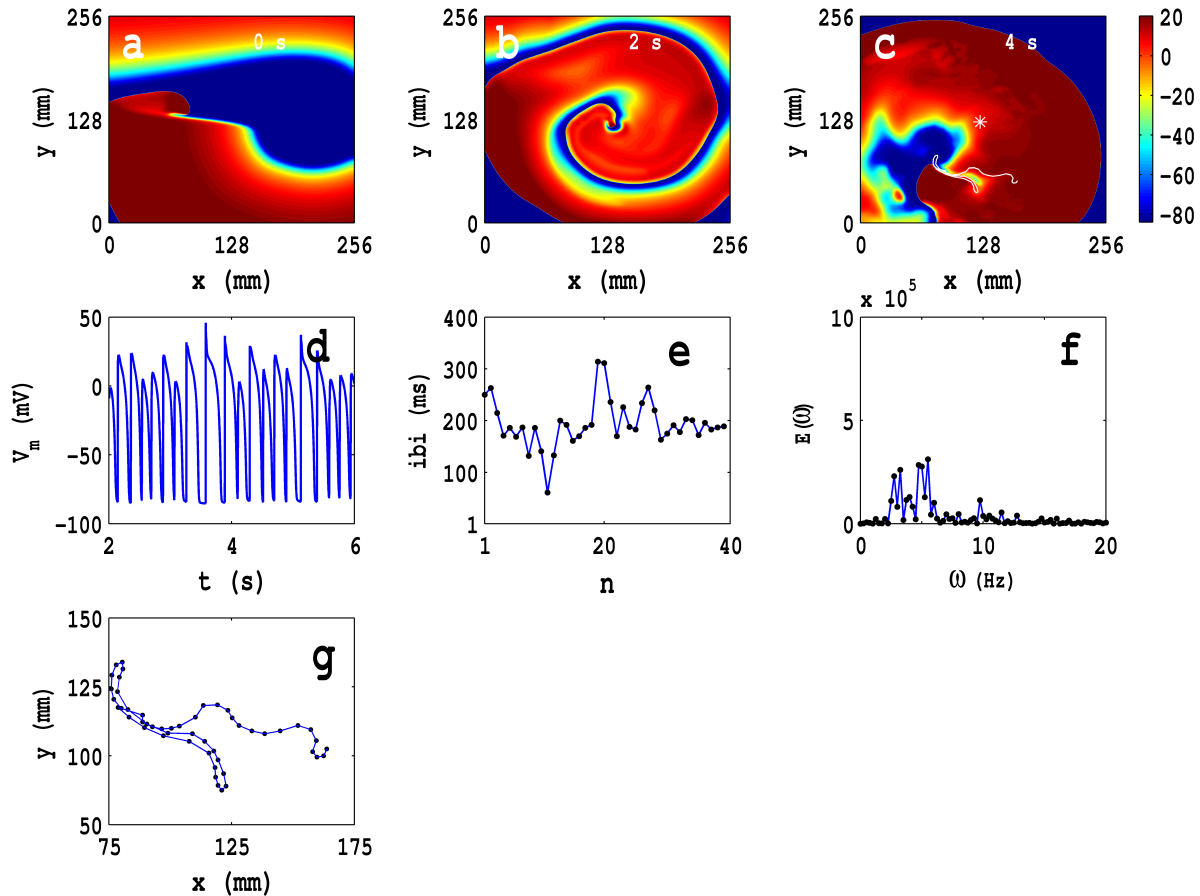


Figure 4.5: Spatiotemporal evolution of V_m for the initial condition $IC2$ for the TP06 model in the absence of PD: (a)-(g) show, for the initial condition $IC2$ in the absence of PD, the exact analogs of Figs. 4.4(a)-(g); and the animation (b) in Video S4 shows the spatiotemporal evolution of V_m for this case. This animation, the pseudocolor plots of V_m ((a)-(c)), the representative local time series of V_m (d), the plot of the ibi (e), the power spectrum $E(\omega)$ (f), and the spiral-tip trajectory (the white curve (c) and the blue one in (g)) show that the initial condition $IC2$ leads to spatiotemporal chaos and spiral turbulence (ST) with a single spiral meandering chaotically in the simulation domain.

V_m for this case. The local time series of $V_m(x, y, t)$, from the representative point ($x = 125$ mm, $y = 125$ mm) (the asterisk in Fig. 4.4(c)), is shown in Fig. 4.4(d) for 2 s $\leq t \leq 6$ s; a plot of the inter beat interval (ibi), which we obtain from this time series, of length 4×10^5 iterations, is given in Fig. 4.4(e), which shows that, after initial transients (roughly the first 10 beats), the spiral wave rotates periodically with an average rotation period $T \simeq 210$ ms. In Fig. 4.4(f), we plot the power spectrum $E(\omega)$, which we have obtained from the local time series of V_m mentioned above; this time series has 2×10^5 data points and the initial 10^5 data points have been removed to eliminate transients; discrete peaks in $E(\omega)$ appear at the fundamental frequency

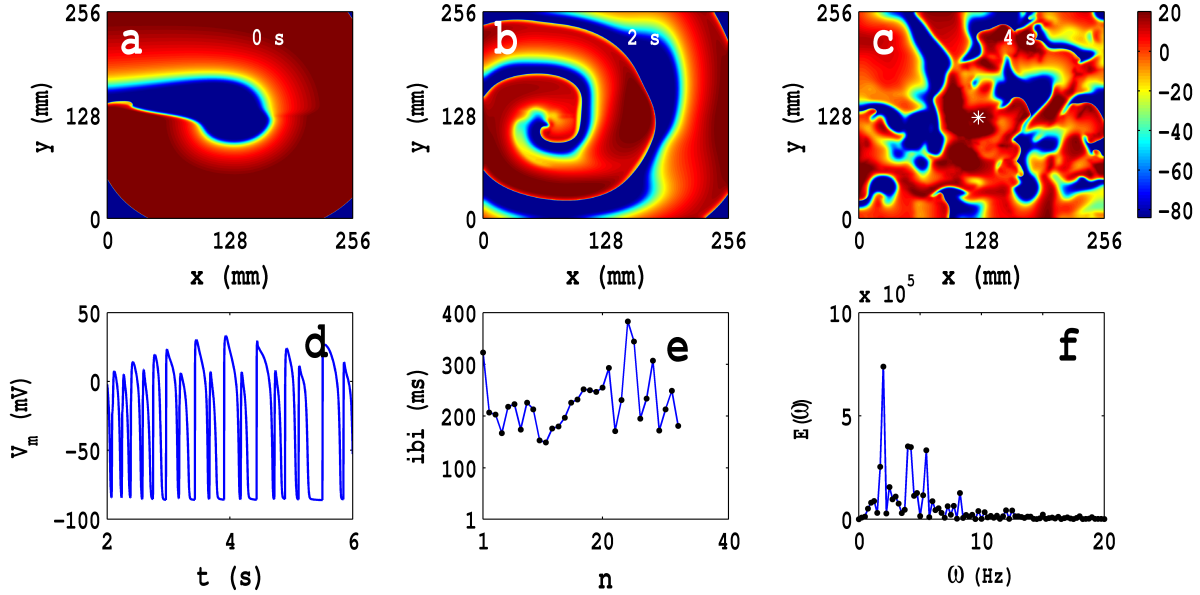


Figure 4.6: Spatiotemporal evolution of V_m for the initial condition $IC3$ for the TP06 model in the absence of PD: (a)-(f) show, for the initial condition $IC3$ in the absence of PD, the exact analogs of Figs. 4.4(a)-(f); and the animation (c) in Video S4 shows the spatiotemporal evolution of V_m for this case. This animation, the pseudocolor plots of V_m ((a)-(c)), the representative local time series of V_m (d), the plot of the ibi (e), and the power spectrum $E(\omega)$ (f) show that the initial condition $IC3$ leads to spatiotemporal chaos and spiral turbulence (ST) with broken spirals in the simulation domain; the life-span of a given spiral-wave segment is small so we do not track the trajectories of spiral tips in this case.

$\omega_f \simeq 4.75$ Hz and its harmonics. The periodic nature of the local time series of V_m , the flattening of the ibi, and the discrete peaks in $E(\omega)$ show that the temporal evolution of the spiral wave is periodic; therefore, the spiral-tip trajectory traces a roughly circular path with radius $l_c \simeq 20$ mm; this circular path is shown, for $3.6 \text{ s} \leq t \leq 4 \text{ s}$, by the white line that has been superimposed on the pseudocolor plot of V_m in Fig. 4.4(c); an expanded version of this path is shown in Fig. 4.4(g).

In Figs. 4.5(a)-(g) we show, for the initial condition $IC2$ in the absence of PD, the exact analogs of Figs. 4.4(a)-(g); and the animation (b) in Video S4 shows the spatiotemporal evolution of V_m for this case. This animation, the pseudocolor plots of V_m (Figs. 4.5(a)-(c)), the representative local time series of V_m (Fig. 4.5(d)), the plot of the ibi (Fig. 4.5(e)), the power spectrum $E(\omega)$ (Fig. 4.5(f)), and the spiral-tip trajectory (the white curve in Fig. 4.5(c) and the blue one in Fig. 4.5(g)) show that the initial condition $IC2$ leads to spatiotemporal chaos and spiral turbulence (ST), with a single spiral meandering chaotically in the simulation domain.

In Figs. 4.6(a)-(f) we show, for the initial condition *IC3* in the absence of PD, the exact analogs of Figs. 4.4(a)-(f); and the animation (c) in Video S4 shows the spatiotemporal evolution of V_m for this case. This animation, the pseudocolor plots of V_m (Figs. 4.6(a)-(c)), the representative local time series of V_m (Fig. 4.6(d)), the plot of the ibi (Fig. 4.6(e)), and the power spectrum $E(\omega)$ (Fig. 4.6(f)) show that the initial condition *IC3* leads to spatiotemporal chaos and spiral turbulence (ST) with broken spirals in the simulation domain; the life-span of a given spiral-wave segment is small so we do not track the trajectories of spiral tips in this case.

Figures S4(a)-(g), Figs. S5(a)-(g), and Figs. S6(a)-(f) (Supplementary Material S1) show, respectively, the TNNP04 analogs of the TP06 Figs. 4.4(a)-(g) (for *IC1*), Figs. 4.5(a)-(g) (for *IC2*), and Figs. 4.6(a)-(f) (for *IC3*); the spatiotemporal evolution of V_m for these three initial conditions for the TNNP04 model are given in animations (d), (e), and (f) in Video S4. From these animations and the Figs. S4(a)-(g), S5(a)-(g), and S6(a)-(f) (Supplementary Material S1) we conclude that the spatiotemporal evolution of V_m in the TNNP04 model, without PD, is similar to, but not identically the same as, that in the TP06 model for the initial conditions *IC1*, *IC2*, and *IC3*. One difference is that, in the TNNP04 model, we have a *Z*-type, spiral-tip trajectory in Figs. S5(c) and (g) (Supplementary Material S1), whereas, for the same initial condition, we have an open spiral-tip trajectory (Figs. 4.5(c) and (g)) in the TP06 model.

4.3.3 Spiral Waves with PD

As we have mentioned in Sec. 4.2, it is important to check the curvature of the front of an expanding wave that emerges from a point at which we apply a stimulus. Therefore, we apply a stimulus of current density 450 pA/pF for 9 ms at the center of our square simulation domain of side $L_x = L_y = 512$ mm. Our numerical results show that fronts of the expanding wave do not deviate substantially from circles, even when we include PD along both x and y directions, with amplitudes and frequencies in the ranges $0 \leq A_x = A_y \leq 0.5$ and $1.0 \text{ Hz} \leq f_x = f_y \leq 7.0 \text{ Hz}$, respectively. The spatiotemporal evolution of such expanding waves is shown for three representative cases of PD, with amplitude and frequency (a) $A_x = A_y = 0.1$, $f_x = f_y = 5 \text{ Hz}$, (b) $A_x = A_y = 0.3$, $f_x = f_y = 5 \text{ Hz}$, and (c) $A_x = A_y = 0.5$, $f_x = f_y = 5 \text{ Hz}$, respectively, in Video S5 by animations of pseudocolor plots (top panel) and contour plots (bottom panel) of V_m .

We turn now to systematic studies of spiral-wave dynamics by using *IC1*, *IC2*, and *IC3* initial configurations in the presence of PD. In the TP06 model, these initial configurations lead, respectively, to (a) an RS state with a roughly circular

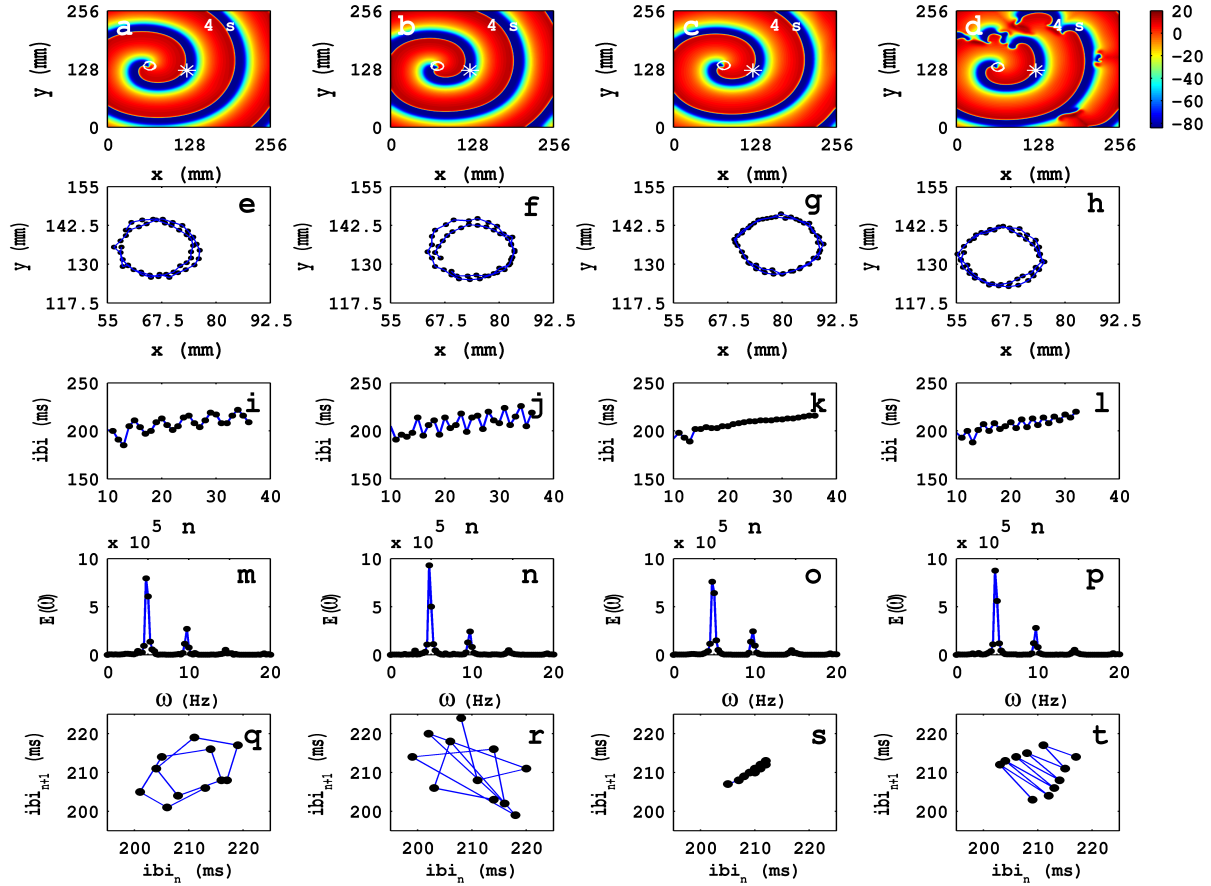


Figure 4.7: Time evolution of the RS state in the TP06 model in the presence of PD with a fixed amplitude: Pseudocolor plots of V_m at time $t = 4$ s for (a) $A_x = A_y = 0.1$, $f_x = f_y = 1.0$ Hz, (b) $A_x = A_y = 0.1$, $f_x = f_y = 3.0$ Hz, (c) $A_x = A_y = 0.1$, $f_x = f_y = 5.0$ Hz, and (d) $A_x = A_y = 0.1$, $f_x = f_y = 7.0$ Hz, respectively; the animations (a1), (b1), (c1), and (d1) in Video S6 show the spatiotemporal evolution of V_m for these cases in the time interval $0 \text{ s} \leq t \leq 4 \text{ s}$. (e-h) Spiral-tip trajectories, which follow from these spatiotemporal evolutions, for $3.6 \text{ s} \leq t \leq 4 \text{ s}$ (in (h) we give the tip trajectory for the main, central spiral (d)). We obtain the local time series of $V_m(x, y, t)$, from the representative point ($x = 125 \text{ mm}, y = 125 \text{ mm}$) (the asterisks in (a-d)), and therefrom the plots of the ibi (i)-(l) and the power spectra (m)-(p). The discrete peaks in $E(\omega)$ appear at the following frequencies: (m) $\omega_1 = 4.75$ Hz, $\omega_2 = 9.5$ Hz, $\omega_3 = 14.25$ Hz, (n) $\omega_1 = 4.75$ Hz, $\omega_2 = 9.5$ Hz, $\omega_3 = 14.25$ Hz, and small peaks at $\omega_1 = 3$ Hz, $\omega_2 = 7.75$ Hz, $\omega_3 = 11$ Hz, $\omega_4 = 12.5$ Hz, $\omega_5 = 15.75$ Hz, (o) $\omega_1 = 4.75$ Hz, $\omega_2 = 9.5$ Hz, $\omega_3 = 14.25$ Hz, and (p) $\omega_1 = 4.75$ Hz, $\omega_2 = 9.5$ Hz, $\omega_3 = 14.25$ Hz. In (i)-(l) we see that the ibi shows a slight upward trend; this implies that, although the temporal evolution is nearly periodic, there is a slight drift, towards lower frequencies, in the rotation rate of the dominant spiral; note also the mild oscillations in the ibi in (i) a 5-cycle, (j) a 3-cycle, and (l) a 2-cycle, but not in (k) a 1-cycle; the natures of these oscillations and their cycle lengths are confirmed by the Poincaré-type return maps, shown in (q), (r), (s), and (t), respectively; in these return maps, successive points are connected by lines.

spiral-tip trajectory, (b) a single meandering spiral with turbulence (we refer to this as SMST henceforth), and (c) multiple-spiral turbulence (MST) with broken spiral waves in the absence of PD, as we have described above. For the TNNP04 model the analogs of these states are (a) RSC, a state with a rotating spiral whose tip trajectory is roughly circular, (b) RSZ, a state with a rotating spiral whose tip trajectory is roughly Z -type, and (c) an MST state.

We first consider the time evolution of *IC1* for the TP06 model in the presence of PD, for which we deform the medium periodically along both x and y directions, with amplitudes and frequencies in the ranges $0.1 \leq A_x = A_y \leq 0.5$ and $1.0 \text{ Hz} \leq f_x = f_y \leq 7.0 \text{ Hz}$, respectively.

In Figs. 4.7(a)-(d) we show pseudocolor plots of V_m at time $t = 4 \text{ s}$ for (a) $A_x = A_y = 0.1$, $f_x = f_y = 1.0 \text{ Hz}$, (b) $A_x = A_y = 0.1$, $f_x = f_y = 3.0 \text{ Hz}$, (c) $A_x = A_y = 0.1$, $f_x = f_y = 5.0 \text{ Hz}$, and (d) $A_x = A_y = 0.1$, $f_x = f_y = 7.0 \text{ Hz}$, respectively. The RS state, which we obtain in the absence of PD, does not evolve into an MST state in cases (a), (b) and (c); however, in case (d) the spiral arm splits into multiple spirals to yield an MST state with mild spatiotemporal chaos, in so far as the dominant spiral does not break down but continues to evolve somewhat like a mother rotor [43–46]; the animations (a1), (b1), (c1), and (d1) in Video S6 show the spatiotemporal evolution of V_m for these cases in the time interval $0 \text{ s} \leq t \leq 4 \text{ s}$; this video uses 10 frames per second (fps) and each pseudocolor plot of V_m is separated from its predecessor by 8 ms. The spiral-tip trajectories, which follow from this spatiotemporal evolution, are shown in Figs. 4.7(e)-(h) for $3.6 \text{ s} \leq t \leq 4 \text{ s}$ (in Fig. 4.7(h) we give the tip trajectory for the main, central spiral in 4.7(a)-(d)); these tip trajectories are nearly circular with radii $l_c \simeq 18 \text{ mm}$, but, as we show below, the temporal evolution of V_m is different in these cases. To examine this evolution, we obtain the local time series of $V_m(x, y, t)$, from the representative point ($x = 125 \text{ mm}, y = 125 \text{ mm}$) (the asterisks in Figs. 4.7(a-d)), and therefrom the plots of the ibi shown in Figs. 4.7(i)-(l) and the power spectra of Figs. 4.7(m)-(p). To obtain the plots of the ibi, we use this local time series with 4×10^5 data points; for the power spectra $E(\omega)$ we use the local time series with 2×10^5 data points after the initial 10^5 data points have been removed to eliminate transients; discrete peaks in $E(\omega)$ appear at the fundamental frequency $\omega_f \simeq 4.75 \text{ Hz}$ and a few other frequencies (see the caption of Fig. 4.7). From Figs. 4.7(i)-(l) we see that the ibi displays a slight upward trend; this implies that, although the temporal evolution is nearly periodic, there is a slight drift, towards lower frequencies, in the rotation rate of the dominant spiral. Furthermore, there are small oscillations in the ibi in Figs. 4.7(i) (a 5-cycle), (j)(a 3-cycle), and (l)(a 2-cycle), but not in Fig. 4.7(k)(a 1-cycle); the natures of these oscillations

and their cycle lengths are confirmed by the Poincaré-type return maps, shown in Figs. 4.7(q)-(t) and corresponding to the ibi plots in Figs. 4.7(i)-(l), respectively; in these return maps, successive points are connected by lines.

Similarly, we study the dependence of spiral-wave dynamics on the amplitudes A_x and A_y of the PD, with the frequencies $f_x = f_y$ held at a fixed value. In Fig. 4.8 we show the pseudocolor plots of V_m at time $t = 4$ s for (a) $A_x = A_y = 0.1$, $f_x = f_y = 1.0$ Hz, (b) $A_x = A_y = 0.2$, $f_x = f_y = 1.0$ Hz, (c) $A_x = A_y = 0.3$, $f_x = f_y = 1.0$ Hz, and (d) $A_x = A_y = 0.4$, $f_x = f_y = 1.0$ Hz. The spiral wave does not split into multiple spirals for these representative values of the amplitudes and frequencies. The animations (a1), (a2), (a3), and (a4) in Video S6 show the spatiotemporal evolution of these spiral waves for the interval $0 \text{ s} \leq t \leq 4 \text{ s}$; these animations use 10 frames per second (fps) and each frame is separated from the preceding one by 8 ms. To examine this evolution, we obtain the local time series of $V_m(x, y, t)$, from the representative point ($x = 125 \text{ mm}$, $y = 125 \text{ mm}$) (the asterisks in Figs. 4.8(a-d)) and the corresponding tip trajectories of spiral waves, in the time interval $3.6 \text{ s} \leq t \leq 4 \text{ s}$ (blue lines with black points in Figs. 4.8(e) and (h), respectively); these tip trajectories trace nearly circular paths, with radii $l_c \simeq 18 \text{ mm}$ in Figs. 4.8(e)-(f); they are of the meandering type in Figs. 4.8(g) and (h), with linear extents $l_c \simeq 24 \text{ mm}$ and $l_c \simeq 75 \text{ mm}$, respectively. From the local time series of V_m mentioned above, we obtain the plots of the ibi shown in Figs. 4.8(i)-(l) and the power spectra of Figs. 4.8(m)-(p); the plots of the ibi use 4×10^5 data points; for the power spectra $E(\omega)$ we use 2×10^5 data points after the initial 10^5 data points have been removed to eliminate transients; discrete peaks in $E(\omega)$ appear at the fundamental frequency $\omega_f \simeq 4.75 \text{ Hz}$ and at the frequencies listed in the caption of Fig. 4.8; these peaks indicate that, in Figs. 4.8(m) and (n), we also have some high-order cycles; the broad-band power spectra in Figs. 4.8(o) and (p) provide evidence for spiral turbulence with a meandering spiral (SMST). In Figs. 4.8(q)-(t), we show Poincaré-type return maps of that we obtain from the ibi plots in Figs. 4.8(i)-(l); in these maps successive points are connected by lines. These plots give additional evidence for 5 cycles in Figs. 4.8(i)-(j) and Figs. 4.8 (m)-(n) and of chaotic behavior in Figs. 4.8(k)-(l) and Figs. 4.8(o)-(p). The lines in Figs. 4.8(q) and (r) move from the bottom-left corner to the top-right corner; this suggests a low-frequency modulation of the spiral-wave dynamics because of the PD; this is associated with the upward trend in the ibi plots of Figs. 4.8(i) and (j).

We focus next on the types of ST states that we obtain, with PD applied along both x and y axes, when we start with the *IC1* initial condition. In Figs. 4.9 we show three representative ST states; Figs. 4.9(a), (b), and (c) show, respectively,

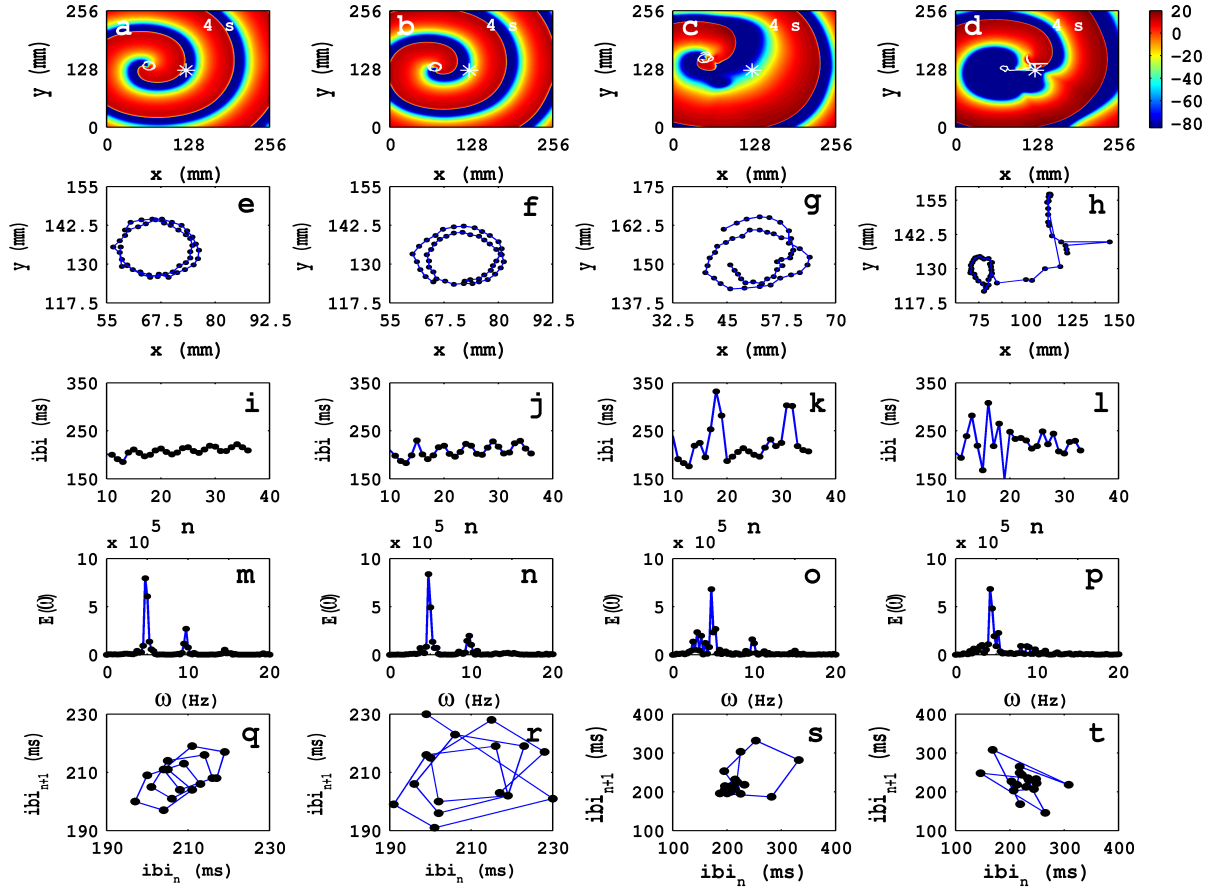


Figure 4.8: Time evolution of the RS state in the TP06 model in the presence of PD with a fixed frequency: Pseudocolor plots of V_m at time $t = 4$ s for (a) $A_x = A_y = 0.1$, $f_x = f_y = 1.0$ Hz, (b) $A_x = A_y = 0.2$, $f_x = f_y = 1.0$ Hz, (c) $A_x = A_y = 0.3$, $f_x = f_y = 1.0$ Hz, and (d) $A_x = A_y = 0.4$, $f_x = f_y = 1.0$ Hz. The animations (a1), (a2), (a3), and (a4) in Video S6 show the spatiotemporal evolution of these spiral waves for the interval $0 \text{ s} \leq t \leq 4 \text{ s}$. (e-h) Spiral-tip trajectories, which follow from these spatiotemporal evolutions, for $3.6 \text{ s} \leq t \leq 4 \text{ s}$. We obtain the local time series of $V_m(x, y, t)$, from the representative point ($x = 125 \text{ mm}, y = 125 \text{ mm}$) (the asterisks in Figs. 4.8(a-d)) and therefrom the plots of the ibi shown in (i)-(l), the power spectra $E(\omega)$ in (m)-(p), and the Poincaré-type return maps, which we obtain from the ibi plots and which show (q) a 5-cycle, (r) a 5-cycle, (s) chaotic behavior, and (t) chaotic evolution; discrete peaks in $E(\omega)$ appear at the following frequencies: (m) $\omega_1 = 4.75 \text{ Hz}$, $\omega_2 = 9.5 \text{ Hz}$, $\omega_2 = 14.25 \text{ Hz}$, (n) $\omega_1 = 4.75 \text{ Hz}$, $\omega_2 = 9.5 \text{ Hz}$, $\omega_2 = 14.25 \text{ Hz}$ and small peaks at $\omega_1 = 3.75 \text{ Hz}$, $\omega_2 = 8.5 \text{ Hz}$, $\omega_3 = 13.25 \text{ Hz}$, $\omega_4 = 15 \text{ Hz}$, $\omega_5 = 17.75 \text{ Hz}$, (o) $\omega_1 = 4.75 \text{ Hz}$, $\omega_2 = 9.5 \text{ Hz}$, and (p) $\omega_1 = 4.5 \text{ Hz}$, $\omega_2 = 9.5 \text{ Hz}$.

pseudocolor plots of the transmembrane potential V_m for PD with (a) $A_x = A_y = 0.3$, $f_x = f_y = 3.0 \text{ Hz}$, (b) $A_x = A_y = 0.3$, $f_x = f_y = 5.0 \text{ Hz}$, and (c) $A_x = A_y = 0.4$, $f_x = f_y = 7.0 \text{ Hz}$; and the animations (b3), (c3), and (d4) in Video S6 show, respectively, the spatiotemporal evolution of V_m for these cases in the time interval $0 \text{ s} \leq t \leq$

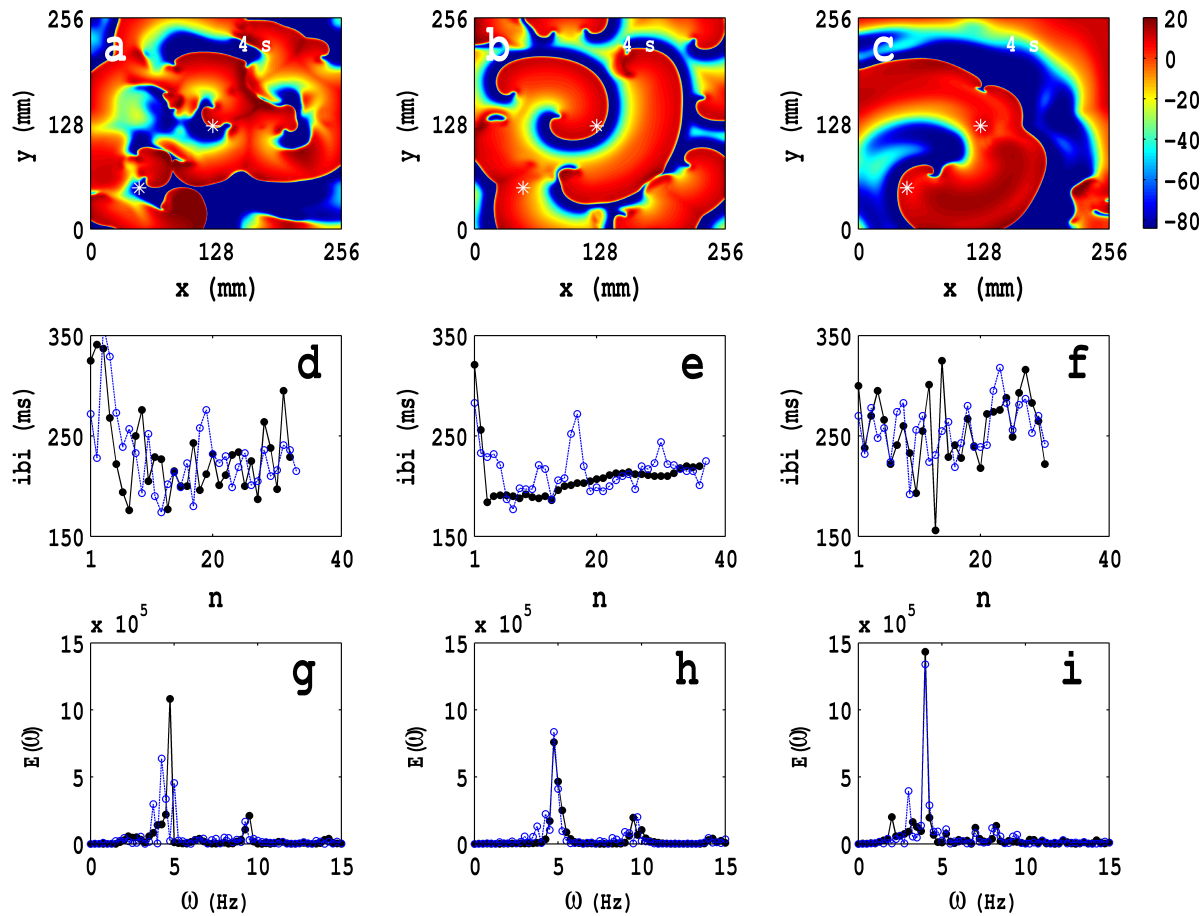


Figure 4.9: Temporal evolution of representative ST states in the TP06 model with PD along both spatial directions: Three ST states, which we obtain with the initial condition $IC1$ and PD, are shown via pseudocolor plots of the transmembrane potential V_m with (a) $A_x = A_y = 0.3$, $f_x = f_y = 3.0$ Hz, (b) $A_x = A_y = 0.3$, $f_x = f_y = 5.0$ Hz, and (c) $A_x = A_y = 0.4$, $f_x = f_y = 7.0$ Hz; the animations (b3), (c3), and (d4) in Video S6 show, respectively, the spatiotemporal evolution of V_m for these cases in the time interval $0 \text{ s} \leq t \leq 4 \text{ s}$. We obtain the local time series of $V_m(x, y, t)$, from the representative points ($x = 125 \text{ mm}, y = 125 \text{ mm}$) and ($x = 50 \text{ mm}, y = 50 \text{ mm}$), shown by asterisks in (a)-(c); from these local time series, we obtain the plots of the ibi (d)-(f) and the power spectra (g)-(i), with open-blue and black-filled circles for the time series from ($x = 125 \text{ mm}, y = 125 \text{ mm}$) and ($x = 50 \text{ mm}, y = 50 \text{ mm}$), respectively. These pseudocolor plots and animations of V_m and the plots of the ibi and power spectra show that we have, roughly speaking, three types of ST states with (a) multiple spirals, (b) a stable spiral core with broken spiral arms, and (c) a single dominant meandering spiral; the second case (b) displays a coexistence of a quasiperiodic and an ST state because of the dominant spiral at the center and the broken spirals generated from its arm.

4 s. To examine this evolution, we obtain the local time series of $V_m(x, y, t)$, from the representative points ($x = 125 \text{ mm}, y = 125 \text{ mm}$) and ($x = 50 \text{ mm}, y = 50 \text{ mm}$), both of which are indicated by asterisks in Figs. 4.9(a)-(c); from these local time

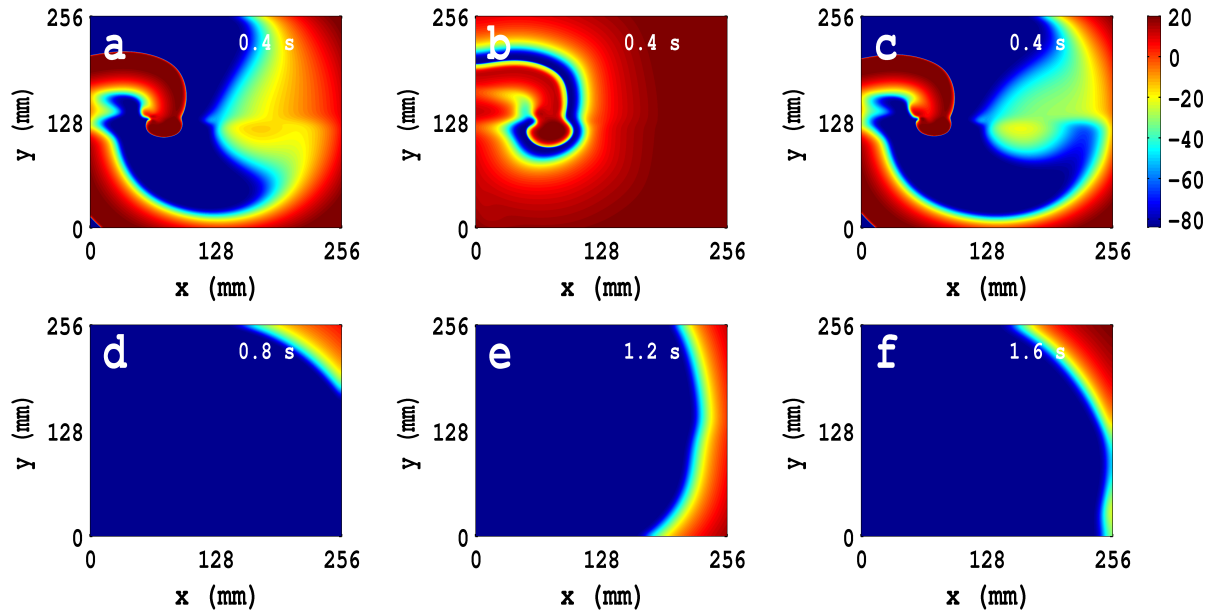


Figure 4.10: Pseudocolor plots of the transmembrane potential V_m for the TP06 model, with PD, illustrating spiral-wave absorption: Pseudocolor plots of V_m , for (a)-(c) $t = 0.4$ s, and (d), (e), and (f), for $t = 0.8$ s, $t = 1.2$ s, and $t = 1.6$ s, respectively, for three representative cases of spiral-wave absorption with the following PDs: (a) and (d) $A_x = A_y = 0.4$, $f_x = f_y = 3.0$ Hz, (b) and (e) $A_x = A_y = 0.5$, $f_x = f_y = 1.0$ Hz, and (c) and (f) $A_x = A_y = 0.5$, $f_x = f_y = 3.0$ Hz; the spatiotemporal evolution of V_m for these cases is shown, respectively, in the animations (b4), (a5), and (b5) in Video S6 for the time interval $0 \leq t \leq 4$ s.

series, we obtain the plots of the ibi shown in Figs. 4.9(d)-(f) and the power spectra of Figs. 4.9(g)-(i), with open-blue and black-filled circles for the time series from $(x = 125 \text{ mm}, y = 125 \text{ mm})$ and $(x = 50 \text{ mm}, y = 50 \text{ mm})$, respectively. The plots of the ibi use 4×10^5 data points; for the power spectra $E(\omega)$ we use 2×10^5 data points after the initial 10^5 data points have been removed to eliminate transients. These pseudocolor plots and animations of V_m and the plots of the ibi and power spectra show that we have, roughly speaking, three types of ST states with (a) multiple spirals (Fig. 4.9(a)), (b) a stable spiral core with broken spiral arms (Fig. 4.9(b)), and (c) a single, dominant, meandering spiral (Fig. 4.9(c)); the second case (b) displays a coexistence of a quasiperiodic and an ST state because of the dominant spiral at the center and the broken spirals generated from its arm. Such coexistence behaviors have been observed in both computational [10, 11, 47] and experimental studies [48, 49], which include *in vivo* experiments.

We also obtain quiescent (Q) states with no spirals because of the absorption of spiral waves at the boundaries of the simulation domain. Typically, this occurs because a single spiral wave drifts towards the boundaries, as we illustrate by the

Type of domain	Dimension of domain (mm)	Parameter sets	Amplitude of PD	Frequency of PD (Hz)
Tissue	$L_x = 1024, L_y = 1024$	(a1)	$A_x = 0.1, A_y = 0.1$	$f_x = 1, f_y = 1$
	$L_x = 1024, L_y = 1024$	(a2)	$A_x = 0.2, A_y = 0.2$	$f_x = 1, f_y = 1$
	$L_x = 1024, L_y = 1024$	(a3)	$A_x = 0.3, A_y = 0.3$	$f_x = 1, f_y = 1$
	$L_x = 1024, L_y = 1024$	(a4)	$A_x = 0.4, A_y = 0.4$	$f_x = 1, f_y = 1$
	$L_x = 1024, L_y = 1024$	(a5)	$A_x = 0.5, A_y = 0.5$	$f_x = 1, f_y = 1$
	$L_x = 1024, L_y = 1024$	(b1)	$A_x = 0.1, A_y = 0.1$	$f_x = 3, f_y = 3$
	$L_x = 1024, L_y = 1024$	(b2)	$A_x = 0.2, A_y = 0.2$	$f_x = 3, f_y = 3$
	$L_x = 1024, L_y = 1024$	(b3)	$A_x = 0.3, A_y = 0.3$	$f_x = 3, f_y = 3$
	$L_x = 1024, L_y = 1024$	(b4)	$A_x = 0.4, A_y = 0.4$	$f_x = 3, f_y = 3$
	$L_x = 1024, L_y = 1024$	(b5)	$A_x = 0.5, A_y = 0.5$	$f_x = 3, f_y = 3$
	$L_x = 1024, L_y = 1024$	(c1)	$A_x = 0.1, A_y = 0.1$	$f_x = 5, f_y = 5$
	$L_x = 1024, L_y = 1024$	(c2)	$A_x = 0.2, A_y = 0.2$	$f_x = 5, f_y = 5$
	$L_x = 1024, L_y = 1024$	(c3)	$A_x = 0.3, A_y = 0.3$	$f_x = 5, f_y = 5$
	$L_x = 1024, L_y = 1024$	(c4)	$A_x = 0.4, A_y = 0.4$	$f_x = 5, f_y = 5$
	$L_x = 1024, L_y = 1024$	(c5)	$A_x = 0.5, A_y = 0.5$	$f_x = 5, f_y = 5$
	$L_x = 1024, L_y = 1024$	(d1)	$A_x = 0.1, A_y = 0.1$	$f_x = 7, f_y = 7$
	$L_x = 1024, L_y = 1024$	(d2)	$A_x = 0.2, A_y = 0.2$	$f_x = 7, f_y = 7$
	$L_x = 1024, L_y = 1024$	(d3)	$A_x = 0.3, A_y = 0.3$	$f_x = 7, f_y = 7$
	$L_x = 1024, L_y = 1024$	(d4)	$A_x = 0.4, A_y = 0.4$	$f_x = 7, f_y = 7$
	$L_x = 1024, L_y = 1024$	(d5)	$A_x = 0.5, A_y = 0.5$	$f_x = 7, f_y = 7$

Table 4.3: Parameters for the PD that we use to study the wave dynamics in our square simulation domain in both TP06 and TNNP04 ventricular models.

pseudocolor plots of V_m in Figs. 4.10(a)-(c), for $t = 0.4$ s, and Figs. 4.10(d), (e), and (f), for $t = 0.8$ s, $t = 1.2$ s, and $t = 1.6$ s, for three representative cases with the following PDs: (a) $A_x = A_y = 0.4$, $f_x = f_y = 3.0$ Hz (Figs. 4.10(a) and (d)), (b) $A_x = A_y = 0.5$, $f_x = f_y = 1.0$ Hz (Figs. 4.10(b) and (e)), and (c) $A_x = A_y = 0.5$, $f_x = f_y = 3.0$ Hz (Figs. 4.10(c) and (f)); the pseudocolor plots of V_m near the final, spiral-absorption states are shown in Figs. 4.10(d)-(f). The spatiotemporal evolution of V_m is shown in the animations (b4), (a5), and (b5) in Video S6 for the time interval $0 \text{ s} \leq t \leq 4 \text{ s}$.

To illustrate the rich variety of spatiotemporal patterns here, we summarize our results for the TP06 model, with the initial condition *IC1*, by presenting a selection of pseudocolor plots of V_m in Figs. 4.11 (a1)-(d5) (for parameter sets see Table. 4.3). The animations in Video S6 show the spatiotemporal evolution of V_m for these cases in the time interval $0 \text{ s} \leq t \leq 4 \text{ s}$. To examine this evolution, we obtain the local time series of $V_m(x, y, t)$, from the representative points ($x = 125$ mm, $y = 125$ mm); these are shown in Fig. S7 (Supplementary Material S1); from these local time series, we obtain the plots of the ibi (Fig. S8 in the Supplementary Material S1) and the

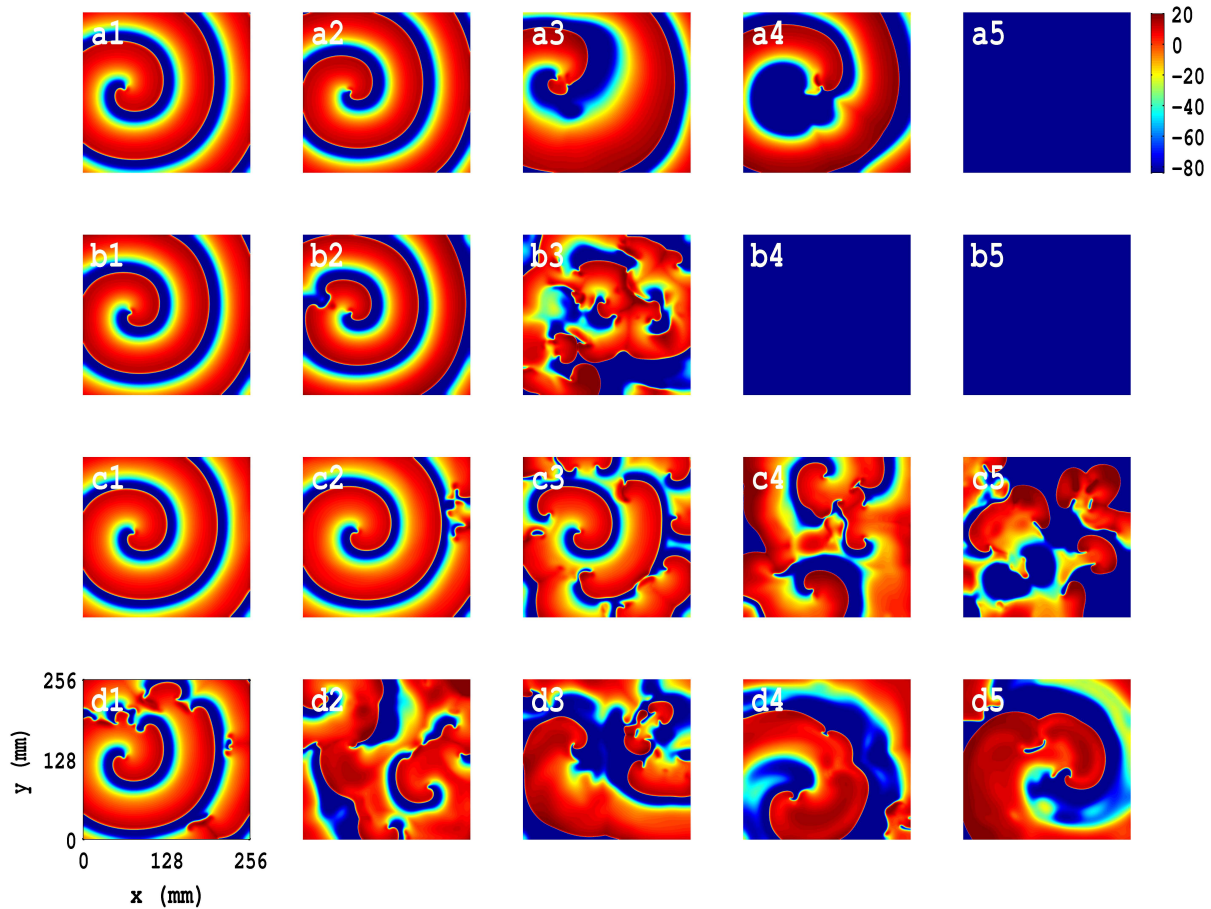


Figure 4.11: Illustrations of the rich variety of spatiotemporal patterns for the TP06 model, with PD and the initial condition $IC1$: Representative pseudocolor plots of V_m with the initial condition $IC1$ (Fig. 4.3(c)) and the parameter sets given in Table. 4.3. The animations in Video S6 show the spatiotemporal evolution of V_m for these cases in the time interval $0 \text{ s} \leq t \leq 4 \text{ s}$. To examine this evolution, we obtain the local time series of $V_m(x, y, t)$, from the representative points ($x = 125 \text{ mm}, y = 125 \text{ mm}$); these are shown in Fig. S7 in the Supplementary Material S1; from these local time series, we obtain the plots of the ibi (Fig. S8 in the Supplementary Material S1) and the power spectra (Fig. S9 in the Supplementary Material S1).

power spectra (Fig. S9 in the Supplementary Material S1). The plots of the ibi use 2×10^5 data points; for each one of the power spectra $E(\omega)$ we use 2×10^5 data points.

The analogs of the pseudocolor plots of V_m in Figs. 4.11 (a1)-(d5) for initial conditions $IC2$ for $IC3$ are given, respectively, in Figs. 4.12 (a1)-(d5) and Figs. 4.13 (a1)-(d5); and the counterparts of Figs. S7, S8, and S9 in the Supplementary Material S1 for initial conditions $IC2$ for $IC3$ are given, respectively, in Figs. S10, S11, and S12 and Figs. S13, S14, and S15 in the Supplementary Material S1.

For the initial conditions $IC2$ and $IC3$ the analogs of the animations in Video S6 are given, respectively, in Videos S7 and S8. For $IC2$, with PD along both axes and

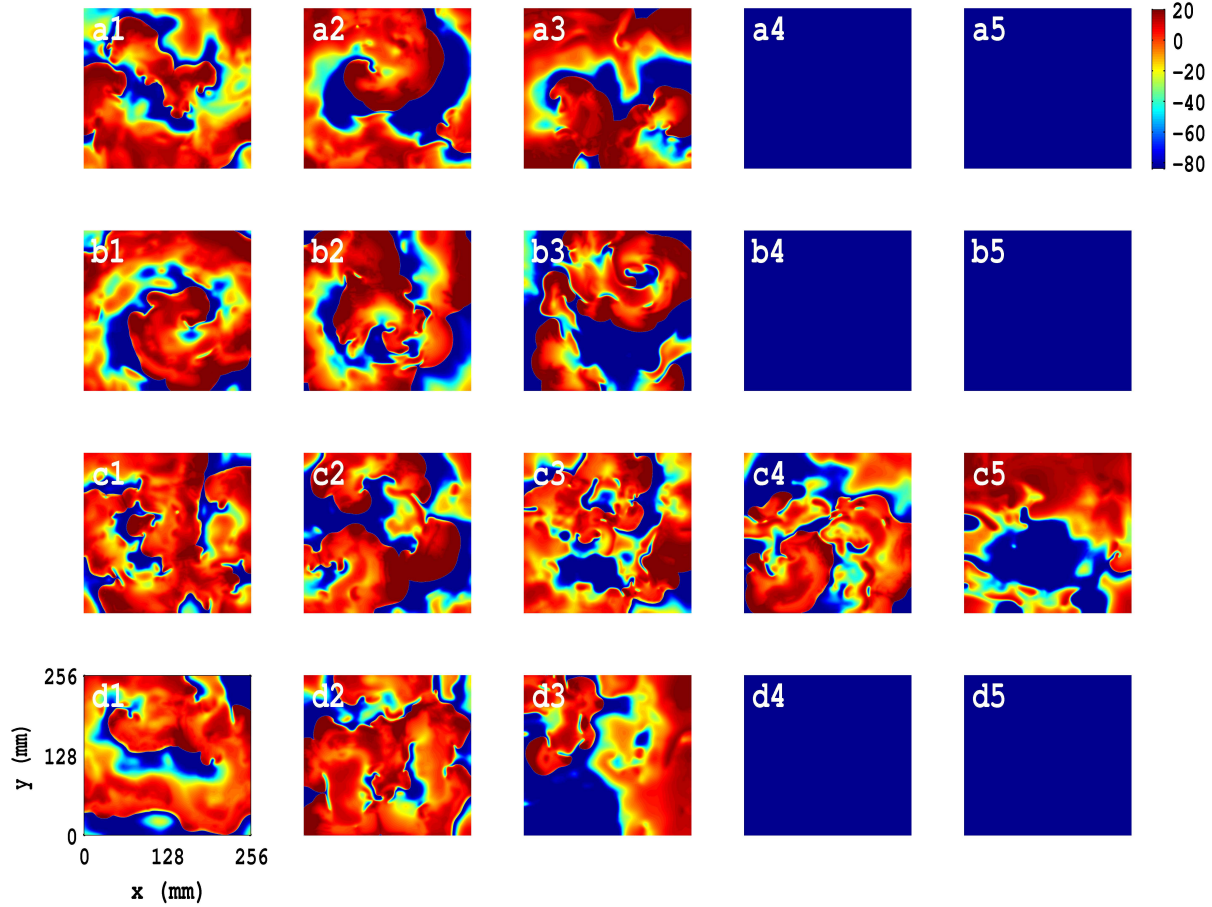


Figure 4.12: Illustrations of the rich variety of spatiotemporal patterns for the TP06 model, with PD and the initial condition $IC2$: The analogs of the pseudocolor plots of V_m in Figs. 4.11 for the initial conditions $IC2$; the plots (a1)-(d5) here use the same PD parameters as their counterparts in Figs. 4.11; the Video S4 shows the spatiotemporal evolution of V_m for these cases for the time interval $0 \leq t \leq 4$ s; and the counterparts of Figs. S7, S8, and S9 in the Supplementary Material S1 for initial condition $IC2$ are Figs. S10, S11, and S12 in the Supplementary Material S1.

different values of the amplitude and the frequency, we examine the time series of $V_m(x, y, t)$, from a representative point in the simulation domain (Figs. S10 in the Supplementary Material S1), the plots of the ibi (Figs. S11 in the Supplementary Material S1) and the power spectrum $E(\omega)$ (Figs. S12 in the Supplementary Material S1), and the spatiotemporal evolution of V_m (given by the the animations in Video S7) and conclude therefrom that, in this case, we obtain either (a) a Q state with no spirals (see animations (a4), (a5), (b4), (b5), (d4) and (d5) in Video S7) or (b) an MST state with broken spiral waves (see the remaining animations in Video S7). A similar analysis, for $IC3$ and PD along both x and y axes, based on time series of V_m (Figs. S13 in the Supplementary Material S1), plots of the ibi (Figs. S14 in the

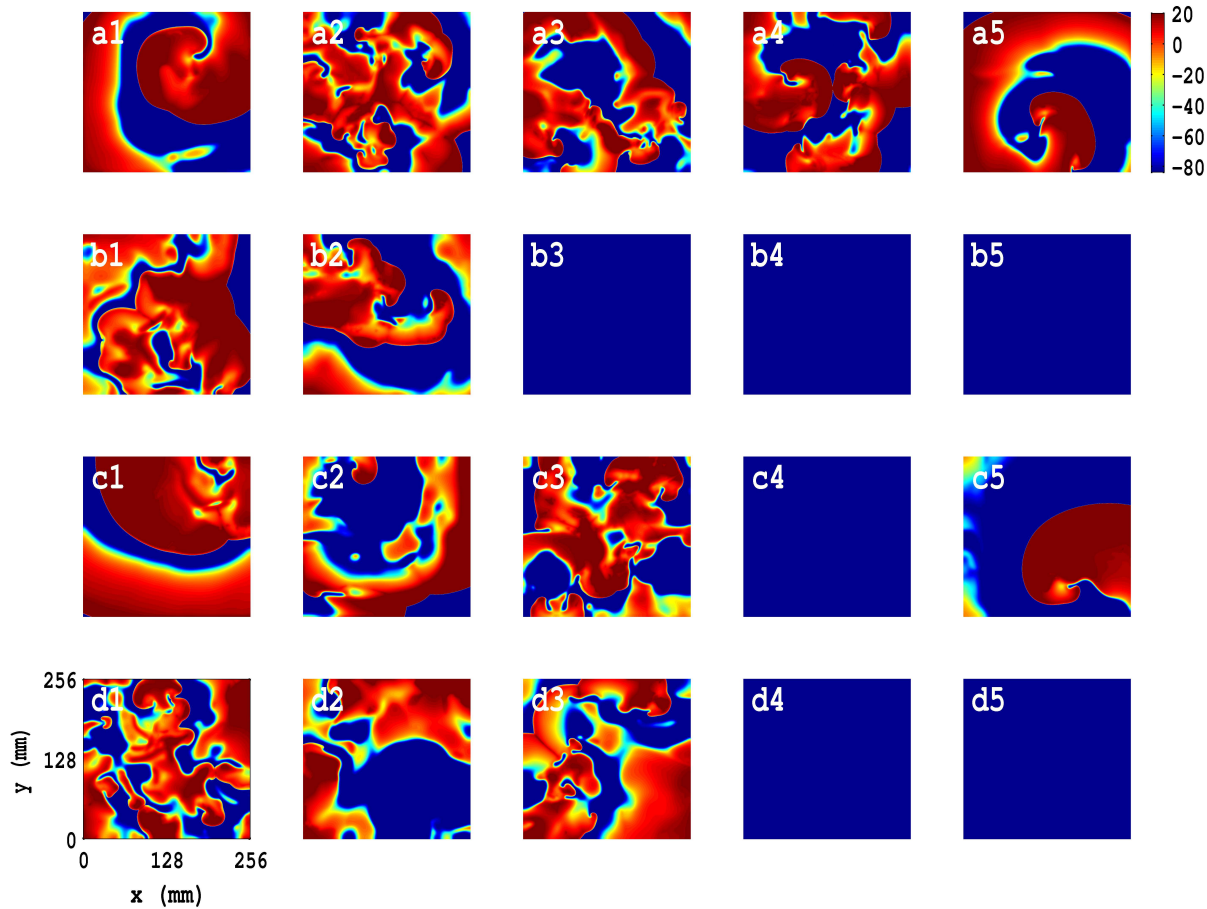


Figure 4.13: Illustrations of the rich variety of spatiotemporal patterns for the TP06 model, with PD and the initial condition $IC3$: The analogs of the pseudocolor plots of V_m in Figs. 4.11 for the initial conditions $IC3$; the plots (a1)-(d5) here use the same PD parameters as their counterparts in Figs. 4.11; the Video S6 shows the spatiotemporal evolution of V_m for these cases for the time interval $0 \leq t \leq 4$ s; and the counterparts of Figs. S7, S8, and S9 in the Supplementary Material S1 for initial condition $IC2$ are Figs. S13, S14, and S15 in the Supplementary Material S1.

Supplementary Material S1), the power spectrum (Figs. S15 in the Supplementary Material S1), and the spatiotemporal evolution of V_m (the animations in Video S8) suggests that here we can have (a) a Q state with no spirals (see animations (b3) (b4), (b5), (c4), (d4) and (d5) in Video S8), (b) an SMST state (see animations (a1) and (a5) in Video S8), or (c) an MST state with with broken spiral waves (see the rest of the animations in Video S8).

The TNNP04 model with PD also exhibits a rich variety of spatiotemporal patterns with spiral waves like the TP06 model. The initial conditions we use are shown via pseudocolor plots of V_m in Fig. S3 in the Supplementary Material S1. In particular, for initial conditions of types $IC1$, $IC2$, and $IC3$ (Fig. S3(c), (f), and

(i), respectively, in the Supplementary Material S1), the TNNP04 analogs of the pseudocolor plots of V_m (Fig. 4.11, Fig. 4.12, and Fig. 4.13 for the TP06 model) are given in Fig. S16, Fig. S17, and Fig. S18, respectively, in the Supplementary Material S1, and the Videos S9, S10, and S11. The time series of $V_m(x, y, t)$, from a representative point in the simulation domain, and the associated plots of the ibi and the power spectra are given in Figs. S19, S20, and S21, for *IC1*, Figs. S22, S23, and S24, for *IC2*, and Figs. S25, S26, and S27, for *IC3*, in the Supplementary Material S1. These figures and videos show that spiral-wave dynamics with PD in the TNNP04 model is quantitatively different from, but qualitatively similar to, that in the TP06 model. In particular, the TNNP04 model shows several quiescent states Q, e.g. (i) for *IC1*, in Fig. S16(b5) (Supplementary Material S1) and the animation (b5) in Video S9, (ii) for *IC2*, in Figs. S17(d4) and (d5) (Supplementary Material S1) and the animations (d4) and (d5) in Video S10, and (iii) for *IC3*, in Figs. S18(a1), (b2), (b3), (c4) and (c5) (Supplementary Material S1) and the animations (a1), (b2), (b3), (c4), and (c5) in Video S11; we obtain states with RS, which are associated with cyclic motions of various orders, in Figs. S20(a2), (a3), (c1), (c3), (c4), (d1), (d2), (d3) and (d4) in the Supplementary Material S1, for *IC1*, Figs. S23(a1), (a2), (a3), (b1), (c1), (c2) and (d1) in the Supplementary Material S1, for *IC2*; finally, we observe a variety of states with spiral-wave turbulence in Fig. S20(c5) in the Supplementary Material S1 and the animation (c5) in Video S9, for *IC1*, Figs. S23(b5), (c4) and (c5) in the Supplementary Material S1 and the animations (b5), (c4) and (c5) in Video S10, for *IC2*, and Figs. S26(a2), (a3), (a4), (a5), (b1), (b4), (b5), (c1), (c2), (c3), (d1), (d2), (d3), (d4) and (d5) in the Supplementary Material S1 and the animations (a2), (a3), (a4), (a5), (b1), (b4), (b5), (c1), (c2), (c3), (d1), (d2), (d3), (d4) and (d5) in Video S11, for *IC3*.

We have discussed spiral-wave dynamics in TP06 and TNNP04 models in the presence of PD along both x and y directions, with initial conditions of types *IC1*, *IC2*, and *IC3*. We have also carried out systematic simulations of spiral-wave dynamics in both these models, with PD along only one (say x) direction. Here too our results are, in the main, qualitatively similar to those we have presented above. Of course, there is anisotropic diffusion if the PD is only along one direction. However, Q, RS, and ST states appear; an overview of their spatiotemporal evolution is given in Figs. S28, S29, S30, S31, S32 and S33, in the Supplementary Material S1, and Videos S12, S13, S14, S15, S16 and S17.

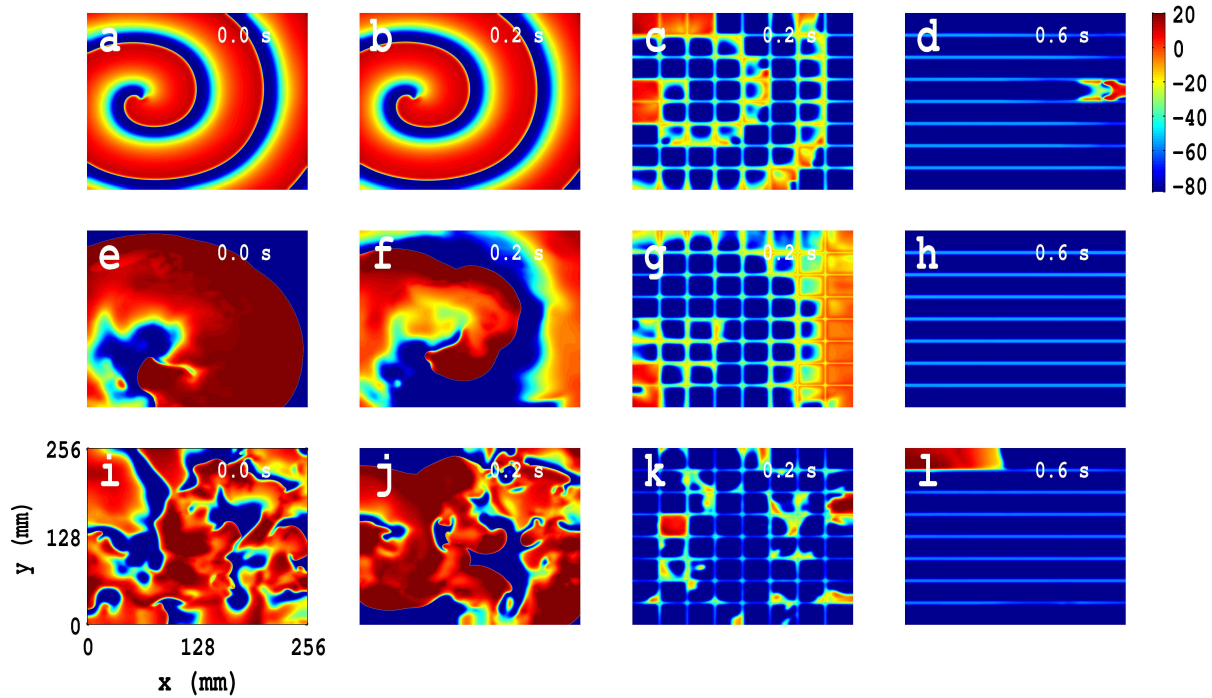


Figure 4.14: Spiral-wave control in the TP06 model, in the absence of PD, by low-amplitude pulses on square and line meshes: We illustrate spiral-wave control, via low-amplitude control pulses, in the TP06 model, in the absence of PD, by presenting pseudocolor plots of V_m . The spiral state, at time $t = 0$ s (a), with the *IC1* initial condition, evolves, in the absence of the control, to an RS state (b), at time $t = 0.2$ s; this state is suppressed by the both square- and line-mesh control methods as shown in (c) and (d), at $t = 0.2$ s and $t = 0.6$ s, respectively. Similar plots for the *IC2* and *IC3* initial conditions are given, respectively, in (e)-(h) and (i)-(l). The Video S18, which comprises nine animations of pseudocolor plots of V_m , show the spatiotemporal evolution of these spiral waves, with and without control pulses, for the time interval $0 \text{ s} \leq t \leq 1 \text{ s}$. In all these cases we apply a control pulse of amplitude 75 pA/pF for $t = 0.2$ ms for the square mesh and an amplitude of 125 pA/pF for $t = 0.6$ ms for the line mesh.

4.3.4 Control of Spiral waves

One of the principal goals of our extensive numerical studies of spiral-wave dynamics in the TP06 and TNNP04 models with PD is to understand its role in enhancing or suppressing spiral-wave turbulence; this is an important step in developing an effective, low-amplitude control technique for the elimination of turbulence with single or multiple spirals. We have provided an overview of some low-amplitude control schemes, in the absence of PD, in earlier studies [18, 33, 34]; the most successful of these is based on an external current stimulus, which is applied on a square mesh on the simulation domain; this control scheme [18, 19, 39] can suppress spiral waves of electrical activation even in the presence of conduction, ionic,

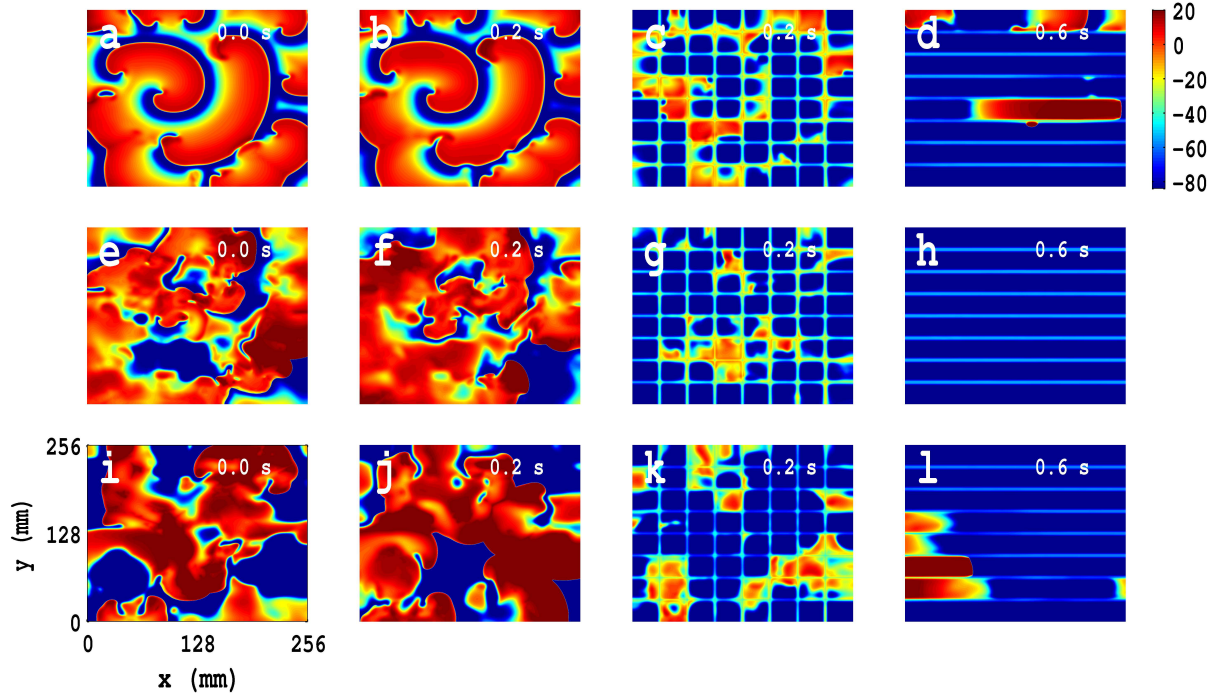


Figure 4.15: Spiral-wave control by low-amplitude pulses in the TP06 model with PD along only the x direction: We impose PD along the x direction and the illustrative amplitude $A_x = 0.3$ and frequency $f_x = 5$ Hz; (a)-(l) are the analogs of Figs. 4.14(a)-(l), respectively. With the initial condition $IC1$, the spiral in (a), at $t = 0$ s, evolves, in the absence of control, to an MST state (b), at $t = 0.2$ s; this MST can be suppressed by both square- and line-mesh control (c) and (d) at $t = 0.2$ s and 0.6 s, respectively. For the $IC2$ and $IC3$ initial configurations, the analogs of these states are shown in (e)-(h) and (i)-(l), respectively; clearly, both our control schemes are successful in eliminating spiral turbulence with PD along one direction. For the spatiotemporal evolution of these spiral waves see Video S19 in the Supplementary Material.

and fibroblast heterogeneities [18, 19, 39]. We now investigate the efficacy of this mesh-based control scheme for both TP06 and TNNP04 models in the presence of PD.

In this mesh-based control scheme, we apply a current pulse of amplitude 75 pA/pF for 0.2 s over a mesh that divides our square simulation domain with $L = 256$ mm into 64 square cells of side $l = 32$ mm each; this pulse makes the links of the mesh refractory and, thereby, effectively imposes Neumann boundary conditions for any block inside the mesh; therefore, spiral waves inside a block are absorbed on the links of the mesh that bound the block. We have also extended this mesh-based scheme to one that uses control pulses on a set of parallel lines; in this line-based scheme, we apply a current pulse of amplitude 125 pA/pF for 0.6 s over a set of parallel lines separated from each other by $l = 32$ mm. As we show below, both these

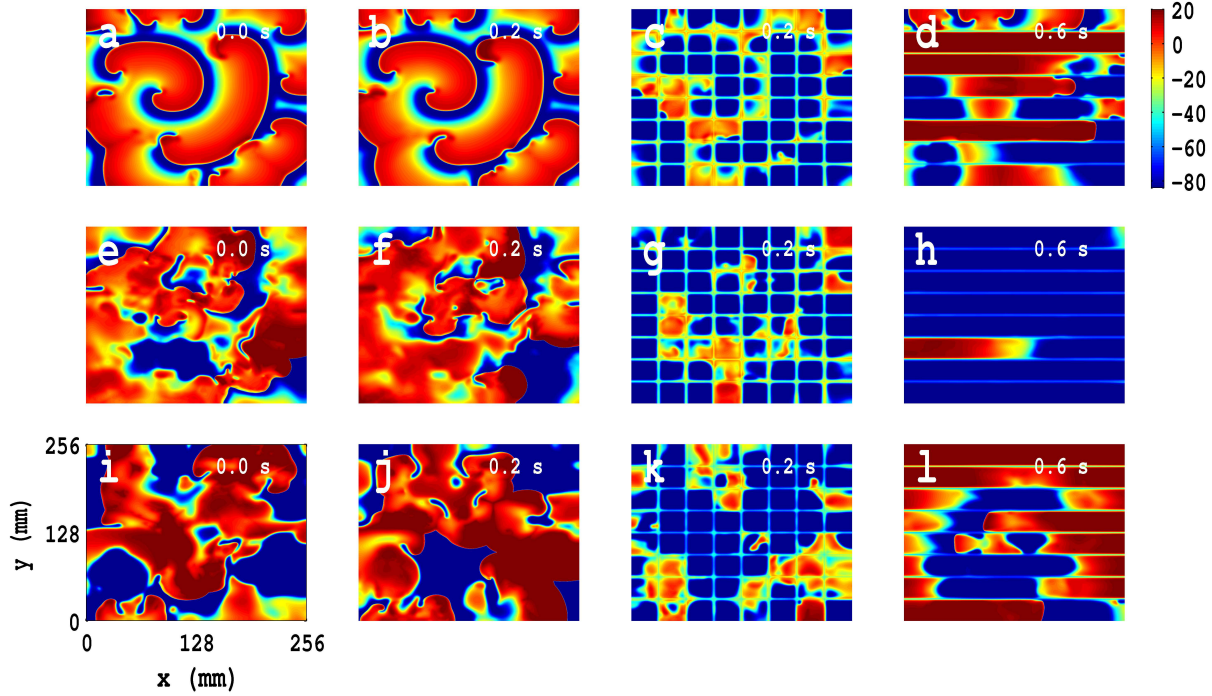


Figure 4.16: Spiral-wave control by low-amplitude pulses in the TP06 model with PD along both x and y directions: We impose PD along both x and y directions with the illustrative amplitudes $A_x = A_y = 0.3$ and frequencies $f_x = f_y = 5$ Hz; for this case (a)-(l) are the analogs of Figs. 4.15 (a)-(l), respectively. With the initial condition $IC1$, the spiral in (a), at $t = 0$ s, evolves, in the absence of the control, to the MST state in (b), at $t = 0.2$ s; this MST can be suppressed by the square-mesh technique but not by the line-mesh technique as we show in (c) and (d) at $t = 0.2$ s and 0.6 s, respectively; the parameters on the control mesh are as in Fig. 4.15. For the initial conditions $IC2$ and $IC3$, the analogs of these states are shown, respectively, in (e)-(h) and (i)-(l). Thus, with PD along both directions, spiral turbulence can be suppressed by our square-mesh control but not the line-mesh method for $IC1$ and $IC3$ initial conditions (see the animations in Video S20 in the Supplementary Material).

schemes succeed in controlling spiral-wave turbulence in the TP06 and TNNP04 models without PD; the line-based scheme uses a higher amplitude for the control pulse and a longer duration of application than the mesh-based one because the former has fewer control-pulse segments than the latter. Furthermore, we show below that the line-based scheme works with PD only if the PD is applied along one spatial direction. However, a slight modification of our line-based control scheme can suppress spiral-wave turbulence; this is a rectangular-mesh-based control scheme, in which we add a few control lines perpendicular to the parallel lines of the line-based control scheme; here we apply a current pulse of amplitude

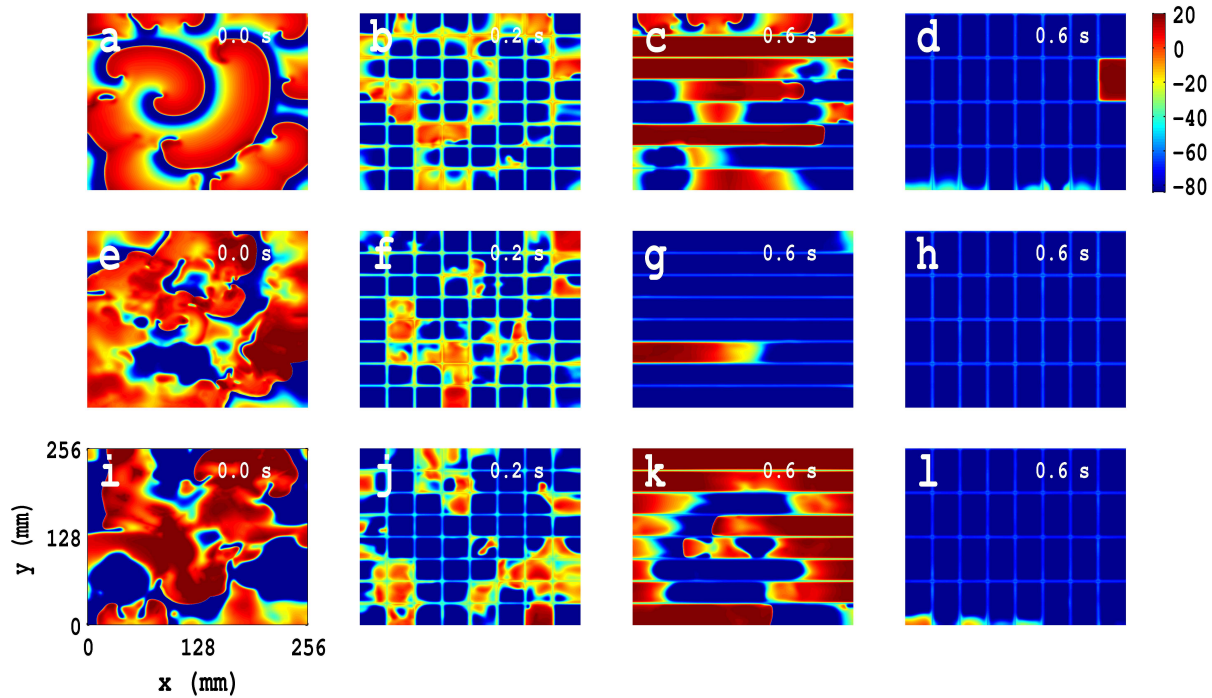


Figure 4.17: Comparison of spiral-wave control by low-amplitude pulses on square, line, and rectangular control meshes in the TP06 model, with PD along both x and y directions: We impose PD along both x and y directions with the illustrative amplitudes $A_x = A_y = 0.3$ and frequencies $f_x = f_y = 5$ Hz for the initial configurations $IC1$, $IC2$, and $IC3$ (pseudocolor plots of V_m in (a), (e), and (f), respectively). We apply the following control pulses: amplitude 75 pA/pF for $t = 0.2$ s over a square mesh ((b), (f), and (j)), with each square block of side $l = 32$ mm; amplitude 125 pA/pF for $t = 0.6$ s over a line mesh ((c), (g), and (k)), with inter-line spacing $l = 32$ mm; amplitude 125 pA/pF for $t = 0.6$ s over a rectangular mesh ((d), (h), and (l)), with block sides $l_x = 32$ mm and $l_y = 64$ mm. These pseudocolor plots of V_m and the associated animations in Video S21 of the Supplementary Material show that these spiral states, with $IC1$, $IC2$, and $IC3$ initial conditions, are suppressed by both square- and rectangular-mesh control but not line-mesh control.

125 pA/pF for 0.6 s over a rectangular mesh whose unit cells have sides $l_x = 32$ mm and $l_y = 64$ mm.

In Fig. 4.14 we illustrate spiral-wave control, via low-amplitude control pulses, in the TP06 model, in the absence of PD, by presenting pseudocolor plots of V_m . The spiral state, at time $t = 0$ ms (Fig. 4.14(a) with the $IC1$ initial condition) evolves, in the absence of the control, to an RS state (Fig. 4.14(b)) at time $t = 0.2$ s; this state is suppressed, by both square- and line-mesh control methods, as shown in Fig. 4.14(c) and Fig. 4.14(d), at $t = 0.2$ ms and $t = 0.6$ ms, respectively. Similar plots for the $IC2$ and $IC3$ initial conditions, Figs. 4.14(e)-(h) and Figs. 4.14(i)-(l), respectively, illustrate square- and line-mesh control of states with spiral turbulence. The

Video S18, which comprises nine animations of pseudocolor plots of V_m , shows the spatiotemporal evolution of these spiral waves, with and without control pulses, for the time interval $0 \text{ s} \leq t \leq 1 \text{ s}$. The results of similar studies for the TNNP04 model are given in Fig. S34 (Supplementary Material S1) and Video S22.

We turn now to spiral-wave control in the TP06 model, with PD along the x direction and the illustrative amplitude $A_x = 0.3$ and frequency $f_x = 5 \text{ Hz}$; for this case Figs. 4.15 (a)-(l) are the analogs of Figs. 4.14(a)-(l), respectively. With the initial condition *IC1*, the spiral in Fig. 4.15(a), at $t = 0 \text{ ms}$, evolves, in the absence of control, to an MST state (Fig. 4.15(b)) at $t = 0.2 \text{ s}$; however, this MST can be suppressed by both square- and line-mesh control techniques as shown in Fig. 4.15(c) and Fig. 4.15(d) at $t = 0.2 \text{ ms}$ and 0.6 ms , respectively. For the *IC2* and *IC3* initial configurations, the analogs of these states are shown in Figs. 4.15(e)-(h) and Figs. 4.15(i)-(l), respectively; clearly, both our control schemes are successful in eliminating spiral turbulence with PD along one direction, as can be seen best in the animations, which show the spatiotemporal evolution of these spiral waves, in Video S19. The results of similar studies for the TNNP04 model are given in Fig. S35 (Supplementary Material S1) and Video S23.

In Fig. 4.16 we illustrate spiral-wave control via pseudocolor plots of V_m by low-amplitude pulses in the TP06 model with PD along both x and y directions and the amplitudes $A_x = A_y = 0.3$ and frequencies $f_x = f_y = 5 \text{ Hz}$; for this case Figs. 4.16 (a)-(l) are the analogs of Figs. 4.15 (a)-(l), respectively. With the initial condition *IC1*, the spiral in Fig. 4.16(a), at $t = 0 \text{ ms}$, evolves, in the absence of the control, to the MST state in Fig. 4.16(b) at $t = 0.2 \text{ s}$; this MST can be suppressed by the square-mesh technique but not by the line-mesh technique as we show in Fig. 4.16(c) and Fig. 4.16(d) at $t = 0.2 \text{ ms}$ and 0.6 ms , respectively. For the initial conditions *IC2* and *IC3* the analogs of these states are shown, respectively, in Figs. 4.16(e)-(h) and Figs. 4.16(i)-(l). Thus, with PD along both directions, spiral turbulence can be suppressed by our square-mesh control but not the line-mesh method for *IC1* and *IC3* initial conditions; this is illustrated clearly by the animations in Video S20. The results of similar studies for the TNNP04 model are given in Fig. S36 (Supplementary Material S1) and Video S24.

A minor modification of our line-based control scheme suppresses spiral-wave turbulence: we use a rectangular-mesh-based control scheme, in which we add a few control lines perpendicular to the parallel lines of the line-based control scheme. We present a comparison of spiral-wave control by low-amplitude pulses on square, line, and rectangular control meshes in the TP06 model, with PD along both x and y directions: We impose PD along both x and y directions with the il-

illustrative amplitudes $A_x = A_y = 0.3$ and frequencies $f_x = f_y = 5$ Hz for the initial configurations $IC1$, $IC2$, and $IC3$ (pseudocolor plots of V_m in Figs. 4.17 (a), (e), and (f), respectively). We apply the following control pulses: (i) pulses with amplitude 75 pA/pF for $t = 0.2$ s over a square mesh (Figs. 4.17 (b), (f), and (j)), with each square block of side $l = 32$ mm; (ii) pulses with amplitude 125 pA/pF for $t = 0.6$ s over a line mesh (Figs. 4.17 (c), (g), and (k)), with inter-line spacing $l = 32$ mm; (iii) pulses with amplitude 125 pA/pF for $t = 0.6$ s over a rectangular mesh (Figs. 4.17 (d), (h), and (l)), with block sides $l_x = 32$ mm and $l_y = 64$ mm. These pseudocolor plots of V_m and the associated animations in Video S21 show that such spiral-wave states, with $IC1$, $IC2$, and $IC3$ initial conditions, are suppressed by both square- and rectangular-mesh control but not by line-mesh control. Our rectangular-mesh control scheme is a significant improvement over the square-mesh one because it uses fewer control lines than the latter. The results of similar studies for the TNNP04 model are given in Fig. S37 (Supplementary Material S1) and Video S25.

4.4 Discussion and Conclusion

We have carried out detailed and systematic numerical studies of the effects of periodic deformation (PD) on spiral-wave dynamics in ionically realistic mathematical models for cardiac tissue by introducing PD in the recently developed TP06 and TNNP04 mathematical models for human ventricular tissue [27, 28], in which we include PD as in Refs. [22–24]. We also investigate, in 2D simulations with PD, the efficacies of square-, rectangular-, and line-mesh-based, low-amplitude control schemes in the suppression of spiral-wave turbulence in these models for cardiac tissue [18, 19, 33, 34].

We have first considered simulations in cable-type domains, which are ideally suited for the calculation of CV and λ . We find that PD leads to a periodic, spatial modulation of CV and a temporally periodic modulation of λ (see Fig. 4.2); the degrees of these modulations depend on the amplitude A_x and frequency f_x of the PD. To the best of our knowledge, such modulations have not been quantified in any earlier study, although a few [23, 24] have suggested, in the context of spiral waves, that such modulations can arise because of a Doppler-type effect [10].

We have considered three types of initial spiral-wave configurations, $IC1$, $IC2$, and $IC3$, which are depicted in Figs. 4.3(c), (f), and (i), for the TP06 model, and Figs. S3(c), (f), and (i) (Supplementary Material S1), for the TNNP04 model. In the TP06 model, these configurations evolve, respectively, to (a) an RSC state, (b) an SMST state, and (c) an MST state, in the absence of PD; in the TNNP04 model

they evolve, respectively, to (a) an RSC state, (b) an RSZ state, and (c) an MST state, in the absence of PD. We have used such initial conditions because various experimental and computational studies [6–8, 10, 18, 27, 50–55] have suggested that spiral-wave dynamics in cardiac tissue can lead to (a) a stable rotor [6, 7, 50], as in our RSC state, (b) a single, meandering rotor whose time series is chaotic [51–53], as in our SMST state, and (c) multiple rotors, which yield a state with spatiotemporal chaos [8, 53–55], as in our MST state. Thus, our initial conditions, *IC1*, *IC2*, and *IC3*, lead to the three major types of spiral-wave evolutions, and slight variants thereof (e.g., RSZ), which have been seen in earlier studies and whose evolution we study now with PD. A rich variety of spiral-wave behaviors result when we add PD to the TP06 and TNNP04 models. We have discussed these in detail above. Our principal findings here can be summarized as follows: In the presence of PD, an RS state may show (a) periodic behavior with high-order cycles in time, (b) temporally quasiperiodic (QP) evolution, (c) a state with spiral-wave turbulence, or (d) a quiescent state Q. For an ST state, which can be of SMST or MST types, PD can either leave the system in an ST state or make it evolve to a Q state, in which all spirals either annihilate each other or are absorbed at the boundaries of the simulation domain. Precisely which one of these states is obtained depends sensitively on our initial conditions and on the PD parameters A_x , A_y , f_x , and f_y of the PD. Thus, our study systematizes the effects of PD on spiral-wave dynamics and turbulence in two, biophysically realistic mathematical models for cardiac tissue; and it complements earlier studies of spiral-wave dynamics, in such models, that have concentrated on the dependence of such dynamics on ion-channel and electrophysiological properties [14–16, 53] and on conduction [17, 18, 21, 56] and ionic inhomogeneities [18–20]. By using the biophysically realistic TP06 and TNNP04 models for cardiac tissue, our study generalizes the work of Refs. [22–24] on spiral-wave instabilities in a simple, two-variable model for cardiac tissue, which is subject to PD.

Moreover, as we have mentioned above, our studies have used three types of spiral-wave initial configurations to examine, via extensive and systematic numerical calculations, the transitions between different states of our system as the amplitude and frequency of the PD are varied. Our work extends significantly earlier studies of periodic deformation, [22–24] and mechanical deformation [25, 26, 29]. In particular, Refs. [22–26, 29] have focused on simple, two-variable, mathematical models for cardiac tissue. Thus, these studies cannot address spiral-wave dynamics in such tissue at the detailed ionic level we consider in our work by using state-of-the-art, ionically realistic mathematical models for ventricular tissue. Further-

more, the authors of Refs. [22–24] study the effects of PD on spiral-wave dynamics for a limited set of initial conditions. For example, in Ref. [22], the authors have studied the behavior of a single rotating spiral (RS) in the presence of PD; the authors of Ref. [23] have used a broken-spiral state as an initial configuration to study the elimination of spirals from the system in the presence of PD; in Ref. [24], the authors have studied an RS initial configuration and its spatiotemporal evolution with PD. The authors in Refs. [25, 26, 29] have used an RS initial configuration to examine the effect of realistic PD on this RS state; they have not investigated the transitions between different spiral-wave states. None of these studies have carried out the detailed numerical investigations of spiral-wave dynamics that we present in our work, which considers a variety of initial conditions.

Furthermore, we have shown that square- and line-mesh-based, low-amplitude control schemes suppress spiral-wave turbulence in both the TP06 and TNNP04 models in the absence of PD; this line-based control scheme is a significant improvement over the square-mesh control scheme of Refs. [18, 19, 33, 34] because it has fewer control lines. However, we have found that the line-based scheme works with PD only if the PD is applied along one spatial direction. We have then shown that a minor modification of our line-based control scheme can suppress spiral-wave turbulence: in particular, we introduce a rectangular-mesh-based control scheme, in which we add a few control lines perpendicular to the parallel lines of the line-based control scheme; this rectangular-mesh scheme is also a significant improvement because it uses fewer control lines than the one based on a square mesh.

The formation of patterns in reaction-diffusion type system with various types of flows have been investigated in Refs. [57–60]; in particular, break up of spiral excitation waves has been observed in a moving excitable medium as suggested in Ref. [57]; these studies have shown that linear shear flow can cause spiral-wave breakup in an excitable medium. Recent studies in Refs. [61–63] have investigated pattern formation in a gel medium that can be oscillated mechanically; the effect of these mechanical oscillations on the underlying spatiotemporal chemical oscillations, because of a Belousov-Zhabotinsky (BZ) reaction, can be studied in such systems. Our work here presents the cardiac-tissue analogs of such chemical-oscillation studies.

Various stretching devices have been developed to control the contraction and expansion of a cell [64–66] and a layer of cells in culture [67–71]. In these devices, both uniaxial and biaxial [72] stretching methods can be used to deform substrates; moreover, in some of these devices, the stretching can be applied in a

cyclic manner at different frequencies. This stretching-induced deformation of the substrate leads, in turn, to the deformation of a layer of culture cells that are attached to the substrate. Examples of such studies include the following: The study in Ref. [64] has measured the strain that develops in cultured vascular smooth muscle cells when they are deformed by the stretching of a substrate to which they adhere. The authors of Ref. [67] have used a device, which applies homogeneous, equibiaxial strains of 0–10% to a cell-culture substrate, to verify quantitatively the transmission of substrate deformation to a 2D sheet of cultured cardiac cells. The studies in Ref. [68] have used endothelial cells in tissue culture, on a silicon elastic membrane, and have designed an apparatus that allows for the control of the magnitude and frequency of the dynamical stretching that is applied uniformly to these cells to produce equibiaxial dynamical stretches, with area changes ranging from 0% to 55% and frequencies ranging from 0 to 2 Hz. The authors of Ref. [69] have developed a system for the imposition of cyclic biaxial strain to stretch cultured pulmonary epithelial cells; similar techniques have been used in Ref. [70] to study the effects of strain in cell cultures and *in vitro* experiments. The authors of Ref. [71] have studied the response to such stretching in cultured neonatal rat atrial cardiomyocytes by using a device that can impose homogeneous equibiaxial deformation. Other recent studies include those of Refs. [65, 66], which have studied the mechanical activities of living cell, fiber, and tissue by applying both equiaxial and uniaxial deformation, and recording the dynamics of the response of these systems by using high-resolution imaging techniques; the former experiment has used fibroblasts and the latter endothelial cells in culture. We suggest that such experimental studies of the responses of cell cultures to an applied stress can be easily generalized to study the types of problems we have concentrated on here. In particular, by imposing a periodic deformation on cardiac tissue or cell cultures, experiments should be able to verify the predictions we have made, on the basis of our *in silico* studies, about the modulations of CV and λ in the presence of PD (Figs. 4.2(a), (b), and (c)) and the effects of PD on spiral-wave dynamics, which we have discussed in detail in the previous Section.

We end with some limitations of our model for PD. The first limitation is that our model does not include stretch-activated currents [25, 26, 29] explicitly; but V_m depends on PD and all ionic currents depend on V_m , so PD affects all such currents implicitly. Next, the PD in our model affects the electrical activation of our medium but it is not, in turn, affected by this activation; by contrast, the model for PD used in Refs. [25, 26, 29] allows for electrical feedback to affect PD; our model does not include soft-tissue mechanics, which can be incorporated in mathemati-

cal models for cardiac tissue by including stress and strain tensors, from elasticity theory [73–75], as in the PD studies of Refs. [25, 26, 29]; however, these studies use only a two-variable model for cardiac tissue and not the ionically realistic TP06 or TNNP04 models that we employ. Moreover, because of the absence of detailed ion-channel dynamics, the simple, two-variable models for cardiac tissue, which have been used in the PD studies of Refs. [25, 26, 29], do not account for the effects of PD on ion-channel activity and the intracellular calcium concentration as suggested in Refs. [76–78]. In spite of the simplicity of our model for PD, our study captures various features of spiral-wave dynamics that have been observed in models that include stretch-activated currents [25]; in particular, our model displays spiral-wave breakup because of PD. The only qualitative effect that our study misses is PD-induced pacemaker activity, for which it has been argued [26, 29, 79] that stretch-activated currents are essential. To the best of our knowledge, our elucidation of the effects of PD on spiral-wave dynamics in mathematical models for cardiac tissue, though simple in its modelling of PD, is the first study that explores the effects of PD on spiral-wave dynamics in *ionically realistic mathematical models for ventricular tissue*. A complete study of a realistic model for PD, with stretch-activated currents, and such ionically realistic mathematical models lies beyond the scope of the present paper. Our model does not include mechano-electrical feedback in a realistic way, as we have described above. Therefore, we have not attempted to study how different mechanical stimuli, other than the PD we consider, initiate or effect spiral-waves in our model; studies of other mechanical stimuli lie beyond the scope of our paper. In Ref. [26] it has been noted that both electrical and mechanical stimuli can cause the formation of a pacemaker in cardiac tissue; and mechanical stimuli can translate the mechanical energy into an electrical stimulus, as argued in Refs. [80, 81]. We use a monodomain description for cardiac tissue; and we do not use an anatomically realistic simulation domain [82, 83], muscle-fiber orientation, and transmural heterogeneity [20, 84]; the inclusion of these features lies beyond the scope of this study. We note, however, that recent studies [85] have compared potentials resulting from normal depolarization and repolarization in a bidomain model with those of a monodomain model; these studies have shown that the differences between results obtained from a monodomain model and those obtained from a bidomain model are extremely small.

1 Supporting Information

Video S1 Spatiotemporal evolution of plane waves in cable-type domains, with PD along the axial-direction of the cables, for the TP06 model, shown via pseudocolor plots of the transmembrane potential V_m ; the time evolution is shown for $0 \text{ s} \leq t \leq 2 \text{ s}$; we use 10 frames per second (fps); in real time each frame is separated from the succeeding frame by 8 ms.

Video S2 Spatiotemporal evolution of plane waves in cable-type domains, with PD along the axial-direction of the cables, for the TNNP04 model, shown via pseudocolor plots of the transmembrane potential V_m ; the time evolution is shown for $0 \text{ s} \leq t \leq 2 \text{ s}$; we use 10 frames per second (fps); in real time each frame is separated from the succeeding frame by 8 ms.

Video S3 Spatiotemporal evolution of the transmembrane potential V_m initiated by the S1-S2 cross field protocol in the TP06 and TNNP04 models; the time evolution is shown for $0 \text{ s} \leq t \leq 0.8 \text{ s}$; we use 10 frames per second (fps); in real time each frame is separated from the succeeding frame by 8 ms.

Video S4 Spiral-wave dynamics in the TP06 and TNNP04 models in the absence of PD; the time evolution of pseudocolor plots of the transmembrane potential V_m is shown for $0 \text{ s} \leq t \leq 4 \text{ s}$; we use 10 frames per second (fps); in real time each frame is separated from the succeeding frame by 8 ms.

Video S5 Spatiotemporal evolution of circular waves for the TP06 model in the presence of PD along both x and y directions with an initial condition of type *IC1*; the time evolution of pseudocolor plots (top panel) and contour plots (bottom panel) of the transmembrane potential V_m are shown for $0 \text{ s} \leq t \leq 0.8 \text{ s}$; we use 10 frames per second (fps); in real time each frame is separated from the succeeding frame by 8 ms.

Video S6 Spiral-wave dynamics for the TP06 model in the presence of PD along both x and y directions with an initial condition of type *IC1*; the time evolution of pseudocolor plots of the transmembrane potential V_m is shown for $0 \text{ s} \leq t \leq 4 \text{ s}$; we use 10 frames per second (fps); in real time each frame is separated from the succeeding frame by 8 ms.

Video S7 Spiral-wave dynamics for the TP06 model in the presence of PD along both x and y directions with an initial condition of type *IC2*; the time evolution of pseudocolor plots of the transmembrane potential V_m is shown for $0 \text{ s} \leq t \leq 4 \text{ s}$; we use 10 frames per second (fps); in real time each frame is separated from the succeeding frame by 8 ms.

Video S8 Spiral-wave dynamics for the TP06 model in the presence of PD along both x and y directions with an initial condition of type *IC3*; the time evolution

of pseudocolor plots of the transmembrane potential V_m is shown for $0 \text{ s} \leq t \leq 4 \text{ s}$; we use 10 frames per second (fps); in real time each frame is separated from the succeeding frame by 8 ms.

Video S9 Spiral-wave dynamics for the TNNP04 model in the presence of PD along both x and y directions with an initial condition of type *IC1*; the time evolution of pseudocolor plots of the transmembrane potential V_m is shown for $0 \text{ s} \leq t \leq 4 \text{ s}$; we use 10 frames per second (fps); in real time each frame is separated from the succeeding frame by 8 ms.

Video S10 Spiral-wave dynamics for the TNNP04 model in the presence of PD along both x and y directions with an initial condition of type *IC2*; the time evolution of pseudocolor plots of the transmembrane potential V_m is shown for $0 \text{ s} \leq t \leq 4 \text{ s}$; we use 10 frames per second (fps); in real time each frame is separated from the succeeding frame by 8 ms.

Video S11 Spiral-wave dynamics for the TNNP04 model in the presence of PD along both x and y directions with an initial condition of type *IC3*; the time evolution of pseudocolor plots of the transmembrane potential V_m is shown for $0 \text{ s} \leq t \leq 4 \text{ s}$; we use 10 frames per second (fps); in real time each frame is separated from the succeeding frame by 8 ms.

Video S12 Spiral-wave dynamics for the TP06 model in the presence of PD along x direction with an initial condition of type *IC1*; the time evolution of pseudocolor plots of the transmembrane potential V_m is shown for $0 \text{ s} \leq t \leq 4 \text{ s}$; we use 10 frames per second (fps); in real time each frame is separated from the succeeding frame by 8 ms.

Video S13 Spiral-wave dynamics for the TP06 model in the presence of PD along x direction with an initial condition of type *IC2*; the time evolution of pseudocolor plots of the transmembrane potential V_m is shown for $0 \text{ s} \leq t \leq 4 \text{ s}$; we use 10 frames per second (fps); in real time each frame is separated from the succeeding frame by 8 ms.

Video S14 Spiral-wave dynamics for the TP06 model in the presence of PD along x direction with an initial condition of type *IC3*; the time evolution of pseudocolor plots of the transmembrane potential V_m is shown for $0 \text{ s} \leq t \leq 4 \text{ s}$; we use 10 frames per second (fps); in real time each frame is separated from the succeeding frame by 8 ms.

Video S15 Spiral-wave dynamics for the TNNP04 model in the presence of PD along x direction with an initial condition of type *IC1*; the time evolution of pseudocolor plots of the transmembrane potential V_m is shown for $0 \text{ s} \leq t \leq 4 \text{ s}$; we use 10

frames per second (fps); in real time each frame is separated from the succeeding frame by 8 ms.

Video S16 Spiral-wave dynamics for the TNNP04 model in the presence of PD along x direction with an initial condition of type *IC2*; the time evolution of pseudocolor plots of the transmembrane potential V_m is shown for $0 \text{ s} \leq t \leq 4 \text{ s}$; we use 10 frames per second (fps); in real time each frame is separated from the succeeding frame by 8 ms.

Video S17 Spiral-wave dynamics for the TNNP04 model in the presence of PD along x direction with an initial condition of type *IC3*; the time evolution of pseudocolor plots of the transmembrane potential V_m is shown for $0 \text{ s} \leq t \leq 4 \text{ s}$; we use 10 frames per second (fps); in real time each frame is separated from the succeeding frame by 8 ms.

Video S18 Spiral-wave dynamics in the TP06 model, in the absence of PD, with and without control pulses, for the time interval $0 \text{ s} \leq t \leq 1 \text{ s}$; we depict pseudocolor plots of V_m and use 10 frames per second (fps); in real time each frame is separated from the succeeding frame by 8 ms. In all these cases we apply a control pulse of amplitude 75 pA/pF for $t = 0.2 \text{ ms}$ for the square mesh and an amplitude of 125 pA/pF for $t = 0.6 \text{ ms}$ for the line mesh.

Video S19 Spiral-wave dynamics in the TP06 model, in the presence of PD along only the x direction ($A_x = 0.3$ and $f_x = 5 \text{ Hz}$), with and without control pulses, for the time interval $0 \text{ s} \leq t \leq 1 \text{ s}$; we depict pseudocolor plots of V_m and use 10 frames per second (fps); in real time each frame is separated from the succeeding frame by 8 ms. In all these cases we apply a control pulse of amplitude 75 pA/pF for $t = 0.2 \text{ ms}$ for the square mesh and an amplitude of 125 pA/pF for $t = 0.6 \text{ ms}$ for the line mesh.

Video S20 Spiral-wave dynamics in the TP06 model, in the presence of PD along both x and y directions ($A_x = A_y = 0.3$ and $f_x = f_y = 5 \text{ Hz}$), with and without control pulses, for the time interval $0 \text{ s} \leq t \leq 1 \text{ s}$; we depict pseudocolor plots of V_m and use 10 frames per second (fps); in real time each frame is separated from the succeeding frame by 8 ms. In all these cases we apply a control pulse of amplitude 75 pA/pF for $t = 0.2 \text{ ms}$ for the square mesh and an amplitude of 125 pA/pF for $t = 0.6 \text{ ms}$ for the line mesh.

Video S21 Comparison of spiral-wave control by low-amplitude pulses on square, line, and rectangular control meshes in the TP06 model, with PD along both x and y directions, for the time interval $0 \text{ s} \leq t \leq 1 \text{ s}$; we depict pseudocolor plots of V_m and use 10 frames per second (fps); in real time each frame is separated from the succeeding frame by 8 ms. In all these cases we apply a control pulse of amplitude

75 pA/pF for $t = 0.2$ ms for the square mesh, an amplitude of 125 pA/pF for $t = 0.6$ ms for the line mesh, and an amplitude of 125 pA/pF for $t = 0.6$ ms for the rectangular mesh.

Video S22 Spiral-wave dynamics in the TNNP04 model, in the absence of PD, with and without control pulses, for the time interval $0 \text{ s} \leq t \leq 1 \text{ s}$; we depict pseudocolor plots of V_m and use 10 frames per second (fps); in real time each frame is separated from the succeeding frame by 8 ms. In all these cases we apply a control pulse of amplitude 75 pA/pF for $t = 0.2$ ms for the square mesh and an amplitude of 125 pA/pF for $t = 0.6$ ms for the line mesh.

Video S23 Spiral-wave dynamics in the TNNP04 model, in the presence of PD along only the x direction ($A_x = 0.3$ and $f_x = 5$ Hz), with and without control pulses, for the time interval $0 \text{ s} \leq t \leq 1 \text{ s}$; we depict pseudocolor plots of V_m and use 10 frames per second (fps); in real time each frame is separated from the succeeding frame by 8 ms. In all these cases we apply a control pulse of amplitude 75 pA/pF for $t = 0.2$ ms for the square mesh and an amplitude of 125 pA/pF for $t = 0.6$ ms for the line mesh.

Video S24 Spiral-wave dynamics in the TNNP04 model, in the presence of PD along both x and y directions ($A_x = A_y = 0.3$ and $f_x = f_y = 5$ Hz), with and without control pulses, for the time interval $0 \text{ s} \leq t \leq 1 \text{ s}$; we depict pseudocolor plots of V_m and use 10 frames per second (fps); in real time each frame is separated from the succeeding frame by 8 ms. In all these cases we apply a control pulse of amplitude 75 pA/pF for $t = 0.2$ ms for the square mesh and an amplitude of 125 pA/pF for $t = 0.6$ ms for the line mesh.

Video S25 Comparison of spiral-wave control by low-amplitude pulses on square, line, and rectangular control meshes in the TNNP04 model, with PD along both x and y directions, for the time interval $0 \text{ s} \leq t \leq 1 \text{ s}$; we depict pseudocolor plots of V_m and use 10 frames per second (fps); in real time each frame is separated from the succeeding frame by 8 ms. In all these cases we apply a control pulse of amplitude 75 pA/pF for $t = 0.2$ ms for the square mesh, an amplitude of 125 pA/pF for $t = 0.6$ ms for the line mesh, and an amplitude of 125 pA/pF for $t = 0.6$ ms for the rectangular mesh.

Bibliography

- [1] American Heart Association (2001) *Heart and Stroke*, Statistical update. (AHA, Dallas, 2001).
- [2] Roger VL, Go AS, Lloyd-Jones DM, *et al.* (2011) Heart disease and stroke statistics-2011 update: a report from the American Heart Association. *Circulation* 123(4): e18.
- [3] Zipes DP, Wellens HJ (1998) Sudden cardiac death. *Circulation* 98: 2334.
- [4] Fogoros RN (2011) Ventricular Fibrillation. *Heart disease, Heart health center*.
- [5] Fenton FH, Cherry EM, Glass L (2008) Cardiac arrhythmia. *Scholarpedia* 3(7): 1665.
- [6] Davidenko JM, Perstov AV, Salomonsz R, *et al.* (1992) Stationary and drifting spiral waves of excitation in isolated cardiac muscle. *Nature* 355: 349.
- [7] Pertsov AM, Davidenko JM, Salomonsz R, *et al.* (1993) Spiral waves of excitation underlie reentrant activity in isolated cardiac muscle. *Circ Res* 72: 631.
- [8] Gray RA, Perstov AM, Jalife J (1998) Spatial and temporal organization during cardiac fibrillation. *Nature* 392: 75.
- [9] Jalife J, Gray RA, Morley GE, *et al.* (1998) Self organization and the dynamical nature of ventricular fibrillation. *Chaos* 8: 5764.
- [10] Fenton FH, Cherry EM, Hastings HM, *et al.* (2002) Multiple mechanisms of spiral wave breakup in a model of cardiac electrical activity. *Chaos* 12(3): 852.
- [11] Cherry EM, Fenton FH (2008) Visualization of spiral and scroll waves in simulated and experimental cardiac tissue. *New J Phys* 10: 125016.
- [12] Garfinkel A, Kim YH, Voroshilovsky O, *et al.* (2000) Preventing ventricular fibrillation by flattening cardiac restitution. *PNAS* 97(11): 6061.

- [13] Koller ML, Riccio MR, Gilmour RJ (1998) Dynamic restitution of action potential duration during electrical alternans and ventricular fibrillation. *Am J Physiol Heart Circ Physiol* 275: H1635.
- [14] Qu Z, Xie F, Garfinkel A, Weiss JN (2000) Origins of spiral wave meander and breakup in a two-dimensional cardiac tissue model. *Ann Biomed Eng* 28: 755.
- [15] Karma A (1994) Electrical alternans and spiral wave breakup in cardiac tissue. *Chaos* 4(3): 461.
- [16] Qu Z, Weiss JN, Garfinkel A (1999) Cardiac electrical restitution properties and stability of reentrant spiral waves: a simulation study. *Am J Physiol Heart Circ Physiol* 276: H269.
- [17] Shajahan TK, Sinha S, Pandit R (2007) Spiral-wave dynamics depends sensitively on inhomogeneities in mathematical models of ventricular tissue. *Phys Rev E* 75: 011929.
- [18] Shajahan TK, Nayak AR, Pandit R (2009) Spiral-wave turbulence and its control in the presence of inhomogeneities in four mathematical models of cardiac tissue. *PLoS One* 4(3): e4738.
- [19] Majumder R, Nayak AR, Pandit R (2011) An overview of spiral- and scroll-wave dynamics in mathematical models for cardiac tissue. *Heart Rate and Rhythm: Molecular Basis, Pharmacological Modulation and Clinical Implications*, Chapter 14, pp 269.
- [20] Majumder R, Nayak AR, Pandit R (2011) Scroll-wave dynamics in human cardiac tissue: lessons from a mathematical model with inhomogeneities and fiber architecture. *PLoS One* 6(4): e18052.
- [21] Xie F, Qu Z, Garfinkel A (1998) Dynamics of reentry around a circular obstacle in cardiac tissue. *Phys Rev E* 58: 6355.
- [22] Zhang H, Ruan X, Hu B, Ouyang Q (2004) Spiral breakup due to mechanical deformation in excitable media. *Phys Rev E* 70: 016212.
- [23] Zhang H, Li BW, Sheng ZM, *et al.* (2006) The effect of mechanical deformation on spiral turbulence. *Europhys Lett* 76: 1109.
- [24] Chen JX, Xu JR, Yuan XP, *et al.* (2009) Influences of Periodic Mechanical Deformation on Spiral Breakup in Excitable Media. *J Phys Chem B* 113: 849.

- [25] Panfilov AV, Keldermann RH, Nash MP (2007) Drift and breakup of spiral waves in reaction-diffusion-mechanics systems. *Proc Natl Acad Sci USA* 104: 7922.
- [26] Weise LD, Nash MP, Panfilov AV (2011) A discrete model to study reaction-diffusion-mechanics systems. *PLoS One* 6(7): e21934.
- [27] ten Tusscher KH, Panfilov AV (2006) Alternans and spiral breakup in a human ventricular tissue model. *Am J Physiol Heart Circ Physiol* 291: H1088.
- [28] ten Tusscher KH, Noble D, Noble PJ, *et al.* (2004) A model for human ventricular tissue. *Am J Physiol Heart Circ Physiol* 286: H1573.
- [29] Panfilov AV, Keldermann RH, Nash MP (2005) Self-organized pacemakers in a coupled reaction-diffusion-mechanics system. *Phys Rev Lett* 95(25): 258104.
- [30] Aliev RR, Panfilov AV (1996) A simple two-variable model of cardiac excitation. *Chaos, Solitons and Fractals* 7: 293.
- [31] Bär M, Eiswirth M (1993) Turbulence due to spiral breakup in a continuous excitable medium. *Phys Rev E* 48(3): R1635.
- [32] Fenton F, Karma A (1998) Vortex dynamics in three-dimensional continuous myocardium with fiber rotation: Filament instability and fibrillation. *Chaos* 8(1): 20.
- [33] Pandit R, Pande A, Sinha S *et al.* (2002) Spiral turbulence and spatiotemporal chaos: characterization and control in two excitable media. *Physica A* 306: 211.
- [34] Sinha S, Pande A, Pandit R (2001) Defibrillation via the elimination of spiral turbulence in model for ventricular fibrillation. *Phys Rev Lett* 86: 3678.
- [35] Clayton RH, Panfilov AV (2008) A guide to modelling cardiac electrical activity in anatomically detailed ventricles. *Prog Biophys Mol Biol* 96: 19.
- [36] Barkley D (1990) Spiral-wave dynamics in a simple model of excitable media: The transition from simple to compound rotation *Phys Rev A* 42(4): 2489.
- [37] Otani NF (2002) A primary mechanism for spiral wave meandering. *Chaos* 12(3): 829.
- [38] Gray RA, Wikswo JP, Otani NF (2009) Origin choice and petal loss in the flower garden of spiral wave tip trajectories. *Chaos* 19(3): 033118.

- [39] Nayak AR, Shajahan TK, Panfilov AV, Pandit R (In press) Spiral-wave dynamics in a Mathematical Model of Human Ventricular Tissue with Myocytes and Fibroblasts. *unpublished manuscript*.
- [40] Noble D (2002) Modelling the heart: insights, failures and progress. *Bioessays* 24: 1155.
- [41] McCulloch AD, Smaill BH, Hunter PJ (1987) Left ventricular epicardial deformation in isolated arrested dog heart. *Am J Physiol* 252: H233
- [42] Bernus O, Wilders R, Zemlin CW, *et al.* (2002) A computationally efficient electrophysiological model of human ventricular cells. *Am J Physiol Heart Circ Physiol* 282: H2296.
- [43] Chen PS, Wu TJ, Ting CT, *et al.* (2003) A Tale of Two Fibrillations. *Circulation* 108: 2298.
- [44] Samie FH, Jalife J (2001) Mechanisms underlying ventricular tachycardia and its transition to ventricular fibrillation in the structurally normal heart. *Cardiovascular Research* 50: 242.
- [45] Ideker RE, Rogers JM (2006) Human ventricular fibrillation: wandering wavelets, mother rotors, or both ? *Circulation* 114: 530.
- [46] Wu TJ, Lin SF, Baher A, *et al.* (2004) Mother Rotors and the Mechanisms of D600-Induced Type 2 Ventricular Fibrillation. *Circulation* 110: 2110.
- [47] Xie F, Qu Z, Weiss JN, Garfinkel A (2001) Coexistence of multiple spiral waves with independent frequencies in a heterogeneous excitable medium. *Phys Rev E* 63: 031905.
- [48] Nash MP, Mourad A, Clayton RH, *et al.* (2006) Evidence for multiple mechanisms in human ventricular fibrillation. *Circulation* 114: 536.
- [49] Massé S, Downar E, Chauhan V, *et al.* (2007) Ventricular fibrillation in myopathic human hearts: mechanistic insights from in vivo global endocardial and epicardial mapping. *Heart Circ Physiol* 292: H2589.
- [50] Beaumont J, Davidenko N, Davidenko JM, Jalife J (1998) Spiral waves in two-dimensional models of ventricular muscle: formation of a stationary core. *Biophys J* 75(1): 1.
- [51] Gray RA, Jalife J, Panfilov AV, *et al.* (1995) Mechanisms of cardiac fibrillation. *Science* 270: 1222.

- [52] Gray RA, Jalife J (1996) Self-organized drifting spiral waves as a mechanism for ventricular fibrillation. *Circulation* 94: 48:
- [53] Qu Z, Weiss JN, Garfinkel A (2000) From local to global spatiotemporal chaos in a cardiac tissue model. *Phys Rev E* 61(1): 727.
- [54] Damle RS, Kanaan NM, Robinson NS, *et al.* (1992) Spatial and temporal linking of epicardial activation directions during ventricular fibrillation in dogs. Evidence for underlying organization *Circulation* 86: 1547.
- [55] Witkowski FX, Leon LJ, Penkoske PA, *et al.* (1998) Spatiotemporal evolution of ventricular fibrillation. *Nature* 392: 78.
- [56] ten Tusscher KHWJ, Panfilov A (2003) Influence of nonexcitable cells on spiral breakup in two-dimensional and three-dimensional excitable media. *Phys Rev E* 68: 062902.
- [57] Biktashev VN, Holden AV, Tsyganov MA, *et al.* (1998) Excitation wave breaking in excitable media with linear shear flow. *Phys Rev Lett* 81: 2815.
- [58] Leconte M, Martin J, Rakotomalala N, Salin D (2003) Pattern of reaction diffusion fronts in laminar flows. *Phys Rev Lett* 90: 128302.
- [59] Kuptsov PV, Satnoianu RA, Daniels PG (2005) Pattern formation in a two-dimensional reaction-diffusion channel with Poiseuille flow. *Phys Rev E* 72: 036216.
- [60] Ermakova EA, Shnol EE, Panteleev MA, *et al.* (2009) On propagation of excitation waves in moving media: the FitzHugh-Nagumo model. *PLoS One* 4(2): e4454.
- [61] Yoshida R (2010) Self-oscillating gels driven by the Belousov-Zhabotinsky reaction as novel smart materials. *Adv Mater* 22: 3463
- [62] Yashin VV, Suzuki S, Yoshida R, Balazs AC (2012) Controlling the dynamic behavior of heterogeneous self-oscillating gels *J Mater Chem* 22: 13625.
- [63] Yashin VV, Kuksenok O, Dayal P, Balazs AC (2012) Mechano-chemical oscillations and waves in reactive gels. *Rep Prog Phys* 75: 066601.
- [64] Barbee KA, Macarak EJ, Thibault LE (1994) Strain measurements in cultured vascular smooth muscle cells subjected to mechanical deformation. *Ann Biomed Eng* 22: 14.

- [65] Huang L, Mathieu PS, Helmke BP (2010) A stretching device for high-resolution live-cell imaging. *Ann Biomed Eng* 38: 1728.
- [66] Wang D, Xie Y, Yuan B (2010) A stretching device for imaging real-time molecular dynamics of live cells adhering to elastic membranes on inverted microscopes during the entire process of the stretch. *Integr Biol* 2: 288.
- [67] Lee AA, Delhaas T, Waldman LK, *et al.* (1996) An equibiaxial strain system for cultured cells. *Am J Physiol* 271: C1400.
- [68] Sotoudeh M, Jalali S, Usami S, *et al.* (1998) A strain device imposing dynamic and uniform equi-biaxial strain to cultured cells. *Ann Biomed Eng* 26: 181.
- [69] Waters CM, Glucksberg MR, Lautenschlager EP, *et al.* (2001) A system to impose prescribed homogenous strains on cultured cells. *J Appl Physiol* 91: 1600.
- [70] Winter LC, Gilbert JA, Elder SH, Bumgardner JD (2002) A device for imposing cyclic strain to cells growing on implant alloys. *Ann Biomed Eng* 30: 1242.
- [71] Rana OR, Zobel C, Saygili E, *et al.* (2008) A simple device to apply equibiaxial strain to cells cultured on flexible membranes. *Am J Physiol Heart Circ Physiol* 294: H532.
- [72] Pang Q (2009) (Thesis) Design and development of a biostretch apparatus for tissue engineering.
- [73] Nash MP, Hunter PJ (2000) Computational mechanics of the heart: from tissue structure to ventricular function. *J Elasticity* 61: 113.
- [74] Nash M, Panfilov A (2004) Electromechanical model of excitable tissue to study reentrant cardiac arrhythmias. *Prog Biophys Mol Biol* 85: 501.
- [75] Keldermann RH, Nash MP, Panfilov AV (2009) Modeling cardiac mechano-electrical feedback using reaction-diffusion-mechanics systems. *Physica D* 238: 100.
- [76] Cherubini C, Filippi S, Nardinocchi P, Teresi L (2008) An electromechanical model of cardiac tissue: constitutive issues and electrophysiological effects. *Prog Biophys Mol Biol* 97: 562.
- [77] Pathmanathan P, Whiteley JP (2009) A numerical method for cardiac mechano-electric simulations. *Ann Biomed Engg* 37: 860.
- [78] Ambrosi D, Arioli G, Nobile F, Quarteroni A (2011) Electromechanical coupling in cardiac dynamics: the active strain approach. *SIAM Journal of Applied Mathematics* 71: 605.

- [79] Kohl P, Hunter P, Noble D (1999) Stretch-induced changes in heart rate and rhythm: clinical observations, experiments and mathematical models. *Prog Biophys Mol Biol* 71: 91.
- [80] Janse MJ, Coronel R, Wilms-Schopman FJ, de Groot JR (2003) Mechanical effects on arrhythmogenesis: from pipette to patient. *Prog Biophys Mol Biol* 82: 187.
- [81] Cooper PJ, Epstein A, Macleod IA, *et al.* (2006) Soft tissue impact characterisation kit (STICK) for ex situ investigation of heart rhythm responses to acute mechanical stimulation. *Prog Biophys Mol Biol* 90: 444.
- [82] Panfilov A, Keener JP (1995) Re-entry in an anatomical model of the heart. *Chaos, Solitons, and Fractals* 5: 681.
- [83] Trayanova NA, Tice BM (2009) Integrative computational models of cardiac arrhythmias- simulating the structurally realistic heart. *Drug Discov Today Dis Models* 6(3): 85.
- [84] Majumder R, Nayak AR, Pandit R (2012) Nonequilibrium arrhythmic States and transitions in a mathematical model for diffuse fibrosis in human cardiac tissue. *PLoS One* 7(10): e45040.
- [85] Potse M, Dube B, Richer J, Vinet A, Gulrajani RM (2006) A comparison of monodomain and bidomain reaction-diffusion models for action potential propagation in the human heart. *IEEE Trans Biomed Eng* 53: 2425.

1 Supplementary Material S1

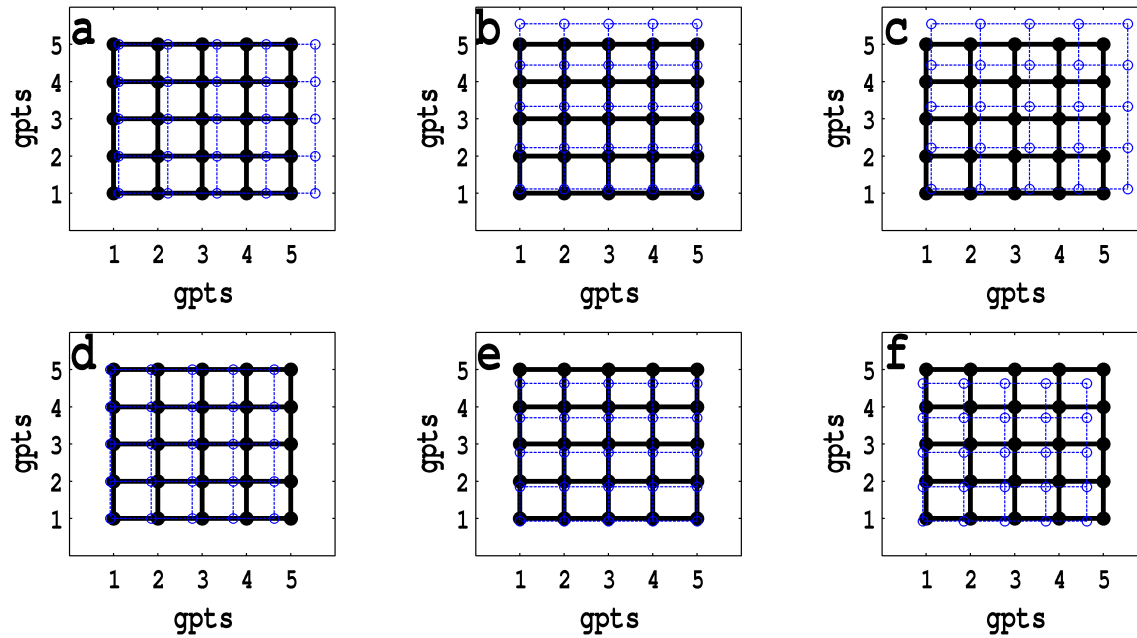


Figure S1: Schematic diagrams for illustrative periodic deformations of a small part of the simulation domain, with 5×5 grid points; in these diagrams, blue, open circles and blue, dashed lines show, at a particular instant of time, the deformed simulation domain superimposed on the undeformed one, which is represented by black, solid circles and black, full lines. The case of expansion, with deformations along only x (with amplitude $A_x = 0.3$ and frequency $f_x = 3$ Hz), only y (with amplitude $A_y = 0.3$ and frequency $f_y = 3$ Hz), or both x and y directions (with amplitudes $A_x = A_y = 0.3$ and frequencies $f_x = f_y = 3$ Hz) are shown, respectively, in (a), (b) and (c), at time $t = 20$ ms; the corresponding plots for contraction, at time $t = 180$ ms, are shown in (d), (e), and (f).

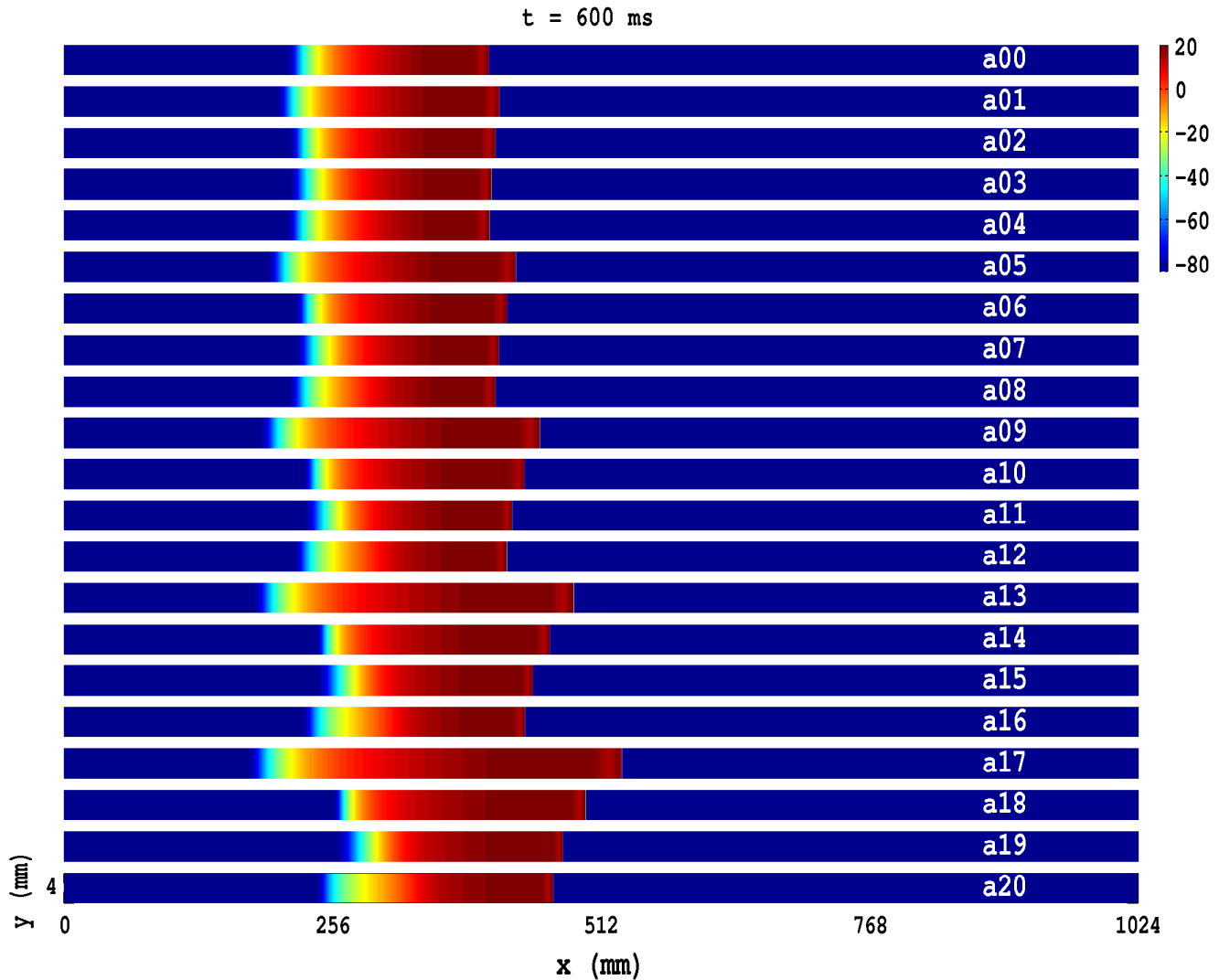


Figure S2: Pseudocolor plots of the transmembrane potential V_m for the TNNP04 model illustrating plane-wave propagation in a cable-type domain, with PD along the axial-direction of the cable, and the following parameter sets: (a00) no PD; (a01) $A_x = 0.1$, $f_x = 1.0$ Hz; (a02) $A_x = 0.2$, $f_x = 1.0$ Hz; (a03) $A_x = 0.3$, $f_x = 1.0$ Hz; (a04) $A_x = 0.4$, $f_x = 1.0$ Hz; (a05) $A_x = 0.5$, $f_x = 1.0$ Hz; (a06) $A_x = 0.1$, $f_x = 3.0$ Hz; (a07) $A_x = 0.2$, $f_x = 3.0$ Hz; (a08) $A_x = 0.3$, $f_x = 3.0$ Hz; (a09) $A_x = 0.4$, $f_x = 3.0$ Hz; (a10) $A_x = 0.5$, $f_x = 3.0$ Hz; (a11) $A_x = 0.1$, $f_x = 5.0$ Hz; (a12) $A_x = 0.2$, $f_x = 5.0$ Hz; (a13) $A_x = 0.3$, $f_x = 5.0$ Hz; (a14) $A_x = 0.4$, $f_x = 5.0$ Hz; (a15) $A_x = 0.5$, $f_x = 5.0$ Hz; (a16) $A_x = 0.1$, $f_x = 7.0$ Hz; (a17) $A_x = 0.2$, $f_x = 7.0$ Hz; (a18) $A_x = 0.3$, $f_x = 7.0$ Hz; (a19) $A_x = 0.4$, $f_x = 7.0$ Hz; and (a20) $A_x = 0.5$, $f_x = 7.0$ Hz. The Video S2 comprises 21 animations that show the spatiotemporal evolution of these plane waves.

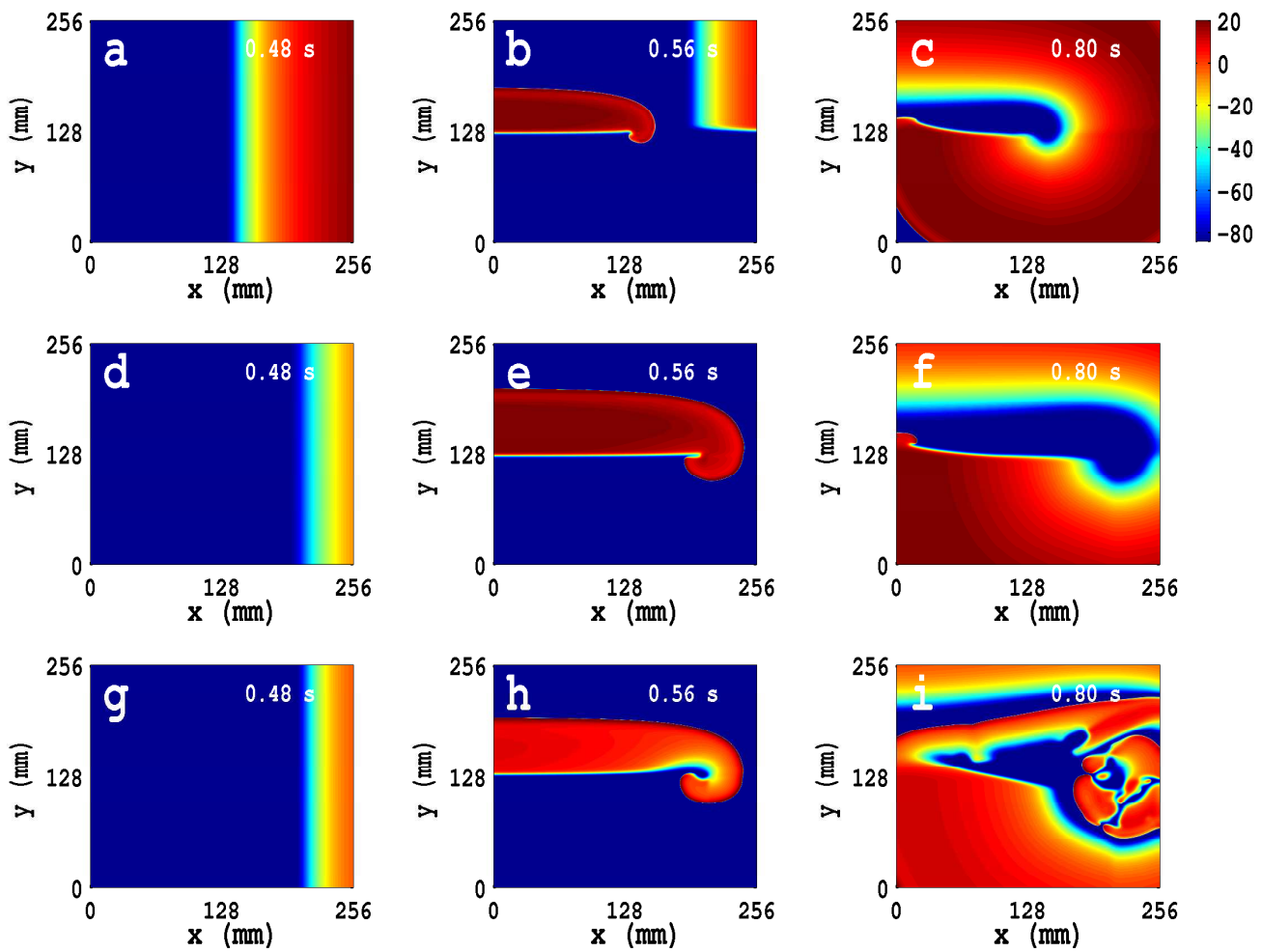


Figure S3: Initiation of spiral waves in the TNNP04 model by the S1-S2 cross field protocol (see main text): Pseudocolor plots of the transmembrane potential V_m showing the time evolution of spiral waves for initial conditions (see text) *IC1* ((a)-(c)), *IC2* ((d)-(f)), and *IC3* ((g)-(i)). The animations (d), (e), and (f) in the Video S3 show the the spatiotemporal evolution of V_m for these cases.

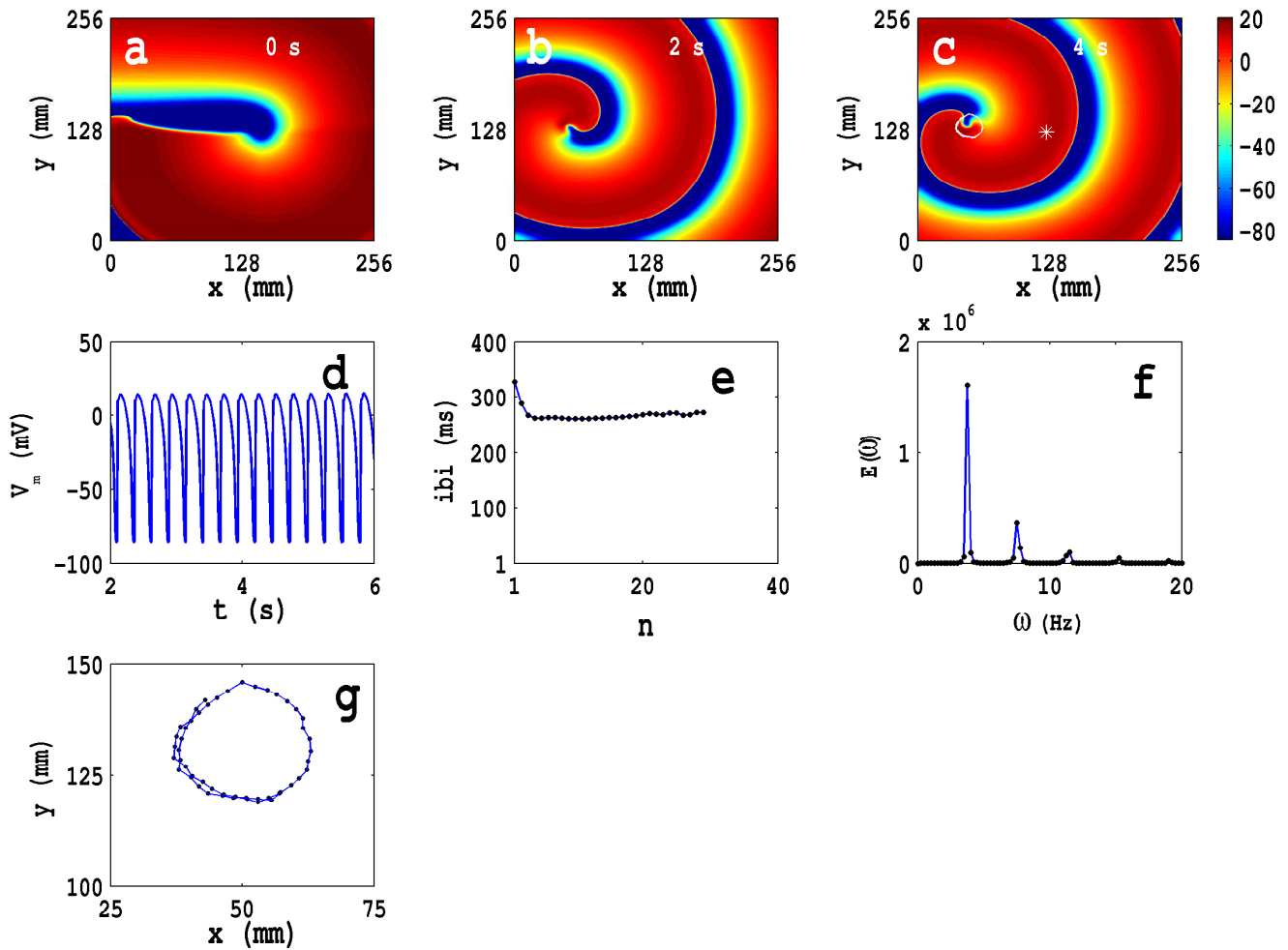


Figure S4: Spatiotemporal evolution of V_m for the initial condition $IC1$ for the TNNP04 model in the absence of PD: (a)-(c) Pseudocolor plots of V_m at times $t = 0$ s, $t = 2$ s, and $t = 4$ s, respectively, showing the evolution towards a state with a rotating spiral (RS); the animation (d) in Video S4 shows the spatiotemporal evolution of V_m for this case. (d) The local time series of $V_m(x, y, t)$, from the representative point ($x = 125$ mm, $y = 125$ mm) (the asterisk in (c)) for 2 s $\leq t \leq 6$ s; (e) a plot of the inter beat interval (ibi), which we obtain from this time series, of length 4×10^5 iterations; (f) the power spectrum $E(\omega)$, obtained from the local time series of (d), with discrete peaks at the fundamental frequency $\omega_f \simeq 3.75$ Hz and its harmonics. The spiral-tip trajectory traces a roughly circular path, with radius $l_c \simeq 25$ mm, which is shown, for 3.6 s $\leq t \leq 4$ s, by the white line that has been superimposed on the pseudocolor plot of V_m in (c); an expanded version of this path is shown in (g).

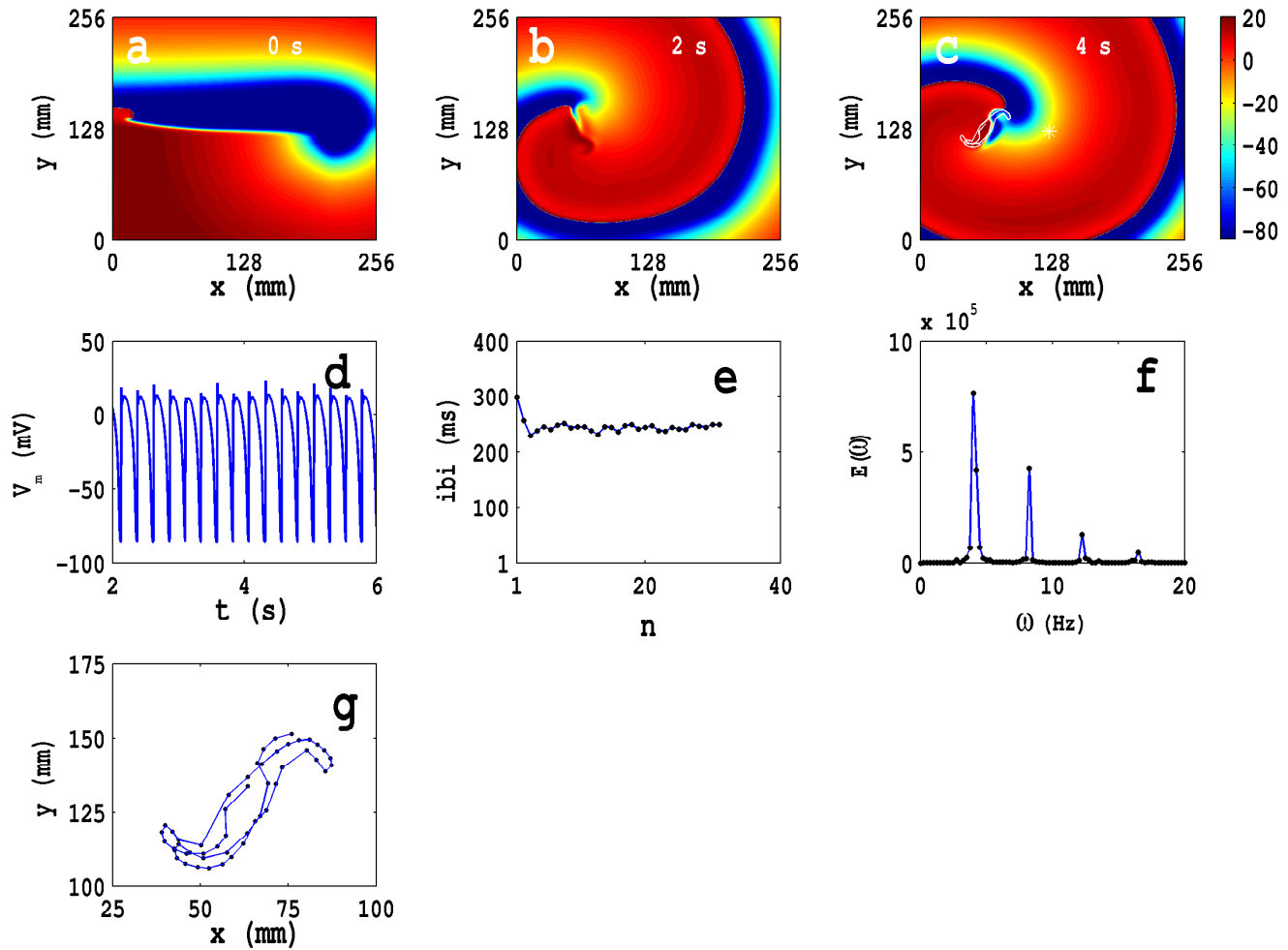


Figure S5: Spatiotemporal evolution of V_m for the initial condition $IC2$ for the TNNP04 model in the absence of PD: (a)-(g) show, for the initial condition $IC2$ in the absence of PD, the exact analogs of Figs. S4(a)-(g); and the animation (e) in Video S4 shows the spatiotemporal evolution of V_m for this case. (d) The local time series of $V_m(x, y, t)$, from the representative point ($x = 125$ mm, $y = 125$ mm) (the asterisk in (c)) for $2 \text{ s} \leq t \leq 6 \text{ s}$; (e) a plot of the inter beat interval (ibi), which we obtain from this time series, of length 4×10^5 iterations; (f) the power spectrum $E(\omega)$, obtained from the local time series of (d), with two principal frequencies, $\omega_1 = 4$ Hz and $\omega_2 = 8.25$ Hz. The spiral-tip trajectory traces a Z-type path, with linear extents $l_c \simeq 43$ mm, which is shown, for $3.6 \text{ s} \leq t \leq 4 \text{ s}$, by the white line that has been superimposed on the pseudocolor plot of V_m in (c); an expanded version of this path is shown in (g). The local time series, the oscillating ibi, and more than one principal frequency in the power spectrum show that the initial condition $IC2$ leads to a quasiperiodic temporal evolution.

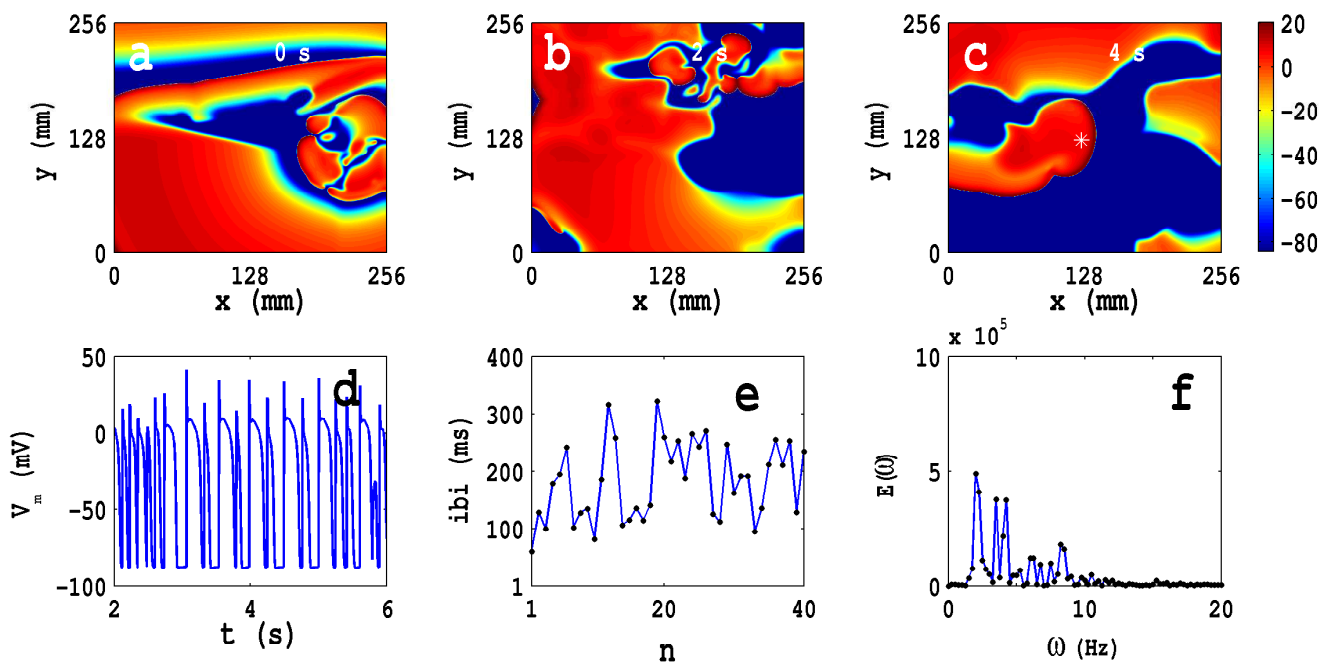


Figure S6: Spatiotemporal evolution of V_m for the initial condition $IC3$ for the TNNP04 model in the absence of PD: (a)-(f) show, for the initial condition $IC3$ in the absence of PD, the exact analogs of Figs. S4(a)-(f); and the animation (f) in Video S4 shows the spatiotemporal evolution of V_m for this case. This animation, the pseudocolor plots of V_m ((a)-(c)), the representative local time series of V_m (d), the plot of the ibi (e), and the power spectrum $E(\omega)$ (f) show that the initial condition $IC3$ leads to spatiotemporal chaos and spiral turbulence (ST) with broken spirals in the simulation domain.

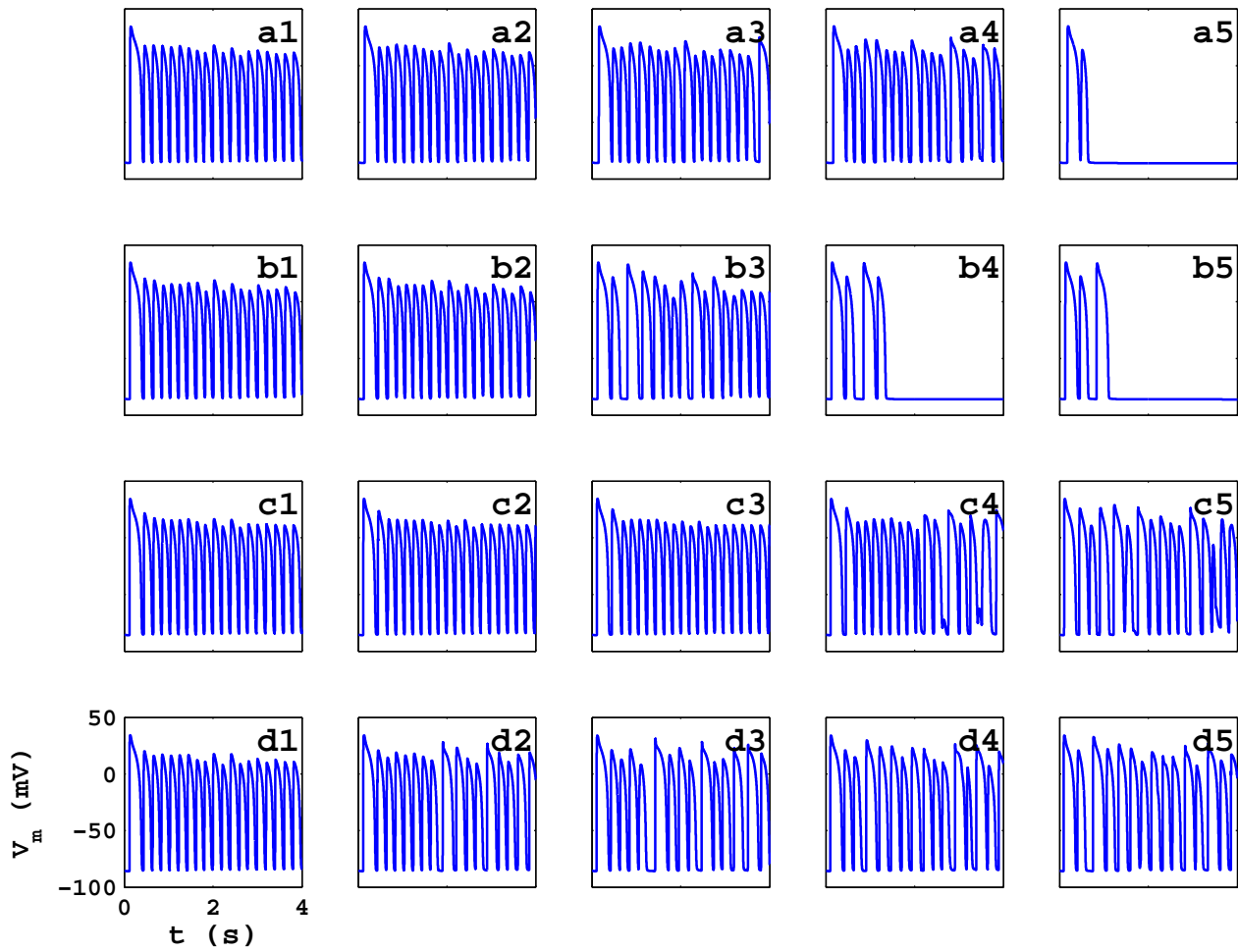


Figure S7: Plots of the local time series of $V_m(x, y, t)$, recorded from the representative points ($x = 125$ mm, $y = 125$ mm), in the TP06 model with the initial condition *IC1* and PD along both spatial directions; the spatiotemporal patterns of V_m are shown in Fig. 11 in the main text.

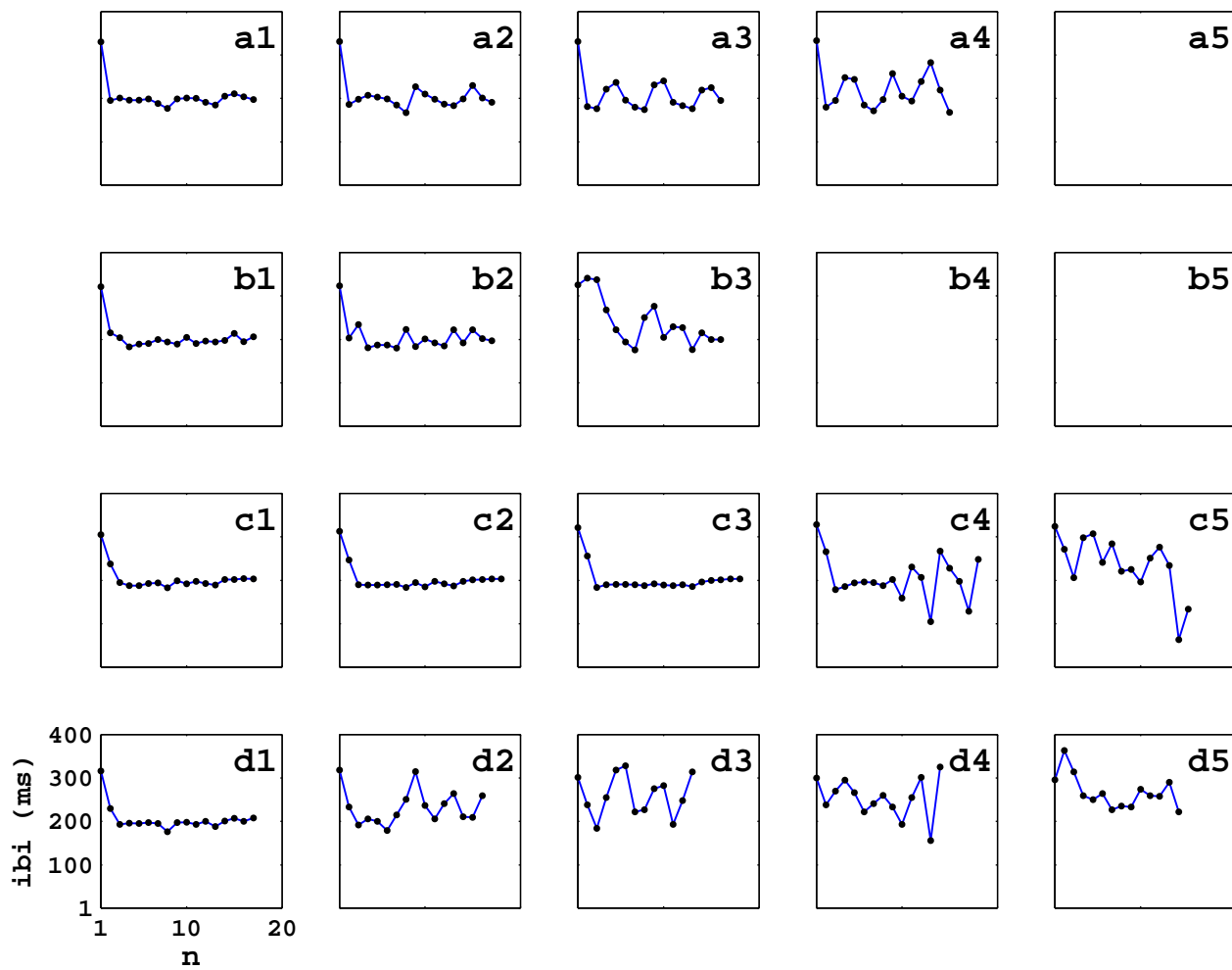


Figure S8: Plots of the ibi versus the beat number n that we obtain from the time series shown in Fig. S7.

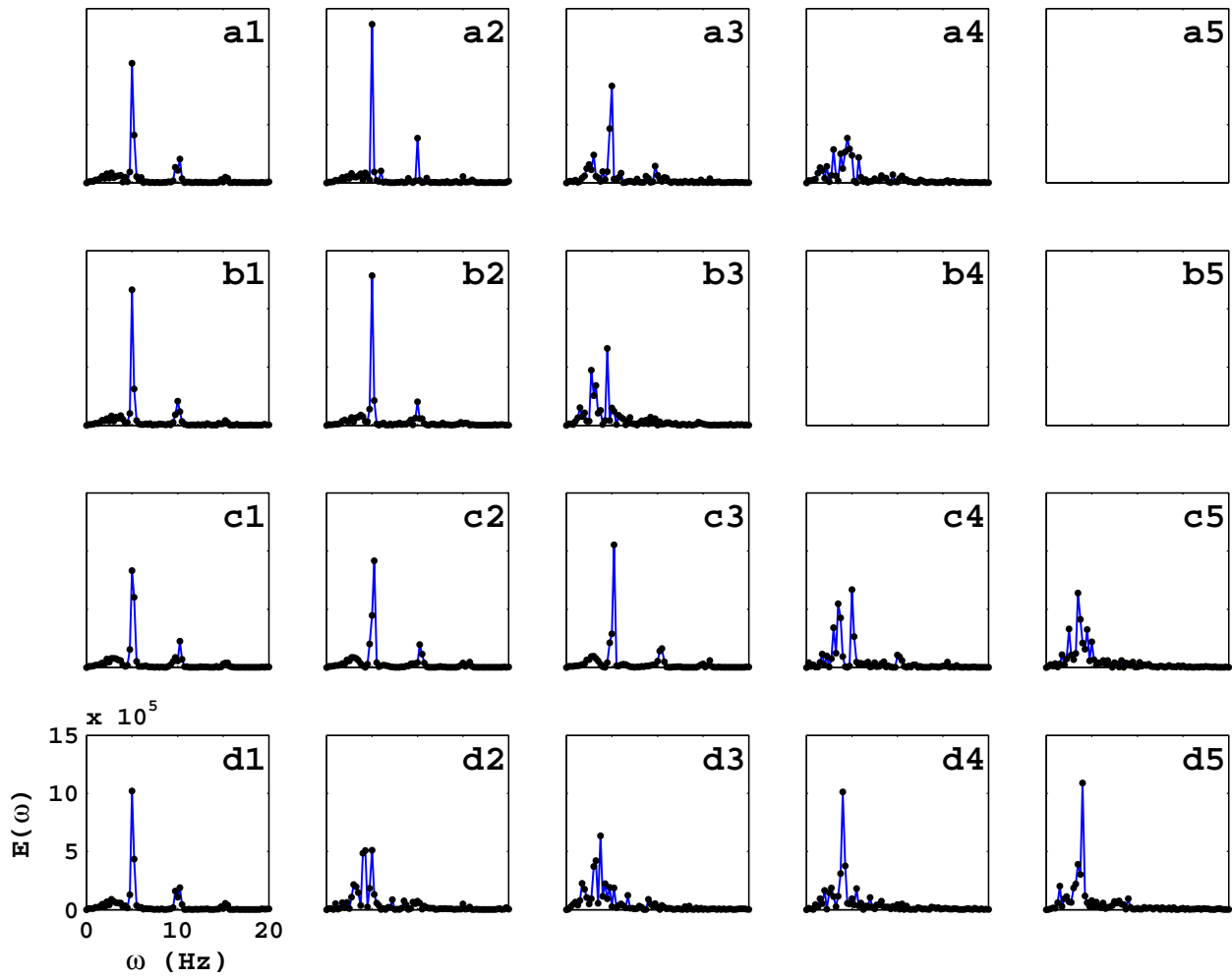


Figure S9: Plots of the power spectrum $E(\omega)$ of V_m obtained from a time series of length 2×10^5 for the data points in Fig. S7.

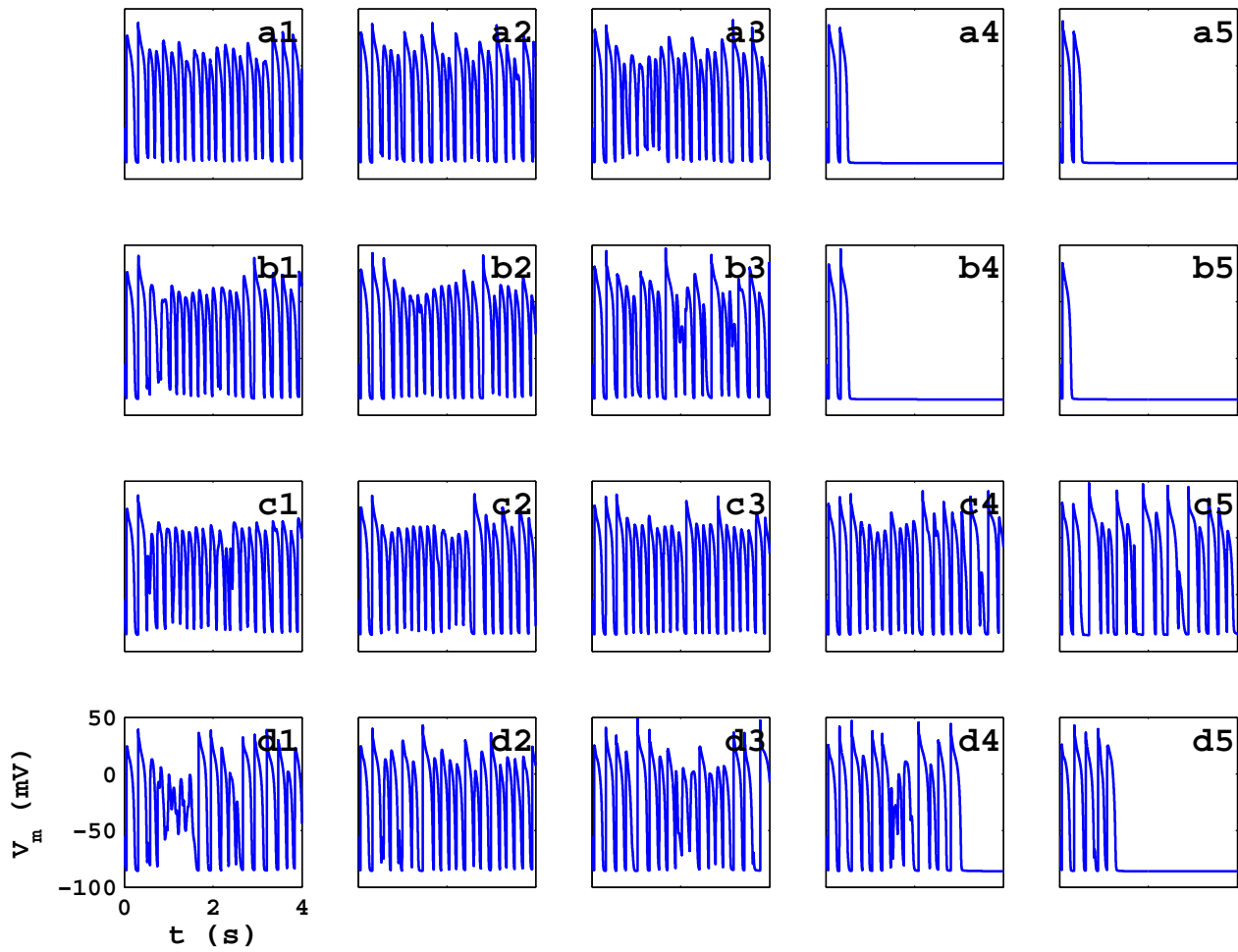


Figure S10: Plots of the local time series of $V_m(x, y, t)$, recorded from the representative points ($x = 125$ mm, $y = 125$ mm), in the TP06 model with the initial condition $IC1$ and PD along both spatial directions; the spatiotemporal patterns of V_m are shown in Fig. 12 in the main text.

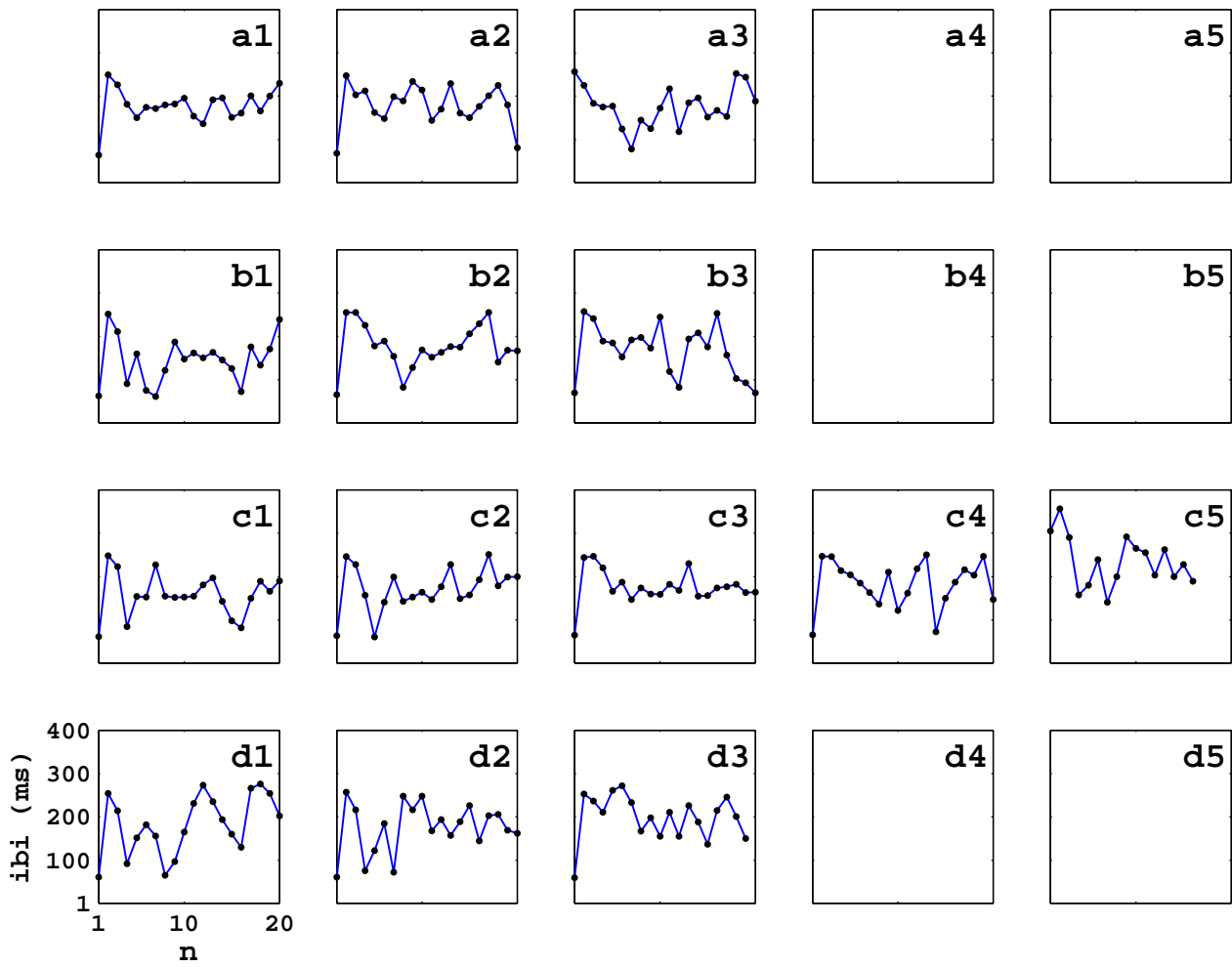


Figure S11: Plots of the ibi versus the beat number n that we obtain from the time series shown in Fig. S10.

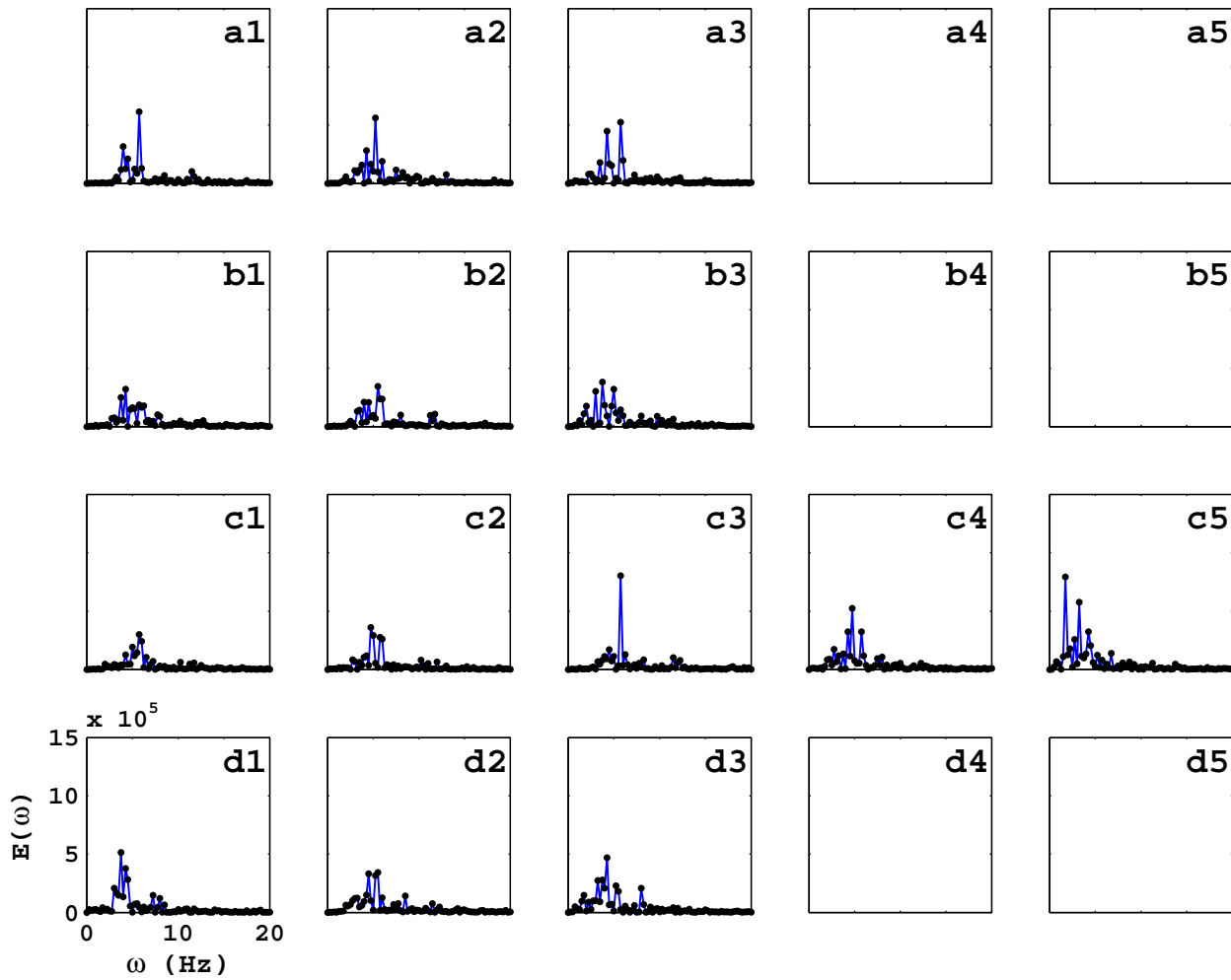


Figure S12: Plots of the power spectrum $E(\omega)$ of V_m obtained from a time series of length 2×10^5 for the data points in Fig. S10.

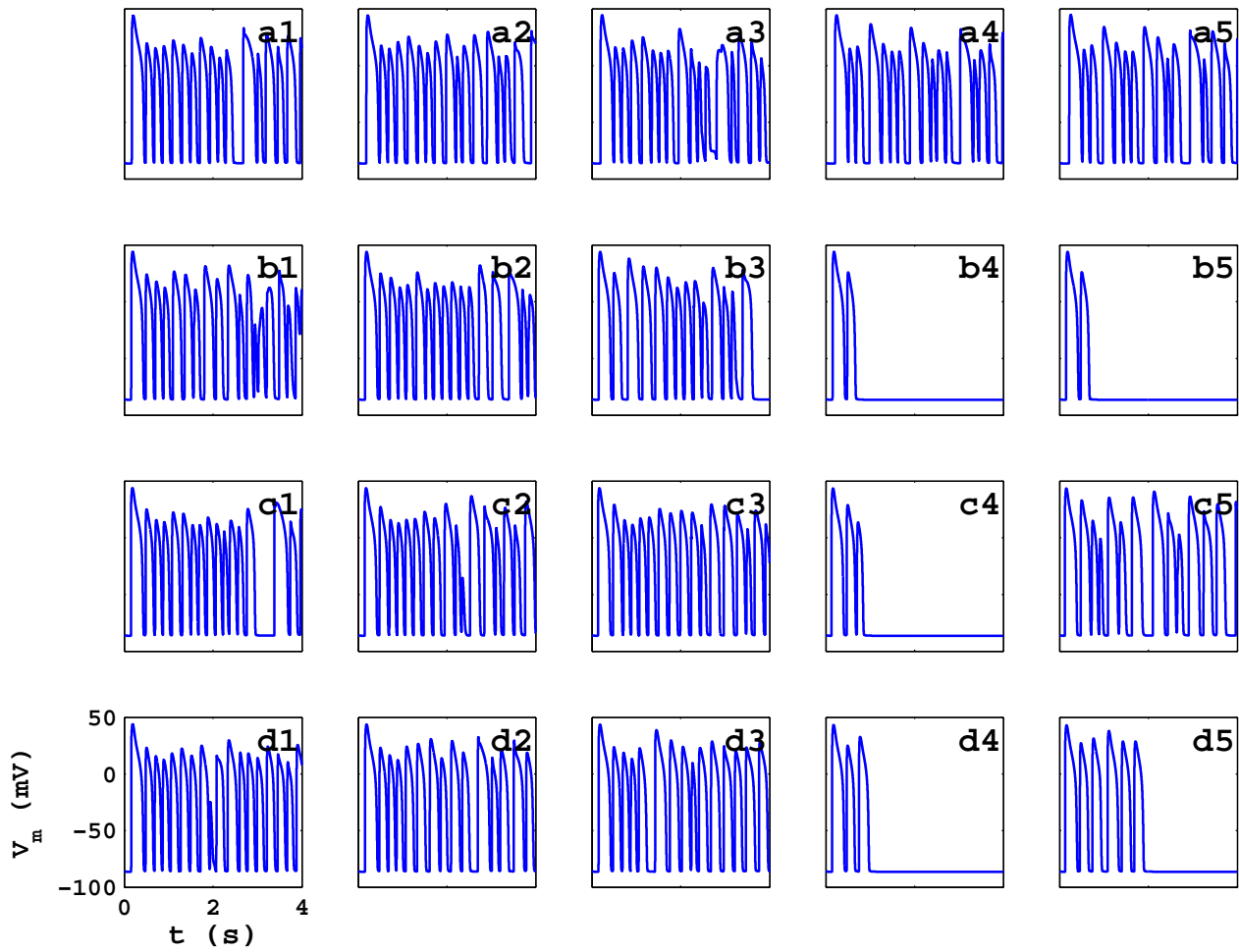


Figure S13: Plots of the local time series of $V_m(x, y, t)$, recorded from the representative points ($x = 125$ mm, $y = 125$ mm), in the TP06 model with the initial condition $IC1$ and PD along both spatial directions; the spatiotemporal patterns of V_m are shown in Fig. 13 in the main text.

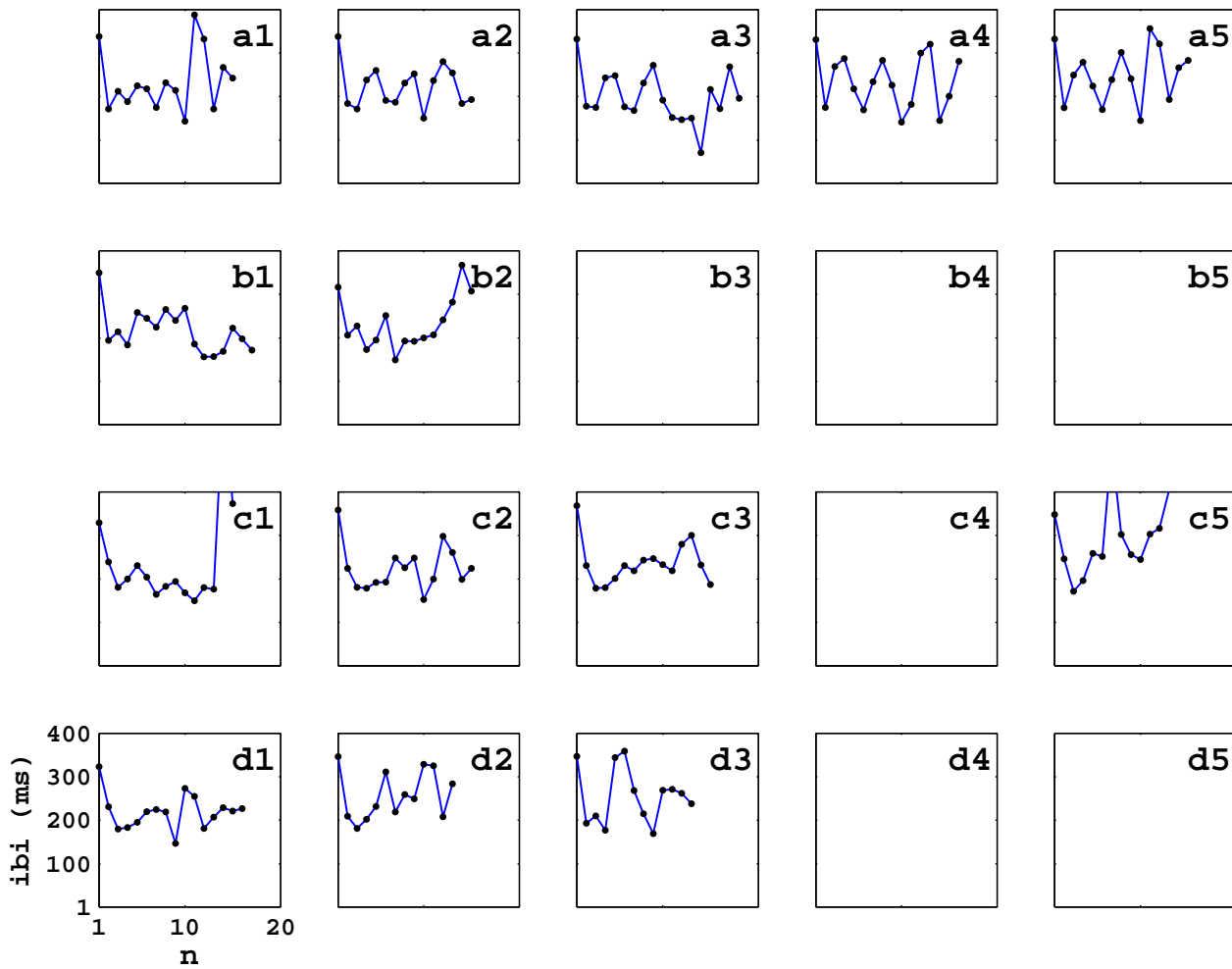


Figure S14: Plots of the ibi versus the beat number n that we obtain from the time series shown in Fig. S13.

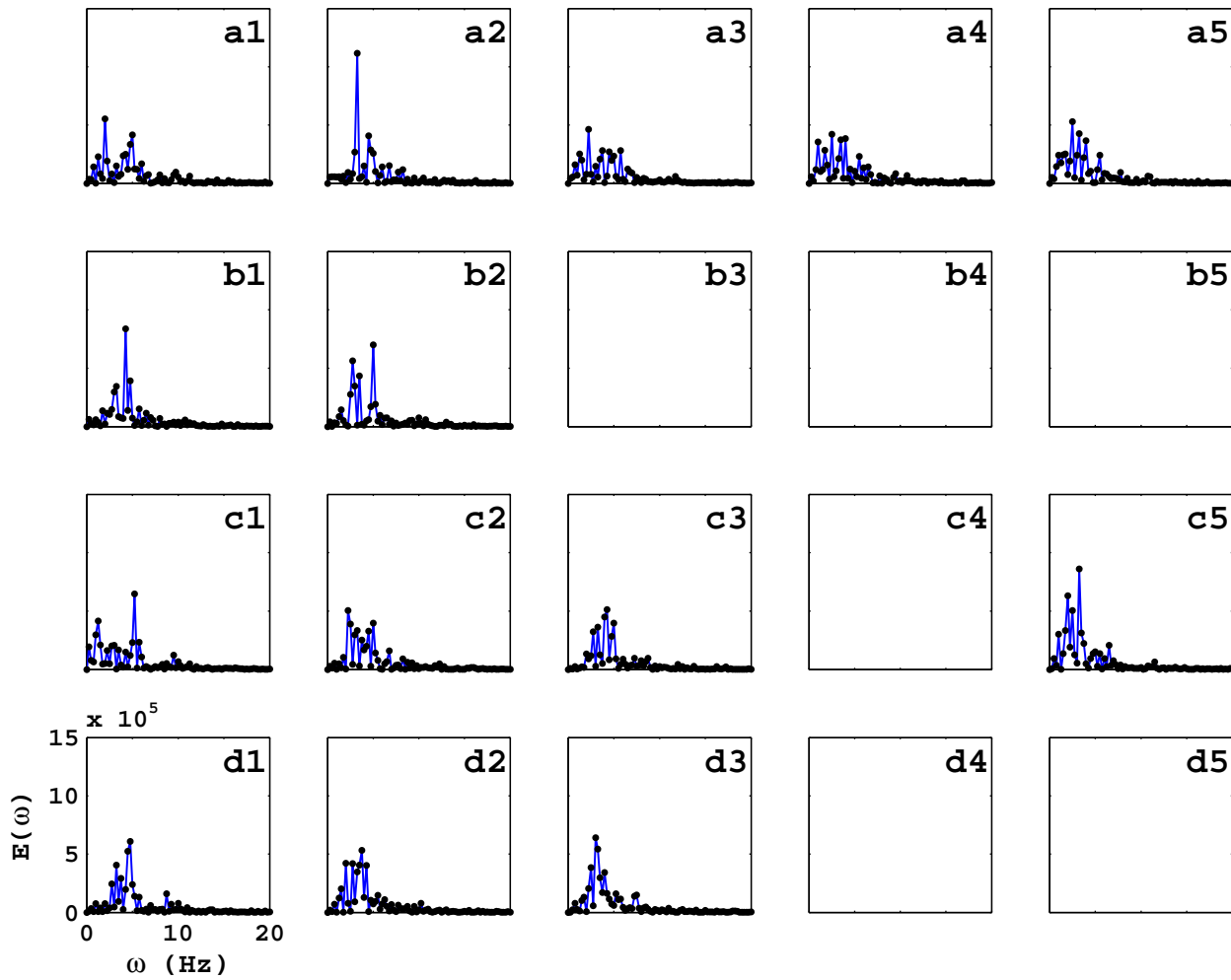


Figure S15: Plots of the power spectrum $E(\omega)$ of V_m obtained from a time series of length 2×10^5 for the data points in Fig. S13.

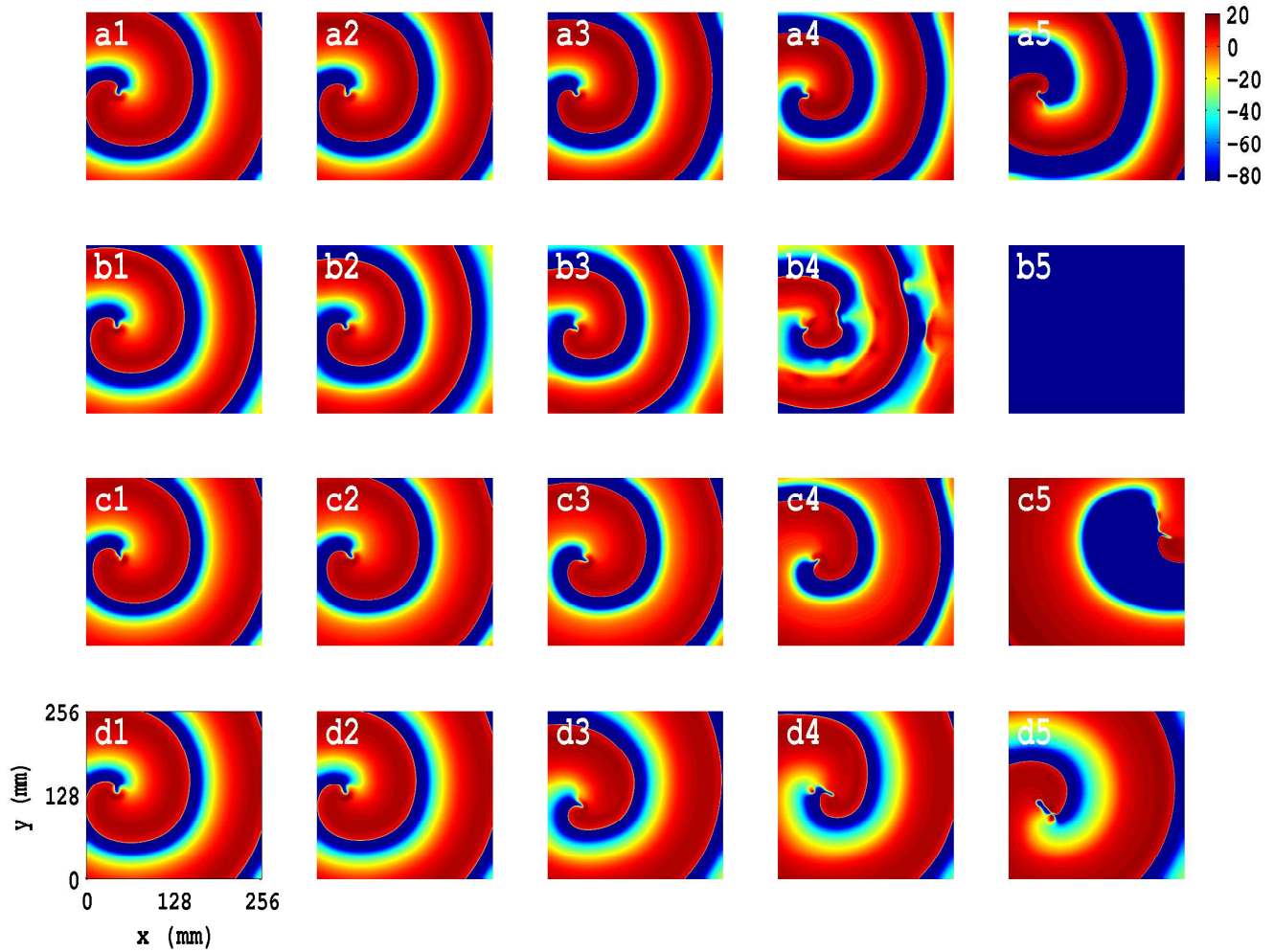


Figure S16: Illustrations of the rich variety of spatiotemporal patterns for the TNNP04 model, with PD along both x and y directions and the initial condition $IC1$: Representative pseudocolor plots of V_m with the initial condition $IC1$ (Fig. S3(c)) and the following PD parameters: (a1) $A_x = A_y = 0.1$, $f_x = f_y = 1.0$ Hz, (a2) $A_x = A_y = 0.2$, $f_x = f_y = 1.0$ Hz, (a3) $A_x = A_y = 0.3$, $f_x = f_y = 1.0$ Hz, (a4) $A_x = A_y = 0.4$, $f_x = f_y = 1.0$ Hz, (a5) $A_x = A_y = 0.5$, $f_x = f_y = 1.0$ Hz, (b1) $A_x = A_y = 0.1$, $f_x = f_y = 3.0$ Hz, (b2) $A_x = A_y = 0.2$, $f_x = f_y = 3.0$ Hz, (b3) $A_x = A_y = 0.3$, $f_x = f_y = 3.0$ Hz, (b4) $A_x = A_y = 0.4$, $f_x = f_y = 3.0$ Hz, (b5) $A_x = A_y = 0.5$, $f_x = f_y = 3.0$ Hz, (c1) $A_x = A_y = 0.1$, $f_x = f_y = 5.0$ Hz, (c2) $A_x = A_y = 0.2$, $f_x = f_y = 5.0$ Hz, (c3) $A_x = A_y = 0.3$, $f_x = f_y = 5.0$ Hz, (c4) $A_x = A_y = 0.4$, $f_x = f_y = 5.0$ Hz, (c5) $A_x = A_y = 0.5$, $f_x = f_y = 5.0$ Hz, (d1) $A_x = A_y = 0.1$, $f_x = f_y = 7.0$ Hz, (d2) $A_x = A_y = 0.2$, $f_x = f_y = 7.0$ Hz, (d3) $A_x = A_y = 0.3$, $f_x = f_y = 7.0$ Hz, (d4) $A_x = A_y = 0.4$, $f_x = f_y = 7.0$ Hz, and (d5) $A_x = A_y = 0.5$, $f_x = f_y = 7.0$ Hz; the animations in Video S9 show the spatiotemporal evolution of V_m for these cases in the time interval $0 \text{ s} \leq t \leq 4 \text{ s}$.

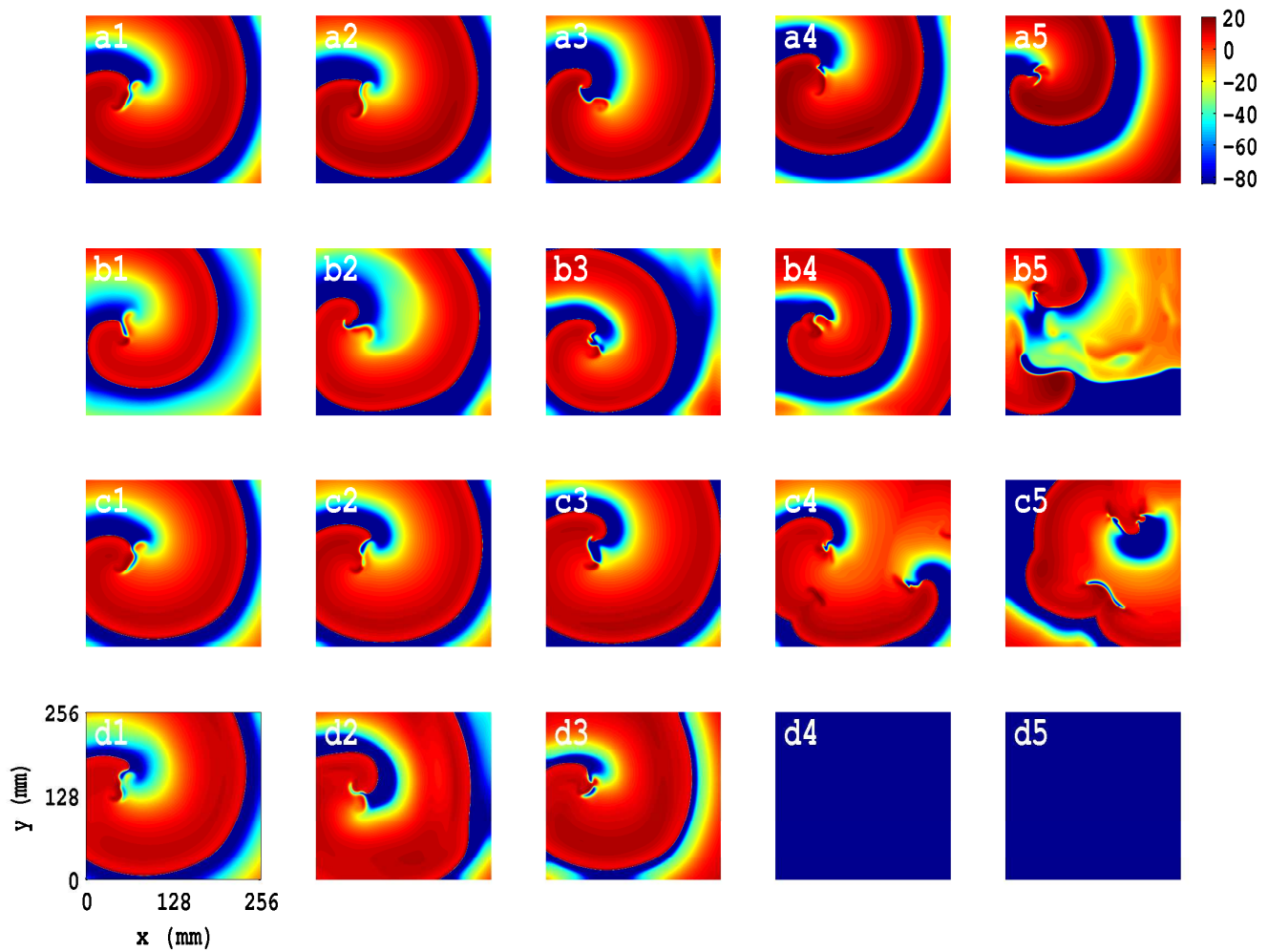


Figure S17: Illustrations of the rich variety of spatiotemporal patterns for the TNNP04 model, with PD along both x and y directions and the initial condition $IC2$: The analogs of the pseudocolor plots of V_m in Fig. S16 for the initial conditions $IC2$; the plots (a1)-(d5) here use the same PD parameters as their counterparts in Fig. S16; the Video S10 shows the spatiotemporal evolution of V_m for these cases for the time interval $0 \leq t \leq 4$ s.

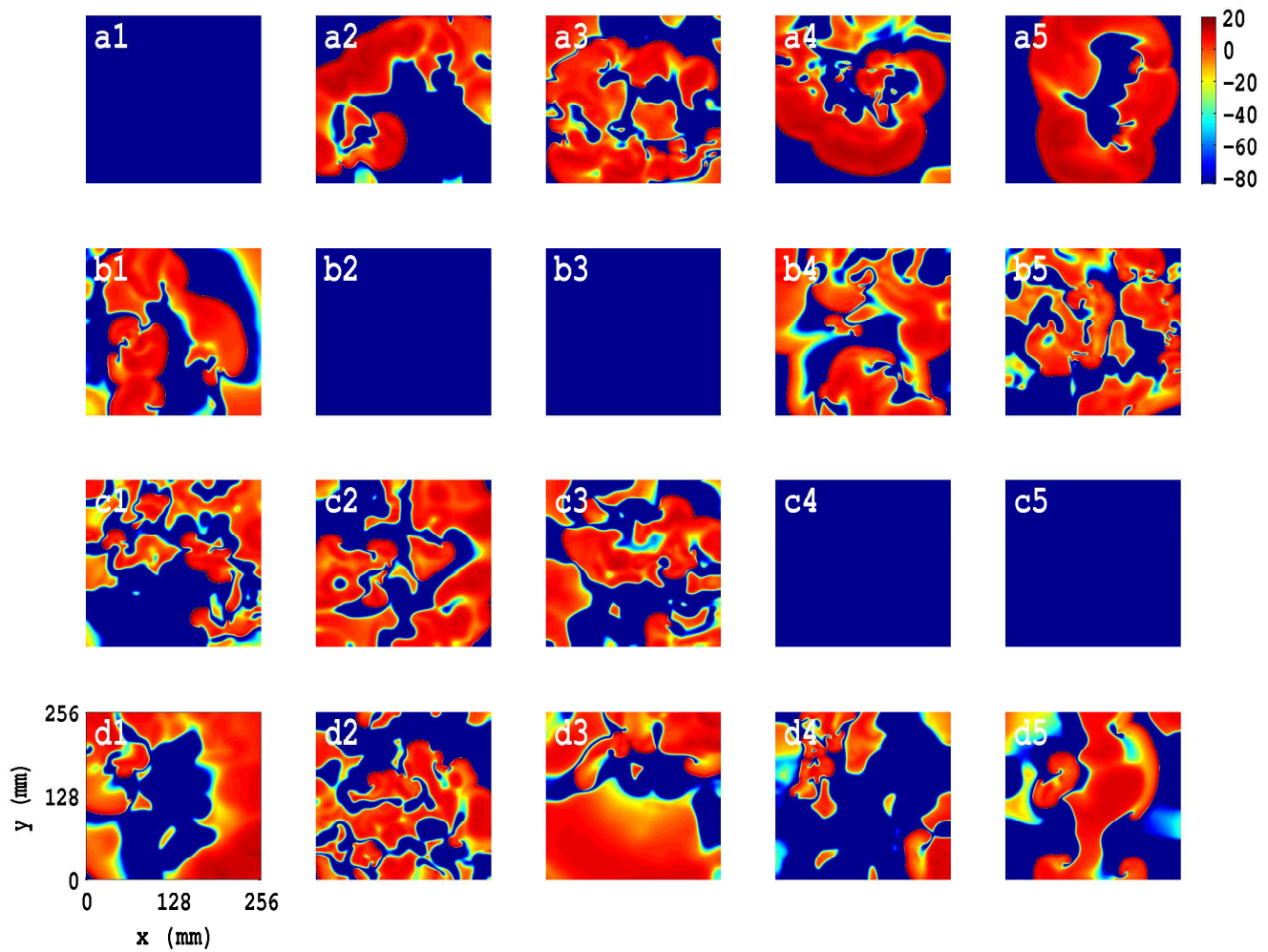


Figure S18: Illustrations of the rich variety of spatiotemporal patterns for the TNNP04 model, with PD along both x and y directions and the initial condition $IC3$: The analogs of the pseudocolor plots of V_m in Fig. S16 for the initial conditions $IC3$; the plots (a1)-(d5) here use the same PD parameters as their counterparts in Fig. S16; the Video S11 shows the spatiotemporal evolution of V_m for these cases for the time interval $0 \leq t \leq 4$ s.

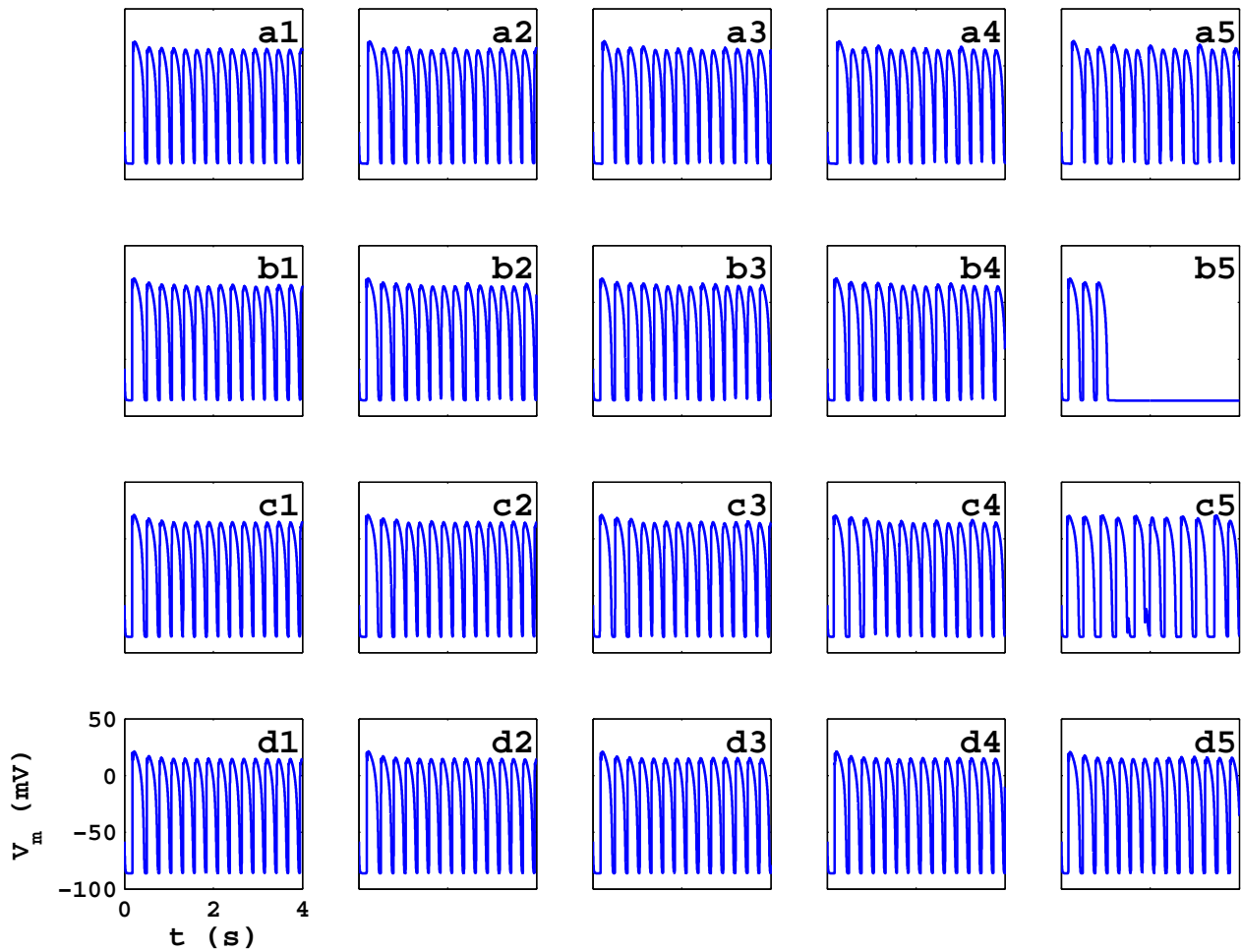


Figure S19: Plots of the local time series of $V_m(x, y, t)$, recorded from the representative points ($x = 125$ mm, $y = 125$ mm), in the TNNP04 model with the initial condition $IC1$ and PD along both spatial directions; the spatiotemporal patterns of V_m are shown in Fig. S16.

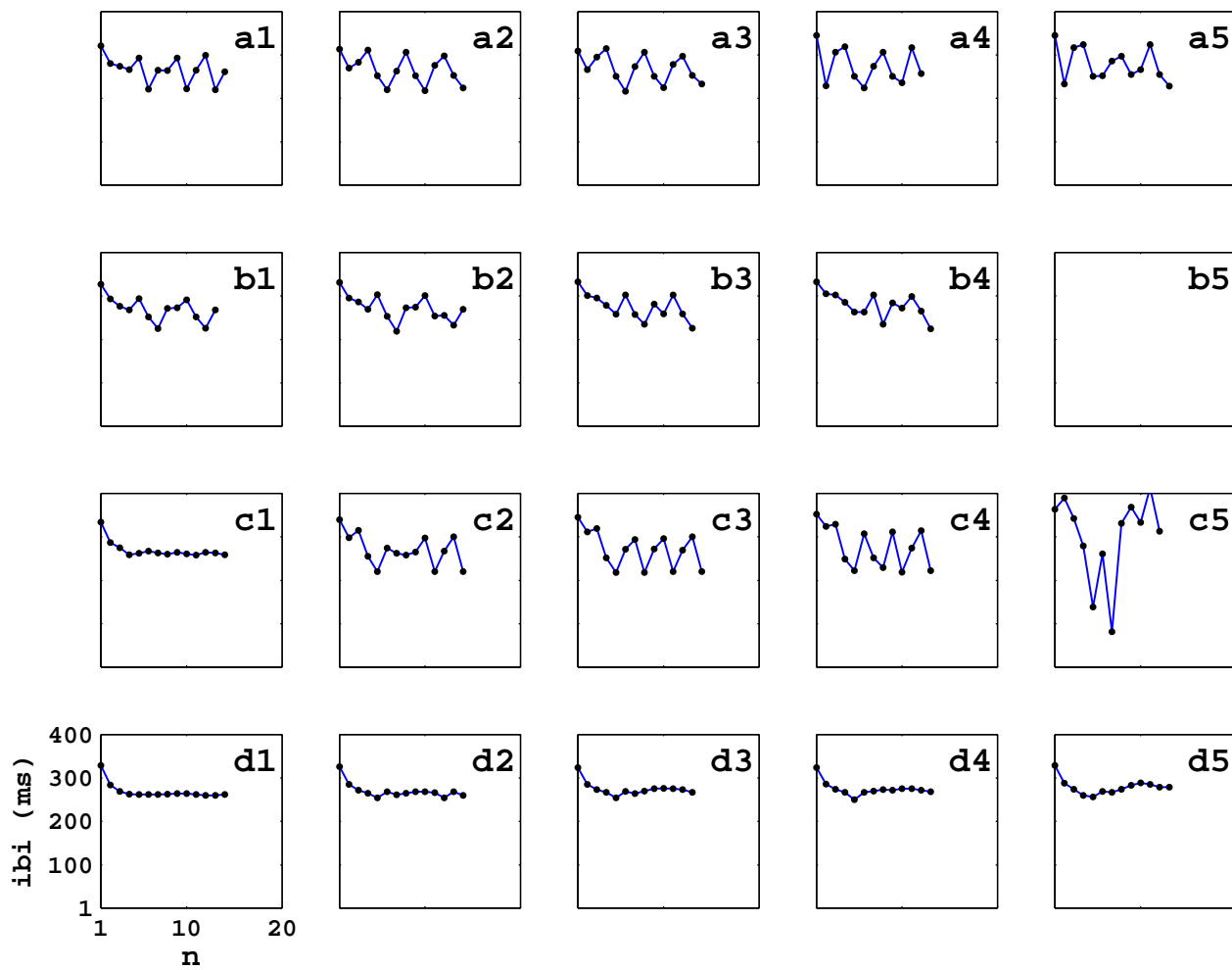


Figure S20: Plots of the ibi versus the beat number n that we obtain from the time series shown in Fig. S19.

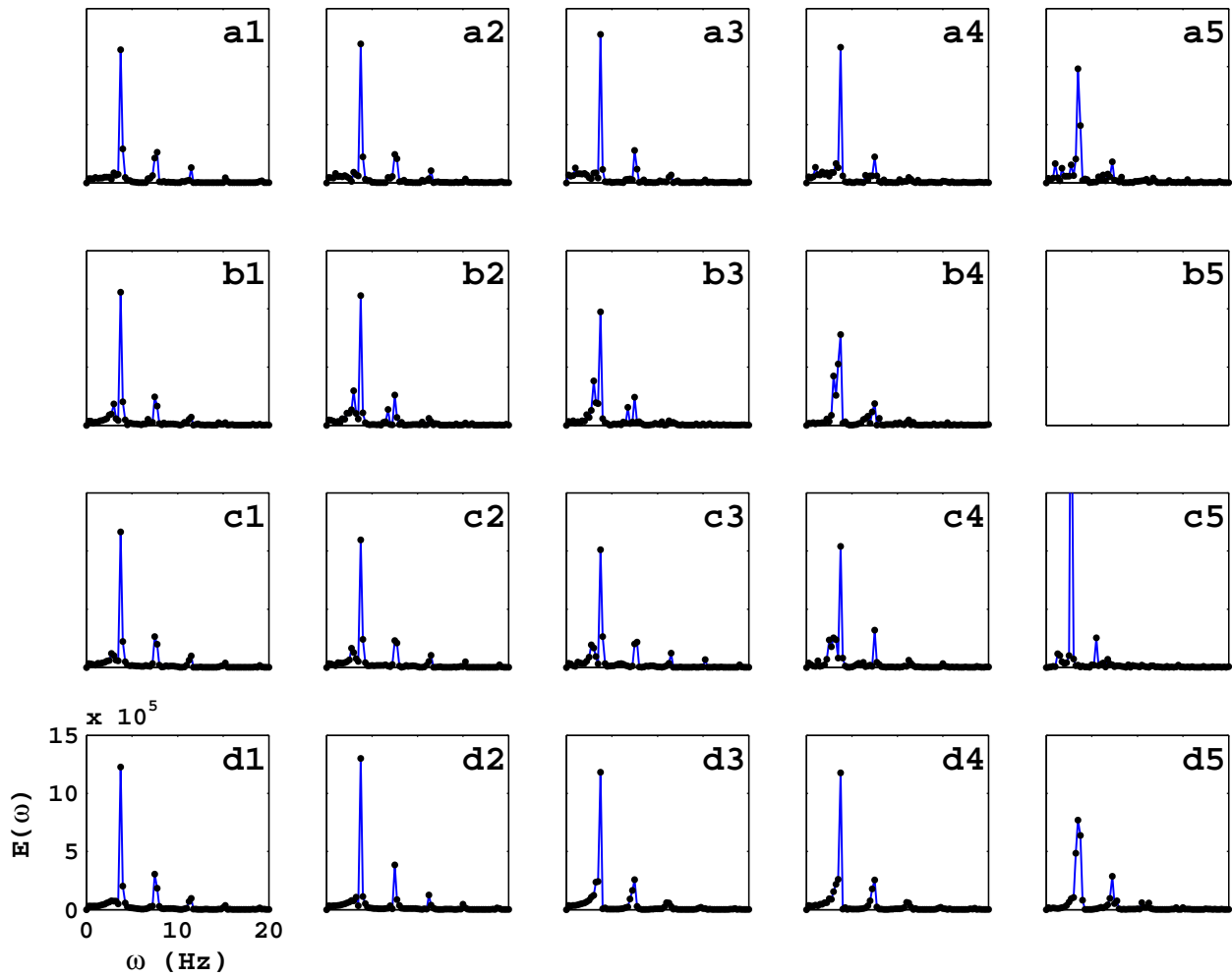


Figure S21: Plots of the power spectrum $E(\omega)$ of V_m obtained from a time series of length 2×10^5 for the data points in Fig. S19.

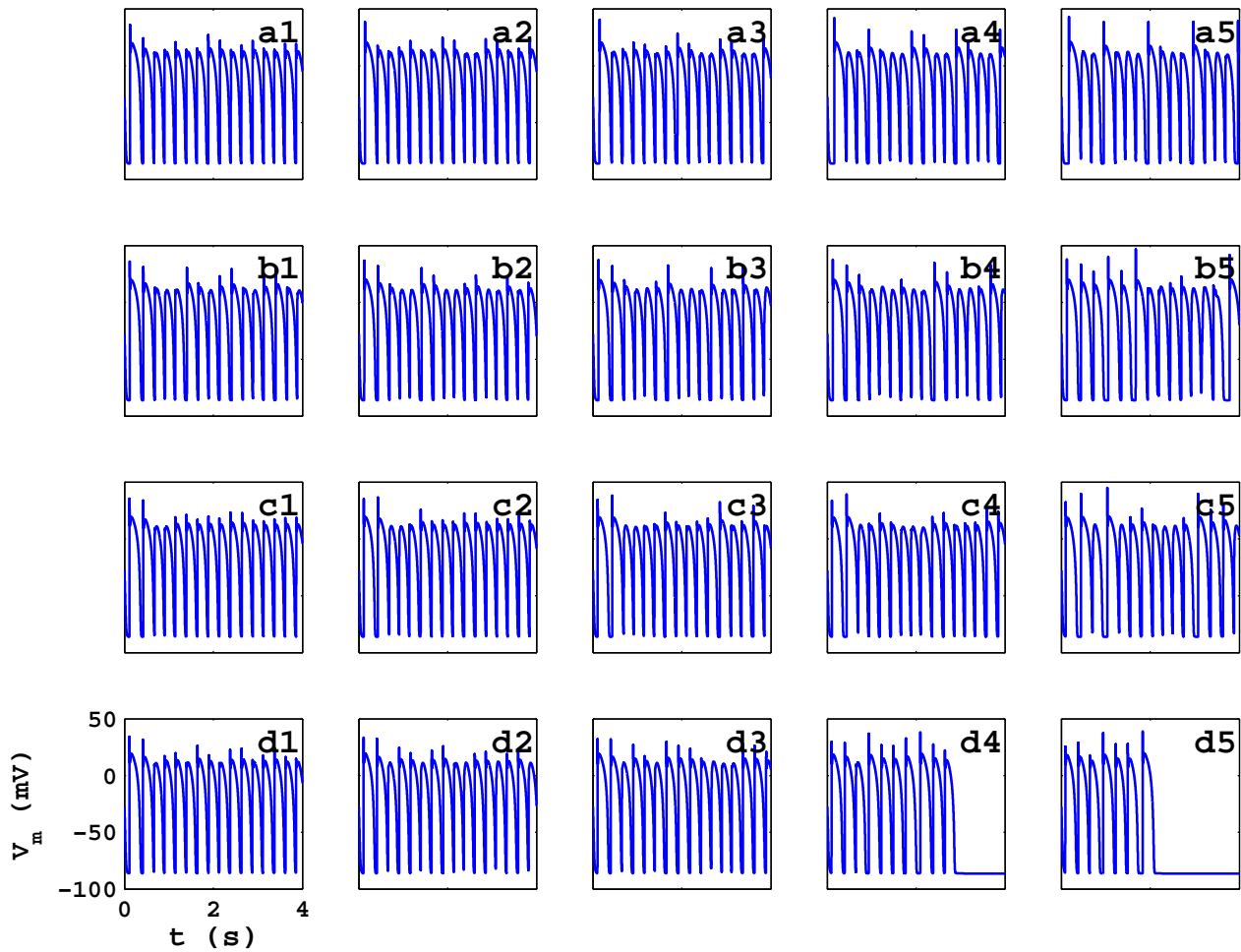


Figure S22: Plots of the local time series of $V_m(x, y, t)$, recorded from the representative points ($x = 125$ mm, $y = 125$ mm), in the TNNP04 model with the initial condition IC2 and PD along both spatial directions; the spatiotemporal patterns of V_m are shown in Fig. S17.

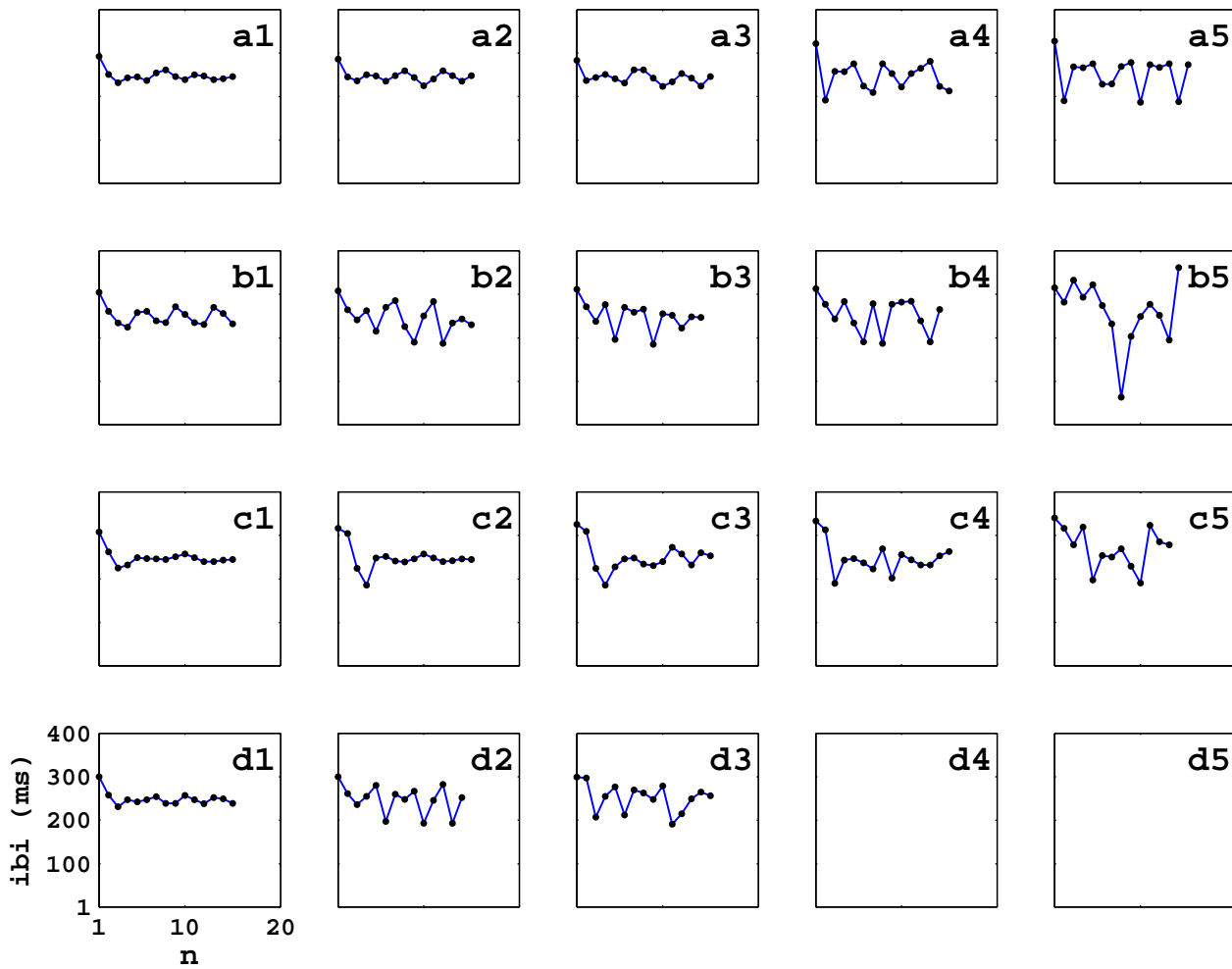


Figure S23: Plots of the ibi versus the beat number n that we obtain from the time series shown in Fig. S22.

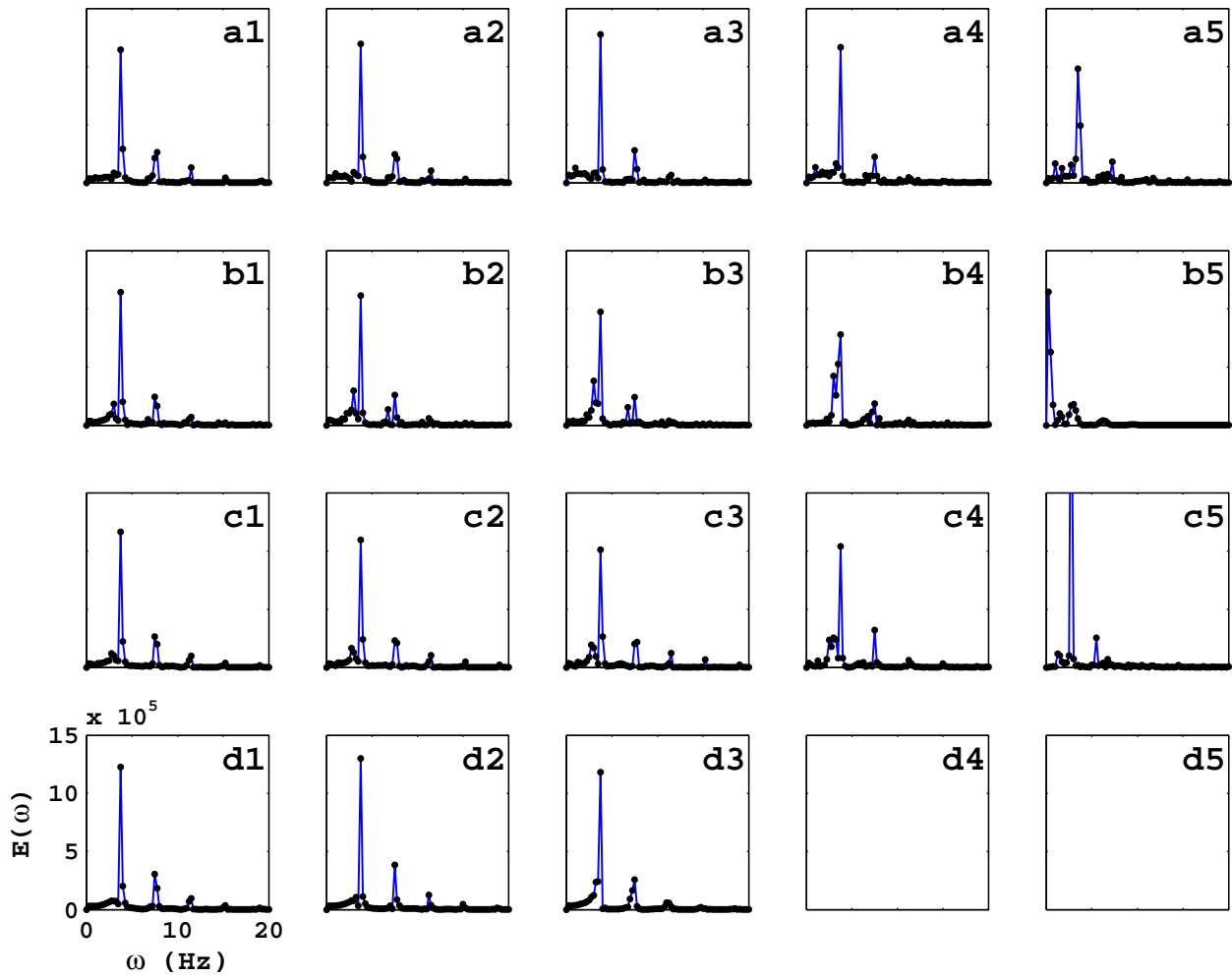


Figure S24: Plots of the power spectrum $E(\omega)$ of V_m obtained from a time series of length 2×10^5 for the data points in Fig. S22.

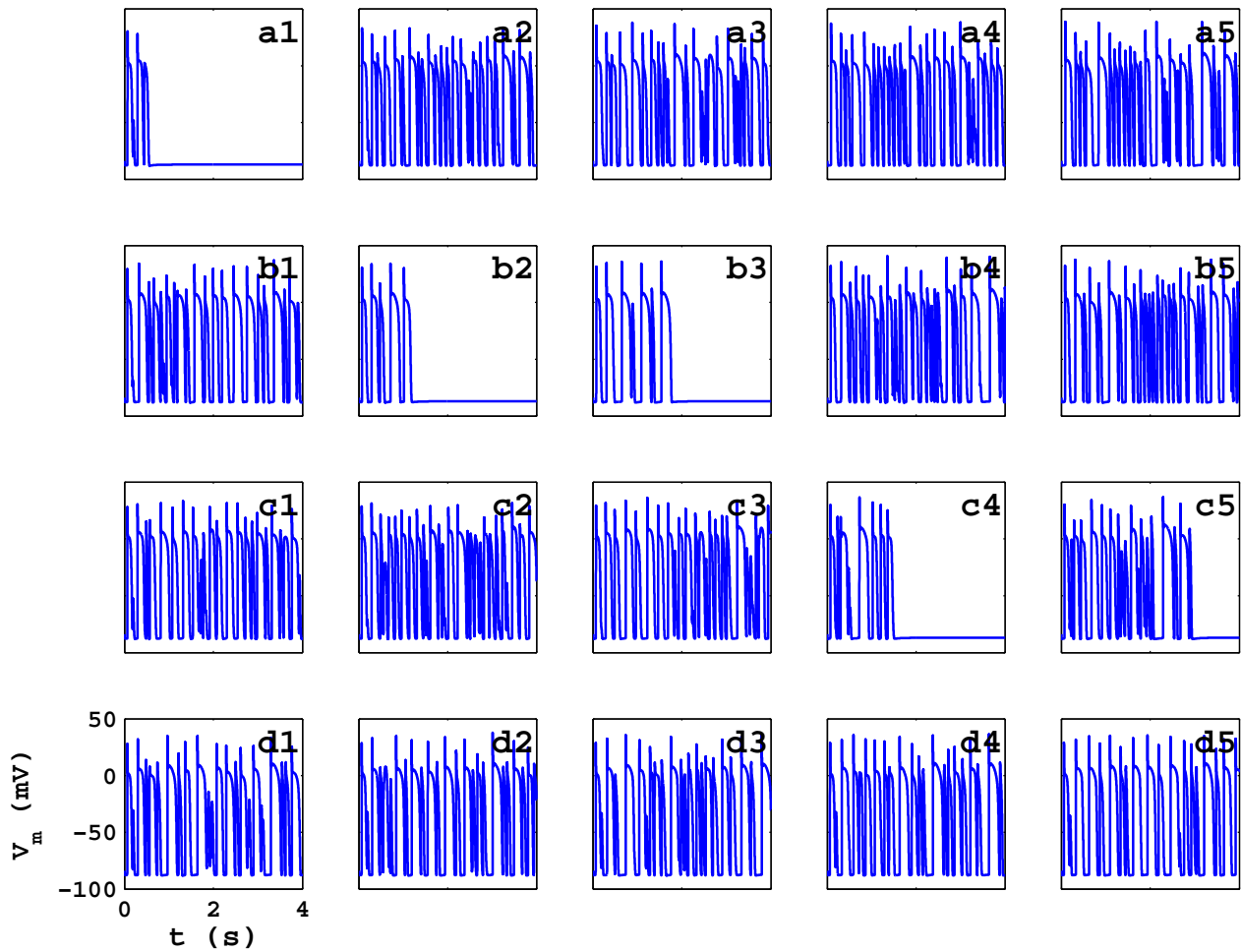


Figure S25: Plots of the local time series of $V_m(x, y, t)$, recorded from the representative points ($x = 125$ mm, $y = 125$ mm), in the TNNP04 model with the initial condition $IC3$ and PD along both spatial directions; the spatiotemporal patterns of V_m are shown in Fig. S18.

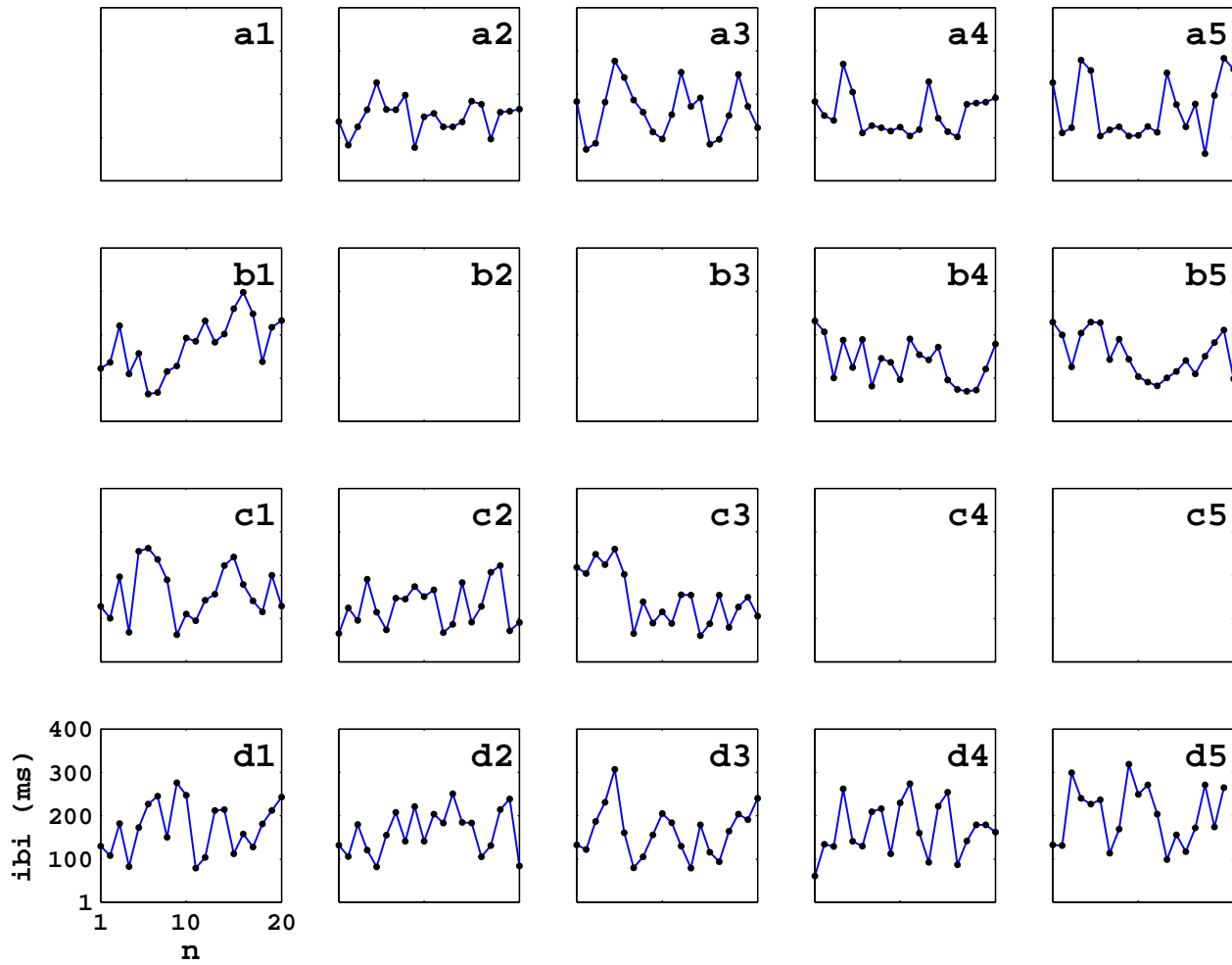


Figure S26: Plots of the ibi versus the beat number n that we obtain from the time series shown in Fig. S25.

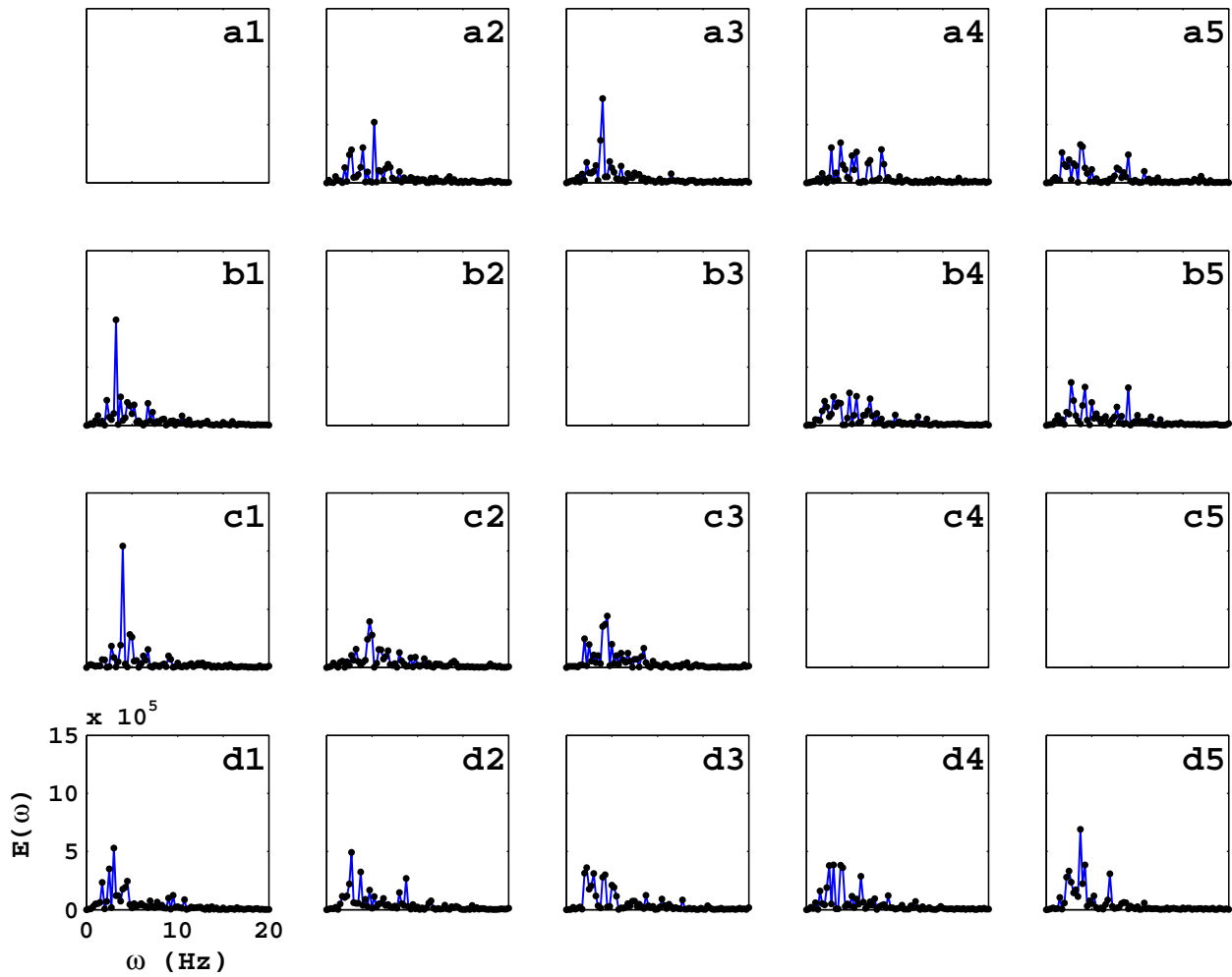


Figure S27: Plots of the power spectrum $E(\omega)$ of V_m obtained from a time series of length 2×10^5 for the data points in Fig. S25.

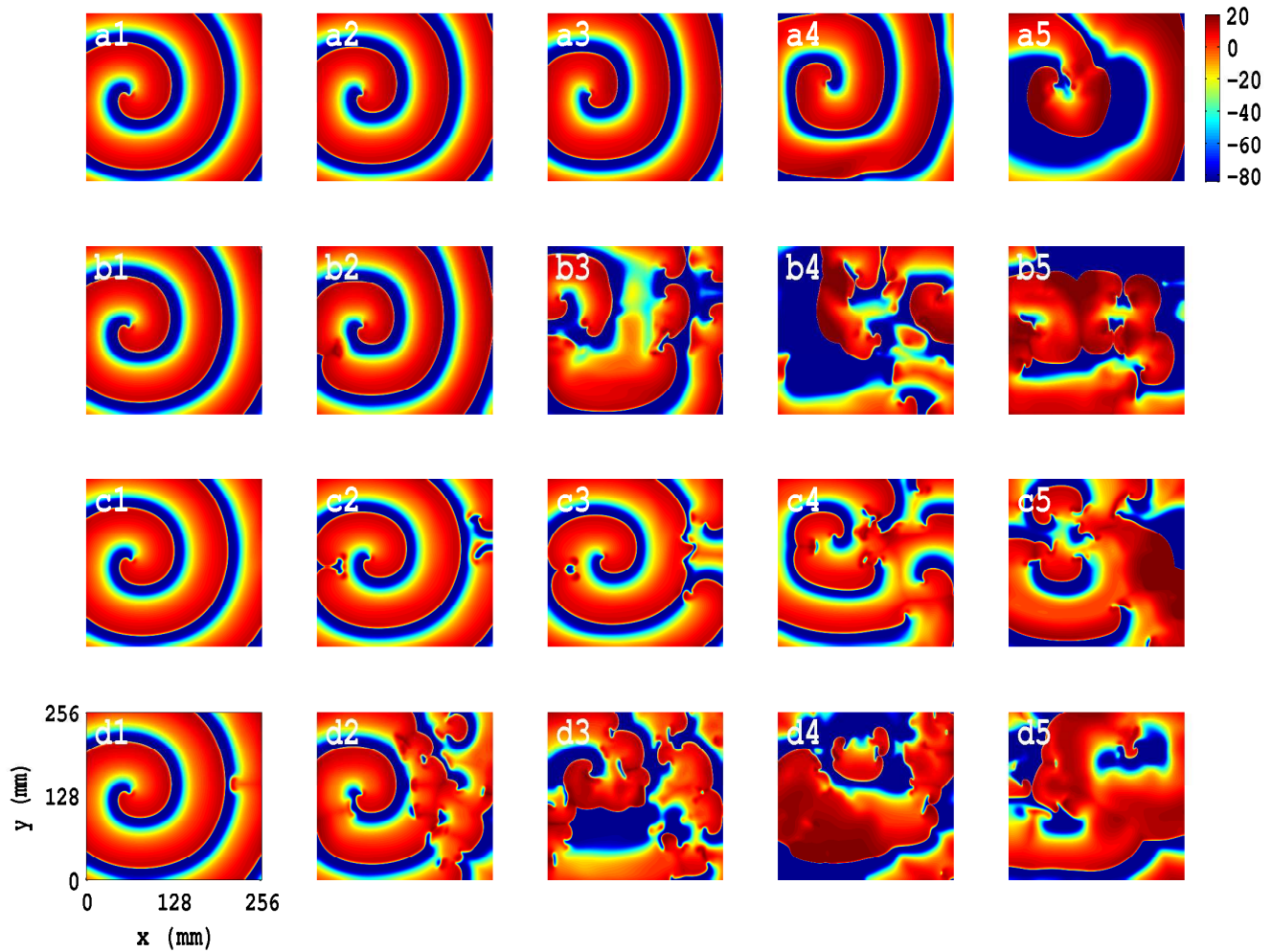


Figure S28: Illustrations of the rich variety of spatiotemporal patterns for the TP06 model, with PD along the x direction and the initial condition $IC1$: Representative pseudocolor plots of V_m with the initial condition $IC1$ (Fig. S3(c)) and the following PD parameters: (a1) $A_x = 0.1$, $f_x = f_y = 1.0$ Hz, (a2) $A_x = 0.2$, $f_x = f_y = 1.0$ Hz, (a3) $A_x = 0.3$, $f_x = f_y = 1.0$ Hz, (a4) $A_x = 0.4$, $f_x = f_y = 1.0$ Hz, (a5) $A_x = 0.5$, $f_x = f_y = 1.0$ Hz, (b1) $A_x = 0.1$, $f_x = f_y = 3.0$ Hz, (b2) $A_x = 0.2$, $f_x = f_y = 3.0$ Hz, (b3) $A_x = 0.3$, $f_x = f_y = 3.0$ Hz, (b4) $A_x = 0.4$, $f_x = f_y = 3.0$ Hz, (b5) $A_x = 0.5$, $f_x = f_y = 3.0$ Hz, (c1) $A_x = 0.1$, $f_x = f_y = 5.0$ Hz, (c2) $A_x = 0.2$, $f_x = f_y = 5.0$ Hz, (c3) $A_x = 0.3$, $f_x = f_y = 5.0$ Hz, (c4) $A_x = 0.4$, $f_x = f_y = 5.0$ Hz, (c5) $A_x = 0.5$, $f_x = f_y = 5.0$ Hz, (d1) $A_x = 0.1$, $f_x = f_y = 7.0$ Hz, (d2) $A_x = 0.2$, $f_x = f_y = 7.0$ Hz, (d3) $A_x = 0.3$, $f_x = f_y = 7.0$ Hz, (d4) $A_x = 0.4$, $f_x = f_y = 7.0$ Hz, and (d5) $A_x = 0.5$, $f_x = f_y = 7.0$ Hz; the animations in Video S12 show the spatiotemporal evolution of V_m for these cases in the time interval $0 \leq t \leq 4$ s.

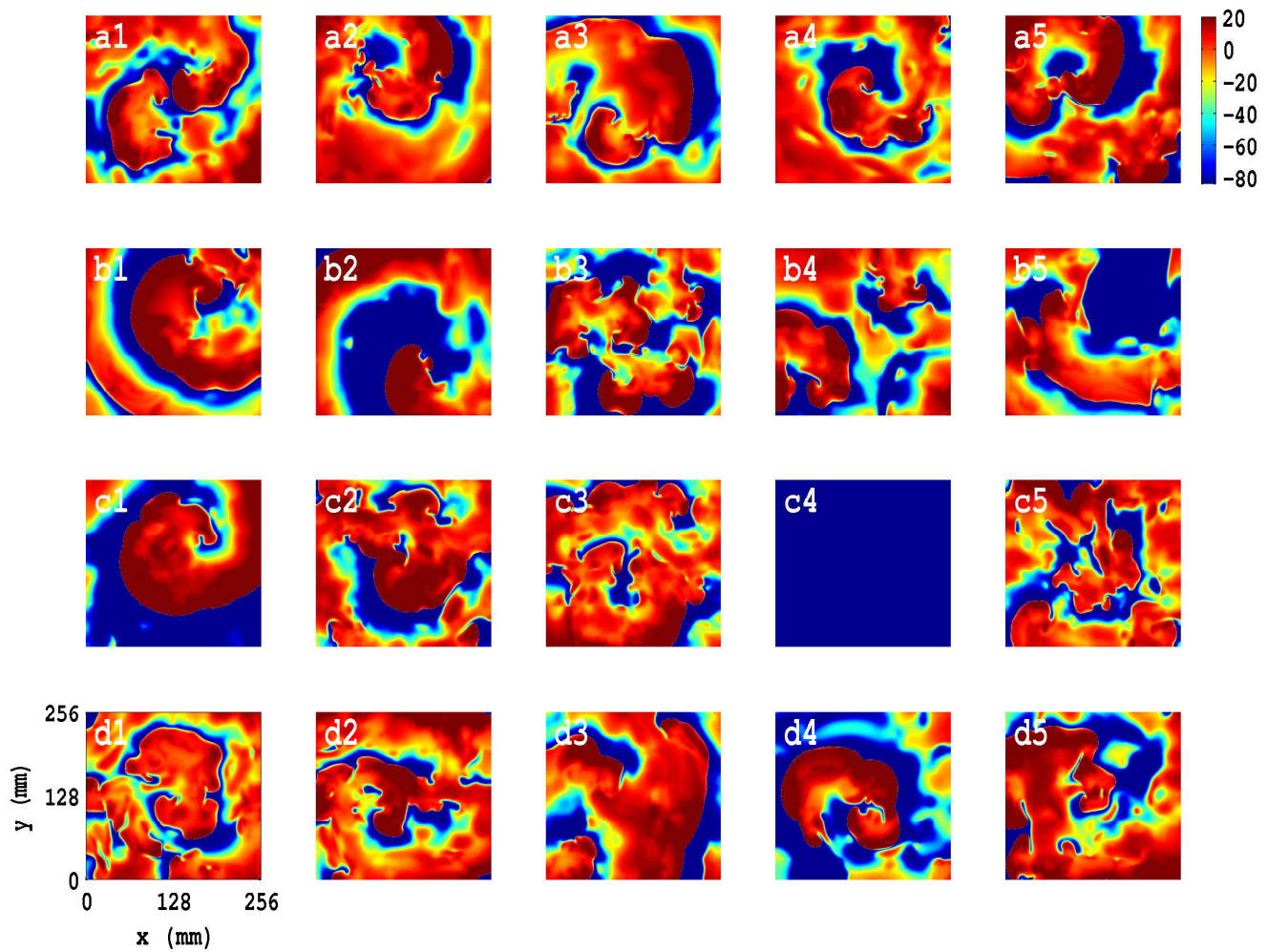


Figure S29: Illustrations of the rich variety of spatiotemporal patterns for the TP06 model, with PD along the x direction and the initial condition $IC2$: The analogs of the pseudocolor plots of V_m in Fig. S28 for the initial conditions $IC2$; the plots (a1)-(d5) here use the same PD parameters as their counterparts in Fig. S28; the Video S13 shows the spatiotemporal evolution of V_m for these cases for the time interval $0 \text{ s} \leq t \leq 4 \text{ s}$.

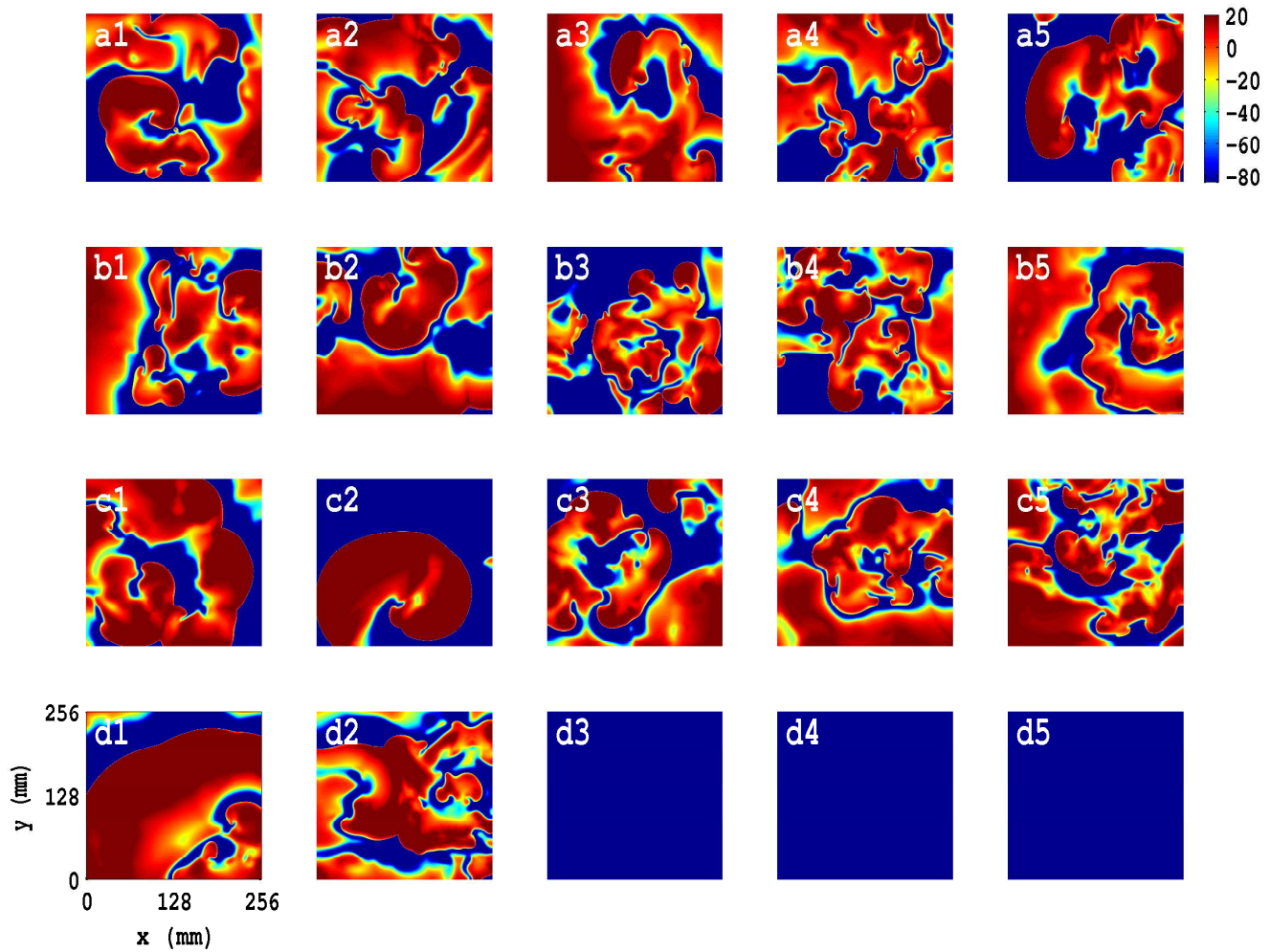


Figure S30: Illustrations of the rich variety of spatiotemporal patterns for the TP06 model, with PD along the x direction and the initial condition $IC3$: The analogs of the pseudocolor plots of V_m in Fig. S28 for the initial conditions $IC3$; the plots (a1)-(d5) here use the same PD parameters as their counterparts in Fig. S28; the Video S14 shows the spatiotemporal evolution of V_m for these cases for the time interval $0 \text{ s} \leq t \leq 4 \text{ s}$.

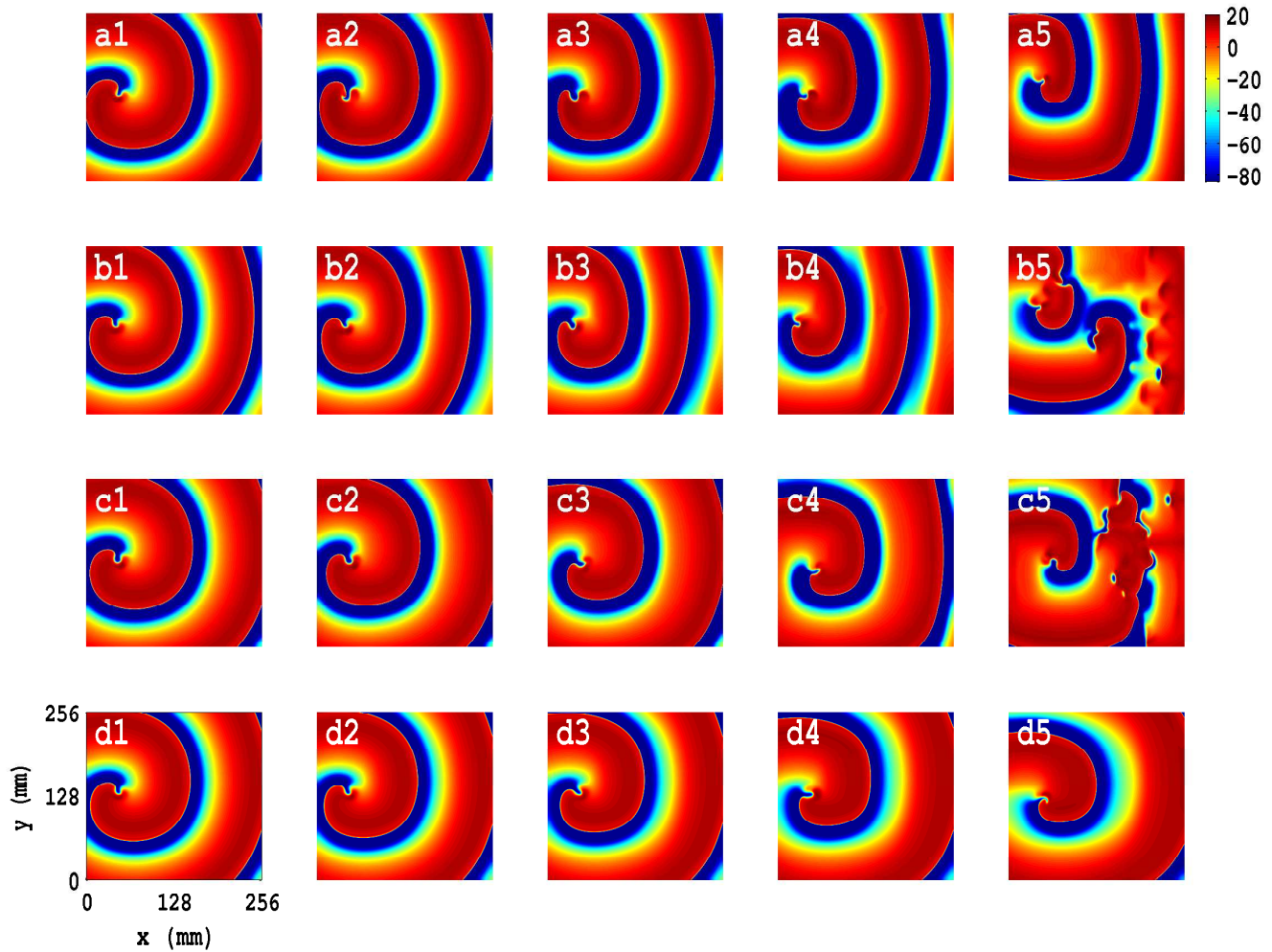


Figure S31: Illustrations of the rich variety of spatiotemporal patterns for the TNNP04 model, with PD along the x direction and the initial condition $IC1$: Representative pseudocolor plots of V_m with the initial condition $IC1$ (Fig. S3(c)) and the following PD parameters: (a1) $A_x = 0.1$, $f_x = f_y = 1.0$ Hz, (a2) $A_x = 0.2$, $f_x = f_y = 1.0$ Hz, (a3) $A_x = 0.3$, $f_x = f_y = 1.0$ Hz, (a4) $A_x = 0.4$, $f_x = f_y = 1.0$ Hz, (a5) $A_x = 0.5$, $f_x = f_y = 1.0$ Hz, (b1) $A_x = 0.1$, $f_x = f_y = 3.0$ Hz, (b2) $A_x = 0.2$, $f_x = f_y = 3.0$ Hz, (b3) $A_x = 0.3$, $f_x = f_y = 3.0$ Hz, (b4) $A_x = 0.4$, $f_x = f_y = 3.0$ Hz, (b5) $A_x = 0.5$, $f_x = f_y = 3.0$ Hz, (c1) $A_x = 0.1$, $f_x = f_y = 5.0$ Hz, (c2) $A_x = 0.2$, $f_x = f_y = 5.0$ Hz, (c3) $A_x = 0.3$, $f_x = f_y = 5.0$ Hz, (c4) $A_x = 0.4$, $f_x = f_y = 5.0$ Hz, (c5) $A_x = 0.5$, $f_x = f_y = 5.0$ Hz, (d1) $A_x = 0.1$, $f_x = f_y = 7.0$ Hz, (d2) $A_x = 0.2$, $f_x = f_y = 7.0$ Hz, (d3) $A_x = 0.3$, $f_x = f_y = 7.0$ Hz, (d4) $A_x = 0.4$, $f_x = f_y = 7.0$ Hz, and (d5) $A_x = 0.5$, $f_x = f_y = 7.0$ Hz; the animations in Video S15 show the spatiotemporal evolution of V_m for these cases in the time interval $0 \leq t \leq 4$ s.

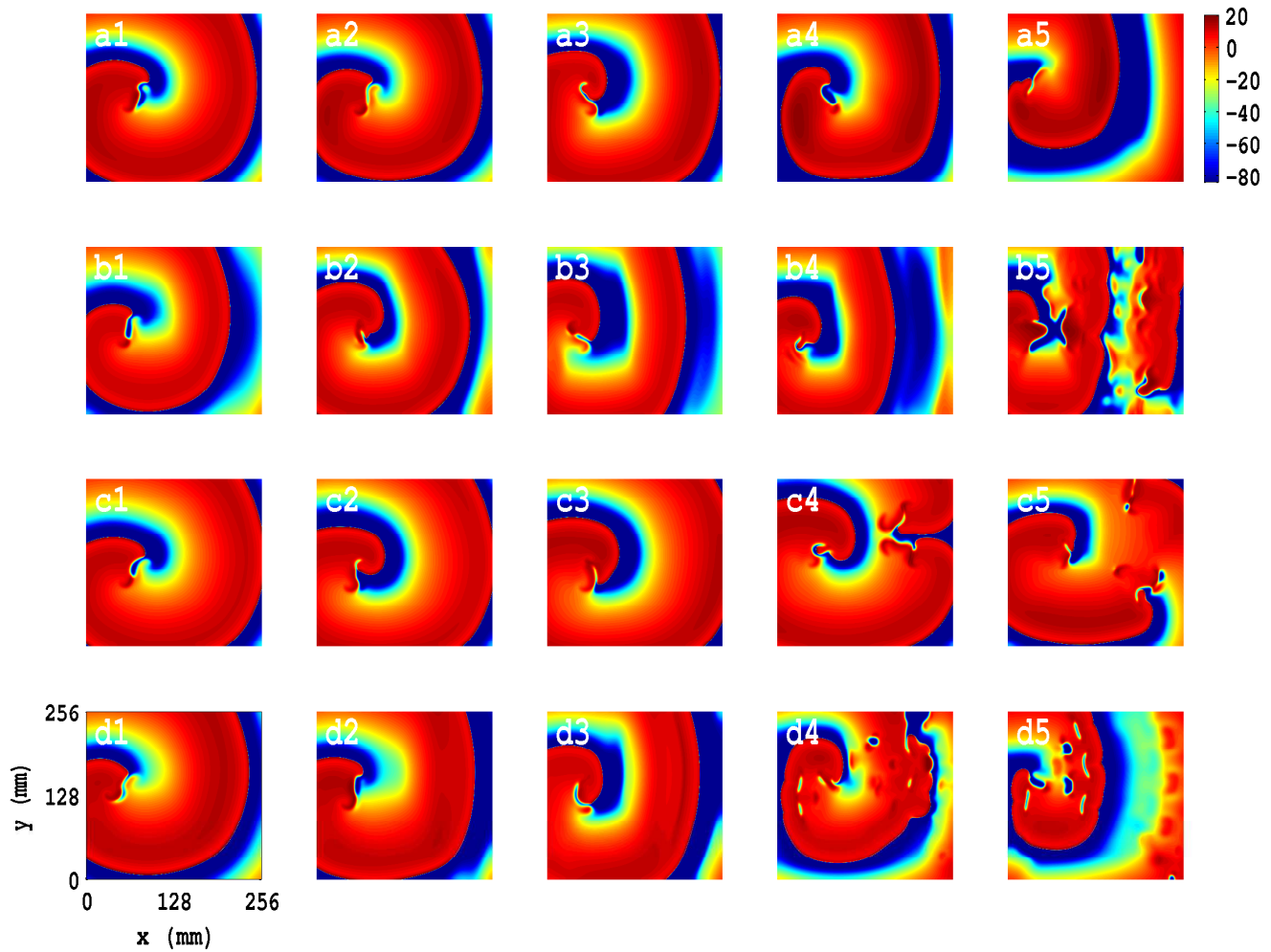


Figure S32: Illustrations of the rich variety of spatiotemporal patterns for the TNNP04 model, with PD along the x direction and the initial condition $IC2$: The analogs of the pseudocolor plots of V_m in Fig. S31 for the initial conditions $IC2$; the plots (a1)-(d5) here use the same PD parameters as their counterparts in Fig. S31; the Video S16 shows the spatiotemporal evolution of V_m for these cases for the time interval $0 \text{ s} \leq t \leq 4 \text{ s}$.

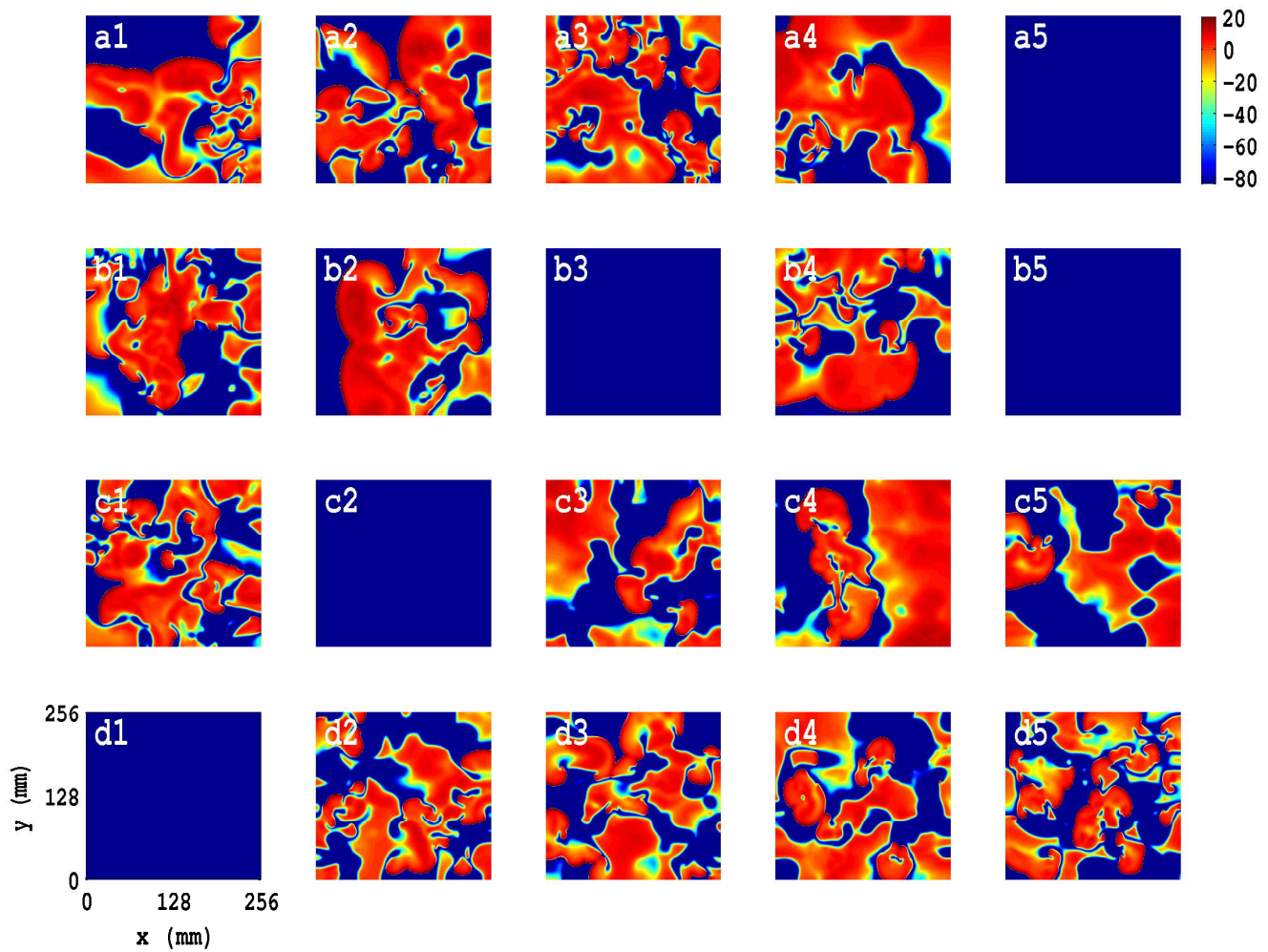


Figure S33: Illustrations of the rich variety of spatiotemporal patterns for the TNNP04 model, with PD along the x direction and the initial condition $IC3$: The analogs of the pseudocolor plots of V_m in Fig. S31 for the initial conditions $IC2$; the plots (a1)-(d5) here use the same PD parameters as their counterparts in Fig. S31; the Video S17 shows the spatiotemporal evolution of V_m for these cases for the time interval $0 \text{ s} \leq t \leq 4 \text{ s}$.

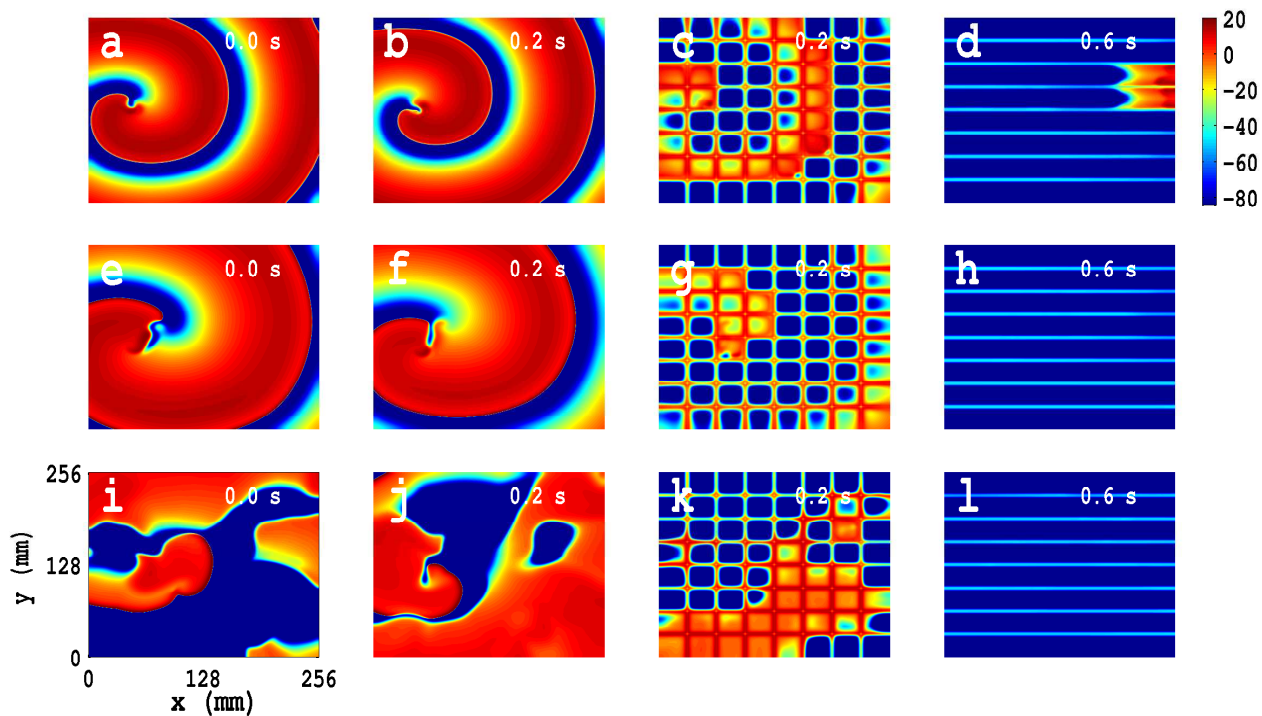


Figure S34: Spiral-wave control in the TNNP04 model, in the absence of PD, by low-amplitude pulses on square and line meshes: We illustrate spiral-wave control, via low-amplitude control pulses, in the TP06 model, in the absence of PD, by presenting pseudocolor plots of V_m . The spiral state, at time $t = 0$ s (a), with the $IC1$ initial condition, evolves, in the absence of the control, to an RS state (b), at time $t = 0.2$ s; this state is suppressed by the both square- and line-mesh control methods as shown in (c) and (d), at $t = 0.2$ s and $t = 0.6$ s, respectively. Similar plots for the $IC2$ and $IC3$ initial conditions are given, respectively, in (e)-(h) and (i)-(l). The Video S22, which comprises nine animations of pseudocolor plots of V_m , show the spatiotemporal evolution of these spiral waves, with and without control pulses, for the time interval $0 \leq t \leq 1$ s. In all these cases we apply a control pulse of amplitude 75 pA/pF for $t = 0.2 \text{ ms}$ for the square mesh and an amplitude of 125 pA/pF for $t = 0.6 \text{ ms}$ for the line mesh.

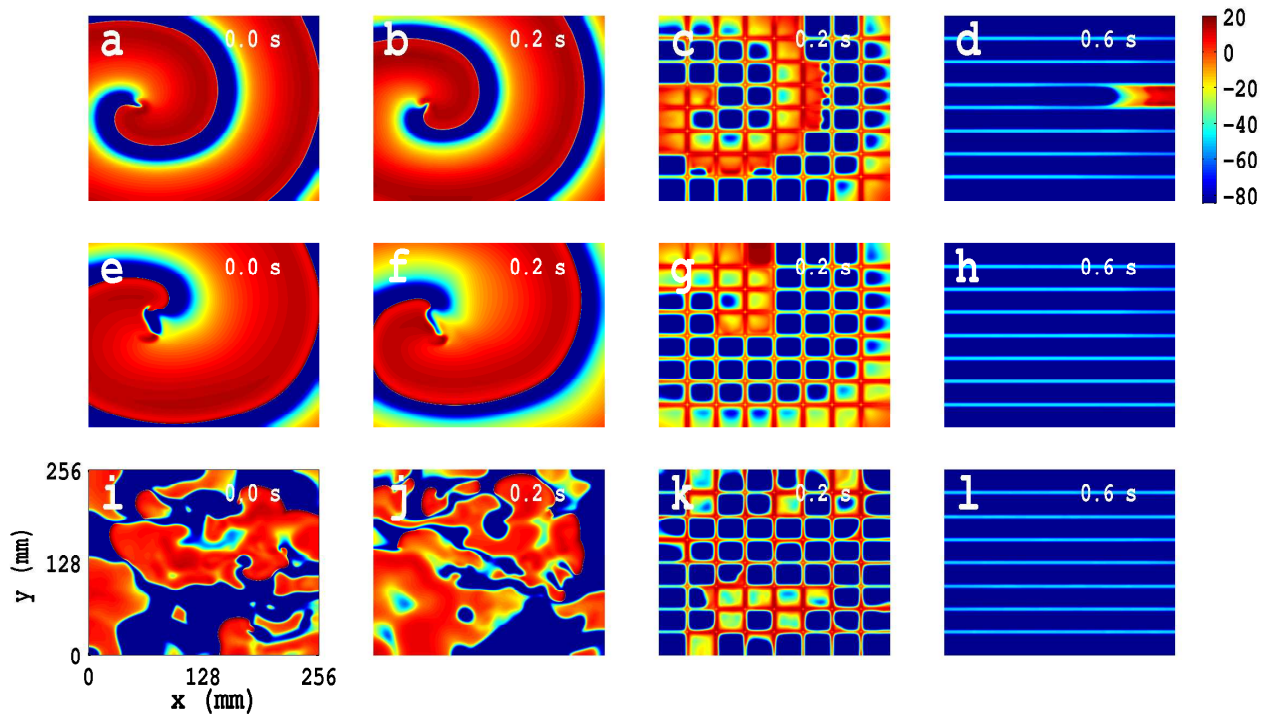


Figure S35: Spiral-wave control by low-amplitude pulses in the TNNP04 model with PD along only the x direction: We impose PD along the x direction and the illustrative amplitude $A_x = 0.3$ and frequency $f_x = 5$ Hz; (a)-(l) are the analogs of Figs. S34(a)-(l), respectively. With the initial condition $IC1$, the spiral in (a), at $t = 0$ s, evolves, in the absence of control, to an MST state (b), at $t = 0.2$ s; this MST can be suppressed by both square- and line-mesh control (c) and (d) at $t = 0.2$ s and 0.6 s, respectively. For the $IC2$ and $IC3$ initial configurations, the analogs of these states are shown in (e)-(h) and (i)-(l), respectively; clearly, both our control schemes are successful in eliminating spiral turbulence with PD along one direction. For the spatiotemporal evolution of these spiral waves see Video S23.

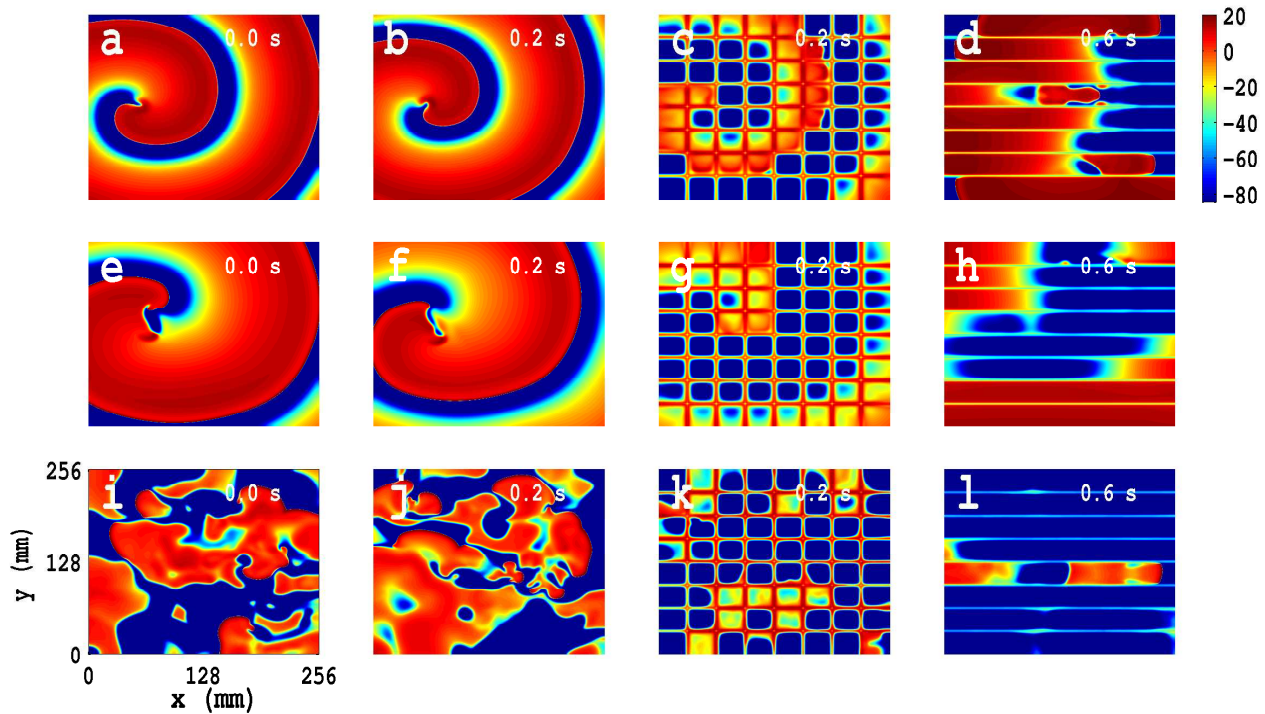


Figure S36: Spiral-wave control by low-amplitude pulses in the TNNP04 model with PD along both x and y directions: We impose PD along both x and y directions with the illustrative amplitudes $A_x = A_y = 0.3$ and frequencies $f_x = f_y = 5$ Hz; for this case (a)-(l) are the analogs of Figs. 4.15 (a)-(l), respectively. With the initial condition $IC1$, the spiral in (a), at $t = 0$ s, evolves, in the absence of the control, to the MST state in (b), at $t = 0.2$ s; this MST can be suppressed by the square-mesh technique but not by the line-mesh technique as we show in (c) and (d) at $t = 0.2$ s and 0.6 s, respectively; the parameters on the control mesh are as in Fig. 4.15. For the initial conditions $IC2$ and $IC3$, the analogs of these states are shown, respectively, in (e)-(h) and (i)-(l). Thus, with PD along both directions, spiral turbulence can be suppressed by our square-mesh control but not the line-mesh method for $IC1$ and $IC3$ initial conditions (see the animations in Video S24).

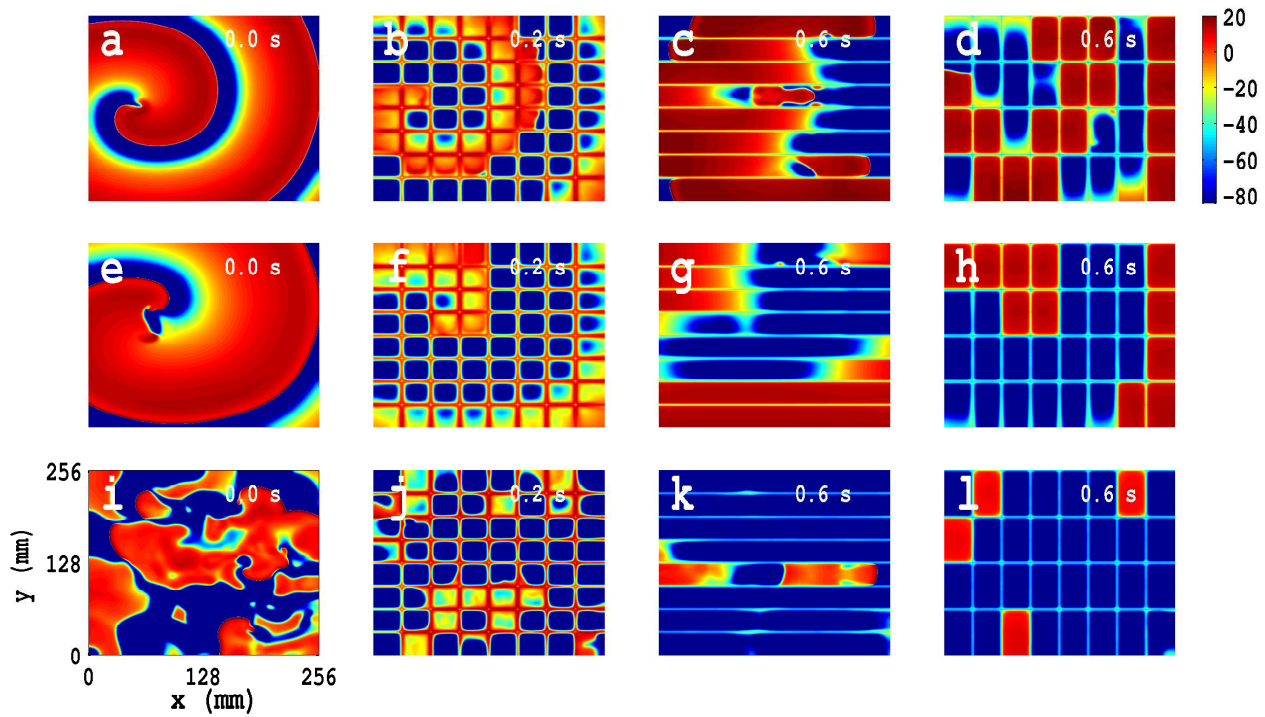


Figure S37: Comparison of spiral-wave control by low-amplitude pulses on square, line, and rectangular control meshes in the TNNP04 model, with PD along both x and y directions: We impose PD along both x and y directions with the illustrative amplitudes $A_x = A_y = 0.3$ and frequencies $f_x = f_y = 5$ Hz for the initial configurations $IC1$, $IC2$, and $IC3$ (pseudocolor plots of V_m in (a), (e), and (f), respectively). We apply the following control pulses: amplitude 75 pA/pF for $t = 0.2$ s over a square mesh ((b), (f), and (j)), with each square block of side $l = 32$ mm; amplitude 125 pA/pF for $t = 0.6$ s over a line mesh ((c), (g), and (k)), with inter-line spacing $l = 32$ mm; amplitude 125 pA/pF for $t = 0.6$ s over a rectangular mesh ((d), (h), and (l)), with block sides $l_x = 32$ mm and $l_y = 64$ mm. These pseudocolor plots of V_m and the associated animations in Video S25 show that this spiral states, with $IC1$, $IC2$, and $IC3$ initial conditions, are suppressed by both square- and rectangular-mesh control but not line-mesh control.

Chapter 5

Spiral-wave dynamics in a Mathematical Model of Human Ventricular Tissue with Myocytes and Purkinje fibres

*This Chapter follows closely a paper that we will submit for publication very soon. The authors are **Alok Ranjan Nayak**, AV Panfilov, and Rahul Pandit.*

5.1 Introduction

In mammalian hearts, *Purkinje fibers* are among the special conduction systems [1] that carry electrical impulses from the *bundle of His* to the interior of ventricular tissue, namely, the endocardium. These impulses excite endocardial myocytes and the resulting excitations propagate across ventricular tissue to develop the mechanical force that is necessary for pumping blood to the whole body. Experiments [1–3] suggest that these Purkinje fibers branch out to form a network that spreads across the interior of the ventricular wall. Computational studies of electrical-wave propagation in the presence such Pukinje-fiber networks are in their infancy compared to studies of electrical-wave propagation in mathematical models of cardiac tissue that include only myocytes. It is important, therefore, to study the dynamics of spiral waves of electrical activation in mathematical models that include both myocytes and networks of Purkinje fibers, because there is a general consensus that such waves can play an important role in life-threatening cardiac arrhythmias like ventricular tachycardia (VT) and ventricular fibrillation (VF), which are often associated, respectively, with an unbroken spiral wave and broken spiral waves of electrical activation in cardiac tissue [4–6]. In mathematical models of cardiac tissue, the simplest analogs of VT and VF are a single, unbroken,

rotating spiral (RS) wave and spiral-wave turbulence (ST) with multiple broken spirals, respectively [4–9].

To study electrical-wave propagation in cardiac tissue in the presence of the Purkinje-fiber conduction network, we must incorporate mathematical models for Purkinje fibers with those for myocytes. Examples of the latter include the Luo-Rudy models [10, 11], the model of ten Tusscher, Noble, Noble, and Panfilov [12], and that of ten Tusscher and Panfilov [13]. Several mathematical models have been developed for ventricular Purkinje cells by including hyperpolarized ionic currents and by modifying the major ionic currents in some ventricular-myocyte models. To the best of our knowledge, 9 models have been developed for ventricular Purkinje fibers; these models are (a) the 1962 model of Noble [14], (b) the 1975 one of McAllister, *et al.* [15], (c) the 1985 model of DiFrancesco, *et al.* [16], (d) the 2008 model of ten Tusscher, *et al.* [17], (e) the 2009 model of Stewart, *et al.* [18], (f) the 2009 model of Aslanidi, *et al.* [19], (g) the 2010 model of Sampson, *et al.* [20], (h) the 2011 model of Li, *et al.* [21], and (i) the 2011 model of Corrias, *et al.* [22]. Short summaries of the Purkinje-fiber models due to Noble [14], McAllister, *et al.* [15], and DiFrancesco [16] can be found in Refs. [17, 18]; we present brief overviews of the remaining Purkinje-fiber models.

We use the model of Stewart, *et al.* [18], who have developed a mathematical model for a human Purkinje cell by modifying two major ionic currents, namely, the transient outward current I_{to} and the inward rectifier K^+ current I_{K1} in the human ventricular-cell mathematical model developed by ten Tusscher and Panfilov (henceforth the TP06 model) [13]; furthermore, this Purkinje-cell model includes two more ionic currents, namely, the sustained K^+ current I_{sus} and the hyperpolarization-activated current I_f ; the maximal channel conductances for the Na^+ current (I_{Na}) and for both rapid and slow delayed rectifier K^+ currents (I_{Kr} and I_{Ks} , respectively) are modified to observe the correct channel kinetics for this Purkinje cell. This group has studied, for an isolated Purkinje cell, the contribution of individual ionic currents to various features of the action-potential morphology (APM), such as, the maximum upstroke velocity, dV/dt_{max} , the maximum AP amplitude, V_{max} , the maximum of the plateau potential, $V_{plateau}$, and the AP duration (measured at 90 % of repolarization in the final phase of repolarization, denoted by APD_{90}), and the resting membrane potential, V_{rest} ; such studies are carried out by the partial (50 %) or complete (100 %) blocking of the channel for a given ionic current. The main focus of this study is to quantify how the autorhythmic cycle length (CL) varies as a function of the individual ionic currents for a single Purkinje cell.

Aslanidi, *et al.* [19] have modelled a canine Purkinje cell by modifying major ionic currents, such as, the L-type and T-type Ca^{2+} currents, I_{CaL} and I_{CaT} , the transient outward current, I_{to} , the fast and slow delayed rectifier currents, I_{Kr} and I_{Ks} , and the inward rectifier K^+ current, I_{K1} , of the original canine model developed for an endocardial cell [23]. They have compared (a) the AP and the ionic currents in their Purkinje-cell model with their counterparts in the original mathematical model for canine myocytes and (b) AP morphological properties, such as, dV/dt_{max} , V_{max} , $V_{plateau}$, APD_{90} , and V_{rest} , and the restitution of the AP with experimental results; they obtain good agreement with such experiments.

Sampson, *et al.* [20] have developed a mathematical model for a Purkinje-cell by using the major membrane currents from experimental data from an isolated canine Purkinje cell. They have also updated the kinetics of the ion channels compared to earlier Purkinje-cell models [18, 19] and have studied the contribution of ionic currents to the Purkinje action potential by suppressing, partially or completely, the corresponding channel conductances; and they have compared their results with experimental results on Purkinje cells (in these experiments drugs are administered to block some specific ion channels).

Li, *et al.* [21] have developed a mathematical model for a canine, Purkinje-cell model by incorporating Ca^{2+} cycling; this part of their model differs greatly from its counterpart in the mathematical model for a canine ventricular myocyte. With these models, they study the properties of the action-potential-duration restitution (APDR) for both isolated Purkinje and myocyte cells and, because their model accounts for Ca^{2+} dynamics in detail, they also study Ca^{2+} alternans.

Corrias, *et al.* [22] have modelled rabbit Purkinje cell with inputs from experimental data; and they have studied the AP morphology for such a cell.

ten Tusscher, *et al.* [17] have developed a mathematical model for a Purkinje cell by modifying their (TP06) model for a human ventricular cell [13]. In essence, they have adjusted two conductances, namely, G_{Na} (associated with the fast sodium current I_{Na}) and G_{Ks} (associated with the slow delayed rectifier current I_{Ks}) in the TP06 model to obtain a higher upstroke velocity \dot{V}_{max} and a longer action potential duration (APD) than those in a ventricular myocyte cell.

One of the basic goals of developing such complex, but ionically realistic, mathematical models for Purkinje cells is to characterize the AP morphology, alternans, APDR, and the ion dynamics in great detail. The results from numerical studies of such models have been compared with experimental results to validate the models. Once this validation has been carried out, as, e.g., in some of the studies mentioned above [18–21], it is important to investigate the contribution of Purkinje fibers to

electrical-impulse propagation in mathematical models for cardiac tissue, which include both myocytes and Purkinje fibers, to enhance our understanding of arrhythmias such as VT and VF (see below). Only a few groups have studied the contribution of Purkinje fibers to the propagation of electrical signals in *in vitro* and *in silico* studies. In these *in silico* studies, Purkinje fibers are modelled as a two-dimensional (2D), network-type structure embedded in the interior of ventricular tissue, namely, the endocardium. We give a brief overview of the results of such studies.

Arnar, *et al.* [24] have studied the origin of focal electrical activities that lead to VT, in canine cardiac tissue, by using an activation-mapping technique. They have shown that more than 60% of the cases of such VT originate from the Purkinje-fiber system; they have also studied the activation delay of such focal electrical activity from the Purkinje fibers to epicardial and endocardial layers. In another study, Arnar, *et al.* [25] have shown that such VT, which originates in the Purkinje-fiber system, can be controlled by changing the electrical-activation properties via α_2 -adrenoceptors in Purkinje fibers. Xing, *et al.* [26], have studied the propagation delay of electrical waves from Purkinje fibers to endocardial tissue, from the endocardium to the mid-myocardium, and from the mid-myocardial to the epicardial layers in *in vitro*, activation-mapping experiments on canine cardiac tissue. Similar studies by Tabereaux, *et al.* [27] have shown that electrical activation can appear focally in the endocardium because of autorhythmic activities in the Purkinje system; such focal activation in the endocardial layer may help to produce abnormal or trigger activities, which can maintain pre-existing VF in the ventricular myocardium. These studies show that the Purkinje system plays a significant role in electrical activation and, thereby, affects VT and VF in cardiac tissue.

Computational studies have also investigated the contribution of the Purkinje network to the electrical activation in ventricular models. In particular, they have studied the electrical-activation sequence and its propagation delay as it travels from the Purkinje system through the ventricular layers. For example, Vigmond, *et al.* [28] have studied the electrical activation in an isolated, anatomically realistic, Purkinje network, which is based on a rabbit heart and with the network embedded in a mathematical model for ventricular tissue; these authors have used the model of DiFrancesco, *et al.* [16] for the Purkinje system and the modified, Beeler-Reuter model [29] for the ventricular system. Numerical simulations have been performed by ten Tusscher, *et al.* [17] of a human-ventricular model in an anatomically realistic geometry and with the His-Purkinje system; they have studied the

electrical-activation sequence here and have also investigated bundle-branch reentry.

Aslanidi, *et al.* [19] have studied the relation between the conduction velocity (CV) and its safety factor (SF), which is the ratio of the charge generated in and the charge consumed by a cell during its excitation, at a Purkinje-ventricular junction (PVJ) of a domain that contains a transmural slice of ventricular tissue connected to a thin strip of Purkinje tissue. In their computational study they have calculated CV and SF for different values of structural and functional parameters, such as, the width d of the Purkinje tissue and its diffusion coefficient D . They have shown that neither very fast nor very slow conduction is safe; but there is an optimal velocity that provides the maximum SF for conduction through the junction; and the conduction-time delay across the PVJ is a natural consequence of the electrophysiological and morphological differences between the Purkinje-fiber system and ventricular tissue.

Bordas, *et al.* [30] have carried out numerical simulations of electrical activation in ventricles, with a realistic, free-running, Purkinje-network system and the bundle of His, and a rabbit-ventricular model in an anatomically detailed geometry, obtained from a high-resolution, magnetic-resonance (MR) data set; their Purkinje network is also obtained from such an MR data set. These authors have shown that the inclusion of the Purkinje system results in slightly faster and more coordinated activation of the ventricles than in a simple, ventricular model that neglects the Purkinje-fiber system.

Recent studies by Cherry, *et al.* [31] have investigated electrical-wave propagation in a two-dimensional (2D) simulation domain comprising a mathematical model for ventricular tissue with a Purkinje system. They have used the canine mathematical model of Hund, *et al.*, [32] to model their ventricular tissue; to model the Purkinje system they have followed Aslanidi, *et al.* [19], for the ionic currents; for the network they have used a digitized-reconstruction technique in conjunction with a high-resolution photograph of a canine ventricle; they have connected their Purkinje network to the endocardial layer at the terminating ends of the network. Their study has shown that the inclusion of the Purkinje network can either accelerate reentry termination or generate wave breakup (which does not occur if the same initial condition is used in the ventricle tissue alone).

To the best of our knowledge, hardly any computational studies have investigated the effects of the Purkinje-fiber system on spiral-wave dynamics in an ionically realistic mathematical model for cardiac tissue, an important exception being the recent study by Cherry *et al.* [31]. To make up for this lacuna, we carry

out a systematic numerical study of spiral-wave dynamics in the human endocardial model developed by ten Tusscher *et al.* [13], in which we include the human, Purkinje-fiber model developed by Stewart *et al.* [18]; because we use both endocardial (E) and Purkinje (P) cells, we refer to our mathematical model as the EP-tissue model. We also study the efficacy of a low-amplitude control scheme, which has been suggested for the control of spiral-wave turbulence in mathematical models for cardiac tissue [8, 9, 33, 34], in our EP-tissue model; such low-amplitude-control schemes have never been studied in mathematical models of cardiac tissue that include Purkinje fibers. We begin with a brief overview of our principal results.

We first carry out systematic numerical studies on a composite, single-unit cell that contains an endocardial cell (E cell) and a Purkinje cell (P cell); we call this unit an EP composite. Our results show that the gap-junctional, diffusive coupling D_{gap} at the PVJ in an EP composite is responsible for the slow cycle length of autorhythmic activity of the P cell. We also observe that the APDR of an E cell in an EP composite can be altered by changing the value of D_{gap} ; thus, we can expect that D_{gap} is an important control parameters that should govern the dynamics of the propagating waves in cardiac tissue.

The remaining part of this paper is organized as follows. In Sec. 5.2, we describe the formulation of our EP model, for a single, composite cell and for 2D tissue; we also describe the numerical schemes that we use. In Sec. 5.3, we present the results of our numerical calculations of spiral-wave dynamics in our EP-tissue model; we then describe the low-amplitude control scheme, which we have developed earlier [33, 34], for the elimination of spiral-wave turbulence in models for cardiac tissue and examine its efficacy in our 2D EP-tissue model. In Sec. 5.4, we discuss the results of our calculations and compare them with results from other experimental and computational studies in this area. The Supplementary Material S1 contains a detailed specification of the human-endocardial and Purkinje models, with a list of all the variable we use, the equations that govern their evolution, their initial values, and the additional figures that augment the results in the main body of this paper.

5.2 Methods

The dynamics of E and P cells is governed by the following ordinary differential equations (ODEs) [35, 36]

$$C_m \frac{\partial V_m}{\partial t} = -I_{ion,m} + I_{ext,m}, \quad (5.1)$$

where m stands either for an E cell or a P cell and, for the cell m , C_m is the capacitance per unit surface area of the cell, V_m is the transmembrane potential, $I_{ion,m}$ is the sum of all the ionic currents that cross the cell membrane, and $I_{ext,m}$ is the externally applied current.

We use biophysically realistic ionic models for human endocardial and Purkinje cells; these models have been developed recently. In particular, we use (a) the ventricular model developed by ten Tusscher, *et al.* (the TP06 model) [13], and (b) the Purkinje model developed by the Stewart, *et al.* [18]. The equations for these models, including the ordinary differential equations for the ion-channel gating variables and the ion dynamics, are given in the Supplementary Material S1.

When an EP composite is coupled, via a heterocellular coupling, at a PVJ site with strength κ [37], the transmembrane potentials for the E and P cells obey the following equations:

$$\frac{\partial V_e}{\partial t} = -\frac{I_{ion,e}}{C_e} - \kappa(V_e - V_p); \quad (5.2)$$

$$\frac{\partial V_p}{\partial t} = -\frac{I_{ion,p}}{C_p} + \kappa(V_e - V_p); \quad (5.3)$$

here, $\kappa = D_{gap}/\Delta z^2$ decides the amount of flux that flows from the Pcell to the E cell (or vice versa) because of the coupling between E and P cells.

In our two-dimensional (2D) model, we arrange Purkinje fibers in a sheet [38] that lies on top of a layer of endocardial cells. We allow the P cells in the top layer to be connected to the E cells in the bottom layer at some, but not necessarily all, sites; at these sites, we have EP composites that follow Eqs. (5.2) and (5.3) [38,39]; the cells in each layer are coupled diffusively, with diffusion constants D_{mm} and D_{pp} for the endocardial and Purkinje layers, respectively. The motivation for developing such bilayer 2D model comes from Refs. [24–26], which study the electrical-activation delay from Purkinje fibers to the epicardial surface in *in vitro* experiments by using an activation-mapping technique; by doing so, these studies construct the electrical-activation pattern of Purkinje, endocardial, and epicardial layers. Our 2D, bilayer, EP-tissue model can be thought of as a very simple approximation for endocardial tissue with Purkinje fibers embedded on its surface.

The transmembrane potentials V_e and V_p of E and P cells, respectively, for such a 2D bilayer simulation domain can be modelled by the following *discrete-reaction-diffusion* equations:

$$\begin{aligned}
\begin{bmatrix} \partial_t V_e(i, j) \\ \partial_t V_p(i, j) \end{bmatrix} &= \begin{bmatrix} 1 & 0 \\ 0 & 1 \end{bmatrix} \begin{bmatrix} \frac{-I_{ion,e}(i, j)}{C_e} \\ \frac{-I_{ion,p}(i, j)}{C_p} \end{bmatrix} + \begin{bmatrix} D_{gap} & 0 \\ 0 & D_{gap} \end{bmatrix} \begin{bmatrix} \frac{V_p(i, j) - V_e(i, j)}{(\Delta z)^2} \\ \frac{V_e(i, j) - V_p(i, j)}{(\Delta z)^2} \end{bmatrix} \\
&+ \begin{bmatrix} D_{ee} & 0 \\ 0 & D_{pp} \end{bmatrix} \begin{bmatrix} \frac{V_e(i+1, j) - 2V_e(i, j) + V_e(i-1, j)}{(\Delta x)^2} + \frac{V_e(i, j+1) - 2V_e(i, j) + V_e(i, j-1)}{(\Delta y)^2} \\ \frac{V_p(i+1, j) - 2V_p(i, j) + V_p(i-1, j)}{(\Delta x)^2} + \frac{V_p(i, j+1) - 2V_p(i, j) + V_p(i, j-1)}{(\Delta y)^2} \end{bmatrix};
\end{aligned} \tag{5.4}$$

here D_{ee} and D_{pp} represent, respectively, diffusion constants in the endocardial and Purkinje layers.

We use a 2D square domain consisting of two layers with 1024×1024 grid points and lattice spacing $\Delta x = \Delta y = 0.25$ mm, so the side of each square domain is $L = 256$ mm; one of these layers contains endocardial cells and the other Purkinje cells. These two layers are separated by a distance $\Delta z = 0.25$ mm. We use a forward-Euler method for the time evolution of the transmembrane potentials with a time step $\Delta t = 0.02$ ms. We use *no-flux* (Neumann) boundary conditions on the edges of the simulation domain.

To examine the spatiotemporal evolution of the transmembrane potentials, we obtain the local time series of $V_m(x, y, t)$, from the representative point ($x = 125$ mm, $y = 125$ mm) that is shown by an asterisk in all pseudocolor plots of V_m ; here the subscript m can be e (endocardial case) or p (Purkinje case), as we have mentioned above. To obtain the plots of the inter-beat interval ibi , we use this local time series with 4×10^5 data points after removing the initial 0.4×10^5 data points; for the power spectra $E(\omega)$ we use the local time series of V_m with 2×10^5 data points, after the initial 2.4×10^5 data points have been removed to eliminate transients. Furthermore, we show animations of pseudocolor plots of transmembrane potentials as videos, which have 10 frames per second and in which each pseudocolor plot is separated from its predecessor by 8 ms.

5.3 Results

We carry out a set of simulations by examining the properties of the AP of an EP composite with the E and P cells coupled via D_{gap} , as described in Sec. 5.2. We perform simulations by varying D_{gap} in the range $0 \leq D_{gap} \leq D_{mm}$; we do not include values of D_{gap} that exceed the value of D_{mm} because the heterocellular, myocyte-Purkinje coupling is always lower than its homocellular counterparts (i.e., myocyte-myocyte and Purkinje-Purkinje diffusive couplings); therefore, the heterocellular,

Parameter sets	G_{Na} (nS/pF)	G_{kr} (nS/pF)	G_{ks} (nS/pF)	G_{pCa} (nS/pF)	G_{pK} (nS/pF)	σ_f
$\mathcal{P}1$	14.838	0.153	0.392	0.1238	0.0146	1
$\mathcal{P}2$	5×14.838	0.153	0.392	0.1238	0.0146	1
$\mathcal{P}3$	14.838	0.172	0.441	0.8666	0.00219	2

Table 5.1: Parameter sets $\mathcal{P}1$, $\mathcal{P}2$, and $\mathcal{P}3$ for an endocardial (E) cell in our model; here, σ_f is the scale factor of the time constant τ_f (see Appendix).

diffusion coefficient D_{gap} is lower than D_{mm} ; in particular, Ref. [40] uses a value for D_{gap} that is about 6% of the homocellular coupling.

In our studies, we vary the *time constant* for the f gate, τ_f (see Appendix) and the four ionic conductances [13] for the E cell; these are (a) G_{Kr} , related to rapid-delayed-rectifier-current of K^+ , namely, I_{Kr} , (b) G_{Ks} , related to slow-delayed-rectifier-current of K^+ , namely, I_{Ks} , (c) G_{pCa} for the plateau Ca^{++} current, I_{pCa} , and (d) G_{pK} for the plateau K^+ current, I_{pK} , to get the parameter sets $\mathcal{P}1$, $\mathcal{P}2$, and $\mathcal{P}3$, which lead, respectively, to states with a rotating-spiral (RS) or broken spirals with spiral turbulence (ST) in the two-dimensional (2D) endocardial, simulation domain (see, Sec. 5.3.2); we list these parameters in Table. 5.1.

5.3.1 An EP composite

Purkinje cells can display autorhythmicity [1, 41] when the sinoatrial node (SAN) fails to fire action potentials; occasionally, premature impulses can be transmitted

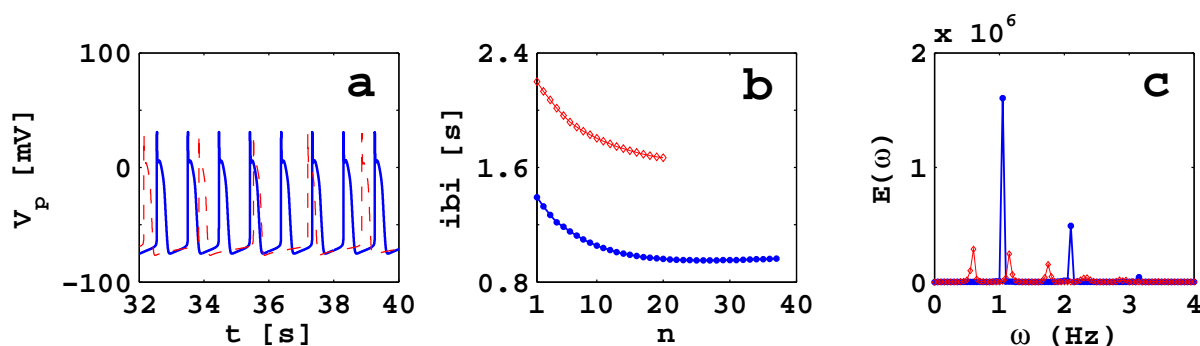


Figure 5.1: Autorhythmic activity of an isolated Purkinje cell and an EP composite with $D_{gap} = D_{mm}/900$. (a) Plots of the Purkinje action potential V_p for an isolated Purkinje cell (blue, solid lines) and an EP composite (red, dashed lines); (b) the inter-beat interval (ibi) versus the beat number n (see Methods for the length of the time series) for an isolated Purkinje cell (blue, filled circles) and an EP composite (red, open diamonds); (c) power spectra $E(\omega)$ versus the frequency ω (see Methods) an isolated Purkinje cell (blue, filled circles) and an EP composite (red, open diamonds).

to the ventricles by Purkinje fibers if a conduction delay occurs in the atrioventricular node (AVN). A Purkinje cell has a longer action potential duration (APD) than a myocyte and it can fire an AP with between 15 – 40 beats per minute. Therefore, we have carried out simulations to examine how the autorhythmic activity of a P cell changes, in our EP composite (Eqs. (5.2) and (5.3)), as a function of D_{gap} . Figure 5.1(a) shows plots of the transmembrane potential V_p for an isolated Purkinje cell (blue solid lines) and an EP composite (red dashed lines), with $D_{gap} = D_{mm}/900$, in the time interval $32 \leq t \leq 40$ s; the corresponding plots of the interval-beat intervals (ibi), calculated with time series data of length 2×10^6 , versus the beat number n are shown in Fig. 5.1(b); Fig. 5.1(c) shows plots of the power spectra $E(\omega)$ versus the frequency ω (obtained from time-series of V_p of length 10^6 after removing the initial 10^6 data points). We find that an isolated Purkinje cell fires APs with a cycle length $CL \simeq 1.3$ s and with $APD_{90\%} \simeq 324$ ms (here, $APD_{90\%}$ is the time at which the AP attains 90% of its final repolarization value); in contrast, $CL \simeq 2.1$ s and $APD_{90\%} \simeq 331$ ms for an EP composite with $D_{gap} = D_{mm}/900$; in both these cases $APD_{90\%}$ is greater than that for an isolated endocardial cell (for which it is $\simeq 304$ ms [17, 42]). We do not calculate the APD and CL of an EP composite by pacing the Purkinje cell externally; such external pulses, with a certain cycle, arise because of the pacemaker activities of the SAN. Therefore, the autorhythmic activity of a P cell is completely suppressed by the SAN pacemaker activities, and the P cell in an EP composite fires a train of APs with the same cycle length as those from the SAN. Hence, the autorhythmic cycle of an EP composite, when paced externally, is independent of D_{gap} .

In our first set of simulations, we excite (a) an endocardial cell, (b) a Purkinje cell, and (c) both cells in an EP composite by applying a current pulse of strength 52 pA/pF for 3 ms; we then observe the AP for these three cases. We also compute the flux that flows from the E to the P cell during the course of an AP. These simulations help us to understand the basic mechanism of the propagation delay of electrical waves as they travel from the Purkinje fibers to the endocardium and vice-versa, which we have described briefly in Sec. 5.1. We show the results of our simulations for an EP composite for two representative values of D_{gap} , namely, $D_{gap} = D_{mm}/10$ and $D_{gap} = D_{mm}/100$. Figure 5.2(a) shows plots of the Purkinje action potential V_p (full symbols and solid lines) and the endocardial action potential V_e (open symbols and dashed lines), when an external stimulus is applied to both cells; here, blue squares and red triangles represent $D_{gap} = D_{mm}/10$ and $D_{gap} = D_{mm}/100$, respectively; and black circles show the plot for an uncoupled endocardial cell. In Fig. 5.2(b) we show plots similar to those in Fig. 5.2(a), but with the stimulus

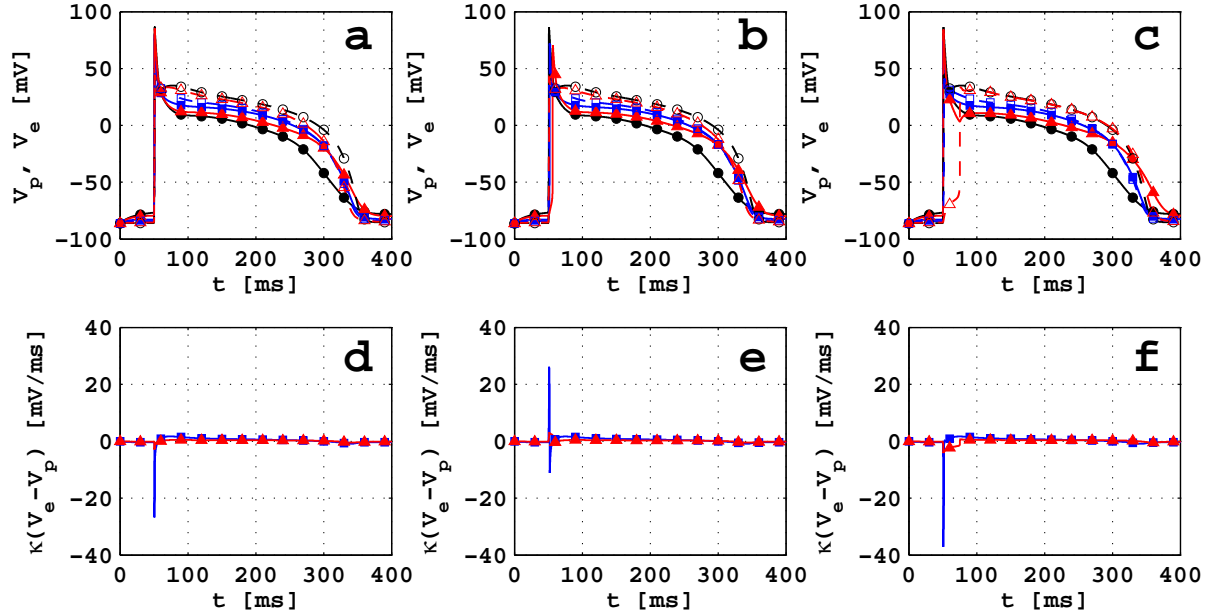


Figure 5.2: Action potentials for E and P cells coupled diffusively via the heterocellular gap-junctional coupling D_{gap} : (a) Plots of the action potentials V_p (full symbols and solid lines) and V_e (open symbols and dashed lines), when a stimulus of strength 52 pA/pF is applied, for 3 ms, to both cells in our EP composite with $D_{gap} = D_{mm}/10$ (blue squares), $D_{gap} = D_{mm}/100$ (red triangles), and uncoupled cells, i.e., $D_{gap} = 0$ (black circles). (b) Plots as in (a), but with a stimulus applied to the E cell only. (c) Plots as in (a), but with a stimulus applied to the P cell only. (d) Plots of the rate of change of potential, $\kappa(V_e - V_p)$, versus t , with parameters and symbols as in (a). (e) and (f): Plots as in (d), but with parameters as in (b) and (c), respectively.

applied only to the endocardial cell in an EP composite; analogous plots are shown in Fig. 5.2(c), but with the stimulus applied only to the Purkinje cell in an EP composite. In Figs. 5.2(d), (e), and (f) we show the rate of change of the potential, i.e., $\kappa(V_e - V_p)$, between E and P cells; we see spikes in the downward direction in the depolarization phase of the AP, when the stimulus is applied to both cells (Fig. 5.2(d)) and P cells only (Fig. 5.2(f)); this implies that the flow of flux from the P cell to the E cell occurs in this early phase of depolarization, i.e., the P cell acts as a stimulation-current source for the E cell. If, instead, we apply a stimulus to the E cell in an EP composite, we see spikes in both directions in the depolarization phase of the AP (Fig. 5.2(e)); this ensures that the flux is in both directions, i.e., a P cell can behave both as a source and a sink.

The restitution of the action potential duration (APD) plays an important role in the stability of spiral waves in mathematical models for cardiac tissue [44–48]. It has been postulated that a steep, increasing, initial segment in the action-potential-duration-restitution (APDR) curve, a plot of the APD versus the diastolic

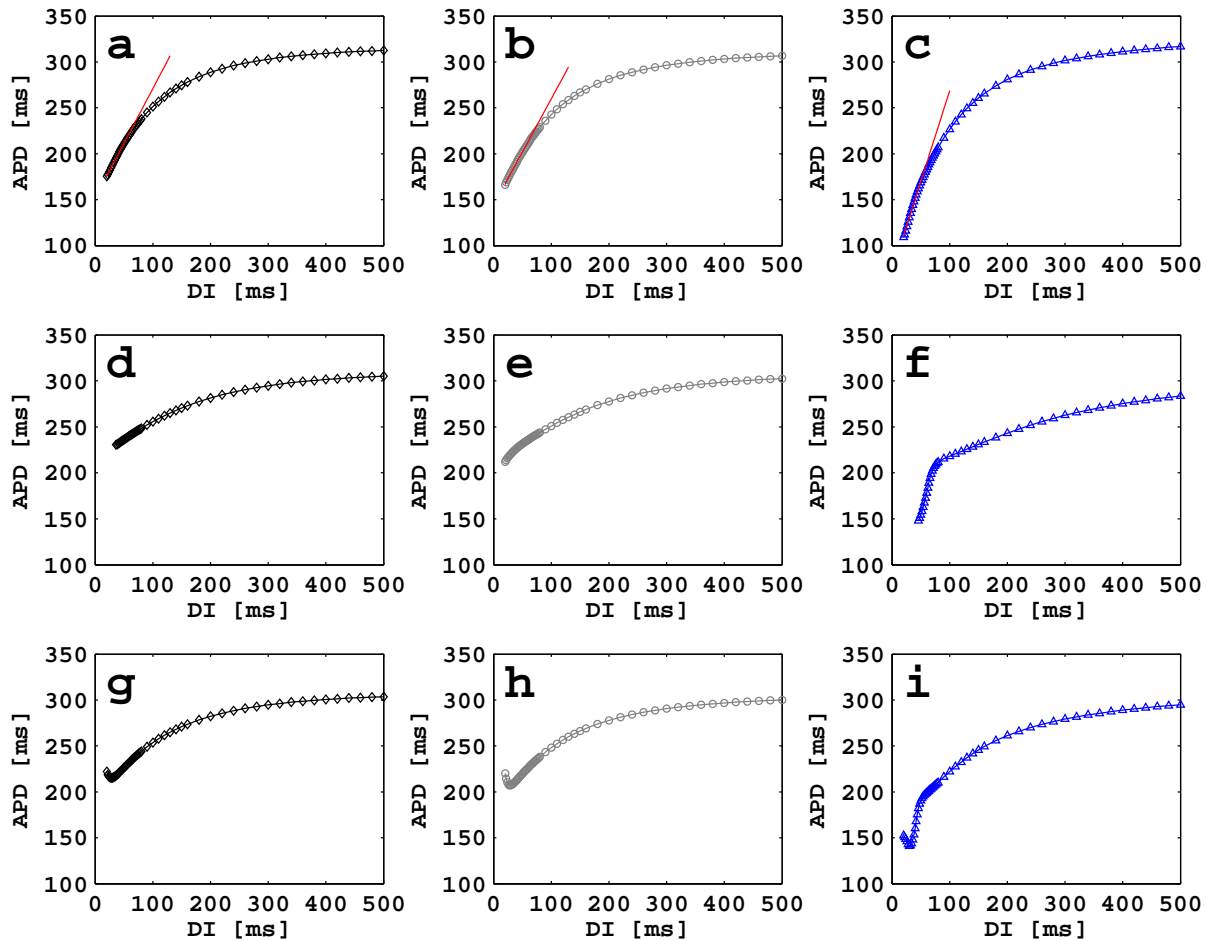


Figure 5.3: Action potential duration restitution (APDR) of an endocardial (E) cell with different sets of parameters (see text). The plots in (a), (b), and (c) show the APDR for an isolated E cell for parameter sets \mathcal{P}_1 , \mathcal{P}_2 , and \mathcal{P}_3 (see Table. 5.1), respectively. The plots in (d), (e), and (f) are, respectively, the analogs of (a), (b), and (c) for our EP composite with $D_{gap} = D_{mm}/10$; and their counterparts, for $D_{gap} = D_{mm}/100$ are shown, respectively, in (g), (h), and (i). We find the slopes of the APDR curve by fitting the initial 20 data points, in such APDR plots, with straight lines, as shown, e.g., in (a), (b), and (c), where the slopes of the APDR are $\simeq 1.1$, $\simeq 1.1$, and $\simeq 2.0$.

interval (DI), leads to a spiral-wave instability. Therefore, we carry out a set of simulations to obtain such a plot for an isolated E cell and an EP composite. In Figs. 5.3(a), (b), and (c), we show, respectively, the static APDR of an endocardial cell for parameter sets \mathcal{P}_1 , \mathcal{P}_2 , and \mathcal{P}_3 (Table. 5.1); we apply a series of 50 S1 pulses, of basic cycle length (BCL) 300 ms and strength 1500 pA/pF, before we apply the final S2 pulse, for which we keep BCL in the range 20 ms to 500 ms. We calculate the slopes of the APDR curves by fitting straight lines to the initial 20 data points (see red straight lines in Figs. 5.3(a), (b), and (c)); these slopes are $\simeq 1.1$, $\simeq 1.1$, and $\simeq 2.0$ for parameter sets \mathcal{P}_1 , \mathcal{P}_2 , and \mathcal{P}_3 , respectively, for an isolated E cell. In

Figs. 5.3(d), (e), and (f), we show similar plots for a P cell coupled to an E cell in an EP composite with $D_{gap} = D_{mm}/10$; analogous plots are shown in Figs. 5.3(g), (h), and (i), for $D_{gap} = D_{mm}/100$. Note that, for the EP composite with $D_{gap} = D_{mm}/10$, the APDR slope decreases, relative to its value for an isolated E cell, for parameter sets $\mathcal{P}1$ and $\mathcal{P}2$, and first increases (for $50 \leq DI \leq 100$ ms) and then decreases for the parameter set $\mathcal{P}3$; However, when $D_{gap} = D_{mm}/100$, the variation of APD as function of DI , for an EP composite, shows biphasic behavior for all these three parameter sets.

5.3.2 Wave dynamics in a 2D simulation domain

We begin with our investigations of wave dynamics in individual layers of E and P cells and then study wave propagation in both cable-type and 2D, bilayer, EP domains, in which E cells in a layer are connected to P cells in the adjoining layer, as we have described in Sec. 5.2. We use the following two representative values of diffusive gap-junctional couplings: (a) $D_{gap} = D_{mm}/10$ and (b) $D_{gap} = D_{mm}/100$, where $D_{mm} = 0.00154 \text{ cm}^2/\text{ms}$. Wave dynamics in a 2D bilayer, whose EP composites are coupled with values that lie in the range $D_{mm}/100 \leq D_{gap} \leq D_{mm}/10$, are qualitatively similar to those for one of the above specified D_{gap} values. We allow for connections between E and P cells in an EP composite bilayer at various, periodically-spaced points in our simulation domain; these points are the analogs of Purkinje-ventricular junctions (PVJs) in our mathematical model. We now study the dependence of spiral-wave dynamics in our EP composite bilayer as a function of the density of PVJs; we use the following values for \mathcal{R} , the ratio of the total number of sites to the number of PVJs in our simulation domain: (a) $\mathcal{R} = 1$, (b) $\mathcal{R} = 2$, (c) $\mathcal{R} = 4$, (d) $\mathcal{R} = 8$, (e) $\mathcal{R} = 16$, and (f) $\mathcal{R} = 32$.

Plane waves in a cable

To study plane-wave propagation we use a cable-type domain, which is a thin domain, consisting of 4096×64 grid points (gpts), with spacing $\Delta x = 0.25$ mm, i.e., edge lengths $L_x = 1024$ mm and $L_y = 16$ mm. We use the parameter sets $\mathcal{P}1$, $\mathcal{P}2$, and $\mathcal{P}3$ (Table 5.1) for the endocardial cable layer. Reference [43] suggests that the conduction velocity CV for a Purkinje-fiber network lies in the range 200–300 cm/s; therefore, we adjust the value of D_{pp} , the diffusive, gap-junctional coupling between P cells, to obtain CV in this range (see below). To initiate a plane wave, we apply a stimulus current $I_{stim} = 150$ pA/pF for 3 ms at the left end of the cable. We then measure CV and the wave length λ , in this cable-type domain, by recording the positions of the wave front at times t and $t + \delta t$ and by using $CV = \delta x / \delta t$, where δx is

the distance travelled by the wave front in the time interval δt . We locate the position of the wave front by finding the value of x at which $V_m \simeq 0$ mV; we define the position of the wave back as the point, behind the wave front, at which a secondary action potential can just be initiated by an additional stimulus (this turns out to occur at a value of $V_m \simeq 75\%$ of the repolarization phase of the AP). We obtain λ by measuring the distance between the wave front and the wave back at time t .

In Figs. S1(a)-(f) in the Supplementary Material S1, we show pseudocolor plots of the transmembrane potential V_m at time $t = 400$ ms in our cable-type domain for (a) E cells with the parameter set $\mathcal{P}1$, (b) E cells with the parameter set $\mathcal{P}2$, (c) E cells with the parameter set $\mathcal{P}3$, (d) P cells with $D_{pp} = D_{mm}$, (e) P cells with $D_{pp} = 2 \times D_{mm}$, and (f) P cells with $D_{pp} = 3 \times D_{mm}$. These plots show that the parameter sets $\mathcal{P}1$, $\mathcal{P}2$, and $\mathcal{P}3$ yield $CV \simeq 71$ cm/s and $\lambda \simeq 216$ mm, $CV \simeq 103$ cm/s and $\lambda \simeq 315$ mm, and $CV \simeq 71$ cm/s and $\lambda \simeq 216$ mm, respectively, for the case of E cells. For P cells we require $D_{pp} = 3 \times D_{mm}$ to obtain a biophysically reasonable value of CV for the Purkinje cable; in particular, we obtain $CV \simeq 210$ cm/s and $\lambda \simeq 580$ mm for $D_{pp} = 3 \times D_{mm}$; therefore, we choose $D_{pp} = 3 \times D_{mm}$ to study wave dynamics in 2D layers of EP composites, in all the calculations that follow. The Video S1 has six animations that show the spatiotemporal evolution of the plane waves depicted in Figs. S1(a)-(f).

We now couple two layers of cable-type domains, with E cells in one layer and P cells in the other, at PVJ sites and examine the dependence, of plane-wave propagation, on \mathcal{R} . In Figs. 5.4, we show the evolution of the transmembrane potential, in both endocardial and Purkinje layers, with $D_{gap} = D_{mm}/10$ and the parameter set $\mathcal{P}1$; we apply the stimulus current (see section on Methods) to the left end of the endocardial simulation domain. Figures 5.4(e1), (e2), (e3), (e4), and (e5) are, respectively, the pseudocolor plots of V_e at time $t = 400$ ms for $\mathcal{R} = 1, 2, 4, 8,$ and 16 ; the corresponding plots for V_p are shown, respectively, in Figs. 5.4(p1), (p2), (p3), (p4), and (p5); the Video S2 has ten animations that show the spatiotemporal evolutions of V_e and V_p for these cases. The presence of D_{gap} at the PVJ within such range of values provides an idealised realization of a Purkinje sheet, albeit one with a regular network. Note that $CV = 202$ cm/s and $\lambda = 615$ mm, in both E and P layers, if $\mathcal{R} = 1$; these are close to the values of CV and λ in an isolated P layer; if $\mathcal{R} = 2$, there is a slight increase of λ and a decrease of CV . For $\mathcal{R} = 1$ and $\mathcal{R} = 2$, plane-wave dynamics in the E layer follows that in the P layer. However, if $\mathcal{R} = 4, 8,$ and 16 , the values of CV and λ in the E layer (in the EP bilayer) are roughly equal to their values in an uncoupled E layer; however, conduction delay occurs in the P layer, and multiple plane waves are initiated after the P layer recovers because of the

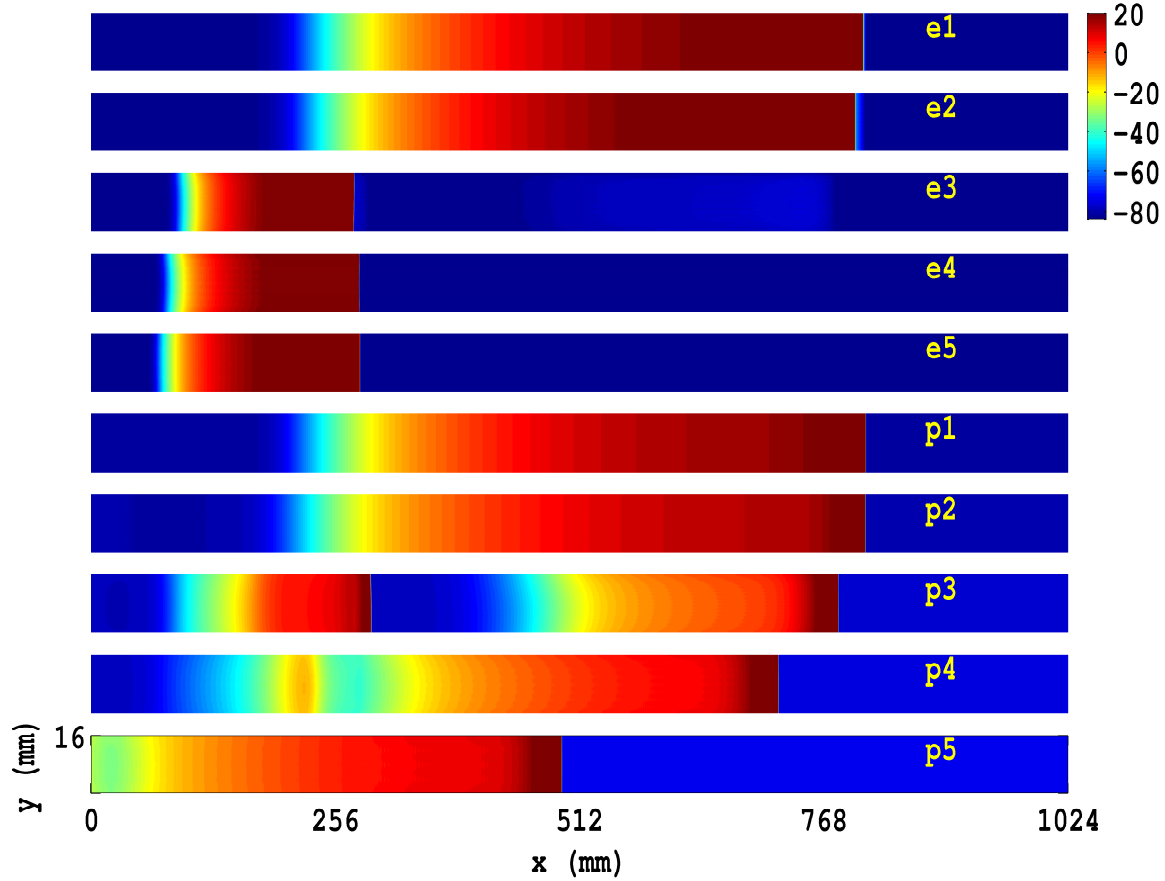


Figure 5.4: Plane-wave propagation in a cable-type, EP-bilayer domain: Pseudocolor plots of V_e ((e1)-(e5)) and V_p ((p1)-(p5)), at $t = 400$ ms in a thin, cable-type EP-bilayer domain (see text), whose dimension is $L_x = 1024$ mm and $L_y = 16$ mm, with the $\mathcal{P}1$ parameter set for the E-cell layer, $D_{gap} = D_{mm}/10$, $D_{pp} = 3 \times D_{mm}$ for the P-cell layer, and $\mathcal{R} = 1$ ((e1),(p1)), $\mathcal{R} = 2$ ((e2),(p2)), $\mathcal{R} = 4$ ((e3),(p3)), $\mathcal{R} = 8$ ((e4),(p4)), and $\mathcal{R} = 16$ ((e5),(p5)). The Video S2 illustrates the spatiotemporal evolution of these plane waves.

flow of flux from the plane-wave front, in the E layer, to the P layer via the PVJs (see Figs. 5.4 and the animations in Video S2). This mismatch of the CV in E-cell and P-cell layers and multiple plane waves in the P-cell layer may cause reentrant activity in 2D simulation domains, as suggested in Refs. [17, 19, 27, 28]; we discuss this below. Similar results follow for plane-wave dynamics for parameter sets $\mathcal{P}2$ and $\mathcal{P}3$, with EP composites coupled diffusively, $D_{gap} = D_{mm}/10$, and the values of \mathcal{R} given above (see Videos S3 and S4 for the spatiotemporal evolution of plane waves for parameter sets $\mathcal{P}2$ and $\mathcal{P}3$, respectively). The Videos S5, S6, and S7 have ten animations that show the spatiotemporal evolutions of the waves for the parameter sets $\mathcal{P}2$, $\mathcal{P}2$, and $\mathcal{P}3$ when EP composite are coupled with $D_{gap} = D_{mm}/100$

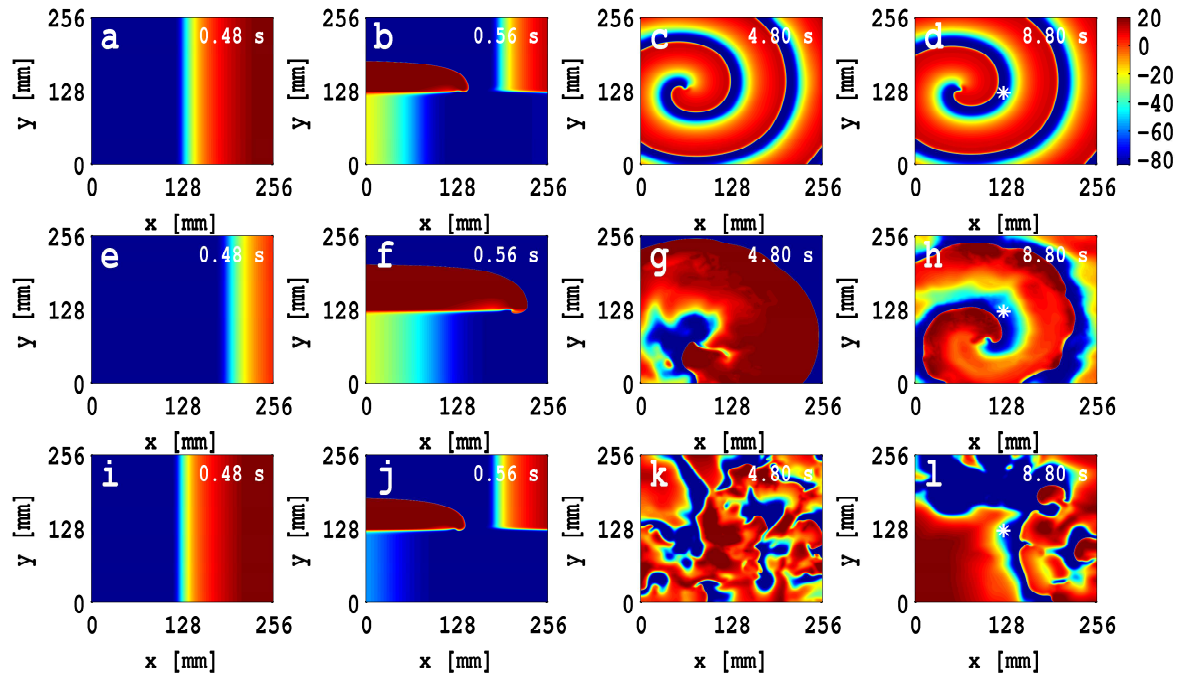


Figure 5.5: Initiation of spiral waves, in a 2D simulation domain consisting of endocardial cells, by using the S1-S2 cross-field protocol. An S2 pulse is applied at time $t = 0.482$ s for all three parameter sets to initiate spirals (see text for details). (a), (b), (c), and (d) show pseudocolor plots of V_e at times $t = 0.48$, 0.56 , 4.8 , and 8.8 s, respectively, for the parameter set $\mathcal{P}1$; their analogs, for the parameter sets $\mathcal{P}2$ and $\mathcal{P}3$ are given, respectively, in (e)-(h) and (i)-(l). The animations (a), (b) and (c) in Video S8 illustrate the spatiotemporal evolution of these spiral waves. To examine the spatiotemporal evolution of V_e , we record the local time series of $V_e(x, y, t)$, from the representative point ($x = 125$ mm, $y = 125$ mm) that is shown by an asterisk in plots (d), (h), and (l).

and $\mathcal{R} = 1, 2, 4, 8$, and 16 ; plane-wave dynamics here are similar to these we have obtained above for $D_{gap} = D_{mm}/10$.

Spiral waves in a 2D domain

We use a slightly modified version of the standard S1-S2 cross-field protocol [49] to initiate a spiral wave in a square simulation domain of side $L = 256$ mm. In this protocol, we apply an S1 stimulus at the left boundary of the domain for a certain interval of time; this initiates a plane wave in the domain. We then apply an S2 stimulus, of the same strength and duration as the S1 stimulus, to the bottom half of the simulation domain; this produces a spiral wave in the medium. We initiate spiral waves in the endocardial, Purkinje, and EP-composite domains by using such S1 and S2 stimuli with strengths 150 pA/pF for 3 ms; we apply the S2 stimulus over the region $0 \text{ mm} \leq y \leq 125 \text{ mm}$.

In Fig. 5.5 we show the initiation of spiral waves in our simulation domain via pseudocolor plots of the endocardial transmembrane potential V_e for a 2D, E layer when an S2 stimulus is applied at time $t = 482$ ms; Figures 5.5 (a), (b), (c), and (d) show V_e at times $t = 480, 560, 4800,$ and 8800 ms, respectively, for the parameter set $\mathcal{P}1$. The exact analogs of the pseudocolor plots of V_e in Figs. 5.5(a)-(d) for parameter sets $\mathcal{P}2$ and $\mathcal{P}3$ are given, respectively, in Figs. 5.5(e)-(h) and Figs. 5.5(i)-(l). The animations (a), (b), and (c) in Video S8 show the time evolution of these spiral waves for the time interval $0 \leq t \leq 8.8$ s and the parameter sets $\mathcal{P}1$, $\mathcal{P}2$, and $\mathcal{P}3$, respectively. To check the spatiotemporal evolution of the transmembrane potential, we examine the local time series of $V_e(x, y, t)$, the inter beat interval (ibi), and the power spectra $E(\omega)$. In Figs. 5.6 (a)-(c) we show these time series; Figures 5.6 (e), (f), and (g) show plots of ibi; in Figs. 5.6 (h), (i), and (j) we show plots of the power spectra $E(\omega)$, which we have obtained from the local time series of V_m . For the parameter set $\mathcal{P}1$, the plots of V_e in Figs. 5.5(c) and (d), and the animation (a) in Video S8, show a single, rotating spiral (RS); the periodic nature of the time series (Fig. 5.6 (a)), the flattening of the ibi (Fig. 5.6 (e)) after the initial 10 beats, and the discrete, strong peaks in $E(\omega)$ (Fig. 5.6 (h)), provide additional evidence for the periodic motion of this spiral wave, whose average rotation period $\tau_{rot} \simeq 210$ ms can be estimated from the ibi plot in Fig. 5.6 (e). The power spectrum shows a peak at the fundamental frequency $\omega_f = 4.75$ Hz and its harmonics; not surprisingly, $\tau_{rot} \simeq 1/\omega_f$. For the parameter set $\mathcal{P}2$, the plots of V_e in Figs. 5.5 (g) and (h) and the animation (b) in Video S8 exhibit single, meandering, spiral turbulence (SMST), in which the spiral arms and core evolve chaotically in space and time; the resulting irregular time series of V_e (Fig. 5.6(b)), the oscillations in the plot of the ibi (Fig. 5.6(f)), and the development of subsidiary peaks in $E(\omega)$ (Fig. 5.6(i)), confirm that the temporal evolution of the SMST state is chaotic. For the parameter set $\mathcal{P}3$, the plots of V_e in Figs. 5.5(k) and (l) and the animation (c) in Video S8 display a state with multiple-spiral turbulence (MST), which leads to an irregular time series for V_e (Fig. 5.6 (c)), a plot of the ibi (Fig. 5.6(g)) that shows irregular oscillations, and a broad-band power spectrum (Fig. 5.6(j)).

In Figs. 5.7(a)-(d) we show pseudocolor plots of the transmembrane potential of the Purkinje layer V_p at the times $t = 360, 440, 4800,$ and 8800 ms, for the diffusive coupling, $D_{pp} = 3 \times D_{mm}$; we apply an S2 stimulus at $t = 360$ ms to initiate spiral wave. The animation (d) in Video S8 shows the spatiotemporal evolution of this spiral wave in the time interval $0 \leq t \leq 8.8$ s; from this animation we see that we have an RS state in the P-cell layer. We also record the time series for V_p from the representative point shown by an asterisk in Fig. 5.7(d); in Fig. 5.7(e) we show

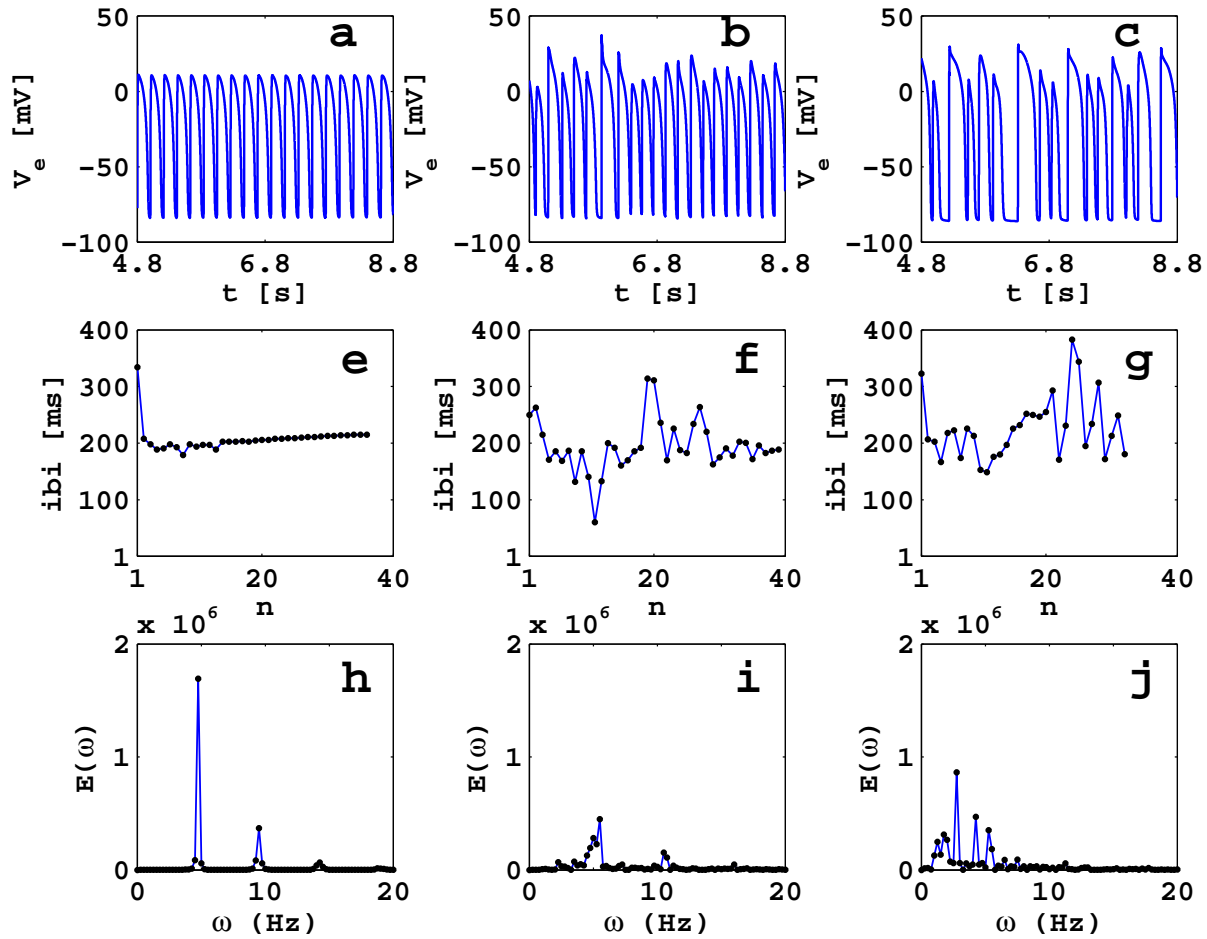


Figure 5.6: Plots of the local time series, inter-beat-interval (ibi), and power spectra $E(\omega)$ for an isolated E-cell layer with the parameter sets $\mathcal{P}1$, $\mathcal{P}2$, and $\mathcal{P}3$. The plots in (a), (b), and (c) show the time series obtained at the position ($x = 125$ mm, $y = 125$ mm), shown by asterisks in Figs. 5.5 (d), (h), and (l), for the parameter sets $\mathcal{P}1$, $\mathcal{P}2$, and $\mathcal{P}3$, respectively. The plots in (d)-(f) and (g)-(i) show, respectively, the ibi and powerspectra calculated by using the above time series (see Methods for the length of time series). The periodic time series (plot (a)), the flattening ibi (plot (d)), after the initial 10 beats, with an average rotation period $\tau_{rot} \simeq 210$ ms, and the discrete, strong peaks in $E(\omega)$ at 4.75 Hz and its harmonics (plot (g)), provide additional evidence for the existence of an RS for the parameter set $\mathcal{P}1$ (see Figs. 5.5(a)-(d) and the animation (a) in Video S8). The irregular time series (plot (b)), the oscillating ibi (plot (f)), and the development of subsidiary peaks in $E(\omega)$ (plot (i)), confirm that the temporal evolution of the state here is quite chaotic; the pseudocolor plots in Figs. 5.5(e)-(h) and the animation (b) in Video S8 show the existence of single, meandering, spiral turbulence (SMST), in which the spiral arms and core evolve chaotically in space and time. An irregular time series (plot (c)), the irregular oscillations in ibi (plot (g)), and a broad-band $E(\omega)$ show the existence of multiple-spiral turbulence (MST) for the parameter set $\mathcal{P}3$ (see Figs. 5.5(i)-(l) and the animation (c) in Video S8).

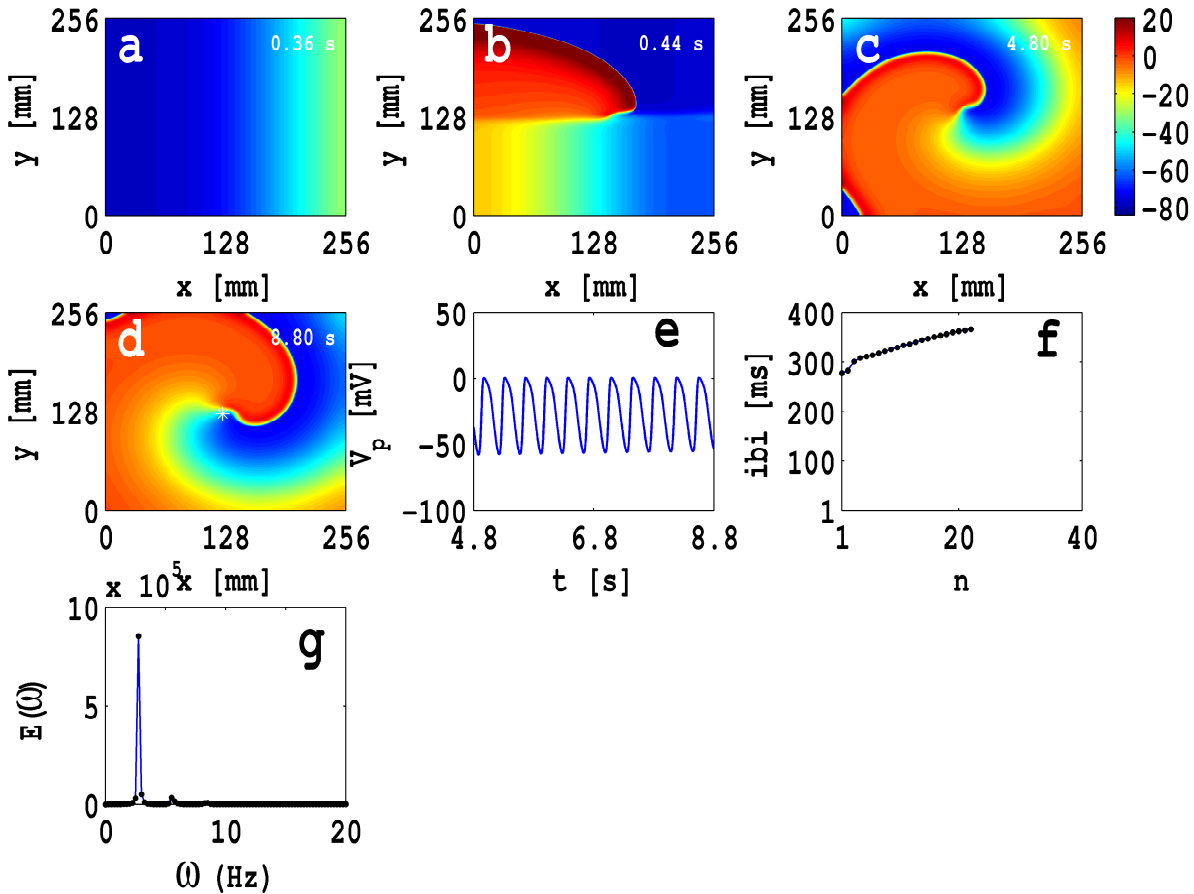


Figure 5.7: Initiation of spiral waves in a 2D simulation domain of Purkinje cells by using S1-S2 cross-field protocol. An S2 pulse is applied at time $t = 0.360$ s to initiate spirals (see text). The plots (a), (b), (c), and (d) show the pseudocolor plots of V_p at times $t = 0.36$, 0.44 , 4.8 , and 8.8 s, respectively, for the diffusive coupling $D_{pp} = 3 \times D_{mm}$. The animation (d) in Video S8 shows the spatiotemporal evolution of this spiral wave. (e) Plot of the local time series recorded at position ($x = 125$ mm, $y = 125$ mm) shown by an asterisk in (d); the plots in (f) and (g) show the ibi and $E(\omega)$ calculated using above time series (see Methods for the length of time series). The periodic time series, and power spectra with discrete peaks with fundamental frequency ($\omega_0 \simeq 2.75$ Hz), are signatures of the existence of a periodic rotating spiral; however, the ibi displays a slight upward trend; this implies that, although the temporal evolution is nearly periodic, there is a slight drift, towards lower frequencies, in the rotation rate of the dominant spiral.

this time series for $4.8 \leq t \leq 8.8$ s. Figure 5.7 (f) displays a plot of the ibi versus n , which shows that, after initial transients that last for the first 5 beats, the spiral wave rotates almost periodically with an average rotation period $\tau_{rot} \simeq 360$ ms. Furthermore, we see that the ibi displays a slight upward trend; this implies that, although the temporal evolution is nearly periodic, there is a slight drift, towards lower frequencies, in the rotation rate of the dominant spiral. In Fig. 5.7 (f) we

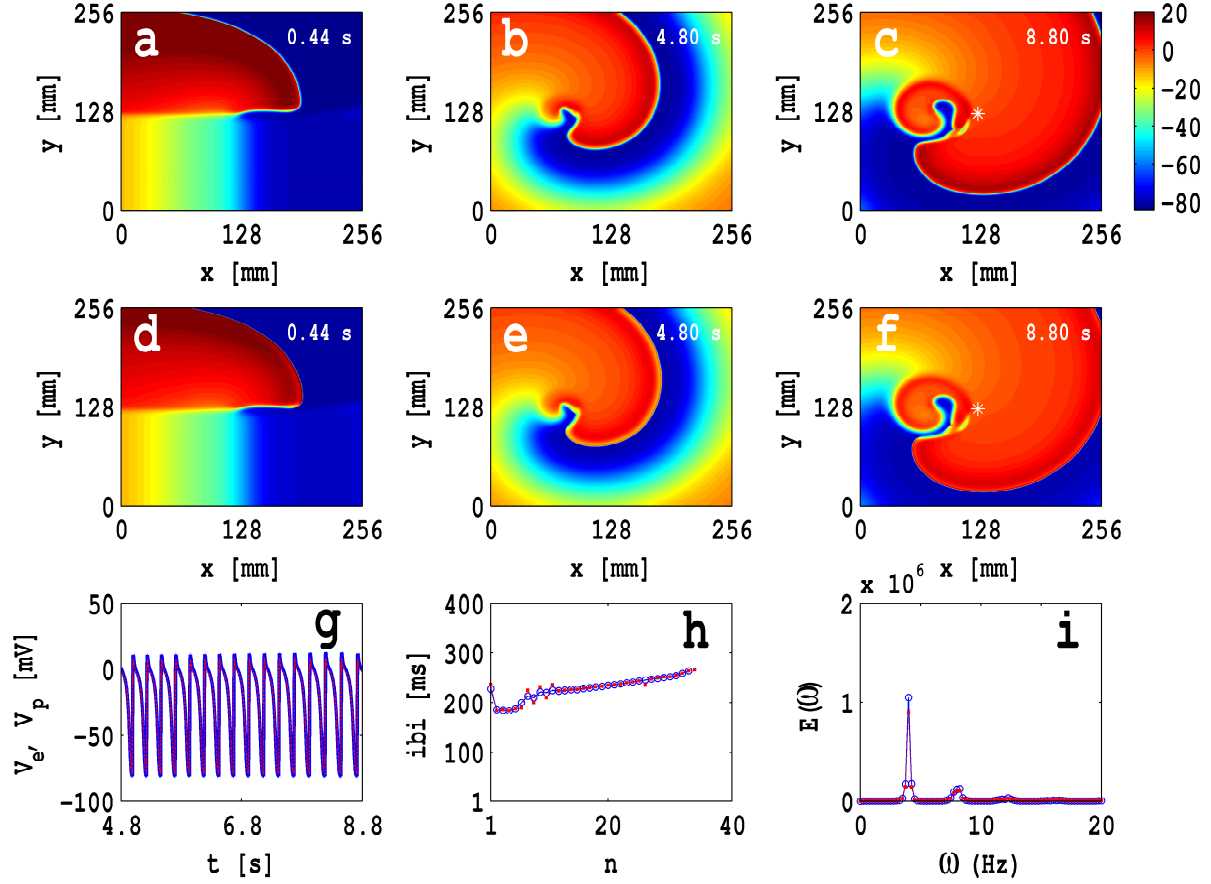


Figure 5.8: Spiral-wave dynamics in our EP-composite bilayer for the parameter set $\mathcal{P}1$, with the S1-S2 cross-field protocol in the E-cell layer, $D_{gap} = D_{mm}/10$, and $\mathcal{R} = 1$ (see Table 5.2); (a)-(c) show pseudocolor plots of V_e ; (d)-(e) show pseudocolor plots of V_p ; the animations in the top-left panel of Video S9 (labelled by $\mathcal{R} = 1$) illustrate the spatiotemporal evolution of these spiral waves. The local time series data, for the transmembrane potential V_e and V_p , are recorded from the representative points ($x = 125$ mm, $y = 125$ mm) of both E- and P- layers (the asterisks in (c) and (f)). (g) Plot of the time series for V_e (blue, solid line) and V_p (red, dashed line); (h) plot of inter-beat interval (ibi) versus the beat number n associated with the E-layer (blue, open circles) and P-layer (filled, red squares); (i) plot of the power spectra $E(\omega)$ versus the frequency ω for the E-layer (blue, open circles) and P-layer (filled, red squares).

show the power spectrum $E(\omega)$ that we have obtained from the local time series of V_p ; $E(\omega)$ has discrete peaks at the fundamental frequency $\omega_f = 2.75$ Hz and its harmonics; not surprisingly, $\omega_f \simeq 1/\tau_{rot}$.

We now carry out a set of simulations to study the spatiotemporal evolutions of spiral waves, for the parameter sets $\mathcal{P}1$, $\mathcal{P}2$, and $\mathcal{P}3$, when an E-cell layer is coupled with a P-cell layer with D_{gap} and \mathcal{R} in the ranges mentioned above. We obtain spiral waves in our EP-composite, 2D bilayer by using the S1-S2 protocol (see Methods) in (a) the E-cell layer, (b) the P-cell layer, or (c) both these layers. The motivation

for this set of simulations comes from the studies in Refs. ??, which study (a) the propagation of electrical signals from the Purkinje system to the endocardium and vice-versa and (b) the propagation delay of these signals under the influence of the SAN system.

In Figs. 5.8(a)-(c), we show, respectively, pseudocolor plots of V_e in the E-cell layer at times $t = 0.44, 4.8,$ and 8.8 s for the parameter set $\mathcal{P}1$ with $D_{gap} = D_{mm}/10$ and $\mathcal{R} = 1$; similar plots are shown in Figs. 5.8(d)-(f) for V_p in the P-cell layer; here, with the S2 stimulus is applied at $t = 360$ ms to the E-cell layer to initiate spiral waves in the EP bilayer; the complete spatiotemporal evolutions of V_e and V_p , given in the first two boxes on the left of the top panel of Video S9, show that the spiral waves in these two layers are very similar and rotate in phase. We record the local time series for V_e and V_p from the representative points, in both E- and P-cell layers, marked by asterisks in Figs. 5.8(c) and 5.8(f); in Fig. 5.8(g), we show these time series for V_e (blue, solid line) and V_p (red, dashed line), which lead to the plots of the ibi versus n shown by blue, open circles (E-cell layer) filled, red squares (P-cell layer) in Fig. 5.8(h); after the initial transients decay, the ibi plots show that the spirals in both layers rotate periodically with an average rotation period $\tau_{rot} = 235$ ms, which is consistent with the inverse of the frequency $\omega_f \simeq 4$ Hz that follows from the power spectra of Figure 5.8(i). Three features are worth noting here: (a) the time series of V_e and V_p (Fig. 5.8(g)) display autorhythmicity, insofar as they show a train of APs that are in phase in the two layers; (b) the plot of the ibi (Figs. 5.8(h)) shows an upward trend, which indicates that the rotation period of the spiral waves increases slowly with time; and (c) τ_{rot} in our EP bilayer assumes an average value that is close to its value in a pure E-cell layer (cf. Fig. 5.6(e)) and considerably smaller than in a pure P-cell layer.

Plots similar to those in Figs. 5.8 are shown in the Supplementary Material in Figs. S2 and S3 for $\mathcal{R} = 2$ and $\mathcal{R} = 4$, respectively, with the S2 stimuli applied at $t = 400$ ms and 480 ms to the E-cell layer to initiate spiral waves in the EP bilayer. The complete spatiotemporal evolution of V_m for these cases is shown in the left part of the middle panel, labelled $\mathcal{R} = 2$, left part of the bottom panel, labelled $\mathcal{R} = 4$, of Video S9. Spiral-wave dynamics, with $\mathcal{R} = 2$ and $\mathcal{R} = 4$, is qualitatively similar to that in the case $\mathcal{R} = 1$ as far as the existence of the RS state is concerned (see above). However, by comparing the animations, which are labelled $\mathcal{R} = 1, \mathcal{R} = 2,$ and $\mathcal{R} = 4$ in Video S9, we see that the width of the spiral-wave arms decreases as \mathcal{R} increases and the rate of rotation of the spiral wave increases; moreover, the premature spiral-wave, which tries to form near the main spiral core for $\mathcal{R} = 1$ and rotates in a sense opposite to that of the principal spiral wave, is suppressed

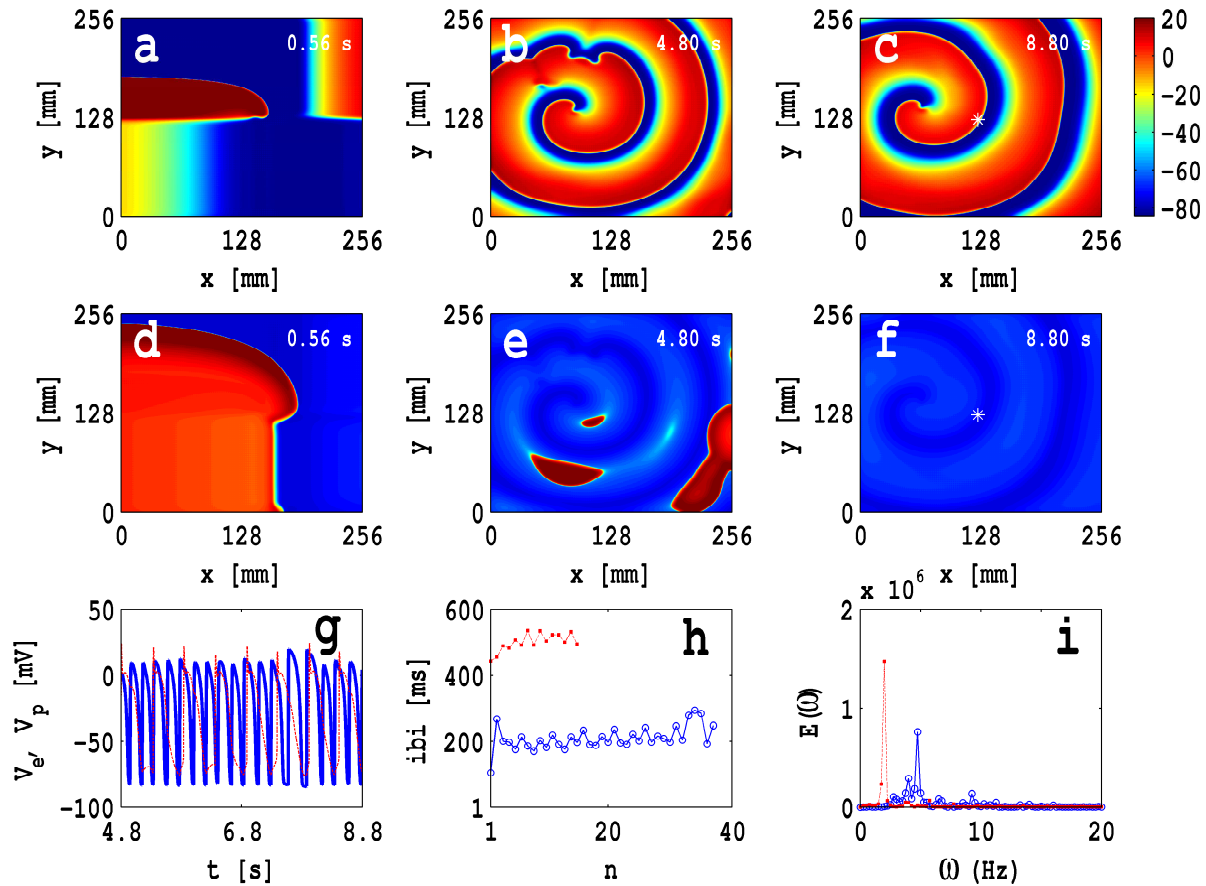


Figure 5.9: Spiral-wave dynamics in an EP-composite bilayer for the parameter set $\mathcal{P}1$, with the S1-S2 cross-field protocol in the E-cell layer, $D_{gap} = D_{mm}/10$, and $\mathcal{R} = 8$ (see Table 5.2); pseudocolor plots of V_e and V_p , the exact analogs of Figs. 5.8(a)-(f), are shown in (a)-(c) and (d)-(f), respectively; the animations in the top-right panel of Video S9 (labelled $\mathcal{R} = 8$) illustrate the spatiotemporal evolution of these spiral waves. The local time series, the ibi, and $E(\omega)$, are shown in plots (g), (h), and (i), respectively.

as \mathcal{R} increases. Therefore, plots of the ibi versus the beat number n flatten with increasing \mathcal{R} (see Fig. S3(h) in the Supplementary Material).

In Fig. 5.9 we show the counterpart of Fig. 5.8 for $\mathcal{R} = 8$, where we initiate the spiral wave by applying an S2 stimulus at $t = 480$ ms to the E-cell layer. The resulting spatiotemporal evolution of V_e and V_p shown, respectively, in Figs. 5.9(a)-(c) and (d)-(f) and in the top-right panel (labelled $\mathcal{R} = 8$) of Video S9, illustrate that, for $\mathcal{R} = 8$, spatiotemporal evolutions of V_e and V_p are not strongly correlated with each other, as they are when $1 \leq \mathcal{R} \leq 4$. Note the spiral-wave breakup occurs far away from the spiral core in the E-cell layer; this is because of the activation of waves in the P-cell layer that causes slow conduction block for the E-cell layer. We record the local time series for V_e and V_p from the representative points, in both E-

and P-cell layers, marked by asterisks in Figs. 5.9(c) and 5.9(f); in Fig. 5.9(g), we show these time series for V_e (blue, solid line) and V_p (red, dashed line), which lead to the plots of the ibi versus n shown by blue, open circles (E-cell layer) filled, red squares (P-cell layer) in Fig. 5.9(h); in Fig. 5.9(i) we show plot of $E(\omega)$ for E- and P-cell layers represented by blue open circles, and filled red squares, respectively. The local time series plot of V_e and its corresponding ibi and $E(\omega)$ confirm that spiral-wave activation in the E-cell layer is not in the form of a periodically rotating spiral. Furthermore, the non-periodic oscillating behavior, associated with focal-wave activations in the P-cell layer, which can be confirmed from the local time series of V_p and the corresponding plots of the ibi and $E(\omega)$, arises because the reflection of a non-periodic, rotating spiral in the E-layer.

The plots shown in Figs. S4 and S5 in the Supplementary Material are the exact analogs of Fig. 5.9 for $\mathcal{R} = 16$ and $\mathcal{R} = 32$, respectively. The complete spatiotemporal evolution of V_m for these cases is shown in the right part of the middle panel, labelled $\mathcal{R} = 16$, and the right part of the bottom panel, labelled $\mathcal{R} = 32$, of Video S9. The spiral-wave dynamics for $\mathcal{R} = 16$ and $\mathcal{R} = 32$ are qualitatively similar to $\mathcal{R} = 8$. However, spiral-wave breakup does not occur at all in the E-cell layer (see $\mathcal{R} = 16$ and $\mathcal{R} = 32$ in Video S9). From the time series of V_e (thick blue line in plots of Figs. S4(g) and S5(g)), the ibi (open blue circles in plots of Figs. S4(h) and S5(h)), and the power spectra (blue open circles in Figs. S4(i) and S5(i)) give the additional evidence for a stable RS in the E layer of the EP-bilayer; the P-cell layer shows autorhythmic excitations, which can be confirmed from the time series (red dashed line in Figs. S4(g) and S5(g)), the ibi (red filled squares in Figs. S4(h) and S5(h)), and the power spectra (red filled squares in Figs. S4(i) and S5(i)); the above time series, ibi, and power spectra for the P-cell layer of the EP-bilayer show that such autorhythmic activities rate decrease as \mathcal{R} decreases.

We now investigate spiral-wave dynamics in the EP-bilayer for the parameter set $\mathcal{P}2$ when an E-cell layer is coupled with a P-cell layer with D_{gap} and \mathcal{R} in the ranges mentioned above; here, we obtain spiral waves in our EP-composite, 2D bilayer by using the S1-S2 protocol in the E-cell layer. Our results for the parameter set $\mathcal{P}2$ are qualitatively similar to those for $\mathcal{P}1$ with two important excitations: With the parameter set $\mathcal{P}2$ our EP-bilayer domain also exhibits spiral-absorption (SA) and single-meandering-spiral-turbulence (SMST) states. We present below the principal results very briefly.

For the parameter set $\mathcal{P}2$ and with $\mathcal{R} = 1$ and $\mathcal{R} = 2$, we observe an RS state in both E- and P-cell layers of our EP-composite bilayer. In Fig. 5.10 we show the exact analogs of Fig. 5.8 for $\mathcal{R} = 1$, where we initiate the spiral wave by applying

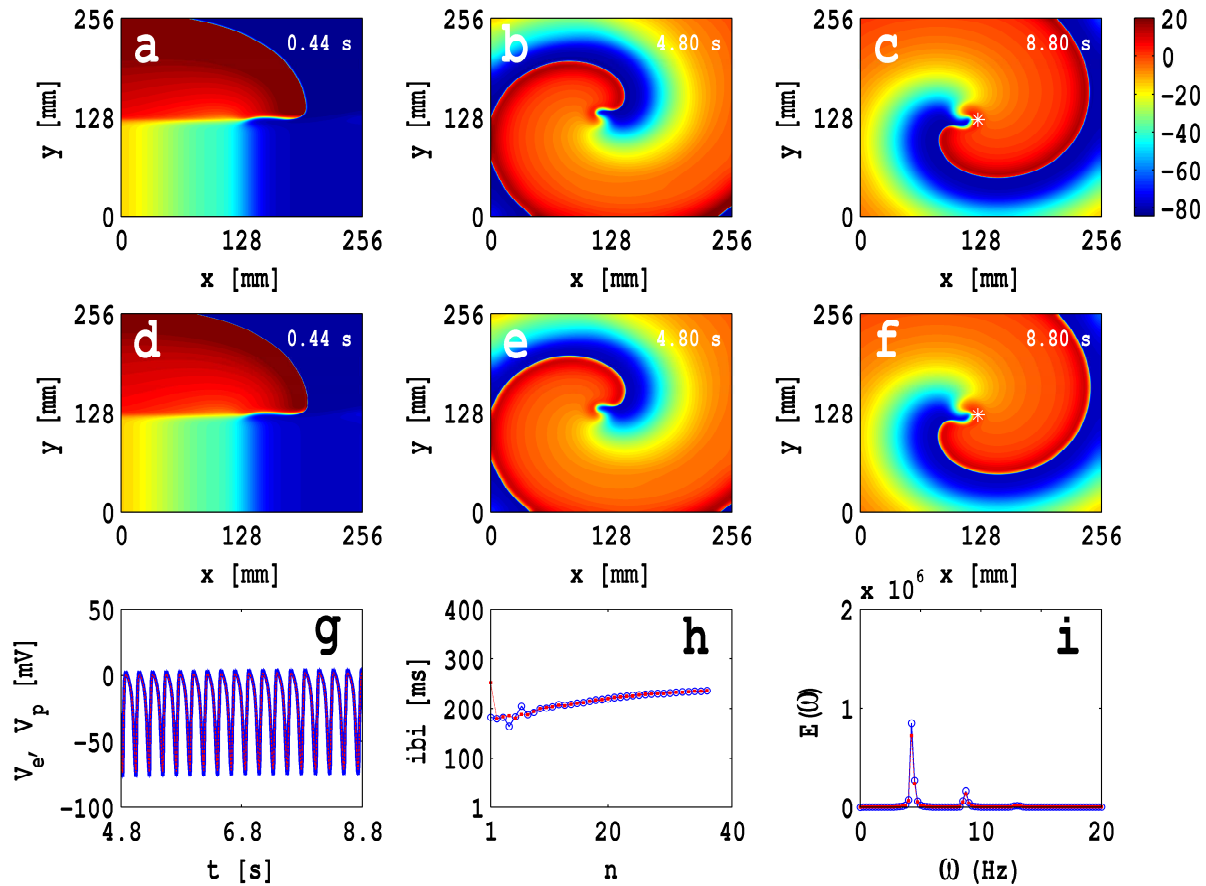


Figure 5.10: Spiral-wave dynamics in an EP-composite bilayer for the parameter set $\mathcal{P}2$, with the S1-S2 cross-field protocol in the E-cell layer, $D_{gap} = D_{mm}/10$, and $\mathcal{R} = 1$ (see Table 5.2); pseudocolor plots of V_e and V_p , the exact analogs of Figs. 5.8(a)-(f), are shown in (a)-(c) and (d)-(f), respectively; the animations in the top-left panel of Video S10 (labelled $\mathcal{R} = 1$) illustrate the spatiotemporal evolution of these spiral waves. The local time series, the ibi, and $E(\omega)$, are shown in plots (g), (h), and (i), respectively.

an S2 stimulus at $t = 480$ ms to the E-cell layer; the animation in the top-left panel (labelled $\mathcal{R} = 1$) of Video S10, illustrates, for $\mathcal{R} = 1$, the spatiotemporal evolutions of V_e and V_p ; analogs plots and animations are shown in Fig. S6 in the Supplemental Material S1 and the animation in the top-middle panel (labelled $\mathcal{R} = 2$) of Video S10, respectively, for $\mathcal{R} = 2$.

In Figs. 5.11(a)-(c) and (d)-(f), respectively, the pseudocolor plots of V_m for the E- and P-layers of our EP-bilayer for $\mathcal{P}2$ and $\mathcal{R} = 4$, we show SA, in both E- and P-layers of EP-bilayer, which occurs because of the absorption of a spiral wave at the boundary (see animation in the bottom-left panel (labelled $\mathcal{R} = 4$) of Video S10).

Plots similar to Figs 5.10, for $\mathcal{P}2$ with $\mathcal{R} = 8$, are shown in Figs. S7 in the Supplementary Material S1; the animation labelled by $\mathcal{R} = 8$ in the top-right panel of

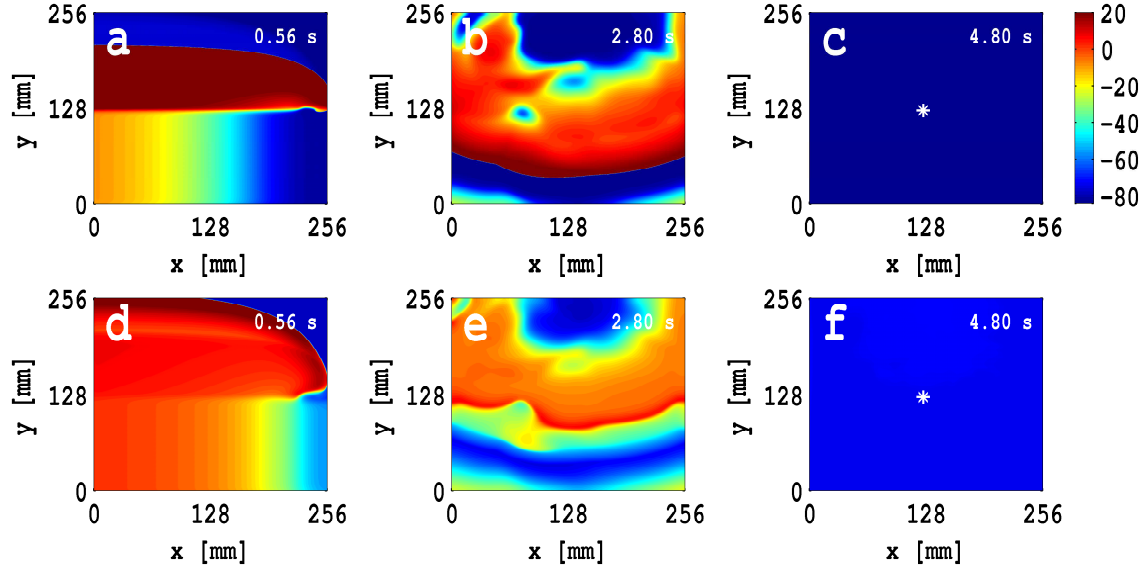


Figure 5.11: Spiral-wave dynamics in an EP-composite bilayer for the parameter set $\mathcal{P}2$, with the S1-S2 cross-field protocol in the E-cell layer, $D_{gap} = D_{mm}/10$, and $\mathcal{R} = 4$ (see Table 5.2); pseudocolor plots of V_e and V_p , the exact analogs of Figs. 5.8(a)-(f), are shown in (a)-(c) and (d)-(f), respectively; the animations in the bottom-left panel of Video S10 (labelled $\mathcal{R} = 4$) illustrate the spatiotemporal evolution of these spiral waves.

Video S10 show the spatiotemporal evolution of V_m ; these illustrate the SMST state in the E-layer; the P-layer produces *non-periodic* focal waves because of SMST state in E-layer of EP-bilayer.

The analogs of the plots in Fig. 5.10, for $\mathcal{P}2$ with $\mathcal{R} = 16$, are shown in Fig. 5.12; and the animation labelled by $\mathcal{R} = 16$ in the middle-right panel of Video S10 shows the spatiotemporal evolution of V_m ; these show that we have an SMST state in the E-layer, whereas the P-layer produces *periodic* focal waves, i.e., autorhythmicity. Such autorhythmic behaviors in the P-layer arises because of the low interaction between EP-composites in the EP-bilayer; we obtain similar results for $\mathcal{P}2$ and $\mathcal{R} = 32$ (see Fig. S8 in the Supplementary Material S1 and the animation labelled by $\mathcal{R} = 32$ in the bottom-right panel of Video S10).

We turn now to spiral-wave dynamics in the EP-bilayer for the parameter set $\mathcal{P}3$ and various ranges of \mathcal{R} (see Sec. 5.2); in all these cases, we initiate spiral waves, in our EP-composite, 2D bilayer, by using the S1-S2 protocol in the E-cell layer. Our results for the parameter set $\mathcal{P}3$ are qualitatively similar to those for either $\mathcal{P}1$ or $\mathcal{P}3$. However, we find that the MST state, which we obtain for an isolated E-layer with parameter set $\mathcal{P}3$, can lead to a transition to (a) an SMST state, (b) an

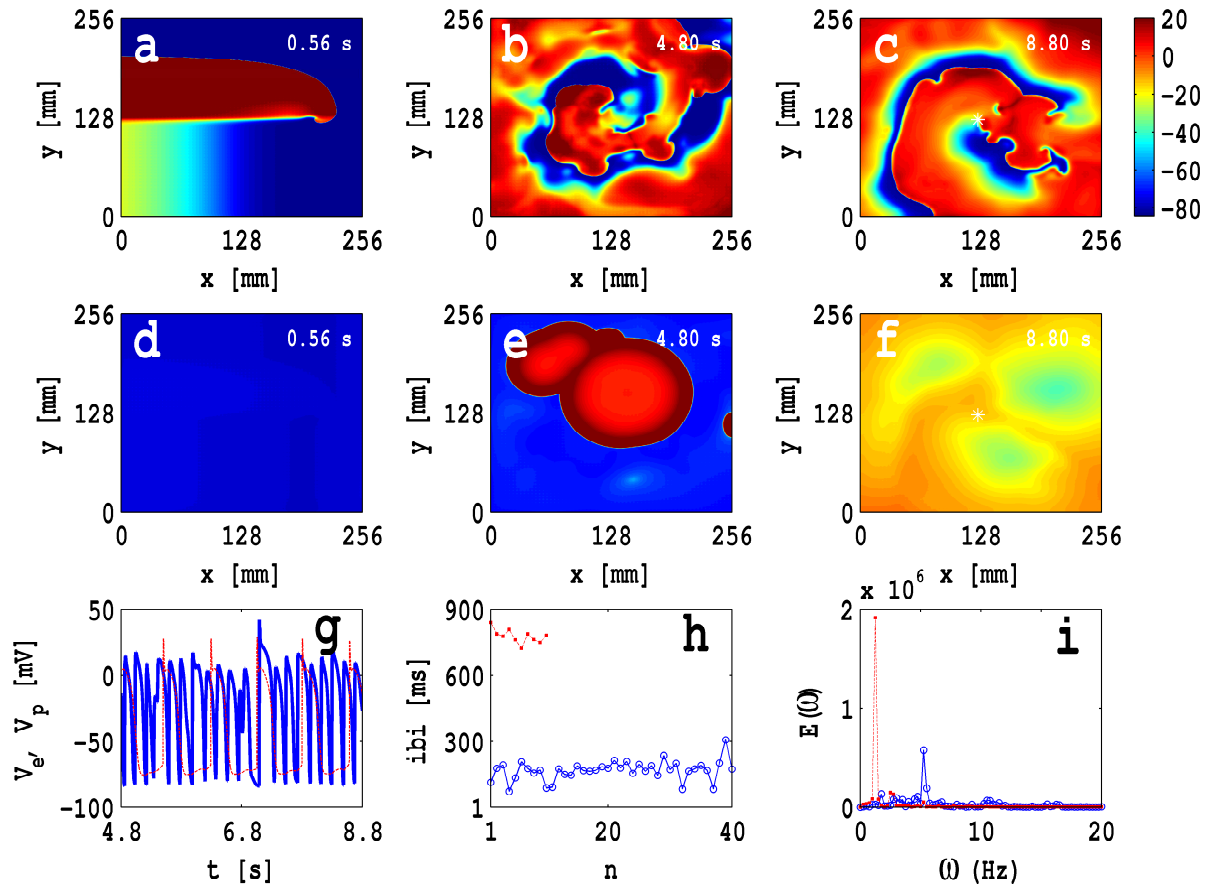


Figure 5.12: Spiral-wave dynamics in an EP-composite bilayer for the parameter set $\mathcal{P}2$, with the S1-S2 cross-field protocol in the E-cell layer, $D_{gap} = D_{mm}/10$, and $\mathcal{R} = 16$ (see Table 5.2); pseudocolor plots of V_e and V_p , the exact analogs of Figs. 5.8(a)-(f), are shown in (a)-(c) and (d)-(f), respectively; the animations in the middle-right panel of Video S10 (labelled $\mathcal{R} = 16$) illustrate the spatiotemporal evolution of these spiral waves. The local time series, the ibi, and $E(\omega)$, are shown in plots (g), (h), and (i), respectively.

RS state, and (c) an SA state depending on the value of \mathcal{R} ; in some cases, the state remain same in the MST state. We present below our principal results very briefly.

For the parameter set $\mathcal{P}3$ and $\mathcal{R} = 1$, we observe an SMST state in both E- and P-cell layers of our EP-composite bilayer. In Fig. S9 in the Supplementary Material S1 we show the pseudocolor plots of V_m (Figs. S9(a)-(c) for V_e and (d)-(f) for V_p), the local time series (Fig. S9(g)), the ibi (Fig. S9(h)), and the power spectra (Fig. S9(i)); the animation in the top-left panel (labelled $\mathcal{R} = 1$) of Video S11, illustrates, for $\mathcal{R} = 1$, the spatiotemporal evolutions of V_e and V_p . Analogs plot and animation, for $\mathcal{R} = 2$, are shown in Fig. 5.13 and the animation in the top-middle panel (labelled $\mathcal{R} = 2$) of Video S11, respectively; from this plot and animation we observe an RS state in both E- and P-cell layers of our EP-composite bilayer. The pseudocolor

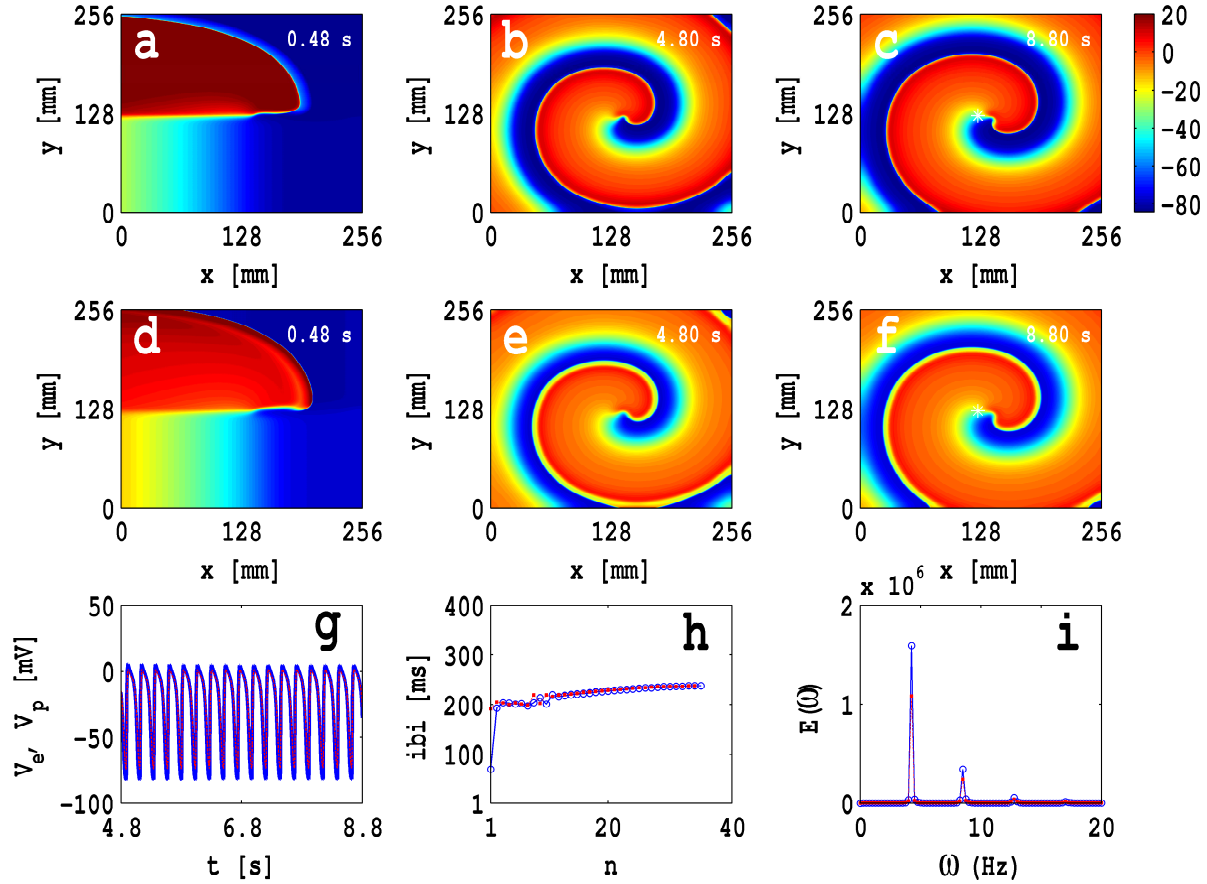


Figure 5.13: Spiral-wave dynamics in an EP-composite bilayer for the parameter set $\mathcal{P}3$, with the S1-S2 cross-field protocol in the E-cell layer, $D_{gap} = D_{mm}/10$, and $\mathcal{R} = 2$ (see Table 5.2); pseudocolor plots of V_e and V_p , the exact analogs of Figs. 5.8(a)-(f), are shown in (a)-(c) and (d)-(f), respectively; the animations in the middle-left panel of Video S11 (labelled $\mathcal{R} = 2$) illustrate the spatiotemporal evolution of these spiral waves. The local time series, the ibi, and $E(\omega)$, are shown in plots (g), (h), and (i), respectively.

plots of V_m for the E- and P-layers of the EP-bilayer, for $\mathcal{P}2$ and $\mathcal{R} = 4$, are shown in Figs. 5.14(a)-(c) and (d)-(f), respectively; animations correspond to V_e and V_p are shown bottom-left panel (labelled $\mathcal{R} = 4$) of Video S11; from these animation we observe that an SA exist in both E- and P-layers of EP-bilayer. Plots similar to Figs 5.13, for $\mathcal{P}2$ with $\mathcal{R} = 8$, are shown in Figs. 5.15; the animation labelled by $\mathcal{R} = 8$ in the top-right panel of Video S11 shows the spatiotemporal evolution of V_m ; these illustrate the SMST state in the E-layer; the P-layer produces *non-periodic* focal waves because of the SMST state in the E-layer of the EP-bilayer. The analogs of the plots in Fig. 5.14, for $\mathcal{P}3$ with $\mathcal{R} = 16$, are shown in Fig. 5.16; and the animation labelled by $\mathcal{R} = 16$ in the middle-right panel of Video S11 shows the spatiotemporal evolution of V_m ; these show that we have an SA state in the E-layer, whereas the P-

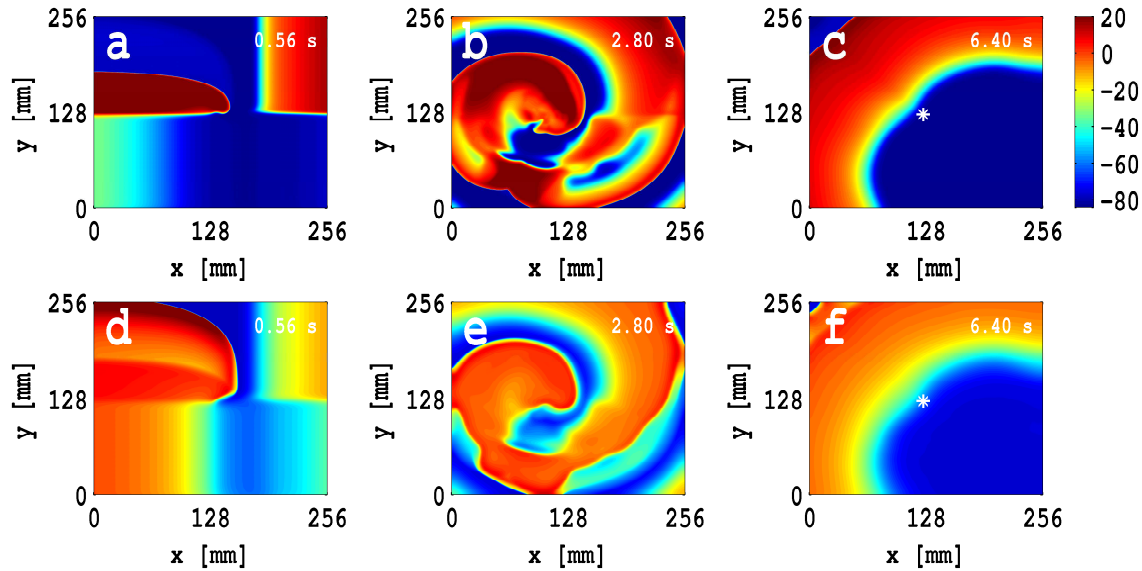


Figure 5.14: Spiral-wave dynamics in an EP-composite bilayer for the parameter set $\mathcal{P}3$, with the S1-S2 cross-field protocol in the E-cell layer, $D_{gap} = D_{mm}/10$, and $\mathcal{R} = 4$ (see Table 5.2); pseudocolor plots of V_e and V_p , the exact analogs of Figs. 5.8(a)-(f), are shown in (a)-(c) and (d)-(f), respectively; the animations in the bottom-left panel of Video S11 (labelled $\mathcal{R} = 4$) illustrate the spatiotemporal evolution of these spiral waves.

layer produces *non-periodic* focal waves. Such non-periodic behaviors in the P-layer arises because of the low interaction between EP-composites in the EP-bilayer. The plots similar to Fig. 5.16 and its corresponding animation, for $\mathcal{P}2$ and $\mathcal{R} = 32$, are shown in Fig. S10 in the Supplementary Material S1 and the animation labelled by $\mathcal{R} = 32$ in the bottom-right panel of Video S11. We observe an MST state in the E-layer, whereas the P-layer produces *periodic* focal waves, i.e., autorhythmicity; note that here the MST state in E-layer can not alter the autorhythmic excitation in P-cell layer of the EP-bilayer because of low coupling. i.e., higher \mathcal{R} value.

The details of our results, that we described above, with parameter sets $\mathcal{P}1$, $\mathcal{P}2$, and $\mathcal{P}31$, E- and P-layers diffusive coupling $D_{gap} = D_{mm}/10$ (high EP-composite coupling), $\mathcal{R} = 1, 2, 4, 8$, and 16 , and S1-S2 protocol to E-layer, are summarized in Table. 5.2. The animations in Videos S9, S10, and S11 show the spatiotemporal evolution of the transmembrane potential V_e and V_p for $0 \leq t \leq 4$ s; all these videos use 10 frames per second and each frame is separated from the succeeding frame by 8 ms.

We also investigate spiral-wave dynamics in the EP-bilayer for the parameter set $\mathcal{P}1$, $\mathcal{P}2$, and $\mathcal{P}3$ when an E-cell layer is coupled with a P-cell layer with

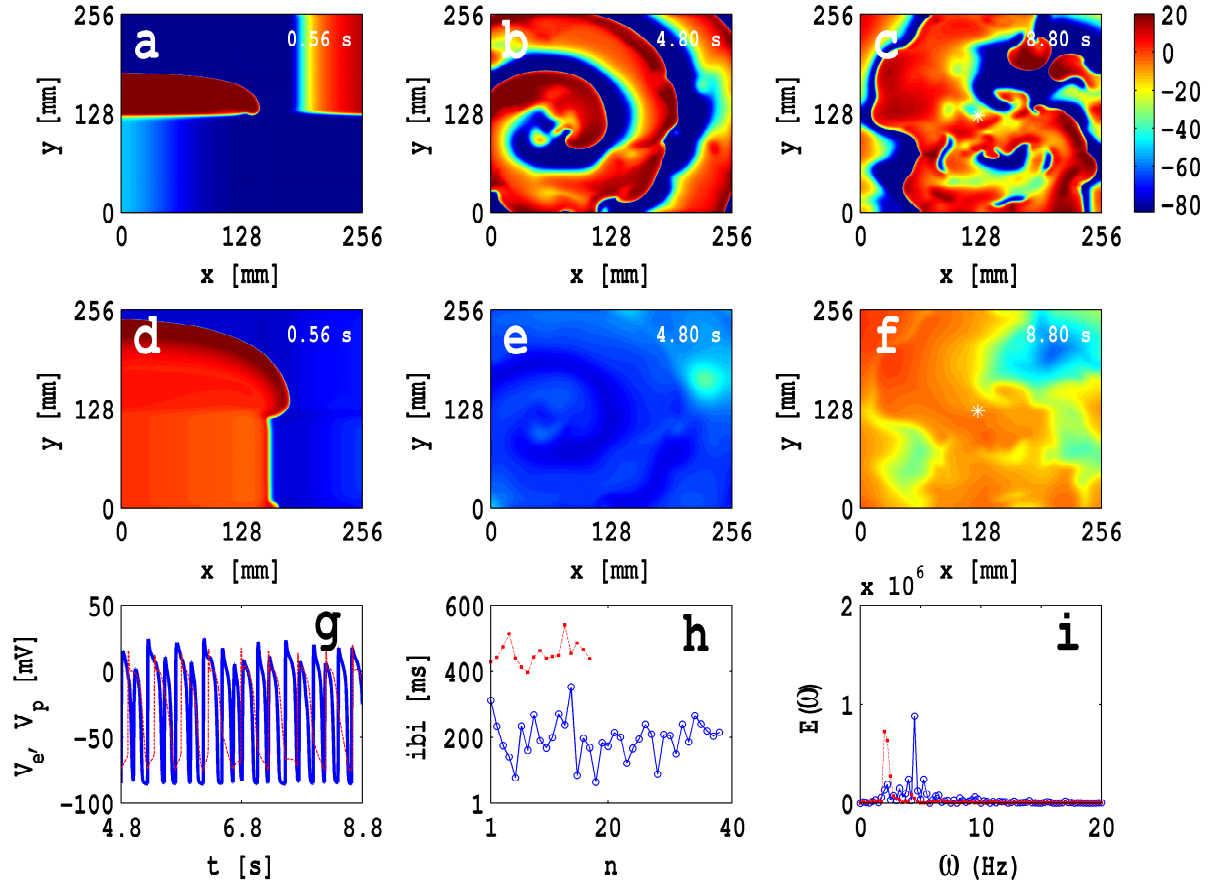


Figure 5.15: Spiral-wave dynamics in an EP-composite bilayer for the parameter set $\mathcal{P}3$, with the S1-S2 cross-field protocol in the E-cell layer, $D_{gap} = D_{mm}/10$, and $\mathcal{R} = 8$ (see Table 5.2); pseudocolor plots of V_e and V_p , the exact analogs of Figs. 5.8(a)-(f), are shown in (a)-(c) and (d)-(f), respectively; the animations in the top-right panel of Video S11 (labelled $\mathcal{R} = 8$) illustrate the spatiotemporal evolution of these spiral waves. The local time series, the ibi, and $E(\omega)$, are shown in plots (g), (h), and (i), respectively.

$D_{gap} = D_{mm}/100$, i.e., low EP-composite coupling, and \mathcal{R} in the ranges mentioned above; here, we obtain spiral waves in our EP-composite, 2D bilayer by using the S1-S2 protocol in the E-cell layer. The Table 5.3 summarizes the final state of E- and P-cell layers. Our qualitative results for such set of simulations remain same depending on the parameter set and the parameter set and \mathcal{R} value. We give some of the illustrative results here: For $\mathcal{P}1$ and $\mathcal{R} = 1$, we observe an RS state in both E- and P-cell layers of our EP-composite bilayer (see Fig. S11 in the Supplementary Material S1); we observe an RS state in the E-layer and the P-layer produces autorhythmic excitation of the EP-bilayer, for $\mathcal{P}1$ and $\mathcal{R} = 8$ (see Fig. S12 in the Supplementary Material S1); for $\mathcal{P}2$ and $\mathcal{R} = 1$, we observe an RS state in both E- and P-cell layers of our EP-composite bilayer (see Fig. S13 in the Supplementary

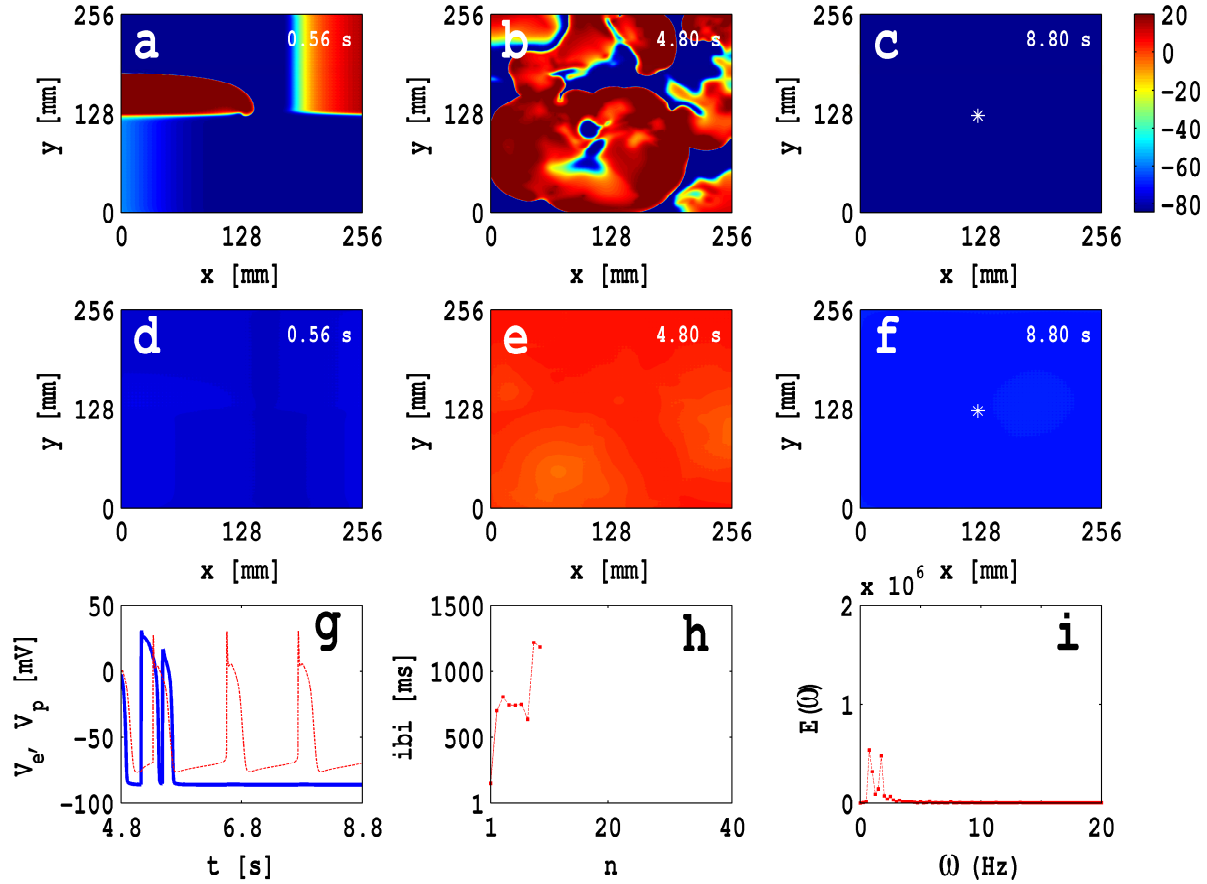


Figure 5.16: Spiral-wave dynamics in an EP-composite bilayer for the parameter set $\mathcal{P}3$, with the S1-S2 cross-field protocol in the E-cell layer, $D_{gap} = D_{mm}/10$, and $\mathcal{R} = 16$ (see Table 5.2); pseudocolor plots of V_e and V_p , the exact analogs of Figs. 5.8(a)-(f), are shown in (a)-(c) and (d)-(f), respectively; the animations in the middle-right panel of Video S11 (labelled $\mathcal{R} = 16$) illustrate the spatiotemporal evolution of these spiral waves. The local time series, the ibi, and $E(\omega)$, are shown in plots (g), (h), and (i), respectively.

Material S1); we observe an SMST state in the E-layer and the P-layer produces autorhythmic excitation of the EP-bilayer, for $\mathcal{P}2$ and $\mathcal{R} = 8$ (see Fig. S14 in the Supplementary Material S1); for $\mathcal{P}3$ and $\mathcal{R} = 1$, we observe an RS with non stationary ibi state in both E- and P-cell layers of our EP-composite bilayer (see Fig. S15 in the Supplementary Material S1); we observe an MST state in the E-layer and the P-layer produces autorhythmic excitation of the EP-bilayer, for $\mathcal{P}3$ and $\mathcal{R} = 8$ (see Fig. S16 in the Supplementary Material S1).

We also study spiral wave dynamics by applying the S1-S2 protocol in (a) the P-cell layer and (b) both EP-cell layers simultaneously of the EP-composite bilayer. We present a few representative cases of our numerical results, which are summarized in Table 5.3. We begin with S1-S2 excitation of the P-cell layer for the

initiation of spiral waves. We observe 4-cycle motion with an RS state in both E- and P-cell layers of our EP-composite bilayer, for $D_{gap} = D_{mm}/10$, $\mathcal{P}1$ and $\mathcal{R} = 1$ (see Fig. S17 in the Supplementary Material S1). An RS state in both E- and P-cell layers of our EP-composite bilayer is observed, for $D_{gap} = D_{mm}/10$, $\mathcal{P}1$ and $\mathcal{R} = 2$ (see Fig. S18 in the Supplementary Material S1). For $D_{gap} = D_{mm}/10$, $\mathcal{P}2$ and $\mathcal{R} = 1$ (Fig. S19 in the Supplementary Material S1), we observe an RS state in both E- and P-cell layers of our EP-composite bilayer. For $D_{gap} = D_{mm}/10$, $\mathcal{P}2$ and $\mathcal{R} = 2$ (Fig. S20 in the Supplementary Material S1), we observe 2-cycle motion in both E- and P-cell layers of our EP-composite bilayer. For $D_{gap} = D_{mm}/10$, $\mathcal{P}3$ and $\mathcal{R} = 1$ (Fig. S21 in the Supplementary Material S1), we observe an SMST state in both E- and P-cell layers of our EP-composite bilayer. For $D_{gap} = D_{mm}/10$, $\mathcal{P}3$ and $\mathcal{R} = 2$ (Fig. S22 in the Supplementary Material S1), we observe an RS state in both E- and P-cell layers of our EP-composite bilayer.

We turn now to cases in which we employ the S1-S2 protocol in both E- and P-cell layers. For $D_{gap} = D_{mm}/10$, $\mathcal{P}1$ and $\mathcal{R} = 4$ (Fig. S23 in the Supplementary Material S1), we observe an RS state in both E- and P-cell layers of our EP-composite bilayer. For $D_{gap} = D_{mm}/10$, $\mathcal{P}2$ and $\mathcal{R} = 4$ (Fig. S24 in the Supplementary Material S1), we observe an SMST state in both E- and P-cell layers of our EP-composite bilayer. For $D_{gap} = D_{mm}/10$, $\mathcal{P}3$ and $\mathcal{R} = 4$ (Fig. S25 in the Supplementary Material S1), we observe an MST state in both E- and P-cell layers of our EP-composite bilayer.

5.3.3 Controlling Spiral Waves in the EP-bilayer Domain

One of the basic goals of our extensive numerical studies of E-cell, P-cell, and EP-bilayer domains in mathematical models is to understand their effects on spiral-wave dynamics, and thus develop effective, low-amplitude control techniques for the elimination of spiral waves, simple or chaotic, of electrical activation in such mathematical models. An overview of some low-amplitude control schemes is given in Ref. [8]. We use the control scheme of Ref. [33]; this eliminates spiral waves by the application of a current pulse on a mesh, which we describe below. The studies of Refs. [8, 9, 33, 34, 49] have shown that such a mesh-based control scheme eliminates spiral waves even when the simulation domain has inhomogeneities [8, 9], ionic [8, 9], fibroblasts [50], or is subjected to periodic deformation [49]. In contrast, control schemes, which use electrical stimuli at a point [51, 52], work well in homogeneous simulation domains but do not eliminate spiral-wave turbulence in domains with inhomogeneities [8].

We begin with a brief review of the mesh-bashed control scheme of Ref. [33, 34] for a mathematical model for cardiac tissue and a 2D, square, homogeneous domain

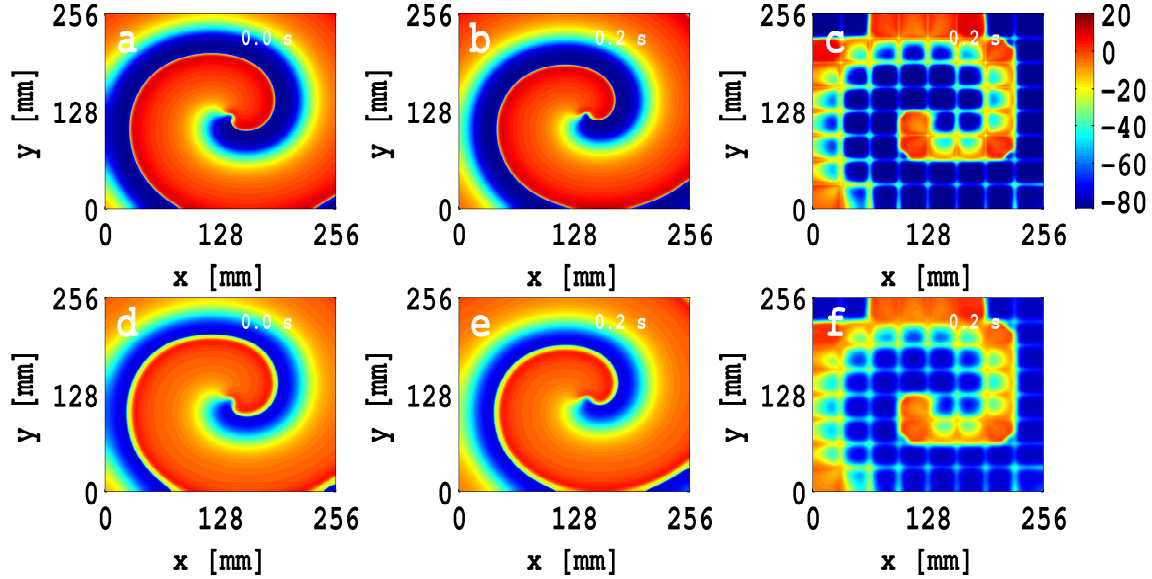


Figure 5.17: Elimination of a single rotating spiral (RS) in a 2D, EP-bilayer, with the parameter set $\mathcal{P}3$, $D_{gap} = D_{mm}/10$, and $\mathcal{R} = 2$. A current pulse of amplitude 75 pA/pF is applied to the E-cell layer for $t = 0.2$ s over a mesh to control spiral waves. (a) Pseudocolor plot of V_e at $t = 0$ s; (b) pseudocolor plot of V_e at $t = 0.2$ s in the absence of the control pulse; and (c) pseudocolor plot of V_e at $t = 0.2$ s in the presence of the control pulse. The plots in (d), (e) and (f), are the analogs of (a), (b), and (c), respectively, for the P-cell layer in the EP-bilayer. The Video S11, which comprises six animations of pseudocolor plots of V_e and V_p , shows the spatiotemporal evolution of the spiral waves for these cases, with and without control pulses.

with side L , which is divided into K^2 smaller blocks by a mesh of lines; a current pulse is applied for a small period of time; the mesh side $\ell = L/K$ is chosen to be small enough that spiral waves cannot persist for a long time inside the blocks. The application of the control-current pulse makes the mesh lines refractory, for a time comparable to the pulse-application time, and so effectively simulates Neumann boundary conditions for any block bounded by the mesh. Thus, spiral waves formed inside the block are absorbed at the bounding mesh lines.

We use such a control scheme to suppress spiral waves in our EP-bilayer domain as follows. We apply a current pulse of amplitude 75 pA/pF to the E-cell layer for $t = 0.2$ s over a mesh that divides our square simulation domain, of side $L = 256$ mm, into $K^2 = 64$ square cells of side $\ell = 32$ mm each. We have carried out a set of simulations to evaluate the efficacy of our control scheme in the EP-bilayer, with the three parameter sets $\mathcal{P}1$, $\mathcal{P}2$, and $\mathcal{P}3$, for the E-cell layer; and we use two representative values of D_{gap} , namely, $D_{gap} = D_{mm}/10$ and $D_{gap} = D_{mm}/100$, and the values of \mathcal{R} that we have listed above. We illustrate the control of spiral waves,

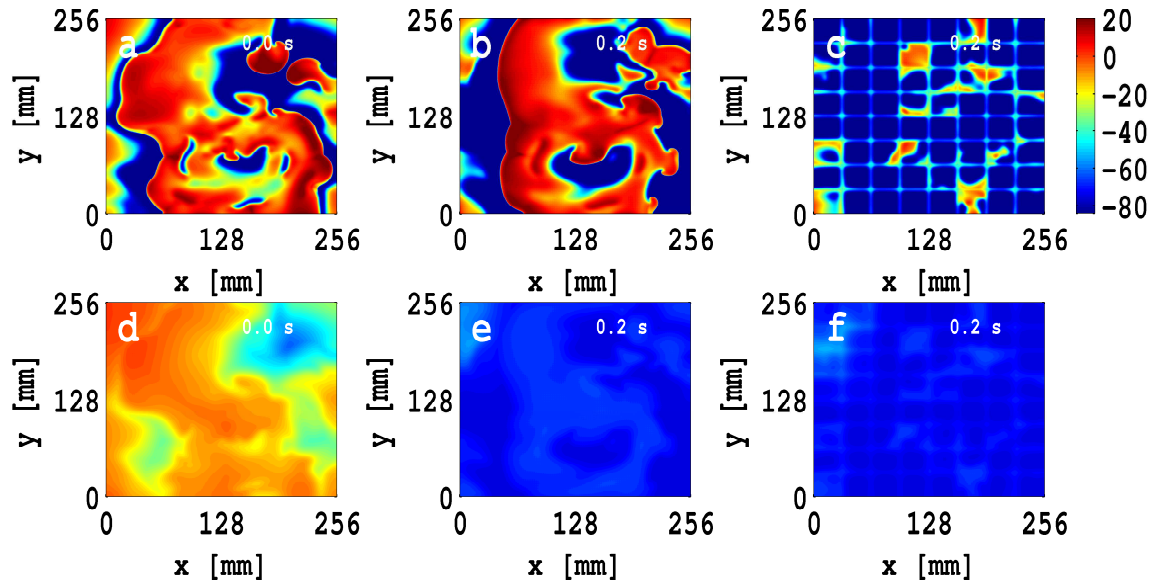


Figure 5.18: Suppression of spiral turbulence (ST) in a 2D, EP-bilayer, with the parameter set $\mathcal{P}3$, $D_{gap} = D_{mm}/10$, and $\mathcal{R} = 8$. A current pulse of amplitude 75 pA/pF is applied to the E-cell layer for $t = 0.2$ s over a mesh to control spiral waves. (a) Pseudocolor plot of V_e at $t = 0$ s; (b) pseudocolor plot of V_e at $t = 0.2$ s in the absence of the control pulse; and (c) pseudocolor plot of V_e at $t = 0.2$ s in the presence of the control pulse. The plots in (d), (e) and (f), are the analogs of (a), (b), and (c), respectively, for the P-cell layer in the EP-bilayer. The Video S12, which comprises six animations of pseudocolor plots of V_e and V_p , shows the spatiotemporal evolution of the spiral waves for these cases, with and without control pulses.

in our 2D, EP-composite simulation domain, by the mesh-based scheme described above, for a few representative cases. In Fig. 5.17 (a) we show a pseudocolor plot of V_e , at time $t = 0$ ms, for the parameter set $\mathcal{P}3$, $D_{gap} = D_{mm}/10$, and $\mathcal{R} = 2$; we give pseudocolor plots of V_e , at $t = 0.2$ s, and in the absence and presence of the control pulse in Figs. 5.17 (b) and (c), respectively. Figures 5.17 (d), (e) and (f), are the analogs of Figs. 5.17 (a), (b), and (c), respectively, for the P-cell layer in the EP-bilayer. The left-half panel of Video S12, which comprises animations of pseudocolor plots of V_e and V_p , shows the spatiotemporal evolution of the spiral waves for these cases, with and without control pulses. From Figs. 5.17(c) and (f), and the animations in the first two boxes at the left of the bottom panel of Video S12, we see that our mesh-based scheme eliminates a single rotating spiral (RS) in less than 0.2 s in a 2D, EP-bilayer simulation domain. In Fig. 5.18, we show the exact analogs of Fig. 5.17 for $\mathcal{P}3$, $D_{gap} = D_{mm}/10$, and $\mathcal{R} = 8$; the animations in the right-half panel of Video S12 show the spatiotemporal evolution of these spiral waves. From the pseudocolor plots of V_e and V_p in Figs. 5.18(c) and (f), and the

animations of the bottom panel of Video S12, we see that our mesh-based scheme eliminates spiral turbulence (ST) in less than 0.2 s. The exact analogs of Video S12 for the parameter set $\mathcal{P}1$, $D_{gap} = D_{mm}/10$, and $\mathcal{R} = 1$, and the parameter set $\mathcal{P}1$, $D_{gap} = D_{mm}/10$, and $\mathcal{R} = 8$, are shown in the left- and right-half panels of Video S13, respectively; Video S14 is the exact analog of Video S13 for the parameter set $\mathcal{P}2$.

5.4 Discussion and Conclusion

We have carried out detailed numerical studies of (a) a single unit of an EP composite and (b) a two-dimensional bilayer, which contains such EP composites at each site. We have considered biophysically realistic ionic models for human endocardial [13] tissue and Purkinje cells [18] to model EP composites.

Our study has been designed to elucidate the sensitive dependence, on parameters and initial conditions, of (a) the dynamics of EP composites and (b) the spatiotemporal evolution of spiral waves of electrical activation in EP-bilayer domains. We examine this dependence on myocyte parameters by using the three different parameter sets $\mathcal{P}1$, $\mathcal{P}2$, and $\mathcal{P}3$; to elucidate the initial-condition dependence we vary the time at which we apply the S2 pulse in our S1-S2 protocol; we also investigate the dependence of the spatiotemporal dynamics of our system on the EP coupling, via D_{gap} , and on the number of PVJs, which are measured here by the ratio \mathcal{R} .

Our studies on EP composite have shown that the frequency of autorhythmic activity of a P cell depends on the diffusive gap-junctional conductance D_{gap} . We have performed a set of simulations to understand the source-sink relation between E and P cells in an EP composite; such a source-sink relation is an important determinant of wave dynamics at the tissue level [19]. Furthermore, we have studied the restitution properties of an isolated E cell and a composite EP unit to uncover their effect on wave dynamics in 2D, bilayers of EP composites. We have also carried out a detailed, systematic, numerical calculation to study plane- and spiral-wave dynamics in a 2D bilayer of EP composites. We discuss the principal finding of our numerical calculations below in the light of earlier studies.

Autorhythmicity is an important property of Purkinje cells; it helps to carry electrical signals rapidly from the *bundle of His* to the endocardium. Our investigation of an EP composite shows that its cycle length (CL) of autorhythmic activity decreases, compared to that of an uncoupled Purkinje cell. Furthermore, we have found that the APD increases for an EP composite, compared to that of an uncoupled P cell.

In our second set of simulations for an EP-composite unit, we have obtained the AP morphological behaviors and the amount of flux that flows from the E to the P cell during the course of the AP. The direction of flow of this flux is an important quantity that identifies which one of these cells act as a source or a sink in this EP composite, and, hence, plays an important role in spiral-wave dynamics at the tissue level [19]. We have found that the P cell in an EP composite acts as a stimulation-current source for the E cell in the depolarization phase of the AP, when the stimulus is applied to both cells or to the P cell only. However, the P cell behaves both as a source and a sink when the stimulus is applied to the E cell only.

In our third set of simulations for an EP composite unit, we have calculated the restitution of the APD; this plays an important role in deciding the stability of spiral waves in mathematical models for cardiac tissue [44–48]. Our simulation shows that, for the EP composite with high intercellular coupling (e.g., $D_{gap} = D_{mm}/10$), the APDR slope decreases, relative to its value for an isolated E cell, for parameter sets $\mathcal{P}1$ and $\mathcal{P}2$, and first increases (for $50 \leq DI \leq 100$ ms) and then decreases for the parameter set $\mathcal{P}3$; however, for low intercellular coupling (e.g., $D_{gap} = D_{mm}/100$), the variation of the APD as a function of DI , for an EP composite, shows biphasic behavior for all these three parameter sets.

We have found that the plane-wave dynamics in EP cable type domains, with EP composites, depends sensitively on \mathcal{R} . This sensitive dependence can be summarized by comparing the final states given in Tables 5.2 for different values of \mathcal{R} . Conduction delays have been observed in *in vitro* studies which use Purkinje and endocardial layers. For example, Xing *et al.* [26], have studied the propagation delay of electrical waves from Purkinje tissue to the endocardium, the endocardium to the midmyocardium, and the midmyocardium to the epicardium in their multi-layer structures in *in vitro* experiments on canine myocytes; they have concluded that the conduction delay occurs because of the weak coupling between the Purkinje layer and the endocardial layer through PVJs. We hope our *in silico* studies of spiral-wave dynamics in EP bilayers will stimulate more, *in vitro* studies that examine such dynamics.

Tabereaux, *et al.* [27] have shown in an *in vitro* studies, that electrical activation can appear focally in the endocardium because of autorhythmic activities in Purkinje system; such focal activation in the endocardial layer may help to produced abnormal or trigger activities, which can maintain the VF in the working ventricular myocardium. Our *in silico* studies are of relevance to such experiments. As we have mentioned in the introduction, other computational studies have studied mathematical models that study the interaction of E and P cells.

These studies range from those that look at isolated EP composites [18–21] to those that investigate the interplay between E and P cells in anatomically realistic domains [28, 30, 31] for a variety mammalian myocytes and Purkinje cells. Some of the models use realistic simulation domains [28, 30, 31] and Purkinje-fiber networks; and they find in general that inclusion of Purkinje system results in slightly faster and more coordinated activation of the ventricles compared to a simplified model that neglects this structure; and they have concluded that the inclusion of the Purkinje-fiber network can either accelerate reentry termination or generate wave breakup (which does not occur when the same initial condition is used in the ventricle alone).

We end with some limitations of our model: We use a monodomain description for cardiac tissue; and we do not use an anatomically realistic simulation domain [53, 54], muscle-fiber orientation, and transmural heterogeneity [55, 56]; the inclusion of these features lies beyond the scope of this study. We note, however, that recent studies [57] have compared potentials resulting from normal depolarization and repolarization in a bidomain model with those of a monodomain model; these studies have shown that the differences between results obtained from a monodomain model and those obtained from a bidomain model are extremely small.

Parameter sets	S1-S2 protocol	D_{gap} value	\mathcal{R}	Figure	Video	Final state in E-layer	Final state in P-layer
$\mathcal{P}1$	E-layer S2 at $t = 360$ ms	$\frac{D_{mm}}{10}$	1	8	S9	periodic RS with fundamental peak at $\omega_e \simeq 4$ Hz	periodic RS with fundamental peak at $\omega_p \simeq 4$ Hz
$\mathcal{P}1$	E-layer S2 at $t = 400$ ms	$\frac{D_{mm}}{10}$	2	S2	S9	periodic RS with fundamental peak at $\omega_e = 4$ Hz	periodic RS with fundamental peak at $\omega_p = 4$ Hz
$\mathcal{P}1$	E-layer S2 at $t = 480$ ms	$\frac{D_{mm}}{10}$	4	S3	S9	periodic RS with fundamental peak at $\omega_e = 3.75$ Hz	periodic RS with fundamental peak at $\omega_p = 3.75$ Hz
$\mathcal{P}1$	E-layer S2 at $t = 480$ ms	$\frac{D_{mm}}{10}$	8	9	S9	non-periodic RS with a strong peak at $\omega_e \simeq 4.75$ Hz	non-periodic excitation with a strong peak at $\omega_p \simeq 2$ Hz
$\mathcal{P}1$	E-layer S2 at $t = 480$ ms	$\frac{D_{mm}}{10}$	16	S4	S9	RS with fundamental peak at $\omega_e = 4.75$ Hz	periodic excitation with fundamental peak at $\omega_p = 1.25$ Hz
$\mathcal{P}1$	E-layer S2 at $t = 480$ ms	$\frac{D_{mm}}{10}$	32	S5	S9	RS with fundamental peak at $\omega_e = 4.75$ Hz	periodic excitation with fundamental peak at $\omega_p = 1$ Hz
$\mathcal{P}2$	E-layer S2 at $t = 360$ ms	$\frac{D_{mm}}{10}$	1	10	S10	RS with fundamental peak at $\omega_e = 4.25$ Hz	RS with fundamental peak at $\omega_p = 4.25$ Hz
$\mathcal{P}2$	E-layer S2 at $t = 400$ ms	$\frac{D_{mm}}{10}$	2	S6	S10	RS with fundamental peak at $\omega_e = 4.25$ Hz	RS with fundamental peak at $\omega_p = 4.25$ Hz
$\mathcal{P}2$	E-layer S2 at $t = 480$ ms	$\frac{D_{mm}}{10}$	4	11	S10	SA	SA
$\mathcal{P}2$	E-layer S2 at $t = 480$ ms	$\frac{D_{mm}}{10}$	8	S7	S10	SMST with a strong peak at $\omega_e \simeq 5.25$ Hz	non periodic excitation with a strong peak at $\omega_p \simeq 2$ Hz
$\mathcal{P}2$	E-layer S2 at $t = 480$ ms	$\frac{D_{mm}}{10}$	16	12	S10	SMST with a strong peak at $\omega_e \simeq 5.25$ Hz	periodic excitation with fundamental peak at $\omega_p = 1.25$ Hz
$\mathcal{P}2$	E-layer S2 at $t = 480$ ms	$\frac{D_{mm}}{10}$	32	S8	S10	SMST with a strong peak at $\omega_e \simeq 5.25$ Hz	periodic excitation with fundamental peak at $\omega_p = 1$ Hz
$\mathcal{P}3$	E-layer S2 at $t = 416$ ms	$\frac{D_{mm}}{10}$	1	S9	S11	SMST with a strong peak at $\omega_e \simeq 4.25$ Hz	SMST with a strong peak at $\omega_p \simeq 4.25$ Hz
$\mathcal{P}3$	E-layer S2 at $t = 400$ ms	$\frac{D_{mm}}{10}$	2	13	S11	RS with fundamental peak at $\omega_e = 4.25$ Hz	RS with fundamental peak at $\omega_p = 4.25$ Hz
$\mathcal{P}3$	E-layer S2 at $t = 480$ ms	$\frac{D_{mm}}{10}$	4	14	S11	SA	SA
$\mathcal{P}3$	E-layer S2 at $t = 480$ ms	$\frac{D_{mm}}{10}$	8	15	S11	SMST with a strong peak at $\omega_e \simeq 4.5$ Hz	non periodic excitation with a strong peak at $\omega_p \simeq 2$ Hz
$\mathcal{P}3$	E-layer S2 at $t = 480$ ms	$\frac{D_{mm}}{10}$	16	16	S11	SA	non periodic excitation with a strong peak at $\omega_p \simeq 0.75$ and 1.75 Hz
$\mathcal{P}3$	E-layer S2 at $t = 480$ ms	$\frac{D_{mm}}{10}$	32	S10	S11	MST	periodic excitation with a strong peak at $\omega_p = 1$ Hz

Table 5.2: Final states in E-cell and P-cell layers of an EP-composite bilayer; here, RS stands for rotating spiral, SMST stands for single-meandering-spiral-turbulence, and MST stands for multiple spiral turbulence.

1 Supporting Information

Video S1: Spatiotemporal evolution of plane waves in cable-type domains for (a) E cells with the parameter set $\mathcal{P}1$, (b) E cells with the parameter set $\mathcal{P}2$, (c) E cells with the parameter set $\mathcal{P}3$, (d) P cells with $D_{pp} = D_{mm}$, (e) P cells with $D_{pp} = 2 \times D_{mm}$, and (f) P cells with $D_{pp} = 3 \times D_{mm}$, shown via pseudocolor plots of the transmembrane potential V_m ; the time evolution is shown for $0 \text{ s} \leq t \leq 0.8 \text{ s}$; we use 10 frames per second (fps); in real time each frame is separated from the succeeding frame by 8 ms.

Video S2: Spatiotemporal evolution of plane waves in cable-type domains of an EP-bilayer, with E cells in one layer and P cells in the other, and the $\mathcal{P}1$ parameter set for the E-cell layer, $D_{pp} = 3 \times D_{mm}$ for the P-cell layer, and gap-junctional coupling between EP-composites $D_{gap} = D_{mm}/10$. (e1) V_e with $\mathcal{R} = 1$, (e2) V_e with $\mathcal{R} = 2$, (e3) V_e with $\mathcal{R} = 4$, (e4) V_e with $\mathcal{R} = 8$, (e5) V_e with $\mathcal{R} = 16$, (p1) V_p with $\mathcal{R} = 1$, (p2) V_p with $\mathcal{R} = 2$, (p3) V_p with $\mathcal{R} = 4$, (p4) V_p with $\mathcal{R} = 8$, and (p5) V_p with $\mathcal{R} = 16$. The pseudocolor plots of the transmembrane potential V_e and V_p are shown for $0 \text{ s} \leq t \leq 1.6 \text{ s}$; we use 10 frames per second (fps); in real time each frame is separated from the succeeding frame by 8 ms.

Video S3: Spatiotemporal evolution of plane waves in cable-type domains of an EP-bilayer, with E cells in one layer and P cells in the other, and the $\mathcal{P}2$ parameter set for the E-cell layer, $D_{pp} = 3 \times D_{mm}$ for the P-cell layer, and gap-junctional coupling between EP-composites $D_{gap} = D_{mm}/10$. (e1) V_e with $\mathcal{R} = 1$, (e2) V_e with $\mathcal{R} = 2$, (e3) V_e with $\mathcal{R} = 4$, (e4) V_e with $\mathcal{R} = 8$, (e5) V_e with $\mathcal{R} = 16$, (p1) V_p with $\mathcal{R} = 1$, (p2) V_p with $\mathcal{R} = 2$, (p3) V_p with $\mathcal{R} = 4$, (p4) V_p with $\mathcal{R} = 8$, and (p5) V_p with $\mathcal{R} = 16$. The pseudocolor plots of the transmembrane potential V_e and V_p are shown for $0 \text{ s} \leq t \leq 1.6 \text{ s}$; we use 10 frames per second (fps); in real time each frame is separated from the succeeding frame by 8 ms.

Video S4: Spatiotemporal evolution of plane waves in cable-type domains of an EP-bilayer, with E cells in one layer and P cells in the other, and the $\mathcal{P}3$ parameter set for the E-cell layer, $D_{pp} = 3 \times D_{mm}$ for the P-cell layer, and gap-junctional coupling between EP-composites $D_{gap} = D_{mm}/10$. (e1) V_e with $\mathcal{R} = 1$, (e2) V_e with $\mathcal{R} = 2$, (e3) V_e with $\mathcal{R} = 4$, (e4) V_e with $\mathcal{R} = 8$, (e5) V_e with $\mathcal{R} = 16$, (p1) V_p with $\mathcal{R} = 1$, (p2) V_p with $\mathcal{R} = 2$, (p3) V_p with $\mathcal{R} = 4$, (p4) V_p with $\mathcal{R} = 8$, and (p5) V_p with $\mathcal{R} = 16$. The pseudocolor plots of the transmembrane potential V_e and V_p are shown for $0 \text{ s} \leq t \leq 1.6 \text{ s}$; we use 10 frames per second (fps); in real time each frame is separated from the succeeding frame by 8 ms.

Video S5: Spatiotemporal evolution of plane waves in cable-type domains of an EP-bilayer, with E cells in one layer and P cells in the other, and the $\mathcal{P}1$ parameter

set for the E-cell layer, $D_{pp} = 3 \times D_{mm}$ for the P-cell layer, and gap-junctional coupling between EP-composites $D_{gap} = D_{mm}/100$. (e1) V_e with $\mathcal{R} = 1$, (e2) V_e with $\mathcal{R} = 2$, (e3) V_e with $\mathcal{R} = 4$, (e4) V_e with $\mathcal{R} = 8$, (e5) V_e with $\mathcal{R} = 16$, (p1) V_p with $\mathcal{R} = 1$, (p2) V_p with $\mathcal{R} = 2$, (p3) V_p with $\mathcal{R} = 4$, (p4) V_p with $\mathcal{R} = 8$, and (p5) V_p with $\mathcal{R} = 16$. The pseudocolor plots of the transmembrane potential V_e and V_p are shown for $0 \leq t \leq 1.6$ s; we use 10 frames per second (fps); in real time each frame is separated from the succeeding frame by 8 ms.

Video S6: Spatiotemporal evolution of plane waves in cable-type domains of an EP-bilayer, with E cells in one layer and P cells in the other, and the $\mathcal{P}2$ parameter set for the E-cell layer, $D_{pp} = 3 \times D_{mm}$ for the P-cell layer, and gap-junctional coupling between EP-composites $D_{gap} = D_{mm}/100$. (e1) V_e with $\mathcal{R} = 1$, (e2) V_e with $\mathcal{R} = 2$, (e3) V_e with $\mathcal{R} = 4$, (e4) V_e with $\mathcal{R} = 8$, (e5) V_e with $\mathcal{R} = 16$, (p1) V_p with $\mathcal{R} = 1$, (p2) V_p with $\mathcal{R} = 2$, (p3) V_p with $\mathcal{R} = 4$, (p4) V_p with $\mathcal{R} = 8$, and (p5) V_p with $\mathcal{R} = 16$. The pseudocolor plots of the transmembrane potential V_e and V_p are shown for $0 \leq t \leq 1.6$ s; we use 10 frames per second (fps); in real time each frame is separated from the succeeding frame by 8 ms.

Video S7: Spatiotemporal evolution of plane waves in cable-type domains of an EP-bilayer, with E cells in one layer and P cells in the other, and the $\mathcal{P}3$ parameter set for the E-cell layer, $D_{pp} = 3 \times D_{mm}$ for the P-cell layer, and gap-junctional coupling between EP-composites $D_{gap} = D_{mm}/100$. (e1) V_e with $\mathcal{R} = 1$, (e2) V_e with $\mathcal{R} = 2$, (e3) V_e with $\mathcal{R} = 4$, (e4) V_e with $\mathcal{R} = 8$, (e5) V_e with $\mathcal{R} = 16$, (p1) V_p with $\mathcal{R} = 1$, (p2) V_p with $\mathcal{R} = 2$, (p3) V_p with $\mathcal{R} = 4$, (p4) V_p with $\mathcal{R} = 8$, and (p5) V_p with $\mathcal{R} = 16$. The pseudocolor plots of the transmembrane potential V_e and V_p are shown for $0 \leq t \leq 1.6$ s; we use 10 frames per second (fps); in real time each frame is separated from the succeeding frame by 8 ms.

Video S8: Spiral-wave dynamics in the E-cell layer for the parameter sets (a) $\mathcal{P}1$, (b) $\mathcal{P}2$, and (c) $\mathcal{P}3$, and (d) the diffusive coupling $D_{pp} = 3 \times D_{mm}$ for the P-cell layer. The pseudocolor plots of the transmembrane potential V_e and V_p are shown for $0 \leq t \leq 6$ s; we use 10 frames per second (fps); in real time each frame is separated from the succeeding frame by 8 ms.

Video S9: Spiral-wave dynamics in the EP-bilayer for the parameter set $\mathcal{P}1$ when an E-cell layer is coupled with a P-cell layer with $D_{gap} = D_{mm}/10$ and $\mathcal{R} = 1$ (two boxes on the top-left panel), $\mathcal{R} = 2$ (two boxes on the middle-left panel), $\mathcal{R} = 4$ (two boxes on the bottom-left panel), $\mathcal{R} = 8$ (two boxes on the top-right panel), $\mathcal{R} = 16$ (two boxes on the middle-right panel), and $\mathcal{R} = 32$ (two boxes on the bottom-right panel); we inject spiral waves by using the S1-S2 protocol in the E-cell layer (see text). The pseudocolor plots of the transmembrane potential V_e and V_p are shown

for $0 \leq t \leq 6$ s; we use 10 frames per second (fps); in real time each frame is separated from the succeeding frame by 8 ms.

Video S10: Spiral-wave dynamics in the EP-bilayer for the parameter set $\mathcal{P}2$ when an E-cell layer is coupled with a P-cell layer with $D_{gap} = D_{mm}/10$ and $\mathcal{R} = 1$ (two boxes on the top-left panel), $\mathcal{R} = 2$ (two boxes on the middle-left panel), $\mathcal{R} = 4$ (two boxes on the bottom-left panel), $\mathcal{R} = 8$ (two boxes on the top-right panel), $\mathcal{R} = 16$ (two boxes on the middle-right panel), and $\mathcal{R} = 32$ (two boxes on the bottom-right panel); we inject spiral waves by using the S1-S2 protocol in the E-cell layer (see text). The pseudocolor plots of the transmembrane potential V_e and V_p are shown for $0 \leq t \leq 6$ s; we use 10 frames per second (fps); in real time each frame is separated from the succeeding frame by 8 ms.

Video S11: Spiral-wave dynamics in the EP-bilayer for the parameter set $\mathcal{P}3$ when an E-cell layer is coupled with a P-cell layer with $D_{gap} = D_{mm}/10$ and $\mathcal{R} = 1$ (two boxes on the top-left panel), $\mathcal{R} = 2$ (two boxes on the middle-left panel), $\mathcal{R} = 4$ (two boxes on the bottom-left panel), $\mathcal{R} = 8$ (two boxes on the top-right panel), $\mathcal{R} = 16$ (two boxes on the middle-right panel), and $\mathcal{R} = 32$ (two boxes on the bottom-right panel); we inject spiral waves by using the S1-S2 protocol in the E-cell layer (see text). The pseudocolor plots of the transmembrane potential V_e and V_p are shown for $0 \leq t \leq 6$ s; we use 10 frames per second (fps); in real time each frame is separated from the succeeding frame by 8 ms.

Video S12: Spiral-wave dynamics, without and with control pulses, in the EP-bilayer for the parameter sets $\mathcal{P}3$, $D_{gap} = D_{mm}/10$ and $\mathcal{R} = 2$ (left-half panel) and $\mathcal{R} = 8$ (right-half panel); we apply control pulse to E-cell layer (see text). The pseudocolor plots of the transmembrane potential V_m are shown for $0 \leq t \leq 1$ s; we use 10 frames per second (fps); in real time each frame is separated from the succeeding frame by 8 ms.

Video S13: Spiral-wave dynamics, without and with control pulses, in the EP-bilayer for the parameter sets $\mathcal{P}1$, $D_{gap} = D_{mm}/10$ and $\mathcal{R} = 1$ (left-half panel) and $\mathcal{R} = 8$ (right-half panel); we apply control pulse to E-cell layer (see text). The pseudocolor plots of the transmembrane potential V_m are shown for $0 \leq t \leq 1$ s; we use 10 frames per second (fps); in real time each frame is separated from the succeeding frame by 8 ms.

Video S14: Spiral-wave dynamics, without and with control pulses, in the EP-bilayer for the parameter sets $\mathcal{P}2$, $D_{gap} = D_{mm}/10$ and $\mathcal{R} = 1$ (left-half panel) and $\mathcal{R} = 8$ (right-half panel); we apply control pulse to E-cell layer (see text). The pseudocolor plots of the transmembrane potential V_m are shown for $0 \leq t \leq 1$ s; we use

10 frames per second (fps); in real time each frame is separated from the succeeding frame by 8 ms.

Parameter sets	S1-S2 protocol	D_{gap} value	\mathcal{R}	Figure	Video	Final state in E-layer	Final state in P-layer
$\mathcal{P}1$	E-layer S2 at $t = 400$ ms	$\frac{D_{mm}}{100}$	1	S11	–	RS with fundamental peak at $\omega_e = 3.75$ Hz	RS with fundamental peak at $\omega_p = 3.75$ Hz
$\mathcal{P}1$	E-layer S2 at $t = 480$ ms	$\frac{D_{mm}}{100}$	8	S12	–	RS with fundamental peak at $\omega_e = 4.75$ Hz	periodic excitation with fundamental peak at $\omega_p = 1$ Hz
$\mathcal{P}2$	E-layer S2 at $t = 400$ ms	$\frac{D_{mm}}{100}$	1	S13	–	RS with fundamental peak at $\omega_e = 4$ Hz	RS with fundamental peak at $\omega_p = 4$ Hz
$\mathcal{P}2$	E-layer S2 at $t = 480$ ms	$\frac{D_{mm}}{100}$	8	S14	–	SMST with a strong peak $\omega_e \simeq 5$ Hz	periodic excitation with fundamental peak at $\omega_p = 1$ Hz
$\mathcal{P}3$	E-layer S2 at $t = 480$ ms	$\frac{D_{mm}}{100}$	1	S15	–	RS with a strong peak at $\omega_e \simeq 3.75$ Hz	RS with a strong peak at $\omega_p \simeq 4$ Hz
$\mathcal{P}3$	E-layer S2 at $t = 480$ ms	$\frac{D_{mm}}{100}$	8	S16	–	MST	periodic excitation with fundamental peak at $\omega_p = 1$ Hz
$\mathcal{P}1$	P-layer S2 at $t = 360$ ms	$\frac{D_{mm}}{10}$	1	S17	–	RS (4-cycle) with fundamental peak at $\omega_e = 4$ Hz	RS (4-cycle) with fundamental peak at $\omega_p = 4$ Hz
$\mathcal{P}1$	P-layer S2 at $t = 360$ ms	$\frac{D_{mm}}{10}$	2	S18	–	RS with fundamental peak at $\omega_e = 4$ Hz	RS with fundamental peak at $\omega_p = 4$ Hz
$\mathcal{P}2$	P-layer S2 at $t = 360$ ms	$\frac{D_{mm}}{10}$	1	S19	–	RS with fundamental peak at $\omega_e = 4.25$ Hz	RS with fundamental peak at $\omega_p = 4.25$ Hz
$\mathcal{P}2$	P-layer S2 at $t = 360$ ms	$\frac{D_{mm}}{10}$	2	S20	–	RS (2-cycle) with fundamental peak at $\omega_e = 4.25$ Hz	RS (2-cycle) with fundamental peak at $\omega_p = 4.25$ Hz
$\mathcal{P}3$	P-layer S2 at $t = 400$ ms	$\frac{D_{mm}}{10}$	1	S21	–	SMST with a strong peak at $\omega_e \simeq 4.25$ Hz	SMST with a strong peak at $\omega_p \simeq 4.25$ Hz
$\mathcal{P}3$	P-layer S2 at $t = 400$ ms	$\frac{D_{mm}}{10}$	2	S22	–	RS with fundamental peak at $\omega_e = 4.25$ Hz	RS with fundamental peak at $\omega_p = 4.25$ Hz
$\mathcal{P}1$	both EP layers S2 at $t = 480$ ms	$\frac{D_{mm}}{10}$	4	S23	–	RS with fundamental peak at $\omega_e = 3.75$ Hz	RS with fundamental peak at $\omega_p = 3.75$ Hz
$\mathcal{P}2$	both EP layers S2 at $t = 480$ ms	$\frac{D_{mm}}{10}$	4	S24	–	SMST with a strong peak at $\omega_e \simeq 4$ Hz	SMST with a strong peak at $\omega_p \simeq 4$ Hz
$\mathcal{P}3$	both EP layers S2 at $t = 480$ ms	$\frac{D_{mm}}{10}$	4	S25	–	MST	MST

Table 5.3: Final states in E-cell and P-cell layers of an EP-composite bilayer; here, RS stands for rotating spiral, SMST stands for single-meandering-spiral-turbulence, and MST stands for multiple spiral turbulence.

Bibliography

- [1] Mangoni ME, Nargeot J (2008) Genesis and regulation of the heart automaticity. *Physiol Rev* 88:919-82.
- [2] Sanchez-Quintana D, Yen Ho S (2003) Anatomy of cardiac nodes and atrioventricular specialized conduction system. *Rev Esp Cardiol* 56(11):1085-92.
- [3] Ono N, Yamaguchi T, Ishikawa H, *et al.* (2009) Morphological varieties of the Purkinje fiber network in mammalian hearts, as revealed by light and electron microscopy. *Arch Histol Cytol* 72(3):139-49.
- [4] Davidenko JM, Perstov AV, *et al.* (1992) Stationary and drifting spiral waves of excitation in isolated cardiac muscle. *Nature* 355: 349
- [5] Gray RA, Pestov AM, Jalife J (1998) Spatial and temporal organization during cardiac fibrillation. *Nature* 392: 75.
- [6] Jalife J, Gray RA, Morley GE, Davidenko JM (1998) Self organization and the dynamical nature of ventricular fibrillation. *Chaos* 8: 5764.
- [7] Fenton FH, Cherry EM, Hastings HM, *et al.* (2002) Multiple mechanisms of spiral wave breakup in a model of cardiac electrical activity. *Chaos* 12(3):852.
- [8] Shajahan TK, Nayak AR and Pandit R (2009) Spiral-wave turbulence and its control in the presence of inhomogeneities in four mathematical models of cardiac tissue. *PLoS ONE* 4(3): e4738.
- [9] Majumder R, Nayak AR, Pandit R (2011) An overview of spiral- and scroll-wave dynamics in mathematical models for cardiac tissue. *Heart Rate and Rhythm: Molecular Basis, Pharmacological Modulation and Clinical Implications*, Chapter 14, pp 269-282.
- [10] Luo CH, Rudy Y (1991) A model of the ventricular cardiac action potential: depolarization, repolarization, and their interaction. *Circ Res* 68: 1501.

- [11] Luo CH, Rudy Y (1994) A dynamic model of the cardiac ventricular action potential. I. Simulations of ionic currents and concentration changes. *Circ Res* 74: 1071.
- [12] ten Tusscher KHWJ, Noble D, Noble PJ, Panfilov AV (2004) A model for human ventricular tissue. *Am J Physiol Heart Circ Physiol* 286: H1573.
- [13] ten Tusscher KHWJ, Panfilov AV (2006) Alternans and spiral breakup in a human ventricular tissue model. *Am J Physiol Heart Circ Physiol* 291: H1088.
- [14] Noble D (1962) A modification of the HodgkinHuxley equations applicable to Purkinje fibre action and pacemaker potentials. *J. Physiol.* 160: 317-352.
- [15] McAllister RE, Noble D, Tsien RW (1975) Reconstruction of the electrical activity of cardiac Purkinje fibres. *J. Physiol.* 251: 1-59.
- [16] DiFrancesco D, Noble D (1985) A model of cardiac electrical activity incorporating ionic pumps and concentration changes. *Philos. Trans. R. Soc. London B* 307: 353398.
- [17] Tusscher KH, Panfilov AV (2008) Modelling of the ventricular conduction system. *Prog Biophys Mol Biol* 96: 152-170.
- [18] Stewart P, Aslanidi OV, Noble D, *et al.* (2009) Mathematical models of the electrical action potential of Purkinje fibre cells. *Philos Transact A Math Phys Eng Sci* 367: 2225-2255.
- [19] Aslanidi OV, Stewart P, Boyett MR, *et al.* (2009) Optimal velocity and safety of discontinuous conduction through the heterogeneous purkinje-ventricular junction. *Biophys J* 97: 20-39.
- [20] Sampson KJ, Iyer V, Marks AR, *et al.* (2010) A computational model of Purkinje fibre single cell electrophysiology: implications for the long QT syndrome. *J Physiol* 588: 2643-2655.
- [21] Li P, Rudy Y (2011) A model of canine purkinje cell electrophysiology and Ca^{2+} cycling: rate dependence, triggered activity, and comparison to ventricular myocytes. *Circ Res* 109: 71-79.
- [22] Corrias A, Giles W, Rodriguez B (2011) Ionic mechanisms of electrophysiological properties and repolarization abnormalities in rabbit Purkinje fibers. *Am J Physiol Heart Circ Physiol* 300: H1806-1813.

- [23] Benson AP, Aslanidi OV, Zhang H, *et al.* (2008) The canine virtual ventricular wall: a platform for dissecting pharmacological effects on propagation and arrhythmogenesis. *Prog Biophys Mol Biol* 96: 187-208.
- [24] Arnar DO, Bullinga JR, Martins JB (1997) Role of the Purkinje system in spontaneous ventricular tachycardia during acute ischemia in a canine model. *Circulation* 96: 2421.
- [25] Arnar DO, Xing D, Lee H, Martins JB (2001) Prevention of ischemic ventricular tachycardia of Purkinje origin: role for α_2 -adrenoceptors in Purkinje? *Am J Physiol Heart Circ Physiol* 280: H1182.
- [26] Xing D, Martins JB (2004) Triggered activity due to delayed afterdepolarizations in sites of focal origin of ischemic ventricular tachycardia. *Am J Physiol Heart Circ Physiol* 287: H2078.
- [27] Tabereaux PB, Walcott GP, Rogers JM, *et al.* (2007) Activation patterns of Purkinje fibers during long-duration ventricular fibrillation in an isolated canine heart model. *Circulation* 116: 1113.
- [28] Vigmond EJ, Clements C (2007) Construction of a computer model to investigate sawtooth effects in the Purkinje system. *IEEE Trans Biomed Eng* 54(3): 389.
- [29] Drouhard JP and Roberge FA (1987) Revised formulation of the Hodgkin-Huxley representation of the sodium current in cardiac cells. *Comput Biomed Res* 20(4): 333.
- [30] Bordas R, Gillow K, Lou Q, *et al.* (2011) Rabbit-specific ventricular model of cardiac electrophysiological function including specialized conduction system. *Prog Biophys Mol Biol* 107: 90.
- [31] Cherry EM, Fenton FH (2012) Contribution of the Purkinje network to wave propagation in the canine ventricle: insights from a combined electrophysiological-anatomical model. *Nonlinear Dyn* 68: 365.
- [32] Hund TJ, Rudy Y (2004) Rate dependence and regulation of action potential and calcium transient in a canine cardiac ventricular cell model. *Circulation* 110: 3168.
- [33] Sinha S, Pande A, Pandit R (2001) Defibrillation via the elimination of spiral turbulence in model for ventricular fibrillation. *Phys Rev Lett* 86: 3678.

- [34] Pandit R, Pande A, Sinha S *et al.* (2002) Spiral turbulence and spatiotemporal chaos: characterization and control in two excitable media. *Physica A* 306: 211.
- [35] Kenner J, Sneyd J (1998) *Mathematical Physiology*. Springer-Verlag New York, Inc. New York, NY, USA.
- [36] Panfilov AV, Holden AV (1996) *Computational Biology of the Heart* Wiley.
- [37] Sato D, Shiferaw Y, Garfinkel A, *et al.* (2006) Spatially discordant alternans in cardiac tissue: role of calcium cycling. *Circ Res* 99:520.
- [38] Oosthoek PW, Virgh S, Lamers WH, *et al.* (2003) Immunohistochemical delineation of the conduction system. II: The atrioventricular node and Purkinje fibers. *Circ Res* 73:482-91.
- [39] Tranum-Jensen J, Wilde AA, Vermeulen JT, Janse MJ (1991) Morphology of electrophysiologically identified junctions between Purkinje fibers and ventricular muscle in rabbit and pig hearts. *Circ Res* 69:429-437.
- [40] Schafferhofer-Steltzer I, Hofer E, Huelsing DJ, Bishop SP, Pollard AE (2005) Contributions of Purkinje-myocardial coupling to suppression and facilitation of early afterdepolarization-induced triggered activity. *IEEE Trans Biomed Eng* 52:1522-31.
- [41] Yu H, Chang F, Cohen IS (1995) Pacemaker current $i(f)$ in adult canine cardiac ventricular myocytes. *J. Physiol.* 485: 469-483.
- [42] Lu HR, Marien R, Saels A, De Clerck F (2001) Species plays an important role in drug-induced prolongation of action potential duration and early afterdepolarizations in isolated Purkinje fibers. *J Cardiovasc Electrophysiol* 12: 93-102.
- [43] Ideker RE, Kong W, and Pogwizd S (2009) Purkinje Fibers and Arrhythmias. *Pacing Clin Electrophysiol* 32: 283.
- [44] Fenton FH, Cherry EM, Hastings HM, *et al.* (2002) Multiple mechanisms of spiral wave breakup in a model of cardiac electrical activity. *Chaos* 12(3): 852.
- [45] Garfinkel A, Kim YH, Voroshilovsky O, *et al.* (2000) Preventing ventricular fibrillation by flattening cardiac restitution. *PNAS* 97(11): 6061.
- [46] Qu Z, Weiss JN, Garfinkel A (1999) Cardiac electrical restitution properties and stability of reentrant spiral waves: a simulation study. *Am J Physiol Heart Circ Physiol* 276: H269.

- [47] Karma A (1994) Electrical alternans and spiral wave breakup in cardiac tissue. *Chaos* 4(3): 461.
- [48] Qu Z, Xie F, Garfinkel A, Weiss JN (2000) Origins of spiral wave meander and breakup in a two-dimensional cardiac tissue model. *Ann Biomed Eng* 28: 755.
- [49] Nayak AR and Pandit R, Spiral-wave dynamics in ionically realistic mathematical models for human ventricular tissue: The effects of mechanical deformation. unpublished.
- [50] Nayak AR, Shajahan TK, Panfilov AV, Pandit R (In press) Spiral-wave dynamics in a mathematical model of human ventricular tissue with myocytes and fibroblasts. unpublished manuscript.
- [51] Zhang H, Hu B, Hu G (2003) Suppression of spiral waves and spatiotemporal chaos by generating target waves in excitable media. *Phys Rev E* 68: 026134.
- [52] Zhang H, Cao Z, Wu NJ, Ying HP, Hu G (2005) Suppress Winfree turbulence by local forcing excitable systems. *Phys Rev Lett* 94: 188301.
- [53] Panfilov A, Keener JP (1995) Re-entry in an anatomical model of the heart. *Chaos, Solitons, and Fractals* 5: 681.
- [54] Trayanova NA, Tice BM (2009) Integrative computational models of cardiac arrhythmias- simulating the structurally realistic heart. *Drug Discov Today Dis Models* 6(3): 85.
- [55] Majumder R, Nayak AR, Pandit R (2011) Scroll-wave dynamics in human cardiac tissue: lessons from a mathematical model with inhomogeneities and fiber architecture. *PLoS One* 6(4): e18052.
- [56] Majumder R, Nayak AR, Pandit R (2012) Nonequilibrium arrhythmic States and transitions in a mathematical model for diffuse fibrosis in human cardiac tissue. *PLoS One* 7(10): e45040.
- [57] Potse M, Dube B, Richer J, Vinet A, Gulrajani RM (2006) A comparison of monodomain and bidomain reaction-diffusion models for action potential propagation in the human heart. *IEEE Trans Biomed Eng* 53: 2425.

1 Supplementary Material S1

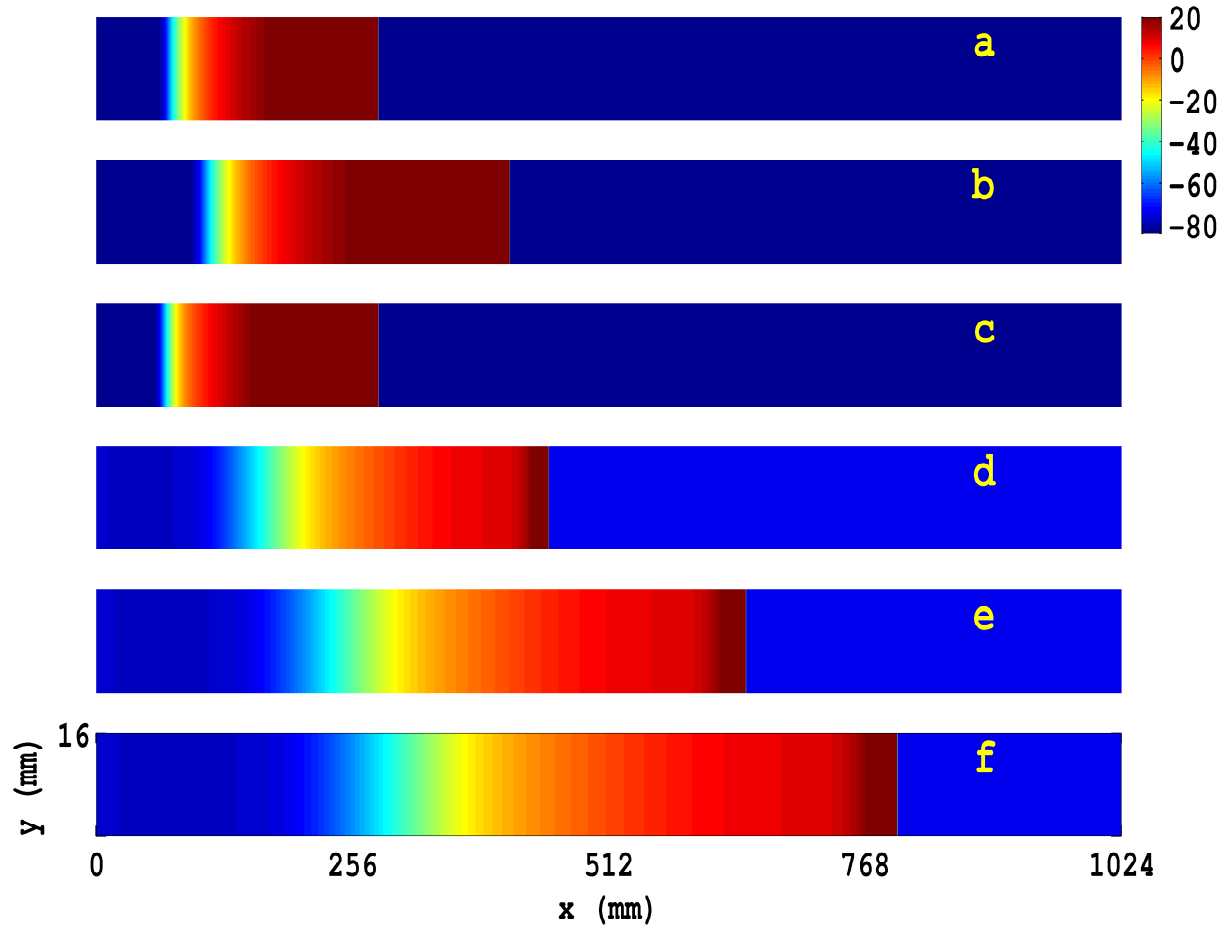


Figure S1: Plane waves, shown via pseudocolor plots of the transmembrane potential V_m , at $t = 400$ ms in a thin strip of tissue of dimensions $L_x = 1024$ mm and $L_y = 16$ mm (basically, a one dimensional cable) for the (a) E-cell layer with parameter set $\mathcal{P}1$, (b) E-cell layer with parameter set $\mathcal{P}2$, (c) E-cell layer with parameter set $\mathcal{P}3$, (d) P-cell layer with $D_{pp} = D_{mm}$, (e) P-cell layer with $D_{pp} = 2 \times D_{mm}$, and (f) P-cell layer with $D_{pp} = 3 \times D_{mm}$ (see text). The animations in Video S1 illustrates the spatiotemporal evolution of these plane waves.

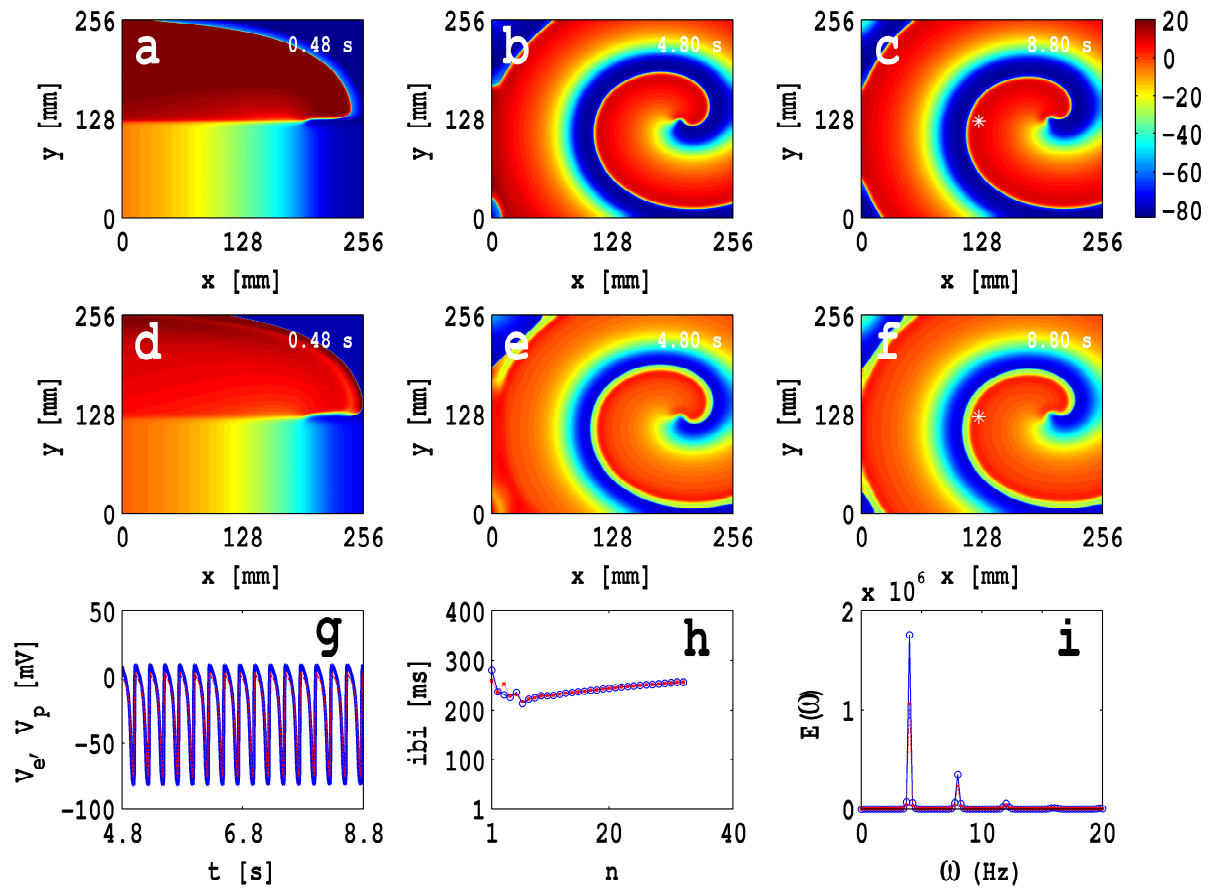


Figure S2: Spiral-wave dynamics in our EP-composite bilayer for the parameter set $\mathcal{P}1$, with the S1-S2 cross-field protocol in the E-cell layer, $D_{gap} = D_{mm}/10$, and $\mathcal{R} = 2$ (see Table 5.2); (a)-(c) show pseudocolor plots of V_e ; (d)-(e) show pseudocolor plots of V_p ; the animations in the middle-left panel of Video S9 (labelled by $\mathcal{R} = 2$) illustrate the spatiotemporal evolution of these spiral waves. The local time series data, for the transmembrane potential V_e and V_p , are recorded from the representative points ($x = 125$ mm, $y = 125$ mm) of both E- and P- layers (the asterisks in (c) and (f)). (g) Plot of the time series for V_e (blue, solid line) and V_p (red, dashed line); (h) plot of inter-beat interval (ibi) versus the beat number n associated with the E-layer (blue, open circles) and P-layer (filled, red squares); (i) plot of the power spectra $E(\omega)$ versus the frequency ω for the E-layer (blue, open circles) and P-layer (filled, red squares).

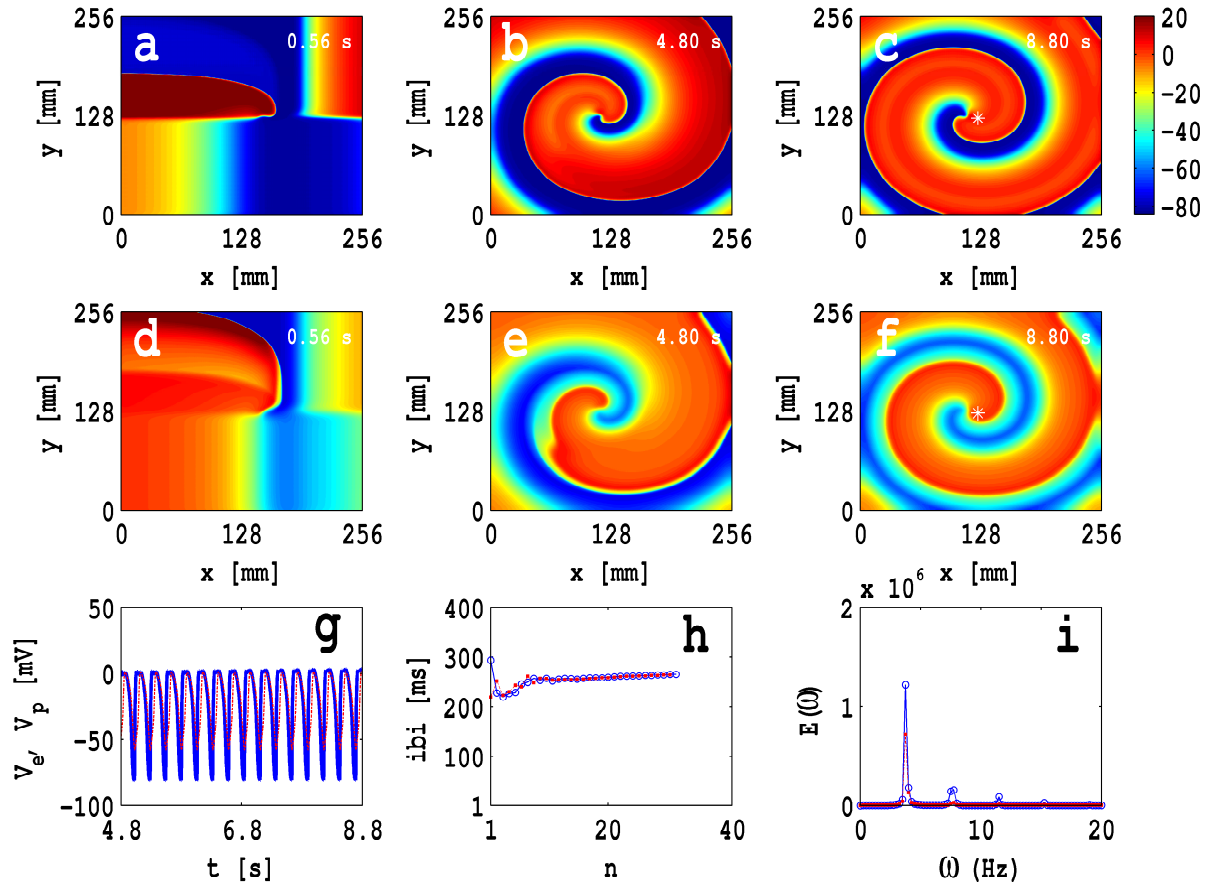


Figure S3: Spiral-wave dynamics in an EP-composite bilayer for the parameter set $\mathcal{P}1$, with the S1-S2 cross-field protocol in the E-cell layer, $D_{gap} = D_{mm}/10$, and $\mathcal{R} = 4$ (see Table 5.2); pseudocolor plots of V_e and V_p , the exact analogs of Figs. S2(a)-(f), are shown in (a)-(c) and (d)-(f), respectively; the animations in the bottom-left panel of Video S9 (labelled $\mathcal{R} = 4$) illustrate the spatiotemporal evolution of these spiral waves. The local time series, the ibi, and $E(\omega)$, are shown in plots (g), (h), and (i), respectively.

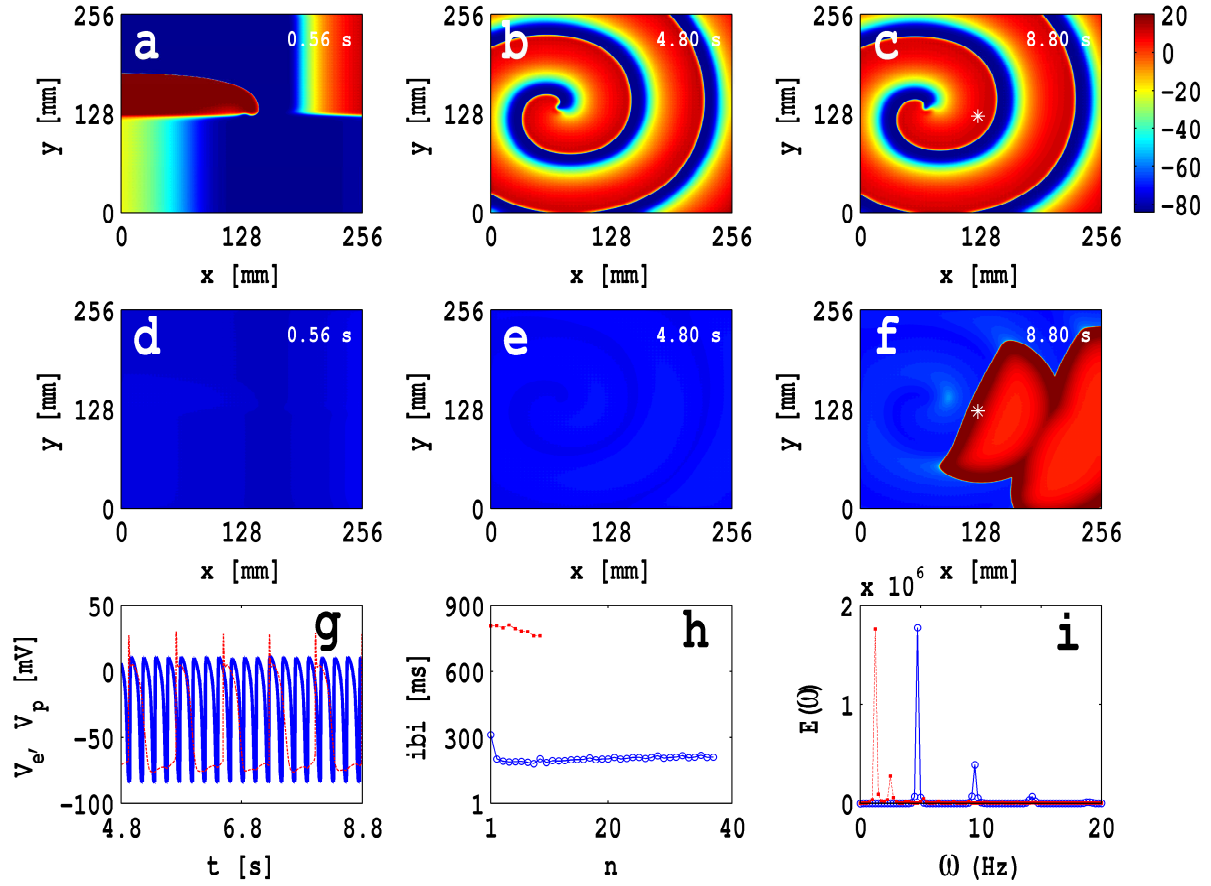


Figure S4: Spiral-wave dynamics in an EP-composite bilayer for the parameter set $\mathcal{P}1$, with the S1-S2 cross-field protocol in the E-cell layer, $D_{gap} = D_{mm}/10$, and $\mathcal{R} = 16$ (see Table 5.2); pseudocolor plots of V_e and V_p , the exact analogs of Figs. S2(a)-(f), are shown in (a)-(c) and (d)-(f), respectively; the animations in the middle-right panel of Video S9 (labelled $\mathcal{R} = 16$) illustrate the spatiotemporal evolution of these spiral waves. The local time series, the ibi, and $E(\omega)$, are shown in plots (g), (h), and (i), respectively.

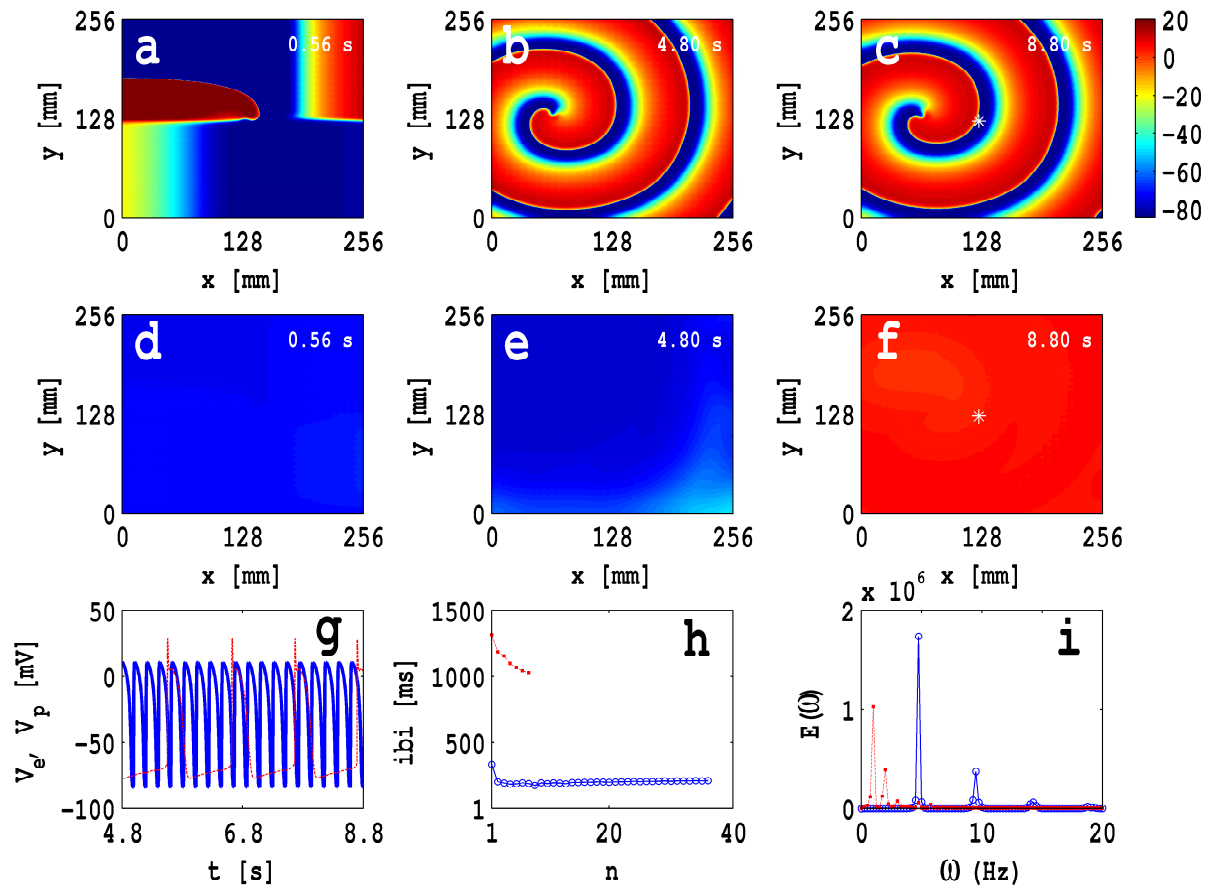


Figure S5: Spiral-wave dynamics in an EP-composite bilayer for the parameter set $\mathcal{P}1$, with the S1-S2 cross-field protocol in the E-cell layer, $D_{gap} = D_{mm}/10$, and $\mathcal{R} = 32$ (see Table 5.2); pseudocolor plots of V_e and V_p , the exact analogs of Figs. S2(a)-(f), are shown in (a)-(c) and (d)-(f), respectively; the animations in the bottom-right panel of Video S9 (labelled $\mathcal{R} = 32$) illustrate the spatiotemporal evolution of these spiral waves. The local time series, the ibi, and $E(\omega)$, are shown in plots (g), (h), and (i), respectively.

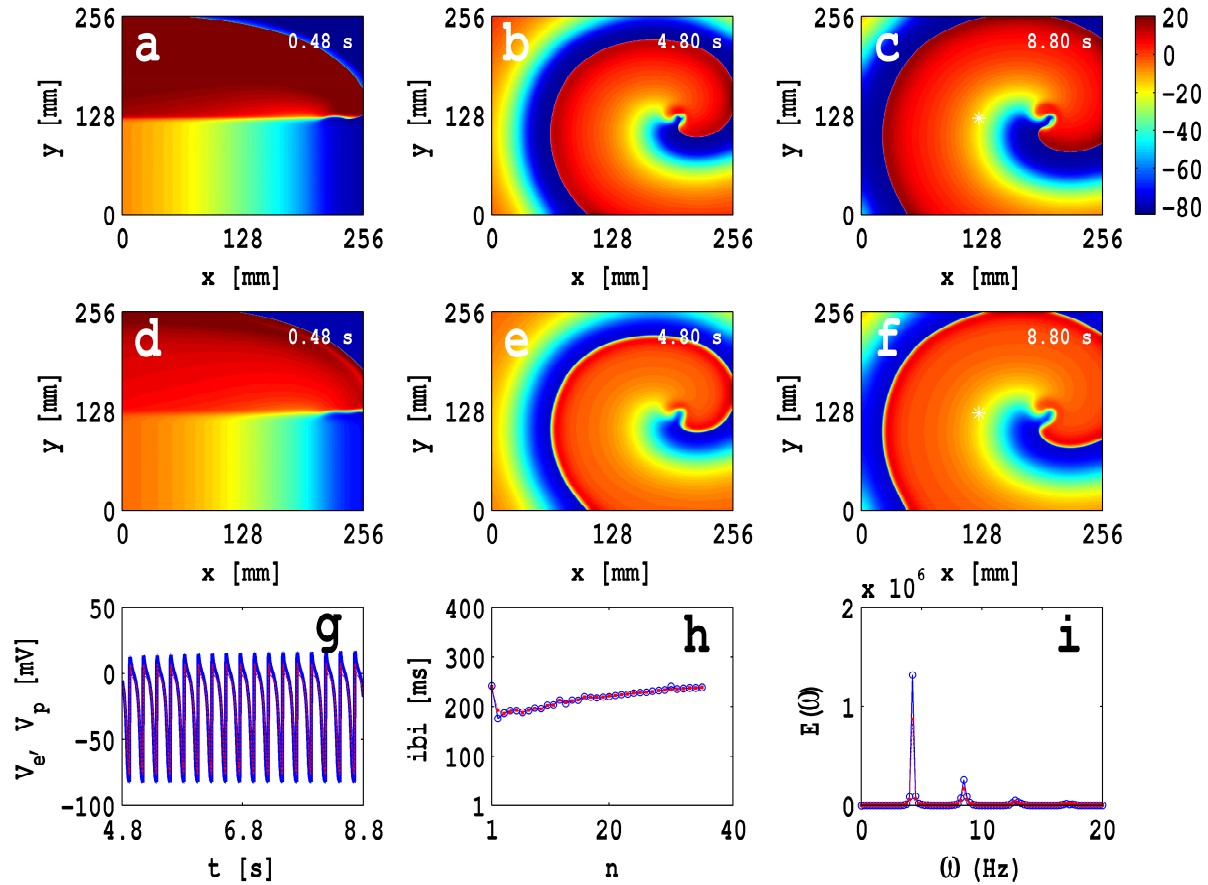


Figure S6: Spiral-wave dynamics in an EP-composite bilayer for the parameter set $\mathcal{P}2$, with the S1-S2 cross-field protocol in the E-cell layer, $D_{gap} = D_{mm}/10$, and $\mathcal{R} = 2$ (see Table 5.2); pseudocolor plots of V_e and V_p , the exact analogs of Figs. S2(a)-(f), are shown in (a)-(c) and (d)-(f), respectively; the animations in the middle-left panel of Video S10 (labelled $\mathcal{R} = 2$) illustrate the spatiotemporal evolution of these spiral waves. The local time series, the ibi, and $E(\omega)$, are shown in plots (g), (h), and (i), respectively.

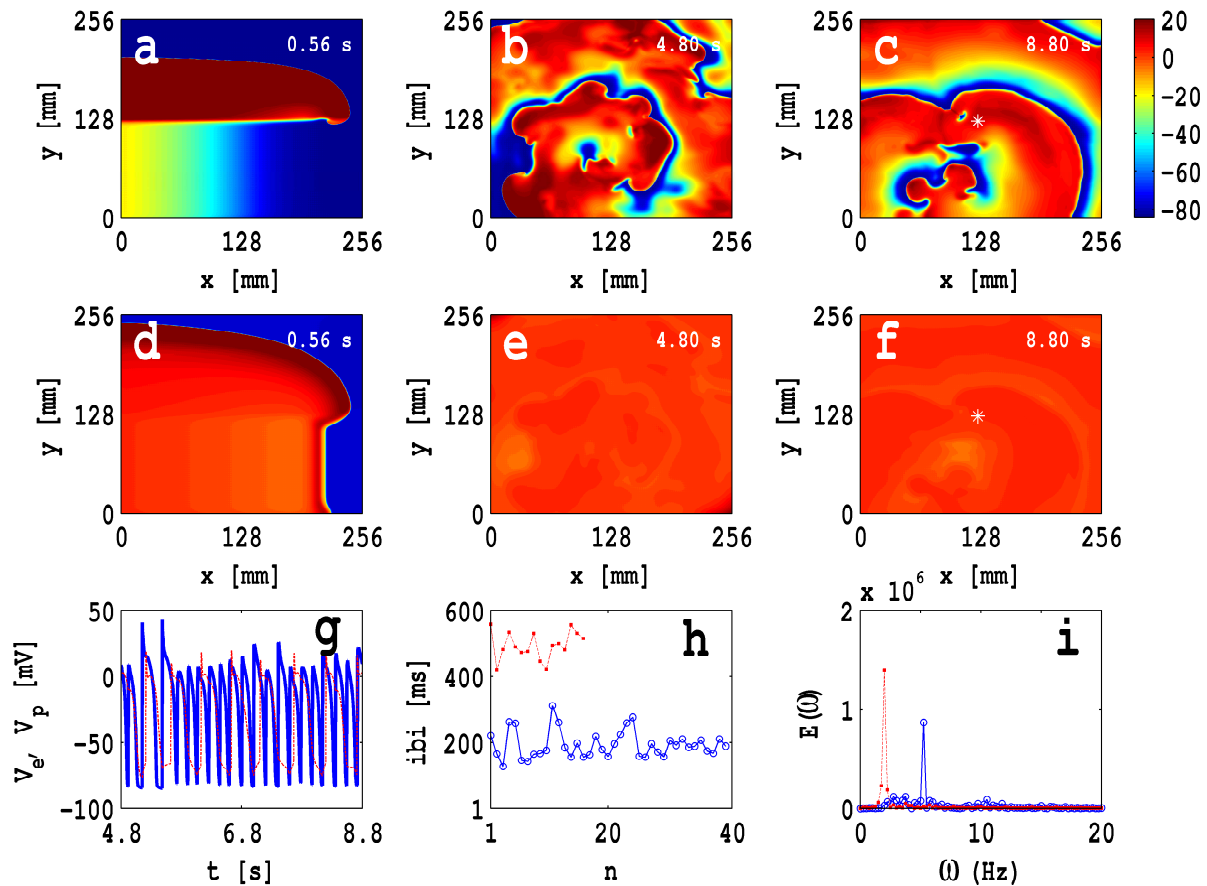


Figure S7: Spiral-wave dynamics in an EP-composite bilayer for the parameter set $\mathcal{P}2$, with the S1-S2 cross-field protocol in the E-cell layer, $D_{gap} = D_{mm}/10$, and $\mathcal{R} = 8$ (see Table 5.2); pseudocolor plots of V_e and V_p , the exact analogs of Figs. S2(a)-(f), are shown in (a)-(c) and (d)-(f), respectively; the animations in the top-right panel of Video S10 (labelled $\mathcal{R} = 8$) illustrate the spatiotemporal evolution of these spiral waves. The local time series, the ibi, and $E(\omega)$, are shown in plots (g), (h), and (i), respectively.

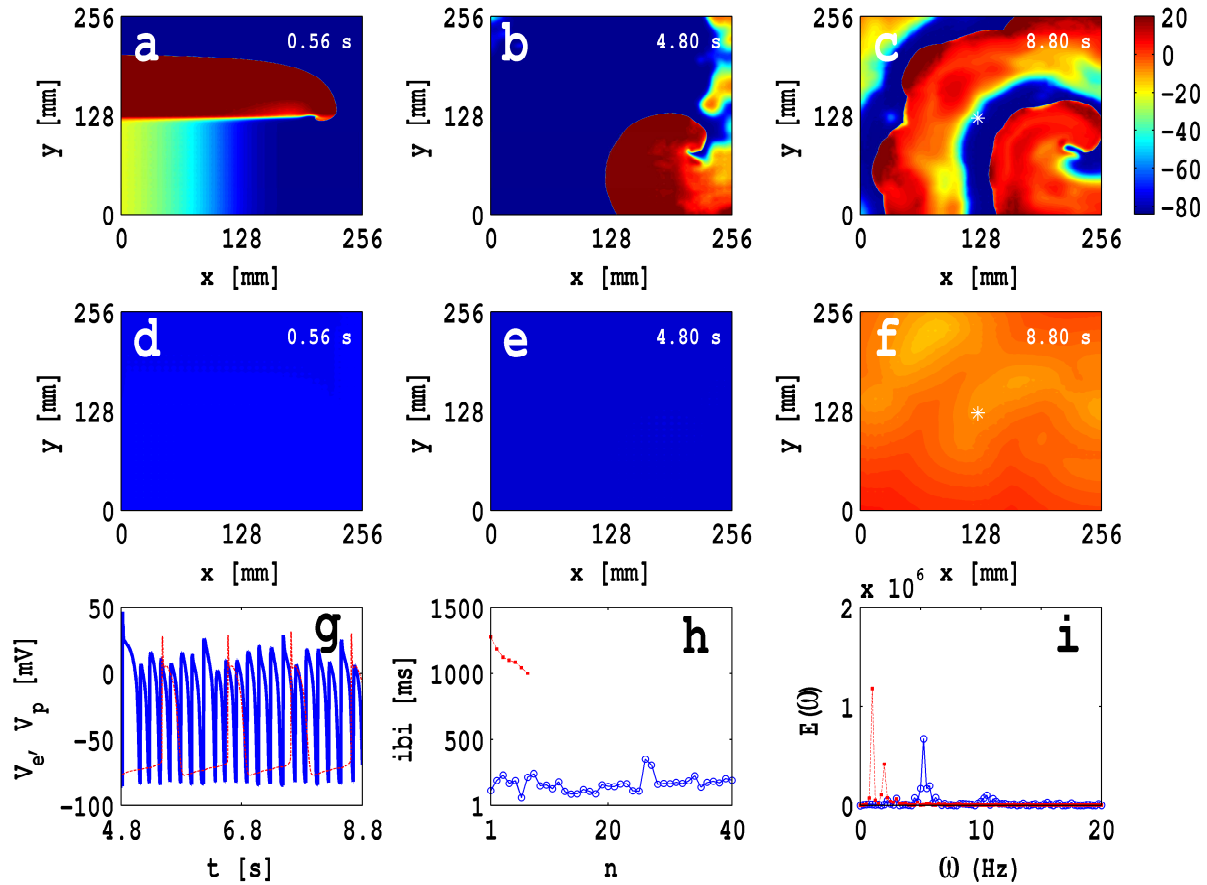


Figure S8: Spiral-wave dynamics in an EP-composite bilayer for the parameter set $\mathcal{P}2$, with the S1-S2 cross-field protocol in the E-cell layer, $D_{gap} = D_{mm}/10$, and $\mathcal{R} = 32$ (see Table 5.2); pseudocolor plots of V_e and V_p , the exact analogs of Figs. S2(a)-(f), are shown in (a)-(c) and (d)-(f), respectively; the animations in the bottom-right panel of Video S10 (labelled $\mathcal{R} = 32$) illustrate the spatiotemporal evolution of these spiral waves. The local time series, the ibi , and $E(\omega)$, are shown in plots (g), (h), and (i), respectively.

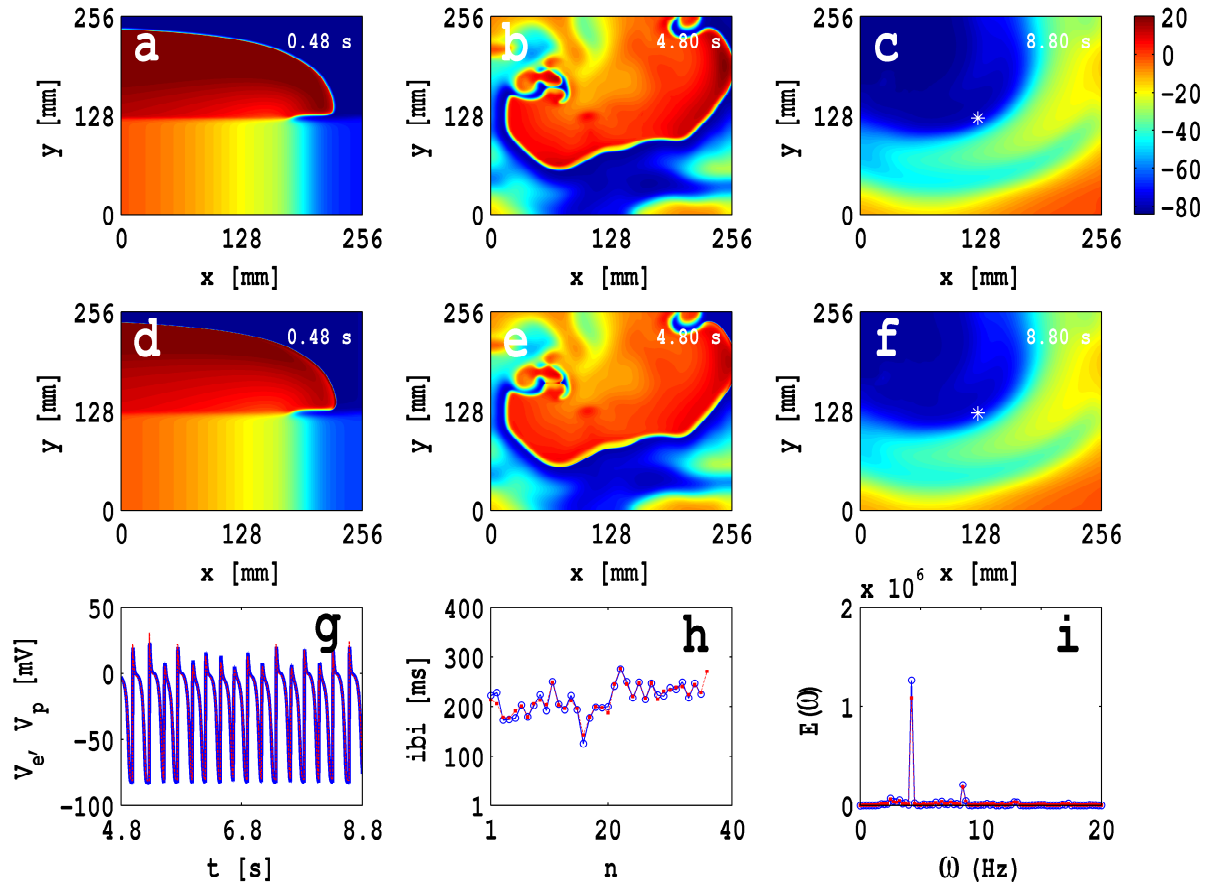


Figure S9: Spiral-wave dynamics in an EP-composite bilayer for the parameter set $\mathcal{P}3$, with the S1-S2 cross-field protocol in the E-cell layer, $D_{gap} = D_{mm}/10$, and $\mathcal{R} = 1$ (see Table 5.2); pseudocolor plots of V_e and V_p , the exact analogs of Figs. S2(a)-(f), are shown in (a)-(c) and (d)-(f), respectively; the animations in the top-left panel of Video S11 (labelled $\mathcal{R} = 1$) illustrate the spatiotemporal evolution of these spiral waves. The local time series, the ibi, and $E(\omega)$, are shown in plots (g), (h), and (i), respectively.

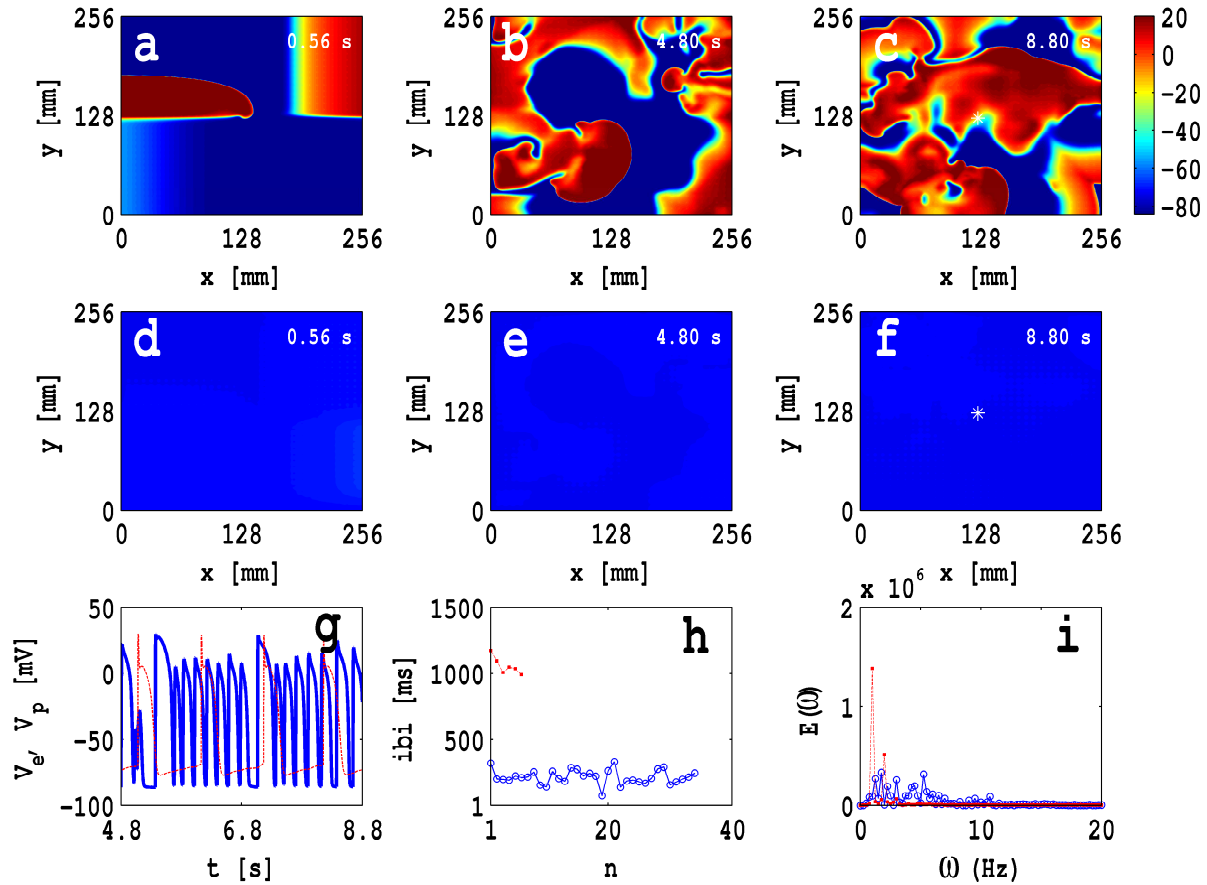


Figure S10: Spiral-wave dynamics in an EP-composite bilayer for the parameter set $\mathcal{P}3$, with the S1-S2 cross-field protocol in the E-cell layer, $D_{gap} = D_{mm}/10$, and $\mathcal{R} = 32$ (see Table 5.2); pseudocolor plots of V_e and V_p , the exact analogs of Figs. S2(a)-(f), are shown in (a)-(c) and (d)-(f), respectively; the animations in the bottom-right panel of Video S11 (labelled $\mathcal{R} = 32$) illustrate the spatiotemporal evolution of these spiral waves. The local time series, the ibi, and $E(\omega)$, are shown in plots (g), (h), and (i), respectively.

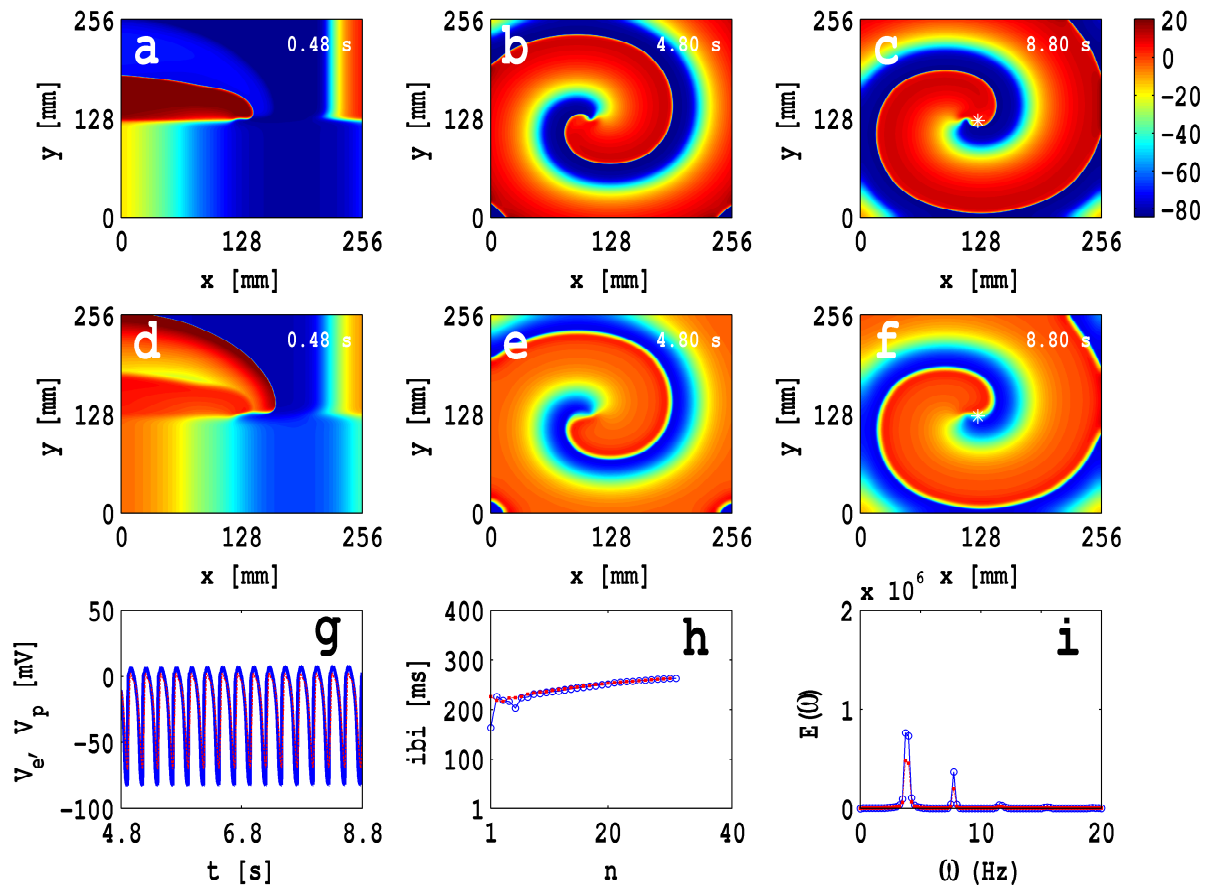


Figure S11: Spiral-wave dynamics in an EP-composite bilayer for the parameter set $\mathcal{P}1$, with the S1-S2 cross-field protocol in the E-cell layer, $D_{gap} = D_{mm}/100$, and $\mathcal{R} = 1$ (see Table 5.3); pseudocolor plots of V_e and V_p , the exact analogs of Figs. S2(a)-(f), are shown in (a)-(c) and (d)-(f), respectively. The local time series, the ibi , and $E(\omega)$, are shown in plots (g), (h), and (i), respectively.

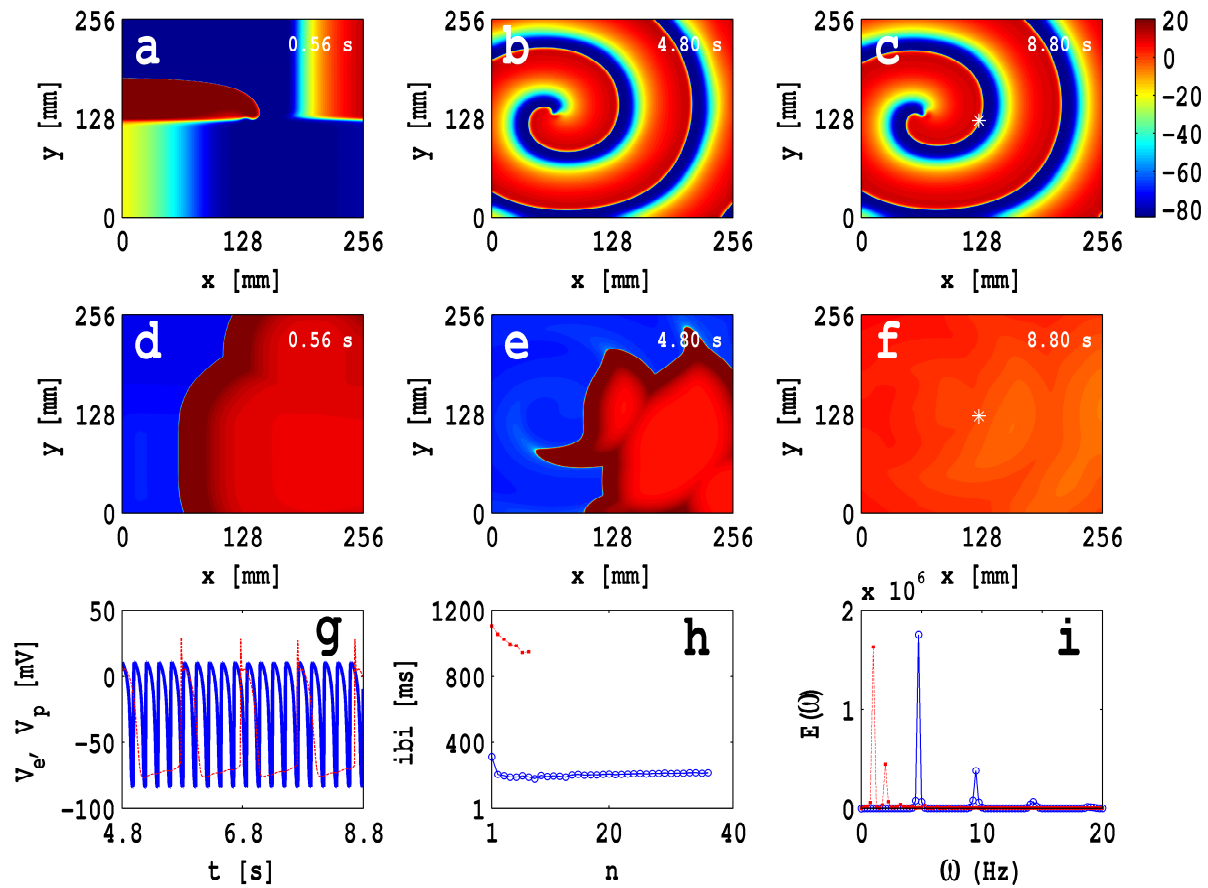


Figure S12: Spiral-wave dynamics in an EP-composite bilayer for the parameter set $\mathcal{P}1$, with the S1-S2 cross-field protocol in the E-cell layer, $D_{gap} = D_{mm}/100$, and $\mathcal{R} = 8$ (see Table 5.3); pseudocolor plots of V_e and V_p , the exact analogs of Figs. S2(a)-(f), are shown in (a)-(c) and (d)-(f), respectively. The local time series, the ibi, and $E(\omega)$, are shown in plots (g), (h), and (i), respectively.

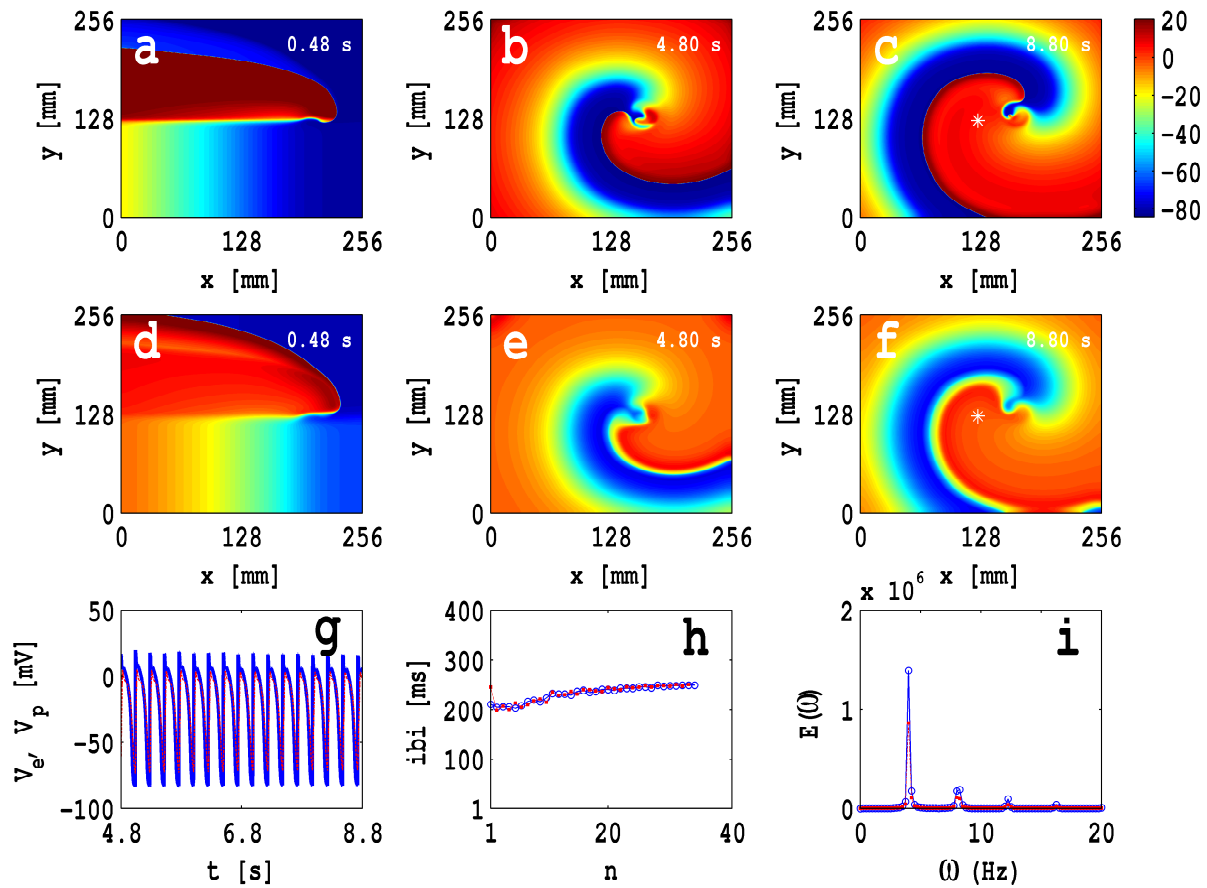


Figure S13: Spiral-wave dynamics in an EP-composite bilayer for the parameter set $\mathcal{P}2$, with the S1-S2 cross-field protocol in the E-cell layer, $D_{gap} = D_{mm}/100$, and $\mathcal{R} = 1$ (see Table 5.3); pseudocolor plots of V_e and V_p , the exact analogs of Figs. S2(a)-(f), are shown in (a)-(c) and (d)-(f), respectively. The local time series, the ibi , and $E(\omega)$, are shown in plots (g), (h), and (i), respectively.

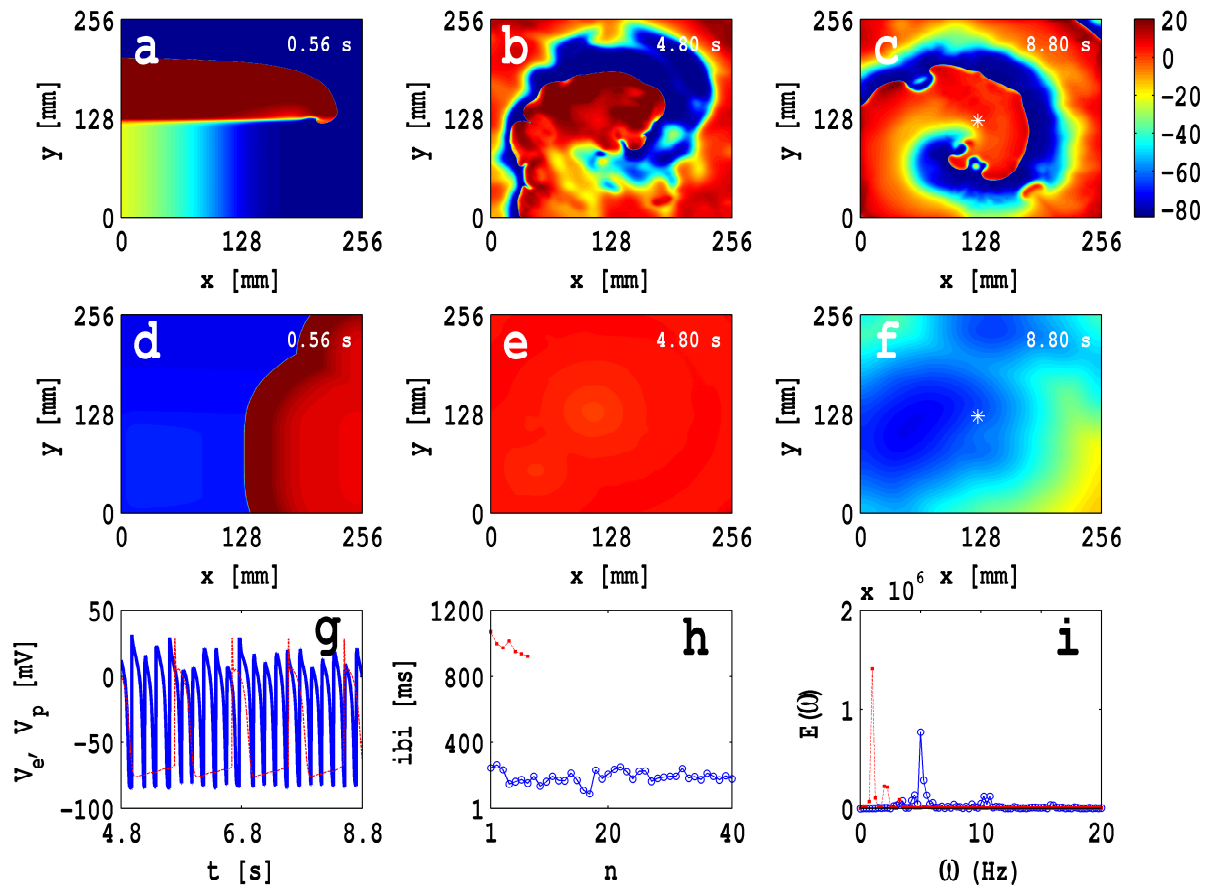


Figure S14: Spiral-wave dynamics in an EP-composite bilayer for the parameter set $\mathcal{P}2$, with the S1-S2 cross-field protocol in the E-cell layer, $D_{gap} = D_{mm}/100$, and $\mathcal{R} = 8$ (see Table 5.3); pseudocolor plots of V_e and V_p , the exact analogs of Figs. S2(a)-(f), are shown in (a)-(c) and (d)-(f), respectively. The local time series, the ibi, and $E(\omega)$, are shown in plots (g), (h), and (i), respectively.

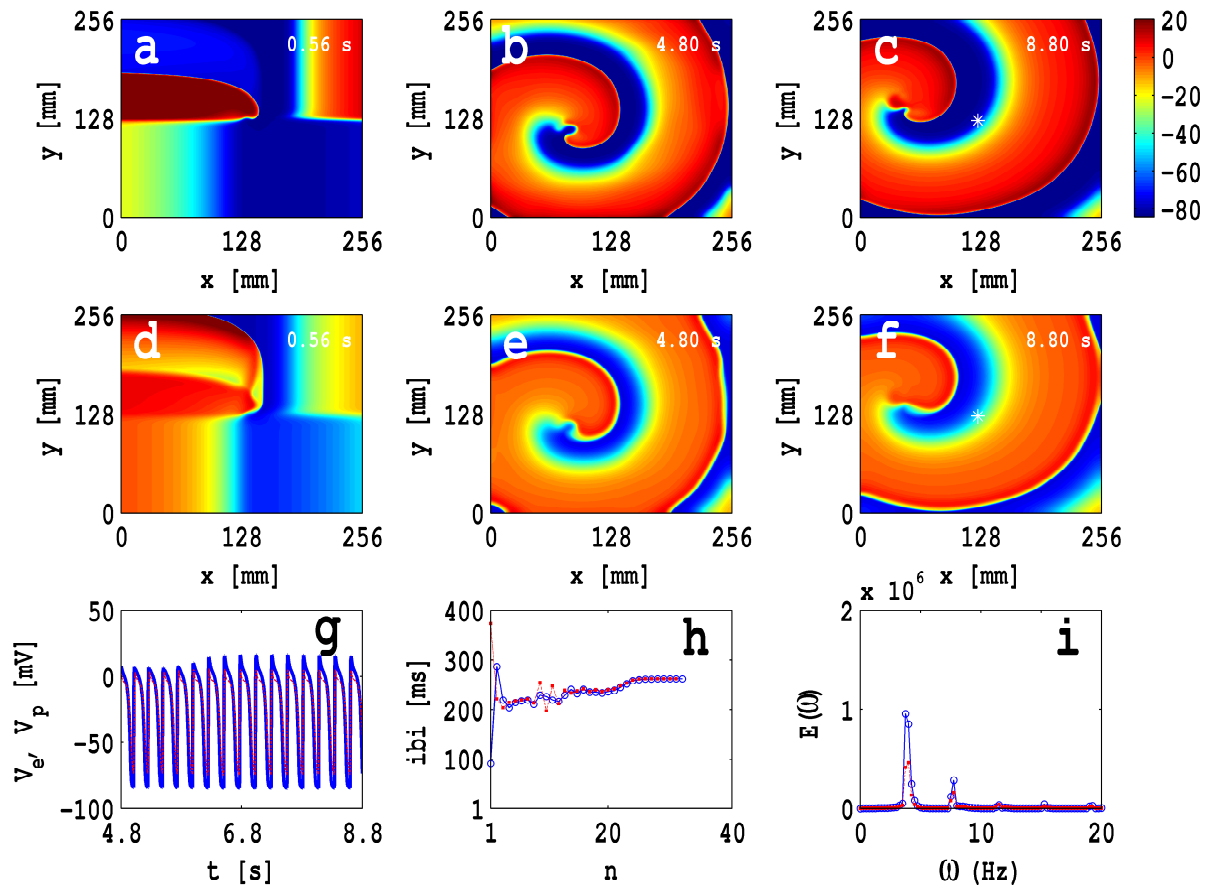


Figure S15: Spiral-wave dynamics in an EP-composite bilayer for the parameter set $\mathcal{P}3$, with the S1-S2 cross-field protocol in the E-cell layer, $D_{gap} = D_{mm}/100$, and $\mathcal{R} = 1$ (see Table 5.3); pseudocolor plots of V_e and V_p , the exact analogs of Figs. S2(a)-(f), are shown in (a)-(c) and (d)-(f), respectively. The local time series, the ibi , and $E(\omega)$, are shown in plots (g), (h), and (i), respectively.

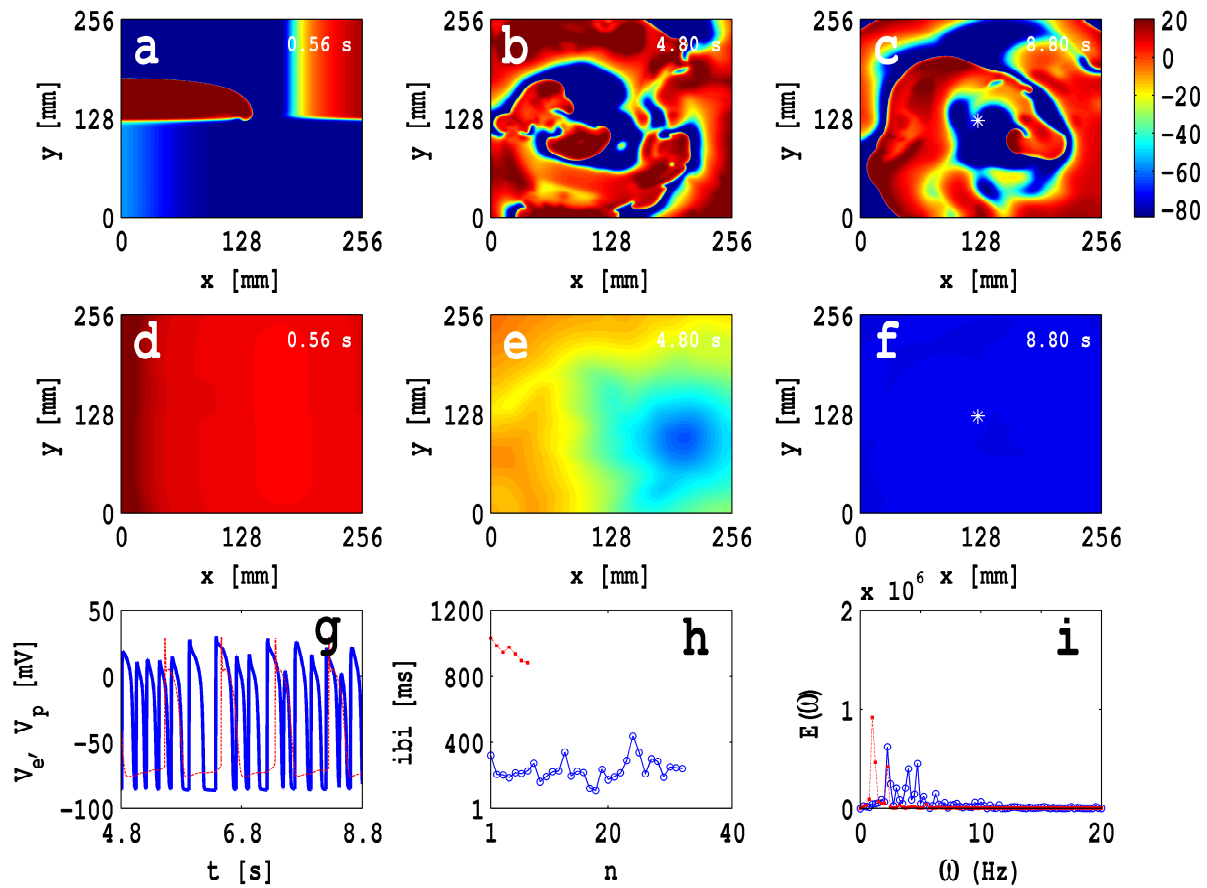


Figure S16: Spiral-wave dynamics in an EP-composite bilayer for the parameter set $\mathcal{P}3$, with the S1-S2 cross-field protocol in the E-cell layer, $D_{gap} = D_{mm}/100$, and $\mathcal{R} = 8$ (see Table 5.3); pseudocolor plots of V_e and V_p , the exact analogs of Figs. S2(a)-(f), are shown in (a)-(c) and (d)-(f), respectively. The local time series, the ibi, and $E(\omega)$, are shown in plots (g), (h), and (i), respectively.

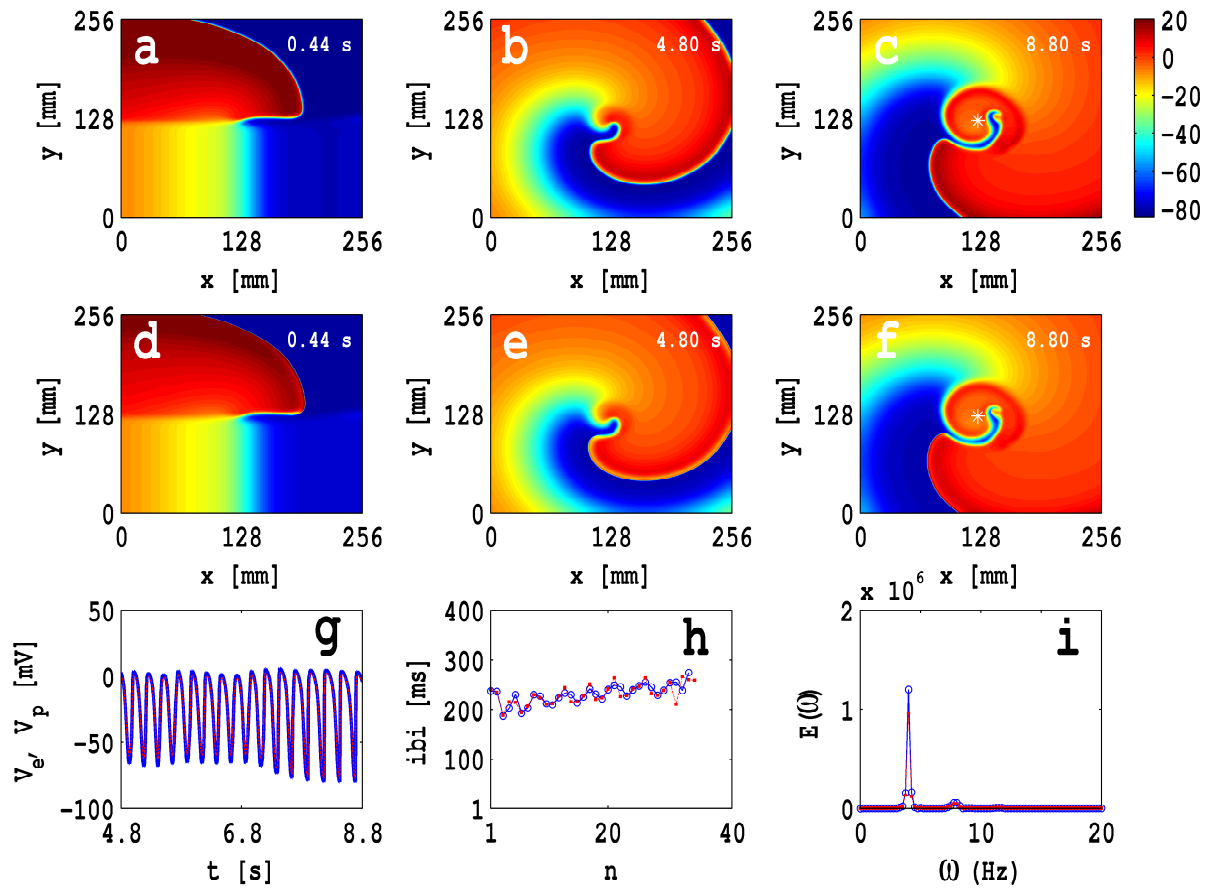


Figure S17: Spiral-wave dynamics in an EP-composite bilayer for the parameter set $\mathcal{P}1$, with the S1-S2 cross-field protocol in the P-cell layer, $D_{gap} = D_{mm}/10$, and $\mathcal{R} = 1$ (see Table 5.3); pseudocolor plots of V_e and V_p , the exact analogs of Figs. S2(a)-(f), are shown in (a)-(c) and (d)-(f), respectively. The local time series, the ibi , and $E(\omega)$, are shown in plots (g), (h), and (i), respectively.

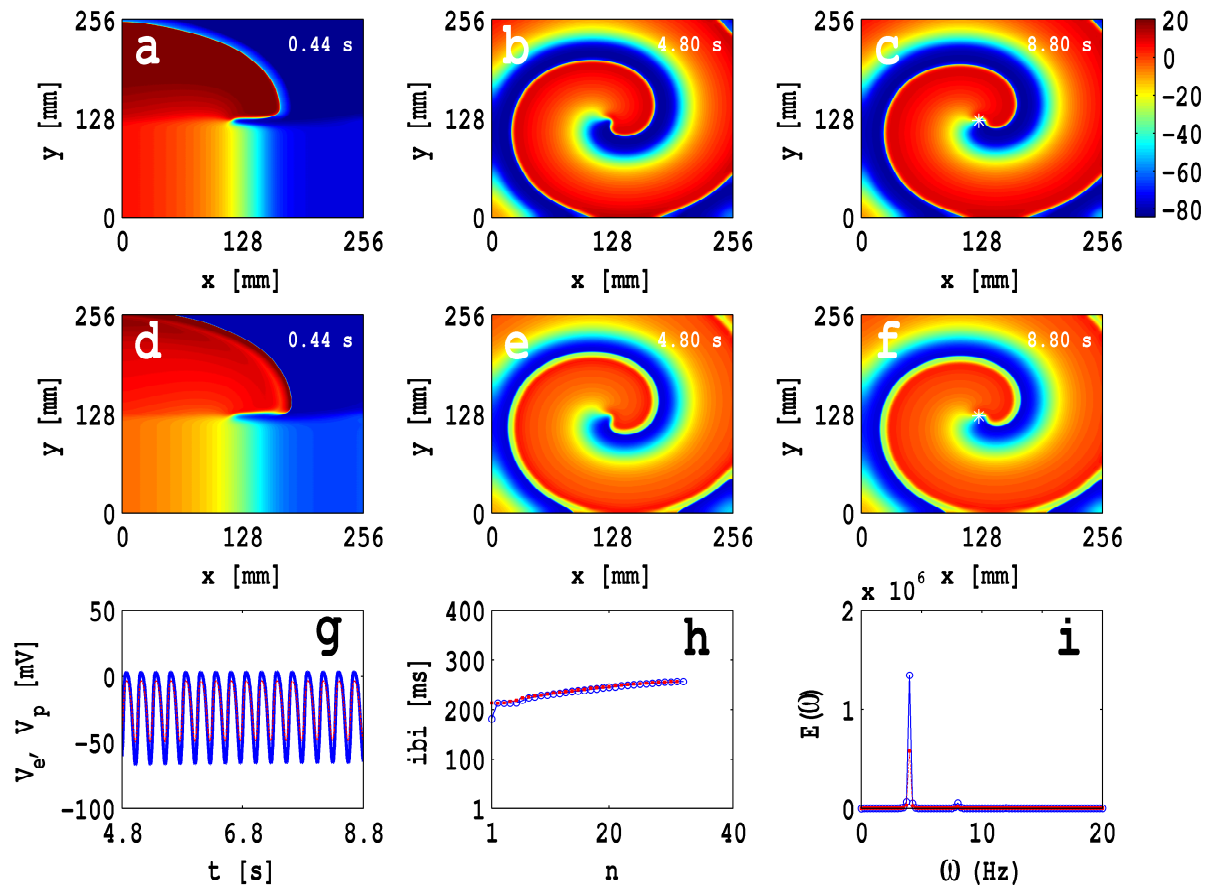


Figure S18: Spiral-wave dynamics in an EP-composite bilayer for the parameter set $\mathcal{P}1$, with the S1-S2 cross-field protocol in the P-cell layer, $D_{gap} = D_{mm}/10$, and $\mathcal{R} = 2$ (see Table 5.3); pseudocolor plots of V_e and V_p , the exact analogs of Figs. S2(a)-(f), are shown in (a)-(c) and (d)-(f), respectively. The local time series, the ibi , and $E(\omega)$, are shown in plots (g), (h), and (i), respectively.

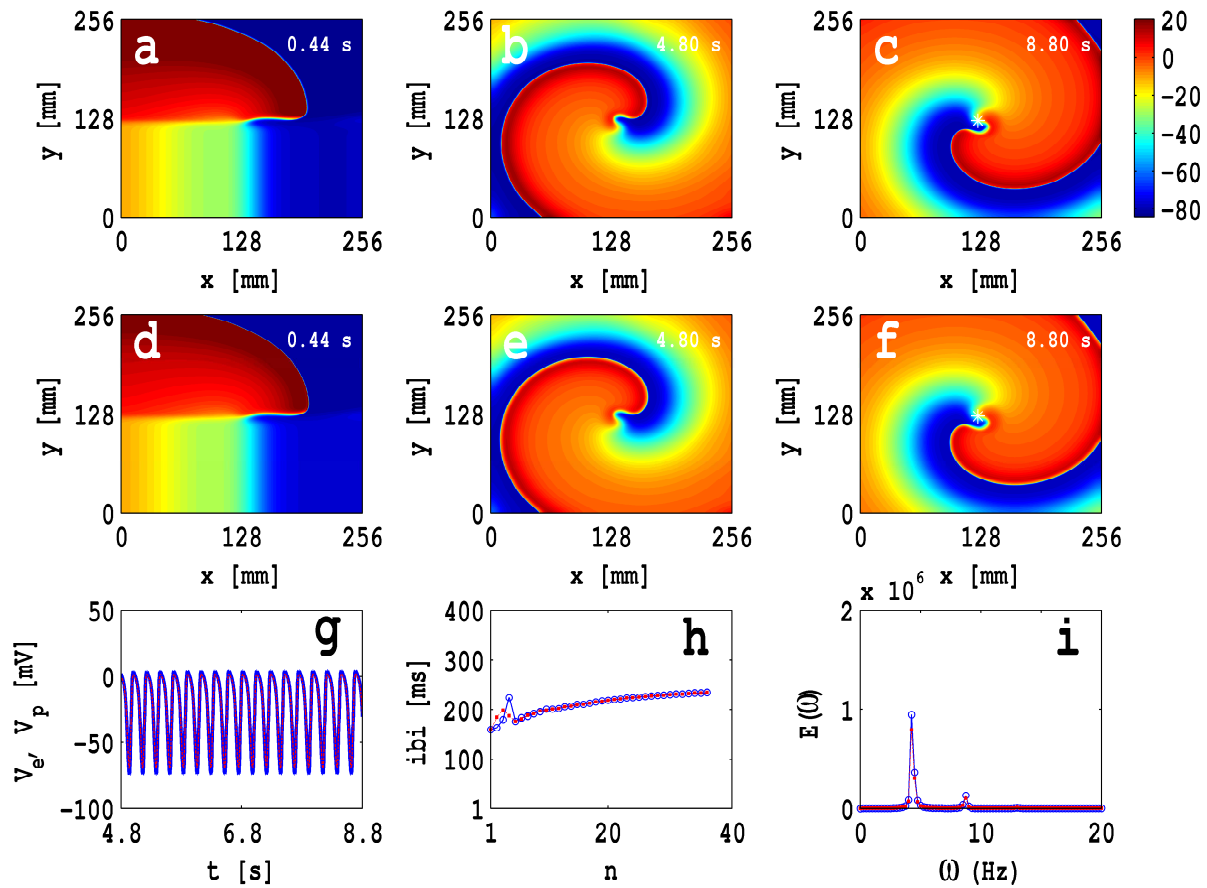


Figure S19: Spiral-wave dynamics in an EP-composite bilayer for the parameter set $\mathcal{P}2$, with the S1-S2 cross-field protocol in the P-cell layer, $D_{gap} = D_{mm}/10$, and $\mathcal{R} = 1$ (see Table 5.3); pseudocolor plots of V_e and V_p , the exact analogs of Figs. S2(a)-(f), are shown in (a)-(c) and (d)-(f), respectively. The local time series, the ibi , and $E(\omega)$, are shown in plots (g), (h), and (i), respectively.

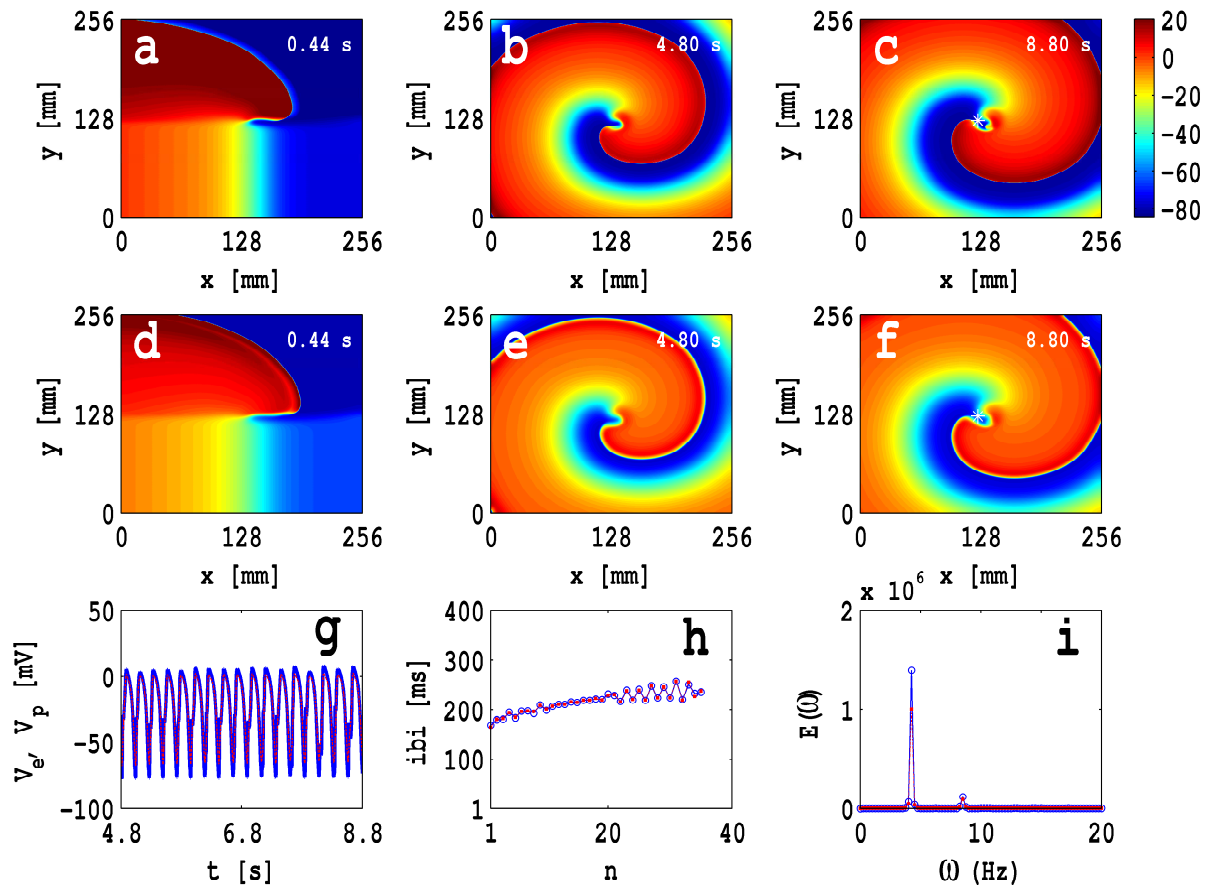


Figure S20: Spiral-wave dynamics in an EP-composite bilayer for the parameter set $\mathcal{P}2$, with the S1-S2 cross-field protocol in the P-cell layer, $D_{gap} = D_{mm}/10$, and $\mathcal{R} = 2$ (see Table 5.3); pseudocolor plots of V_e and V_p , the exact analogs of Figs. S2(a)-(f), are shown in (a)-(c) and (d)-(f), respectively. The local time series, the ibi , and $E(\omega)$, are shown in plots (g), (h), and (i), respectively.

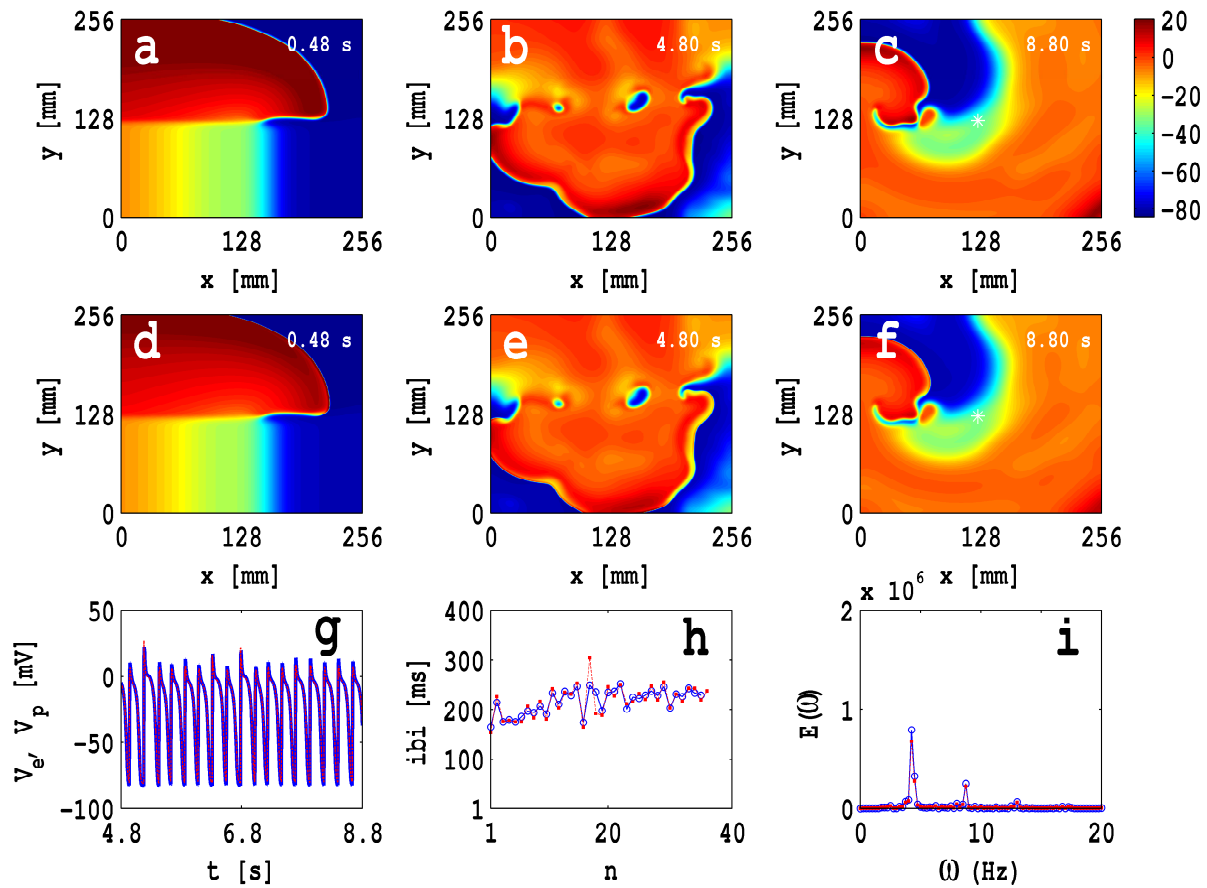


Figure S21: Spiral-wave dynamics in an EP-composite bilayer for the parameter set $\mathcal{P}3$, with the S1-S2 cross-field protocol in the P-cell layer, $D_{gap} = D_{mm}/10$, and $\mathcal{R} = 1$ (see Table 5.3); pseudocolor plots of V_e and V_p , the exact analogs of Figs. S2(a)-(f), are shown in (a)-(c) and (d)-(f), respectively. The local time series, the ibi , and $E(\omega)$, are shown in plots (g), (h), and (i), respectively.

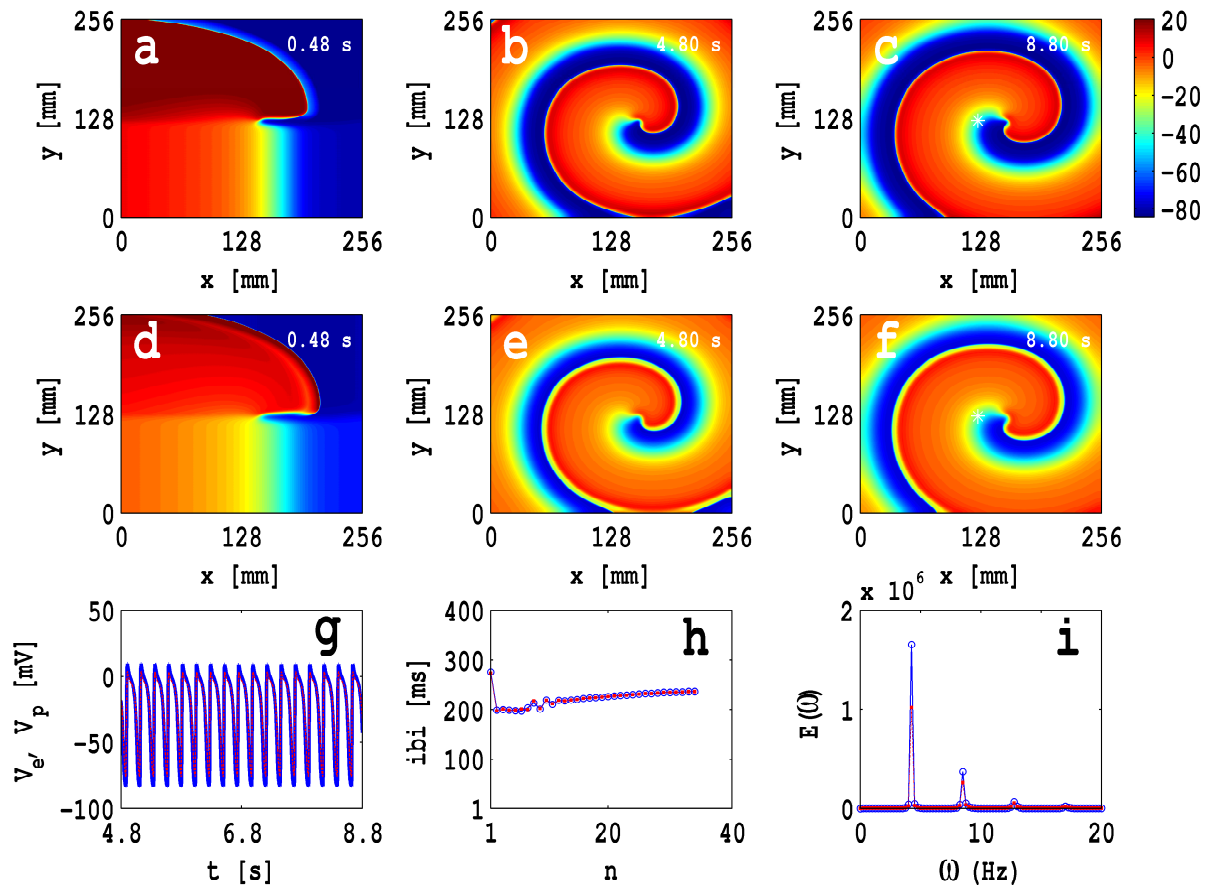


Figure S22: Spiral-wave dynamics in an EP-composite bilayer for the parameter set $\mathcal{P}3$, with the S1-S2 cross-field protocol in the P-cell layer, $D_{gap} = D_{mm}/10$, and $\mathcal{R} = 2$ (see Table 5.3); pseudocolor plots of V_e and V_p , the exact analogs of Figs. S2(a)-(f), are shown in (a)-(c) and (d)-(f), respectively. The local time series, the ibi , and $E(\omega)$, are shown in plots (g), (h), and (i), respectively.

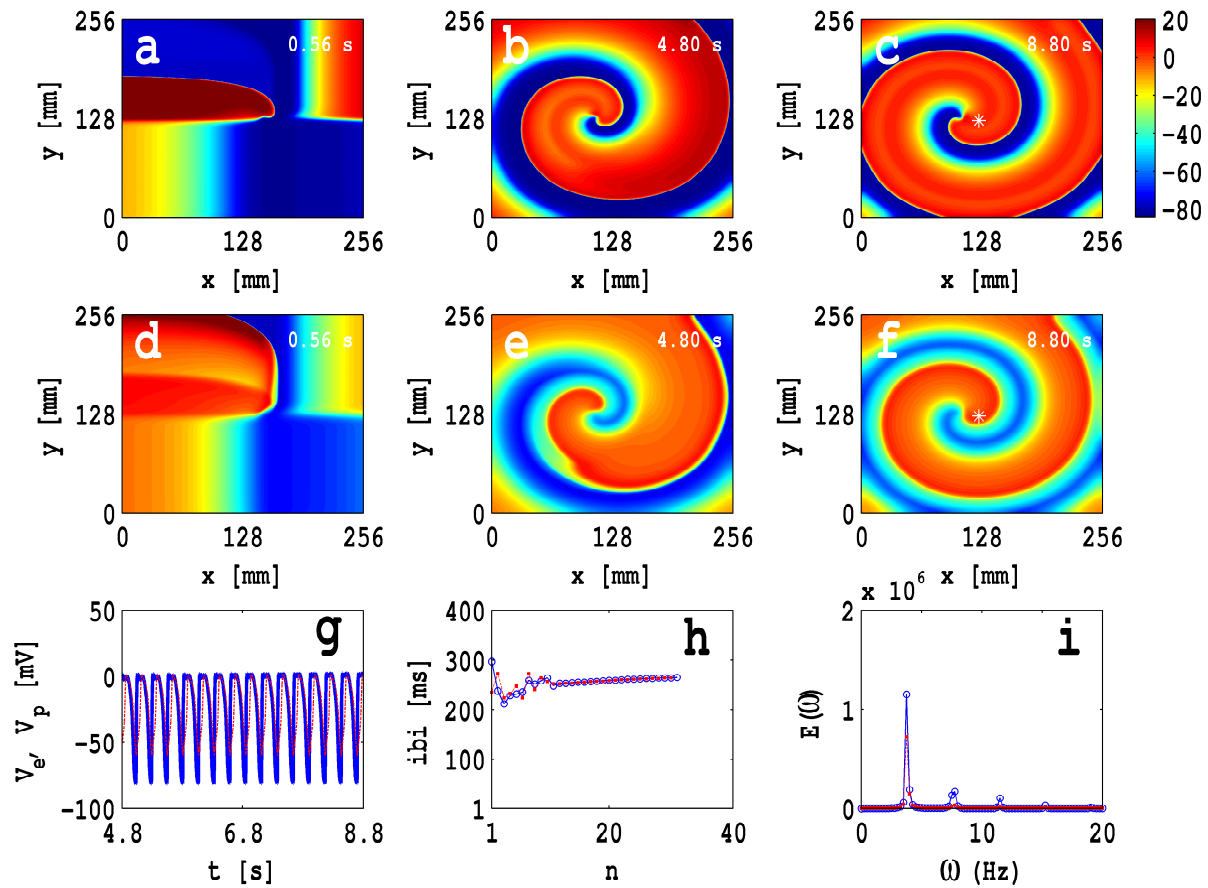


Figure S23: Spiral-wave dynamics in an EP-composite bilayer for the parameter set $\mathcal{P}1$, with the S1-S2 cross-field protocol in the both E- and P-cell layers, $D_{gap} = D_{mm}/10$, and $\mathcal{R} = 4$ (see Table 5.3); pseudocolor plots of V_e and V_p , the exact analogs of Figs. S2(a)-(f), are shown in (a)-(c) and (d)-(f), respectively. The local time series, the $|b_i|$, and $E(\omega)$, are shown in plots (g), (h), and (i), respectively.

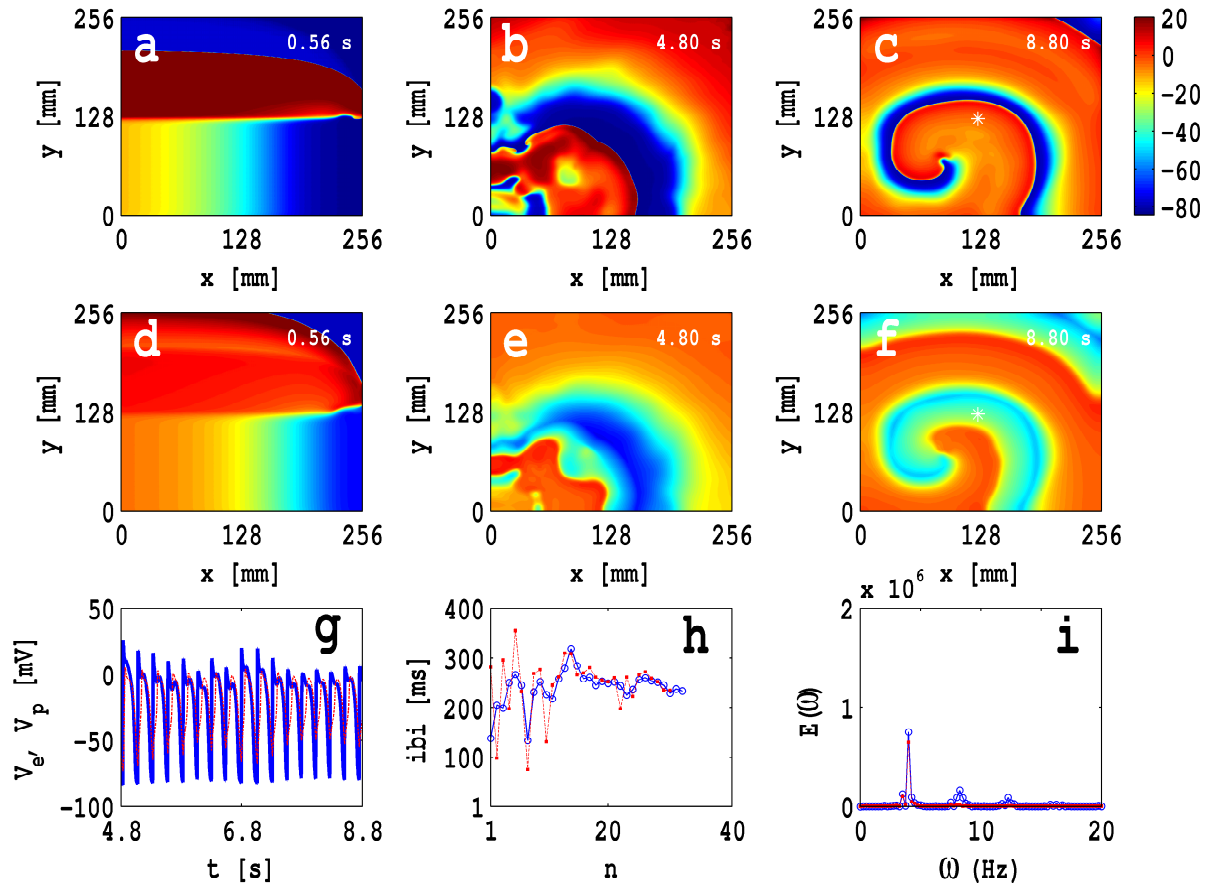


Figure S24: Spiral-wave dynamics in an EP-composite bilayer for the parameter set $\mathcal{P}2$, with the S1-S2 cross-field protocol in the both E- and P-cell layers, $D_{gap} = D_{mm}/10$, and $\mathcal{R} = 4$ (see Table 5.3); pseudocolor plots of V_e and V_p , the exact analogs of Figs. S2(a)-(f), are shown in (a)-(c) and (d)-(f), respectively. The local time series, the $|b_i|$, and $E(\omega)$, are shown in plots (g), (h), and (i), respectively.

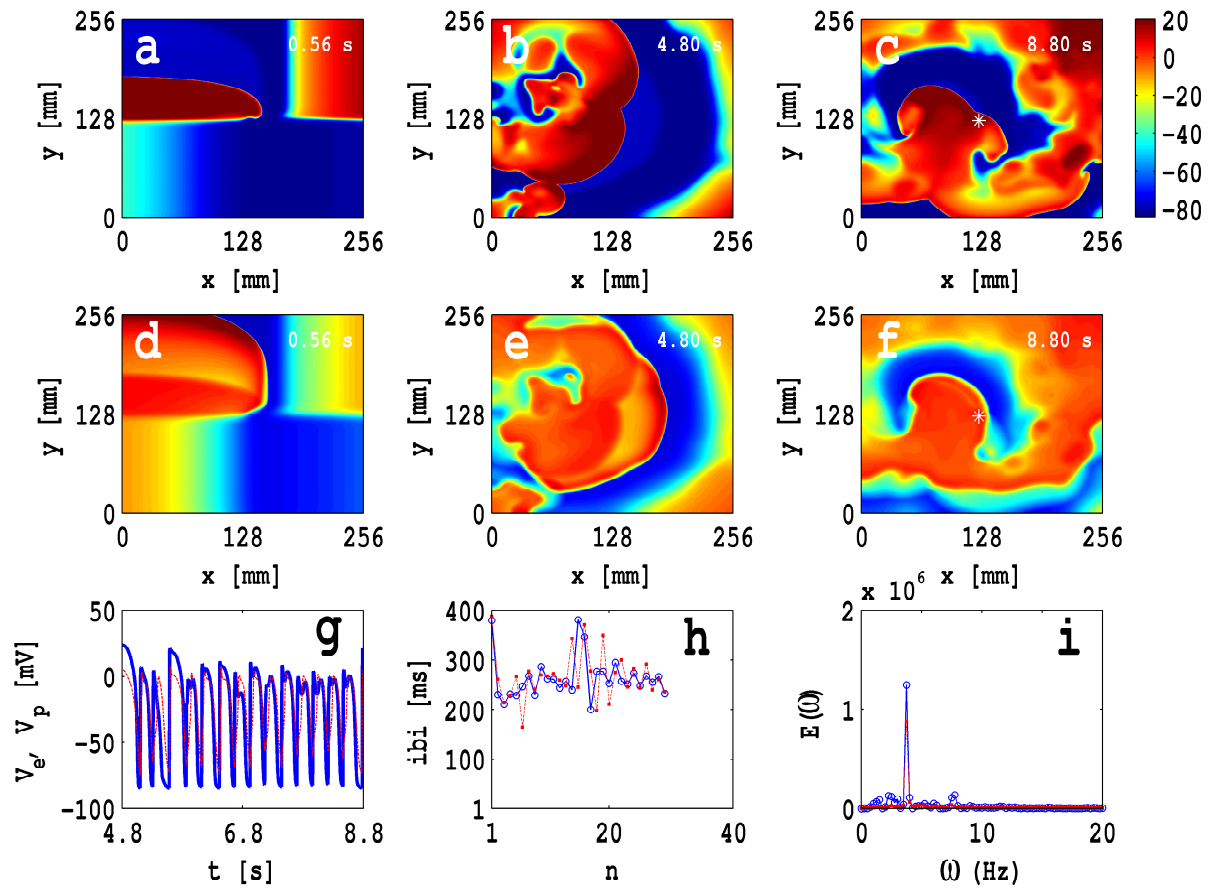


Figure S25: Spiral-wave dynamics in an EP-composite bilayer for the parameter set $\mathcal{P}3$, with the S1-S2 cross-field protocol in the both E- and P-cell layers, $D_{gap} = D_{mm}/10$, and $\mathcal{R} = 4$ (see Table 5.3); pseudocolor plots of V_e and V_p , the exact analogs of Figs. S2(a)-(f), are shown in (a)-(c) and (d)-(f), respectively. The local time series, the $|b_i|$, and $E(\omega)$, are shown in plots (g), (h), and (i), respectively.

Appendix A

A.1 The TNNP04 Model

This model has been developed for human cardiac cell [1], especially to study the action potential morphology of endocardium, epicardium, and midmyocardium cells. The model consists of 12 components of the ionic current, namely, the fast inward Na^+ current I_{Na} , the L-type slow inward Ca^{2+} current I_{CaL} , the transient outward current I_{to} , the slow delayed rectifier current I_{Ks} , the rapid delayed rectifier current I_{Kr} , the inward rectifier K^+ current I_{K1} , the Na^+/Ca^{2+} exchanger current I_{NaCa} , the Na^+/K^+ pump current I_{NaK} , the plateau Ca^{2+} current I_{pCa} , the plateau K^+ current I_{pK} , the background Na^+ current I_{bNa} , and the background Ca^{2+} current I_{bCa} . It uses 17 variables: (a) 1 for the transmembrane potential V_m , (b) 12 for ion channel gates, namely, m , h , j , d , f , f_{Ca} , r , s , x_s , x_{r1} , x_{r2} , and g , and (c) 4 for ion concentrations dynamics, namely, Na_i , K_i , Ca_i , and Ca_{sr} .

All current densities are measured in the units of pA/pF, V_m in mV, and ion concentrations in mM/L; the ionic currents are determined by the time-dependent ion-channel gating variables, as given above, generically denoted by ξ , which follow ordinary differential equations of the type

$$\frac{d\xi}{dt} = \frac{\xi_\infty - \xi}{\tau_\xi},$$

where $\xi_\infty = \alpha_\xi / (\alpha_\xi + \beta_\xi)$ is the steady-state value of ξ and $\tau_\xi = \frac{1}{\alpha_\xi + \beta_\xi}$ is its time constant; here, α_ξ and β_ξ are voltage-dependent rate constants associated with the gate ξ .

Reversal potentials

At equilibrium the reversal potentials obey the Nernst equation:

$$E_X = \frac{RT}{zF} \log \frac{X_o}{X_i} \quad \text{for } X = Na^+, K^+, Ca^{2+} \quad (\text{A.1})$$

$$E_{Ks} = \frac{RT}{F} \log \frac{K_o + p_{KNa} Na_o}{K_i + p_{KNa} Na_i}, \quad (\text{A.2})$$

where R is the gas constant, T the temperature, z the valence of the ion, F the Faraday constant, X_o and X_i the extra- and intra-cellular ionic concentrations, p_{KNa} the relative I_{Ks} permeability to Na^+ .

Ionic currents

Fast Na^+ current (inward)

$$I_{Na} = G_{Na} m^3 h j (V - E_{Na}) \quad (\text{A.3})$$

$$m_\infty = \frac{1}{[1 + \exp(\frac{-56.86 - V}{9.03})]^2} \quad (\text{A.4})$$

$$\alpha_m = \frac{1}{1 + \exp(\frac{-60 - V}{5})} \quad (\text{A.5})$$

$$\beta_m = \frac{0.1}{1 + \exp(\frac{V + 35}{5})} + \frac{0.1}{1 + \exp(\frac{V - 50}{200})} \quad (\text{A.6})$$

$$\tau_m = \alpha_m \beta_m \quad (\text{A.7})$$

$$h_\infty = \frac{1}{[1 + \exp(\frac{V + 71.55}{7.43})]^2} \quad (\text{A.8})$$

$$\begin{aligned} \alpha_h &= 0 \quad \text{if } V \geq -40 \\ &= 0.057 \exp\left(\frac{-(V + 80)}{6.8}\right) \quad (\text{otherwise}) \end{aligned} \quad (\text{A.9})$$

$$\beta_h = \frac{0.77}{0.13 \left[1 + \exp\left(\frac{-(V+10.66)}{11.1}\right) \right]} \quad \text{if } V \geq -40 \quad (\text{A.10})$$

$$= 2.7 \exp(0.079V) + 3.1 \times 10^5 \exp(0.3485V) \quad (\text{otherwise})$$

$$\tau_h = \frac{1}{\alpha_h + \beta_h} \quad (\text{A.11})$$

$$j_\infty = \frac{1}{\left[1 + \exp\left(\frac{V+71.55}{7.43}\right) \right]^2} \quad (\text{A.12})$$

$$\alpha_j = 0 \quad \text{if } V \geq -40 \quad (\text{A.13})$$

$$= \frac{(-2.5428 \times 10^4 \exp(0.2444V) - 6.948 \times 10^{-6} \exp(-0.04391V))(V + 37.38)}{1 + \exp(0.311(V + 79.23))} \quad (\text{otherwise})$$

$$\beta_j = \frac{0.6 \exp(0.057V)}{1 + \exp(-0.1(V + 32))} \quad \text{if } V \geq -40 \quad (\text{A.14})$$

$$= \frac{0.02424 \exp(-0.01052V)}{1 + \exp(-0.1378(V + 40.14))} \quad (\text{otherwise})$$

$$\tau_j = \frac{1}{\alpha_j + \beta_j} \quad (\text{A.15})$$

L-type Ca²⁺ current (inward)

$$I_{CaL} = G_{CaL} df_{Ca} 4 \frac{VF^2}{RT} \frac{Ca_i \exp(\frac{2VF}{RT}) - 0.0341 Ca_o}{\exp(\frac{2VF}{RT}) - 1} \quad (\text{A.16})$$

$$d_\infty = \frac{1}{1 + \exp(\frac{-5-V}{7.5})} \quad (\text{A.17})$$

$$\alpha_d = \frac{1.4}{1 + \exp(\frac{-35-V}{13})} + 0.25 \quad (\text{A.18})$$

$$\beta_d = \frac{1.4}{1 + \exp(\frac{V+5}{5})} \quad (\text{A.19})$$

$$\gamma_d = \frac{1}{1 + \exp(\frac{50-V}{20})} \quad (\text{A.20})$$

$$\tau_d = \alpha_d \beta_d + \gamma_d \quad (\text{A.21})$$

$$f_\infty = \frac{1}{1 + \exp(\frac{V+20}{7})} \quad (\text{A.22})$$

$$\alpha_f = 1125 \exp\left(\frac{-(V+27)^2}{240}\right) \quad (\text{A.23})$$

$$\beta_f = \frac{165}{1 + \exp(\frac{25-V}{10})} \quad (\text{A.24})$$

$$\gamma_f = 80 \quad (\text{A.25})$$

$$\tau_f = \alpha_f + \beta_f + \gamma_f \quad (\text{A.26})$$

$$\alpha_{fCa} = \frac{1}{1 + \left(\frac{Ca_i}{0.000325}\right)^8} \quad (\text{A.27})$$

$$\beta_{fCa} = \frac{0.1}{1 + \exp(\frac{Ca_i - 0.0005}{0.0001})} \quad (\text{A.28})$$

$$\gamma_{fCa} = \frac{0.2}{1 + \exp(\frac{Ca_i - 0.00075}{0.0008})} \quad (\text{A.29})$$

$$f_{Ca\infty} = \frac{\alpha_{fCa} + \beta_{fCa} + \gamma_{fCa} + 0.23}{1.46} \quad (\text{A.30})$$

$$\frac{df_{Ca}}{dt} = k \frac{f_{Ca\infty} - f_{Ca}}{\tau_{fCa}} \quad (\text{A.31})$$

$$k = 0 \quad \text{if } f_{Ca\infty} > f_{Ca} \quad \text{and } V > -60 \text{ mV}$$

$$= 1 \quad (\text{otherwise})$$

$$\tau_{fCa} = 2 \text{ ms} \quad (\text{A.32})$$

Transient outward current (outward)

$$I_{to} = G_{to} r_s (V - E_K) \quad (\text{A.33})$$

$$r_\infty = \frac{1}{1 + \exp\left(\frac{20-V}{6}\right)} \quad (\text{A.34})$$

$$\tau_r = 9.5 \exp\left(\frac{-(V+40)^2}{1800}\right) + 0.8 \quad (\text{A.35})$$

$$s_\infty = \frac{1}{1 + \exp\left(\frac{V+28}{5}\right)} \quad \text{for endocardial cell types} \quad (\text{A.36})$$

$$= \frac{1}{1 + \exp\left(\frac{V+20}{5}\right)} \quad \text{for epicardial and M-cell types} \quad (\text{A.37})$$

$$\tau_s = 1000 \exp\left(\frac{-(V+67)^2}{1000}\right) + 8 \quad \text{for endocardial cell types} \quad (\text{A.38})$$

$$= 85 \exp\left(\frac{-(V+45)^2}{320}\right) + \frac{5}{1 + \exp\left(\frac{V-20}{5}\right)} + 3 \quad \text{for epicardial and M-cell types} \quad (\text{A.39})$$

Slow delayed rectifier current (outward)

$$I_{Ks} = G_{Ks} x_s^2 (V - E_{Ks}) \quad (\text{A.40})$$

$$x_{s\infty} = \frac{1}{1 + \exp\left(\frac{-5-V}{14}\right)} \quad (\text{A.41})$$

$$\alpha_{xs} = \frac{1100}{\sqrt{1 + \exp\left(\frac{-10-V}{6}\right)}} \quad (\text{A.42})$$

$$\beta_{xs} = \frac{1}{1 + \exp\left(\frac{V-60}{20}\right)} \quad (\text{A.43})$$

$$\tau_{xs} = \alpha_{xs} \beta_{xs} \quad (\text{A.44})$$

Rapid delayed rectifier current (outward)

$$I_{Kr} = G_{Kr} \sqrt{\frac{K_o}{5.4}} x_{r1} x_{r2} (V - E_K) \quad (\text{A.45})$$

$$x_{r1\infty} = \frac{1}{1 + \exp\left(\frac{-26-V}{7}\right)} \quad (\text{A.46})$$

$$\alpha_{xr1} = \frac{450}{1 + \exp\left(\frac{-45-V}{10}\right)} \quad (\text{A.47})$$

$$\beta_{xr1} = \frac{6}{1 + \exp\left(\frac{V+30}{11.5}\right)} \quad (\text{A.48})$$

$$\tau_{xr1} = \alpha_{xr1} \beta_{xr1} \quad (\text{A.49})$$

$$x_{r2\infty} = \frac{1}{1 + \exp\left(\frac{V+88}{24}\right)} \quad (\text{A.50})$$

$$\alpha_{xr2} = \frac{3}{1 + \exp\left(\frac{-60-V}{20}\right)} \quad (\text{A.51})$$

$$\beta_{xr2} = \frac{1.12}{1 + \exp\left(\frac{V-60}{20}\right)} \quad (\text{A.52})$$

$$\tau_{xr2} = \alpha_{xr2} \beta_{xr2} \quad (\text{A.53})$$

Inward rectifier K⁺ current (outward)

$$I_{K1} = G_{K1} \sqrt{\frac{K_o}{5.4}} x_{K1\infty} (V - E_K) \quad (\text{A.54})$$

$$\alpha_{K1} = \frac{0.1}{1 + \exp(0.06(V - E_K - 200))} \quad (\text{A.55})$$

$$\beta_{K1} = \frac{3 \exp(0.0002(V - E_K + 100)) + \exp(0.1(V - E_K - 10))}{1 + \exp(-0.5(V - E_K))} \quad (\text{A.56})$$

$$X_{K1\infty} = \frac{\alpha_{K1}}{\alpha_{K1} + \beta_{K1}} \quad (\text{A.57})$$

Na⁺-Ca²⁺ exchanger current

$$I_{NaCa} = k_{NaCa} \frac{\exp\left(\frac{\gamma VF}{RT}\right) Na_i^3 Ca_o - \exp\left(\frac{(\gamma-1)VF}{RT}\right) Na_o^3 Ca_i \alpha}{(K_{mNa_i})^3 + Na_o^3} (K_{mCa} + Ca_o) \left(1 + k_{sat} \exp\left(\frac{(\gamma-1)VF}{RT}\right)\right) \quad (\text{A.58})$$

Na⁺-K⁺ pump current

$$I_{NaK} = P_{NaK} \frac{K_o Na_i}{(K_o + K_{mK})(Na_i + K_{mNa})(1 + 0.1245 \exp\left(\frac{-0.1VF}{RT}\right) + 0.0353 \exp\left(\frac{-VF}{RT}\right))} \quad (\text{A.59})$$

Plateau Ca^{2+} current (outward)

$$I_{pCa} = G_{pCa} \frac{Ca_i}{K_{pCa} + Ca_i} \quad (\text{A.60})$$

$$(\text{A.61})$$

Plateau K^+ current (outward)

$$I_{pK} = G_{pK} \frac{V - E_K}{1 + \exp\left(\frac{25-V}{5.98}\right)} \quad (\text{A.62})$$

Background Na^+ current (inward)

$$I_{bNa} = G_{bNa}(V - E_{Na}) \quad (\text{A.63})$$

$$(\text{A.64})$$

Background Ca^{2+} current (inward)

$$I_{bCa} = G_{bCa}(V - E_{Ca}) \quad (\text{A.65})$$

Ion dynamics **Ca^{2+} dynamics**

$$I_{leak} = V_{leak}(Ca_{sr} - Ca_i) \quad (\text{A.66})$$

$$I_{up} = \frac{V_{maxup}}{1 + \left(\frac{K_{up}}{Ca_i}\right)^2} \quad (\text{A.67})$$

$$I_{rel} = \left(a_{rel} \frac{Ca_{sr}^2}{b_{rel}^2 + Ca_{sr}^2} + c_{rel} \right) dg \quad (\text{A.68})$$

$$g_{\infty} = \frac{1}{1 + \left(\frac{Ca_i}{0.00035}\right)^6} \quad \text{if } Ca_i \leq 0.00035 \quad (\text{A.69})$$

$$= \frac{1}{1 + \left(\frac{Ca_i}{0.00035}\right)^{16}} \quad (\text{otherwise})$$

$$\tau_g = 2 \text{ ms} \quad (\text{A.70})$$

$$\frac{dg}{dt} = k \frac{g_{\infty} - g}{\tau_g} \quad (\text{A.71})$$

$$k = 0 \quad \text{if } g_{\infty} > g \quad \text{and } V > -60 \text{ mV}$$

$$= 1 \quad (\text{otherwise})$$

$$Ca_{ibufc} = \frac{Ca_i \times Bufc}{Ca_i + K_{bufc}} \quad (\text{A.72})$$

$$\frac{dC_{a_{itotal}}}{dt} = -\frac{I_{CaL} + I_{bCa} + I_{pCa} - 2I_{NaCa}}{2V_C F} + I_{leak} - I_{up} + I_{rel} \quad (\text{A.73})$$

$$C_{a_{srbufsr}} = \frac{C_{a_{sr}} \times B_{ufsr}}{C_{a_{sr}} + K_{bufsr}} \quad (\text{A.74})$$

$$\frac{dC_{a_{srtotal}}}{dt} = \frac{V_C}{V_{SR}} (-I_{leak} + I_{up} - I_{rel}) \quad (\text{A.75})$$

Na⁺ dynamics

$$\frac{dNa_i}{dt} = -\frac{I_{Na} + I_{bNa} + 3I_{NaK} + 3I_{NaCa}}{V_C F} \quad (\text{A.76})$$

K⁺ dynamics

$$\frac{dK_i}{dt} = -\frac{I_{K1} + I_{to} + I_{Kr} + I_{Ks} - 2I_{NaK} + I_{pK} + I_{stim} - I_{ax}}{V_C F} \quad (\text{A.77})$$

Model parameters

Channel conductances

G_{Na} : Maximal fast Na^+ current (I_{Na}) conductance = 14.838 nS/pF

G_{CaL} : Maximal L-type Ca^{2+} current (I_{CaL}) conductance = $1.75 \times 10^{-4} \text{ cm}^2 \cdot \mu\text{F}^{-1} \cdot \text{s}^{-1}$

G_{to} : Maximal transient outward current (I_{to}) conductance = 0.294 nS/pF (for epicardial and M-cell), 0.073 nS/pF (for endocardial cell)

G_{Ks} : Maximal slow delayed rectifier current (I_{Ks}) conductance = 0.245 nS/pF (for epicardial and endocardial), 0.062 nS/pF (for M-cell)

G_{Kr} : Maximal rapid delayed rectifier current (I_{Kr}) conductance = 0.096 nS/pF

G_{K1} : Maximal inward rectifier K^+ current (I_{K1}) conductance = 5.405 nS/pF

G_{pCa} : Maximal plateau Ca^{2+} current (I_{pCa}) conductance = 0.825 nS/pF

G_{pK} : Maximal plateau K^+ current (I_{pK}) conductance = 0.0146 nS/pF

G_{bNa} : Maximal background Na^+ current (I_{bNa}) conductance = 0.00029 nS/pF

G_{bCa} : Maximal background Ca^{2+} current (I_{bCa}) conductance = 0.000592 nS/pF

Ion concentration

Na_o : Extracellular Na^+ concentration = 140 mM

Ca_o : Extracellular Ca^{2+} concentration = 5.4 mM

K_o : Extracellular K^+ concentration = 2 mM

Cell geometry (Volume)

V_C : Cytoplasmic volume = 16404 μm^3

V_{SR} : Sarcoplasmic reticulum volume = 1094 μm^3

Other parameters

p_{KNa} : Relative I_{Ks} permeability to Na^+ = 0.03

k_{NaCa} : Maximal Na^+/Ca^{2+} exchanger current (I_{NaCa}) = 1000 pA/pF

k_{mNa_i} : Na_i half-saturation constant for I_{NaCa} = 87.5 mM

k_{mCa} : Ca_i half-saturation constant for I_{NaCa} = 1.38 mM

k_{sat} : Saturation factor for I_{NaCa} = 0.1

α : Factor enhancing outward nature of I_{NaCa} = 2.5

γ : Voltage dependence parameter of I_{NaCa} = 0.35

P_{NaK} : Maximal I_{NaK} = 1.362 pA/pF

K_{mK} : K_o half-saturation constant of I_{NaK} = 1 mM

K_{mNa} : Na_i half-saturation constant of I_{NaK} = 40 mM

K_{pCa} : Ca_i half-saturation constant of I_{pCa} = 0.0005 mM

V_{leak} : Maximal I_{leak} = 0.00008 ms^{-1}

V_{maxup} : Maximal I_{up} = 0.000425 mM/ms

K_{up} : Half-saturation constant of I_{up} = 0.00025 mM

a_{rel} : Maximal Ca_{SR} -dependent I_{rel} = 0.016464 mM/ms

b_{rel} : Ca_{SR} half-saturation constant of I_{rel} = 0.25 mM

c_{rel} : Maximal Ca_{SR} -independent I_{rel} = 0.008232 mM/ms

B_{ufc} : Total cytoplasmic buffer concentration = 0.15 mM

B_{ufsr} : Total sarcoplasmic reticulum buffer concentration = 10 mM

K_{bufc} : Ca_i half-saturation constant for cytoplasmic buffer = 0.001 mM

K_{bufsr} : Ca_{SR} half-saturation constant for sarcoplasmic reticulum buffer = 0.3 mM

Initialized gating variables and ion concentrations

m : Activation gate for I_{Na} = 0;

h : Fast inactivation gate for I_{Na} = 0.75;

j : Slow inactivation gate for I_{Na} = 0.75;

d : Activation gate for I_{CaL} = 0;

f : Inactivation gate for I_{CaL} = 1;

f_{Ca} : Intracellular calcium-dependent inactivation gate for I_{CaL} = 1;

r : Activation gate for I_{to} = 0;

s : Inactivation gate for I_{to} = 1;

x_s : Activation gate for $I_{Ks} = 0$;

x_{r1} : Activation gate for $I_{Kr} = 0$;

x_{r2} : Inactivation gate for $I_{Kr} = 1$;

g : Calcium-dependent inactivation gate for $I_{rel} = 1$;

Na_i : Intracellular Na^+ concentration = 11.6 mM

Ca_i : Intracellular Ca^{2+} concentration = 0.0002 mM

K_i : Intracellular K^+ concentration = 138.3 mM

Ca_{sr} : Free Ca^{2+} concentration in the sarcoplasmic reticulum (SR) = 0.2 mM

A.2 The TP06 Model

We use the model developed by ten Tusscher and Panfilov [2] (the TP06 model) to model an endocardial cell; this model is based on experimental data and is more realistic than other human ventricular models [1,3–7]; this model has been developed to study the action-potential morphology, alternans, intracellular ion dynamics (in particular, calcium dynamics) at the single-cell level for epicardial, midmyocardial, and endocardial cells. The model consists of 12 components of the ionic current, namely, the fast inward Na^+ current I_{Na} , the L-type slow inward Ca^{2+} current I_{CaL} , the transient outward current I_{to} , the slow delayed rectifier current I_{Ks} , the rapid delayed rectifier current I_{Kr} , the inward rectifier K^+ current I_{K1} , the Na^+/Ca^{2+} exchanger current I_{NaCa} , the Na^+/K^+ pump current I_{NaK} , the plateau Ca^{2+} current I_{pCa} , the plateau K^+ current I_{pK} , the background Na^+ current I_{bNa} , and the background Ca^{2+} current I_{bCa} . It uses 19 variables: (a) 1 for the transmembrane potential V_m , (b) 13 for ion-channel gates, namely, m , h , j , d , f , f_2 , f_{cass} , r , s , x_s , x_{r1} , x_{r2} , and \bar{R} , and (c) 5 for intracellular, ion-concentration dynamics, namely, Na_i , K_i , Ca_i , Ca_{sr} , and Ca_{ss} .

All current densities are measured in the units of pA/pF, V_m in mV, and ion concentrations in mM/L; the ionic currents are determined by the time-dependent ion-channel gating variables, as given above, generically denoted by ξ , which follow ordinary differential equations of the type

$$\frac{d\xi}{dt} = \frac{\xi_\infty - \xi}{\tau_\xi},$$

where $\xi_\infty = \alpha_\xi / (\alpha_\xi + \beta_\xi)$ is the steady-state value of ξ and $\tau_\xi = \frac{1}{\alpha_\xi + \beta_\xi}$ is its time constant; here, α_ξ and β_ξ are voltage-dependent rate constants associated with the gate ξ .

Reversal potentials

At equilibrium the reversal potentials obey the Nernst equation:

$$E_X = \frac{RT}{zF} \log \frac{X_o}{X_i} \quad \text{for } X = Na^+, K^+, Ca^{2+} \quad (\text{A.78})$$

$$E_{Ks} = \frac{RT}{F} \log \frac{K_o + p_{KNa} Na_o}{K_i + p_{KNa} Na_i}, \quad (\text{A.79})$$

where R is the gas constant, T the temperature, z the valence of the ion, F the Faraday constant, X_o and X_i the extra- and intra-cellular ionic concentrations, p_{KNa} the relative I_{Ks} permeability to Na^+ .

Ionic currents

Fast Na^+ current (inward)

$$I_{Na} = G_{Na} m^3 h j (V - E_{Na}) \quad (\text{A.80})$$

$$m_\infty = \frac{1}{[1 + \exp(\frac{-56.86 - V}{9.03})]^2} \quad (\text{A.81})$$

$$\alpha_m = \frac{1}{1 + \exp(\frac{-60 - V}{5})} \quad (\text{A.82})$$

$$\beta_m = \frac{0.1}{1 + \exp(\frac{V + 35}{5})} + \frac{0.1}{1 + \exp(\frac{V - 50}{200})} \quad (\text{A.83})$$

$$\tau_m = \alpha_m \beta_m \quad (\text{A.84})$$

$$h_\infty = \frac{1}{[1 + \exp(\frac{V + 71.55}{7.43})]^2} \quad (\text{A.85})$$

$$\begin{aligned} \alpha_h &= 0 \quad \text{if } V \geq -40 \quad (\text{A.86}) \\ &= 0.057 \exp\left(\frac{-(V + 80)}{6.8}\right) \quad (\text{otherwise}) \end{aligned}$$

$$\beta_h = \frac{0.77}{0.13 \left[1 + \exp\left(\frac{-(V+10.66)}{11.1}\right) \right]} \quad \text{if } V \geq -40 \quad (\text{A.87})$$

$$= 2.7 \exp(0.079V) + 3.1 \times 10^5 \exp(0.3485V) \quad (\text{otherwise})$$

$$\tau_h = \frac{1}{\alpha_h + \beta_h} \quad (\text{A.88})$$

$$j_\infty = \frac{1}{\left[1 + \exp\left(\frac{V+71.55}{7.43}\right) \right]^2} \quad (\text{A.89})$$

$$\alpha_j = 0 \quad \text{if } V \geq -40 \quad (\text{A.90})$$

$$= \frac{(-2.5428 \times 10^4 \exp(0.2444V) - 6.948 \times 10^{-6} \exp(-0.04391V))(V + 37.38)}{1 + \exp(0.311(V + 79.23))} \quad (\text{otherwise})$$

$$\beta_j = \frac{0.6 \exp(0.057V)}{1 + \exp(-0.1(V + 32))} \quad \text{if } V \geq -40 \quad (\text{A.91})$$

$$= \frac{0.02424 \exp(-0.01052V)}{1 + \exp(-0.1378(V + 40.14))} \quad (\text{otherwise})$$

$$\tau_j = \frac{1}{\alpha_j + \beta_j} \quad (\text{A.92})$$

L-type Ca²⁺ current (inward)

$$I_{CaL} = G_{CaL} d f f_2 f_{Ca} 4 \frac{(V-15)F^2}{RT} \frac{0.25 C_{aSS} \exp(\frac{2(V-15)F}{RT}) - C_{a_o}}{\exp(\frac{2(V-15)F}{RT}) - 1} \quad (\text{A.93})$$

$$d_\infty = \frac{1}{1 + \exp(\frac{-8-V}{7.5})} \quad (\text{A.94})$$

$$\alpha_d = \frac{1.4}{1 + \exp(\frac{-35-V}{13})} + 0.25 \quad (\text{A.95})$$

$$\beta_d = \frac{1.4}{1 + \exp(\frac{V+5}{5})} \quad (\text{A.96})$$

$$\gamma_d = \frac{1}{1 + \exp(\frac{50-V}{20})} \quad (\text{A.97})$$

$$\tau_d = \alpha_d \beta_d + \gamma_d \quad (\text{A.98})$$

$$f_\infty = \frac{1}{1 + \exp(\frac{V+20}{7})} \quad (\text{A.99})$$

$$\alpha_f = 1102.5 \exp\left(\frac{-(V+27)^2}{225}\right) \quad (\text{A.100})$$

$$\beta_f = \frac{200}{1 + \exp(\frac{13-V}{10})} \quad (\text{A.101})$$

$$\gamma_f = \frac{180}{1 + \exp(\frac{V+30}{10})} + 20 \quad (\text{A.102})$$

$$\tau_f = \alpha_f + \beta_f + \gamma_f \quad (\text{A.103})$$

$$f_{2\infty} = \frac{0.67}{1 + \exp(\frac{V+35}{7})} + 0.33 \quad (\text{A.104})$$

$$\alpha_{f2} = 600 \exp\left(\frac{-(V+25)^2}{170}\right) \quad (\text{A.105})$$

$$\beta_{f2} = \frac{31}{1 + \exp(\frac{25-V}{10})} \quad (\text{A.106})$$

$$\gamma_{f2} = \frac{16}{1 + \exp(\frac{V+30}{10})} \quad (\text{A.107})$$

$$\tau_{f2} = \alpha_{f2} + \beta_{f2} + \gamma_{f2} \quad (\text{A.108})$$

$$f_{Cass\infty} = \frac{0.6}{1 + \left(\frac{C_{aSS}}{0.05}\right)^2} + 0.4 \quad (\text{A.109})$$

$$\tau_{fCass} = \frac{80}{1 + \left(\frac{C_{aSS}}{0.05}\right)^2} + 2 \quad (\text{A.110})$$

Transient outward current (outward)

$$I_{to} = G_{to} r_s (V - E_K) \quad (\text{A.111})$$

$$r_\infty = \frac{1}{1 + \exp\left(\frac{20-V}{6}\right)} \quad (\text{A.112})$$

$$\tau_r = 9.5 \exp\left(\frac{-(V+40)^2}{1800}\right) + 0.8 \quad (\text{A.113})$$

$$s_\infty = \frac{1}{1 + \exp\left(\frac{V+28}{5}\right)} \quad (\text{A.114})$$

$$\tau_s = 1000 \exp\left(\frac{-(V+67)^2}{1000}\right) + 8 \quad (\text{A.115})$$

Slow delayed rectifier current (outward)

$$I_{Ks} = G_{Ks} x_s^2 (V - E_{Ks}) \quad (\text{A.116})$$

$$x_{s\infty} = \frac{1}{1 + \exp\left(\frac{-5-V}{14}\right)} \quad (\text{A.117})$$

$$\alpha_{xs} = \frac{1400}{\sqrt{1 + \exp\left(\frac{5-V}{6}\right)}} \quad (\text{A.118})$$

$$\beta_{xs} = \frac{1}{1 + \exp\left(\frac{V-35}{15}\right)} \quad (\text{A.119})$$

$$\tau_{xs} = \alpha_{xs} \beta_{xs} + 80 \quad (\text{A.120})$$

Rapid delayed rectifier current (outward)

$$I_{Kr} = G_{Kr} \sqrt{\frac{K_o}{5.4}} x_{r1} x_{r2} (V - E_K) \quad (\text{A.121})$$

$$x_{r1\infty} = \frac{1}{1 + \exp\left(\frac{-26-V}{7}\right)} \quad (\text{A.122})$$

$$\alpha_{xr1} = \frac{450}{1 + \exp\left(\frac{-45-V}{10}\right)} \quad (\text{A.123})$$

$$\beta_{xr1} = \frac{6}{1 + \exp\left(\frac{V+30}{11.5}\right)} \quad (\text{A.124})$$

$$\tau_{xr1} = \alpha_{xr1} \beta_{xr1} \quad (\text{A.125})$$

$$x_{r2\infty} = \frac{1}{1 + \exp\left(\frac{V+88}{24}\right)} \quad (\text{A.126})$$

$$\alpha_{xr2} = \frac{3}{1 + \exp\left(\frac{-60-V}{20}\right)} \quad (\text{A.127})$$

$$\beta_{xr2} = \frac{1.12}{1 + \exp\left(\frac{V-60}{20}\right)} \quad (\text{A.128})$$

$$\tau_{xr2} = \alpha_{xr2} \beta_{xr2} \quad (\text{A.129})$$

Inward rectifier K⁺ current (outward)

$$I_{K1} = G_{K1} \sqrt{\frac{K_o}{5.4}} x_{K1\infty} (V - E_K) \quad (\text{A.130})$$

$$\alpha_{K1} = \frac{0.1}{1 + \exp(0.06(V - E_K - 200))} \quad (\text{A.131})$$

$$\beta_{K1} = \frac{3 \exp(0.0002(V - E_K + 100)) + \exp(0.1(V - E_K - 10))}{1 + \exp(-0.5(V - E_K))} \quad (\text{A.132})$$

$$X_{K1\infty} = \frac{\alpha_{K1}}{\alpha_{K1} + \beta_{K1}} \quad (\text{A.133})$$

Na⁺-Ca²⁺ exchanger current

$$I_{NaCa} = k_{NaCa} \frac{\exp\left(\frac{\gamma VF}{RT}\right) Na_i^3 Ca_o - \exp\left(\frac{(\gamma-1)VF}{RT}\right) Na_o^3 Ca_i \alpha}{(K_{mNa_i})^3 + Na_o^3} (K_{mCa} + Ca_o) \left(1 + k_{sat} \exp\left(\frac{(\gamma-1)VF}{RT}\right)\right) \quad (\text{A.134})$$

Na⁺-K⁺ pump current

$$I_{NaK} = P_{NaK} \frac{K_o Na_i}{(K_o + K_{mK})(Na_i + K_{mNa}) \left(1 + 0.1245 \exp\left(\frac{-0.1VF}{RT}\right) + 0.0353 \exp\left(\frac{-VF}{RT}\right)\right)} \quad (\text{A.135})$$

Plateau Ca²⁺ current (outward)

$$I_{pCa} = G_{pCa} \frac{Ca_i}{K_{pCa} + Ca_i} \quad (\text{A.136})$$

$$(\text{A.137})$$

Plateau K⁺ current (outward)

$$I_{pK} = G_{pK} \frac{V - E_K}{1 + \exp\left(\frac{25-V}{5.98}\right)} \quad (\text{A.138})$$

Background Na⁺ current (inward)

$$I_{bNa} = G_{bNa} (V - E_{Na}) \quad (\text{A.139})$$

$$(\text{A.140})$$

Background Ca²⁺ current (inward)

$$I_{bCa} = G_{bCa} (V - E_{Ca}) \quad (\text{A.141})$$

Ion dynamics

Ca²⁺ dynamics

$$I_{leak} = V_{leak}(Ca_{sr} - Ca_i) \quad (A.142)$$

$$I_{up} = \frac{V_{maxup}}{1 + \left(\frac{K_{up}}{Ca_i}\right)^2} \quad (A.143)$$

$$I_{rel} = V_{rel}O(Ca_{sr} - Ca_{ss}) \quad (A.144)$$

$$I_{xfer} = V_{xfer}(Ca_{ss} - Ca_i) \quad (A.145)$$

$$O = \frac{k_1 Ca_{ss}^2 \bar{R}}{k_3 + k_1 Ca_{ss}^2} \quad (A.146)$$

$$\frac{d\bar{R}}{dt} = -k_2 Ca_{ss} \bar{R} + k_4(1 - \bar{R}) \quad (A.147)$$

$$k_1 = \frac{k'_1}{k_{casr}} \quad (A.148)$$

$$k_2 = k'_2 k_{casr} \quad (A.149)$$

$$k_{casr} = max_{sr} - \frac{max_{sr} - min_{sr}}{1 + \left(\frac{EC}{Ca_{sr}}\right)^2} \quad (A.150)$$

$$Ca_{ibufc} = \frac{Ca_i \times Bufc}{Ca_i + K_{bufc}} \quad (A.151)$$

$$\frac{dCa_{itotal}}{dt} = -\frac{I_bCa + I_pCa - 2I_{NaCa}}{2V_C F} + \frac{V_{SR}}{V_C} (I_{leak} - I_{up}) + I_{xfer} \quad (A.152)$$

$$Ca_{srbufsr} = \frac{Ca_{sr} \times Bufsr}{Ca_{sr} + K_{bufsr}} \quad (A.153)$$

$$\frac{dCa_{srtotal}}{dt} = (-I_{leak} + I_{up} - I_{rel}) \quad (A.154)$$

$$Ca_{ssbufss} = \frac{Ca_{ss} \times Bufss}{Ca_{ss} + K_{bufss}} \quad (A.155)$$

$$\frac{dCa_{sstotal}}{dt} = -\frac{1}{2V_{SS} F} I_{CaL} + \frac{V_{SR}}{V_{SS}} I_{rel} - \frac{V_C}{V_{SS}} I_{xfer} \quad (A.156)$$

Na⁺ dynamics

$$\frac{dNa_i}{dt} = -\frac{I_{Na} + I_{bNa} + 3I_{NaK} + 3I_{NaCa}}{V_C F} \quad (A.157)$$

K⁺ dynamics

$$\frac{dK_i}{dt} = -\frac{I_{K1} + I_{to} + I_{Kr} + I_{Ks} - 2I_{NaK} + I_{pK} + I_{stim}}{V_C F} \quad (A.158)$$

Model parameters

Channel conductances

- G_{Na} : Maximal fast Na^+ current (I_{Na}) conductance = 14.838 nS/pF
 G_{CaL} : Maximal L-type Ca^{2+} current (I_{CaL}) conductance = 3.98×10^{-5} cm $\cdot\mu$ F $^{-1}\cdot$ ms $^{-1}$
 G_{to} : Maximal transient outward current (I_{to}) conductance = 0.073 nS/pF
 G_{Ks} : Maximal slow delayed rectifier current (I_{Ks}) conductance = 0.392 nS/pF
 G_{Kr} : Maximal rapid delayed rectifier current (I_{Kr}) conductance = 0.153 nS/pF
 G_{K1} : Maximal inward rectifier K^+ current (I_{K1}) conductance = 5.405 nS/pF
 G_{pCa} : Maximal plateau Ca^{2+} current (I_{pCa}) conductance = 0.1238 nS/pF
 G_{pK} : Maximal plateau K^+ current (I_{pK}) conductance = 0.0146 nS/pF
 G_{bNa} : Maximal background Na^+ current (I_{bNa}) conductance = 0.00029 nS/pF
 G_{bCa} : Maximal background Ca^{2+} current (I_{bCa}) conductance = 0.000592 nS/pF

Ion concentration

- Na_o : Extracellular Na^+ concentration = 140 mM
 Ca_o : Extracellular Ca^{2+} concentration = 5.4 mM
 K_o : Extracellular K^+ concentration = 2 mM

Cell geometry (Volume)

- V_C : Cytoplasmic volume = 16404 μ m 3
 V_{SR} : Sarcoplasmic reticulum volume = 1094 μ m 3
 V_{SS} : Diadic subspace volume = 54.68 μ m 3

Other parameters

- p_{KNa} : Relative I_{Ks} permeability to Na^+ = 0.03
 k_{NaCa} : Maximal Na^+/Ca^{2+} exchanger current (I_{NaCa}) = 1000 pA/pF
 k_{mNa_i} : Na_i half-saturation constant for I_{NaCa} = 87.5 mM
 k_{mCa_i} : Ca_i half-saturation constant for I_{NaCa} = 1.38 mM
 k_{sat} : Saturation factor for I_{NaCa} = 0.1
 α : Factor enhancing outward nature of I_{NaCa} = 2.5
 γ : Voltage dependence parameter of I_{NaCa} = 0.35
 P_{NaK} : Maximal I_{NaK} = 2.724 pA/pF
 K_{mK} : K_o half-saturation constant of I_{NaK} = 1 mM
 K_{mNa} : Na_i half-saturation constant of I_{NaK} = 40 mM
 K_{pCa} : Ca_i half-saturation constant of I_{pCa} = 0.0005 mM
 V_{leak} : Maximal I_{leak} conductance = 0.00036 mM/ms

V_{maxup} : Maximal I_{up} conductance = 0.006375 mM/ms
 K_{up} : Half-saturation constant of I_{up} = 0.00025 mM
 V_{rel} : Maximal I_{rel} conductance = 0.102 mM/ms
 V_{xfer} : Maximal I_{xfer} conductance = 0.0038 mM/ms
 k'_1 : R to O and RI to I I_{rel} transition rate = 0.15 $mM^{-2} \cdot ms^{-1}$
 k'_2 : O to I and R to RI I_{rel} transition rate = 0.045 $mM^{-1} \cdot ms^{-1}$
 k_3 : O to R and I to RI I_{rel} transition rate = 0.06 ms^{-1}
 k_4 : I to O and RI to I I_{rel} transition rate = 0.005 ms^{-1}
 EC : Ca_{SR} half-saturation constant of k_{casr} = 1.5 mM
 max_{sr} : Maximum value of k_{casr} = 2.5
 min_{sr} : Minimum value of k_{casr} = 1.0
 Bu_{fc} : Total cytoplasmic buffer concentration = 0.2 mM
 Bu_{fsr} : Total sarcoplasmic reticulum buffer concentration = 10 mM
 Bu_{fss} : Total diadic subspace buffer concentration = 0.4 mM
 $K_{bu_{fc}}$: Ca_i half-saturation constant for cytoplasmic buffer = 0.001 mM
 $K_{bu_{fsr}}$: Ca_{SR} half-saturation constant for sarcoplasmic reticulum buffer = 0.3 mM
 $K_{bu_{fss}}$: Ca_{SS} half-saturation constant for diadic subspace buffer = 0.00025 mM

Initialized gating variables and ion concentrations

m : Activation gate for I_{Na} = 0;
 h : Fast inactivation gate for I_{Na} = 0.75;
 j : Slow inactivation gate for I_{Na} = 0.75;
 d : Activation gate for I_{CaL} = 0;
 f : Slow inactivation gate for I_{CaL} = 1;
 f_2 : Fast inactivation gate for I_{CaL} = 1;
 f_{Cass} : Diadic subspace free calcium-dependent inactivation gate for I_{CaL} = 1;
 r : Activation gate for I_{to} = 0;
 s : Inactivation gate for I_{to} = 1;
 x_s : Activation gate for I_{Ks} = 0;
 x_{r1} : Activation gate for I_{Kr} = 0;
 x_{r2} : Inactivation gate for I_{Kr} = 1;
 \bar{R} : Proportion of close I_{rel} channel = 1;
 O : Proportion of open I_{rel} channel = 0;
 Na_i : Intracellular Na^+ concentration = 7.67 mM
 Ca_i : Intracellular Ca^+ concentration = 0.00007 mM
 K_i : Intracellular K^+ concentration = 138.3 mM

Ca_{sr} : Free Ca^{2+} concentration in the sarcoplasmic reticulum (SR) = 1.3 mM

Ca_{ss} : Free Ca^{2+} concentration in the diadic subspace (SS) = 0.00007 mM

A.3 The Purkinje Model

We use the model developed by the Stewart *et al.* [8] to model a Purkinje cell. This model has been developed for a human Purkinje cell by modifying two major ionic currents, namely, transient outward current, I_{to} , and inward rectifier K^+ current, I_{K1} , of the TP06 model; the Stewart *et al.* model also includes two more ionic currents, namely, the sustained K^+ current, I_{sus} , and the hyperpolarization-activated current, I_f ; hence, the model consists of 14 ionic currents. Furthermore, the maximum channel conductances for Na^+ current, I_{Na} , and both rapid and slow delayed rectifier K^+ currents, I_{Kr} and I_{Ks} , are modified to obtain the correct channel kinetics for a Purkinje cell. The model can reproduce the contribution of individual ionic currents to the action potential morphology for a human Purkinje cell in both healthy and disease cases. It uses 20 variables: (a) 1 for the transmembrane potential V_m , (b) 14 for ion channel gates, namely, m , h , j , d , f , f_2 , f_{cass} , r , s , x_s , x_{r1} , x_{r2} , y , and \bar{R} , and (c) 5 for intracellular, ion-concentration dynamics, namely, Na_i , K_i , Ca_i , Ca_{sr} , and Ca_{ss} .

All current densities are measured in the units of pA/pF, V_m in mV, and ion concentrations in mM/L; the ionic currents are determined by the time-dependent ion-channel gating variables, as given above, generically denoted by ξ , which follow ordinary differential equations of the type

$$\frac{d\xi}{dt} = \frac{\xi_\infty - \xi}{\tau_\xi},$$

where $\xi_\infty = \alpha_\xi / (\alpha_\xi + \beta_\xi)$ is the steady-state value of ξ and $\tau_\xi = \frac{1}{\alpha_\xi + \beta_\xi}$ is its time constant; here, α_ξ and β_ξ are voltage-dependent rate constants associated with the gate ξ .

Reversal potentials

At equilibrium the reversal potentials obey the Nernst equation:

$$E_X = \frac{RT}{zF} \log \frac{X_o}{X_i} \quad \text{for } X = Na^+, K^+, Ca^{2+} \quad (\text{A.159})$$

$$E_{Ks} = \frac{RT}{F} \log \frac{K_o + p_{KNa} Na_o}{K_i + p_{KNa} Na_i}, \quad (\text{A.160})$$

where R is the gas constant, T the temperature, z the valence of the ion, F the Faraday constant, X_o and X_i the extra- and intra-cellular ionic concentrations, p_{KNa} the relative I_{Ks} permeability to Na^+ .

Ionic currents

Fast Na^+ current (inward)

$$I_{Na} = G_{Na} m^3 h j (V - E_{Na}) \quad (\text{A.161})$$

$$m_\infty = \frac{1}{\left[1 + \exp\left(\frac{-56.86 - V}{9.03}\right)\right]^2} \quad (\text{A.162})$$

$$\alpha_m = \frac{1}{1 + \exp\left(\frac{-60 - V}{5}\right)} \quad (\text{A.163})$$

$$\beta_m = \frac{0.1}{1 + \exp\left(\frac{V + 35}{5}\right)} + \frac{0.1}{1 + \exp\left(\frac{V - 50}{200}\right)} \quad (\text{A.164})$$

$$\tau_m = \alpha_m \beta_m \quad (\text{A.165})$$

$$h_\infty = \frac{1}{\left[1 + \exp\left(\frac{V + 71.55}{7.43}\right)\right]^2} \quad (\text{A.166})$$

$$\begin{aligned} \alpha_h &= 0 \quad \text{if } V \geq -40 \\ &= 0.057 \exp\left(\frac{-(V + 80)}{6.8}\right) \quad (\text{otherwise}) \end{aligned} \quad (\text{A.167})$$

$$\beta_h = \frac{0.77}{0.13 \left[1 + \exp\left(\frac{-(V + 10.66)}{11.1}\right)\right]} \quad \text{if } V \geq -40 \quad (\text{A.168})$$

$$= 2.7 \exp(0.079V) + 3.1 \times 10^5 \exp(0.3485V) \quad (\text{otherwise})$$

$$\tau_h = \frac{1}{\alpha_h + \beta_h} \quad (\text{A.169})$$

$$j_\infty = \frac{1}{\left[1 + \exp\left(\frac{V + 71.55}{7.43}\right)\right]^2} \quad (\text{A.170})$$

$$\alpha_j = 0 \quad \text{if } V \geq -40 \quad (\text{A.171})$$

$$= \frac{(-2.5428 \times 10^4 \exp(0.2444V) - 6.948 \times 10^{-6} \exp(-0.04391V))(V + 37.38)}{1 + \exp(0.311(V + 79.23))} \quad (\text{otherwise})$$

$$\beta_j = \frac{0.6 \exp(0.057V)}{1 + \exp(-0.1(V + 32))} \quad \text{if } V \geq -40 \quad (\text{A.172})$$

$$= \frac{0.02424 \exp(-0.01052V)}{1 + \exp(-0.1378(V + 40.14))} \quad (\text{otherwise})$$

$$\tau_j = \frac{1}{\alpha_j + \beta_j} \quad (\text{A.173})$$

L-type Ca^{2+} current (inward)

$$I_{CaL} = G_{CaL} d f_2 f_{Ca} 4 \frac{(V-15)F^2}{RT} \frac{0.25 C_{aSS} \exp(\frac{2(V-15)F}{RT}) - C_{a_o}}{\exp(\frac{2(V-15)F}{RT}) - 1} \quad (\text{A.174})$$

$$d_\infty = \frac{1}{1 + \exp(\frac{-8-V}{7.5})} \quad (\text{A.175})$$

$$\alpha_d = \frac{1.4}{1 + \exp(\frac{-35-V}{13})} + 0.25 \quad (\text{A.176})$$

$$\beta_d = \frac{1.4}{1 + \exp(\frac{V+5}{5})} \quad (\text{A.177})$$

$$\gamma_d = \frac{1}{1 + \exp(\frac{50-V}{20})} \quad (\text{A.178})$$

$$\tau_d = \alpha_d \beta_d + \gamma_d \quad (\text{A.179})$$

$$f_\infty = \frac{1}{1 + \exp(\frac{V+20}{7})} \quad (\text{A.180})$$

$$\alpha_f = 1102.5 \exp\left(\frac{-(V+27)^2}{225}\right) \quad (\text{A.181})$$

$$\beta_f = \frac{200}{1 + \exp(\frac{13-V}{10})} \quad (\text{A.182})$$

$$\gamma_f = \frac{180}{1 + \exp(\frac{V+30}{10})} + 20 \quad (\text{A.183})$$

$$\tau_f = \alpha_f + \beta_f + \gamma_f \quad (\text{A.184})$$

$$f_{2\infty} = \frac{0.67}{1 + \exp(\frac{V+35}{7})} + 0.33 \quad (\text{A.185})$$

$$\alpha_{f2} = 600 \exp\left(\frac{-(V+25)^2}{170}\right) \quad (\text{A.186})$$

$$\beta_{f2} = \frac{31}{1 + \exp(\frac{25-V}{10})} \quad (\text{A.187})$$

$$\gamma_{f2} = \frac{16}{1 + \exp(\frac{V+30}{10})} \quad (\text{A.188})$$

$$\tau_{f2} = \alpha_{f2} + \beta_{f2} + \gamma_{f2} \quad (\text{A.189})$$

$$f_{Cass\infty} = \frac{0.6}{1 + \left(\frac{C_{aSS}}{0.05}\right)^2} + 0.4 \quad (\text{A.190})$$

$$\tau_{fCass} = \frac{80}{1 + \left(\frac{C_{aSS}}{0.05}\right)^2} + 2 \quad (\text{A.191})$$

Transient outward current (outward)

$$I_{to} = G_{tors}(V - E_K) \quad (\text{A.192})$$

$$r_{\infty} = \frac{1}{1 + \exp\left(\frac{20-V}{13}\right)} \quad (\text{A.193})$$

$$\tau_r = 10.45 \exp\left(\frac{-(V+40)^2}{1800}\right) + 7.3 \quad (\text{A.194})$$

$$s_{\infty} = \frac{1}{1 + \exp\left(\frac{V+27}{13}\right)} \quad (\text{A.195})$$

$$\tau_s = 85 \exp\left(\frac{-(V+25)^2}{320}\right) + \frac{5}{1 + \exp\left(\frac{V-40}{5}\right)} + 42 \quad (\text{A.196})$$

Sustained K⁺ current (outward)

$$I_{to} = G_{sus} a_{\infty} (V - E_K) \quad (\text{A.197})$$

$$a_{\infty} = \frac{1}{1 + \exp\left(\frac{5-V}{17}\right)} \quad (\text{A.198})$$

Slow delayed rectifier current (outward)

$$I_{Ks} = G_{Ks} x_s^2 (V - E_{Ks}) \quad (\text{A.199})$$

$$x_{s\infty} = \frac{1}{1 + \exp\left(\frac{-5-V}{14}\right)} \quad (\text{A.200})$$

$$\alpha_{xs} = \frac{1400}{\sqrt{1 + \exp\left(\frac{5-V}{6}\right)}} \quad (\text{A.201})$$

$$\beta_{xs} = \frac{1}{1 + \exp\left(\frac{V-35}{15}\right)} \quad (\text{A.202})$$

$$\tau_{xs} = \alpha_{xs} \beta_{xs} + 80 \quad (\text{A.203})$$

Rapid delayed rectifier current (outward)

$$I_{Kr} = G_{Kr} \sqrt{\frac{K_o}{5.4}} x_{r1} x_{r2} (V - E_K) \quad (\text{A.204})$$

$$x_{r1\infty} = \frac{1}{1 + \exp\left(\frac{-26-V}{7}\right)} \quad (\text{A.205})$$

$$\alpha_{xr1} = \frac{450}{1 + \exp\left(\frac{-45-V}{10}\right)} \quad (\text{A.206})$$

$$\beta_{xr1} = \frac{6}{1 + \exp\left(\frac{V+30}{11.5}\right)} \quad (\text{A.207})$$

$$\tau_{xr1} = \alpha_{xr1} \beta_{xr1} \quad (\text{A.208})$$

$$x_{r2\infty} = \frac{1}{1 + \exp\left(\frac{V+88}{24}\right)} \quad (\text{A.209})$$

$$\alpha_{xr2} = \frac{3}{1 + \exp\left(\frac{-60-V}{20}\right)} \quad (\text{A.210})$$

$$\beta_{xr2} = \frac{1.12}{1 + \exp\left(\frac{V-60}{20}\right)} \quad (\text{A.211})$$

$$\tau_{xr2} = \alpha_{xr2} \beta_{xr2} \quad (\text{A.212})$$

Inward rectifier K⁺ current (outward)

$$I_{K1} = G_{K1} x_{K1\infty} (V - 8 - E_K) \quad (\text{A.213})$$

$$x_{K1\infty} = \frac{1}{1 + \exp(0.1(V + 75.44))} \quad (\text{A.214})$$

Hyperpolarization-activated current

$$I_f = I_{fK} + I_{fNa} \quad (\text{A.215})$$

$$I_{fK} = G_{fK} y (V - E_K) \quad (\text{A.216})$$

$$I_{fNa} = G_{fNa} y (V - E_{Na}) \quad (\text{A.217})$$

$$y_{\infty} = \frac{1}{1 + \exp\left(\frac{V+80.6}{6.8}\right)} \quad (\text{A.218})$$

$$\alpha_y = \exp(-2.9 - 0.04V) \quad (\text{A.219})$$

$$\beta_y = \exp(3.6 + 0.11V) \quad (\text{A.220})$$

$$\tau_y = \frac{4000}{\alpha_y + \beta_y} \quad (\text{A.221})$$

Na⁺-Ca²⁺ exchanger current

$$I_{NaCa} = k_{NaCa} \frac{\exp\left(\frac{\gamma VF}{RT}\right) Na_i^3 Ca_o - \exp\left(\frac{(\gamma-1)VF}{RT}\right) Na_o^3 Ca_i \alpha}{(K_{mNa_i})^3 + Na_o^3} (K_{mCa} + Ca_o) \left(1 + k_{sat} \exp\left(\frac{(\gamma-1)VF}{RT}\right)\right) \quad (\text{A.222})$$

Na⁺-K⁺ pump current

$$I_{NaK} = P_{NaK} \frac{K_o Na_i}{(K_o + K_{mK})(Na_i + K_{mNa}) \left(1 + 0.1245 \exp\left(\frac{-0.1VF}{RT}\right) + 0.0353 \exp\left(\frac{-VF}{RT}\right)\right)} \quad (\text{A.223})$$

Plateau Ca²⁺ current (outward)

$$I_{pCa} = G_{pCa} \frac{Ca_i}{K_{pCa} + Ca_i} \quad (\text{A.224})$$

$$(\text{A.225})$$

Plateau K⁺ current (outward)

$$I_{pK} = G_{pK} \frac{V - E_K}{1 + \exp\left(\frac{25-V}{5.98}\right)} \quad (\text{A.226})$$

Background Na⁺ current (inward)

$$I_{bNa} = G_{bNa} (V - E_{Na}) \quad (\text{A.227})$$

$$(\text{A.228})$$

Background Ca²⁺ current (inward)

$$I_{bCa} = G_{bCa} (V - E_{Ca}) \quad (\text{A.229})$$

Ion dynamics

Ca²⁺ dynamics

$$I_{leak} = V_{leak}(Ca_{sr} - Ca_i) \quad (\text{A.230})$$

$$I_{up} = \frac{V_{maxup}}{1 + \left(\frac{K_{up}}{Ca_i}\right)^2} \quad (\text{A.231})$$

$$I_{rel} = V_{rel}O(Ca_{sr} - Ca_{ss}) \quad (\text{A.232})$$

$$I_{xfer} = V_{xfer}(Ca_{ss} - Ca_i) \quad (\text{A.233})$$

$$O = \frac{k_1 Ca_{ss}^2 \bar{R}}{k_3 + k_1 Ca_{ss}^2} \quad (\text{A.234})$$

$$\frac{d\bar{R}}{dt} = -k_2 Ca_{ss} \bar{R} + k_4(1 - \bar{R}) \quad (\text{A.235})$$

$$k_1 = \frac{k'_1}{k_{casr}} \quad (\text{A.236})$$

$$k_2 = k'_2 k_{casr} \quad (\text{A.237})$$

$$k_{casr} = max_{sr} - \frac{max_{sr} - min_{sr}}{1 + \left(\frac{EC}{Ca_{sr}}\right)^2} \quad (\text{A.238})$$

$$Ca_{ibufc} = \frac{Ca_i \times Bufc}{Ca_i + K_{bufc}} \quad (\text{A.239})$$

$$\frac{dCa_{itotal}}{dt} = -\frac{I_bCa + I_pCa - 2I_{NaCa}}{2V_C F} + \frac{V_{SR}}{V_C}(I_{leak} - I_{up}) + I_{xfer} \quad (\text{A.240})$$

$$Ca_{srbufsr} = \frac{Ca_{sr} \times Bufsr}{Ca_{sr} + K_{bufsr}} \quad (\text{A.241})$$

$$\frac{dCa_{srtotal}}{dt} = (-I_{leak} + I_{up} - I_{rel}) \quad (\text{A.242})$$

$$Ca_{ssbufss} = \frac{Ca_{ss} \times Bufss}{Ca_{ss} + K_{bufss}} \quad (\text{A.243})$$

$$\frac{dCa_{sstotal}}{dt} = -\frac{1}{2V_{SS} F} I_{CaL} + \frac{V_{SR}}{V_{SS}} I_{rel} - \frac{V_C}{V_{SS}} I_{xfer} \quad (\text{A.244})$$

Na⁺ dynamics

$$\frac{dNa_i}{dt} = -\frac{I_{Na} + I_{bNa} + I_{fNa} + 3I_{NaK} + 3I_{NaCa}}{V_C F} \quad (\text{A.245})$$

K⁺ dynamics

$$\frac{dK_i}{dt} = -\frac{I_{K1} + I_{to} + I_{Kr} + I_{Ks} + I_{fK} + I_{sus} - 2I_{NaK} + I_{pK} + I_{stim}}{V_C F} \quad (\text{A.246})$$

Model parameters

Channel conductances

G_{Na} : Maximal fast Na^+ current (I_{Na}) conductance = 130.5744 nS/pF

G_{CaL} : Maximal L-type Ca^{2+} current (I_{CaL}) conductance = 3.98×10^{-5} cm $\cdot\mu$ F $^{-1}\cdot$ ms $^{-1}$

G_{to} : Maximal transient outward current (I_{to}) conductance = 0.08184 nS/pF

G_{sus} : Maximal sustained K^+ current (I_{sus}) conductance = 0.0227 nS/pF

G_{Ks} : Maximal slow delayed rectifier current (I_{Ks}) conductance = 0.2352 nS/pF

G_{Kr} : Maximal rapid delayed rectifier current (I_{Kr}) conductance = 0.0918 nS/pF

G_{K1} : Maximal inward rectifier K^+ current (I_{K1}) conductance = 0.065 nS/pF

G_{fK} : Maximal hyperpolarization-activated K^+ current (I_{fK}) conductance = 0.0234346 nS/pF

G_{fNa} : Maximal hyperpolarization-activated Na^+ current (I_{fNa}) conductance = 0.0145654 nS/pF

G_{pCa} : Maximal plateau Ca^{2+} current (I_{pCa}) conductance = 0.1238 nS/pF

G_{pK} : Maximal plateau K^+ current (I_{pK}) conductance = 0.0146 nS/pF

G_{bNa} : Maximal background Na^+ current (I_{bNa}) conductance = 0.00029 nS/pF

G_{bCa} : Maximal background Ca^{2+} current (I_{bCa}) conductance = 0.000592 nS/pF

Ion concentration

Na_o : Extracellular Na^+ concentration = 140 mM

Ca_o : Extracellular Ca^{2+} concentration = 5.4 mM

K_o : Extracellular K^+ concentration = 2 mM

Cell geometry (Volume)

V_C : Cytoplasmic volume = 16404 μ m 3

V_{SR} : Sarcoplasmic reticulum volume = 1094 μ m 3

V_{SS} : Diadic subspace volume = 54.68 μ m 3

Other parameters

p_{KNa} : Relative I_{Ks} permeability to Na^+ = 0.03

k_{NaCa} : Maximal Na^+/Ca^{2+} exchanger current (I_{NaCa}) = 1000 pA/pF

k_{mNai} : Na_i half-saturation constant for I_{NaCa} = 87.5 mM

k_{mCa} : Ca_i half-saturation constant for I_{NaCa} = 1.38 mM

k_{sat} : Saturation factor for I_{NaCa} = 0.1

α : Factor enhancing outward nature of I_{NaCa} = 2.5

γ : Voltage dependence parameter of I_{NaCa} = 0.35

P_{NaK} : Maximal $I_{NaK} = 2.724 \text{ pA/pF}$
 K_{mK} : K_o half-saturation constant of $I_{NaK} = 1 \text{ mM}$
 K_{mNa} : Na_i half-saturation constant of $I_{NaK} = 40 \text{ mM}$
 K_{pCa} : Ca_i half-saturation constant of $I_{pCa} = 0.0005 \text{ mM}$
 V_{leak} : Maximal I_{leak} conductance $= 0.00036 \text{ mM/ms}$
 V_{maxup} : Maximal I_{up} conductance $= 0.006375 \text{ mM/ms}$
 K_{up} : Half-saturation constant of $I_{up} = 0.00025 \text{ mM}$
 V_{rel} : Maximal I_{rel} conductance $= 0.102 \text{ mM/ms}$
 V_{xfer} : Maximal I_{xfer} conductance $= 0.0038 \text{ mM/ms}$
 k'_1 : R to O and RI to I I_{rel} transition rate $= 0.15 \text{ mM}^{-2} \cdot \text{ms}^{-1}$
 k'_2 : O to I and R to RI I_{rel} transition rate $= 0.045 \text{ mM}^{-1} \cdot \text{ms}^{-1}$
 k_3 : O to R and I to RI I_{rel} transition rate $= 0.06 \text{ ms}^{-1}$
 k_4 : I to O and RI to I I_{rel} transition rate $= 0.005 \text{ ms}^{-1}$
 EC : Ca_{SR} half-saturation constant of $k_{casr} = 1.5 \text{ mM}$
 max_{sr} : Maximum value of $k_{casr} = 2.5$
 min_{sr} : Minimum value of $k_{casr} = 1.0$
 Bu_{fc} : Total cytoplasmic buffer concentration $= 0.2 \text{ mM}$
 Bu_{fsr} : Total sarcoplasmic reticulum buffer concentration $= 10 \text{ mM}$
 Bu_{fss} : Total diadic subspace buffer concentration $= 0.4 \text{ mM}$
 K_{bufc} : Ca_i half-saturation constant for cytoplasmic buffer $= 0.001 \text{ mM}$
 K_{bufsr} : Ca_{SR} half-saturation constant for sarcoplasmic reticulum buffer $= 0.3 \text{ mM}$
 K_{bufss} : Ca_{SS} half-saturation constant for diadic subspace buffer $= 0.00025 \text{ mM}$

Initialized gating variables and ion concentrations

m : Activation gate for $I_{Na} = 0$;
 h : Fast inactivation gate for $I_{Na} = 0.75$;
 j : Slow inactivation gate for $I_{Na} = 0.75$;
 d : Activation gate for $I_{CaL} = 0$;
 f : Slow inactivation gate for $I_{CaL} = 1$;
 f_2 : Fast inactivation gate for $I_{CaL} = 1$;
 f_{Cass} : Diadic subspace free calcium-dependent inactivation gate for $I_{CaL} = 1$;
 r : Activation gate for $I_{to} = 0$;
 s : Inactivation gate for $I_{to} = 1$;
 x_s : Activation gate for $I_{Ks} = 0$;
 x_{r1} : Activation gate for $I_{Kr} = 0$;
 x_{r2} : Inactivation gate for $I_{Kr} = 1$;
 y : Activation gate for I_{fK} and $I_{fNa} = 0$;

\bar{R} : Proportion of close I_{rel} channel = 1;

O : Proportion of open I_{rel} channel = 0;

Na_i : Intracellular Na^+ concentration = 7.67 mM

Ca_i : Intracellular Ca^+ concentration = 0.00007 mM

K_i : Intracellular K^+ concentration = 138.3 mM

Ca_{sr} : Free Ca^{2+} concentration in the sarcoplasmic reticulum (SR) = 1.3 mM

Ca_{ss} : Free Ca^{2+} concentration in the diadic subspace (SS) = 0.00007 mM

Bibliography

- [1] ten Tusscher KHWJ, Noble D, Noble PJ, Panfilov AV (2004) A model for human ventricular tissue. *Am J Physiol Heart Circ Physiol* 286: H1573.
- [2] ten Tusscher KHWJ, Panfilov AV (2006) Alternans and spiral breakup in a human ventricular tissue model. *Am J Physiol Heart Circ Physiol* 291: H1088.
- [3] Iyer V, Mazhari R, Winslow RL (2004) A computational model of the human left-ventricular epicardial myocyte. *Biophys J* 87: 1507.
- [4] Priebe L, Beuckelmann DJ (1998) Simulation study of cellular electric properties in heart failure. *Circ Res* 82: 1206.
- [5] Bernus O, Wilders R, Zemlin CW, et al. (2002) A computationally efficient electrophysiological model of human ventricular cells. *Am J Physiol Heart Circ Physiol* 282: H2296.
- [6] Bueno-Orovio A, Cherry EM, Fenton FH (2008) Minimal model for human ventricular action potentials in tissue. *J Theor Biol* 253: 544.
- [7] Grandi E, Pasqualini FS, Bers DM (2010) A novel computational model of the human ventricular action potential and Ca transient. *J Mol Cell Cardiol* 48: 112.
- [8] Stewart P, Aslanidi OV, Noble D, et al. (2009) Mathematical models of the electrical action potential of Purkinje fibre cells. *Philos Transact A Math Phys Eng Sci* 367: 2225.